Experimental and theoretical studies of the inhibition potential of *Lippia javanica* plant extracts for the corrosion of aluminium, mild steel, and zinc metals in acidic medium

by

TSHIMANGADZO NESANE

Student Number: 11627022

A thesis submitted in fulfillment of the requirements for the degree of

Doctor of Philosophy in Chemistry (MNPDPC)

Department of chemistry

Faculty of Science, Engineering, and Agriculture

University of Venda

Supervisor: Prof. L.C. MURULANA

Co-Supervisor: Prof. M.M KABANDA

Co-Supervisor: Prof. N.E MADALA

November 2022

Declaration

I hereby declare that the work in this thesis is my own and was done under the supervision of Prof. L.C Murulana, Prof. M.M Kabanda, and Prof. N.E Madala as my co-supervisors. The information derived from literature has been duly acknowledged in text and a list of references provided. This work is being submitted for the degree of Doctor of Philosophy in Chemistry at the university of Venda and has not been submitted before for any degree or examination at any other university.

Full Names: Tshimangadzo Nesane Date: 11/27/2022

Signature: 

Dedication

This thesis is dedicated to my mother, **Alugumi Tshivhundo,** for her never-ending love and for ensuring I get the best possible education and life.

Table of Contents

Acknowledgements

First and foremost, with humility and reverence, I would like to thank the Almighty God for the protection and guidance He bestowed on me throughout my study.

It is a privilege to extend my sincere gratitude to my research supervisor, **Prof. L.C. Murulana**, for his consistent support of my Ph.D. studies and associated research and his patience, enthusiasm, and extensive expertise. He gave me all the resources I could need, and his guidance was crucial as I was conducting my research and writing this thesis. My growth as a student, researcher, and aspiring scientist has been significantly encouraged and influenced by his expertise in the field of corrosion science. I am grateful to him, and I will honour the work ethic he gave me.

I thank my co-supervisor, **Prof. M.M. Kabanda,** for his helpful suggestions, counsel, and tremendous support. His help in the execution of computational calculations and the analysis of the resulting data was essential to finishing this work successfully and expanding my knowledge of computational chemistry.

I want to thank **Prof. N.E. Madala** for his crucial contribution to this study and his discerning inquiries, which encouraged me to consider some parts of my research from numerous angles rather than simply adhering to the norm. His expertise in green chemistry is one of the factors that contributed to the success of this research, and I would like to express my gratitude for his help in the characterization of the plant extracts.

I want to thank the **Sasol scholarship and the Sasol-National Research Foundation of South Africa** for the financial support and the **Centre of High-Performance Computing (CHPC),** Cape Town, South Africa, for the Materials Studio 2020 license and platform to perform computational calculations. I sincerely thank the technicians at the **Department of Chemistry** at the **University of Pretoria** for assisting in conducting SEM/EDS studies and for their valuable suggestions and insights.

I thank the **Department of Chemistry** and my colleagues in the **CorroSci Research Group** for their encouragement and advice. Finally, I thank my **Family**, my brother **Mashudu Nesane** and my sister **Murendeni Nesane** for being an inspiration and for their encouragement.

Abstract

Corrosion is a natural phenomenon considered a chemical and an electrochemical process of metals interacting with the surrounding corrosive environment. Inhibition is a preventive measure used by corrosion engineers to reduce the effects of corrosion on metals, the environment, society, and the economy. The current study investigates the use of the *Lippia javanica* plant as an eco-friendly green inhibitor for mild steel (MS), aluminium (Al), and zinc (Zn) corrosion in a 1 M HCl environment. The leaf extracts were prepared by the Soxhlet extraction method using methanol, ethanol, and acetone as solvents. The leaf extracts of *L. javanica* were characterized using Fourier-transform infrared spectroscopy (FT-IR) and Liquid chromatography-mass spectrometry (LC/MS) analysis. The inhibitory potential of *L. javanica* extracts was established by performing weight loss measurements, electrochemical methods such as potentiodynamic polarization (PDP), and electrochemical impedance spectroscopy (EIS) techniques. The weight loss assessment was carried out at different temperatures (303 to 333 K) and varying concentrations of the extracts from 200 to 800 ppm. The technique was also used to determine the stability of the extract with varying immersion times. Weight loss measurements showed that the inhibition efficiency increased with increasing concentration of the extracts up to 800 ppm for all three metals. Increasing the temperature of the corrosive environment resulted in a decrease in the inhibition efficiency of Al and MS corrosion, with that of Zn increasing with temperature. The variation of inhibition efficiency with time showed a similar trend, with the protective efficiency of Al and MS decreasing with time and Zn increasing with immersion time. Increasing Zn's inhibition efficiency with temperature and immersion time implies a chemical protection mode. The reduction in the inhibition efficiency with temperature and immersion time for Al and MS suggests a physical protection mode. According to EIS measurements, the extracts adsorb onto Al, Zn, and MS surfaces to create a protective coating with pseudo-capacitive properties. The only component of the Zn and MS Nyquist plots in the high frequency was a capacitive loop, but the Al plots also showed an inductive loop at a lower frequency. The higher frequency loop represents the resistance for the charge transfer during the corrosion process.

In contrast, the lower frequency loop represents the relaxing of hydrogen ions and the adsorption of corrosive chloride ions onto the oxide film. The PDP results revealed that for Al and MS, the three extracts had a similar impact on both the anodic and cathodic half-reactions. In contrast, both half-reactions were affected for Zn, but the cathodic area was more significantly impacted.

Undulation Tafel curves for MS and Zn were observed with and without the extracts; however, a longer passive region was detected for Al, particularly in the presence of the plant extracts. The investigational extracts function as mixed-type corrosion inhibitors for Al, Zn, and MS, as indicated by the control of both the anodic and cathodic areas with the introduction of the extracts. Among the many plotted isotherms for the three extracts on the metal surfaces, the Langmuir adsorption isotherm was determined to be the best-fit isotherm. The isotherm confirmed the mechanism of adsorption, which was a mixed-type adsorption for Al, Zn, and MS. Spectroscopy studies revealed that the interaction of the three extracts with Al, Zn, and MS resulted in the formation of metal-inhibitor complexes, which slowed the corrosion process. Scanning electron microscopy/energy dispersive X-ray spectroscopy (SEM/EDS) studies demonstrated that *L. javanica* leaf extracts form a protective film on Al, Zn, and MS surfaces, protecting them from the corrosive environment. Theoretical simulations showed that the primary extract constituent (verbascoside) had binding energy greater than 13 kcal/mol on the surfaces of Zn(110), Al(111), and Fe(110). The high binding energy indicates a mixed-type binding process that includes chemisorption and physisorption. All corrosion experiments revealed that the three extracts exhibited superior inhibition performance for all the three metals studied with comparable results in 1 M HCl corrosive solution.

List of abbreviations

%IE	Inhibition efficiency
ΔG^{o}_{ads}	Change in free energy of adsorption
ΔH^{*}_{a}	Enthalpy of activation
ΔS^{*}_{a}	Entropy of activation
AC	Alternating current
Al	Aluminium
ALJCE	Acetonolic *L. javanica* crude leaf extract
AM1	Austin Model 1
API	Atmospheric pressure ion source
BCC	Body-centred cubic
BFGS	Broyden-Fletcher-Goldfarb-Shanno
BP	Becke-Perdew
C_{dl}	Double-layer capacitor
C_{inh}	Concentrations of inhibitors/extracts
CMC	Critical micelle concentration
CNDO	Complete neglect of differential overlap
COSMO	Conductor-like screening model
COSMO-RS	COSMO for real solvent
COSMO-SAC	COSMO for segment activity coefficient
CPE	Constant-phase element
C_R	Corrosion rate
DC	Direct current

DFT	Density functional theory
DIIS	Iterative subspace direct inversion
DN	Double numeric
DND	Double-numerical +d
DNP	Double numeric with polarization functions
DPPH·	Free radical 1,1-diphenyl2-picryl hydrazyl
DSPP	DFT semi-core pseudopotential
E_a	Activation energy
E_{corr}	Corrosion potential
EEC	Equivalent electric circuit
EIS	Electrochemical impedance spectroscopy
ELJCE	Ethanolic *L. javanica* crude leaf extract
E_{OCP}	Evolution of open-circuit potential
E_{OCP}	Open circuit potential
E_{pp}	Passivation potential
ESI	Electrospray ionization
E_W	Equivalent weight
Ɛ	COSMO dielectric
FCC	Face-centred cubic
$Fe(OH)_2$	Ferrous hydroxide
$Fe(OH)_3$	Ferric hydroxide
$FeCO_3$	Siderite or ferrous carbonate
FeS	Iron sulfide
FHWA	Federal Highway Administration
FRA	Frequency response analyzer

FRAP	Ferric reducing antioxidant power
FT-IR	Fourier-transform infrared spectroscopy
GDP	Gross domestic product
GGA	Generalized gradient approximation
GSE	General solubility equation
GTO	Gaussian-type orbitals
H_2CO_3	Carbonic acid
H_2S	Hydrogen sulfide
H_2SO_4	Sulfuric acid
H_3PO_4	Phosphoric acid
HCl	Hydrochloric acid
HF	Hartree-Fock
HPLC	High-performance liquid chromatography
I	Electric current
I_{corr}	Corrosion current density
IEFPCM	Integral equation formalism for PCM
INDO	Intermediate neglect of differential overlap
I_{pass}	Passive current density
ISM	Implicit solvation models
K_L	Dimensionless constant; separation factor
L	Inductance
LC	Liquid chromatography
LC/MS	Liquid chromatography/mass spectrometry

LDA	Local density approximation
LYP	Lee-Yang-Parr
ME	Mimusaps Elangi
MF	Molecular formula
MIN	Minimal
MLJCE	Methanolic *L. javanica* crude leaf extract
MM	Molecular mechanics
MNDO	Modified Neglect of Diatomic Overlap
MS	Mild steel
MW	Molecular weight
n	CPE exponent
NAO	Numerical atomic orbitals
NCPP	Norm-conserving pseudopotentials
NDDO	Neglect of differential diatomic overlap
O_2	Oxygen
OCP	Open-circuit potential
PAC	Performance, availability, and cost
PBC	Periodic boundary conditions
PBE	Perdew-Burke-Ernzerhof
PCM	Polarizable continuum model
Pd	Palladium
PDP	Potentiodynamic polarization
PES	Potential energy surface

PM3	Parameterized Model number 3
PM6	Parameterized method number 6
ppb	Parts per billion
ppm	Parts per million
PW86	Perdew-Wang 86
PW91	Perdew-Wang
Q_{ads}	Heat of adsorption
QM	Quantum mechanical
QSAR	Quantitative structure-activity relationship
QSPR	Quantitative structure-property relationship
R	Resistance
R_{ct}	Charge transfer resistance:
RE	Reference electrode
R_L	Inductive resistance
RPBE	Revised Perdew-Burke-Enzerhof
RT	Retention time
SCE	Saturated calomel electrode
SCF	Self-consistent field
SEM/EDS	Scanning electron microscopy/energy dispersive X-ray spectroscopy
SHE	Standard hydrogen electrode
STO	Slater-type orbital
S_θ	Synergism parameter
TNP	Triple numerical polarized

UPLC	Ultra-performance liquid chromatography
US	United States
UV–Vis	Ultraviolet-visible spectroscopy
V	Voltage
VBS	Verbascoside
VCA	Video contact angle system
WE	Working electrode
ZDO	Zero Differential Overlap
Zn	Zinc
α-FeOOH	Goethite
β_a	Anodic Tafel constant/slope
β_c	Cathodic Tafel constant/slope
π-FeOOH	Lepidocrocite

List of Figures

List of tables

CHAPTER 1

Introduction

The thesis titled "**Experimental and theoretical studies of the inhibition potential of *Lippia javanica* plant extracts for the corrosion of aluminium, mild steel, and zinc metals in acidic medium**," is divided into eight chapters.

This first chapter specifically examines the impacts of corrosion, including the costs and significance of corrosion management, and explores the potential of plant extracts as corrosion inhibitors for metals such as zinc, aluminium, and mild steel. It also delves into the effects of corrosion on the oil and gas industry, as well as the benefits of using hydrochloric acid as a cleaning solution in this industry. Additionally, this chapter discusses various corrosion control methods, with a focus on using plant extracts as environmentally friendly corrosion inhibitors. The study's objectives and goals are also discussed in this chapter.

1. Introduction and problem statement

Metals and alloys play an essential part in the industrial world today. They are utilized to construct industrial and residential buildings, vehicles, pipelines, bulkheads, ports, passenger trains, piers, railway cars, engine construction, ships, and storage tanks [1]. They have always played such a role in past civilizations, but in the world today, a variety of coated metals/alloys with multifunctional materials (smart materials) are required [2]. The wide usage of metals such as copper, aluminium (Al), mild steel (MS), and carbon steel in several engineering and construction industries results from their low cost, workability, and specific physical, chemical, and mechanical properties [3-7]. During their use, metallic materials are susceptible to degradation [8, 9]. The phenomenon by which metallic properties are generally degraded and destroyed over time is called corrosion [9]. Corrosion delays industrialization and economic growth, and it is the worldwide most damaging factor for metallic components [10]. It affects almost all types of materials, including wood and polymers, due to their environmental conditions. Materials are most effective if their corrosion rate is slow and they work for many years before corrosion failure occurs. Metal corrosion is a hybrid process that includes a chemical reaction that converts metal atoms to metal ions and transfers metal valence electrons to electrochemically active ions and molecules in the metal environment. Therefore, metallic corrosion is termed an electrochemical process that contributes to the spontaneous degradation of a material subject to adverse environmental conditions over time [10-12]. Corrosion is primarily a slow process, typically on the metal's surface, but the losses brought about by corrosion are of varying magnitude. Consequently, metallic objects like equipment and structures are rendered ineffective and inefficient [13].

Corrosion can cause significant economic and human losses in the modern world because of metal's expanded utilization. Some of these financial and human losses include the collapse of buildings and bridges, road accidents due to wear and tear of nuts and bolts at joints, etc. [14]. Corrosion has been previously considered a problem for only metallurgists and chemists, but it is now considered an interdisciplinary field as metals are universal. Because of a growing awareness of the enormous losses caused by corrosion damage, material corrosion has taken considerable importance over the years. Due to corrosion problems, defence industries and other institutions lose trillions of dollars a year worldwide [15].

In 2002, the United States (US) published a landmark report Federal Highway Administration (FHWA) on the costs associated with the corrosion of metallic products in various industries. The study showed that $276 billion, equal to 3.1% of the US gross domestic product (GDP), was the overall annual approximate direct cost of corrosion in the US per year, as shown in Figure 1.1 [16]. Evaluating corrosion concluded such determination of the expenses in different industries like production, design, construction, and management [17]. Besides significant economic losses, metal corrosion damages or destroys the environment in which it occurs [18]. It is, however, expected that savings of between 15 and 35% of corrosion costs could be made annually - approximately $375 billion and around $875 billion worldwide - using various corrosion control techniques [19].

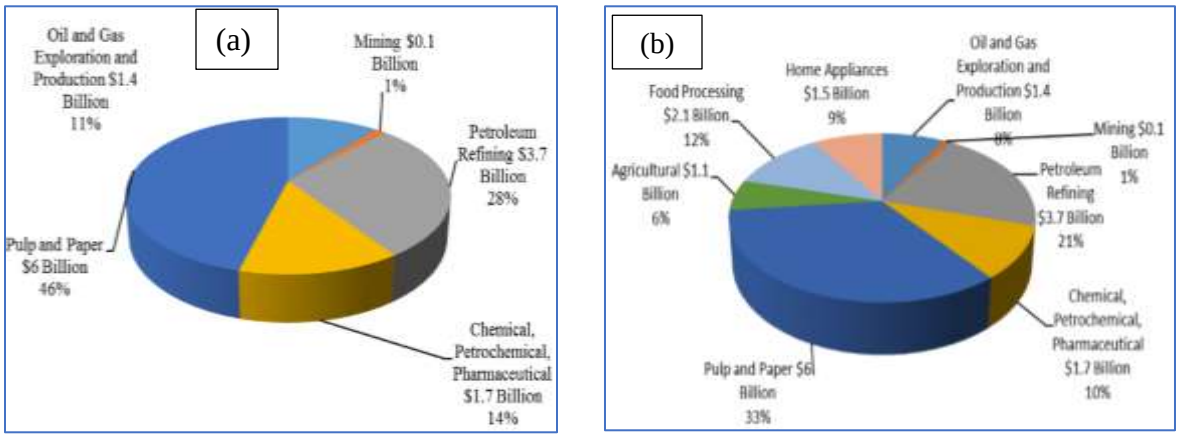

Figure 1.1: The total overall costs of corrosion in key industrial fields that contribute to these costs (a) and the annual cost of corrosion in the manufacturing and processing sectors (b) [16]

Corrosion cost is part of building an appealing appearance for buildings, the direct cost of repair and maintenance, and the resulting economic loss due to interruptions in development. It also incorporates additional costs for using expensive materials and other measures to prevent corrosion and product loss or disposal. In addition to financial costs, consideration should be given to safety risks and environmental pollution due to corrosion. Personal damage may occur due to structural fractures (failure), pressure tank failure, and leakage of toxic or hostile liquids into containers [20].

“Rust never sleeps”; this is because metals tend to return to their lower energy following processing and shaping; the law of entropy controls such a process. In the stainless-steel industry, considerable effort is made to turn naturally occurring iron ore into steel. Exposing the steel to

oxygen (O_2) and moisture, on the other hand, reverses the energy used to convert the ore into steel [21, 22]. Thus, corrosion affects global metal supplies by removing the already refined components or structures from their service, which consumes a part of the earth's total material supply. Therefore, corrosion scientists are keen on preserving the already available metals to reduce solid waste at recycling centres or landfills (Figure 1.2). Also, increasing the lifespan of a metal product allows further development or treatment, thus reducing greenhouse gas emissions [1].

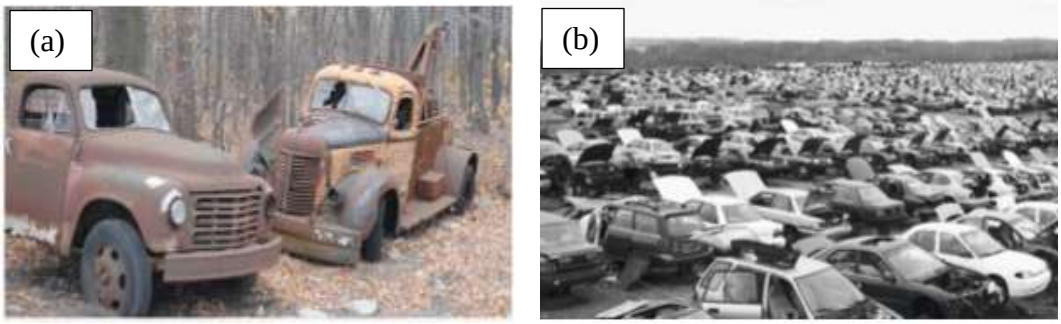

Figure 1.2: Vintage car deterioration (a), including a land field view of the recycling, reclamation, and storage of used cars (b) [1]

Most corrosion agents or causes are gaseous materials, oils, liquid substances, and humidity in the air [23]. The petroleum and petrochemical industries are some of the sectors that suffer the most from corrosion. Corrosion affects these industries' oil and gas pipelines internally due to the chemicals they transport. Such effects are due to the corrosive environment that builds up within the pipelines and causes extensive damage across the entire supply chain, leading to an approximate cumulative annual cost of $1.372 billion [24-26]. The pipelines' internal corrosion is a significant hazard to the initial production stage in industries [27]. Accordingly, from 1990 to 2012, more than 9000 internal corrosion failures were registered, comprising 54.8% of all spills [28]. Figure 1.3 illustrates schematically some forms of internal corrosion that are likely to occur in pipelines.

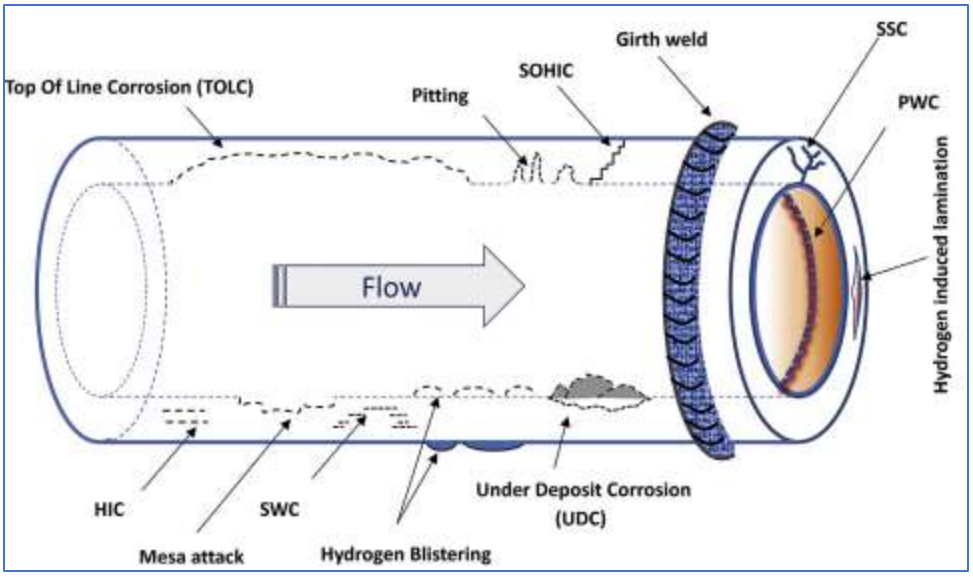

Figure 1.3: Various forms of internal corrosion in hydrocarbon pipelines [29]

The corrosion forms that develop in pipelines are primarily due to a localized attack and welds' corrosion due to pitting or galvanic corrosion. These attacks are becoming harder to anticipate, leading to pipeline failure [30]. Pipeline operators' annual profit margins are frequently reduced as a result of corrosion-related failures. As a result, operators must learn to identify and assess the potential impact of corrosion on pipeline failure, as well as estimate the total cost of corrosion. This knowledge can help operators reduce the risks and costs associated with corrosion while also improving overall efficiency and profitability [31].

While systemic measures to reduce corrosion-related damage in this field, such as increased corrosion assessment education, may be beneficial. One of the most difficult challenges in pipeline corrosion prevention is the fact that internal corrosion defects are frequently difficult to detect. Technicians who have received adequate training in corrosion detection and mitigation techniques, as well as a thorough understanding of the corrosion process, are required. It is difficult to implement effective remedy techniques without this knowledge and expertise, which can result in additional corrosion and damage to the pipeline. The economic cost of such an effort also makes it challenging. Consequently, the oil and gas industry has used corrosion prediction models that consider various assumptions to determine whether and what form of corrosion will occur during hydrocarbon extraction and production [32]. Acidic solutions are commonly used in the industrial process, such as acid washing, oil refining equipment washing, and acid pickling. Still, the problem

with such solutions is that they accelerate the corrosion of metallic materials, which affects their performance [33].

Because of their relatively low cost, ease of manufacturing, and excellent mechanical and physical properties, carbon steels are commonly used as metallic structures for industrial applications [34]. Low carbon steel (i.e., mild steel) is used in metallurgy, desalination plants, storage tanks, chemical processing, screwdriver, petroleum refineries, pharmaceuticals, construction materials, gas industry, boilers, automobiles, electronics, and pickling processes, etc. [35-39]. Despite their benefits, corrosion from carbon steel limits their flexibility and application [40-42]. The corrosion processes on carbon steels result from redox electrochemical reactions on their metallic surfaces in environments consisting predominantly of Cl^-, SO_4^{2-}, NO_3^- anions, etc., which slowly degrade the metallic alloy [43].

However, some progress has been made to mitigate the effects of corrosion on materials, particularly metals. Some of the solutions used for such processes include various defensive/protective measures, particularly environmental modifications, metal selection, coatings, cathodic protection, and corrosion inhibitors, which are particularly interesting in the present study [44-46]. While there are many options to prevent metal corrosion, inhibitors are considered one of the best methods for shielding metals from corrosion [47-50]. Conventional organic and inorganic synthetic inhibitors are proven effective inhibitors of metal corrosion; however, their use is limited due to their toxicity and broadening the definition of "green chemistry" in science, technology, and engineering [51-53]. Green chemistry is a science and technology field that uses various concepts that minimize and apply environmental malignancies to natural and eco-friendly substances [54-56].

Even though some synthetic inhibitors are considered safe [57, 58], current research mainly focuses on utilizing plant extracts that exhibit more robust anti-corrosive properties while being environmentally sound. Many chemical compounds, particularly heterocyclic compounds, are present in plant extracts and contribute to corrosion inhibition [57-59]. Plants' effectiveness as inhibitors against metallic corrosion is due to molecules containing heteroatoms such as O_2, nitrogen, sulfur, and phosphorus [60, 61]. This is because a metal protector(s) must have properties that can adsorb to the metal surface and delay the metal's breakdown. The chemisorbed inhibitor's resulting film protects the process by retarding it or as a shield against the metal and the corrosive

environment [62-68]. Although most studies have discovered new green corrosion inhibitors in different plant sections, a few have produced realistic coatings that can solve corrosion problems in oil and gas pipelines where corrosion is highly encountered. As such, molecules and the arrangement of their bond structures in plant extracts responsible for corrosion prevention should be first identified before any inhibition studies are conducted [69]. Therefore, studying the prevention of metals' dissolution using plant-based corrosion inhibitors is of great interest. Several advantages are associated with using plant extracts as corrosion inhibitors. Plants are plentiful, easily accessible, cost-effective, biodegradable, biocompatible, and less or non-toxic [70].

Computational methods for studying corrosion inhibitors are now standard practice with technological advancements. The method is used in studying corrosion inhibitors because it helps elucidate compounds' electronic structure and reactivity and understand inhibition mechanisms [71, 72]. Density functional theory (DFT) [73] is a veritable technique used to establish new standards for predicting and interpreting chemical processes. DFT methods have been used to study the inhibitory mechanism of organic molecules on the metal surface as a complementary measure to augment experimental data [74-79]. Computational techniques have been employed in this study to model the corrosion inhibitors' behaviour in the bulk aqueous medium and near the metal-water interface.

The research seeks to address several key questions: Can these previously unexplored plant extracts effectively inhibit corrosion within controlled experimental conditions? What molecular interactions underline their inhibition properties? How does temperature and immersion time affect the inhibition properties of the extracts.? These questions collectively contribute to an enriched comprehension of the inhibition capabilities inherent in natural compounds and the hypothesis for the study is that the exploration of *L. javanica* as a novel green inhibitor against the corrosion of various metals will result in the discovery of an efficient inhibitor as a result of the many chemical constituents produced by the plant with little or non-toxic effects.

1.1. Scope and objectives of the current study

The purpose of the current work is to highlight the potential of utilizing plant-based compounds, such as *L. javanica* leaf extracts, in inhibiting corrosion on metals like Al, MS, and Zn in a 1 M HCl solution. The effectiveness of plant extracts in this regard is demonstrated in the study. There has been no study or research on using *L. javanica* leaf extracts as a corrosion inhibitor. The study

investigates how temperature affects inhibition effectiveness, evaluates some thermodynamic parameters using chemical and electrochemical techniques, and investigates the binding geometry and energy of plant extract's main constituent on metal surfaces using quantum chemical techniques. The following primary objectives guided the current investigation:

- The determination of the active phytochemical constituents in *L. javanica* leaf extracts obtained through Soxhlet extraction using methanol, ethanol, and acetone solvents by employing LC/MS analysis and FT-IR characterization
- Investigation of the mechanism of interaction of the metal-inhibitor by the use of different adsorption isotherms
- Quantitative assessment of the corrosion resistance, degradation, and corrosion inhibition mechanisms of the inhibitors by electrochemical techniques
- Determination of the wettability of the metal's surface before and after protection by the extracts using water contact angle studies
- Quantum chemical calculation to obtain the electronic structures of the active constituents of plant extracts and their stable adsorption structures on the various metal surfaces
- Investigation of interactions between Al, Zn, and MS surface and the studied *L. javanica* leaf extracts in the corrosive 1 M HCl solution using spectroscopic techniques (FT-IR and UV-vis)
- Assessment of the characteristics of the protective film formed on metal surfaces and determination of the elemental composition of these surfaces by SEM/EDS
- Investigation of the influence of immersion period, temperature, and concentration of the extracts on the inhibition efficiency and corrosion rate of the 1 M HCl corrosive environment

CHAPTER 2

Literature review

The current study's literature review is covered in this chapter. It provides a general overview of corrosion's basic principles, theories, and classification. This chapter also goes over various types of corrosion, such as sweet and sour corrosion. A more detailed explanation of corrosion control and the various methods available for this purpose are also provided. Corrosion inhibitors of various types have been discussed, including the corrosion inhibition process in acidic and near-neutral solutions. Adsorption methods on metal surfaces, such as physisorption and chemisorption, have also been discussed. This chapter presents a history of using plant extracts as corrosion inhibitors to demonstrate their ability to control metal corrosion. It also provides a detailed description of the specific plant chosen for the study and discusses various corrosion monitoring techniques, with a focus on computational and electrochemical methods.

2. Definition of corrosion

Corrosion is an electrochemical process due to a physicochemical interaction between metals and their surroundings. During this process, metal electrons are released from the metal's surface into an external electron receiver, releasing metal ions into the surrounding medium, leading to progressive degradation [80], loss, or, in extreme cases, structural metal failure. This process involves a series of anodic and cathodic reactions of compounds in direct contact with or close to the metal surface [80]. Corrosion occurs in almost all environments, including air and water, industrial atmospheres (gases, alkaline, acids, and so on), salty and fresh water, and other organic or inorganic solutions or mediums [81-84]. Corrosion is also thermodynamically favourable, i.e., it is spontaneous and, given time, inevitable. On that basis, corrosion cannot be prevented but only slowed down by appropriate corrosion control measures. Wet and dry corrosion is another pervasive distinction. Wet corrosion involves liquids such as the aqueous electrolyte involved in the electrochemical corrosion of steel. It often occurs in the absence of fluid processes such as carburization and metal dusting and is associated with high temperatures [85]. Analyzing corrosion chemistry is essential before examining its various forms and control methods. As such, the chemistry of corrosion is discussed below.

2.1. Chemistry of corrosion

Due to the high temperatures and pressures within the pipelines, as well as the presence of species such as carbon dioxide (CO_2), oxygen (O_2), and hydrogen sulphide (H_2S), the corrosion process in oil and gas pipelines is complex and dynamic. This complexity is exacerbated by factors such as the type of metal used in pipeline construction, pH conditions at various processing stages, and corrosion material surface morphology. Figure 2.1 depicts the two half-reactions that occur on the surface of a metal during corrosion [86]: the cathodic reaction, in which the metal is reduced and gains electrons, and the anodic reaction, in which the metal is oxidized and loses electrons. The potential difference between different microstructural areas of the metal drives these reactions, which result in the movement of electrons or ions between the cathodic and anodic regions. The metal is dissolved into positively charged metal ions at the anodic region, which are carried away by the electrolytic solution, leaving excess electrons on the metal surface.

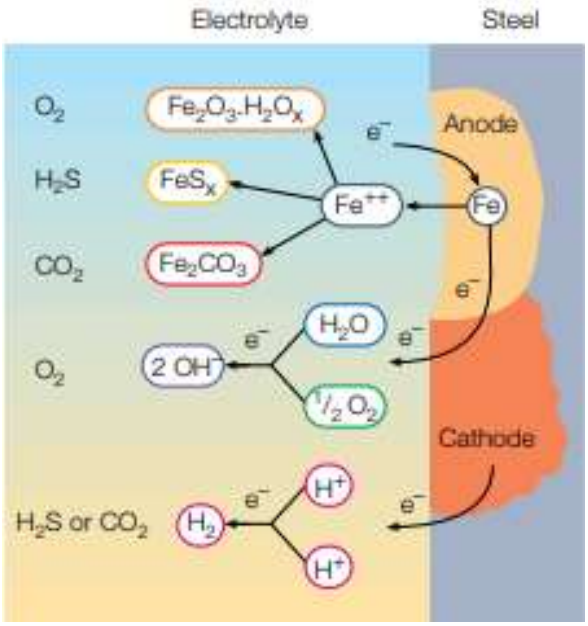

Figure 2.1: Acidic steel corrosion: a visualization of typical chemical reactions and their products [86]

$$M(s) \rightarrow M^{n+}(aq) + ne^{-} \quad (1)$$

M is the atom on the surface of the metal, M^{n+} is the solution ion(s), n is the reaction number of valence electrons and e^{-} are the electron(s).

The cathode reaction depends on the type of environment. Electrochemically active species take up the excess electrons that are released during anodic reaction at the cathodic region of the metal, balancing the anodic reaction above. In acidic solutions (pH < 4), the primary cathodic reaction is typically hydrogen production by proton reduction:

$$2H^{+}(aq) + 2e^{-} \rightarrow H_2(g) \quad (2)$$

Dissolved O_2 is the principal cathodic reactant in aerated near-neutral solutions, as shown in the following reaction:

$$O_2(aq) + 2H_2O(l) + 4e^{-} \rightarrow 4OH(aq) \quad (3)$$

Even though the reduction of O_2 occurs in aerated acidic solutions, it is usually not the primary cathodic reaction. Although that might be the case, the direct water reduction in the absence of dissolved O_2 can be written as:

$$2H_2O(l) + 2e^- \rightarrow H_2(g) + 2OH(aq) \quad (4)$$

At low pH, where there is plenty of H^+ ions in solution (more precisely, H_3O^+), the primary cathodic reaction becomes:

$$2H^+(aq) + 2e^- \rightarrow H_2(g) \quad (5)$$

The cathodic reaction of interest in this study takes place in a strongly acidic solution of hydrochloric acid (HCl), but other cathodic reactions can be observed in a weakly acidic solution of carbonic acid (H_2CO_3) at a pH of around 4, which is typical of sweet oilfield environments. At pH values greater than 5, the direct reduction of H_2CO_3 may become a significant cathodic reaction as the concentration of H^+ ions decrease to the point where they are no longer the dominant reactant [87-91]. Despite decades of research, the detailed mechanisms of this cathodic chemistry are still unknown.

As previously stated, the above reactions (2 to 5) are half-cell electrochemical reactions, and the general corroding reaction consists of a charge transfer and electrons exchange between electrodes. The anode oxidation and cathode reduction process are simultaneous activities that must occur at the same time. Furthermore, as a carrier for ions such as H^+ or M^+, a conducting solution (electrolyte) is required. The overall corrosion cycle for iron corrosion in water is demonstrated in Figure 2.1 [22, 87, 88].

The environment influences the formation of corrosion products on metallic surfaces such as those of iron and carbon steel, which can either promote or inhibit corrosion. Iron is typically bare and free of corrosion scales or films in strongly acidic conditions, and corrosion reactions occur directly on the metal's surface. However, corrosion scales or films are more commonly observed in higher pH environments, and they may include compounds such as lepidocrocite (π-FeOOH), goethite (α-FeOOH), ferric hydroxide ($Fe(OH)_3$), and ferrous hydroxide ($Fe(OH)_2$) [90]. The primary corrosion scale in sweet, carbon dioxide-rich aqueous environments with low levels of dissolved oxygen is typically siderite ($FeCO_3$), which may or may not provide substrate protection depending on factors such as temperature.

The metallic surface of pipelines acquires corrosive species like hydroxides, carbides, oxides, and carbonates due to the oils and gases passed through them. Bare metal surfaces have been observed depending on the acidic conditions of the pipelines [92]. This is illustrated by Figure 2.2 which

details iron's thermodynamics in an aqueous water environment at 25 ^{o}C. The Pourbaix diagram can be divided into three regions: passivation, corrosion, and immunity. However, the diagram limitation is that there is very little knowledge concerning the reaction rates, and the information provided is derived from pure metals and environments [93]. Therefore, it should be noted that such a diagram provides only partial reaction rate information. The benefit of this sort of diagram is that it provides a straightforward method for predicting the condition of the potential and pH state in which any metal can potentially react with an electrolyte. Such a theoretical model-based pH and potential predictor diagram strongly correlate with actual corrosion situations [93]. For instance, this situation can be considered when the iron is partially covered with its oxide and immersed in a neutral solution at pH 7. If the potential in relation to a standard hydrogen electrode (SHE) falls to -0.6 V, it is in a resistant state (Figure 2.2).

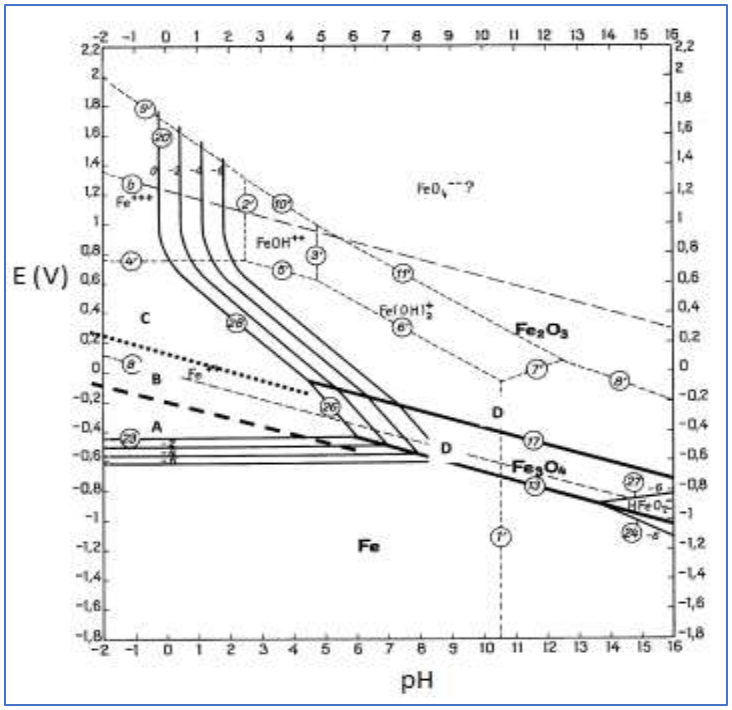

Figure 2.2: The Pourbaix diagram for iron: a visualization of the active dissolution region (A), stable metal oxides (B and C), and stable oxide phase (D) [95]

Similarly, if the conditions are the same as before but with a potential that only falls to -0.2 V concerning the saturated calomel electrode (SCE), the iron would still be in a corrosion state. At pH < 7, the iron is in a corrosion zone, but at pH > 7, the iron is in a passivation region. To protect

the iron from corrosion, protection has to be based on reducing the potential to the extent that the iron corrosion does not theoretically become part of the immunity domain. For example, E_v = -0.62 V (SHE) = -0.89 V (SCE) if the pH is below 10 [93]. The graph demonstrates that the state of iron at pH $\leq$ 2 can vary between Fe^0, Fe^{2+}or Fe^{3+} along a wide range of potential, impacting the metastable states on the metal's surface [94].

Stainless steels comprising of more than 10% chromium have a very small top surface layer up to the nanometer-scale of chromium oxide (Cr_2O_3), which provides enhanced corrosion resistance [96]. However, factors such as the surface texture of the metal, which can create crevices, pits, and other imperfections that promote corrosion, can also influence the corrosion rate of these steels. These surfaces can become anodic, resulting in increased iron ion dissolution, which occur at faster rate in the presence of corrosive species like chloride ions [86]. Furthermore, the dissolution process can alter the metal surface structures by forming thin films of corrosion products, complicating the corrosion mechanisms even further. These examples highlight the complexity of the metal surface structures used in oil and gas pipelines, which are affected by a range of factors such as temperature, strain, electrochemical potential, pH, solvation, alloy preparation process, and solvated species [86]. Due to the many system-specific conditions that affect corrosion mechanisms in oil and gas pipelines, it is difficult to generalize the findings of research in this field. One of the most cost-saving measure to reduce the degradation of metallic substrates in oil and gas wells is to use lower-grade carbon steels in conjunction with corrosion inhibitors. [97].

2.2. Classification of Corrosion

Corrosion can be classified in various ways depending on the nature of the corrosive system. Some key considerations include temperature, chemical composition, and the presence of moisture. For example, when a metal comes into contact with an electrolytic solution or when two dissimilar metals are combined, wet corrosion may occur. This type of corrosion is often responsible for metal oxidation and the electrochemical corrosion of steel [22]. Dry corrosion, often seen at high temperatures, occurs without the presence of a liquid phase and can manifest as carburization or metal dusting. In the oil and gas industry, the most common forms of corrosion are sweet corrosion caused by CO_2 and sour corrosion caused by H_2S [10, 98, 99]. Metal surfaces and equipment in oil and gas production facilities can be severely damaged by this type of corrosion. Extensive research on these mechanisms has been conducted, though most research has focused on pipeline

corrosion rather than downhole corrosion. Furthermore, systems such as, but not limited to, workover fluids, sulfur solvents, and hydrate-prevention fluids can introduce O_2 in surface pipelines, which also facilitates the corrosion process [100]. Some of the most common corrosion types in the oil and gas pipelines resulting from the chemicals transported through them are briefly discussed below.

2.2.1. Oxygen (O_2) induced corrosion

Although O_2 is not typically present in oil and gas reservoirs, it can enter these environments through various channels such as leaking pump seals, process vents, casing, and open hatches. This can increase the electrochemical process of the cathodic reaction and accelerate the anodic dissolution of metals [98]. The presence of O_2 can also enhance the corrosive effects of CO_2 and H2S gases, resulting in higher levels of corrosion. In sour wells, the presence of oxygen can be especially harmful, as it can interfere with the formation of protective iron sulfide (FeS) by dissolving elemental sulfur. Previous research has shown that concentrations of O_2 as small as 5 parts per billion (ppb) could be very harmful to oil and gas pipelines and needs to be extracted with an O_2 scavenger [101]. Figure 2.3 displays typical corrosion in a pipeline caused by the presence of O_2.

Figure 2.3: Oxygen-induced corrosion in the oil and gas pipelines [98]

2.2.2. Sweet or carbon dioxide (CO_2) corrosion

Carbon dioxide (CO_2), naturally present in oil and gas fields, is pumped intentionally into wells to boost oil recovery. Corrosion of CO_2, also known as “sweet corrosion,” is among the significant issues in the petroleum industry, costing billions of dollars annually [102]. On its own, dry CO_2 is

not corrosive at the temperatures typically found in oil and gas processing. However, when it is dissolved in water, it forms H_2CO_3, which makes the liquid acidic and can corrode steel. This is why CO_2 corrosion is only a concern when it is mixed or dissolved in an aqueous phase [103].

$$Fe(s) + CO_2(g) + H_2O(l) \rightarrow FeCO_3(s) + H_2(g) \quad (6)$$

This sweet corrosion is often influenced by elevated temperatures and is widespread in gas pipelines [99, 104]. Corrosion increases as CO_2, system pressure, and temperature increase. Usually, this corrosion is gradual, localized, and leads to pitting. Pits are tough to detect because of their small size and the corrosion materials that cover them [102]. Figure 2.4 illustrates a typical example of mesa corrosion resulting from CO_2 in the pipeline. The morphology of the attack is influenced by factors like the flow system, partial CO_2 and H_2S pressure, the presence of other gasses, and the water composition produced from the wells [100]. Carbon dioxide (CO_2) that dissolves in water forms carbonic acid, which lowers the pH of the system and initiates a corrosion cycle on pipeline steel. This reaction results in the precipitation of corrosion products, such as iron carbonate, on the surface of the metal [105]. The CO_2 in oilfields can come from various sources, including mineral dissolution and by-products of petroleum formation processes, particularly injection processes [10]. On its own, bare steel is extremely corrosive. However, exposure to a corrosive environment causes the accumulation of corrosion products on its surface, which eventually provides protection by slowing the corrosion rate. To further reduce CO_2 corrosion, corrosion inhibitors have been used to create a protective film on the metal surface, which minimizes its interaction with water or other corrosive elements. The morphology of the corrosion layer, which is thick and composed of carbonate, can determine whether the corrosion attack is continuous and dissolution-free with protective films, or whether it results in low protective corrosion rates or localized corrosion with pitting and mesa attacks [106].

Figure 2.4: A typical example of mesa corrosion as a result of CO_2 in the pipeline **[107]**

2.2.3. Sour or hydrogen sulfide (H_2S) corrosion

Hydrogen sulfide (H_2S) corrosion occurs when water and H_2S are present in the fluid in the pipeline [108]. The presence of H_2S in the oilfield is more problematic than CO_2 since it is highly toxic and because the H_2S concentration above 700 parts per million (ppm) kills instantly; therefore, its leakage should be prevented [109]. Like CO_2, H_2S alone does not cause corrosion; it becomes highly corrosive in the presence of water leading to the cracking of pipelines [10]. The majority of H_2S in the oilfield comes from various natural processes like the volcanic process, dissolution of the mineral deposits, bacterial activities, and sweet wells that can be transformed into a sour well with age or specific processing activities, including injection of water [10]. In understanding the kinetics of the scale formation and its growth, knowledge of the reliance on the surface-scale layer formed on the surface of the metal is always helpful. In comparison to CO_2, which only forms ferrous carbonate ($FeCO_3$) scale on the surface of the metal, H_2S forms different iron sulfides, including amorphous ferrous sulfides, smythite, ferrous cubic sulfide, pyrrhythite, greigite, troilite and pyrite [110].

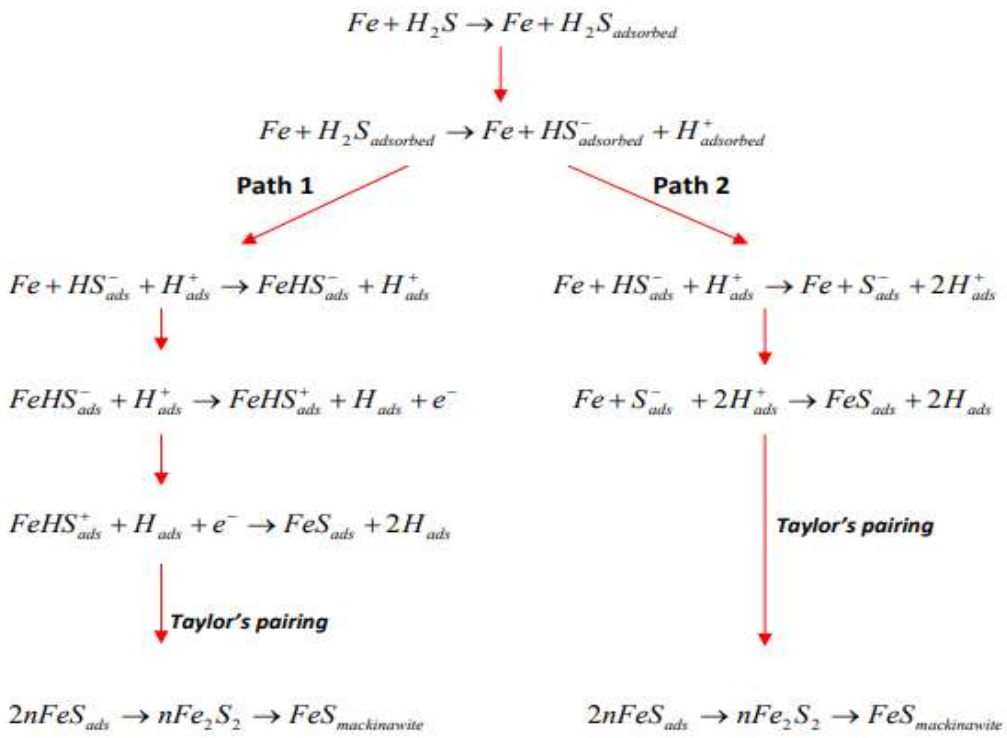

Figure 2.5: Proposed mechanisms for mild steel dissolution in aqueous solutions containing H_2S **[110, 111]**

The interaction of Fe with H_2S in aqueous environments proceeds toward mackinawite formation through the reaction paths shown in Figure 2.5, according to Sun *et al.* [110, 111]. After the initial adsorption of H_2S on Fe's surface, mackinawite may be formed by either Path 1 or Path 2 from an amorphous FeS. Smith and Miller [112] investigated the mechanisms of sour corrosion. They identified that mackinawite is first produced and converted to other forms of iron sulfide when exposed to H_2S in the longer term [113]. Sour corrosion can be prevented using various control methods, such as injection of H_2S scavengers, pH monitoring by caustic injection, corrosion inhibitors, and alloy selection according to the sulfide stress cracking prevention standard [114].

Other forms of corrosion experienced in metallic-based materials include galvanic, crevice, fretting and pitting corrosion, and environmentally induced cracking, among others, based on the attack's morphology, as shown in Figure 2.6.

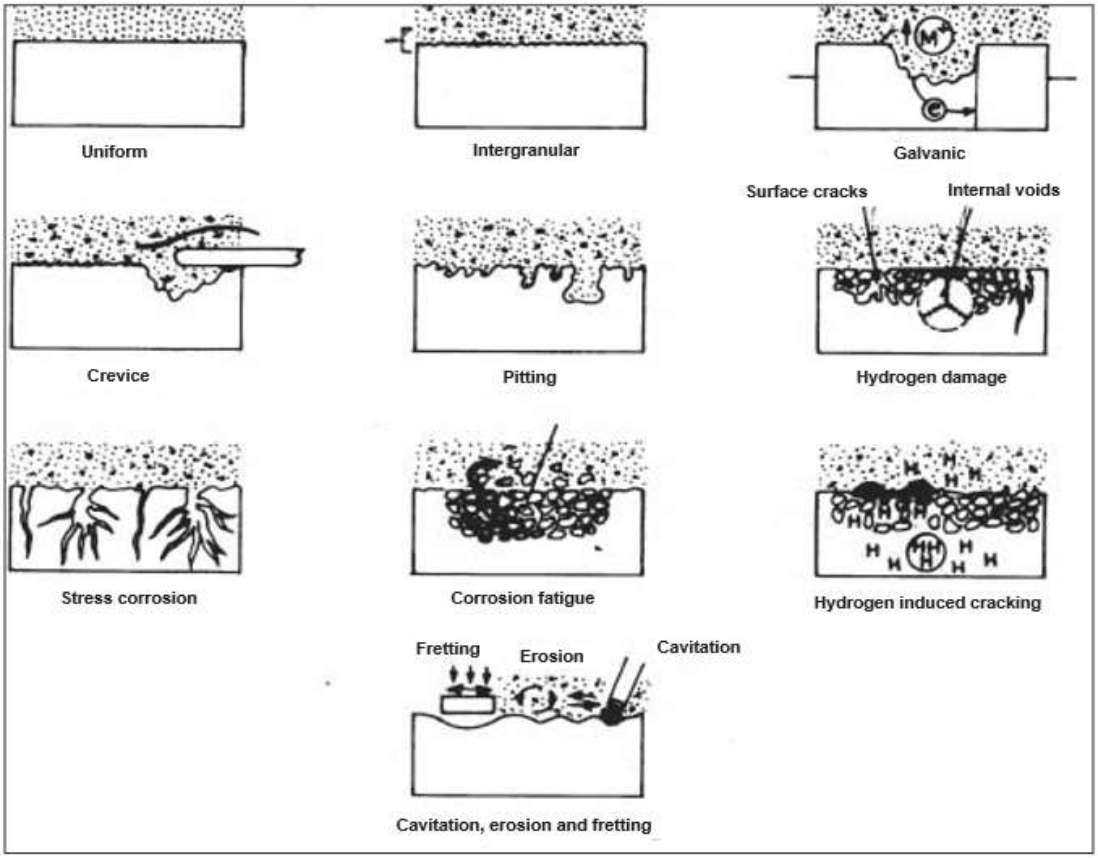

Figure 2.6: Diagrammatic summary of the various corrosion types [115]

2.3. Corrosion control

Various methods for protecting metals/alloys from corrosion have been developed over the years. The complexity and scope of these methods vary greatly. They can, however, be classified as variants of one or more of the three main methods: creating a barrier between the material and its surroundings (i.e., environmental modification), material selection, and surface engineering [116]. It is not always easy to decide which corrosion control method is most appropriate for a specific application. Still, the so-called PAC rule, i.e., performance, availability, and cost, can be used to select the proper technique [117]. Furthermore, more than one method is frequently used at the same time.

2.3.1. Surface engineering

Surface engineering requires ex-situ alteration of the metal/alloy surface to decrease its corrosion rate (i.e., before service). There is a vast variety of these technologies, which vary widely in complexity and expense, for example, the application of surface modification induced by paint and

laser. Outstanding performance can be achieved using the appropriate technique, but the engineered surface condition must be controlled carefully, as the protective action may be lost due to degradation [117].

2.3.2. Material selection

The selection of material is, as its name suggests, selecting the most appropriate material for a particular application and environment. One would initially assume that the best option for protection against corrosion is to choose metals highly resistant to deterioration during the engineering process. However, an engineer must consider the costs and availability of such types of metal. Metal experience different kinds of attacks in different environments and knowing the type of corrosion that affects specific metals is vital. For instance, choosing a high-end corrosion-resistant alloy for a long oil export pipeline is not very practical because it would cost prohibitively. Also, no sufficient source quantity can be available for such material [117]. Titanium is often the preferred choice for materials due to its exceptional resistance to corrosion. However, steel is sometimes used in its place because it is less expensive and durable. In the oil industry, steel is commonly used for its mechanical properties and cost-effectiveness in the production of vessels, pipes, tanks, and wells [118].

2.3.3. Environmental adjustment

Since corrosion is a reaction between the metal and its surroundings, a specific environmental adjustment can reduce corrosion. Such changes are cost-effective if the problem is limited to a small area since environmental modifications are limited to particular applications or techniques. This technique is most effective when the building raw material for a specific environment has already been selected, such as the piping system. In such cases, it is possible to change the environment in which they are located. Factors influencing corrosion rates, such as concentration or the flow velocity of the corrosive species, or temperature, can be manipulated to prevent corrosion. In general, lowering one of these factors slows down the corrosion process. However, changing the corrosive system temperature has little or no effect on the corrosion rate in some cases [85].

Protective barriers or substances can also be inserted into an environment to make it less corrosive. The inducement of protective barriers involves adding a chemical that interacts with the corroding metal/alloy to form a corrosion-resistant interfacial barrier. No modification is made to the

concentration of corrosive species in the bulk fluid [117]. One prime example of the inducement of protective barriers is corrosion inhibition, which is the central theme of this thesis, and will, therefore, be discussed further in the following sections.

2.4. Corrosion inhibitors

One of the most economical ways of dealing with corrosion is using corrosion inhibitors. Various scholars have used several definitions to describe and define what corrosion inhibitors are. Godlinez-Alvarez *et al.* [119] identified inhibitors according to their chemical properties, inhibition mechanism, chemical structure, etc. A chemical that can thus be referred to as a corrosion inhibitor is a substance that can be added or sprayed into a corrosive environment to reduce the corrosiveness (i.e., corrosion rate) of the environment to appropriate concentrations while not significantly altering the concentration of the aggressive ions [120].

This description excludes O_2 scavengers, which are known to reduce the corrosion rate by modifying the environmental composition [10]. Corrosion inhibitors work by inducing a shift at or near the substrate's surface, which is achieved through an adsorption process that leads to barrier formation on the surface of the metal. The exact form of this barrier varies with the corrosion inhibitor's type and condition.

The critical use of inhibitors is to monitor general corrosion in sweet environments. Different inhibitors are available to control mesa and pitting corrosion, which occurs in sweet and sour conditions. Intensive laboratory tests can be conducted to select corrosion inhibitors combined with chemical surfactants and biocides to create a commercial package that is eventually inserted into pipelines. Successfully developed inhibitor molecules interact with corrosion processes, decreasing the corrosion rate by at least two orders of magnitude [121]. It is vital to select an appropriate inhibitor type to control a particular form of corrosion [122]. It is critical to use caution when selecting an inhibitor for a specific system. An inhibitor that protects one metal well in one corrosive environment may actually worsen corrosion in other metals in the same environment. [123]. The selection also requires consideration of numerous parameters, including solution flow, pH, system temperature, metallurgy, and the presence of dissolved organic or inorganic substances.

Consequently, when selecting an inhibitor to protect pipelines, corrosion scientists must consider several influencing factors. Generally, long-chain nitro-based compounds, such as amides or amines, are used in hydrocarbon pipelines as corrosion inhibitors. Organophosphates can also be used to prevent corrosion in pipelines. They prevent corrosion by forming a bond between the compound's charged active group and the pipeline's metal walls. The inhibitor is said to be physically adsorbed to the wall before being chemically attached to its surface as a result of a charge transfer between the inhibitor and the metal surface of the pipeline, resulting in the formation of a chemical bond. Because hydrocarbons are present in the inhibitors' structures, it is assumed that they control corrosion by forming a hydrophobic layer between the metal walls and the corrosive solution [122].

The mechanism by which inhibitors prevent metal corrosion is said to be twofold: the displacement of adsorbed water molecules from the metallic pipe walls via the formation of an adsorption layer and the modification of the surface potential, which inhibits both oxidation and reduction corrosion reactions. For the optimum delivery and storage properties of the inhibitor, inhibitors are used with a solvent carrier liquid and other addictive substances, such as surfactants. Corrosion inhibitors are known not completely to stop corrosion, but they are designed to slow it down to a manageable rate [122]. Over time the inhibitor's effectiveness is decreased by equilibrium desorption, mechanical shearing, or chemical reactions. For an inhibitor to be effective, it must be dispersed/injected into the water-wet surface and be capable of achieving and maintaining a proactive film in this location. Transporting the inhibitor to all corroding sections along the pipeline length is critical, regardless of where the corrosion occurs [124].

2.5. Classification of corrosion inhibitors

Many compounds can be used as corrosion inhibitors, and an effective inhibitor in one system might not work in another, indicating that inhibitors are not uniformly applicable [10]. Thus, different inhibitors are required for specific conditions or environments. Corrosion inhibitors are classified based on their protective mechanism (anodic, cathodic, or both) or chemical composition (organic and inorganic). They may also be classified as "green inhibitors" in other classes. The inhibitors are classified as anodic, cathodic, or mixed based on their electrochemical defence mechanism [125, 126].

2.5.1. Anodic mechanism of protection

As the name suggests, anodic inhibitors work by modifying the anodic process. This can result in a significant shift in the corrosion potential (E_{corr}) in a positive direction, forcing the metal's surface into the passive region. This, in turn, reduces the corrosion current density (I_{corr}). This is achieved by supporting the natural tendencies of the passivation of metal surfaces or forming an insoluble film surface layer. Anodic corrosion inhibitors are typically used in near-neutral solutions where corrosion products with low solubilities, such as salts, oxides, and hydroxides, are produced. These inhibitors inhibit metal anodic corrosion reactions by facilitating the formation of a passive layer; thus, they are known as passive corrosion inhibitors [127]. The inhibitor's interaction with the corrosion products on the metal surface results in the formation of a cohesive and insoluble layer [128]. These corrosion inhibitors have no effect on the cathodic reaction [129], but they can increase the anodic electrochemical potential, as shown in Figure 2.7. This shifts the anodic and cathodic curves so that they intersect at a lower corrosion current and higher corrosion potential. Anodic inhibitors are most effective when used at high concentrations and in environments with high levels of chloride [130].

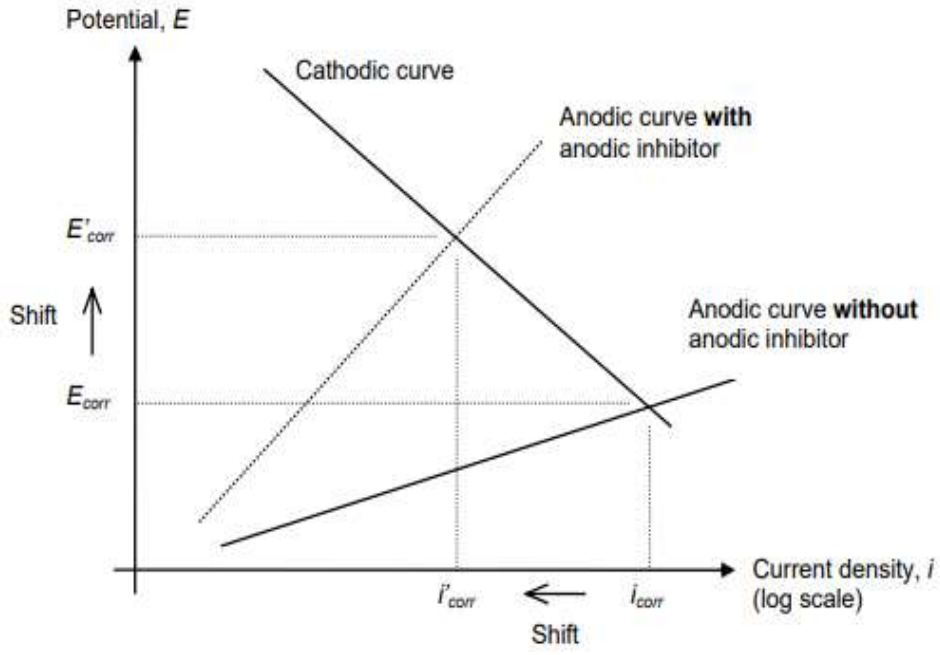

Figure 2.7: Corrosion potential with anodic inhibiting effect [129]

2.5.2. Cathodic mechanism of protection

Cathodic inhibitors work by preventing the cathodic reaction on the steel during the corrosion cycle [128]. They do this by producing insoluble compounds that precipitate on the cathodic regions of the metal, forming a barrier that restricts the diffusion of O_2 and conduction electrons [128, 129]. This reduces the supply of O_2 during the corrosion cycle [128], which in turn decreases the corrosion rate and shifts the corrosion potential to lower negative values [128, 129]. If corrosion's potential is reduced, it's customary to assume a lower chance of decay [129]. A cathodic inhibitor's presence promotes a 'hang' in the potential for corrosion and corrosion rate to E_{corr} and $I_{corr,}$ respectively, as shown in Figure 2.8. Cathodic inhibitors operate by either slowing the cathodic reaction by moving the E_{corr} to a more negative value or selectively increasing the surface impedance. This limits the migration of reducible species to areas where the I_{corr} has decreased, as shown in Figure 2.8. [131-133]. As the potential for corrosion decreases to lower values, the rate of corrosion decreases [129], leading to cathodic polarization. Some common cathodic inhibitors include carbonates, phosphates, polyphosphates, and silicates [129]. Zinc oxide has also been shown to have cathodic inhibitor properties by Rincón *et al*. [134]. Sodium hydroxide and sodium carbonate are among the most commonly used cathodic inhibitors [135], as they increase the pH of the steel, reduce O_2 transport, and form a film on the surface of the steel. Cathodic inhibitor concentrations tend to be higher than those of anodic inhibitors, as their effect on suppressing the corrosion process is weaker than that of anodic inhibitors [136].

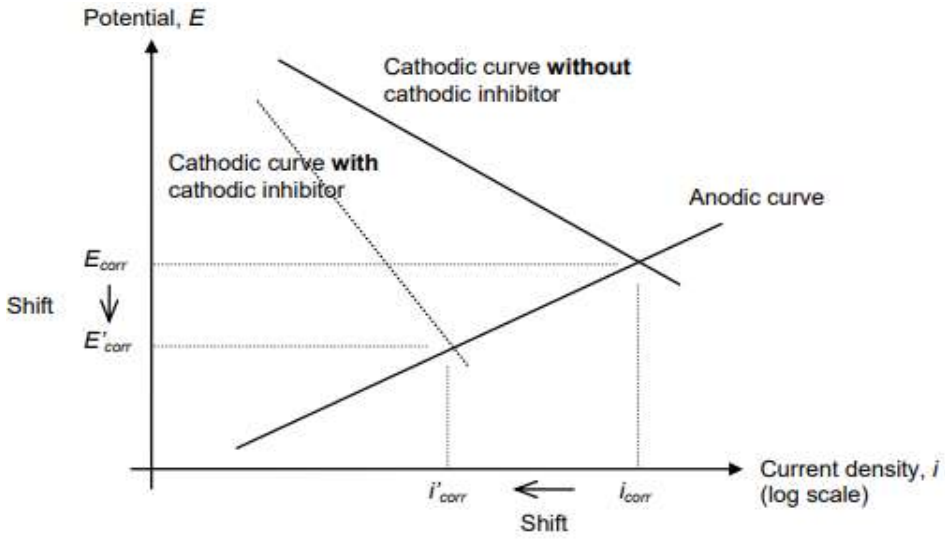

Figure 2.8: Corrosion potential with cathodic inhibiting effect [129]

2.5.3. Mixed mechanism of protection

In current practice, using inhibitors in the form of single compounds is unusual. It is more popular to use formulations that consist of two or more inhibitors. This formulation is because single inhibitors are successful with only a small number of metals, and multi-metal system protection demands more than one inhibitor to be present. Chemicals with different properties (e.g., anodic and cathodic inhibition) often complement each other's deficiency, and the mixed inhibitor's efficacy increases. Consequently, dosage concentration can be decreased dramatically, reducing the production costs and the environmental impacts caused by chemicals [10]. The mixed inhibitors work on both the cathodic and anodic regions, usually by adsorption on the metal surface, forming a protective layer [135], thus being known as adsorption inhibitors [137] or inhibitors of pellicular formation [138]. Some corrosion inhibitors act as mixed inhibitors when there is little change in E_{corr} with a decrease in I_{corr}, as shown in Figure 2.9. The inhibitor decreases the corrosion rate and does not change the corrosion potential significantly. These inhibitors reduce the corrosion rate without significantly altering the corrosion potential. They have minimal effects on the corrosion potential of the anodic or cathodic site, regardless of which reaction is most affected [129]. The type of inhibitor used can be determined using anodic and cathodic Tafel slopes (βa, βc) [139]. An anodic inhibitor is indicated by an increase in only the anodic Tafel slope, whereas a cathodic inhibitor is indicated by an increase in only the cathodic Tafel slope. While an increase in both slopes indicates a mixed-type corrosion inhibitor.

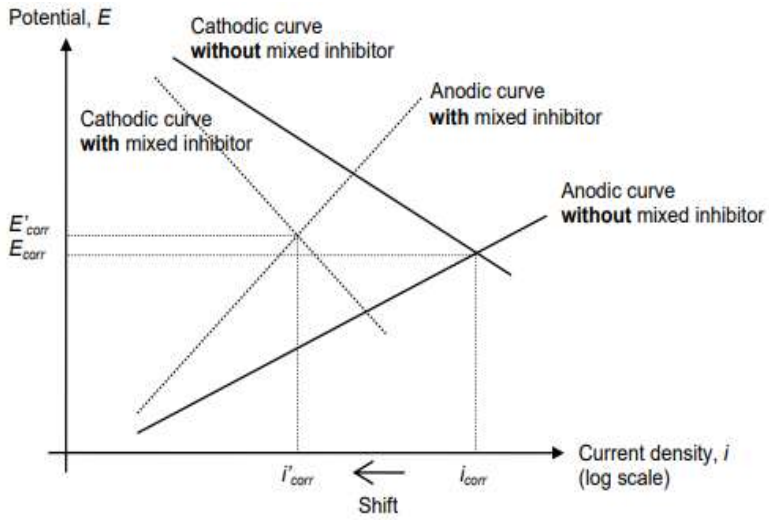

Figure 2.9: Corrosion potential with mixed inhibiting effect [129]

2.6. Chemical composition

The action of mechanisms and the use of inhibitors are derived from their chemical composition. Various inhibitors are divided into inorganic and organic chemical compounds [140].

2.6.1. Inorganic inhibitors

Nitrites stand out as the most widely used inorganic inhibitors. These inhibitors were primarily applied as a protective measure mixed with concrete in the 1950s. Sodium nitrite has been researched in the past. However, it was substituted with calcium nitrite, the first commonly sold inhibitor, because of the side effects of sodium nitrites, such as a weaker concrete strength and an increased risk of alkali-silica reactions and adverse effects on the concrete [141]. Nitrites also inhibit the chloride and sulfate ions' action in the corrosion process [142]. Nitrites accelerate the setting of fresh concrete and increase their strength gains among concrete side effects [129]. While nitrites effectively reduce the corrosion rate of reinforced concrete structures in many European countries, such as Germany and Switzerland [143], they are prohibited due to their carcinogenic and toxic effects [144]. This prohibition has culminated in the investigation of alternative inhibitors.

2.6.2. Organic inhibitors

Like inorganic inhibitors, organic inhibitors have been widely used in recent years, with many studies focusing on their modes of action and efficacy [145-148]. Organic compounds can donate or receive electrons from the metal surface, form a covalent bond, and are considered suitable corrosion inhibitors [148]. Ryu *et al*. [149] argue that organic inhibitors are common in reinforced concrete, even in the presence of chloride ions, and are often used to prevent corrosion. Organic inhibitors are often composed of compounds with O_2, nitrogen, and sulfur atoms, and multiple bonds within the molecules. These structural features enable the inhibitor to adsorb to the metal surface, and the efficacy of the inhibitor is often related to its adsorption properties. The effectiveness of adsorption can depend on the condition and type of metal surface, the corrosive environment, and the chemical structure of the inhibitor [150]. The adsorption of these inhibitors on the metal surface depends on various factors [151, 152]. These include the inhibitor group's physical-chemical properties, the functional group, the p-orbital character, and the donated atom's electronic mass. Therefore, the efficiency of inhibition depends on the molecular electronic structure comprising active adsorption centres, the method of absorption, the molecular size, the

inhibitor cover rate on the metal surface, and the formation of metallic compounds [148]. Amines and alkanolamines are commonly used as corrosion inhibitors because they are highly water-soluble and have a limited effect on the properties of concrete in its fresh and hardened states [145]. These inhibitors are effective at spreading through concrete and are known as volatile inhibitors or migration inhibitors because they can be mixed into the concrete, fixed mortar, or applied to the concrete surface during operation [141]. Amines are organic compounds that contain a lone pair of nitrogen atoms, which allows them to bind to the metal surface and form a protective layer. This layer shields the metal from corrosion [145] and can also extract corrosion products from the metal surface, ensuring direct contact between the protective layer and the metallic surface [141]. Another class of organic inhibitors is carboxylates, which are distinguished by the presence of carboxylic acids (-COOH) [145]. Like amines, these compounds can bind to the metal surface and create an organic layer that protects the steel from corrosion [129].

2.6.3. Green inhibitors

Inhibitors can be either synthetic or natural [128]. Synthetic inhibitors are artificially manufactured and can have negative effects on both humans and the environment, particularly synthetic organic inhibitors. As a result, there has been increasing interest in using green or natural inhibitors, which are environmentally sustainable and often more effective than synthetic inhibitors [153-155]. Natural inhibitors are derived from plants, spices, and other sources and are biodegradable[154, 156]. They are also inexpensive to extract using simple methods, making them a cost-effective alternative to synthetic inhibitors. Thus, extensive research has been conducted to extract natural roots, leaves, or seeds from plants [153-156]. Red mud, a compound based on ferric oxide and alumina and a residue generated for Al production in bauxite processing, is included in the green inhibitor's classification. There is no universally accepted definition of corrosion. However, Darling and Rakshpal [157] defined green chemistry as a technique for synthesizing, manufacturing, and using chemicals in a way that minimizes harm to human health and the environment.

2.7. Corrosion inhibition in acidic media

Inhibitors that inhibit the corrosion of metallic materials in an acidic environment are typically organic species that form an adsorbed 2-D layer based on the above-mentioned corrosion inhibitor classifications [158]. Organic corrosion inhibitors are effective because they contain both

hydrophilic and hydrophobic moieties. With varying lengths of carbon numbers, these molecules typically have a hydrocarbon chain attached to a polar or ionic head group. The mechanism by which these inhibitors reduce corrosion is not fully understood, but it is thought that the polar molecule group allows surface water molecules to be displaced (Figure 2.10) [159], which relies on its polarizability and electron density [158]. The polar head and hydrocarbon tail of corrosion inhibitors work together to facilitate adsorption onto the metal surface from an aqueous solution. The concentration of the inhibitor plays a crucial role in its effectiveness. At low concentrations, the inhibitor adsorbs onto the steel surface in a parallel or inclined orientation [160]. As the concentration increases, the hydrophobic tail groups extend into the aqueous phase, allowing for more surfactant molecules to be accommodated and increasing the surface coverage.

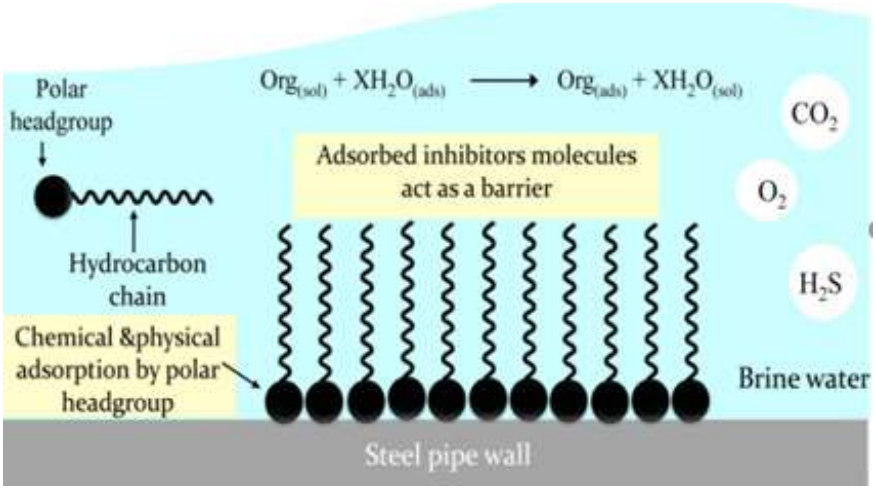

Figure 2.10: The action of inhibitor molecules on steel pipe wall corrosion is depicted schematically, with examples of some of the chemical fragments for each part of the inhibitor [159]

At the critical micelle concentration (CMC), a monolayer distribution of the inhibitor is formed. The tail groups are arranged parallel to each other and perpendicular to the metal surface [160], which becomes hydrophobic. McMahon [161] showed that the adsorption of inhibitor molecules (e.g., oleic imidazoline) on steel produces a hydrophobic surface with no water affinity. This creates a waterproof barrier between the corrosive aqueous phase and the steel pipe.

Ramachandran *et al*. [162, 163] studied the inhibition of iron corrosion by a series of imidazoline derivatives and proposed a self-assembled monolayer mechanism for corrosion inhibition. This model suggests the following criteria for an effective inhibitor molecule:

- Adequate solubility and inhibitor conveyance rate from solution to the surface
- The surfactant headgroups strongly bind to the metal surface
- Self-assembly of headgroups forming a thick and orderly layer
- Hydrocarbon tail self-assembly to form a hydrophobic barrier

In terms of organic corrosion inhibitor bonding, these inhibitors are said to adsorb onto the metal surface via physical, chemical, or a combination of the two [158].

2.8. Corrosion inhibition of near-neutral solutions

Because of the corrosion cycle mechanisms variations between acid and near-neutral solutions, the inhibitors used in acid solutions typically have little to no inhibition effect in near-neutral solutions. The inhibition activity in acid solutions is due to the adsorption on metal surfaces free of oxides. The principal cathodic mechanism in these media is the evolution of hydrogen. The corrosion cycle of metals results in sparsely soluble surface materials, such as oxides, hydroxides, or salts, in almost neutral solutions. The partial cathodic reaction is the reduction of O_2. In near-neutral aqueous solutions, inorganic or organic compounds and chelating agents are used as inhibitors. Inorganic corrosion inhibitors may be classified according to their modes of action:

1. The metallic content is self-passivated by oxidizing agents such as chromates and nitrites. Maintaining the concentration of these inhibitors above a safety level is crucial. If not, the oxidizer can cause severe corrosion due to pitting or localized attack.
2. Carbonate precipitation on metal surfaces forms a protective film. This typically occurs due to Ca^{2+} and Mg^{2+} ions commonly found in polluted waters.
3. Protective film formation and maintenance can be achieved by adding inorganic anions, such as polyphosphates, phosphates, silicates, and borates.
4. The surface film's protective properties are modified by adding Ni^{2+}, Co^{2+}, Zn^{2+}, or Fe^{2+}.

Organic acid sodium salts such as benzoate, salicylate, cinnamon, tartrate, and azelate can substitute inorganic inhibitors, particularly in ferrous solutions. When such compounds are used in solutions containing other anions, such as chlorides or sulfates, the concentration of inhibitors

required for successful defence may depend on the aggressive anions' concentration. Therefore, instead of the critical concentration, the critical pH value for inhibition must be considered [164].

2.9. Adsorption process

Adsorption is a mechanism that allows a molecule (adsorbent) to reach the surface (adsorbent), resulting in the molecule being held close to the surface. The bonding mechanism involved in the adsorption process is distinguished from its physical origin [165, 166]. Adsorption is classified into two types based on the strength of the interaction between the adsorbate molecules and the adsorbent:

2.9.1. Chemical adsorption (chemisorption)

Chemisorption occurs due to the binding/attraction of the molecule-metal surface interface marked by a covalent chemical bond between the inhibitor and the surface of the metal. During this adsorption process, the electronic structure of the chemisorbing molecule dramatically changes. Chemisorption binding is the creation of a shared pair of electrons with the metal surface from inhibitor molecules. As such, a transfer of electrons leaves the inhibitor molecule with a formal positive charge. Although the receiver (metal) may have orbitals for more than one pair of electrons, it is unlikely that more than one electron pair will be donated per molecule. A short equilibrium distance between the adsorbate and substrate occurs during chemisorption. Hence, the van der Waals forces are not dominant in such surface systems.

2.9.2. Physical adsorption (physisorption)

Physisorption involves weak adsorbate-substrate interactions, such as the two substituents' polarization or van der Waals interactions. Therefore, no significant chemical changes arise from the adsorption process on the adsorbent's chemical composition (i.e., no exchange of electrons is observed) [158, 167]. Thus, physisorption is easily reversible since no permanent bonds are formed between the adsorbate and the surface. The energy interaction comparable to the vaporization heat (condensation) is characteristic of physisorption adsorption. The standard binding energies of physisorption are a few kcal/mole at most [168]. Among the most important parameters for effective corrosion inhibition are the surface coverage and the strength of the inhibitor binding to the substrate. Usually, it is assumed that inhibitors must adhere to a more significant proportion of active surface sites to protect the metal properly. The fraction of the corrosion inhibitor's metal

surface may be connected to the bulk solution's inhibitor concentration [158]. The surface coverage typically rises as the concentration of the inhibitor increases [169].

The adsorption degree depends on the adsorbate and adsorbent's nature, activation of the adsorbent, adsorbent surface area, and experimental conditions such as temperature, pressure, etc. The adsorption mechanism is commonly analyzed through graphs known as the isotherm of adsorption. This is the sum of adsorbate on the adsorbent as a function of its pressure or concentration at a constant temperature. The adsorbed quantity is almost always normalized by the adsorbent's mass so that different materials can be compared [170]. In 1916, Irving Langmuir published a new isothermal model for solid-adsorbed gases, the Langmuir adsorption isotherm [171, 172]. It is a semi-empirical isotherm derived from the proposed kinetic mechanism. This isotherm is believed to occur between adsorbed gaseous molecules and free gaseous molecules under several different conditions. The isotherm is based on various assumptions: only a monolayer is formed at maximum adsorption so that adsorbent molecules do not deposit on the other adsorbent molecules that are already adsorbed but adsorb only on the free adsorbent surface; adsorbent molecules do not interact with each other; the adsorbent surface is uniform, meaning that all adsorbent sites are equivalent; and all adsorption occurs through the same adsorption mechanism [170]. Irving Langmuir proposed that the mechanism of adsorption takes place through the following equation:

$$A\,(g) + B\,(s) \underset{Desorption}{\overset{Adsorption}{\rightleftharpoons}} AB \tag{7}$$

A is the unadsorbed gaseous molecule, B is an unoccupied metal surface, and AB is the adsorbed gaseous molecule. The direct and inverse rate constants are k and k^{-1}. According to the Langmuir adsorption mechanism, the surface coverage (θ) and concentration of the inhibitor (C_{inh}) in bulk solution are related by the following equation:

$$\theta = \frac{KC}{1+KC} \tag{8}$$

K is the equilibrium constant of adsorption, θ is the fractional surface coverage, and C is the inhibitor concentration in solution. It is often suggested that the fractional surface coverage (θ) may be directly linked to a corrosion inhibitor's inhibition efficiency. Still, the validity of this statement is largely untested and therefore questionable. In addition, assuming monolayer

coverage for good inhibition efficiency is debatable, and it may be that the inhibited surface is covered by $\theta < 1$ monolayer or multiple layers (e.g., a bilayer). Other standard adsorption isotherms include the Freundlich [173], Frumkin [174], and Temkin [175] adsorption isotherms, amongst others.

Inhibitors adsorption blocks the active sites on the metal surface, thereby restricting the corrosion process; this is one possible mechanism for inhibiting corrosion. The adsorption of a substance on the metal surface involves its build-up at the connection between two phases, like the liquid and solid interface or the gas and solid. At the interface, the molecule that builds up, or adsorbs, is known as adsorbate, and the adsorbent is the solid on which the adsorption process occurs. Desorption is a reverse process by which the inhibitor molecules desorb (i.e., detach) from a solid or liquid surface to a gas or liquid [176]. As mentioned above, there are two significant forms of adsorption: chemical adsorption and physical adsorption. Polar groups in molecular structures that can adsorb heavily into the metal surface or react to the surface corrosion product to form a protective layer promote most organic inhibitors' adsorption. The adsorption of organic molecules at the interface between metal and solution is significant in surface chemistry and can significantly alter metals' corrosion-resistant properties [177]. Below are some crucial factors influencing the inhibitor molecules' adsorption and inhibition efficiency on the metal's surface.

2.9.3. Interaction of the inhibitor with water molecules

The propensity of an adsorbent molecule depends on its water affinity in contrast with its adsorption affinity. Organic inhibitors can be adsorbed by displacing adsorbed water molecules on an electrode/electrolyte interface on the electrode's inner Helmholtz plane, as shown in the equation below [178].

$$Org(sol) + nH_2O(ads) \rightarrow Org(ads) + nH_2O(sol) \quad (9)$$

In this equation, n represents the number of water molecules that are adsorbed for each inhibitor molecule extracted from the metal surface, and Org(sol) and Org(ads) represent the organic inhibitor molecules in the electrolyte and the adsorbed inhibitor molecules on the metal surface, respectively [179]. The adsorption of organic inhibitor molecules onto the metal surface is driven by the higher energy of interaction between the metal and the substrate compared to the metal and water molecules.

2.9.4. Influence of surface charge on the metal

The adsorption of corrosion inhibitors onto the metal surface may be driven by electrostatic forces, which attract ionic charges or dipoles on the adsorbed species and electric charges on the metal at the metal-solution interface. The charge on a metal surface is often expressed in terms of its potential relative to the zero-charge potential, which is more relevant to adsorption than the potential on the hydrogen scale. The signs of these two potentials may differ. As the potential of a metallic surface becomes more positive, anion adsorption is favored, and as the zero-charge potential becomes more negative, cation adsorption is favored. At zero-load potential, the electrode has no ion-double layer and adsorbs substances dissolved in the electrolyte. In cases of potential variations in the ionic double layer, an electrode's ability to adsorb organic molecules is decreased. This is because the field pulls organic molecules from the metal surface into water molecules with a high dielectric constant. Thus, an electrode's adsorbent power is below the zero-charge potential at its limit [180].

2.9.5. Influence of molecule structure and functional group

Inhibitors may also bind to metal surfaces by transferring an electron to the metal to form a coordinate bond type. This process is favored by the presence of vacant low-energy electron orbitals, which are commonly found in transition elements/metals. The availability of loosely bound electrons in anions and neutral organic molecules containing lone pairs or multiple bonds (e.g., triple bonds or aromatic rings) promotes electron transfer from adsorbed species. At the functional group, the electron density decreases as the inhibitive capacity increases in various compounds. As a result of the easy transfer of electrons, the strength of the coordinate bonds forms increases, resulting in greater adsorption of the inhibitor on the surface of the metal [181].

2.9.6. Changes in the electrical double layer

One of an inhibitor's effects is created by altering the electrical double-layer structure at the interface between metal and solution. The electrostatic adsorption of ionized inhibitor molecules or species causes this effect. An inhibitor's introduction into the electric double layer causes the alteration of its structure and composition. The presence of inhibitor molecules on the metal surface can affect the electric double layer by inducing changes in the dielectric properties of the water molecules in the layer. This can alter the orientation of the water molecule dipoles, leading to a decrease in the dielectric constant and double-layer capacitance. The decrease in double-layer

capacitance may be due to the reduced electrolyte area resulting from the formation of an inhibitor film [182].

2.10. Synergism of corrosion inhibitors

Some corrosion inhibitors with decent inhibitory ability have been widely criticized for their environmental problems or high costs. The use of environmentally friendly inhibitors that do not interrupt environmental equilibrium or adversely affect human health has increased. This class of inhibitors has been classified by Ivusic *et al*. [183] on an ad hoc basis as green inhibitors (plant extracts). The use of corrosion inhibitors is no longer just about their ability to prevent metal corrosion. The effectiveness of the inhibitor is now also a key consideration. The effectiveness of an inhibitor can be grouped into three categories based on the inhibition efficiency they can provide, which can either be poor (those with %IE < 40), moderate (those with %IE between 40 and 69), and excellent inhibitors (those with %IE > 70). To address the problems of poor or moderate inhibitor's ability and exorbitant prices in recent years, corrosion scientists have taken steps to find substances that may have synergistic effects when combined with the inhibitor. Such a combination should decrease the price of inhibitors or increase their efficiency [184]. Synergism is a nonlinear cumulative effect observed when two or more substances combine to create a sequential or complementary impact more significant than either of which would have manifested on their own. That effect is referred to as a "synergistic effect" [185, 186]. Synergism is one of the most significant effects in the inhibition mechanism, and it is regarded as the basis for most modern anticorrosion formulations [187, 188]. It is also essential in improving inhibitors' ability to inhibit, minimize waste or use of individual compounds and diversify the use of inhibitors in corrosive media [189]. Corrosion scientists must recognize, explore and apply synergy in complex corrosive media. Aramaki and Hackerman [190] assessed the effect in terms of synergism parameter (S_θ) as follows:

$$S_\theta = \frac{1-\theta_{1,2}}{1-\theta'_{1,2}} \tag{10}$$

where $\theta_{1,2} = (\theta_1 + \theta_2) - (\theta_1\theta_2)$, θ_1 is the surface coverage by inhibitor, θ_2 is the surface coverage by the additive and $\theta'_{1,2}$ is the surface coverage measured for the combination of the inhibitor and the additive. When the value of S_θ is greater than unity ($S_\theta > 1$), it implies the existence of a synergistic inhibition effect between the two substances or inhibitors, and when S_θ

is less than unity ($S_\theta < 1$), it is an indication that the synergistic effect is not significant. While if S_θ is equal to 1 ($S_\theta = 1$), there is no synergistic effect between inhibitors.

Plant extracts can be considered multi-component inhibitors because they have more than one molecule capable of inhibiting corrosion. It is essential to investigate their synergistic effect to determine each molecule's contribution to the metal surface coverage and inhibition efficiency.

2.11. Plants extracts as corrosion inhibitors

Plants undergo several metabolic and biochemical processes during development, forming and accumulating various chemical substances that shape the plant's chemical composition [191, 192]. A plant extract is a material with unique properties typically obtained from a plant's tissues by treatment with a solvent for a particular reason [193]. Plant extracts are complicated and often contain several different chemical compositions in different plant sections [194-196]. Plant metabolites range from alkaloids, tannins, flavonoids, saponins, terpenes, glycosides, etc. They have a wide range of heterogenic atoms such as sulfur, phosphorous, nitrogen, aromatic tendencies, pi and sigma connections (double and triple bonds), etc. These plant metabolites have a strong surface binding tendency. They can displace water molecules concentrated on the metal surfaces and create a film barrier that prevents corrosive agents from attacking the protected (metal) surface [14, 197-199]. Parts of the plants that control corrosion include seeds, flowers, fruit, leaves, etc. Natural products such as plant extracts are entirely biodegradable, non-toxic, and readily available [170]. Tannic acid is regarded as one of the most effective and well-known plant extracts used as a corrosion inhibitor to treat rusted iron [200]. It is found in various plant materials and can be extracted commercially from oak, sumac, and willow galls. It is also found in about one-third of the flowering plant families, fungi, brown seaweed, green algae, mosses, and ferns [201]. Tannic acid prevents corrosion by forming a protective layer with corrosion-inhibiting properties by reacting with metallic iron or rust and precipitating ferric tannates, as illustrated in Figure 2.11 [202].

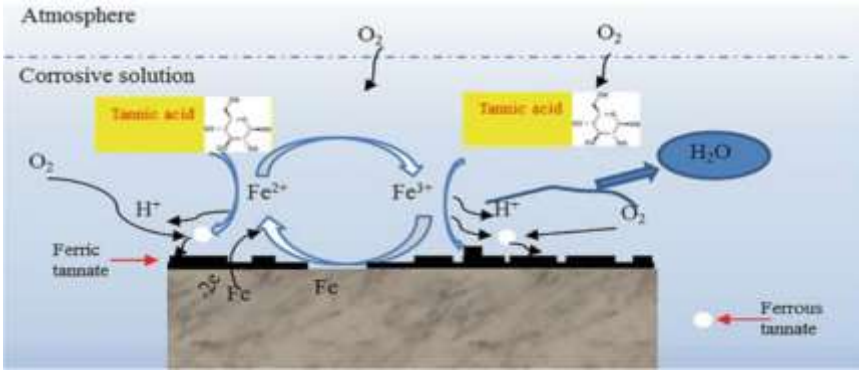

Figure 2.11: Schematically illustration of carbon steel corrosion process in a corrosive environment with tannic acid as a corrosion inhibitor [202]

Plant-derived oils can also be used as corrosion inhibitors. These include carboxylic acid salts extracted from colza, palm, and sunflower are some of the most well-known vegetable oils that have been studied for the conservation of metals such as copper, iron, and lead alloys [203]. The most common classification for these inhibitors is surfactant-type corrosion inhibitors.

The literature review also reveals the use of Moringa oleifera gum exudate [204], Hibiscus sabdariffa [205], Argemone Mexicana [206], and other plants as environmentally friendly corrosion inhibitors in neutral and acidic media, as they cover organic compounds with higher electron density in hetero atoms. The use of phytochemicals as corrosion inhibitors can be traced back to the 1960s, when tannins and their derivatives were used to protect steel, iron, and other metals from corrosion. In 1973, Srivatsava and Sanyal studied caffeine and nicotine's effect on mild steel corrosion in neutral media as an effective inhibitor [35].

Haida *et al*. [207] identified Cistus monspeliensis plant as a potent antioxidant and corrosion inhibitor. Extracts from the plant were obtained through maceration in a mixture of water and acetone solvents. The extracts were then subjected to phytochemical testing to determine their composition. The antioxidant capacity of the extracts was assessed using two methods: the DPPH reduction test and the FRAP test. EIS and PDP were used to investigate the extract's ability to inhibit corrosion. The results showed that the extract, with a yield of 27.6%, contains phenolic compounds, flavonoids, saponins, tannins, reducing sugars, and glycosides. The extract had an antioxidant potential similar to ascorbic acid, with an inhibition concentration of 0.077 mg/mL and 0.102 mg/mL for the DPPH and FRAP tests, respectively. Tafel plots showed that the extract was an effective inhibitor of cathodic reactions, with maximum inhibition of 92% achieved at 298 K

with 0.25 g/L of the inhibitor. The impedance plot was characterized by a single capacitive loop, indicating that the inhibitor works by adsorbing onto the metal surface and forming a protective film that inhibits corrosion of ordinary steel.

Odidika *et al*. [208], in 1 M H_2SO_4 solutions with ethanol extract of Commelina benghalensis leaves, have determined the corrosion inhibition of mild steel using the gravimetric technique. The extract was analyzed phytochemically, and its concentration effect, temperature, time of immersion, and acid concentration were determined on the corrosion cycle. The extract's corrosion inhibition efficiency increased with an increase in the extract concentration and decreased with the temperature rise. The corrosion rate of mild steel increased with an increase in the temperature of the H_2SO_4 solution with and without various concentrations of the extract. Adsorption isotherms, Langmuir and Freundlich, were the isotherms followed by the extracts. The inhibition efficiency trends with temperature indicated a physical adsorption mechanism and measured Gibbs free energy, activation energy, and enthalpy of adsorption values. The amount of %IE of the plant extract has been assigned to the plant-derived phytochemical constituents. The study also showed that Commelina benghalensis could serve as a strong mild steel corrosion inhibitor in an acid medium. It reached a corrosion inhibition efficiency of 91.91% at a concentration of 2.0 g/L extract.

Sivakumar and Srikanth [209] performed a comparative analysis of the inhibitory effect of different sections of the Mimusaps Elangi (ME) plant extract (leaves, fruits, barks, seeds) on the mild corrosion of 1 N HCl medium by weight loss, PDP and EIS. Polarization studies have shown that plant extracts act as mixed inhibitors. The weight loss approach has demonstrated that ME extracts inhibition efficiency increases in a concentration-dependent manner, which electrochemical techniques tests have also confirmed. Maximum inhibition efficiency for ME leaves extract was found at a concentration of 20 ppm to be 98.50%. The surface coverage values were graphically tested for appropriate adsorption. Temperature studies revealed a decrease in inhibition efficiency with temperature increase, suggesting a mechanism for physisorption.

Essential oils isolated from the aerial parts of the Artemisia herba-alba plant were hydrodistilled by Boudalia *et al*. [210], and their chemical composition was studied using capillary gas chromatography and gas chromatography-mass spectrometry. The main extracted components were 1,8-cineole (35,6%) and camphor (24,1%). Using PDP, EIS, and SEM studies, the oils were

tested as a stainless-steel corrosion inhibitor in 1 M H_3PO_4. The results of this study suggest that Artemisia essential oils can reduce the rate of corrosion. The Tafel polarization approach indicated that the plant extract acts as a mixed-type inhibitor, and the efficiency of inhibition increased with the concentration of the inhibitor, reaching a maximum of 88% at 298 K and 1 g/L of oil. Nyquist diagrams obtained from impedance studies also confirm the anti-corrosive effects of the plant. The temperature effect on the corrosion of stainless steel in 1 M H3PO4 without and with Artemisia herba-alba oil at 1 g/L was studied in a range of 298 to 353 K. The thermodynamic parameters suggest that the adsorption process is spontaneous and exothermic, supporting the mechanism of physical adsorption. The experimental evidence fits well with the Langmuir adsorption isothermal model.

Ogunleye *et al*. [211], using gravimetric, depth of attack, and surface analysis techniques, investigated Luffa cylindrica leaf extract's corrosion inhibition. The effect of inhibitor concentrations, temperatures, and immersion time on the extract's inhibition efficiency on mild steel immersed in a 0.5 M HCl solution was observed. The proposed inhibitor's constituents were identified using gas chromatography-mass spectroscopy. Using an FT-IR spectrophotometer, the media solutions and adsorbed film on MS have been described.

The ethanol extract of Musa sapientum peels (banana) was used by Eddy and Ebenso [212] as a corrosion inhibitor of mild steel. Classical Langmuir and Frumkin adsorption models showed that the inhibitor worked by adsorbing onto the MS surface. The physical adsorption process description was consistent with the inhibitor's adsorption properties. Musa sapientum peels' inhibitory effects were primarily regulated by temperature, immersion time, pH, potential electrodes, and inhibitor concentration.

Singh [213] studied Adhatoda vasica extract's inhibition effect in an aqueous solution of 0.5 M H_2SO_4 on mild steel corrosion and its corrosion inhibition mechanism by weight loss, potentiodynamic polarization, and electrochemical impedance spectroscopy. Adhatoda vasica's inhibition efficiency of mild steel corrosion in 0.5 M H_2SO_4 solution increased with an increase in concentration and decreased with an increase in temperature. The PDP measurement results showed that the extract acted as a blended type of inhibitor, and Langmuir isotherm was found to be best suited to the adsorption of the extract on a mild steel sheet.

The inhibition effect of the Garcinia Mangostana fruit pericarp acid extract on mild steel corrosion was studied in HCl. The study shows that the corrosion inhibitor extract's efficacy increased with the inhibitor dosage and decreased as the temperature increased. Electrochemical parameters indicated a mixed but predominantly cathodic mode of inhibition. Kumar *et al*. [214] proposed that the metal surface's adsorption was due to heteroatoms in the extract's organic components.

Cocos nucifera, palmyra palm (Borassus flabellifer Linn.) shell, and coconut shell extract were studied for their ability to inhibit the corrosion of mild steel by Vijayalakshmi *et al*. [215]. The researchers used mass loss, polarization, and electrochemical impedance techniques to evaluate the effectiveness of the extracts as inhibitors. The results showed that the extracts acted as strong inhibitors for the corrosion of mild steel. The inhibitor adsorption on the MS surface was random, endothermic, and consistent with the assumptions of the Langmuir adsorption isotherm. Electrochemical measurements indicated that the extracts acted as mixed-type inhibitors.

Okafor *et al*. [216] used weight loss and Gasometric techniques to investigate the inhibitory action of Azadirachta indica leaves, roots, and seed extracts on the corrosion of mild steel in H_2SO_4 solutions. They found that the inhibition efficiency increased with both the concentration and temperature of the extracts. The researchers proposed a mechanism for the chemical adsorption of the phytochemical components of the extracts onto the metal surface. The experimental data were consistent with the Freundlich adsorption isotherm.

Ekanem *et al*. [217] studied the inhibition properties of Pineapple leaf extract on a mild steel surface in the HCl system by gravimetric and hydrogen gas evolution at a temperature range of 30-60 °C. Weight loss studies revealed that pineapple leaf extract protects mild steel from corrosion using a concentration and temperature-dependent model. They also studied the corrosion inhibition mechanism of the Langmuir adsorption model.

Satapathy *et al*. [218] researched the methanol extract of Justicia gendarussa leaves in the HCl acid medium for the inhibition of MS corrosion. The authors used the gas chromatography-mass spectrometric technique to classify the organic compounds present in the methanol extract. The findings showed that the compounds in the methanol extract were difficult to isolate because most of the compounds' retention times were similar. Electron spectroscopy was used for chemical analysis and atomic force microscopy to obtain film formation details on a mild steel specimen's surface.

The use of natural plant extracts as corrosion inhibitors for metals has gained significant attention in recent years due to their environmentally friendly and cost-effective nature. In a study, the inhibitory action of leaves, seeds, and a combination of leaves and seeds extracts of the Phyllanthus amarus plant were tested on the corrosion of mild steel in HCl and H_2SO_4 solutions. The results showed that the extracts functioned as strong inhibitors in both conditions, and their inhibition efficiency improved with an increase in the inhibitor concentration. Temperature studies also showed that the inhibition efficiency improved with an increase in temperature, and the activation energy decreased in the presence of the extract. The researchers proposed a mechanism of chemical adsorption of plant components onto the metal surface to explain the inhibition behavior. The Temkin isotherm was used to model the adsorption properties of the inhibitor on the surface of the metal [35].

Using gravimetric and electrochemical methods, Singh *et al.* [219] extracted natural chemicals from Piper Longum Fruit and studied their corrosion inhibition action on mild steel surfaces in a 1 M HCl environment. Results of weight loss showed that plant extract molecules' inhibition properties depend mainly on their concentration, time, and temperature. The Tafel plot showed that plant extracts could prevent mild steel corrosion through a mixed-type inhibition mechanism. Scanning electron microscopy, Fourier infrared spectroscopy, and dispersive X-ray spectroscopy techniques confirmed the protective layer formed on a mild steel sheet.

Vijayalakshmi *et al.* [220] investigated the inhibitive effect and adsorption properties of the petiole extract produced by the destructive distillation of Cocos nucifera for mild steel corrosion at 0.5 M H_2SO_4 and 1 M HCl. The constant values of Tafel β_a and β_c confirmed that the extract of coconut palm petiole acts as a mixed inhibitor. The inhibitor adsorption on a mild steel surface was spontaneous, endothermic, and consistent with Langmuir adsorption isotherm assumptions.

The corrosion inhibition action of alkaloids extracted from the Annona squamosa plant for C38 steel was demonstrated in 1 M HCl solution. PDP and AC impedance were used to test the anti-corrosion action of the extract. It was found that inhibition of corrosion efficiency increased as the concentration of plant extracts increased. PDP studies have shown that extracts from Annona squamosa are a mixed-type HCl corrodent inhibitor. The experimental results predicted that the corrosion inhibition efficiency of Annona squamosa extract is temperature-dependent and increases the corrosion activation energy. This revealed the physical adsorption of the corrosion

inhibitor molecules present in the extract on the metal surface. The Langmuir adsorption isotherm was discovered to be the preferred adsorption model, and the extract's inhibitive effect was attributed to the presence of organic compounds in it. The study also discovered that the extract was not cytotoxic [221].

2.12. Description of *L. javanica*

Common names: Fever tea (English), Lemoenbossie (Afrikaans), Umsuzwane (Zulu), Inzinziniba (Xhosa), Musukudu (Tswana), Musuzugwane (Tshivenda)

Scientific name: *L. javanica*

Domain: Eukaryota

Genus: Lippia

Class: Asteridae

Species: Javanica

Family: Verbenaceae

Order: Lamiales

Kingdom: Plantae

Phylum: Magnoliophyta

Subphylum: Magnoliopsida,

L. javanica was previously classified as a member of the Lamiaceae family [222], but it is now a Verbena or Verbenaceae family member. There are over 200 species of Lippia, ranging from shrubs and herbs to small trees [223]. *L. javanica* (f. Burm.) Spreng (Fever Tea), a species of interest for this study, is an upright, multi-stemmed, woody bush [224] with high aromatic leaves that emit lemon fragrance when compacted [222]. Lippia is distinguished among the genera by the two sepals, which are 2-4 toothed in general. Three or four petals, four stamens, and an ovary are found in these plants, which have two chambers and one ovule per chamber. The margins of the leaves on both sides are finely dense and hairy, while the flowers are creamy-white, clustered together in a thick circular spike at the tip of the stem, and the seeds are tiny brown nuts. The fruits are small, dry and located at the base of the flower clusters. When looked at in cross-section, the stems appear to have a square shape. The plant is said to be one of the most aromatic of the indigenous shrubs of South Africa [222, 225-227]. Six indigenous Lippia species have been identified in South Africa and are widespread throughout the country, except for the Western Cape [227]. They grow from the Eastern Cape northwards, extending to tropical Africa, including

Swaziland, Botswana, Malawi, Mozambique, Kenya, Tanzania, and Zambia [228]. They can be grown from seeds but can also be quickly grown from cuttings of different plant sections. They proliferate in open fields, bush and forest edges, preferably in sunny areas. Generally, the genus Lippia appears to have a clear chemical composition and pharmacological activities [227]. The most common use of Lippia species is in the treatment of respiratory disorders. Various sections (leaves, twigs, and sometimes roots) of the plant are used for multiple purposes. Infusion from its leaves is widely used in Africa as a tea to treat colds, coughs, bronchitis, and fever. It also treats conditions such as chest ailments, stomach problems, measles, flu, malaria, rashes, and headaches [226, 229-232]. Zulu people also use cold infusions of plant leaves to treat gangrenous rectitis. The Xhosa people combine weak leaf and stem infusions to treat colds, coughs and bronchial diseases. It is also helpful for managing skin conditions, scalp infections, scabies and disinfecting anthrax-infected meat. In West Africa, leaves and roots are used for fever, headache, and skin diseases. Zimbabweans use the leaves for asthma, headaches, fever, respiratory issues, and seizures. While Batswana use the plant's roots for bronchitis, sore eyes, and food poisoning. Vhavenda people use leaf infusions for respiratory and febrile diseases and prophylactics against dysentery, diarrhoea, and malaria [227, 231]. The plant contains a high concentration of volatile oils, including ipsdenone, limonene, cariophyllene, carvone, sabinene, linalool, piperiteone, p-cymenone, myrcenone, ocimenone, tagetenone [224, 233-236], some of which are used in the production of fragrances. Research by Viljoen *et al*. [224] has shown that *L. javanica* essential oil profiles are characterized by interspecies and intraspecies variations due to different metabolic production pathways. The plant is also used ritually in cleansing ceremonies when someone has been in contact with a corpse and also for protection against dogs, crocodiles, and lightning strikes [224, 227, 237]. Because there have been no reports of *L. javanica* extracts being used as anti-corrosive agents in the literature to date, it can be deduced that the plant could be used as a potential corrosion inhibitor against metal corrosion because it contains a diverse range of molecules that may act as effective inhibitors. They are non-toxic, eco-friendly, low-cost, easily accessible, and renewable. Therefore, this study aims to extract different chemical compounds from *L. javanica* leaves and test their potential to prevent the corrosion of precious everyday metals (Al, Zn, and MS) in an acidic solution.

2.13. Understanding corrosion inhibition through computational models

Experimental surface chemistry techniques can provide detailed information about the atomic bonding between the metal surface and molecules of interest [238]. However, uncovering such information can be challenging and the data obtained may not always be sufficient to fully understand the mechanisms of interaction. Atomistic simulation techniques can be useful in complementing experimental results, particularly for complex systems, to provide deeper insight into the behaviour of molecules adsorbed on the surface [239-241]. The computational simulation approach is the most widely utilised method for gaining insight into the atomistic information related to metal surface molecule interactions. Computational simulations are divided into three categories: those that utilise classical mechanics methodology, those that utilise quantum mechanics approaches, and those that combine classical mechanics approaches and quantum mechanics approaches. In the next subsections, a detailed review of methods that utilise the classical approach and quantum approaches to understanding surface molecule interactions are reviewed.

2.13.1. Molecular mechanical methods

Molecular mechanics (MM) is a computational method that is based on the laws of classical mechanics for structure and property prediction. It is characterized by a “force field” that enables the measurement of the potential energy surface for a particular arrangement of atoms of a molecule under study [242]. MM aims to find the lowest energy structure, i.e., the equilibrium geometry of the molecule. According to MM, a molecule is composed of atoms that are interconnected by various interatomic forces [243]. The bonded atoms in these molecules are modelled as balls constrained by springs (bonds). The electrons around the nucleus and the nucleus itself are treated as a perfect sphere. The force fields associated with each spring are used to calculate the molecules potential energy. A force field is a set of equations and associated constants designed to reproduce molecular geometry and the selected properties of the structures studied. It is used in MM simulations to determine the potential energy of the atomic system or the coarse-grained particles [244]. The energy of the molecule can be calculated via the mechanic’s force field as shown in Equation (11) below;

$$E_{steric} = \sum_{bonds} K_r\left(r - r_{eq}\right)^2 + \sum_{angles} K_\theta\left(\theta - \theta_{eq}\right)^2 + \sum_{dihedrals} \frac{V_n}{2}[1 + cos(n\phi - \gamma)] +$$

$$\sum_{non-bonding} \left[\frac{A_{ij}}{R_{ij}^{12}} - \frac{B_{ij}}{R_{ij}^{6}} + \frac{q_i q_j}{\varepsilon R_{ij}}\right] + \sum_{H-bonding} \left[\frac{C_{ij}}{R_{ij}^{12}} + \frac{D_{ij}}{R_{ij}^{10}}\right] \quad (11)$$

The potential functions are based on experimental parameters, which includes the force constants and equilibrium values. In a given force field, the potential energy function is the sum of each of the functions for bonding, bending of angles, torsional energies and non-bonding interactions (Figure 2.12) [242, 245].

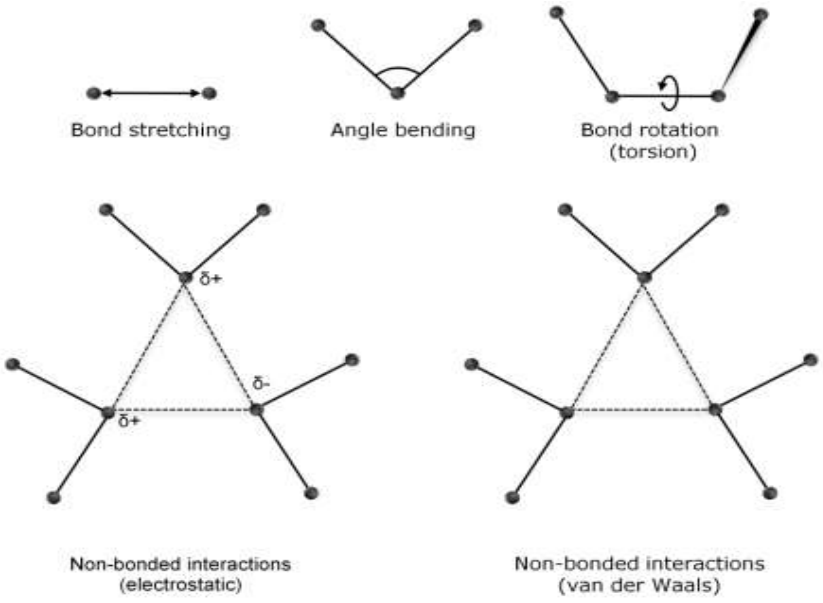

Figure 2.12: Schematic representation of the various molecular mechanical force field contributions; bending of angle, bond stretching, torsional terms, and non-bonded interactions (Figure adapted from reference [246])

The force field approach to molecular modelling provides no insight into processes involving bond-making or bond-breaking which are all chemical processes. The bond formation mechanism will be investigated in the current study and, as the force field approach does not take into account bond formation, it will not be used in this study. This can only be done by quantum mechanical (QM) or semi-empirical methods [247]. The method is also restricted by parameters of equations (i.e. it requires a different force-field for different types of atoms), and it is also not applicable for

electronic properties as it ignores the motion of electrons and only calculates the potential energy of the system as a function of nuclear position. However, its advantage is that it requires less computational time as compared to quantum mechanics and it is widely used to give accurate structures and energies for molecules [248].

2.13.2. Quantum mechanics methods

Quantum Mechanics (QM) approach is the mathematical description of electronic behaviour within a system of interest and employs the laws of quantum mechanics to predict the geometry and properties of atoms or molecules. In principle, QM can be employed to predict the characteristics of an atom or molecule reliably. QM equations have only been precisely solved for a one-electron system. A multitude of methods has been developed to estimate the solution for multiple electron systems [249]. Quantum mechanics approaches the study of chemistry by assuming that the behaviour of a molecule can be fully understood in terms of the interactions between the electronic charges within the molecule. Unlike MM, the quantum model assumes that molecules are composed of both electrons and nuclei. This allows for a more accurate description of the behaviour of molecules at the atomic level [250]. Such electronic methods are defined either by the way the wavefunction is approximated, and the Schrödinger equation is solved or by the methodology used to determine the electron probability density. The Schrödinger equation is regarded as the most fundamental equation in the field of QM. By solving the Schrödinger equation for multi-body systems, both dynamic properties such as adhesion and diffusion, and static characteristics, such as geometric configurations or vibrational frequencies can be satisfied and are vital when studying chemical reactions. However, it is difficult to solve the Schrödinger equation analytically, except for the most trivial of systems, due to the difficulty of multi-body interactions.

2.13.2.1. The Schrödinger equation

Electrons exhibit a unique property known as wave-particle duality, which means that they cannot be fully described by classical mechanics. Instead, they must be studied using the principles of quantum mechanics. The Schrödinger equation, developed in 1926 by Erwin Schrödinger, is a fundamental equation in quantum mechanics that provides a basis for determining the wavefunction of any system [251]. The time-independent Schrodinger many-body equation is particularly important for studying the behavior of multiple particles in a quantum system,

$$\hat{H}\,(r_1, r_2, r_3, \ldots, r_N)\,\psi\,(r_1, r_2, r_3, \ldots, r_N) = E\,\psi\,(r_1, r_2, r_3, \ldots, r_N) \qquad (12)$$

where r_N is the three-dimensional position vector for particle N, ψ is the many-body wavefunction, E is the total energy of the system and $\hat{H}$ is the Hamiltonian operator defined as the sum of the kinetic energy operator ($\hat{T}$) and the electron-electron interaction potential energy operator ($\hat{V}$) of the system:

$$\hat{H} = \hat{T} + \hat{V} \tag{13}$$

A key distinction of classical mechanics and quantum mechanics is that the latter is probabilistic, meaning that it can only predict the possibility of obtaining particles in a given location. According to the Schrödinger equation, the probability of finding all N particles simultaneously at positions $(r_1, r_2, r_3, \ldots, r_N)$ is given by $|\psi(r_1, r_2, r_3, \ldots, r_N)|^2$. This equation also provides the relationship between energy and nuclear coordinates, which is crucial for studying chemistry, physics, and other fields. However, most systems do not have an analytical solution to the Schrödinger equation, so approximations are often used to make it feasible to solve. When such approximations are applied to a system consisting of a set of atoms, they easily obtain their ground state energy. The Born-Oppenheimer approximation [252] is one of the most significant approximations in quantum mechanics. It allows for the separation of the nuclear and electronic motion in a molecule, enabling the Schrödinger equation solution for the electrons while treating the nuclei as fixed parameters. This is possible because the nuclei are much more massive than the electrons, making their quantum behaviour insignificant in many situations. However, solving the Schrödinger equation for multi-electron systems remains a complex task, requiring further calculations.

2.13.2.2. Hartree-Fock (HF) theory

The Hartree-Fock (HF) theory is an ab initio method for solving the Schrödinger equation in quantum mechanics. It is based on the approximation that the motion of each electron is independent of the others, allowing for a simplified treatment of the electron distribution in a given system. This approach, known as an isolated-particle model, is commonly used as a starting point for more advanced methods. The total wavefunction (ψ) in the HF theory is expressed as a combination of individual electron orbitals, making it possible to describe the wavefunction of a system with N electrons according to the following equation [170];

$$\psi_{total} = (r_1, r_2, r_3, \ldots, r_N) = \psi_1(r_1)\psi_2(r_2) \ldots\ldots\ldots (r_N) \tag{14}$$

where ψ_{total} is the total wavefunction, $\psi_1, \psi_2 \ldots \psi_N$ are the wavefunction for electrons 1, 2 … N, respectively. $r_1, r_2, \ldots r_N$ are space and spin coordinates for electrons 1, 2, …N, respectively.

One limitation of the above equation (12) is that it does not account for Pauli's exclusion principle, which states that fermions, such as electrons, cannot occupy the same quantum state [253]. This can be addressed by using a linear combination of wavefunctions to describe a system of N electrons, as shown in the following equation:

$$\psi_{total}(1,2,\ldots N) = \frac{1}{\sqrt{N!}}\sum(-1)^p \psi_1(k_1), \psi_2(k_2) \ldots\ldots\ldots \psi_N(k_N) \quad (15)$$

In the HF theory, the normalization factor $\frac{1}{\sqrt{N!}}$ ensures that the wavefunction is properly normalized, while the factor $(-1)^p$ accounts for the sign of the wavefunction. This factor ensures that the sign of the wavefunction remains unchanged for an even number of transpositions, but changes for an odd number of transpositions [254]. This property is important for properly describing systems of fermionic particles, such as electrons, which must obey Pauli's exclusion principle. A common tool used in the HF theory for expressing the linear combination of spin-orbital wavefunctions is the Slater determinant, shown in the following equation:

$$\begin{vmatrix} \psi_1(r_1) & \psi_1(r_2) & \psi_1(r_3)\ldots\ldots\ldots & \psi_1(r_N) \\ \psi_2(r_1) & \psi_2(r_2) & \psi_2(r_3)\ldots\ldots\ldots & \psi_2(r_N) \\ \psi_3(r_1) & \psi_3(r_2) & \psi_3(r_3)\ldots\ldots\ldots & \psi_3(r_N) \\ \ldots\ldots\ldots\ldots & \ldots\ldots\ldots & \ldots\ldots\ldots\ldots\ldots & \ldots\ldots\ldots \\ \psi_1(r_1) & \psi_1(r_2) & \psi_1(r_3)\ldots\ldots\ldots & \psi_1(r_N) \end{vmatrix}$$

The variational theorem is a principle of quantum mechanics that states that the energy of any trial wavefunction, or approximation of the true wavefunction of a system, is always greater than or equal to the ground-state energy of the system. This theorem provides a way to approximate the ground-state energy of a system by testing different trial wavefunctions and selecting the one that gives the lowest energy. However, a limitation of the Hartree-Fock method is that it assumes the potential of the electrons to be an average contribution from all the electrons in the system, neglecting the potential of each individual electron. This can lead to significant errors in the calculated geometric and energetic parameters of a system, compared to experimental results.

2.13.3. Semi-empirical methods

Semi-empirical methods are a type of computational approach used to approximate the solution of the Schrödinger equation in quantum mechanics. They aim to simplify and accelerate the computational cost of ab initio Hartree-Fock methods by empirical parameterization[255], while still retaining a high degree of accuracy. These methods typically focus on the valence electrons of a system, using different approximations to account for the core electrons, such as nuclear charge reduction or effective core potentials. The computational cost of evaluating two-electron integrals in quantum chemistry can be greatly reduced by making the Zero Differential Overlap (ZDO) assumption, which states that the product of two basis functions of the same type that are located on different atoms is equal to zero. This assumption allows for significant simplifications in the calculation of two-electron integrals, reducing the computational cost of these calculations. Examples of semi-empirical methods include AM1 (Austin Model 1) [256] and PM3 (Parameterized Model 3) [257]. Usually, these methods have relatively fast computational time especially for large molecules such as proteins, polymers, or transition metal compounds [247]. These semi-empirical methods differ from each other as to how they approximate Schrödinger's equation and what values are included in their set of parameters. Given that each approximation and parameter list have a limited scope, choosing a semi-empirical method that is well suited to the molecule and properties being examined becomes significant. Compared to MM, semi-empirical calculations are slightly slower, however faster than *ab initio* calculations. The weakness of semi-empirical calculations is that the outcome can be unpredictable and only a few properties can be accurately predicted if the molecules in record used to parameterize a method are considered the results can be very good. However, if the molecule in the parameterization set varies from what is already in the record, the results could be largely negative [258]. Below is a brief description of some of the semi-empirical methods.

2.13.3.1. Modified Neglect of Diatomic Overlap (MNDO)

The method is based on the neglect of differential diatomic overlap (NDDO) integral approximation, which is regarded as an advanced version of the intermediate neglect of differential overlap (INDO) method. INDO itself represents an improvement over the complete neglect of differential overlap (CNDO) approximation. The method uses spectroscopic data generated for all isolated atoms and parameterizes the one centre-two-centre integrals. The MNDO method is a semi-empirical approach to solving the Schrödinger equation, which uses a combination of s and

p-orbital basis sets. The most recent MNDO/d model extends this approach by adding d-orbital basis sets, allowing for the classification of d-block elements and hypervalent sulphur species. However, the MNDO method has some limitations, such as its inability to accurately describe hydrogen bonding and its low accuracy in predicting heats of formation [259].

2.13.3.2. Austin Model 1 (AM1)

AM1 is a semi-empirical method that is based on NDDO integral approximation. In particular, it is a generalization of the modified MNDO approximation. Dewar *et al.* [256] are responsible for designing the method. An AM1 method uses approximations to evaluate the two-electron integrals and a different expression for nuclear-nuclear core repulsions. This expression accounts for van der Waals interactions, which can introduce non-physical attractive forces. AM1 is a useful tool for characterizing hydrogen bonds, but it has a tendency to systematcally overestimate the basicity of substances or molecules [259].

2.13.3.3. Parameterized model number 3 (PM3)

PM3 is a semi-empirical method that is based on the NDDO integral approximation, just like the AM1 method. The two methods use the same equations and formalism, but there are some differences in the way they are parameterized. PM3 uses two Gaussian functions for its core repulsion function, whereas AM1 uses a variable number of functions. Additionally, the numerical values of the parameters in PM3 are optimized, whereas some of the parameters in AM1 are taken from spectroscopic measurements. These differences in the parameterization of the two methods result in slightly different predictions of molecular properties [257]. PM3 advantage resides in estimating heats of formation. Several of the drawbacks associated with PM3 include the lack of precision of molecular conformational energies, the overestimation of activation barriers and the fact that radical theories are not quite precise [260].

2.13.3.4. Parameterized method number 6 (PM6)

The PM6 method is a semi-empirical approach based on the integral approximation of the MNDO method, similar to the ZDO assumption. However, the parameters in the PM6 model are optimized to reproduce molecular properties rather than atomic properties. The PM6 model was developed to address the limitations of the MNDO/AM1/PM3 system, such as its limited coverage of main group elements and poor treatment of transition elements. The PM6 model features modifications to the core-core approximations and includes tailored parameters for

transition elements, enabling the accurate description of over 70 different elements, with a particular emphasis on biochemical compounds [261].

2.13.4. Density Functional Theory

In DFT, the solution to the Schrödinger equation is approximated by a combination of one-electron densities, similar to the HF method. This allows for the calculation of the total energy of a system without the need to solve the computationally demanding multi-electron wavefunction. Instead, the only variable required is the total electron density, $\rho(r)$, which is expressed as a function of real-space coordinates, $r = (x, y, z)$. The energy of a system in DFT ($E[\rho(r)]$) is known as a functional, because it is a function of the electron density, which is itself a function of the real-space coordinates. In DFT, the ground-state energy of a system is given by the expression [262]:

$$E[\rho(r)] = T_s + U + V_{nuc} + E_{xc}[\rho] \quad (16)$$

where T_s is the kinetic energy of the non-interacting Kohn-Sham orbitals, $E[\rho(r)]$ is ground-state energy, U is the Coulomb energy, V_{nuc} is the nuclear-electron potential, and $E_{xc}[\rho]$ is the exchange-correlation energy. The main advances of DFT over the HF method lie in the development of the expressions for T_s and $E_{xc}[\rho]$.

2.13.4.1. Exchange-correlation functional

DFT is implemented in practice using the well-received Kohn-Sham method [263, 264]. The theory measures the self-consistent electronic field structure, including the approximation of the exchange-correlation energy functional, $E_{xc}[\rho]$, for the ground state properties of the atoms. Densities must be approximated only when the $E_{xc}[\rho]$ is measured, depending on the electron spin up, $n_{\uparrow}(r)$, and spin down $n_{\downarrow}(r)$. In DFT, $E_{xc}[\rho]$, is approximated using one of two forms: the local density approximation (LDA) or the generalized gradient approximation (GGA). The LDA was widely used in the 1970s and 1980s to calculate the electronic structure of solid materials, but it has several limitations [265]. For example, it relies on the calculation of $E_{xc}[\rho]$ based solely on the value of the electron density at each point in real space, assuming a uniform electron gas. This can lead to overestimations of binding energies in molecules, and it does not accurately describe the ground state of bulk Fe. In contrast, the GGA is more accurate for molecules and bulk materials and is the focus of the current study. The outcome of the LDA results is not the exact result of the Schrödinger equation but is suitable for structures that share some of the characteristics of the uniform electron gas (e.g., simple metals). It explains the atomic structure, vibrational and elastic

properties for a broad variety of structures realistically, but energy, such as activation energy and reaction energy, are not precise enough due to the LDA overestimation of the binding energies of molecules and solids [264, 266-270]. GGA is an improvement over the LDA and uses both the local density and the local density gradient. It provides more realistic energy barriers, molecular energies and structural energy differences and increases the accuracy of measured parameters such as bond lengths and lattice spacing compared to LDA in general, but is not always more reliable than LDA [263, 266]. In the late 1980s, GGAs were popularized and represent most of the functionals currently in use. The other difference between GGAs and LDAs is that GGAs does not only account for ρ at each point in space but also considers the gradient ∇ρ. There are many GGA exchange-correlation functionals, but the functional developed by Perdew-Burke-Ernzerhof (PBE) [263] and that developed by Perdew-Wang (PW91) [271] are the two most commonly used functionals.

The GGA functional can be expressed mathematically as:

$$E_{XC}^{GGA}[n_{\uparrow}, n_{\downarrow}] = \int f(n_{\uparrow}, n_{\downarrow}, \nabla n_{\uparrow}, \nabla n_{\downarrow}) d^3r \quad (17)$$

where $n_{\uparrow}$ and $n_{\downarrow}$ are the up and down spin densities, respectively, then the GGA exchange-correlation functionals can be related to the energy per particle of a uniform electron gas $\epsilon_{xc}^{GGA}(\rho(r), \nabla\rho)$, as shown in the equation below [263, 264]:

$$E_{XC}^{GGA}[\rho(r)] = \int \rho(r)\epsilon_{xc}^{GGA}(\rho(r), \nabla\rho(r))dr \quad (18)$$

In addition to PBE and PW91, other common GGA exchange-correlation functions include [263, 264, 271], Revised Perdew-Burke-Enzerhof (RPBE), Lee-Yang-Parr (LYP), Becke-Perdew (BP) and Perdew-Wang 86 (PW86). PW91 is regarded as the first reasonable GGA functional, and is reliable for a broad range of systems, but has some difficulties, as reported by Perdew *et al* [263], as it leads to "spurious wiggles" in the exchange-correlation potential. PBE on the other hand gives an accurate explanation of the linear responses of the uniform electron gas, a smoother potential and correct behaviour under uniform scaling. For the modelling of the adsorption of molecules on the surface of metals, PBE functional is the most commonly used functional, since the functional does not report strong over-binding compared to PW91 for adsorption on metal surfaces such as platinum surfaces [272-274]. Accurate chemisorption adsorption findings have been observed with RPBE functional on metallic surfaces and also its ability to describe surface adsorbates without over-binding, but only in the absence of substantial contributions from van der Waals interactions

and in such situation lower energies are observed that what is reported experimentally [274-276]. While both PBE and RPBE are capable of predicting adsorption energies without significant over-binding, only PBE produces results for lattice and molecular bond lengths that are consistent with experimental values in the presence of strong adsorbate species such as atomic OH and O [277, 278].

2.13.4.2. Plane-waves and Blöch theorem

The simplest way to model an ideal surface or solid is to construct a unit cell that is repeated in two or three dimensions. This is even more true for metallic systems when valence electrons are delocalized, and bands are formed. The unit cell is replicated to achieve a perfect periodic system. The periodicity of the systems is the product of the plane wave basis sets used in the calculation. This means that a translation operator is being used, and that operator must communicate with the Hamiltonian systems:

$$[\hat{H}, \hat{T}] = 0 \tag{19}$$

To minimize the infinite number of one-electron wave functions to be computed to the number of electrons in the unit cell, the Blöch theorem [279] uses translation symmetry. The one-electron wave-functions can then be represented as the product of a periodic part of a cell and a wave-like part (i.e., Blöch functions). For the Hamiltonian, Blöch functions can be picked as eigenvectors, and from the crystalline orbitals, the Schrödinger equation can be solved. Thus, the Hamiltonian's eigenfunctions will include or contain the translational symmetry. A linear combination of base functions can be used to expand crystalline orbitals. Such an expansion is made possible by plane waves which are common in the fields of physics and electromagnetism. Solid-state physics employs them to model the band structure of solids. The Blöch theorem is stated as follows:

$$\psi_{\vec{k}}(\vec{r}) = u_{\vec{k}}(\vec{r})e^{i\vec{k}.\vec{r}} \tag{20}$$

where $\psi_{\vec{k}}(\vec{r})$ the Blöch wave, $\vec{r}$ is the position vector, $u_{\vec{k}}$ is the periodic Bloch function, and $\vec{k}$ is the crystal wave vector. This representation allows for the convenient mathematical treatment of crystalline systems using plane waves follows:

$$\psi_{\vec{k}}(\vec{r}) = \sum_{\vec{G}} u_{\vec{k}}(\vec{G})e^{i(\vec{k}+\vec{G}).\vec{r}} \tag{21}$$

where $\vec{G}$ is the reciprocal lattice vector. In principle, the basis set should be complete and therefore contain an infinite number of plane waves, in order to represent any possible form of $\psi_{\vec{k}}(\vec{r})$. The goal of using a complete basis set is to ensure that the wavefunction is accurately represented. However, this is not feasible in practice, so a cut-off energy is used to limit the plane waves to those with kinetic energy below a certain threshold. This allows for a more practical implementation of the basis set.

$$\frac{\hbar^2|\vec{G}+\vec{k}|^2}{2m} < E_{cut-off} \tag{22}$$

For near k-points, the modification of $\psi_{\vec{k}}(\vec{r})$ with $\vec{k}$ becomes negligible. In DFT, the study of a solid or surface is often performed using a finite number of k-points, which approximate the infinitely many $\vec{k}$ vectors in the system. The number of k-points chosen is known as the k-point sampling, and it is one of the parameters that must be carefully evaluated to ensure convergence of the calculation, typically with respect to the total energy of the system. A plane wave basis set has several advantages, including a single convergence criterion, equal treatment of all space, and the natural incorporation of periodic boundary conditions (PBC) for solid-state calculations. However, some disadvantages of using a plane wave basis set can be addressed by using an atom-centered basis set instead. For example, the number of plane waves needed is determined by the wavefunction's greatest curvature, which can be challenging for some systems. This issue can be addressed using pseudopotentials, which are commonly used in solid-state calculations.

2.13.4.3. Pseudopotentials

To provide a proper description of the core electrons of an atom it is vital to have a huge number of plane waves. This is true even when using the Blöch theorem and calculating only the plane waves with a certain kinetic energy, and pseudopotentials are used to address this issue. It is known that core electrons do not participate in chemical bonds, so if one only wants to deal with chemical processes, it is not necessary to describe them explicitly. Therefore, the pseudopotential concept is a result of the fact that bonding electrons (i.e., valence electrons) determine the chemical properties of most atoms [280]. This justifies the use of the approximation of so-called frozen-core electrons, where core electrons are calculated in the reference configuration and remain constant in other calculations. The valence electron wavefunctions are then replaced by pseudo-wave functions, which reproduce the energetic levels obtained by the measurement of all-electrons.

These pseudo-wave functions differ from the all-electron wave functions, as they are designed not to have any nodes in the inner region, near the nucleus. This results in a substantial reduction in the number of plane-waves required. There are various forms of pseudopotentials available, such as non-preservative pseudopotentials [281], US pseudopotentials [282], and PAW pseudopotentials [281, 283]. The general form of norm-conserving pseudopotentials (NCPP) is given by [280]:

$$V_{pseudo}(r) = \sum_{l,m} |Y_{lm}\rangle \, V_{lm}(r) \, \langle Y_{lm}| \tag{23}$$

where the spherical harmonics are referred to as $|Y_{lm}\rangle$ and considered to be semi-local since they are only local in the radial part but non-local in the angular part. $|Y_{lm}\rangle$ projects a one-particle wavefunction, such as one Kohn-Sham orbital, to the angular momentum labelled by l, m. The pseudopotentials are represented by $V_{lm}(r)$, and acts on the projected component.

Troullier and Martins [284] and Rappe *et al.* [285] were the first to implement the pseudopotential approach for plane-wave basis sets successfully. The pseudopotentials of the Troullier-Martins are built to offer exceptionally soft potentials. The comparison with the corresponding all-electron results between the standard pseudo-wave function and the Pseudopotential is shown in Figure 2.13 for a 3s state. In the case of the use of suitable pseudopotentials (i.e., NCPP), the cost of computing is substantially reduced due to the simultaneous maintenance of an accurate description for most systems. For instance, the use of NCPP reduces the number of electrons that would normally be accounted for during the computation of palladium (Pd) from a total of 46 electrons to 10 d electrons [286].

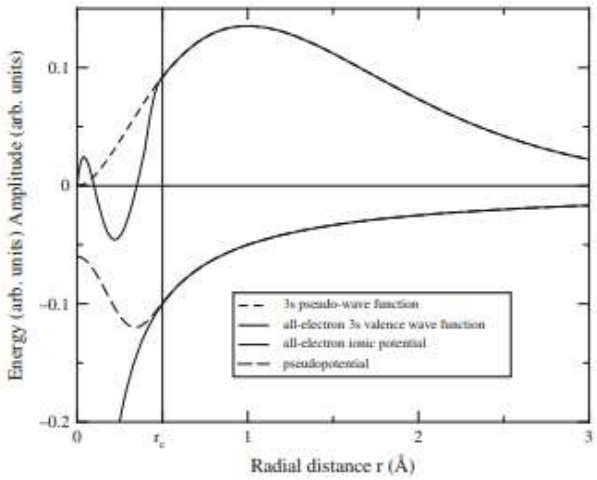

Figure 2.13: Schematic illustration of the difference between the all-electron (solid line) and the pseudo 3s (dashed line) wave function. The vertical line indicates the core radius r_c [280]

2.13.5. Basis sets

Ab initio and DFT methods use a mathematical definition of molecular orbitals called basis sets to perform calculations. Most quantum chemical computations use atom-centred basis sets to describe the electronic wave function. Such a description uses the natural localization of electrons within molecules, thereby offering a very rapid convergence (compared to the fully-delocalized plane waves) of energies and molecular properties in terms of base-set size [287, 288]. A balance needs to be struck between the size and the accuracy when selecting a base set. If the basis set used is small, it is inaccurate, and if too large, it goes beyond the capabilities of the available computers [289]. The analytical Gaussian-type orbitals (GTO) and Slater-type orbital (STO) are the most widely employed atom-centred bases. They represent the radial component of the orbital as a linear combination of the functions of Gaussian or Slater and are centralized in particular spatial locations usually, but not always, on the nuclei of a molecule [287, 288]. STO advantage is that they conform to the Schrodinger equation radial solutions for the hydrogen atom and as a consequence possess correct asymptotic solution at zero and large distances, thus providing better convergence (as opposed to the pure GTO) [287, 288]. STO mathematical expression is given as follows:

$$\phi_i(\zeta, n, l, m; r, \theta, \phi) = Nr^{n-1}e^{-\zeta\tau}Y_{lm}(\theta, \phi) \quad (24)$$

where Y_{lm} is the angular momentum part, r, θ and φ are the spherical coordinates, N is a normalization constant, and ζ is called the exponent. The n, l and m are quantum numbers: principal, angular momentum and magnetic respectively.

GTO advantage on the other hand is that it is capable of computing the two-electron integrals represented by Gaussian functions quickly analytically. This is in contrast to the STO in which numerical assessment of the two-electron integrals is required [287, 288]. GTO is usually introduced due to the computational demand required by STO and is represented by the equation:

$$g(\alpha, l, m, n; x, y, z) = Ne^{-\alpha r^2}x^l y^m z^n \quad (25)$$

where N is a normalization constant. The x, y and z are the cartesian coordinates.

An alternative to the two above-mentioned analytical basis in molecular electronic-structure computations are the numerical atomic orbitals (NAO):

$$\psi_i(r,R) = u_i(|r-R|)Y_{lm}(\Omega)/|r-R| \quad (26)$$

where r and R are the electron coordinates and the basis-set centre, $u_i(|r-R|)$ is the radial shape, and $Y_{lm}(\Omega)$ are the spherical harmonics. The radial form is tabled numerically during the basis-set construction. This offers additional flexibility in the representation of the radial component of the atomic orbitals, which contribute to a greater convergence of energies and molecular properties compared to the analytical bases. The NAO can be implemented at the DFT level [288] and the present study makes use of the DFT program referred to as DMol^3 contained in the BOVIA Materials Studio software package. The basis sets used by the DMol^3 module are denoted as minimal (MIN), double numeric (DN), double-numerical +d (DND), triple numerical polarized (TNP) and double numeric with polarization functions (DNP) basis sets. The NAO basis sets are reported to be much more accurate than the Gaussian basis set of the same scale. For example, DNP is one of the most reliable bases set in the DMol^3 module, and the literature review shows that it is comparable to the 6-31G ** Gaussian basis set [290-293], hence, the current work uses the DNP basis set.

2.13.6. Geometry optimization

Geometry optimization is required to determine the equilibrium or stable geometry of the systems under study when searching for a structure with the lowest total energy. This is done by analyzing the total energy minima along the potential energy surface (PES), which is always a very expensive computational task and whose complexity is reduced by starting with a good initial estimate of geometry. Typically, the minima are determined using the first and second derivatives, where the first derivatives find the PES stationary points, and the second derivatives allow for their characterization. Generally, the most desirable stationary point is when the second derivatives are positive. The other type of a stationary point, however, is where the second derivatives are all negative and are referred to as the “maximum”. Saddle points are also found where the second derivative is negative but positive in all other directions, as shown in Figure 2.14 [294]. These minimum points refer to the stable conformers of the minimized structures, the saddle points are transition states and the ground state structures are the global minimum.

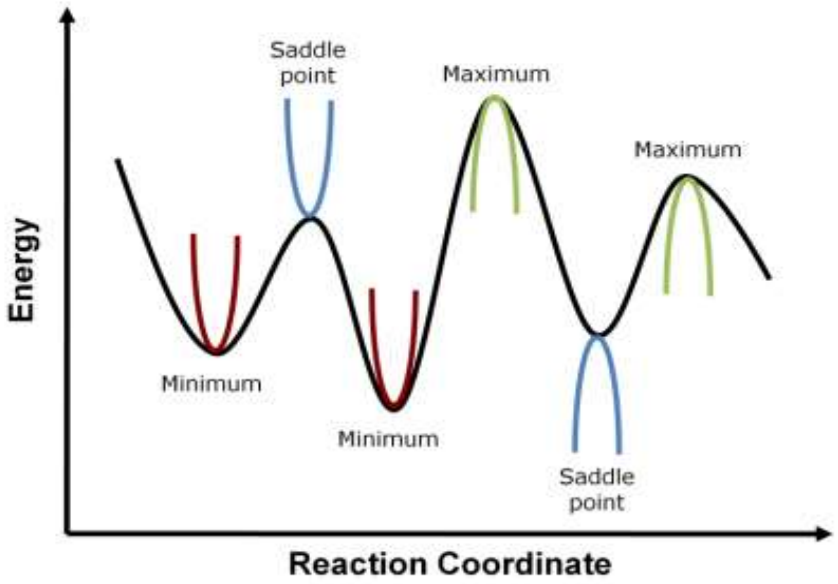

Figure 2.14: An illustration of a multidimensional PES, displaying the maxima, the minima and the saddle points [294]

There are various methods available to solve this dynamic multidimensional problem of minimization, which requires a great deal of freedom to be optimized [295]. One of these methods is the Steepest Descent method, a simple method in which the system is guided towards the minimum energy function E(x), by moving downward along the gradient measured at each point. The direction being searched is the negative direction (d) of the gradient (g), where $g_i = \frac{\delta E}{\delta X_i}$ and the step size is either fixed or reliant on the gradient magnitude. This approach will always approach a minimum, but it can be very slow to converge. The Conjugant Gradient approach is another method that can be employed to achieve convergence, but the technique is slightly more complicated. The method converges to a minimum a lot faster and operates by looking in a direction at step, n, which is a combination of the current gradient and the previous search directions, d_{n-1}.

$$d_n = -g_n + \beta_n d_{n-1} \tag{27}$$

where β is a coefficient that determines the level of mixing. This approach simply utilizes the history of the gradient to decide a better path for the next step.

Although the above methods function quite well, they can be very slow in non-linear systems. A version of the Newton-Raphson [296] method is included in most modern nuclear simulation software packages. This method converges with a very limited number of steps to the nearest stationary point, but it can be very costly to calculate. The Newton-Raphson method speed is derived from its calculation of the second derivative matrix (Hessian matrix) which allows it to predict the distance from the current geometry to the stationary point, as well as the form of the stationary point upon arrival. The minimum can be verified if all the correct values produced by the Hessian diagonalization are valid and positive (i.e., positive definite Hessian), otherwise, the stationary point with the negative eigenvalues value N is the N-th order transition state. Newton-Raphson's only big disadvantage is that it can only find local minima and that the construction and inversion of the Hessian matrix can become very expensive. Several methods can be used to estimate Hessian using gradient history so that cost-consuming analytic Hessian analysis is not measured at every step. There are various algorithms that can be used to achieve convergence with respect to a particular property, such as the geometry of the system. One effective approach is to use the Broyden-Fletcher-Goldfarb-Shanno (BFGS) minimization algorithm, which employs both first and second energy derivatives to identify the minima of the system. This leads to achieving convergence much faster than just implineting the first derivative, as is the case with the steepest descent algorithm. The choice of convergence algorithm can significantly impact the efficiency and accuracy of the calculation.

2.13.7. DFT-based DMol^3 code

The local orbital density functional (DMol^3) method is a standard, commercial and academic software package based on a numerical base set that uses the DFT method [297]. DMol^3 calculates the different characteristics of the electro-structural, optical, vibrational, cluster, molecular, crystalline solid materials and nanomaterial surfaces from the first calculation principles [298]. DMol^3 is currently a package of BIOVIA-designed Material Studio software. DMol^3 can be used in solid-based materials or low-dimensional periodicity modelling in either vacuum (gas-phase conditions; non-periodic) or three-dimensional periodic boundary conditions (PBC). DMol^3 has many functions, including single-point calculation, dynamics, restricted and unrestricted DFT calculations, geometry optimization, transition search, frequency calculation, etc. Two favourable DMol^3 functions are possibly DFT and dynamics. In general, DMol^3 permits the optimization of geometry and the calculation of different characteristics depending on the electronic configuration.

This function is useful for searching for a saddle point with and without geometric constraints. DMol^3 has increasingly been used for structural, electronic, optical and vibrational properties of metal oxide clusters [299, 300], polymers [301, 302], and biomolecules [303, 304].

2.13.8. Surface slab

The combination of DFT with plane-wave basis sets and pseudopotentials has become a popular technique for studying condensed matter systems [272, 305]. These calculations are often performed in periodic supercells to accurately represent the physical system being investigated. However, this method can also be applied to non-periodic systems, such as defects in a crystal or a crystal surface. In these cases, it is necessary to construct an appropriate periodic representation for the calculation, which requires special attention. Overall, this approach allows for the accurate and efficient calculation of the electronic structure of a wide range of condensed matter systems. Although with the bulk metal calculations periodicity is satisfied naturally, the introduction of surface results in the removal of the periodicity in one direction. Considering that the surface is normal to the z-direction, a semi-infinite vacuum and bulk region along the z-axis (orthogonal to the surface plane) will have to be addressed with periodicity being only maintained in the x-y plane [280, 286, 306]. However, with the slab approach, the semi-infinite metal is replaced by a slab that consists of two surfaces along with a finite number of layers. In doing so, a two-dimensional lattice is obtained in which periodicity is provided by the surface unit cell. The slab is repeated in the z-direction to restore the three-dimensional periodicity through the addition of a sufficiently large vacuum region between the layers as shown in Figure 2.15. This makes it possible to extend the wavefunction computationally in a plane-wave basis set, even in the case of non-periodic surface problems.

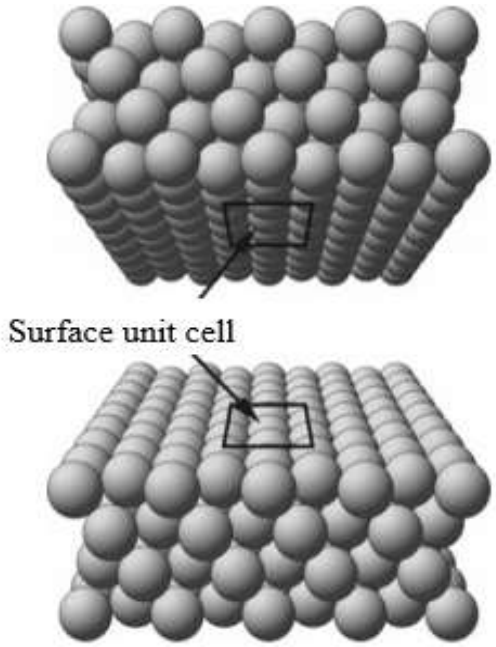

Figure 2.15: Illustration of the supercell approach to the metal surface model representing a slab comprising a finite number of layers and a large vacuum space repeated periodically [280]

The chosen vacuum must be large enough ($\Delta z \geq 10$ Å) to ensure that the slab surfaces are effectively separated to prevent non-physical interaction between the solid surfaces and/or adsorbates, which ensures that the artificial supercell is still close enough to the physical reality. Also, the slab should be thick enough to model the bulk states and any surface relaxation with precision. To ensure realistic behaviour, enough bulk and surface layers should be used, four or more layers are already ideal for convergence on low-index metal surfaces. Finally, the cell surface unit size must be chosen in such a way that it corresponds to known experimental coverage or is broad enough to exclude lateral interactions between adsorbates. In general, the bulk atomic surface coordinates are frozen, while the layers of the solid surface are allowed to relax along with any molecule adsorbed on the metal surface (Figure 2.16). This approach allows for a more accurate representation of the system under investigation.

2.13.9. Surface energy

It is preferable to use the optimized unit cell to build a slab surface during its modelling as this decreases the computation cost. Surfaces can be considered to be generated through the cleavage of an infinite solid. Such a process requires some amount of energy, or else the crystal would

cleave spontaneously. Therefore, surface energy is the amount of energy required to split a crystal along a specific surface plane into two halves.

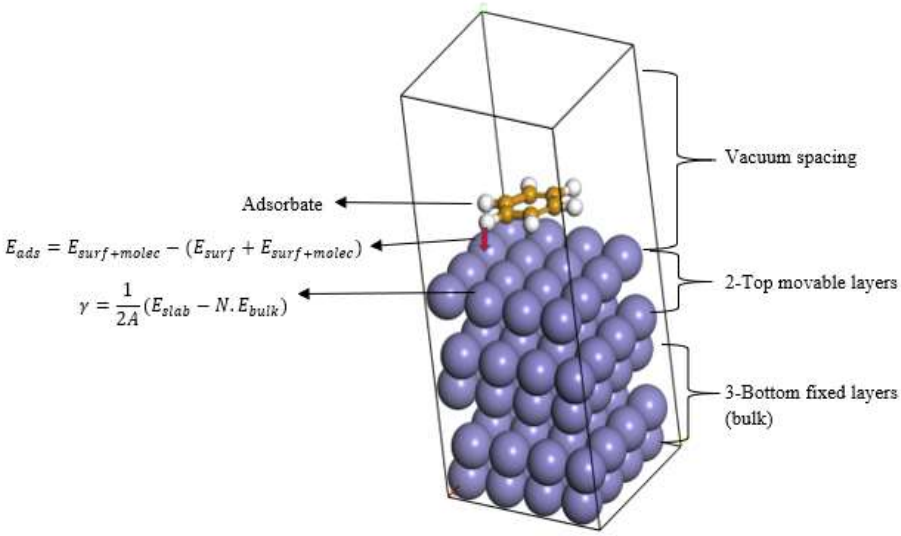

Figure 2.16: An example of a surface supercell showing the top surface, adsorbate, bulk, and vacuum layers (modified from [280])

Surface energies (γ) of a monoatomic solid at 0 K can be calculated as follows [280, 307]:

$$\gamma = \frac{1}{2A}(E_{slab} - N.E_{bulk}) \tag{28}$$

where E_{slab} denotes the total energy of the slab per supercell, N denotes the number of slab atoms, E_{bulk} denotes the total energy of the bulk material per atom, and A denotes the supercell's surface area. The 1/2 factor accounts for the formation of the two halves of the surface formed during crystal cleavage. However, this equation can give incorrect results for certain systems, such as when the slab thickness is increased [307-309]. In these cases, a correction must be made to account for the difference between the well-converged E_{bulk} and the bulk energy associated with the surface slab's lower portion. One solution is to use the Boettger equation, which calculates the slab-derived bulk energy using incrementally thicker slab energies [308]. The equation can be written as:

$$E_{bulk} = E^{i}_{slab} - E^{i-1}_{slab} = \frac{\Delta E_{slab}}{\Delta N}, \tag{29}$$

where i is the slab thickness. The Boettger method makes use of the average values of ΔE_{slab} for different i increments results to improve the method predictions.

2.13.9.1. Adsorption energy

In DFT computations of chemical reactions, the electrons of the reactants are often expected to follow their nuclei adiabatically in their respective ground state. This is true for most reactions, although there are significant exceptions such as photochemical reactions or scattering processes involving charge transfer processes [310]. Due to these constraints, the total DFT energy per supercell is obtained by a fixed set of ionic coordinates. The adsorption energies (E_{ads}) were obtained by considering the positive sign value of E_{int} ($E_{ads} = -E_{int}$) [311] calculated from total energies from DFT data according to equation 29:

$$E_{int} = E_{total} - (E_{slab} + E_{molecule}) \quad (30)$$

where E_{total} is the total energy of the slab with an adsorbed molecule, $E_{molecule}$ is the total energy of the free molecule, and E_{slab} is the total energy of the clean metal slab.

Such calculation gives an insight into the type of interaction (adsorption mechanism) between the molecule to be adsorbed and the surface of a metal.

2.13.10. Solubility prediction models

An adequate simulation model is essential for accurate theoretical justifications and experimental predictions. Such a model includes atoms and interactions that play an important role in the mechanisms studied. This requirement presupposes suitable methods for comprehensively measuring forces and molecular models. The solvent model used in the calculations is particularly important [312, 313]. Most of the chemistry occurs in solution and practically all of the biochemistry. The solvent significantly affects the solution, especially the water-like polar solvent. Precise thermodynamic modelling of solvent effects is time-consuming and often supplemented by solvent continuum modelling or other simplified methods [314]. Solubility can be defined as the amount of solute that will dissolve in a given volume of solvent at a specific temperature, pressure, and pH [315]. Solubility can be divided into four categories: kinetic, intrinsic, thermodynamic, and apparent solubility. Among these, intrinsic solubility is of most interest for most theoretical models and refers to the solubility of unionized molecules in a saturated solution [316]. In computational chemistry, solubility models can be grouped into the following categories: informatics models, explicit models, and implicit models [317]. These categories reflect the different approaches used to model and predict solubility in a given system.

2.13.10.1. Informatics

Informatics is the science of processing, storing, and mining data [317]. Models are used in this field to predict the physical properties of a molecule by comparing its structural features to those of other known molecules. The quantitative structure-property relationship (QSPR) and the quantitative structure-activity relationship (QSAR) are the most common models in this category, which use regression analyses to relate structural properties to empirical data and predict the properties of a molecule based on its structure [316-318]. QSAR is typically used to predict chemical or biological properties, while QSPR is used to predict physical properties. These models are not generally applicable, but are effective for molecules with high structural similarity to those used in the training set [316, 317]. The general solubility equation (GSE) is a common QSPR model that uses a solute's partition coefficient and melting point as input to predict its solubility. Although these models have proven successful in predicting solubility, they are not always effective for molecules that differ from those used in their training sets, and do not fully interpret physical properties in all cases [319, 320].

2.13.10.2. Explicit solvation models (ESM)

A measurement of explicit solvent examines the direct effects of a solvent on a molecule, including any changes to the solvent or the molecule's properties as a result of their interaction. This allows for a detailed examination of the physical interactions between a solvent and a molecule. ESM uses methods such as molecular dynamics, Monte Carlo [317, 321], MM, and water as the most commonly used solvent due to its well-known microscopic properties relative to other solvents. Although explicit solvent calculations are a very realistic method for determining solvent effects, they are generally associated with high computational costs and convergence problems. For example, it is important to incorporate Newton's laws of motion into all atoms by measuring all atomic forces at each measured phase during a molecular dynamics simulation. In addition, the fact that non-bound interactions are particularly difficult to quantify for long-range electrostatic interactions between atoms, and such approximations are implemented in a way that restricts the system to a finite size and limits the number of pairwise interactions to those within a specific radius [322]. The use of boundary conditions and the spherical cut-off are examples of these. These approximations, however, can result in inaccurate representations of Lennard-Jones interactions, dielectric properties, and full-charge systems, resulting in artefacts [323].

2.13.10.3. Implicit solvation models (ISM)

ISM, also known as continuous solvent models, treat solvents as a continuous isotropic medium with known permittivity. These models assume that an implicit treatment can adequately capture solvent effects by representing the solvent as a continuous medium, rather than as individual solvent molecules. This approach is less computationally demanding than explicit solvent models but lacks the structural details of explicit solvent models. The polarizable continuum model (PCM), the integral equation formalism for PCM (IEFPCM), and the conductor-like screening model are all examples of implicit solvent models (COSMO) [296, 317].

2.13.10.4. Conductor-like screening model (COSMO)

The COSMO model is an implicit solvent model that describes the behavior of a solute molecule in a conductor-like solvent [324]. The model allows for the calculation of solubility without the need to explicitly consider the solvent molecules. This can make the calculations more efficient and allow for the study of larger systems. The solute is assumed to be sufficiently polar to interact with the solvent, and the resulting uneven distribution of charges on the polar surface of the solute leads to the formation of a molecularly shaped cavity in the solvent. This cavity is created according to specific rules and the atomic radii of the solute's constituent atoms, as shown in Figure 2.17 [325]. The dipole and higher moments of the solute molecule attract the charges of the surrounding solvent molecules to neutralize the charges on the cavity surface. This results in a net surface potential of zero, and the solvent is said to have screened, solvated, and stabilized it.

The amount of screening is determined by the size of the cavity surface screening charges, with larger cavities resulting in more screening. The COSMO model is considered to be a highly effective continuum solvation model and has advanced versions, including COSMO-RS and COSMO-SAC [326, 327], which offer improved performance for real solvent systems and segment activity coefficient calculations. The surface screening charge, q^*, refers to the total potential, Φ_{tot}, generated on the cavity surface, and the potential, Φ_{sol} due to charge distribution in the solute only by [325, 328]:

$$\Phi_{tot} = 0 = \Phi_{sol} + Aq^* \quad (31)$$

where A is the Coulomb interaction matrix accounting for the probability of interactions between surface charges and is a function of the cavity geometry [329].

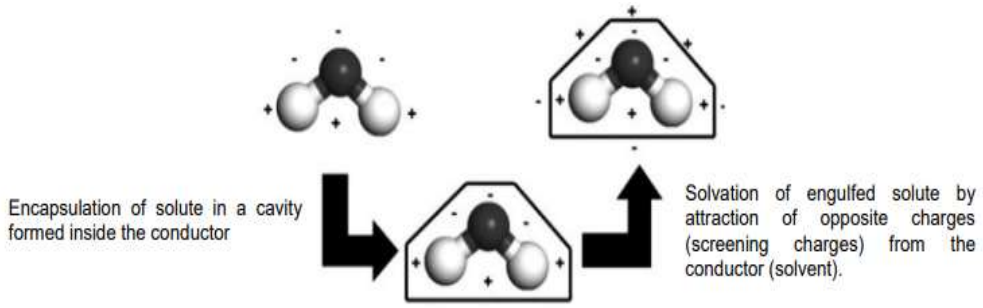

Figure 2.17: Schematic representation of the ideal solvation process with the molecule positioned in a cavity and conductive medium based on the COSMO solvation model [325]

By simply scaling the distribution of the surface charge within the conductor (σ*), the surface-charging distribution in a finite dielectric solvent can be approximated. In this way, COSMO significantly reduces computation costs with a small loss of precision [329]. The screening charge q* in the finite dielectric given by equation 32 is adjusted by a scaling factor for a dielectric system (solvent) with a finite permittivity value, Ɛ:

$$F(\varepsilon) = \frac{\varepsilon - 1}{\varepsilon + 0.5} \tag{32}$$

The COSMO approach is unique in that it uses a boundary condition called the vanishing electrostatic surface potential, which does not require an electrostatic conductive potential on cavity surfaces. Compared to the typical dielectric boundary condition employed in the polarized continuum model, this boundary condition is more straightforward and numerically stable. COSMO is effective, elegant, scalable, and less computationally intensive for liquid and solution phase calculations. Because the solute charge density optimization is carried out automatically to incorporate the screening potential into the self-consistent field cycle (SCF), the COSMO technique is also flexible. COSMO calculations are carried out by building the Ɛ to infinity, which describes solvents as a perfect conductors [317], but any solvent of interest can be identified using a finite value of the dielectric constant [328].

COSMO-RS is a version of COSMO specifically designed to estimate the thermodynamic properties of pure liquids. The model is a non-empirical approach that uses only molecular structures as input for its calculations. It consists of two basic stages: first, each variable in the system is subjected to a unimolecular quantum chemical calculation; second, a statistical thermodynamic calculation is conducted utilizing the results of the quantum chemical calculation

[326, 330, 331]. The COSMO-RS model is known for its ability to accurately predict the solubility of molecules in a wide range of solvents without the need for experimental data. This makes it a valuable tool for predicting the solubility of new or unknown molecules. Based on the surface polarization/screening charge densities of the solution's component parts and their corresponding absolute energies in the conductor from the quantum chemical COSMO calculation, COSMO-RS determines the chemical potential of the solution. COSMO-RS deals with any interaction between mixture components or solutions (especially the electrostatic and hydraulic connections) as contact between surfaces of components that can be connected to the screening charge densities σ and σ' of the contact surfaces of the respective surfaces [328, 331]. From a statistical thermodynamic perspective, a solute in a solvent can be divided into patches, and the surface charge density, σ, can be calculated for each patch using the COSMO model. The ensemble is defined based on the distribution of surface charge densities across the patches, and is known as the sigma profile, $p_s(\sigma)$, which is a plot of the corresponding probability distribution. For a solvent with n components, the sigma profile $p_s(\sigma)$ is related to the surface charge density of each component X_i by the following expression:

$$P_S(\sigma) = \frac{\sum_i^n x_i \, p^{x_i}(\sigma)}{\sum_i^n x_i} \tag{33}$$

Where x_i and $p^{x_i}(\sigma)$ are the molar fraction and sigma profile, respectively, of each ensemble component.

For example, $p_s(\sigma)$ is derived using the calculation output from the DMol^3 program after a COSMO-RS run. The presence of peaks near the zero-screening charge density (x-axis) confirms the occurrence of screening. The COSMO-RS calculations can also provide important thermodynamic properties, including hydraulic free energy, vapour pressure, and octanol-water activity coefficient.

2.14. High-performance liquid chromatography/mass spectrometry

Liquid chromatography in its high-performance (HPLC) or ultra-performance (UPLC) forms are the most widely used analytical technique for confirming the active components of extracts. It is frequently combined with detection instruments such as mass spectrometry (MS), resulting in the hyphenated technique known as LC/MS [332-336]. In LC, analytes are transported through a stationary phase column using a liquid mobile phase. In the column, the extract mixtures are

separated into their components. LC can achieve chemical separation because different compounds migrate at different rates in each column and mobile phase [337, 338]. The choice of stationary and mobile phases primarily determines the extent of the separation. The amount of water in a mobile phase determines how strongly the hydrophobic analyte is repelled and retained in the stationary phase. How the analyte is retained also depends on the chemical nature of the stationary phase. As a result, LC is a selectivity-driven technique accomplished through two interacting phases [339, 340]. The separated components can be manipulated by selecting different mobile and stationary phases [341, 342]. Following retention and separation, the separated samples are sprayed into an atmospheric pressure ion source , which converts them into gas-phase ions, with most of the eluent pumped to waste. The ions are then organized based on their mass-to-charge ratio (*m/z*). The mass analyzer can separate ions based on charge ratios or scan overall ion *m/z* values. Ions exiting the mass analyzer are counted, and the signal produced by each ion can be amplified. A high vacuum is used for all mass analysis and detection, which is achieved by combining foreline (roughing) and turbomolecular pumps [170], this is to avoid the ions to have interaction with other gases from the surrounding environment which may influence the trajectory of ions inside the mass analyzer, thereby resulting erroneous *m/z* measurement. Contact angle and surface hydrophobicity

The addition of inhibitor compounds, such as plant extracts, to the corrosive solution, can affect the wettability of surfaces such as Al, MS, and Zn. Adsorption of inhibitors to metal surfaces or corrosion products via the metal-surface-oriented hydrophilic portion of the molecule and the liquid-phase oriented hydrophobic portion results in a more hydrophobic metal surface, thereby reducing liquid water wettability [343]. The contact angle is one of the simplest ways to determine the hydrophobicity of a substance. Hydrophilic surfaces have a water contact angle of less than 90° because the liquid spreads along the surface. While highly hydrophobic surfaces have a contact angle greater than 90° [344]. Surface tension is caused by intermolecular bonds or cohesive forces between water molecules. When water comes into contact with the surface of solid surfaces such as metals, mutual attraction usually occurs. During the liquid phase (water) interaction with a solid phase (metal), adhesive forces between the material and water compete with cohesive forces in water. Water tends to spread along the material's surface when the adhesive forces are stronger than the cohesive forces. Water forms a droplet on the material surface when the adhesive surfaces are weaker than the cohesive forces. The geometry of a sessile or resting drop is commonly used

to describe wettability [345]. Figure 2.18 shows that different contact angles can be observed on the solid surface, including a small contact angle propagating along the solid surface of the material and a large contact angle observed when the liquid rolls/beads off the surface. When the surface contact angle is less than 90°, wetting is favourable, and the liquid tends to spread over a large surface area of the material/solid. A contact angle greater than 90° indicates unfavourable surface wetting, resulting in a smaller surface-liquid contact area and a compact liquid droplet. Complete wetting of the solid surface occurs when the contact angle is 0° because the placement of the water droplet on the surface results in a shallow puddle of water. For superhydrophobic surfaces, the contact angle formed by a tactile drop of water is usually greater than 150°, indicating that the contact between the drop and the solid surface is minimal [346].

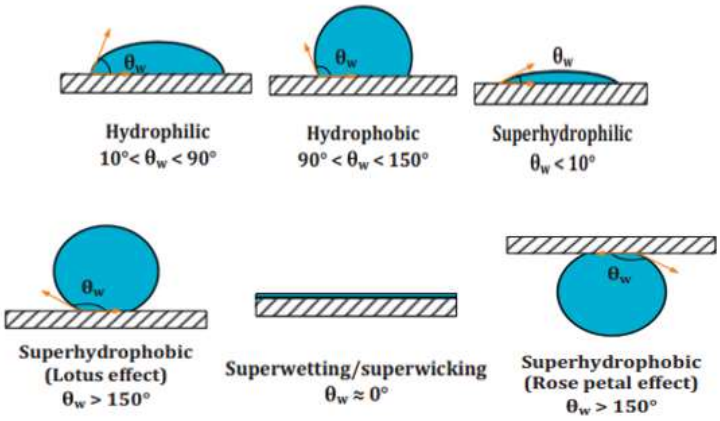

Figure 2.18: Different wetting behaviour based on the static water contact angle (θ_w) on a smooth, homogeneous solid surface, which leads to different contact angles [347]

The contact angle geometry is defined as the angle a water droplet makes at the three-phase interface were a liquid, a gas, and a solid intersect, with three different forces acting on it, as shown in Figure 2.19.

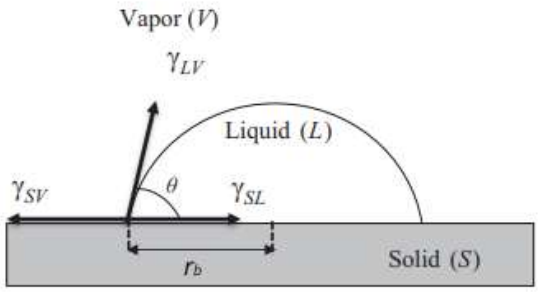

Figure 2.19: The profile of a contact angle formed by a droplet of water on the surface of a solid material showing three interfacial tensions between a solid, a droplet of water, and air [348]

The γ_{sv} is the surface tension of a solid material (i.e., surface free energy), the surface tension of the water droplet is given by γ_{lv}, while γ_{sl} is the interfacial tension between the solid material and the water droplet. The balance at the three-phase contact is described by the well-known Young´s equation below:

$$\gamma_{sv} = \gamma_{sl} + \gamma_{lv} cos\theta_Y \quad (34)$$

Young´s contact angle θ_Y is the equilibrium contact angle of wetting formed by the interfacial tensions, γ_{sv}, γ_{sl}, and γ_{lv}.

2.15. Electrochemical techniques for corrosion rate measurements

2.15.1. Open-circuit potential (OCP)

The open-circuit potential (OCP) is the value determined between the working electrode (WE) and the reference electrode (RE) when no current is transferred. The WE assume an intrinsic potential, E_{corr} (relative to a reference electrode), which is the OCP when it is in contact with a given corrosive electrolyte and is not attached to any instrumentation, as it would be 'in service.' A specimen at E_{corr} has the anodic and cathodic half-currents taking place simultaneously on its surface so that no net current can be measured. OCP can be defined as the potential at which the oxidation rates are the same as the reduction rates. Open circuit-related experiments are referred to as potentiometric studies. The potential of a metal dissolved in aquatic solutions depends on the metal's fundamental reactivity and the oxidizing strength of the aqueous solution. These potential measurements aim to determine the working electrode's potential without influencing electrochemical reactions occurring on the surface. These potential measurements must be made with respect to a stable reference electrode to compare any changes in the measured potential with changes at the sample/resolution interface. The specifications for the reference electrode are that its potential should be reproducible and stable. If an adequate reference is used, it is possible to control the working electrode's potential reproducibly and confidently relate changes in the measured potential in the test to the changes in the working electrode potential. Unbalanced or contaminated reference electrodes are unacceptable and lead to aborted or improper experiments [349]. OCP calculation can be run over some time to analyze corrosion behaviour. Information obtained through the simple measurement of OCP is only minimal, but corrosion's relative probability can be evaluated. Potential increase (i.e., a more positive OCP value) may be due to the formation of a physical barrier onto the metal surface, which reduces its susceptibility to electrochemical dissolution. However, this is not true for cases where an increased cathodic reaction rate produces a more positive OCP. The potential of a metal in a negative direction indicates that it is in an active state and may undergo dissolution. Fluctuations or noise in the OCP versus time curve suggest localized corrosion, which indicates damage and rebuilding of the passive metal surface film. OCP only provides information on the phase of corrosion and not on the rate of corrosion. Additionally, using OCP as part of another parameter, such as the addition of corrosion inhibitors, can help to understand the system's response to perturbation. In addition,

EIS and PDP depend on OCP stability, and their usefulness is questionable if OCP changes dramatically during testing.

2.15.2. Potentiodynamic polarization (PDP)

With a PDP scan, essential insights can be gained into the processes at the working electrode. This technique provides information on the corrosion rate, susceptibility to pitting, passivity, and the cathode behaviour of the electrochemical system [349]. Several parameters must be specified when configuring the instrument to perform a potentiodynamic scan. The first is the starting and ending potential to define the path of the scan. The starting point depends on the type of information requested. Anodic (scanning progressing toward positive potentials) and cathodic (scanning progressing toward negative potentials) scanning should ideally be initiated from the open circuit potential. Scans are started primarily at a slightly anodic (potentially positive) OCP during the cathodic (negative) scan. With anodic scanning, the open circuit potential is slightly cathodic. Although in many cases, these deviations from the open circuit potential do not affect the experiment, they do modify the surface of the metal. Such modifications may take the form of increased or decreased oxide thickness or deposits on the metal surface by the solution's components. The greater the difference to the open circuit potential, the greater the effect. The positioning of the final potential also depends on the type of knowledge one wishes to acquire. The scan also runs until the target current is reached, and then the scan ends. For example, if pitting is initiated for a passive metal in a chloride-containing electrolyte, the potential increases even further; thus, no useful information is generated.

Similarly, when the potential for hydrogen evolution in a cathodic scan is sufficiently negative, the increasing potential does not provide additional detail. On the other hand, when a current or potential has been reached, the scan is reversed, after which the scan moves to another endpoint. For the passive metal system, inversion of the scan allows the determination of the re-passivation potential (potential at which active pits/wells re-passivate) [350]. For reactions that are activation controlled (i.e., charges transfer-controlled reactions or mass transfer-controlled reactions occurring at a rate much lower than the limiting rate), the current density can be expressed as a function of the overpotential (η), where $\eta = E_{applied} - E_{OCP}$ as shown in equation 35:

$$\eta = \beta \log\left(\frac{i}{i_o}\right) \quad (35)$$

This term is known as the Tafel equation [351], where β is the Tafel slope, i is the applied current density (reaction current), and i_o is the current exchange density. When in equilibrium, it can be defined as equal and opposite rates for cathodic and anodized reactions. Therefore, the Tafel slope for anodic and cathodic (β_a and β_c) reactions in the open circuit can be obtained from the linear polarization curve regions, as highlighted in Figure 2.19.

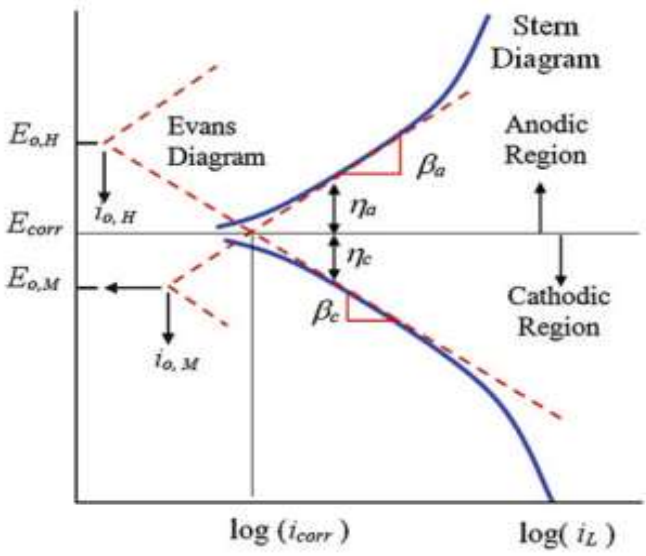

Figure 2.20: Schematic potentiodynamic polarization curve showing Tafel extrapolation [352]

When these slopes have been established, both anodic and cathodic areas can be extrapolated to an equivalent anodic and cathodic reaction rate (i.e., currents). At this point, the current density is referred to as the I_{corr}, and the potential at which it falls is the E_{corr}. The corrosion current density [350] can be combined with the Faradays law to give equation 36:

$$M = \frac{AW \times Q}{z \times F} \tag{36}$$

Where M is the mass of the material removed during the reaction, AW is the working electrode atomic weight, Q is the total charge passed (i.e., $I_{corr} \times$ time), z is the number of transmitted electrons in the reaction, and F is the Faraday constant. Most potentiodynamic polarization tests are performed on alloys instead of pure metals, and this equation must be considered in such cases.

2.15.3. Electrochemical impedance spectroscopy (EIS)

EIS is a perturbation characterization of the electrochemical dynamic process. The data obtained from EIS far exceeds the data produced by direct current (DC) or single-frequency measurement techniques. EIS can distinguish between two or more chemical reactions and detect diffusion-limited reactions (e.g., diffusion through a passive film). This makes EIS the ideal technique for studying metal corrosion and adsorption/desorption phenomena on electrode surfaces [353]. Electrical resistance is the ability of the circuit element to withstand the flow of electrical current. Ohm's law (V = IR) describes the relationship between resistance (R), electric current (I), and voltage (V) when DC is applied through a circuit. Although this relationship is well established, its implementation is restricted to an ideal less complex resistor with simplified characteristics [354]. These characteristics include that the ideal resistor obeys Ohm's Law at all currents and voltages, that its resistance value is independent of the frequency, and that the resistor's AC and voltage signals are in-phase with each other. In the real world, however, circuit elements demonstrate a dynamic behaviour as opposed to the simplistic behaviour of the ideal resistor [354]. Therefore, a more general circuit parameter called impedance (Z_ω) ($\omega = 2\pi f$ is the angular frequency of the applied AC voltage) is introduced to replace the simple concept of resistance and is observed when an AC voltage is applied to an electrochemical cell. Impedance implies the relation of the voltage with the current that demonstrates that the circuit is capable of withstanding current flow and can be represented as (V_ω/I_ω), which is the equation for Ohm's law in an AC circuit [354].

$$Z_\omega = \frac{'_\omega}{I_\omega} = \frac{V' \sin(\omega t)}{I_m \sin(\omega t - \emptyset)}, \tag{37}$$

where V_ω' is the frequency-dependent voltage while I_ω is the frequency-dependent current, and V_m and I_m represent the maximum values of V and I, respectively.

The expression for V and I in the above equation can be modified by using the complex function $j = \sqrt{-1} = e^{\left(\frac{j\pi}{2}\right)}$, to give the two equations below:

$$V = V_m e^{(j\omega t)}, \tag{38}$$

$$I = I_m e^{[j(\omega t - \emptyset)]}. \tag{39}$$

Therefore, the impedance Z_ω can be expressed as:

$$Z_\omega = \frac{V_\omega}{I_\omega} = \frac{V_m e^{(j\omega t)}}{I_m e^{[j(\omega t - \emptyset)]}} = \frac{V_m}{I_m} e^{(j\emptyset)}. \quad (40)$$

Euler's formula, $e^{(j\emptyset)} = cos(\emptyset) + jsi'(\emptyset)$, can be used to modify equation 40 to give:

$$Z_\omega = \frac{V_\cdot}{I_m} e^{(j\emptyset)} = \frac{V_m}{I_m}[cos(\emptyset) + 'jsin(\emptyset)] = Z_o[cos(\emptyset) + jsin(\emptyset)]. \quad (41)$$

The following equation can be obtained by dividing the above equation into real and imaginary parts:

$$Z_\omega = Z_o[cos(\emptyset) + jsin(\emptyset)]j, \quad (42)$$

$* Z'_{real} = Z_o \cos(\emptyset) : R(resistance)$

$* Z''_{img} = Z_o \cos(\emptyset) : C(capacitance) + L(inductance)$

Two different plots can be used to interpret the impedance spectrum based on equation (42); this includes the Nyquist and Bode plots (Figure 2.21). Using cartesian coordinates, the Nyquist plots represent the impedance's real and imaginary parts. In contrast, the Bode plots show the phase shift and magnitude changes in the applied frequency ranges. The Bode plot has excellent benefits for observing phase margins under which the system becomes unstable (violent phase or magnitude changes). It is also helpful for studying sensors, filters, and transistors in electronic devices. The Nyquist plot offers insight into possible processes or phenomena in an equivalent circuit model system [354].

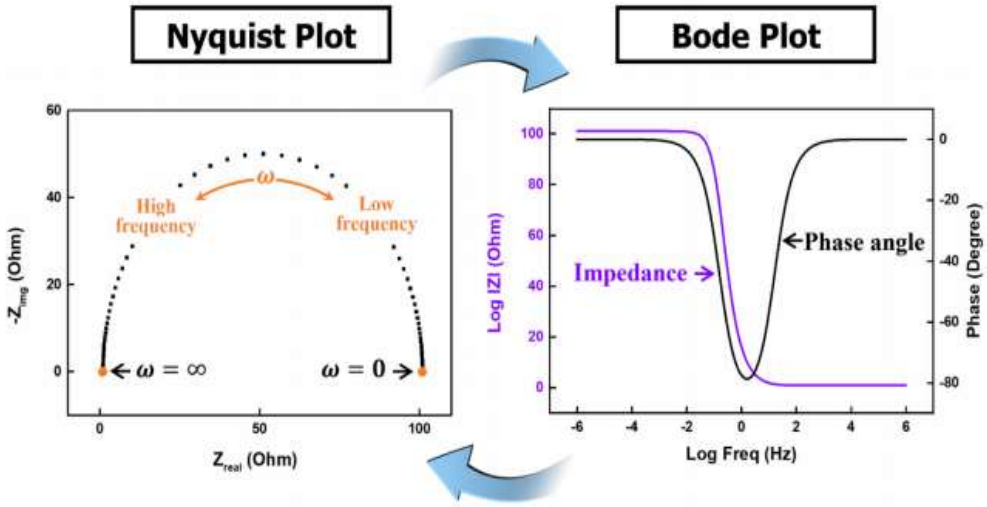

Figure 2.21: Representation of EIS by Nyquist (left) and Bode diagrams (right) [354]

CHAPTER 3

Experimental

The chapter describes the materials and methods used to define and determine the qualitative and quantitative outcomes of this work, which include the following steps:

3.1. Chemicals used

3.2. Metallic materials used

3.3. Extraction of plant material and preparation of the inhibitor solution

3.4. Corrosive and inhibitory electrolytic test environments

3.5. Chromatographic Separation

3.6. Weight loss analysis

3.7. Electrochemical experiments

3.8. FT-IR Spectrometry

3.9. Electronic Spectroscopy

3.10. Water contact angle measurement

3.11. Scanning electron microscope/energy dispersive x-ray spectroscopy (SEM/EDS) analysis

3.12. DFT adsorption energy calculation

3.1. Chemicals used

The following analytical grade chemicals or solutions were used during the extraction and corrosion studies.

- Methanol (CH_3OH), D = 0.791 g/mL at 25 °C (lit.), M = 32.04 g/mol
- Ethanol (CH_3CH_2OH), D = 0.789 g/mL at 25 °C (lit.), M = 46.07 g/mol
- Acetone (CH_3COCH_3), D = 0.791 g/mL at 25 °C (lit.), M = 58.08 g/mol
- Hydrochloric acid (HCl), D = 1.161 g/mL at 25 °C, M = 36.460 g/mol
- Distilled water

3.2. Metallic materials used

The Zn, Al, and MS samples used in this study were obtained from the University of North-West. Each film was 0.04 cm thick and mechanically pressed into 3×2 cm coupons. The coupons had a 0.375 cm radius hole through which the glass rods used to hang the metals could be inserted. The metal coupons were cleaned with a paper towel to remove any dust particles from their surfaces before being stored in the desiccator until use. The chemical composition of the MS used in the experiments is as follows: (Mn = 0.37), (Ni = 0.039), (P = 0.02), (S = 0.03), (C = 0.21), (Fe = 99.32) and (Mo = 0.01). Al and Zn coupons with an approximate composition of 99% were also used. Before electrochemical measurements, the surfaces of all specimens were polished with different grades of emery paper (Struers silicon carbide grinding discs #220 and #500) under running water and rinsed with distilled water.

3.3. Extraction of plant material and preparation of the inhibitor solution

L. javanica leaves were collected and air-dried at room temperature for about a week. The air-dried materials were blended until they were approximately the same size. About 25 g of the leaf powder was extracted in 200 mL of 100% acetone, methanol, and ethanol using Soxhlet extraction. The extraction was repeated three times with a fresh solvent extractor for three hours. The solutes were then passed through a rotary evaporator to remove the solvents used for the extraction, yielding 2.5504, 6.5709, and 5.8797 g of the crude acetone, methanol, and ethanol extracts, respectively. The procedure was repeated to extract more crude extract when necessary.

3.4. Corrosive and inhibitory electrolytic test environments

An acid-corrosive environment was used in this work to investigate the dissolution of Al, Zn, and MS coupons and the inhibitive effect of *L. javanica* plant extracts. A corrosive 1 M HCl test solution was prepared by diluting 32% analytical grade HCl with distilled water. The inhibitor/extract solutions of different concentrations (200, 400, 600, and 800 ppm) were prepared by dissolving the crude extracts in a 1 M HCl test solution and then storing them in a dark place for later use.

3.5. Chromatographic Separation

The chromatographic separation of the *L. javanica* extract was performed using a UHPLC-qTOF-MS 9030 mass spectrometer (Shimadzu, Japan) equipped with an end-capped C18-bonded column phase known as Shim-Pack Velox C18 (2.1×100 mm, 2.7 μm particle) provided by Shimadzu (South Africa). A mobile phase consisting of two solvents, solvent A (0.1% formic acid in Milli-Q water) and solvent B (methanol with 0.1% formic acid), were used. The analytes were separated chromatographically using a 53-minute gradient procedure that included the following steps: the use of 10% B for 3 minutes, a steep gradient to 60% B over 37 minutes, and a hold at 60% B for 3 minutes, another gradient to 90% B for 2 minutes, an isocratic hold at 90% B for 3 minutes and the final steps involved restoring the initial conditions (10% B) in 2 minutes and re-equilibrating the column for the next run at 10% B for 3 minutes. The MS detection parameters involved the use of negative electrospray ionization (ESI) mode, and an m/z range of 100–1000 was used. Parameters were set as follows: interface voltage of 4.0 kV, interface temperature of 300 ◦C, nebulization and dry gas flow 3 $L.min^{-1}$, DL temperature of 280 ◦C, detector voltage of 1.8 kV and the flight tube temperature at 42 ◦C. For monitoring high mass accuracy, sodium iodide was used as a calibration solution. MS1 and MS2 were generated concurrently (via data-dependent acquisition) for all ions with a m/z range between 100 and 1000 Da with an intensity threshold above 5000. Argon was used as a collision gas for the MS2 experiments, at a collision energy of 30 eV. The components contained within the crude acetone extract were determined using Sirius software (version 5.5.7) [355-363].

3.6. Weight loss analysis

The weight loss analysis technique was performed first because it is simple, accurate, and can be used to determine whether the extract has inhibitory abilities against Al, MS, and Zn corrosion.

The procedure involved conducting two series of tests, the first involved immersing weighed metal coupons in the corrosive test solution without the corrosion inhibitor. In the second series of tests, the weighed metal coupons were immersed in the corrosive test solution containing varying concentrations of the extract (200 to 800 ppm) used as a corrosion inhibitor. Approximately 60 ml of the test solution in a 100 ml beaker was used to immerse the specimens using glass rod hooks while covering their entire surface area. The technique was performed in a thermostatic water bath at 30, 40, 50, and 60 °C for 7 hours. After a 7-hour immersion time, the coupons were removed from the test solutions, scrubbed with a brush, washed with distilled water, air dried, and weighed to determine the total weight change. The final weight loss obtained was then used to measure the inhibition efficiency (%IE) and corrosion rate (C_R) using the following equations:

$$C_R = \left(\frac{\Delta W}{St}\right) \tag{43}$$

where ΔW is the weight difference of the metal coupons before and after immersion in the uninhibited and inhibited corrosive environments. S and t are the surface area of the metal samples and the immersion time in hours, respectively.

$$\%IE = \left\{\frac{C_{R(unh)} - C_{R(inh)}}{C_{R(unh)}}\right\} x100 \tag{44}$$

where $C_{R(inh)}$ and $C_{R(unh)}$ are the corrosion rate of the metals samples exposed to the inhibited and uninhibited corrosive test solutions, respectively.

3.7. Electrochemical experiments

A single-channel potentiostat/galvanostat BioLogic–SP150 with a built-in frequency response analyzer (FRA) was used to perform PDP, and EIS tests at 303 K. PDP results were analyzed using EC-Lab software, and EIS results using ZSimp software. Approximately 80 ml of the inhibited and uninhibited corrosive test solution was used in a three-electrode cell. The electrodes used in the tests included a working electrode (WE) made of Al, MS, and Zn metal coupons with a 1 cm^2 exposed surface area, a reference, and auxiliary electrodes, which were Ag/AgCl and graphite electrodes, respectively. EIS and PDP measurements were performed after the electrodes reached a steady-state potential under an open circuit (approximately 1 hour of immersion time). The potential of the electrodes was recorded each time the potential changed by 10 mV for at least 30 seconds while the potential range was set at ±10 V. The OCP results showed graphs with time as

the x-axis and voltage of the working electrodes relative to the reference electrode (E_{we} vs Ag/AgCl) as the y-axis. PDP curves were obtained by scanning from a slightly higher cathodic potential (−0.150 V/Ag/AgCl) from the OCP towards a positive potential (1.100 V/Ag/AgCl) to observe the pitting potential. The potential was changed at a scan rate of 1 mV/s for the unstirred, uninhibited, and inhibited solutions. EIS measurements were performed from the start and end frequency sampling rates from 100 kHz to 10 mHz at OCP. At OCP, EIS measurements were taken from the initial and final frequency scan rates of 100 kHz to 10 mHz. The sinus amplitude was set to 10 mV, and the potential range for adjusting the potential resolution with the system of interest was also chosen to be ±10 V for both the PDP and EIS measurements.

3.8. FT-IR Spectrometry

FT-IR spectroscopic analysis was performed on dried *L. javanica* plant extracts using a Bruker spectrum instrument to determine the extract's functional groups. The techniques were also used to characterize the corrosion products/inhibitory films formed on the surface of zinc metals in the presence and absence of the optimal concentration (800 ppm) of the extract/inhibitor solution after immersion in 1 M HCl solution for 7 hours, as well as the solutions of the two systems. At room temperature, the spectra were recorded from 4000 to 400 cm^{-1}.

3.9. Electronic Spectroscopy

Ultraviolet-visible spectroscopy (UV–vis) was performed to help elucidate the electronic absorption properties of the different *L. javanica* leaf extracts and their adsorption behaviour on the Al, MS, and Zn surfaces. As molecules, electrons are known to absorb energy from the visible to the UV range (200–780 nm), which excites them from the ground state to a higher energy state. UV analysis in this work was performed from 199.9 nm to 1000 nm using a Jenway 7305 spectrophotometer in a quartz cell at room temperature. For the experiments, the optimal concentration of the extract (800 ppm) was analyzed without performing a gravimetric analysis. To examine the stability of the extract on the Al, MS, and Zn surfaces, the three metal samples were immersed in 60 ml of 1 M HCl containing an effective concentration (800 ppm) of the *L. javanica* extract and subjected to weight loss analysis at 303 K for 7 hours. After 7 hours, test samples were drawn out, and the solution was analyzed with UV–Vis. After immersing the samples in 1 M HCl in the absence of the extracts, the solution was also examined in addition to the 1 M HCl control for comparison purposes.

3.10. Water contact angle measurement

The wettability effect of the Al, MS, and Zn coupons by *L. javanica* extracts was determined by measuring the contact angle of water on the three metal surfaces. A video contact angle system, or VCA, is commonly used to estimate contact angles. These systems tend to be expensive, but smartphones can be used as an alternative [364-366]. This study used a smartphone, pipette, macro lens, and lens mount to capture the image of a water droplet. The data were analyzed with an open-source image editor (ImageJ version 1.53), which allows the contact angle to be calculated directly from the image. The macro lens was clipped over the smartphone's camera lens after attaching it to the lens mount. In a well-lit environment, the sample was placed flush with the edge of a workbench. The pipette was used to dispense a small drop of ultrapure water (one microliter) near the leading edge of the sample. The smartphone was placed about 1-2 cm from the droplet to capture a sharp image with the highest possible resolution. The analysis was performed on a grayscale image (32-bit) with sufficient magnification to facilitate static contact angle measurement. A drop analysis plugin (Drop analysis-LBADSA) [367] was used to measure the static contact angle. The metal specimens were sanded with silicone paper, rinsed with water, and dried at room temperature before testing. After that, they were immersed in uninhibited and inhibited (800 ppm) corrosive solutions for 7 hours. After a 7-hour immersion period, the samples were scrubbed with a brush, washed with distilled water, dried, and stored in a desiccator until testing.

3.11. Scanning electron microscope/energy dispersive x-ray spectroscopy (SEM/EDS) analysis

SEM analysis was performed as an effective method to evaluate Al, MS, and Zn surface morphology before and after exposure to the corrosive medium (1 M HCl) in the presence and absence of different *L. javanica* leaf extracts. The surface morphological changes of the Al, MS, and Zn electrodes were evaluated using the Zeiss Gemini Ultra Plus FEG SEM instrument coupled with an EDS detector for elemental composition analysis. Before SEM/EDX analysis, the samples were first subjected to gravimetric analysis performed for a 7-hour immersion period at an ambient temperature of 30°C. Then, after this period, the samples were removed from the reaction environment, scrubbed with a stubble brush, washed with distilled water, washed again with ethanol, and finally dehydrated with acetone. Photographs were taken of the portion of the samples from which better data was obtained. To get a detailed picture of the effect of the extracts on the

surface morphology of the three metal samples, the morphology of the untreated polished metal samples were also analyzed, and the results were compared to the samples exposed to 1 M HCl with and without different concentrations of *L. javanica* extracts.

3.12. DFT adsorption energy calculation

Theoretical quantum chemical calculations based on DFT provided in the DMol^3 code were performed to study the adsorption geometries and energies using the Material Studio 2020 package [368]. The minimization of the adsorption geometries was acquired by the GGA/PBE/DNP level in conjunction with the COSMO-based solvent model [369-371]. To account for the core electrons and to accelerate the convergence of the self-consistent field (SCF) charge density, DFT semi-core pseudopotential (DSPP) and iterative subspace direct inversion (DIIS) were used [372]. For the sampling of the Brillouin zone, a 3×3×1 Monkhorst–Pack grid was used. To achieve geometry optimization, the convergence criteria for electronic energy, gradient, and atom displacement were set to 0.00001 Ha, 0.002 Ha/Å, and 0.005 Å, respectively. The Fe(110), Zn(110), and Al(111) slab surfaces were constructed with three layers, with the uppermost layer of metal atoms relaxed along with the adsorbates and the remaining two layers constrained. The slab was repeated in 8x8, 5x5, and 7x7 cells for the Fe, Zn, and Al surfaces, respectively, with a 30 Å separation between clean slabs to prevent contact between the sorbate and its periodic image. Figure 3.1 depicts a schematic summary of the methodology used to conduct the current study.

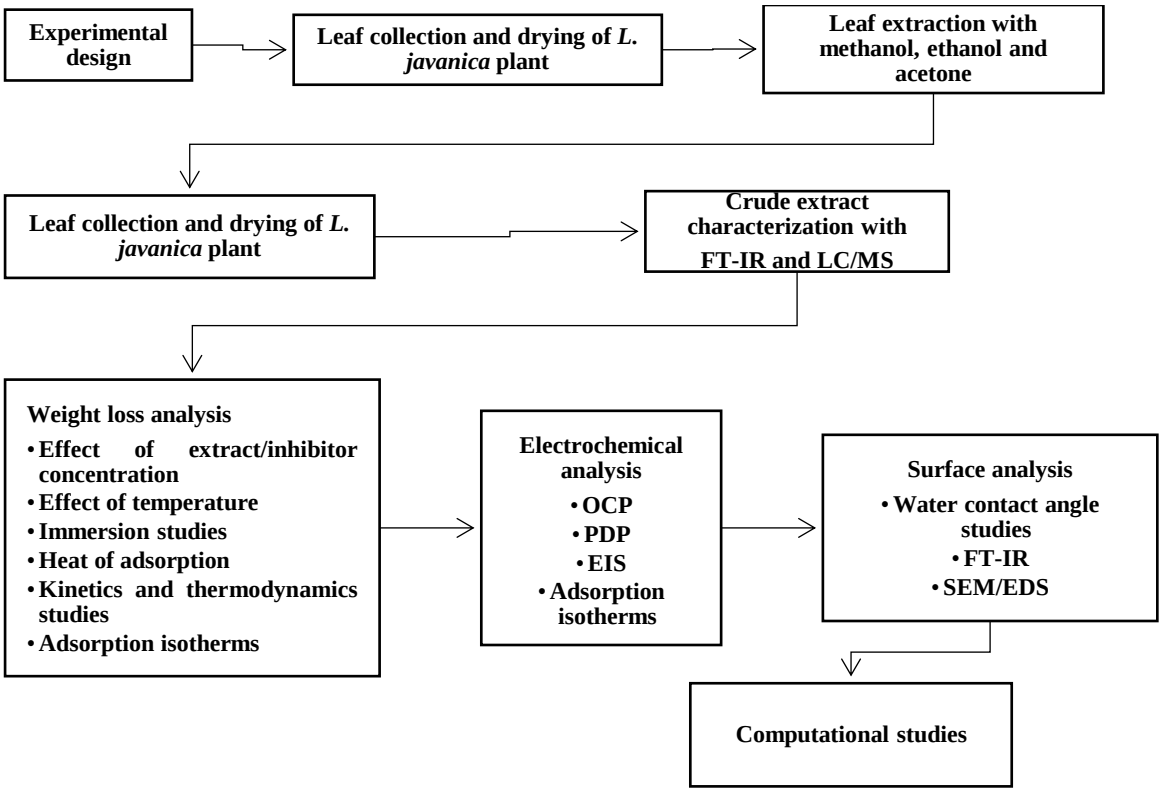

Figure 3.1: The techniques used to characterise and evaluate *L. javanica* leaf extracts as green inhibitors of Al, MS, and Zn corrosion in 1 M HCl solution are depicted schematically

CHAPTER 4

Methanolic extract results and discussions

This chapter summarises and discusses the findings from the Methanolic *L. javanica* crude leaf extract (MLJCE). The crude extracts were characterised using LC/MS and FT-IR spectroscopies. Weight loss analysis with a focus on the effect of temperature and inhibitor concentration, adsorption isotherms and thermodynamic parameters, and adsorption film analysis were all used to assess the corrosion potential of MLJCE. Electrochemical techniques were used to assess the corrosion resistance, degradation, and corrosion inhibition mechanisms of the inhibitors. Surface analysis of the extracts' protective film on metal surfaces was also performed.

4. Methanolic *L. javanica* crude leaf extract (MLJCE) as a green inhibitor for Zn, Al, and MS corrosion

4.1. HPLC analysis of MLJCE

Optimum chromatographic conditions were achieved by optimizing the mobile phase, elution program, and mass conditions. Under the conditions described in experimental section 3.4, a typical total ion current chromatogram in a negative ESI mode ($[M-H]^-$) was obtained. The figure demonstrates that the constituents in MLJCE were well separated using the developed method. Several major peaks were tentatively detected in the crude extract with diverse retention time (RT), molecular formula (MF), and molecular weight (MW) (Table 4.1). With reference to the literature, a phenylethanoid glycoside, acetonide, or, as commonly referred to, verbascoside (VBS) (RT = 7.36 minutes) [373] was identified as the major component of the extract (Figure 4.1). The primary molecular ion at m/z 623.1958 ($C_{29}H_{36}O_{15}$) for Verb ($[M-H]^-$) was observed in the mass spectrum with its proposed fragmentation pathway, as presented in Figure 4.2. The sugar skeleton of β-glucose and monosaccharides make up the bulk of the VBS molecule, as depicted in Figure 4.1, with caffeoyl rhamnose and hydroxyl phenylethyl aglycons replacing the hydroxyl groups of C4 and C1 of β-glucose, respectively.

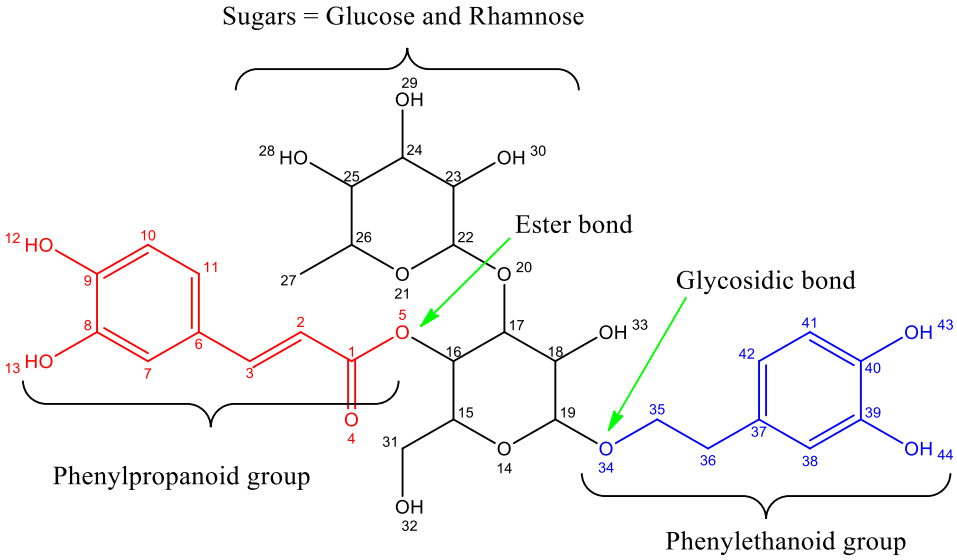

Figure 4.1: The VBS molecule's sugar groups (glucose and rhamnose) and two antioxidants (phenylpropanoid and phenylethanoid) linked through an ester and glycosidic linkages

Though VBS was identified as the major component of MLJCE, other phytochemical compounds were identified (Figure 4.3). These include compounds that contain molecules mainly composed of oxygen, nitrogen, and π-electrons. The presence of carbonyl and aromatic groups and the carbon double bonds in the structures of the identified phytochemical compounds could act as the adsorption centres on the surfaces of the three metals. The complex chemical makeup of the MLJCE suggests a possible synergistic inhibition mechanism, making it difficult to assign the inhibition mechanism for the corrosion of the three metals to an individual compound in the extract.

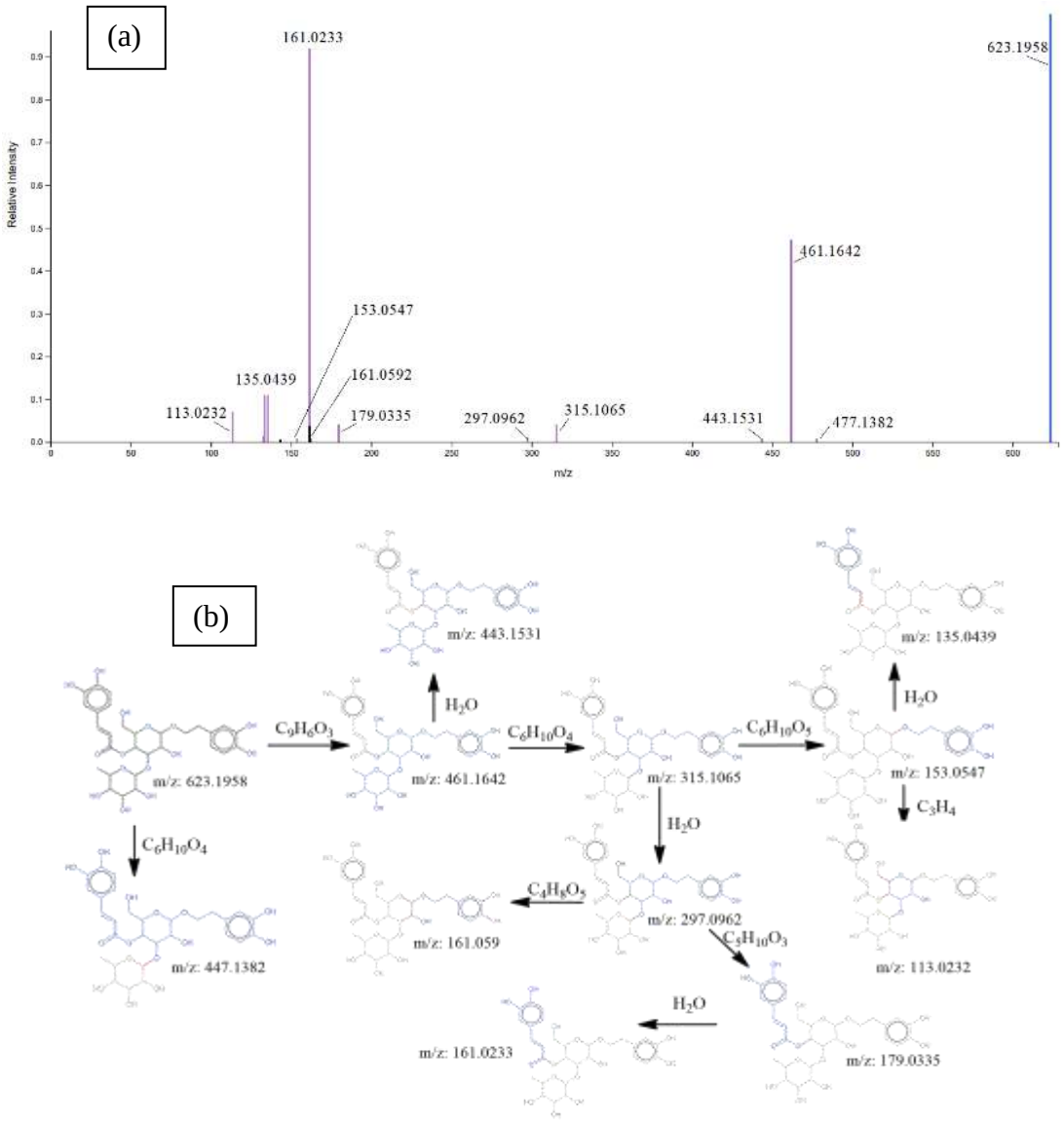

Figure 4.2: MS-ESI spectra (a) and proposed fragmentation pattern (b) of Verb

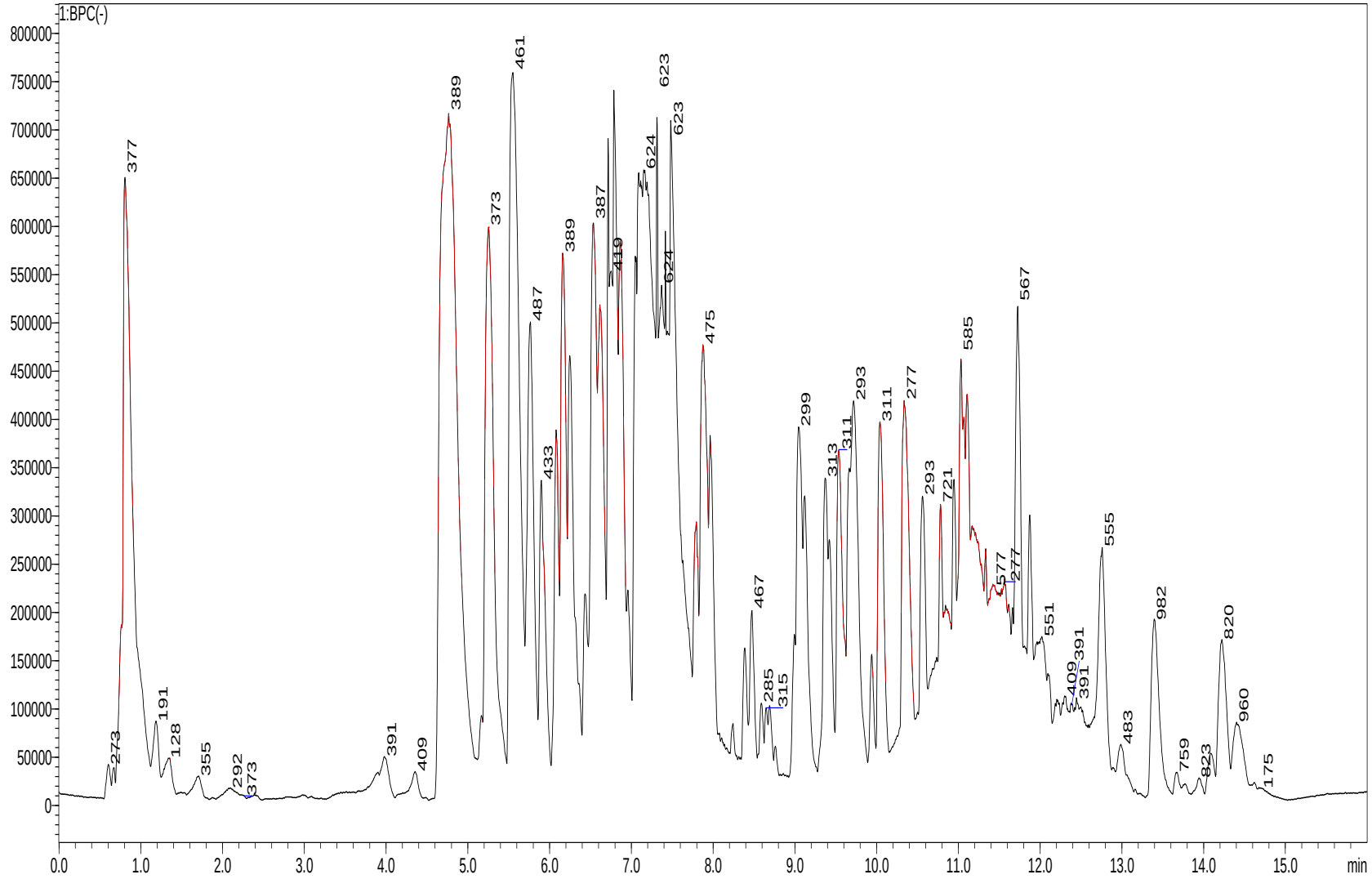

Figure 4.3: Total ion chromatograms of phytochemicals mixtures of MLJCE measured by LC/MS in negative ion mode

Table 4.1: Phytochemicals identified in the MLJCE

S.No.	RT (min)	Name of the compound	MF	MW
1	5.20	Geniposidic acid	$C_{16}H_{22}O_{10}$	373.11
2	5.45	Decaffeoyl-acteoside	$C_{20}H_{30}O_{12}$	461.17
3	6.22	(1S)-4abeta-[(6-Deoxy-alpha-L-mannopyranosyl)oxy]-1-(beta-D-glucopyranosyloxy)-7-methyl-4a,7abeta-dihydrocyclopenta[c]pyran-5(1H)-one	$C_{21}H_{30}O_{13}$	471.15
4	6.33	Glomeratose A	$C_{24}H_{34}O_{15}$	561.18
5	7.19	Verbascoside	$C_{29}H_{36}O_{15}$	623.20
6	7.57	6-O-[2-O,3-O-Diacetyl-alpha-D-glucopyranosyl]-3-O-(2-O,3-O,4-O,6-O-tetraacetyl-alpha-D-glucopyranosyl)-1-O,2-O-(ethylidene)-alpha-D-glucopyranose 4-acetate	$C_{34}H_{48}O_{23}$	805.24
7	10.78	(2S)-3-[(6-O-β-L-glucopyranosyl-β-L-galactopyranosyl)oxy]-2-hydroxypropyl (9Z,12Z,15Z)-octadeca-9,12,15-trienoate	$C_{33}H_{56}O_{14}$	675.36
8	11.88	[6-[6-[[10-(5,6-Dimethyloxan-2-yl)oxy-5-methoxy-9,16-dimethyl-2-oxo-7-(2-oxoethyl)-4-propanoyloxy-1-oxacyclohexadeca-11,13-dien-6-yl]oxy]-5-hydroxy-2-methyl-4-propan-2-yloxan-3-yl]oxy-4-hydroxy-2,4-dimethyloxan-3-yl] 3-methylbutanoate	$C_{51}H_{84}O_{16}$	951.57
9	12.25	3-((6-(dihydroxymethyl)-3,4,5-trihydroxytetrahydro-2H-pyran-2-yl)oxy)propane-1,2-diyl bis(octadeca-9,12,15-trienoate)	$C_{47}H_{74}O_{11}$	789.51
10	13.36	[(2S)-1-[(9E,12E,15E)-octadeca-9,12,15-trienoyl]oxy-3-[(2R,5R,6R)-3,4,5-trihydroxy-6-[[(2R,5R,6R)-3,4,5-trihydroxy-6-(hydroxymethyl)oxan-2-yl]oxymethyl]oxan-2-yl]oxypropan-2-yl] (6E,9E,12E)-octadeca-6,9,12-trienoate	$C_{51}H_{84}O_{15}$	935.57

4.2. FT-IR screening of phytochemicals from MLJCE

FT-IR spectroscopy is an analytical technique that can examine a wide range of samples, from pure substances to mixtures [374]. Through this technique, the characterization of the MLJCE components was achieved, and the spectrum obtained is shown in Figure 4.4. The spectrum is characterized by strong absorption bands of a saturated hydrocarbon group at 2923 $cm^{-1,}$ corresponding to a methyl group (C–H_3), and at 2853 cm^{-1}, which corresponds to a methylene group (C–H_2) [375]. These two peaks could be due to alkanes and alkyl in the extract [376]. A broad, intense absorption band was observed at around 3349 cm^{-1}, which could be due to the presence of a hydroxyl group (H–O) in alcohols [377], amine (N–H), and amide groups (N–H) in the plant extract [378]. The absorption band at about 1737 cm^{-1} corresponds to the stretching vibration of C–O. The band at 1032 cm^{-1} corresponds to the bending vibration of C–O–C groups and could indicate the presence of carbohydrates [375].

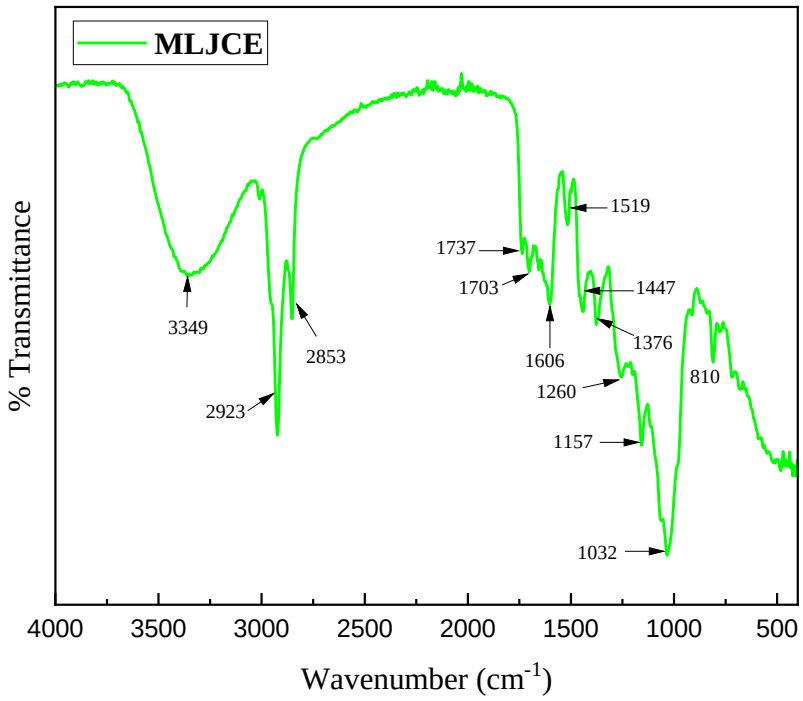

Figure 4.4: FTIR spectrum of the MLJCE used for the inhibition of Zn, MS, and Al corrosion

The peak at 1606 cm^{-1} is due to the asymmetric and symmetric vibrational stretching of the carboxyl ion (COO^{-}), indicating the presence of ester, carbonyl, and carboxylic acid groups in the MLJCE [379, 380]. The absorption bands at 1032, 1519, and 1157 cm^{-1} correspond to the skeletal stretching vibration of aromatic rings and the =C–O–C group, which could be flavonoids. The

vibrational band at 1447 cm^{-1} could be an indication that the extract contains sulfate (S=O), alkane (C–H), and aromatic (C=C) functional groups in the extract. The presence of alkyl halide (C–F), sulfonyl chloride (S=O), and nitro (N=O) groups are suggested by the band at 1376 cm^{-1} [378]. In the range of 1260 cm^{-1}, phosphoramide (P=O), amine (C–N), carboxylic acid (C–O), alkyl halide (C–F), ether (C–O) and ester (C–O) groups are indicated to also be in the extract [378]. The peak observed at around 1703 cm^{-1} is indicative of the aromatic (–C=C–) absorption band [381, 382]. The absorption bands in the 800–1750 cm^{-1} region can be attributed to the contribution of aromatic ring stretches, while those from 820 to 760 cm^{-1} result from ring vibrations [380].

4.3. Variation of the open circuit potential (OCP) with immersion period

OCP is the potential of the WE (Al, MS, and Zn) relative to the reference electrode when no current or potential is flowing in the system. A change in OCP causes polarization of the electrodes as a result of current flow near the electrode/electrolyte interface [383]. OCP measurements were performed for 1 hour to allow the system to reach a stable corrosion potential, allowing the corrosion protection of MLJCE to be evaluated for Al, MS, and Zn at different concentrations. The OCP–time plots of Zn, Al, and MS in 1 M HCl in the absence and presence of various concentrations (200 ppm to 800 ppm) of 303 K are shown in Figures 4.5–4.7. Figure 4.5 shows that the OCP for MS gradually moved positive and negative during the first 500 seconds of immersion until it reached stable values in the blank solution at around 2000 seconds. The drop in MS potential could be due to the dissolution of the native oxide that had previously formed on the MS surface due to exposure to the atmosphere.

In contrast, stabilization at around 2000 seconds could be attributed to the formation of corrosion products which protect the MS surface and reduce uniform corrosion. The OCP variations showed a similar trend at 400 and 600 ppm of MLJCE, except for 200 and 800 ppm, which showed movement in a negative direction from the start. In the presence of the extracts, the long movement of OCP in the negative direction indicates that they form a protective film on the surface of the MS electrode. The shift of the OCP values to both positive and negative values until reaching stable values indicates the occurrence of two opposing processes. One of the processes is forming a protective adsorption layer on the MS working electrode by the extracted compounds, resulting

in corrosion inhibition, while the other is the dissolution of MS due to the decreasing potential in the negative direction [384-387].

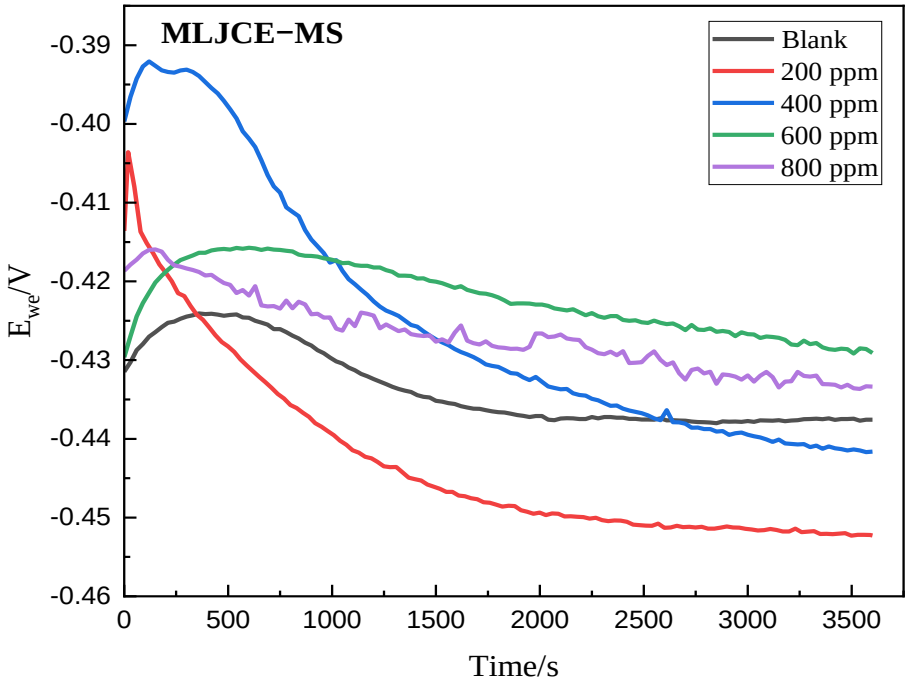

Figure 4.5: Evolution of open-circuit potential (E_{OCP}) versus exposure time for MS with and without MLJCE in 1 M HCl solution

For concentrations of 200, 400, and 800 ppm, a steady-state potential was instantly attained and maintained over time, according to the OCP curves for the Zn electrode (Figure 4.6). The potential of the Zn sample in 1 M HCl shows an abrupt change during the first few minutes of immersion in the blank solution and the presence of MLJCE at 600 ppm. An increase in potential was also observed, as well as a subsequent movement and stabilization toward positive values. Although the Zn surface initially undergoes active dissolution in the presence of 600 ppm MLJCCE, the extracts were effective in reducing the corrosion rate of zinc, as indicated by the shorter time taken to reach the stable potential in the presence of the inhibitor (170 seconds) compared to the blank (895 seconds).

The stabilized OCP for the blank was about the same as that of the MLJCE at about 0.44V. OCP can classify inhibitors as anodic, cathodic, or mixed-type based on their OCP value compared to the blank values. Anodic inhibitors have lower OCP values than the blank, while cathodic inhibitors have higher values than the blank. The inhibitor is said to be a mixture of cathodic and

anodic forms when the OCP of the blank and inhibitor are nearly equal. Because anomalies can occur, this classification is not always followed. The OCP values for Zn show that the metal experience similar OCP values for the blank and in the presence of MLJCE, indicating that the methanolic extracts have mixed-type inhibitory abilities. In the presence of the MLJCE for MS, higher and lower OCP values were obtained compared to the blank value of -0.44V. This indicates that the MLJCE contains compounds that inhibit anodic reactions and those that inhibit cathodic reactions of MS [388].

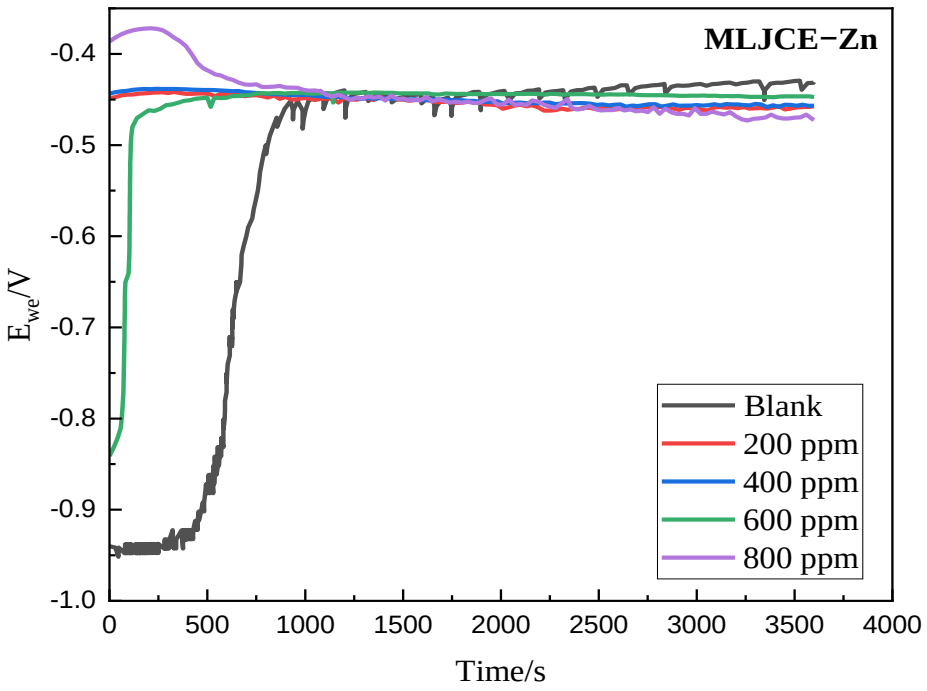

Figure 4.6: Evolution of open-circuit potential (E_{OCP}) versus exposure time for Zn with and without MLJCE in 1 M HCl solution

The OCP for Al (Figure 4.7) shows that MLJCE shifts the steady-state potential slightly positively and reaches stable values at around 500 seconds. The slight positive shift indicates that MLJCE has minimal effect on the anodic reaction. However, the OCP time plots also show that although there is a slightly positive OCP value, the steady-state MLJCE potential was more negative than the uninhibited Al sample, indicating that the extracts primarily act on the cathodic reaction [389]. The OCP curves are straight lines for both uninhibited and inhibited Al systems, indicating that the equilibrium potential has been reached in both cases [390].

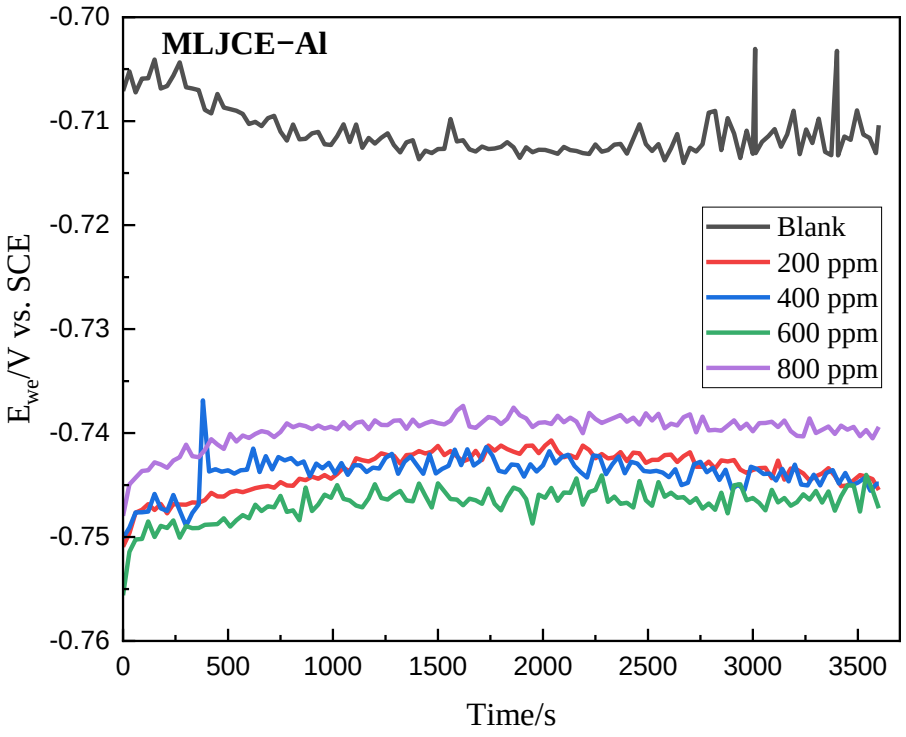

Figure 4.7: Evolution of open-circuit potential (E_{OCP}) versus exposure time for Al with and without MLJCE in 1 M HCl solution

4.4. Potentiodynamic polarization

PDP is an electrochemical technique in which the corrosion system is stimulated with a linearly changing potential, and the system's current flow's instantaneous value is recorded. PDP measurements were performed after the electrodes (Al, MS, and Zn) had reached a steady state potential under an open circuit after approximately 1 hour of immersion time. The measurements were carried out in the absence and presence of the MLJCE for Al, Zn, and MS corrosion in 1 M HCl at 303 K. PDP curves were obtained by scanning from a slightly more cathodic potential (−0.150 V/Ag/AgCl) from the OCV towards a positive potential (1.100 V/Ag/AgCl) to observe the pitting potential. PDP curves were used to determine electrochemical parameters such as the corrosion potential (E_{corr}), which is the potential at which hydrogen evolution starts, anodic and cathodic Tafel slopes (β_a, β_c), corrosion current density (I_{corr}), which is the current densities at hydrogen evolution potentials, and the PDP inhibition efficiencies (%IE_{PDP}). This was achieved by extrapolating the anodic and cathodic Tafel branches to the point where the reaction rates of the two branches are equivalent using the EC-Lab software, as shown in Figure 4.8.

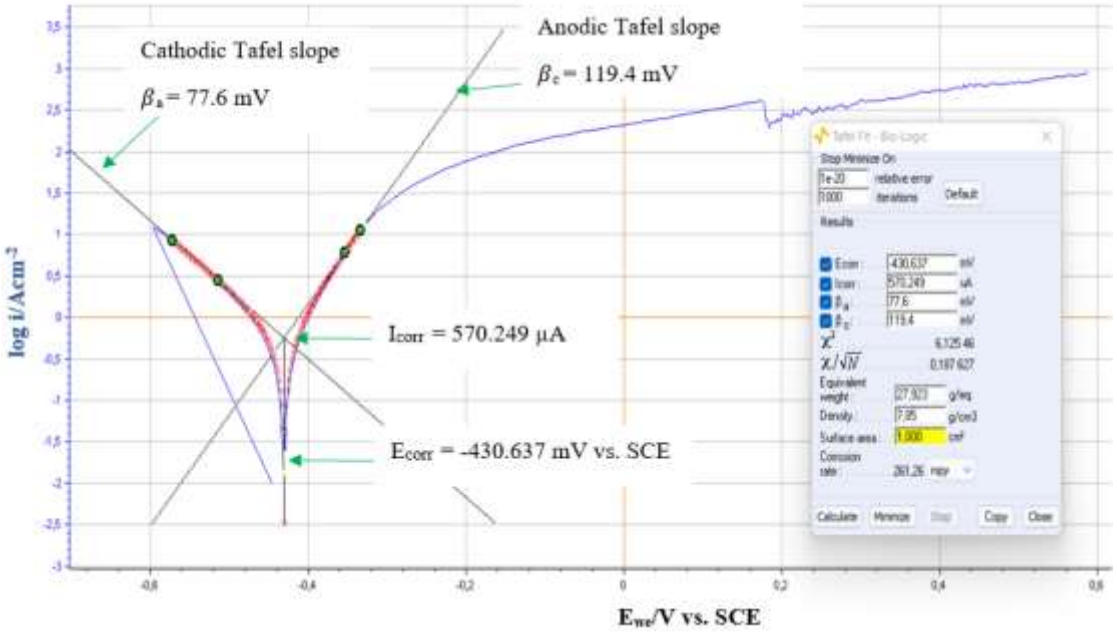

Figure 4.8: Tafel extrapolation using EC-Lab software for the uninhibited MS sample immersed in 1.0 M HCl solution

The corrosion rate (milli-inch per year, mpy) was calculated according to the equation:

$$C_R(mpy) = \frac{I_{corr} k E_W}{dA}. \quad (45)$$

Where k, A, d, and E_W are the corrosion rate constant (k = 128.800 milli-inches (amp cm year)), metal electrode surface area (1 cm^2), metal density, and metal equivalent weight (E_W) in grams/equivalent. For an alloy, the E_W can be expressed as the weighted average of its constituents. Knowledge of each constituent's oxidation state and the alloy's molecular fraction is needed to determine the E_W for an alloy. The E_W or material mass per unit load is the same as the element's atomic weight divided by its valence. As such, the E_W of Al^{3+}, $Zn^{2+,}$ and Fe^{2+} was determined as 26.982/3, 65.409/2, and 55.845/2. The $\%IE_{PDP}$ was calculated as follows:

$$IE_{PDP}(\%) = \frac{I_{corr} - I_{corr(inh)}}{I_{corr}} \times 100, \quad (46)$$

where I_{corr} and $I_{corr(inh)}$ are the corrosion current densities in the absence and presence of MLJCE.

Scanning of the PDP curves from the OCP to a slightly more cathodic potential revealed no pitting potentials or passive areas on the surface of MS or Zn in the presence or absence of MLJCE. In the absence of methanolic extracts, the lack of pitting or passive areas suggests that corrosion products formed on the Zn surface or an oxide layer formed on the surface of MS because of previous exposure to the atmosphere, protecting the two surfaces from severe attack by Cl^- ions. The absence of pitting in the presence of MLJCE could be attributed to the extract components forming a protective film on the surface. Due to its natural ability to develop a natural oxide layer (i.e., passive layer) on the surface, Al is somewhat resistant to corrosion; however, this layer can delaminate when exposed to Cl^- environments, resulting in corrosion-like pitting [391-394]. The anodic Tafel curves (Figure 4.11) in the presence and absence of MLJCE show an increase in the potential, which rises to the passivation potential (E_{pp}) point due to activation-control behaviour. Beyond that, there is a sharp decrease in corrosion current density, indicating the formation of a protective or passive film on the Al surface. In the presence of the passive layer on the Al surface, the anodic current density tends to drop to the lowest value called the passive current density (I_{pass}). The curves also point out some current fluctuations that indicate the formation of metastable pits during the measurements. The occurrence of the metastable pits suggests that the passive layer on the Al surface is locally destroyed first before the dissolution process occurs, then after the surface re-passivates again [395]. The non-uniformity of the passive area makes it difficult to determine

the exact value of I_{pass}; even in such a case, the I_{pass} values were obtained from the middle passive area and decreased from 1.7399 to 1.3376 μA.cm^{-2} with increasing concentration (200 to 600 ppm) of MLJCE. Higher I_{pass} values in the presence of the plant extracts imply a degradation of the protective adsorption layer in addition to the natural protective oxide layer [396] of the Al surface. This also suggests that the protective or passive film on the Al surface was less stable. The lack of a pronounced passive region at 800 ppm MLJCE indicates that the extract compounds successfully formed an effective protective film on the surface of Al at the maximum concentration. As such, the susceptibility of the Al surface to pitting corrosion was reduced at the highest concentration of MLJCE.

PDP data for Al and MS collected in 1 M HCl indicate a visible but small change in OCP in the presence of MLJCE concentrations compared to blank. This is consistent with other work [397, 398] and shows that MLJCE acts as a mixed-type corrosion inhibitor, implying that the extracts inhibit both the cathodic and anodic reactions of Al and MS to a similar extent [399, 400]. However, the shift in the OCP for Zn to more negative values indicates that the extracts impede the cathodic dissolution process more than the anodic. This is supported by the fact that the difference in cathodic slope between all MLJCE concentrations studied and the blank is greater than the difference in anodic slopes. The shape of the curves in the absence of inhibitors appears to be similar to the curves in the presence of MLJCE for all three samples, indicating that the presence of plant extracts in the corrosive solution does not affect the metal's corrosion mechanisms [401]. Adding MLJCE to the corrosive solution inhibits the corrosion process, as evidenced by the systematic shift of the curves to lower current densities with increasing extract concentration for all three metal systems. For instance, the corrosion current density for the blank was 570.249, 1144.688, and 5831.281 μA.cm^{-2} for MS, Zn, and Al, respectively. These values decreased in the presence of MLJCE to a low of 37.630, 36.533, and 711.796 μA.cm^{-2} at the maximum concentration for MS, Zn, and Al, respectively, indicating that the extracts formed an effective protective film on the surfaces of the metals.

The MS anodic and cathodic Tafel slopes were reduced by about a decade or more in the presence of MLJCE compared to the sample immersed in its absence. The change in corrosion potential, $\Delta E_{corr} = E_{corr} - E^{\circ}_{corr}$, where E°_{corr} is the potential of the uninhibited system, can be used to indicate the inhibitor's electrochemical form [402]. According to the literature [403, 404], if E_{corr}

exceeds ±85 mV, the inhibitor prevents the metal from corroding by controlling either the anodic or cathodic reactions. On the other hand, when E_{corr} < ±85 mV, the inhibitor is considered to prevent both the anodic and cathodic reactions and is referred to as a mixed-type corrosion inhibitor. In the presence of MLJCE, the maximum shift in E_{corr} relative to the blank is 8, 16, and 50 mV for Al, MS, and Zn, respectively. Since in the presence of MLJCE, E_{corr} values are lower than 85 mV with respect to the blank solution, it is assumed that the inhibitor acts against Al, MS, and Zn corrosion through a mixed mode inhibition mechanism involving both the anodic dissolution and reduction of hydrogen ions on the metals [405]. Compared to the values of the uninhibited corrosive system, the E_{corr} values for MS showed a potential increase in the positive direction in most cases of the extract concentration. This indicates that the extracts, although mixed-type, showed predominantly anodic behaviour [406, 407].

In contrast, the E_{corr} values for the Al and Zn surface showed a movement in the negative direction compared to the values of the uninhibited corrosive system in the presence of MLJCE, indicating that the extracts mainly controlled the cathodic reaction [408]. Tafel slope values can also be used to support the inference derived from the E_{corr} shift in classifying the inhibitory effects of an extract or inhibitor as cathodic, anodic, or mixed type. The β_a and β_c values from the current work (Table 4.2) show that these values vary with inhibitor concentration. Although there is no clear trend in the variation of the Tafel slopes with MLJCE concentration, the results show that adding the extracts into the corrosive solution causes changes in the values of both β_a and β_c, indicating that the extracts can be classified as mixed-type corrosion inhibitors [33].

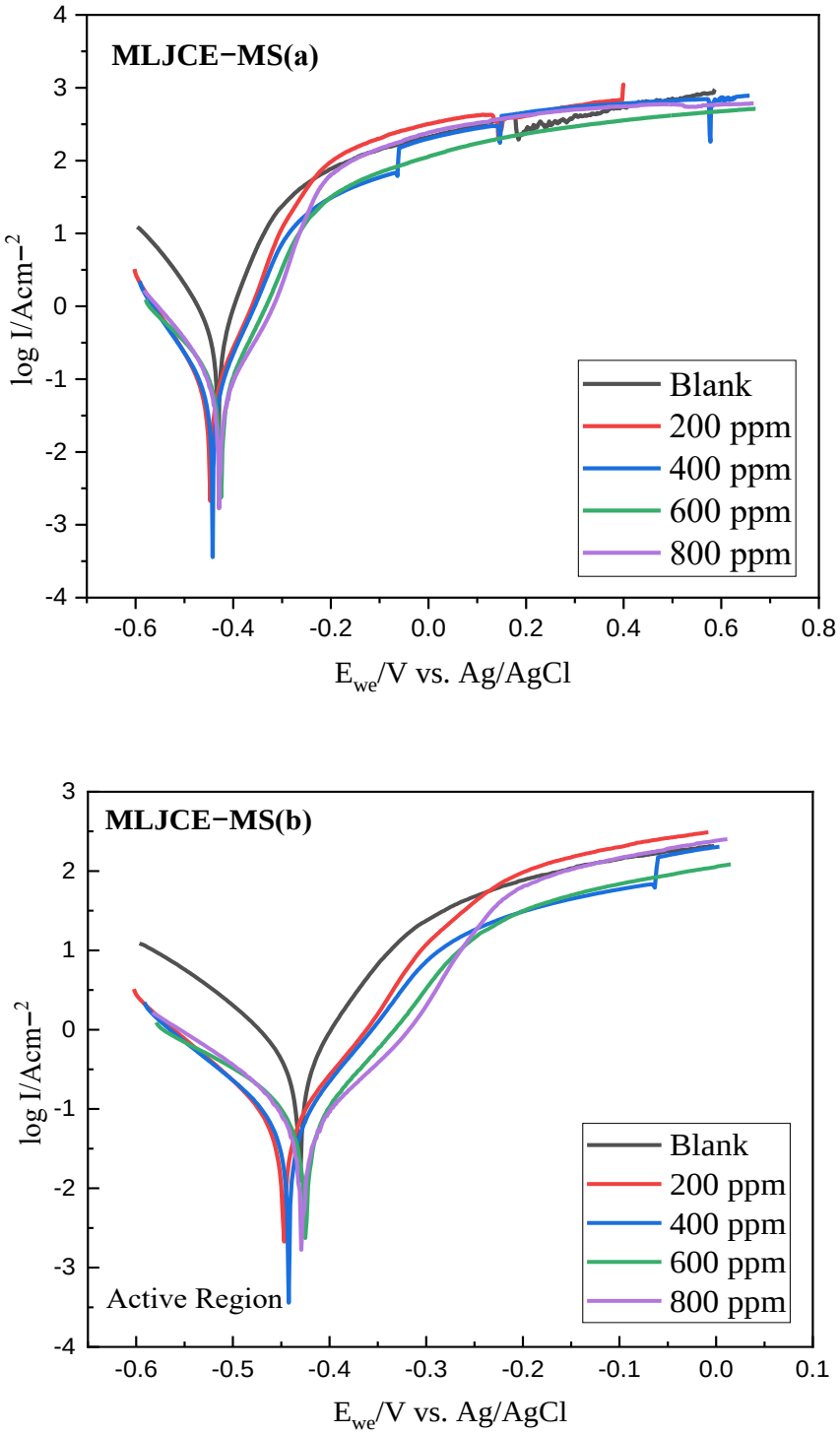

Figure 4.9: Tafel PDP curves for MS dissolution in 1 M HCl with and without different concentrations of MLJCE to observe pitting (a). The extrapolated (b) active area at 303 K, respectively

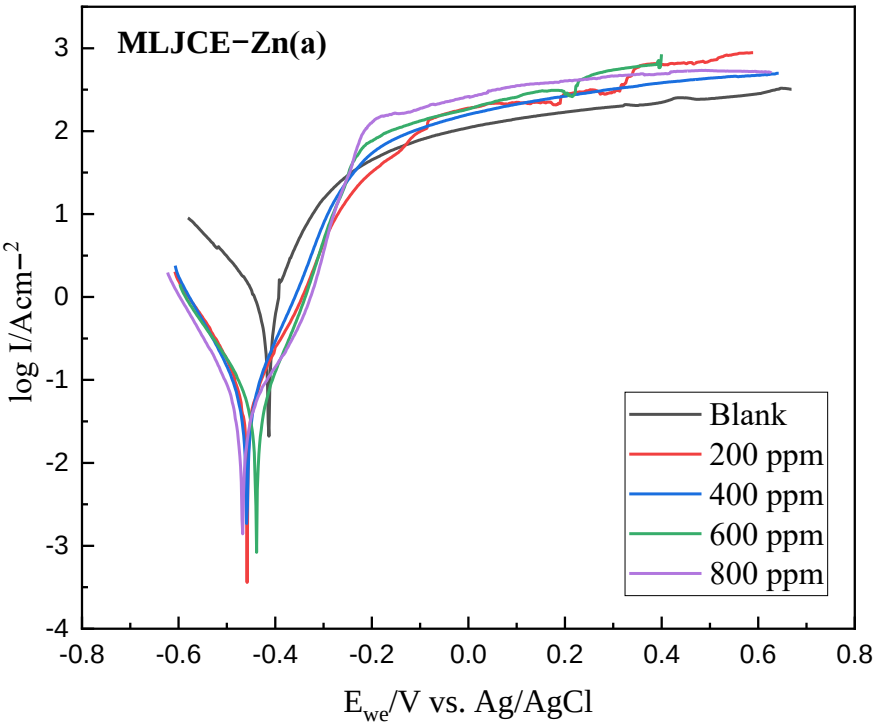

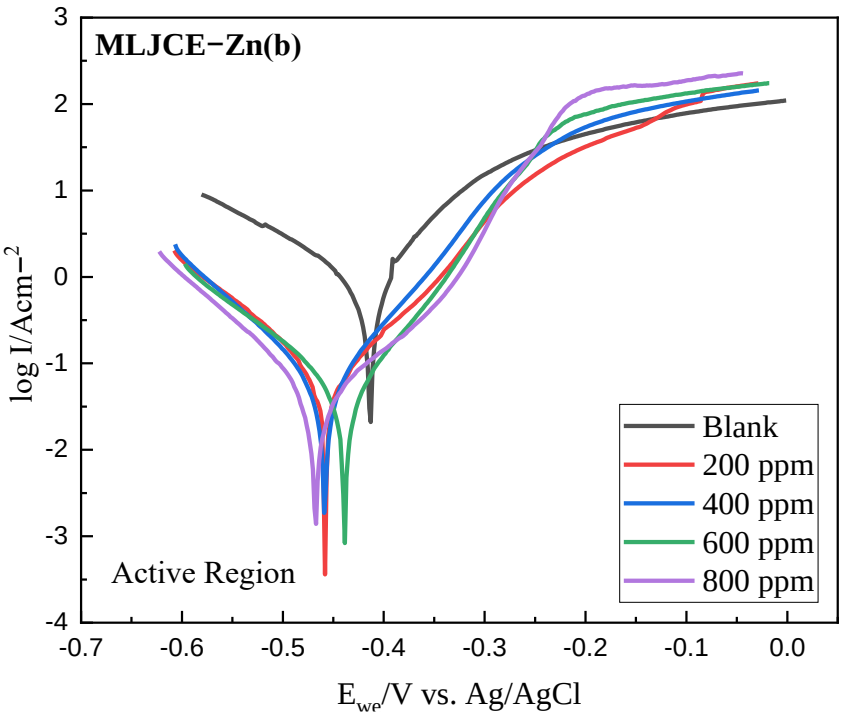

Figure 4.10: Tafel PDP curves for Zn dissolution in 1 M HCl with and without different concentrations of MLJCE to observe pitting (a). The extrapolated (b) active area at 303 K, respectively

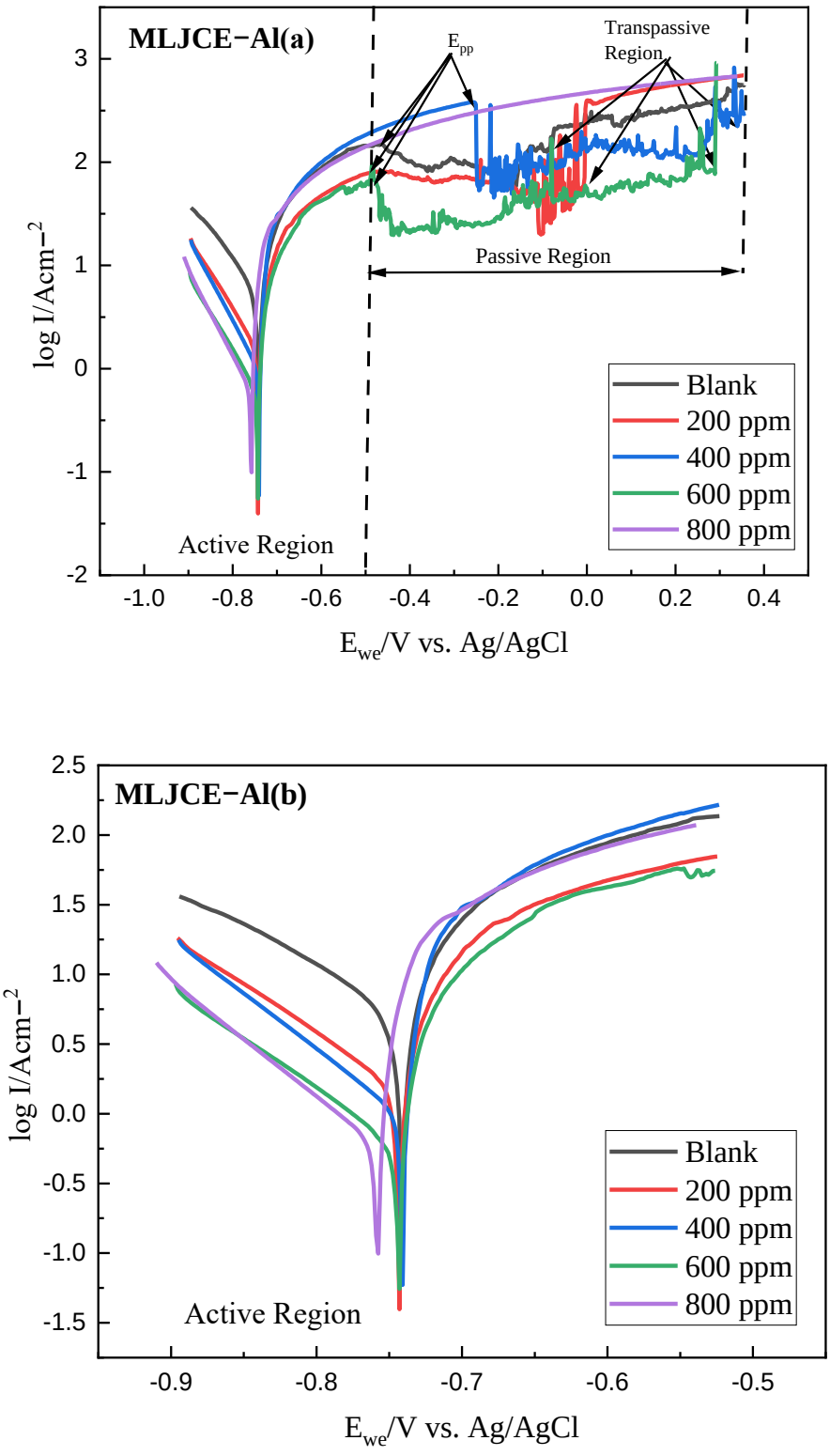

Figure 4.11: Tafel PDP curves for Al dissolution in 1 M HCl with and without different concentrations of MLJCE to observe pitting (a). The extrapolated (b) active area at 303 K, respectively

Table 4.2: Polarization electrochemical parameters of Al, Zn and MS after 1-hour immersion at 303 K in 1 M HCl with and without different concentrations of MLJCE

Metal	Conc. of MLJCE (ppm)	C_R (mpy)	E_{corr} (mV vs Ag/AgCl)	β_a (mV.dec^{-1})	β_c (mV.dec^{-1})	I_{pass} (µA.cm^{-2})	I_{corr} (µA.cm^{-2})	%IE_{PDP}
MS	**Blank**	261.26	−430.637	77.6	119.4	−	570.249	−
	200	26.9287	−447.343	65.7	91.4	−	58.777	89.69
	400	24.2605	−438.539	64.3	98.5	−	52.953	90.71
	600	23.3135	−421.667	67.7	90.5	−	50.886	91.08
	800	17.2402	−425.230	65.9	69.5	−	37.630	93.40
Zn	**Blank**	675.025	−413.435	96.8	196.8	−	1144.688	−
	200	44.8816	−457.905	88.7	107.5	−	76.109	93.35
	400	31.9135	−458.490	75.3	92.8	−	54.118	95.27
	600	28.3818	−435.418	67.3	114.8	−	48.129	95.80
	800	21.5436	−463.541	107.3	93.3	−	36.533	96.84
Al	**Blank**	2492.66	−740.497	64.6	183.6	1.7399	5831.281	−
	200	660.105	−742.190	32.6	144.7	1.8380	1544.235	73.52
	400	476.918	−741.174	17.0	136.7	2.1007	1115.692	80.87
	600	324.027	−743.678	27.5	167.1	1.3376	758.023	87.00
	800	304.267	−758.395	19.2	133.4	−	711.796	87.79

4.5. Electrochemical impedance spectroscopy (EIS)

Al, MS, and Zn electrodes were immersed in the corrosive environment (1 M HCl) with and without varying concentrations (200 to 800 ppm) of MLJCE for 1 hour before EIS measurements were made. The measurements were performed to quantitatively assess the inhibitors' corrosion resistance, degradation, and corrosion inhibition mechanisms. Figures 4.12−4.14 shows the development of the impedance spectra based on Nyquist and Bode phase diagrams. The Nyquist and Bode diagrams for the uninhibited and inhibited systems show comparable behaviour, suggesting that the MLJCE has no significant effect on the Al, MS, and Zn corrosion mechanism. The impedance of the Nyquist curves in the low-frequency range in the presence of MLJCE is greater for all three metals than that of the uninhibited system. It increases with increasing concentration of the MLJCE. The increase in the diameter of the Nyquist semicircles indicates that the metal/electrolyte system impedance increases while the corrosion rate in the presence of MLJCEs decreases. The increase in semicircle diameter with inhibitor concentration is associated with an increase in charge transfer resistance (R_{ct}) through the metal–solution interface [409]. The Nyquist plots for MS and Zn are represented by imperfect semicircular loops whose centres appear below the impedance axis due to unavoidable frequency dispersion effects inherent in solid metal electrodes [410-412]. The behaviour could also be explained by surface inhomogeneity caused by MLJCE adsorption on the Zn and MS surfaces and by the microscopic surface roughness of the metals [413].

The Al-Nyquist plots in Figure 4.14 show the capacitive loops in the higher frequency range and an inductive loop in the lower frequency range. The presence of indicative loops in the low-frequency range may result from the appearance of adsorbed intermediates on the Al surface. Therefore, adsorbed intermediates such as Al^{+} and Al^{3+} ions could be involved in the Al dissolution process [414]. Brett [415] suggested that high-frequency capacitive loops are involved in the charge transfer process due to the oxide layer formed on the Al surface. The oxide layer results from the formation of Al^{+} ions at the metal/oxide interface and their migration through the oxide/solution interface, where they are oxidized to Al^{3+} ions. In addition, OH^{-} or O^{2-} ions are formed at the oxide/solution interface. Capacitive loops represent all of these processes. The ionic conduction occurring in the oxide film and the dielectric properties suggest that the oxide film acts as a parallel circuit of a resistor or a capacitor [416]. The induction loop observed in the low-frequency range may result from the surface relaxation of oxide film species [416]. The roughness

and inhomogeneity of the electrode surface can also contribute to the imperfect Nyquist curves that characterize capacitive Al loops [417]. For all three metals, the depression in these loops indicates a departure from an ideal capacitor [417]. To account for deviations from ideal behaviour, a constant-phase element (CPE) was used in the mathematical analysis of impedance plots instead of a real capacitor to compensate for the depression of the Al, MS, and Zn capacitive loops [418].

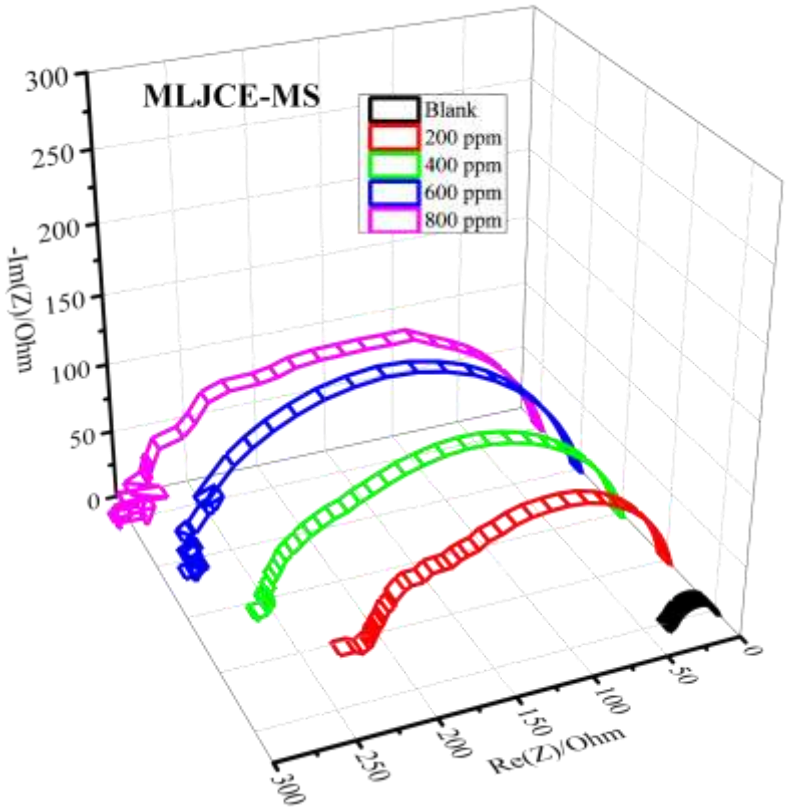

Figure 4.12: MS Nyquist plots in 1 M HCl solution with and without MLJCE at various concentrations at 303 K

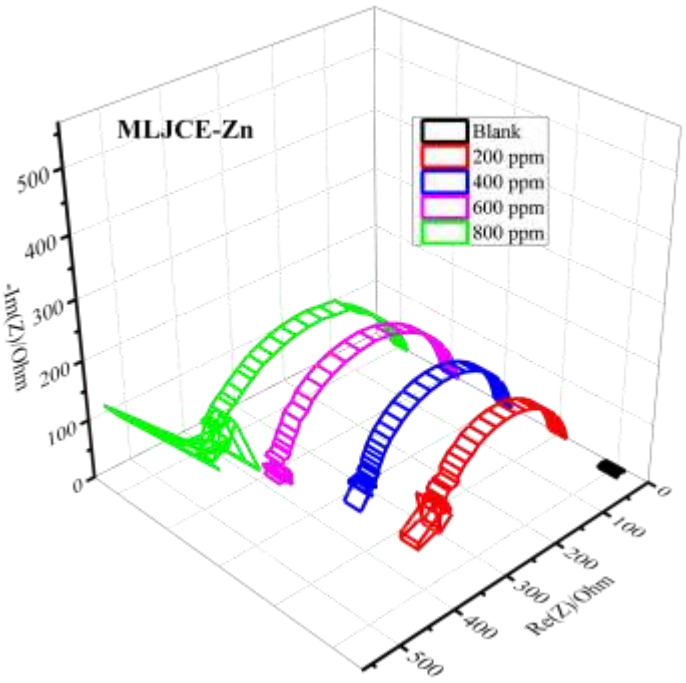

Figure 4.13: Zn Nyquist plots in 1 M HCl solution with and without MLJCE at various concentrations at 303 K

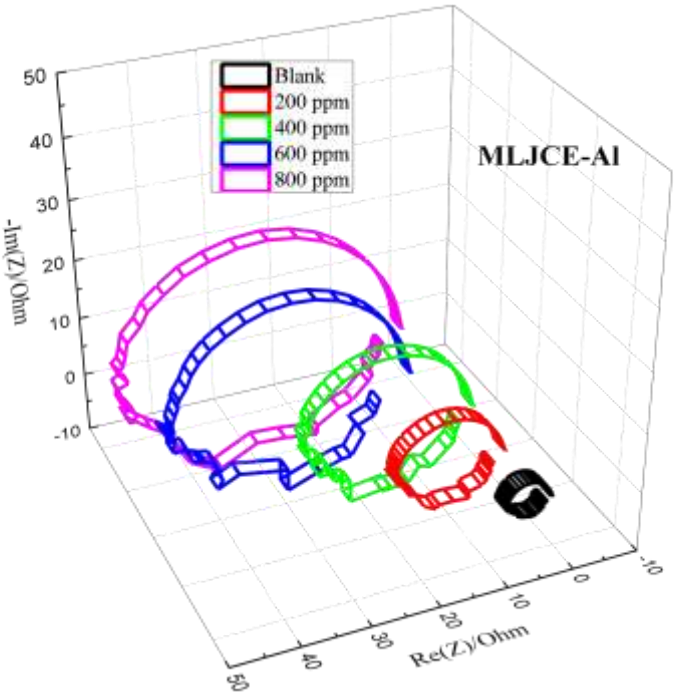

Figure 4.14: Al Nyquist plots in 1 M HCl solution with and without MLJCE at various concentrations at 303 K

The magnitude log (|Z|/Ohm) and Phase(Z)/deg plotted on the ordinate against log (freq/Hz) on the abscissa represent the Bode plots in Figure 4.15−4.17. These plots also show an increase in absolute impedance at low frequencies as the concentration of MLJCE increased from 200 to 800 ppm, indicating that MLJCE provides excellent protection against Al, MS, and Zn corrosion. Single maximums represent the phase angle plots at a medium frequency range (1–2 Hz) for both MS and Zn with and without MLJCE in 1 M HCl solution, which indicates a one-time constant in the corrosion process [419]. The presence of a one-time constant in the presence of MLJCE means that the charge-transfer process controls the corrosion of MS and Zn metals in the test solution [420], whereas the gradual broadening of the phase maxima intermediate frequency accounts for the formation of a protective layer on the electrode surfaces [421, 422].

The Bode plot for Al (Figure 4.17) shows two peaks, suggesting that the corrosion process has two-time constants. The presence of a capacitive semicircle at high frequencies and an inductive loop at low frequencies also demonstrate the participation of a two-time constant in the corrosion process of Al. The electron charge transfer process across the double layer at the interface and the native oxide layer on the Al surface is said to be responsible for the two-time constant [423, 424]. The magnitude of the phase angle |θ| and slope values calculated at intermediate frequencies from the linear part of the log (|Z|/Ohm) against log (Freq/Hz) are frequently used to explain the adsorption mechanism and the nature of the adsorption film formed on the electrode surfaces. An ideal capacitor has a |θ| of −90º and a slope of −1 [425-427]. However, electrochemical systems do not always behave in an ideal manner. In the present study, the linear part of the log (|Z|/Ohm) versus log (Freq/Hz) reveals phase angles near −70º and slope values around −0.8 for MS and Zn in the presence of MLJCE compared to the uninhibited system. These values also deviate from ideal behaviour for the Al sample but show an approximation of ideal behaviour as MLJCE concentration increases.

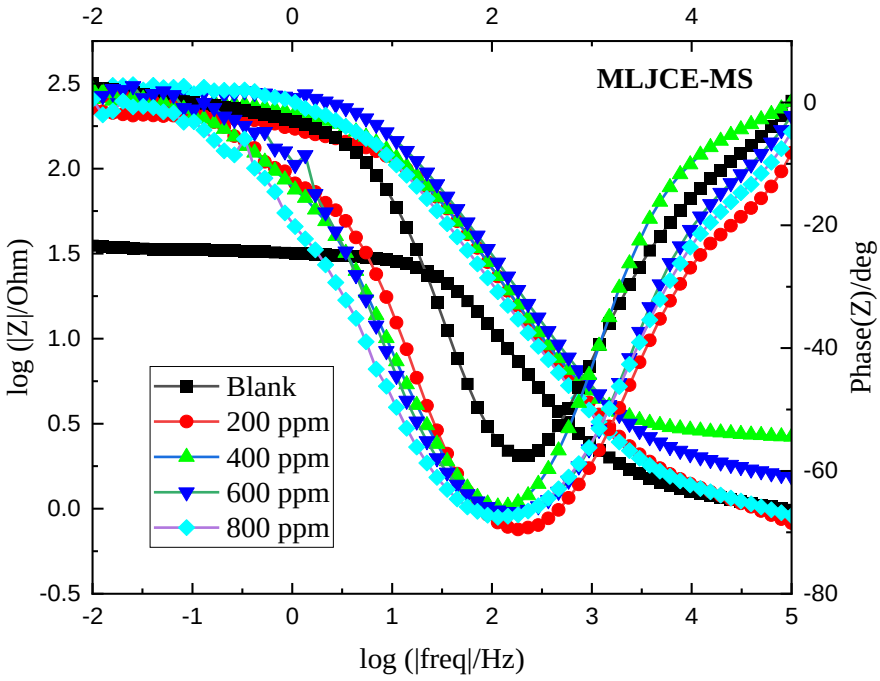

Figure 4.15: MS Bode modulus and phase angle plot in 1 M HCl solution with and without MLJCE at various concentrations at 303 K

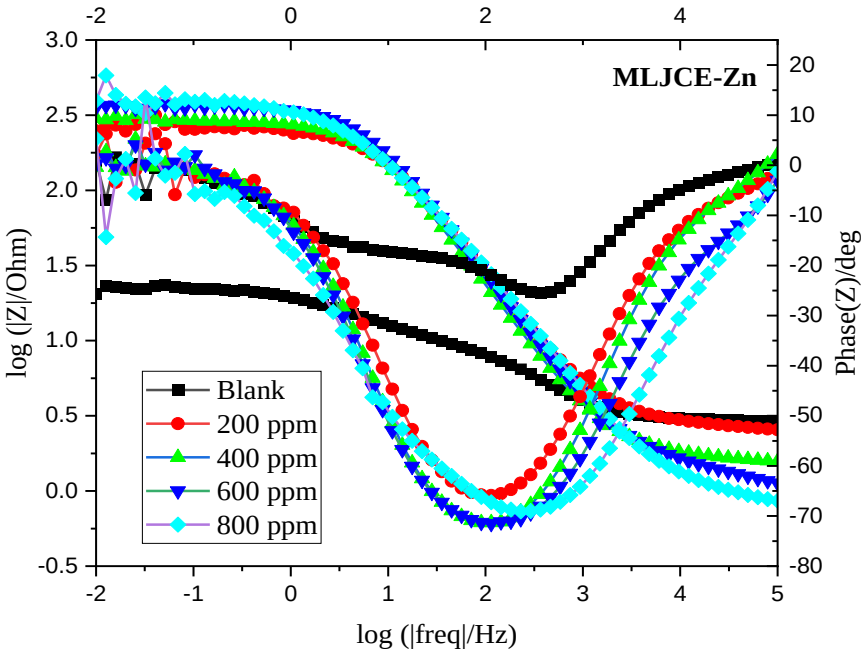

Figure 4.16: Zn Bode modulus and phase angle plot in 1 M HCl solution with and without MLJCE at various concentrations at 303 K

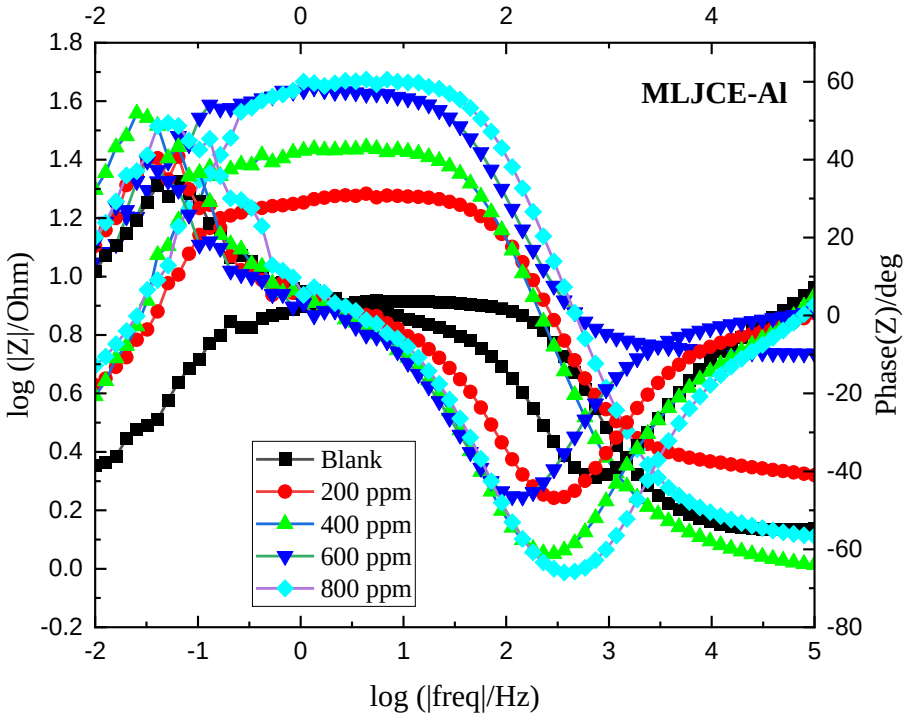

Figure 4.17: Al Bode modulus and phase angle plot in 1 M HCl solution with and without MLJCE at various concentrations at 303 K

EIS data were also analyzed by drawing an analogy between experimental data and an equivalent electric circuit (EEC). An EEC employs discrete electrical circuit elements to represent the corroding electrode interface and the electrochemical phenomena that occur using capacitors, resistors, inductors, and elements that mimic diffusion processes. The modified Randles EEC (Figure 4.18) [428, 429] was selected to fit the experimental data for MS and Zn using the ZSimp 3.3 software. The Randles circuit was chosen because it requires only one time constant since the Nyquist plots for n and MS are represented by a continuous semicircle indicative of a one-time constant.

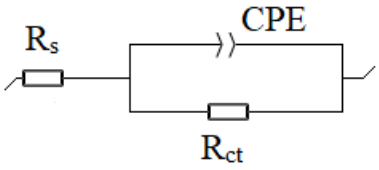

Figure 4.18: The Randles equivalent circuit diagram used to model the experimental impedance data for MS and Zn with and without MLJCE in 1 M HCl

where R_s, CPE, and R_{ct} represent the uncompensated solution resistance, constant phase element, and charge transfer resistance, respectively. R_s on the impedance curve is where the curve intersects the real axis in the high-frequency region (i.e., near the origin). The totality of R_s and R_{ct} is considered when the impendence curve meets the real axis in the low-frequency section. As a result, the diameter of the impedance curve in a Nyquist plot equals R_{ct}.

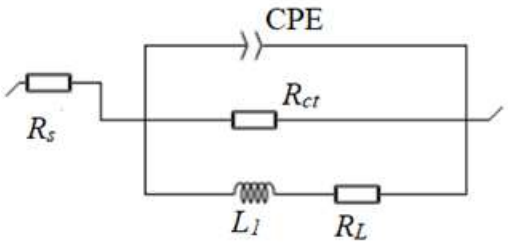

Figure 4.19: Equivalent electrical circuit used to model the experimental impedance data for Al with and without MLJCE in 1 M HCl

The EEC used to fit the Al data is shown in Figure 4.19 and shows the addition of inductance (L) and inductive resistance (R_L) elements to the modified Randles EEC to represent the inductive behaviour of the impedance. As with MS and Zn, a CPE was used to describe the electrical double-layer capacitance and to account for the dispersion effect. The validity of the EIS results for the three systems (Al, MS, and Zn) with ECCs was estimated by considering the quality of the fitted curves in addition to the chi-square (χ^2) values. An example of the estimated percentage errors for MS electrical components of the modified Randel EEC is shown in Figure 4.20. The figure shows the measured and calculated/predicted plots for MS immersed in 1 M HCl in the absence of MLJCE, used to validate the fitting of the EIS results. It also indicates a good fit with acceptable error values and a χ^2 in the 10^{-3} range, confirming that the fitted data and the experimentally measured data agree well, which is valid for Al and Zn when using the appropriate EEC.

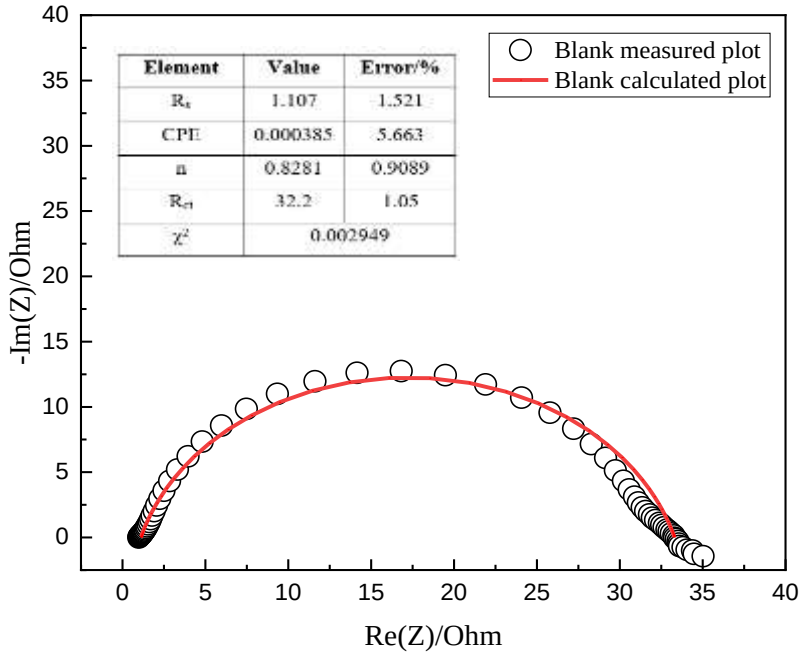

Figure 4.20: An EEC for simulating the EIS data with a focus on the uninhibited corrosive MS system (1 M HCl)

Table 4.3 lists the fitted data of the electrochemical parameters and shows that as the concentration of MLJCE increases, the R_{ct} values increase, which implies that MLJCE forms a protective film on the metal surface, leading to a decrease in CPE values. For example, the R_{ct} increased from 20.76 (blank) to 403.1 Ω (800 ppm) for Zn metal by increasing the concentration of MLJCE in bulk solution. The same increase trend in R_{ct} values in the presence and subsequent increase of MLJCE concentration were observed for MS and Al. The increase in R_{ct} indicates that the charge transfer process is slowed down due to a reduction in the exposed metal surface vulnerable to corrosion attack. The R_{ct} values with (R_{ct}) and without (R°_{ct}) MLJCE were used to calculate the inhibition efficiency using equation 47:

$$IE_{EIS}(\%) = \left(1 - \frac{R^{\circ}_{ct}}{R_{ct}}\right) \times 100 \quad (47)$$

The increase in R_{ct} values is consistent with the inhibition efficiency, with the efficiency increasing to a maximum of 89.13, 94.84, and 85.08% for MS, Zn, and Al, respectively, at the optimum concentration of MLJCE.

Table 4.3: Electrochemical impedance parameters of Al, Zn, and MS after 1-hour immersion at 303 K in 1 M HCl with and without different concentrations of MLJCE

Metal	Conc. of MLJCE (ppm)	R_s ($\Omega.cm^2$)	CPE parameters		L_1 (H)	R_{ct} ($\Omega.cm^{-2}$)	(|θ|)	Slope	R_L ($\Omega.cm^{-2}$)	$\%IE_{EIS}$	χ^2 $\times10^{-3}$
			Y_0 ($S.sec^n$) $\times10^{-3}$	n							
MS	**Blank**	1.107	0.385	0.8281	–	32.2	−57.4165	−0.6904	–	–	2.949
	200	0.9677	0.2001	0.8157	–	195.6	−69.5415	−0.8028	–	83.54	7.874
	400	2.674	0.1846	0.8364	–	238.6	−65.8056	−0.7685	–	86.50	2.821
	600	1.68	0.1513	0.8295	–	280.2	−66.6531	−0.7663	–	88.51	1.509
	800	1.014	0.2816	0.7959	–	296.2	−67.5375	−0.7481	–	89.13	3.277
Zn	**Blank**	2.628	6.051	0.5031	–	20.76	−25.5302	−0.2366	–	–	4.598
	200	2.697	0.1527	0.8434	–	268.8	−65.8949	−0.7539	–	92.28	2.867
	400	1.663	0.1478	0.8776	–	293	−71.288	−0.8186	–	92.91	1.119
	600	1.309	0.1419	0.8552	–	365.8	−71.5051	−0.8137	–	94.32	3.196
	800	0.8784	0.1938	0.8021	–	403.1	−69.0552	−0.7682	–	94.85	8.669
Al	**Blank**	1.392	0.1029	0.9548	10.24	6.617	−41.5066	−0.5775	1.076	–	2.707
	200	2.245	0.1451	0.9257	29.01	16.34	−46.8247	−0.6263	2.009	59.50	2.061
	400	1.149	0.1779	0.9166	45.92	25.95	−61.215	−0.7788	2.448	74.50	5.334
	600	5.575	0.1291	0.9454	89.89	36.73	−46.5043	−0.6323	6.056	81.98	1.677
	800	1.396	0.07373	0.9426	36.57	44.35	−65.9513	−0.8008	4.289	85.08	4.049

The proximity of the CPE exponent (n) values to unity supports that the electrode/electrolyte systems are pseudocapacitive in nature due to their surfaces' inhomogeneities. The CPE exponent values for Al and MS did not differ significantly in the presence of the MLJCE when compared to the blank. Their stability demonstrates that the charge transfer process controls the dissolution mechanism of the electrodes in 1 M HCl solution with and without the extracts [430]. The increase in CPE exponent values for Zn in the presence of MLJCE compared to the blank (0.5073) indicates that the Zn surface became more homogeneous.

The CPE can be replaced by the respective double-layer capacitor (C_{dl}) in all three corrosive/inhibited systems to enable a more precise fit of the data; a frequency-dependent element used to represent the surface roughness of the metal samples. The impedance function of CPE can be calculated using equation 48 [431, 432]:

$$Z_{CPE} = \frac{1}{(Y_o j\omega)^n} \tag{48}$$

where Y is a proportional factor that indicates a combination of properties that relates to the metal surface and also the electroactive species independent of frequency, ω is the angular frequency ($2\pi f_{max}$, where f is the frequency), j is an imaginary number equal to $\sqrt{-1}$ and n is the phase shift, commonly referred to as the deviation parameter, which describes the nature of the Al, MS, and Zn surface and reflects microscopic fluctuations of the surface [37]. When n = 0, the Z_{CPE} represents the resistance of the Al, MS, and Zn surface with $R = Y^{-1}$; n = –1 representing an inductance with $L = Y^{-1}$ [433], while n = 1, the CPE is indicative of an ideal capacitor with Y being equal to the capacitance (C = Y) [434]. The phase shift values obtained in this work are close to 1 with the inclusion of *L. javanica* into the acidic solution, implying that the CPE resembles capacitive behaviour and the correction of capacity to its real values can be expressed by:

$$f(-Z''_{max}) = \left(\frac{1}{2\pi R_{ct} C_{dl}}\right) \tag{49}$$

where $-Z''_{max}$ is the maximum imaginary component of the impedance.

Lower C_{dl} values imply an increase in the electrical double layer and/or a lowering in the local dielectric constant (ε), indicating that the inhibitors molecules get adsorbed onto the Al, MS, and Zn surface at both the anodic and cathodic locations [55]. The thickness of the protective layer (d) is related to C_{dl} according to the following equation 50 [53]:

$$C_{dl} = \frac{\varepsilon \varepsilon_o}{d} \tag{50}$$

where ε_o is the permittivity of the free space.

4.6. Weight loss measurement

4.6.1. The effect of MLJCE concentration on the anti-corrosive behaviour of Zn, Al, and MS

Weight loss measurements at different temperatures (303 K to 333 K) over 7 hours were used to provide a preliminary framework for the anti-corrosive nature of MLJCE in 1M HCl solution for Al, MS, and Zn. Table 4.4 displays the calculated corrosion rate and inhibition efficiency values to examine the effect of MLJCE concentration in 1 M HCl on Al, MS, and Zn corrosion. The tabulated results show that the corrosion rate was significantly higher for the three metals' uninhibited systems at all temperatures tested. For instance, at the lowest temperature (303 K) evaluated for the uninhibited systems, a corrosion rate of 1.4988×10^{-3}, 2.6325×10^{-3} and 8.6931×10^{-3} $g.cm^{-2}.h^{-1}$ was obtained for MS, Zn, and Al, respectively. However, adding MLJCE into the corrosive solution markedly decreased the corrosion rate of these metals. For MS, the corrosion rate was reduced to 8.6881×10^{-5}, 1.8617×10^{-5}, 1.6135×10^{-5} 1.3653×10^{-5} $g.cm^{-2}.h^{-1}$ in the presence of 200, 400, 600, and 800 ppm of MLJCE respectively. For Zn, the corrosion rate decreased to 1.4000×10^{-3}, 1.3578×10^{-3}, 1.3268×10^{-3} and 1.2970×10^{-3} $g.cm^{-2}.h^{-1}$ in the presence of 200, 400, 600, and 800 ppm MLJCE, respectively. While for Al, the corrosion rate decreased to 1.5266×10^{-3}, 1.2871×10^{-3}, 1.1717×10^{-3} and 9.9293×10^{-4} $g.cm^{-2}.h^{-1}$ in the presence of 200, 400, 600, and 800 ppm MLJCE, respectively. The variation in corrosion rate with respect to MLJCE concentrations (Figure 4.21) demonstrates that increasing inhibitor concentrations resulted in lower corrosion rates. Figure 4.22−4.425 shows that as the MLJCE concentration increases, the inhibition efficiency increases, with 800 ppm providing the best protection. The low corrosion rate and high inhibition efficiency values observed at 800 ppm are due to more MLJCE molecules being available than at 200 ppm, resulting in a greater tendency for MLJCE to adsorb at the metal/solution interface of the three metal surfaces. The protective effect afforded to the three metals by the extracts can be attributed to the adsorbed MLJCE molecules on the metal surfaces, forming a barrier limiting O_2 diffusion and water access to the metal surfaces [435].

Table 4.4: Weight loss parameters for the uninhibited and MLJCE-inhibited Al, MS, and Zn system in 1 M HCl corrosive solution at 303-333 K

Metal	Conc. of MLJCE (ppm)	303 K			313 K			323 K			333 K		
		C_R ($g.cm^{-2}.h^{-1}$)	C_R (mpy^1)	$\%IE_{CR}$	C_R ($g.cm^{-2}.h^{-1}$)	C_R (mpy^1)	$\%IE_{CR}$	C_R ($g.cm^{-2}.h^{-1}$)	C_R (mpy^1)	$\%IE_{CR}$	C_R ($g.cm^{-2}.h^{-1}$)	C_R (mpy^1)	$\%IE_{CR}$
MS	Blank	1.4988×10^{-3}	1.66944	–	2.8038×10^{-3}	3.11683	–	4.8840×10^{-3}	5.42832	–	8.6198×10^{-3}	9.58729	–
	200	8.6881×10^{-5}	0.09665	94.20	1.4025×10^{-4}	0.15609	95.00	7.2856×10^{-4}	0.81004	85.08	2.0554×10^{-3}	2.28432	76.15
	400	1.8617×10^{-5}	0.02068	98.76	1.3032×10^{-4}	0.14485	95.35	3.4256×10^{-4}	0.38091	92.99	8.7377×10^{-4}	0.97084	89.86
	600	1.6135×10^{-5}	0.01794	98.92	8.8122×10^{-5}	0.09791	96.86	2.8547×10^{-4}	0.31703	94.15	5.5480×10^{-4}	0.61639	93.56
	800	1.3653×10^{-5}	0.01516	99.09	7.6952×10^{-5}	0.08560	97.26	2.2837×10^{-4}	0.25397	95.32	4.9274×10^{-4}	0.54744	94.28
Zn	Blank	2.6325×10^{-3}	2.92620	–	4.3130×10^{-3}	4.79488	–	7.2024×10^{-3}	8.00784	–	1.3485×10^{-2}	14.98449	–
	200	1.4000×10^{-3}	1.55536	46.82	1.5887×10^{-3}	1.76742	63.16	1.7103×10^{-3}	1.89950	76.25	3.2853×10^{-3}	3.64937	75.64
	400	1.3578×10^{-3}	1.50944	48.42	1.3417×10^{-3}	1.49020	68.89	1.5092×10^{-3}	1.67704	79.05	1.9002×10^{-3}	2.11173	85.91
	600	1.3268×10^{-3}	1.47530	49.60	1.3280×10^{-3}	1.47689	69.21	1.4993×10^{-3}	1.66869	79.18	1.8270×10^{-3}	2.03194	86.45
	800	1.2970×10^{-3}	1.43924	50.73	1.1543×10^{-3}	1.28285	73.24	1.3826×10^{-3}	1.53717	80.80	1.7637×10^{-3}	1.95844	86.92
Al	Blank	8.6931×10^{-3}	9.65529	–	8.9549×10^{-3}	9.95270	–	1.0930×10^{-2}	12.13168	–	1.1308×10^{-2}	12.57309	–
	200	1.5266×10^{-3}	1.69772	82.44	4.2348×10^{-3}	4.70351	52.71	6.3746×10^{-3}	7.07611	41.68	6.4491×10^{-3}	7.15742	42.97
	400	1.2871×10^{-3}	1.42926	85.19	4.0313×10^{-3}	4.48532	54.98	6.0295×10^{-3}	6.69604	44.84	6.3671×10^{-3}	7.07378	43.69
	600	1.1717×10^{-3}	1.30171	86.52	3.3611×10^{-3}	3.73489	62.47	5.5256×10^{-3}	6.14161	49.45	5.7726×10^{-3}	6.40953	48.95
	800	9.9293×10^{-4}	1.10373	88.58	3.1215×10^{-3}	3.47377	65.14	4.9584×10^{-3}	5.51346	54.63	5.1260×10^{-3}	5.70868	54.67

The corrosion rates in the table were originally measured in grams per square centimeter per hour ($g.cm^{-2}.h^{-1}$). To facilitate better comparison with electrochemical measurements, the values were converted to mils per year (mpy) by considering the density of the metals and using the equation: C_R (mpy) = (C_R ($g.cm^{-2}.h^{-1}$) × 24 × 365.25)/density ($g.cm^{-3}$).

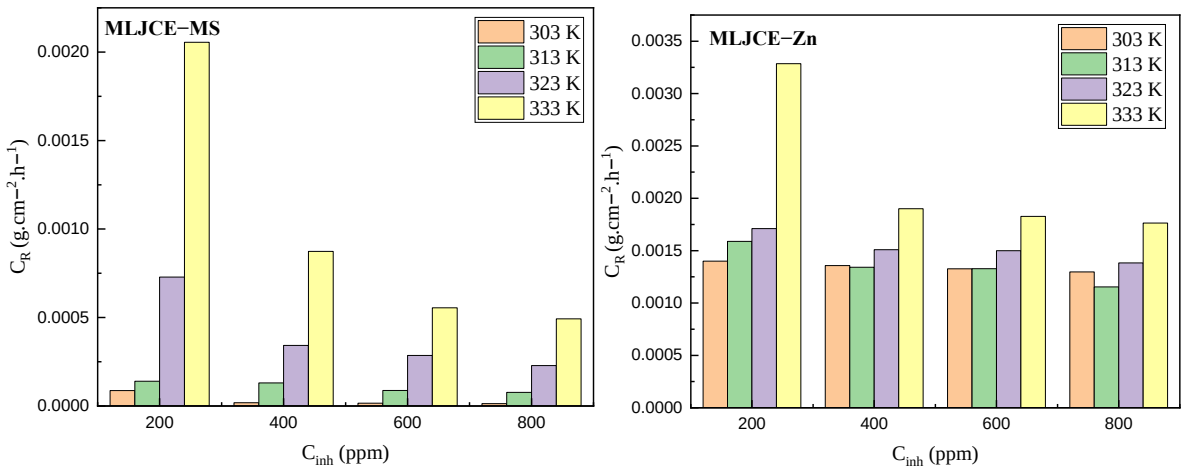

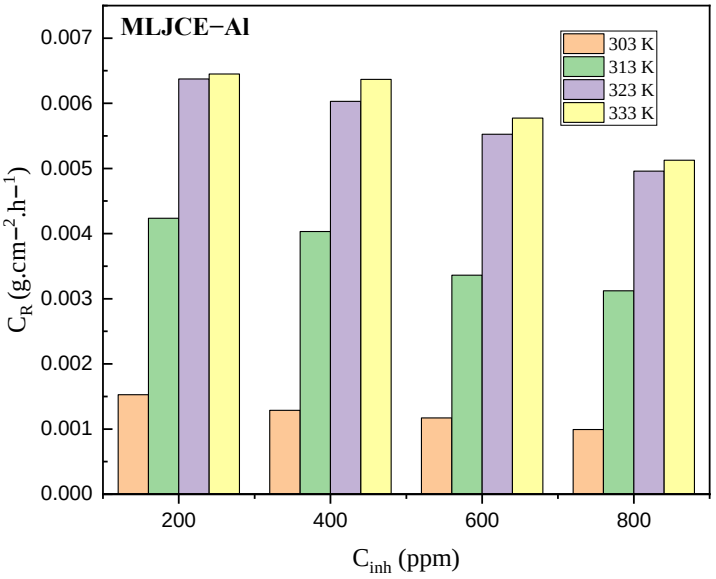

Figure 4.21: Variation of corrosion rate (C_R) obtained from weight loss for Zn, Al, and MS in 1 M HCl as a function of concentration in the presence of MLJCE at 303-333 K

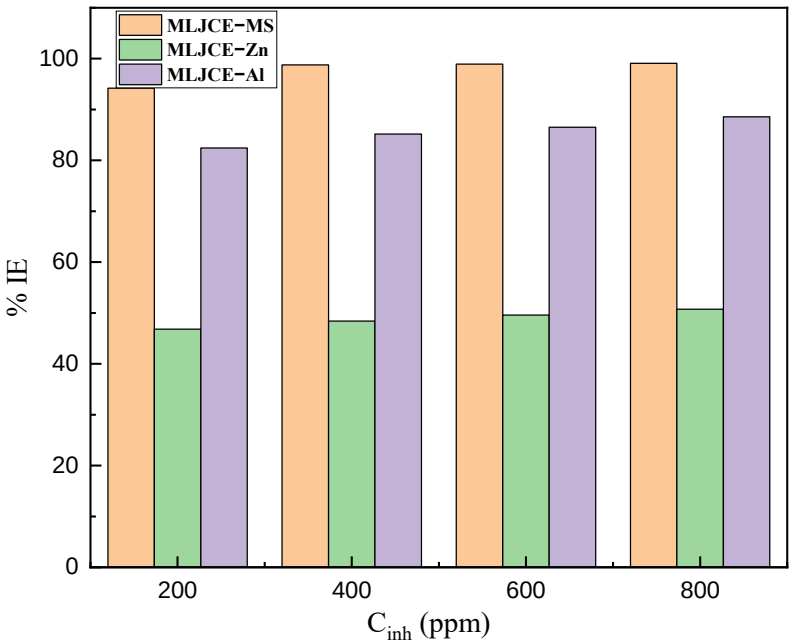

Figure 4.22: The dependence of $\%IE_{WL}$ obtained from weight loss on the concentration of MLJCE after 7 h of immersion of Zn, Al, and MS samples in 1M HCl at 303 K

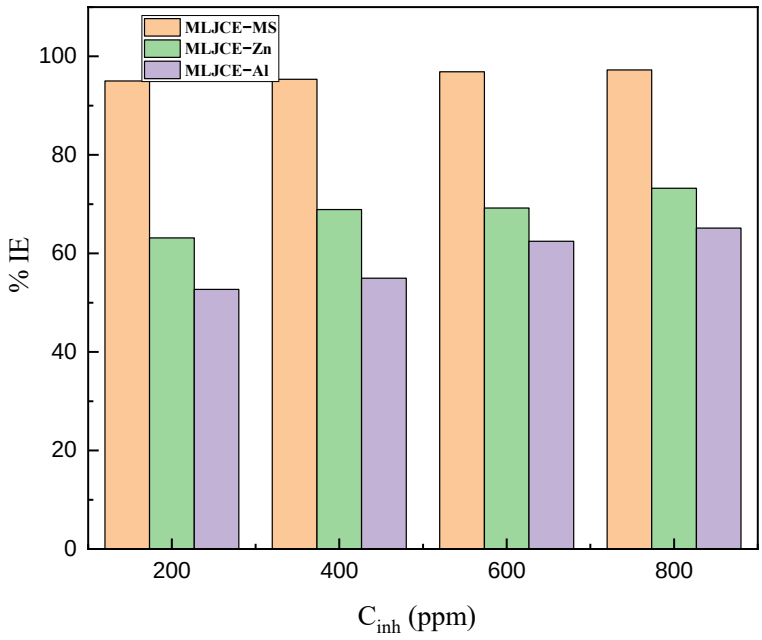

Figure 4.23: The dependence of $\%IE_{WL}$ obtained from weight loss on the concentration of MLJCE after 7 h of immersion of Zn, Al, and MS samples in 1M HCl at 323 K

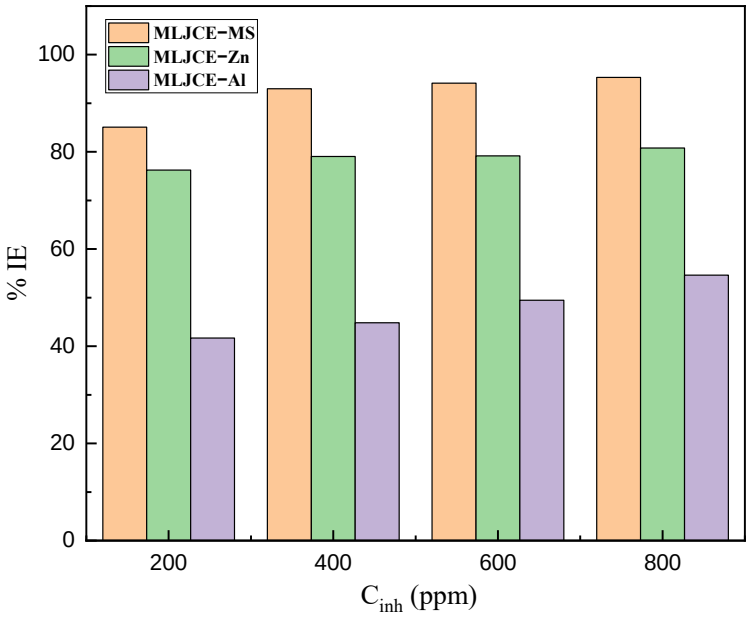

Figure 4.24: The dependence of $\%IE_{WL}$ obtained from weight loss on the concentration of MLJCE after 7 h of immersion of Zn, Al, and MS samples in 1M HCl at 323 K

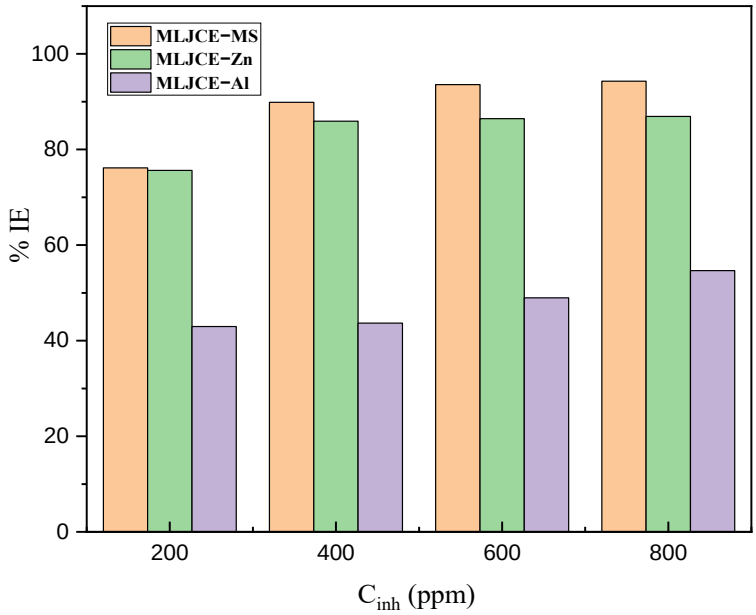

Figure 4.25: The dependence of $\%IE_{WL}$ obtained from weight loss on the concentration of MLJCE after 7 h of immersion of Zn, Al, and MS samples in 1M HCl at 333 K

4.6.2. Influence of immersion time on MS, Al, and Zn corrosion inhibition in 1 M HCl with an optimal concentration of MLJCE at 303 K

Inhibition-time curves of Al, MS, and Zn samples in applicable 1 M HCl solution were determined in the presence and absence of 800 ppm MLJCE, and the results are shown in Figure 4.26 and Table 4.5. The inhibition efficiencies were determined after 6, 7, 12, 18, and 24-hour immersion periods. Table 4.5 shows that after 7 hours of immersion at 303K, the maximum inhibition efficiency for MS was 99.09%. The %IE ranged from 88.29% after 6 hours to 95.99% after 24 hours of immersion. The increase in inhibition efficiency from 88.29% after 6 hours to 99.09% after 7 hours, as well as the achievement of stability at around 90% from 7 hours to 24 hours (Figure 4.26), indicates that MLJCE has formed a relatively stable adsorption film on the surface of MS.

Table 4.5 results support the figure's depiction of a gradual decrease in inhibition efficiency with increasing immersion for Al. The %IE for Al decreases from 73.93% (for 6hrs) to 70.08% (for 24hrs). According to these findings, increasing the immersion time results in the desorption of MLJCE molecules from the surfaces of both Al and MS. The decrease in MLJCE efficiency with increasing immersion time can be attributed to saturation in the thickness of the adsorbed inhibitor

film, which promotes inhibitor desorption from the metal surface [436]. Desorption of the inhibitor from the metal surface decreases the surface coverage exposing the bare metal to attack by the corrosive solution as reflected by the inhibition efficiency [437, 438]. The stability of the adsorbed layer can be compromised by prolonged exposure to the thin film formed by the inhibitor on the metal [439]. MLJCE provided adequate protection for the surface of MS and Al with increasing immersion time, with a %IE of 95.99 and 70.08% at 24 hours, despite inhibition efficiency decreasing with time. The Zn inhibition-time curve demonstrates that the protective effect increases with an immersion time of up to 24 hours. The progressive formation of protective chemical coordinate bonds on the Zn surface by MLJCE can be attributed to the increase in protection values over time [440]. The maximum protection efficiency for the Zn sample was 77.69%. Prabhu *et al*. [441] discovered that the protection efficiency increased with increasing immersion time for Zn samples, reaching a maximum value of 75%. Because of the thermal stability of MLJCE for MS surfaces, the slight decrease in inhibition efficiency cannot be attributed to MLJCE molecule rearrangement, fragmentation, or instability.

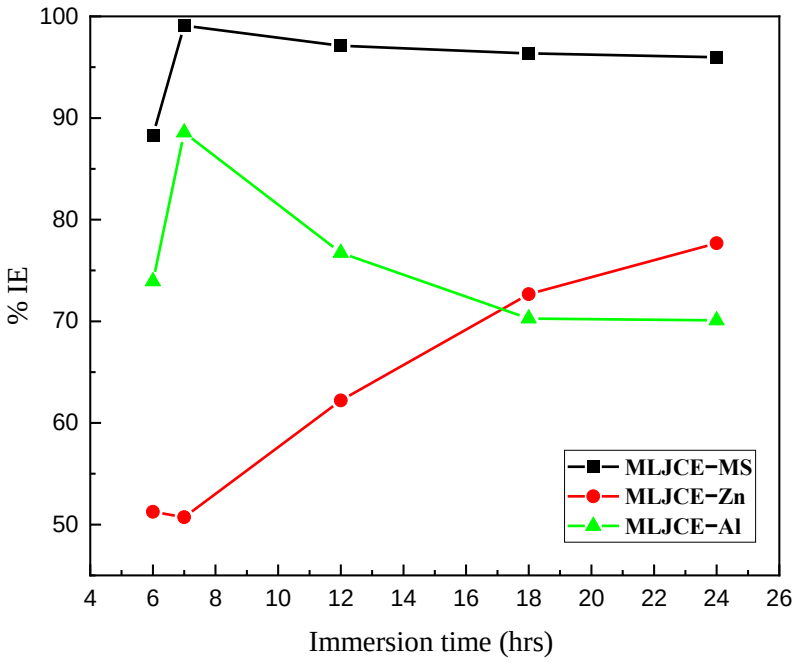

Figure 4.26: Relationship between immersion time and $\%IE_{WL}$ for Al, Zn, and MS corrosion in 1 M HCl in the presence of 800 ppm MLJCE

Table 4.5: Weight loss results showing the %IE for Al, Zn, and MS corrosion in 1M HCl in the absence and presence of 800 ppm MLJCE at various immersion times

Metal	Conc. of MLJCE (ppm)	Immersion period (hours)				
		6	7	12	18	24
		%IE				
MS	800	88.29	99.09	97.10	96.36	95.99
Zn	800	51.25	50.73	62.21	72.67	77.69
Al	800	73.93	88.58	76.73	70.27	70.08

4.6.3. Effect of temperature on the corrosion of Zn, Al, and MS in 1.0 M HCl solution containing MLJCE

Several changes occur at the surface of metals during corrosion inhibition, including rapid etching, inhibitor decomposition, and desorption of inhibitor molecules from the metals' surface, all of which are complex processes influenced by temperature [442]. To understand more about the performance of MLJCE and the mechanisms of adsorption and activation processes, weight loss experiments were performed for 7 hours in 1 M HCl at temperatures ranging from 303 to 333 K. This is because temperature accelerates the corrosion rate of metals, which affects the stability of the adsorption film and as well as the protection efficiency, more particularly in acidic solutions. It is observed that the inhibitory effect of MLJCE against MS and Al corrosion decreases with increasing system temperature, as shown in Figures 4.27 and 4.29, respectively. For example, the MS inhibition efficiency at 333 K decreased from 99.09% to 94.28% at the highest concentration of MLJCE (800 ppm), while the Al inhibition efficiency decreased from 88.58% to 54.67% at the same temperature. The high %IE at 303 K indicates that MLJCE is more effective in preventing the dissolution of MS and Al at lower temperatures, which can be attributed to the physical interaction of the extracts with the metal surfaces of the two samples. The reduction in the inhibition efficiencies with increasing temperature was observed at all concentrations of MLJCE for Al and MS systems. The limited protection that MLJCE offers against Al and MS surfaces corrosion at elevated temperatures can be explained by two possible explanations.

On the one hand, with increasing temperature, the equilibrium between adsorption and desorption becomes the determining factor for the maximum adsorbed equilibrium mass. It is known that adsorption and desorption of inhibitor molecules occur simultaneously on the metal surface, both

processes being in equilibrium at a specific temperature. As the temperature increases, the equilibrium between the two processes shifts to the desorption side until a new equilibrium is reached at a different value of the equilibrium constant, resulting in fewer inhibitor molecules protecting the metal surface [443, 444]. The desorption of the inhibitor molecules from the metal surfaces [445, 446] causes an increase in the dissolution rate of the Al and MS samples as a larger surface area is exposed to the acidic medium. This means a higher inhibitor dosage is required at high temperatures to reach the maximum adsorbing mass. The other explanation is that the rate of metal dissolution affects the impact that MLJCE has on the corrosion process. The increase in temperature causes the surface of metals to become less stable and the rate of metal dissolution to increase. This behaviour can be attributed to the rise in the thermal motion of the corrosive species [447], causing them to attack metal surfaces more frequently. A decrease in the strength of the electrostatic force of attraction between the metal atoms and the adsorbed inhibitor molecules also causes this behaviour.

Meanwhile, increasing the system temperature from 303 to 333 K significantly increased the %IE at all plant extract concentrations for Zn. At the highest concentration of MLJCE (800 ppm), the %IE increased from 50.73, 73.24, 80.80 to 86.92% at temperatures ranging from 303, 313, 323 to 333 K. Among the three metal samples tested, MLJCE provided the highest protection for the MS surface at all temperatures. The increase in %IE with temperature for the Zn sample, on the other hand, indicates that a much stronger protective film was formed on this surface. This observation could be explained by Zn's natural ability to create corrosion byproducts such as basic hydrated sulphates, oxides, or carbonates, which act as a protective layer (along with the inhibitor) capable of significantly reducing its corrosion rate depending on the nature of the corrosive environment [448]. The inhibition efficiency of Zn increases with temperature, suggesting that MLJCE interacts with the metal's surface via a chemical adsorption process at high temperatures to slow down Zn corrosion [449].

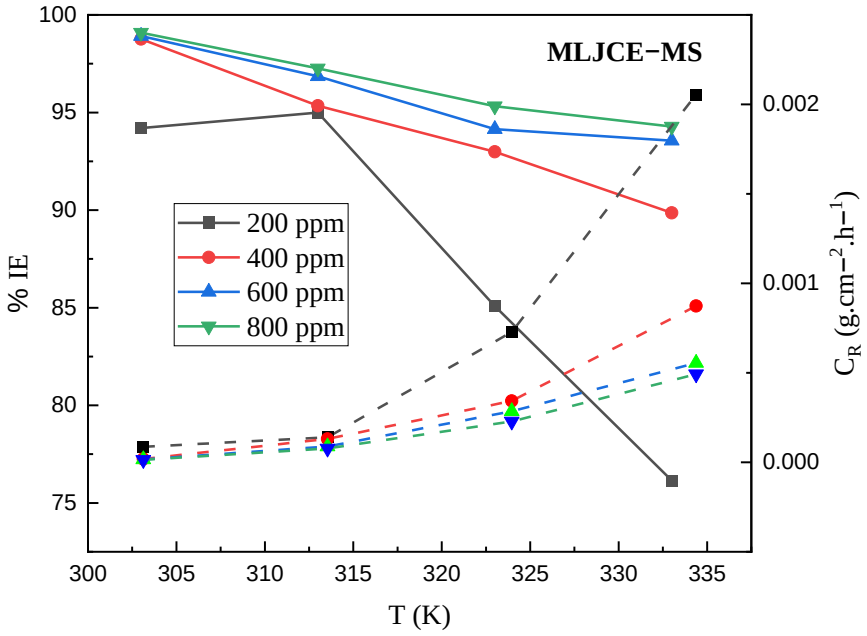

Figure 4.27: The dependence of (a) IE_{WL}(%) (solid lines) and (b) C_R (dashed lines) on temperature after 7 h of immersion of MS samples in 1 M HCl at different MLJCE concentrations

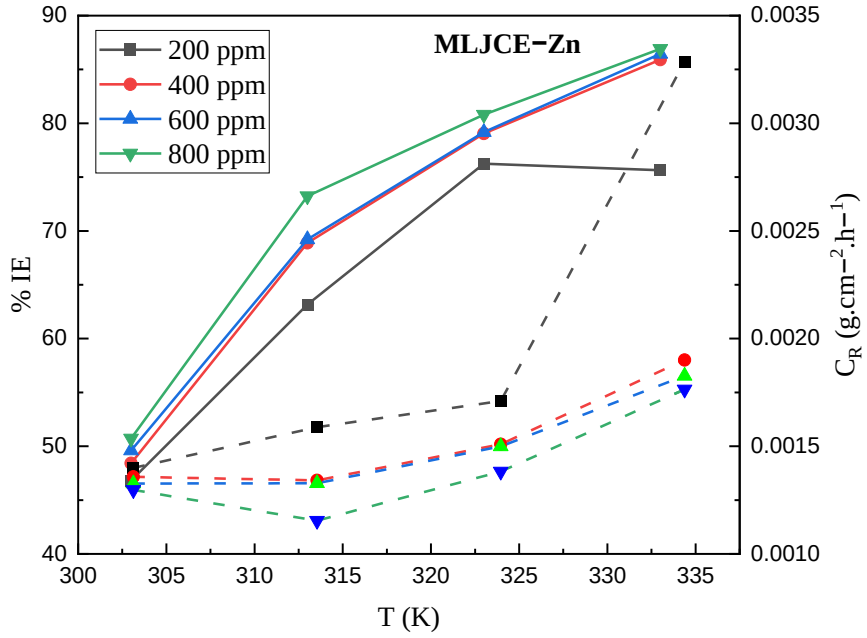

Figure 4.28: The dependence of (a) IE_{WL}(%) (solid lines) and (b) C_R (dashed lines) on temperature after 7 h of immersion of Zn samples in 1 M HCl at different MLJCE concentrations

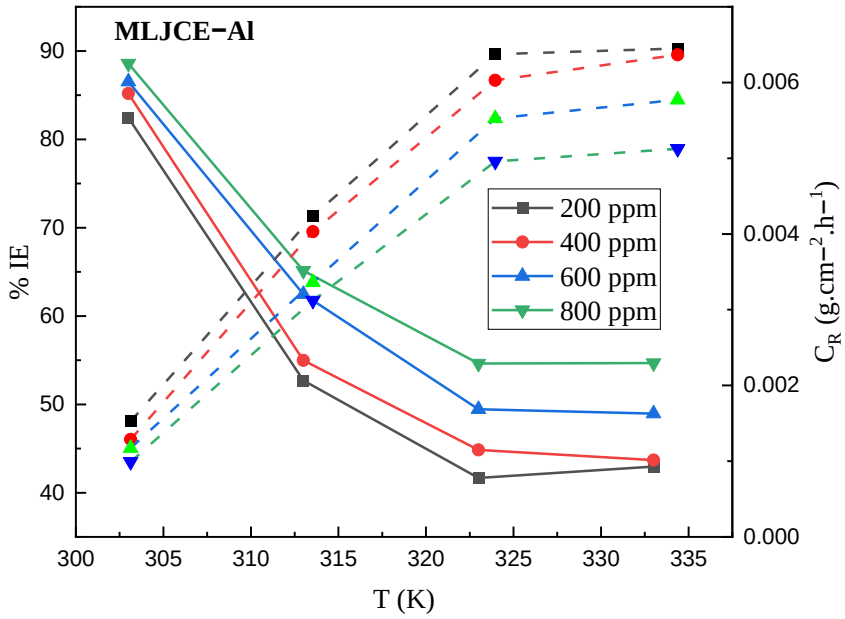

Figure 4.29: The dependence of (a) IE_{WL}(%) (solid lines) and (b) C_R (dashed lines) on temperature after 7 h of immersion of Al samples in 1 M HCl at different MLJCE concentrations

4.6.4. Thermodynamic and kinetic Parameters

Corrosion analysis at various temperatures enables the evaluation of critical thermodynamic activation parameters of the corrosion reaction. The Arrhenius formula and its alternative, the transition state, can express the corrosion rate's temperature dependency, as shown in equations 51 and 52.

$$\log C_R = \log A - \frac{E_a}{2.303RT} \tag{51}$$

$$\log\left(\frac{C_R}{T}\right) = \left[\log\left(\frac{R}{Nh}\right) + \left(\frac{\Delta S_a^*}{2.303R}\right)\right] + \left(\frac{-\Delta H_a^*}{2.303R}\right)\left(\frac{1}{T}\right) \tag{52}$$

In equation 51, E_a represents the apparent effective activation energy for MS corrosion, the smallest amount of kinetic energy required by the reactants to form corrosion products. R represents the general gas constant, equivalent to 8.3145 J.mol^{-1}.K^{-1}, T represents the absolute temperature, and A means the frequency factor. In equation 52, N is the Avogadro's number (6.02252×10^{23} mol^{-1}), h is the Plank's constant (6.626176×10^{-34} J s), 2.303 is a conversion factor from natural log to log10, ΔH_a^* is the enthalpy change of activation and ΔS_a^* is the entropy change of activation. The ΔH_a^* and ΔS_a^* values in Table 4.6 were calculated from the slope ($-\Delta H_a^*/2.303R$) and the intercept of [log (R/Nh) + $\Delta S_a^*/2.303R$] of the straight-line plots of log

(C_R/T) versus (1/T) shown in Figure 4.34−4.36. The variations in the log of C_R versus reciprocal temperature for the uninhibited and MLJCE-inhibited systems are shown in Figure 4.30−4.32, and the plots suggest that the corrosion of MS, Al, and Zn in 1 M HCl can be elucidated with the kinetic model.

The E_a and the effect of temperature on metal corrosion inhibition efficiency can be used to categorize inhibitors into three classes, as defined by Bentiss *et al*. and Hegazy *et al*. [450, 451]:

1. The first classification states that if the %IE decreases with increasing temperature, the value of E_a of the inhibited acid-metal reaction will be greater than that of the uninhabited acid-metal reaction
2. The second classification states that if the %IE does not change with increasing temperature, then no discernible change in E_a value will be observed
3. Lastly, if %IE increases with an increase in temperature, the apparent energy of activation of the inhibited solution will be less than that of the blank solution

According to Table 4.6, the MLJCE slows down the dissolution of MS and Al based on the first classification assumption. The decrease in %IE with increasing temperature from 303 to 333 K and the E_a values for the inhibited acid-metal reaction are larger than those for the uninhabited acid-metal reaction, demonstrating this. This shows that an MLJCE-metal-activated complex was formed by replacing water molecules on the metal surface, slowing down MS and Al dissolution. In the absence of MLJCE from the corrosive solution, the activated complex is described as Al-H_2O and Fe-H_2O for Al and MS, respectively, which decomposes during corrosion to give Al^{3+}, Fe^{2+}, H_2, and OH^- [452]. The increase in temperature and E_a values with inhibitor concentration can be interpreted as evidence of a columbic or physical adsorption mode [453]. The opposite effect suggests the chemisorption mechanism, which corresponds to an increase in the %IE with increasing temperature and a lower E_a in the presence of an inhibitor. [454, 455]. Based on the preceding information for Al and MS, the trend of E_a values for MLJCE suggests a physisorption inhibition mechanism.

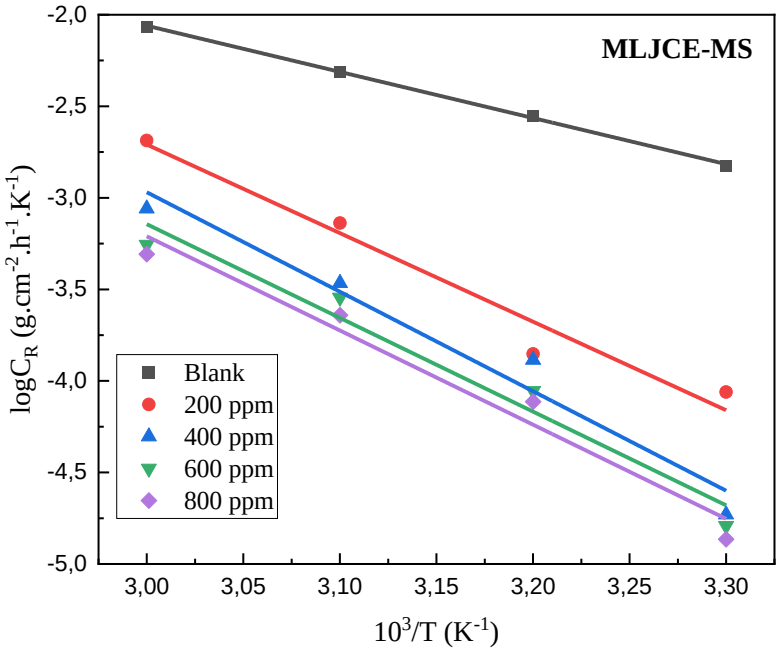

Figure 4.30: Arrhenius diagram (log C_R versus 1/T) for the uninhibited (blank) and MLJCE-inhibited (200 to 800 ppm) MS system in corrosive 1 M HCl solution after 7 hours of immersion

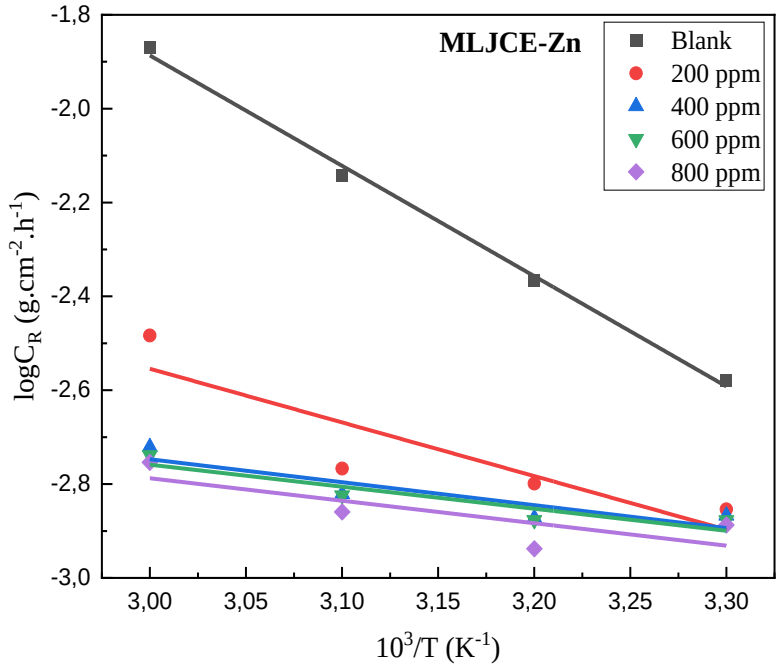

Figure 4.31: Arrhenius diagram (log C_R versus 1/T) for the uninhibited (blank) and MLJCE-inhibited (200 to 800 ppm) Zn system in corrosive 1 M HCl solution after 7 hours of immersion

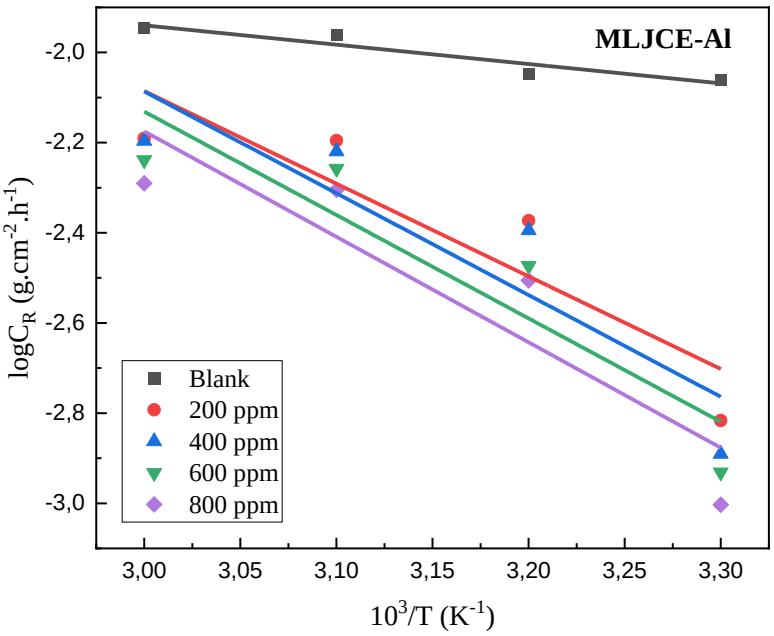

Figure 4.32: Arrhenius diagram (log C_R versus 1/T) for the uninhibited (blank) and MLJCE-inhibited (200 to 800 ppm) Al system in corrosive 1 M HCl solution after 7 hours of immersion

The values of E_a for Zn appear to decrease as the concentration of the extract is increased, which is paradoxical. Although this behaviour is unusual, it is indicative of the chemisorption adsorption mechanism by MLJCE. Putilova *et al*. [456] attributed E_a's paradoxical behaviour to an increase in metal surface coverage by the inhibitors as the temperature of the solution increased and also suggested that at higher temperatures, the rate of formation of the chemisorbed film may be faster than the rate of dissolution of the metal. El-Anadouli *et al*. [457] made the same observation, which they attributed to the modification in the kinetics of the corrosion reaction caused by the formation of alternate reaction paths with lower E_a. As a result, for Zn metal, the plant extracts fall into the third class of classification of corrosion inhibitors as defined by Bentiss *et al*. and Hegazy *et al*. [450, 451].

Table 4.6: Kinetic and activation parameters for MS, Al, and Zn in uninhibited and MLJCE-inhibited 1 M HCl solution

Metal	Conc. of MLJCE (ppm)	E_a ($kJ.mol^{-1}$)	ΔH_a^* ($kJ.mol^{-1}$)	$E_a - \Delta H_a^* = RT$ ($kJ.mol^{-1}$)	ΔS_a^* ($J.mol^{-1}.K^{-1}$)	Q_{ads} ($kJ.mol^{-1}$)		
						303 to 313	313 to 323	323 to 333
MS	Blank	48.2192	45.6457	2.5735	−194.5601	–	–	–
	200	92.6318	90.0142	2.6176	−188.2578	12.3726	−101.1871	−51.8759
	400	104.0557	101.4381	2.6176	−186.7286	−107.0157	−36.6169	−36.0816
	600	98.0278	95.4179	2.6099	−187.8461	−85.8327	−54.6982	−9.1569
	800	98.5103	95.8927	2.6176	−187.8379	−88.4040	−46.7021	−18.9305
Zn	Blank	45.0215	42.4058	2.6157	−194.8944	–	–	–
	200	21.8980	19.2747	2.6233	−199.1860	52.5623	52.7436	−2.9868
	400	9.3654	6.7479	2.6175	−201.3414	67.6848	44.8080	42.9245
	600	8.9882	6.3706	2.6176	−201.4120	65.1416	44.2106	46.2767
	800	9.1701	6.5525	2.6176	−201.4125	77.1039	36.1714	40.8623
Al	Blank	8.2165	5.6009	2.6156	−200.7138	–	–	–
	200	39.3517	36.7341	2.6176	−195.9819	−113.4077	−37.3650	4.7271
	400	43.2330	40.6154	2.6176	−195.3747	−122.2234	−34.2181	−4.1696
	600	43.9204	41.2990	2.6214	−195.3123	−106.4422	−44.6892	−1.7894
	800	44.7993	42.1837	2.6156	−195.2174	−112.2562	−36.9477	0.1444

Inspection of Table 4.6 shows that ΔH_a^* values are positive for the uninhibited systems for all three metals, indicating that the metals were endothermically dissolved. The addition of various concentrations of the extracts into the 1 M HCl corrosive solution resulted in higher ΔH_a^* values for Al and MS. The increase in ΔH_a^* with increasing concentration, the extracts raise the height of the energy barrier required to form the corrosion products as indicated by E_a values. Although the ΔH_a^* values are also positive for Zn metal; they show a decreasing trend as the concentration of the plant's extracts increases, indicating that the Zn specimens were exothermically dissolved.

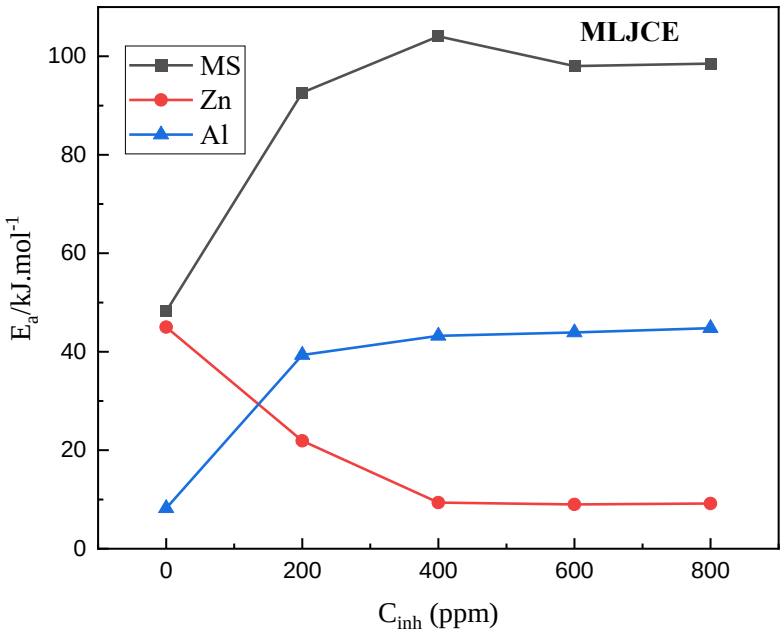

Figure 4.33: Relationship of E_a with the different concentrations of MLJCE for Zn, Al, and MS

ΔS_a^* values decreased negatively with increasing concentration of MLJCE, indicating the formation of an ordered, stable, protective film on the MS and Al surface, implying that the activated complex represents association rather than dissociation in the rate-limiting step [458]. ΔS_a^* values increased negatively in the presence of MLJCE compared to the uninhibited 1 M HCl solution and can be interpreted as a shift towards a less disordered or more ordered system. During the inhibition of corrosion, an increase in ΔS_a^* has been linked to the repulsive force among the adsorptive MLJCE molecules resulting in the disordered arrangement of the extracts molecules on the Zn surface [459]. E_a and ΔH_a^* values similarly vary with the concentration of MLJCE, allowing verification of the corresponding thermodynamic equation ($E_a - \Delta H_a^* = RT$). The calculated values near RT (2.6 kJ.mol^{-1}) indicate that the plant extracts acted equally on E_a and ΔH_a^*.

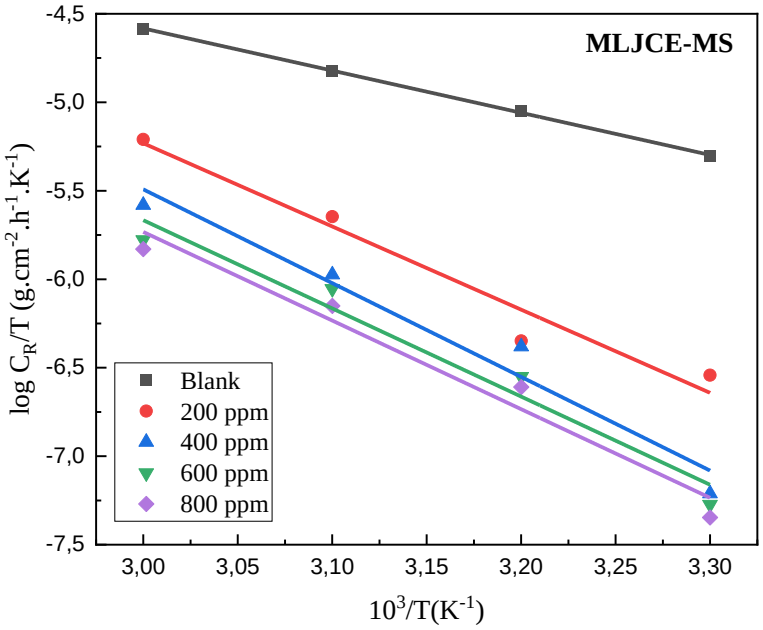

Figure 4.34: Transition state diagram (log C_R/T versus 1/T) for the uninhibited (blank) and MLJCE-inhibited (200 to 800 ppm) MS system in corrosive 1 M HCl solution after 7 hours of immersion

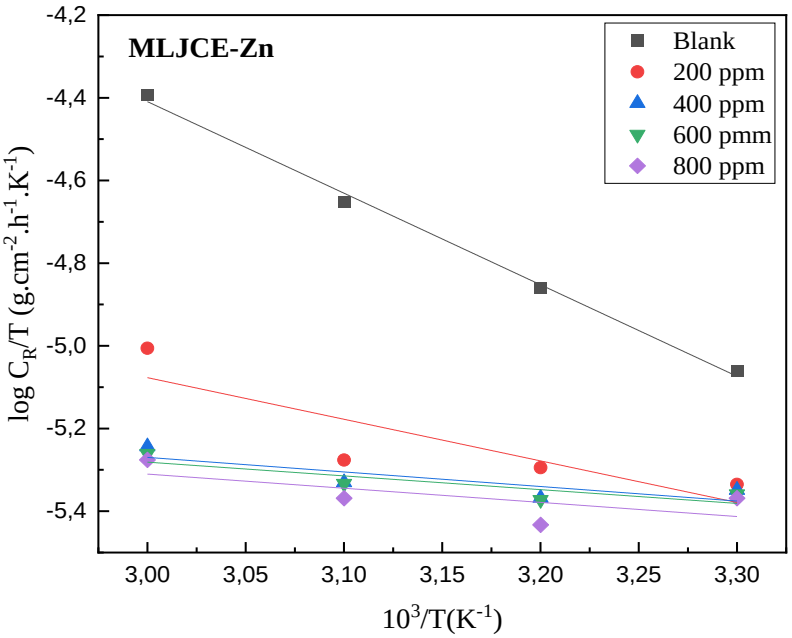

Figure 4.35: Transition state diagram (log C_R/T versus 1/T) for the uninhibited (blank) and MLJCE-inhibited (200 to 800 ppm) Zn system in corrosive 1 M HCl solution after 7 hours of immersion

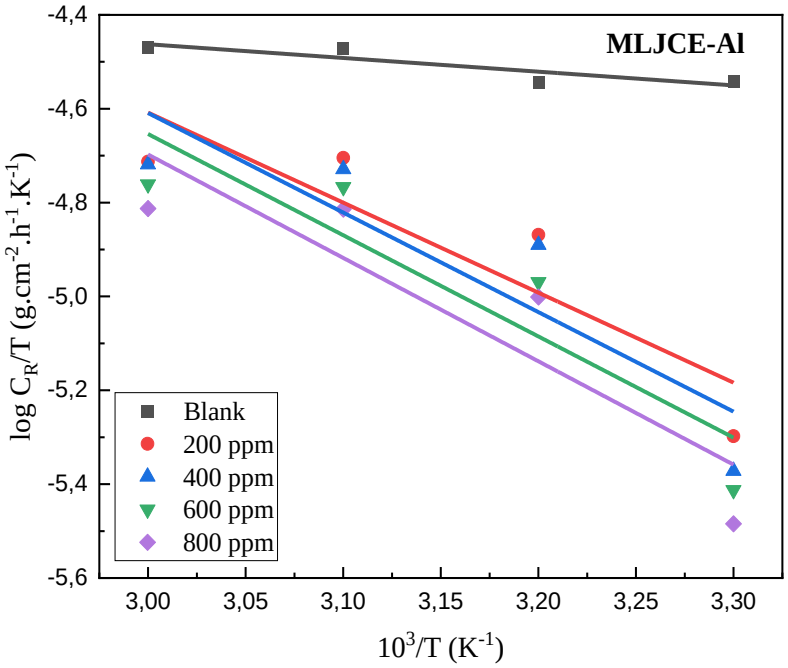

Figure 4.36: Transition state diagram (log C_R/T versus 1/T) for the uninhibited (blank) and MLJCE-inhibited (200 to 800 ppm) Al system in corrosive 1 M HCl solution after 7 hours of immersion

One of the requirements for the adsorption of inhibitor molecules on metal surfaces is that the molecules are drawn from the bulk solution onto the metal surface, which requires the expansion of an amount of energy known as the heat of adsorption (Q_{ads}). To gain more insight into the adsorption mechanism of MLJCE components on MS surface, Q_{ads} were evaluated using the kinetic thermodynamic model expression as follows [453, 460]:

$$Q_{ads} = 2.303R\left\{\log\left(\frac{Q_2}{1-Q_2}\right) - \log\left(\frac{Q_1}{1-Q_1}\right)\right\} \times \left(\frac{T_1 \times T_2}{T_2 - T_1}\right) \quad (53)$$

where θ_1 and θ_2 are the degrees of surface coverage at temperatures T_1 and T_2, and R is the gas constant. Almost all the Q_{ads} values obtained with MLJCE in 1 M HCl solution were negative for Al and MS. The negative sign of these values indicates that most of the extract adsorption process on the Al and MS surface occurred via an exothermic process. The adsorption process was endothermic, progressing from 303 to 313 K for MS at 200 ppm and from 323 to 333 K for Al at 200 and 800 ppm. The negative Q_{ads} values indicate that the extracts' coverage of the metal surfaces decreased as temperature increased, lending support to the proposed physisorption adsorption mechanism for Al and MS [461]. Positive Q_{ads} values, on the other hand, indicate that

the degree of surface coverage increased with increasing temperature, which is more pronounced for the Zn metal, supporting the previously proposed chemisorption mechanism of the MLJCE on the surface of this metal [462]. Since Q_{ads} showed both negative and positive values for all three metal samples, it is assumed that MLJCE adsorption on the metal surfaces is a hybrid adsorption mechanism process that includes both physical and chemical adsorption processes. Both negative and positive Qads are mainly observed at the extract's lowest concentration (200 ppm) as shown in Figure 4.37.

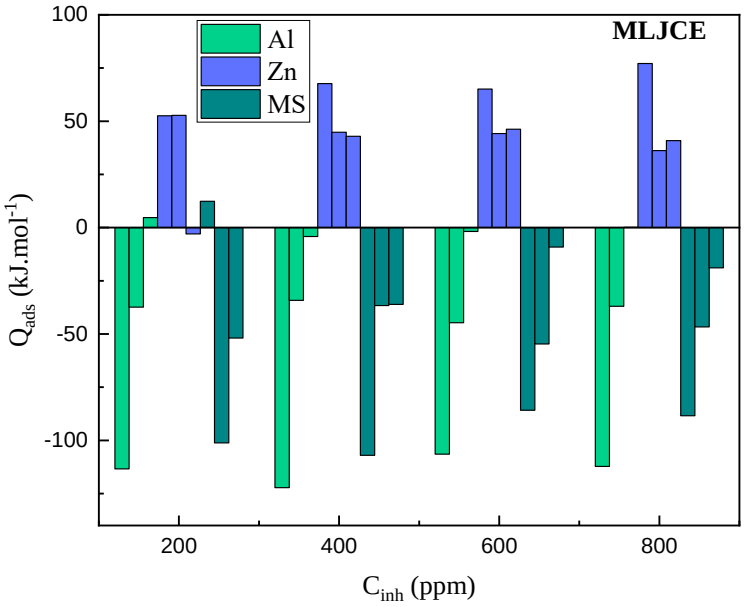

Figure 4.37: Heat of adsorption data for different concentrations of MLJCE for Zn, Al, and MS

4.7. Thermodynamic parameters of adsorption

Essential information regarding the mechanism of interaction between MLJCE and the Al, Zn. and MS surface can be provided by adsorption isotherms [463]. The adsorption process is influenced by the charge, nature, and electronic state of the metal surface, the structure of the inhibitor compounds, the temperature of the corrosion reaction, the nature of the aggressive electrolyte, and the electrochemical potential at the solution interface [464, 465]. For the molecules of the methanolic extract to effectively adsorb on the surface of the metal and slow down the rate of corrosion, the strength of the interaction between the molecules of the extract (inhibitors) and the metal surface must be greater than that between the metal surface and the water molecules [419, 466, 467]. The degree of metal surface coverage (θ = %IE/100) by the inhibitor molecules depends

on the concentrations of inhibitors (C_{inh}). Since θ is the part of the metal surface covered by the inhibitor molecules, 1-θ is described as the part not covered by the inhibitor molecules. To assess the mode of adsorption of MLJCE molecules on three metal surfaces, the θ values obtained in the presence of 200 to 800 ppm inhibitor concentrations were fitted to different adsorption isotherms. Adsorption isotherms are used to distinguish between two forms of adsorption that can take place on metal surfaces, namely, physical or chemical adsorption, if not both. The θ values from the PDP, EIS, and weight loss analysis at 200 to 800 ppm and various temperatures were evaluated using different adsorption isotherms (Temkin, Flory-Huggins, Frumkin, kinetic-thermodynamic, and Langmuir adsorption isotherms). The Langmuir isotherm provided the best description of the experimental data for the adsorption mechanism of the extracts on the surfaces of the three metals. The linearity of the plots C_{inh}/θ versus C_{inh} (Figure 4. 38−4.41) and the correlation coefficient values (R^2) being close to unity supports this.

According to this isotherm, the surface coverage [i.e., θ = IE(%)/100] is related to the concentration of MLJCE, C_{inh} ($g.L^{-1}$), and the adsorption equilibrium constant, K_{ads} through the following expression:

$$\frac{C_{inh}}{\theta} = \frac{1}{K_{ads}} + C_{inh}. \quad (54)$$

The values of K_{ads} were extrapolated from the intercept (intercept = $1/K_{ads}$). The K_{ads}, was used to calculate values of the standard Gibbs free energy of adsorption (ΔG^{o}_{ads}) using equation (55):

$$\Delta G^{\circ}_{ads} = -RT \ln(K_{ads}) \quad (55)$$

T is the absolute temperature, while R is the universal gas constant (8.3145 $J.mol^{-1}.K^{-1}$). The unit for ΔG°_{ads} is commonly known as $J.mol^{-1}$. In equation (55), the K_{ads} must be dimensionless since the unit for the term RT is also $J.mol^{-1}$ [468]. Most of the ΔG^{o}_{ads} values reported in the literature are incorrect due to the use of numerical values of K_{ads} given in units such as ppm; this results in incorrect values for ΔG^{o}_{ads} of the adsorption process [468]. As adsorption is studied in an aqueous environment, the values of K_{ads} obtained from equation 54 in the current study must be in the $g.L^{-1}$ dimension to obtain the correct value of ΔG^{o}_{ads}. As a result, the concentrations of the extracts have been converted from ppm to $g.L^{-1}$ and multiplied by 1000 (1 L = 1000 ml) to make them dimensionless [468, 469] when plotting the isotherms so that they are equal to that of water. As a consequence, the correct values of ΔG^{o}_{ads} can be derived from equation (56):

$$\Delta G°_{ads} = -RT\ ln\ (1000K_{ads}) \quad (56)$$

The adsorption mechanism can be attributed to the electrostatic interaction between the charged metal surface and the charged adsorbate molecules based on the values of $\Delta G°_{ads}$, known as physisorption. It can also refer to a charge-sharing or charge-transfer process from the inhibitor molecules to the metal surface to form coordinate bonds, also known as chemisorption. Values of -20 kJ.mol^{-1} or less negative indicated physisorption, while –40 kJ.mol^{-1} or more negative indicated chemisorption [470-472]. The calculated $\Delta G°_{ads}$ values from PDP, EIS, and weight loss data were found to be greater than –20 kJ.mol^{-1} but less than –40 kJ.mol^{-1}, indicating that MLJCE extracts adsorb onto Zn, Al, and MS surfaces via a mixed-type adsorption process involving both physisorption and chemisorption adsorption. Table 4.7 shows that the $\Delta G°_{ads}$ for Al, MS, and Zn metals are all negative, indicating that the extracts adsorb spontaneously on the metal surfaces and the adsorbed film formed was stable. Although the R^2 values for the Langmuir adsorption isotherm are acceptable, slope values of the Langmuir plots deviate from unity, indicating that the isotherm cannot be applied implicitly. One of the Langmuir adsorption isotherm theories states that adsorbed inhibitor molecules do not interact with each other; however, this is incorrect for large molecules. Large molecules are said to interact with each other through mutual attraction or repulsion, and this behaviour affects the slope. The heat changes during the adsorption process as surface coverage increases have also been suggested as the cause of the slope deviation. The Langmuir isotherm has been said to be ineffective in accounting for these factors [473]. According to Table 4.7, the MS slope values deviate slightly from unity, while Al and Zn deviate significantly more. This implies that the adsorbed species interact with each other on the surfaces of MS, Al, and Zn metals. These discrepancies can be explained by considering another physical property of the adsorption isotherm relevant to the best fit of an isotherm besides the slope and R^2 values [469, 474, 475]. Therefore, the Langmuir isotherm was modified mathematically to account for the dimensionless constant; separation factor (K_L) defined by the relationship:

$$K_L = \frac{1}{1 + K_{ads}\left(\frac{C_{inh}}{1000}\right)} \quad (57)$$

Table 4.7: Gravimetric, EIS, and PDP Langmuir and Temkin adsorption isotherm parameters

Metal	Isotherm	Method	T (K)	R^2	Slope	Intercept	K_{ads} (L.g^{-1})	$\Delta G°_{ads}$ (kJ.mol^{-1})	–a
			303	0.999	0.9933	0.0111	90.0901	–28.7415	

MS	Langmuir	Weight loss	313	0.999	1.0180	0.0090	111.1111	–30.2359	–
			323	0.999	1.0099	0.0305	32.7869	–27.9241	
			333	0.999	0.9769	0.0609	16.4204	–26.8741	
		PDP	303	0.999	1.0592	0.0152	65.7895	−27.9496	
		EIS	303	0.999	1.0950	0.0218	45.8716	−27.0411	
	Temkin	Weight loss	303	0.822	0.0821	1.0065	1.8176×10^{12}	–88.5186	14.0256
			313	0.871	0.0397	0.9752	3.6661×10^{24}	–165.1740	29.0050
			323	0.920	0.1702	0.9791	5.6585×10^{5}	–54.1248	6.7656
			333	0.926	0.3108	0.9946	1.5856×10^{3}	–39.5277	3.7050
		PDP	303	0.7911	0.0534	0.9311	2.7315×10^{17}	−118.5493	–
		EIS	303	0.991	0.0960	0.9032	2.5604×10^{9}	−71.9792	11.9948
Zn	Langmuir	Weight loss	303	0.999	1.9165	0.0517	19.3424	–24.8656	–
			313	0.998	1.3066	0.0608	16.4474	–25.2643	
			323	0.999	1.2176	0.0203	49.2611	–29.0174	
			333	0.999	1.0982	0.0370	27.0270	–28.2537	
		PDP	303	0.999	1.0210	0.0111	90.0901	−28.7415	
		EIS	303	0.999	1.0429	0.0103	97.0874	−28.9300	
	Temkin	Weight loss	303	0.987	0.0636	0.5115	1.1026×10^{8}	–64.0558	18.1053
			313	0.933	0.1534	0.7405	6.7174×10^{4}	–46.9032	7.5065
			323	0.938	0.0701	0.8130	3.9600×10^{11}	–90.2690	16.4265
			333	0.836	0.1895	0.9044	5.9224×10^{4}	–49.5515	6.0765
		PDP	303	303	0.982	0.0556	0.9728	3.1362×10^{17}	118.8973
		EIS	303	303	0.926	0.0441	0.9515	37.6704×10^{20}	142.5626
Al	Langmuir	Weight loss	303	0.999	1.1028	0.0258	38.7597	–26.6167	–
			313	0.993	1.3895	0.1291	7.7459	–23.3046	
			323	0.988	1.6375	0.1937	5.1626	–22.9596	
			333	0.979	1.6519	0.1916	5.2192	–23.7006	
		PDP	303	0.999	1.0564	0.0637	15.6986	−24.3397	
		EIS	303	0.999	1.0037	0.1345	7.4349	−22.4568	
	Temkin	Weight loss	303	0.981	0.0976	0.8914	1.3589×10^{9}	–70.3833	11.7982
			313	0.892	0.2143	0.6641	1.2677×10^{3}	–36.5713	5.3733
			323	0.910	0.2061	0.5494	4.6313×10^{2}	–35.0355	5.5871
			333	0.783	0.1841	0.5409	8.6716×10^{2}	–37.8568	6.2548
		PDP	303	0.977	0.2506	0.9116	4.3421×10^{3}	−38.5046	4.5950
		EIS	303	0.988	0.4344	0.9064	1.2207×10^{2}	−29.5068	2.6508

Table 4.8 shows the calculated values of K_L for the different concentrations of MLJCE at temperatures ranging from 303 to 333 K for Al, Zn, and MS in 1 M HCl. According to Eduok and Khaled [475], KL > 1 or KL = 1 indicates that the adsorption process is unfavourable or considered irreversible and inconsistent with the Langmuir adsorption isotherm. If $K_L < 1$, the experimental data are favourable and fit the Langmuir adsorption isotherm. According to Table 4.8, the K_L values being less than unity for all MLJCE concentrations confirms that the adsorption process

favours the Langmuir isotherm. The value of K_L provides essential information about the nature of adsorption. The K_L values indicate whether the adsorption is irreversible ($K_L = 0$) or favourable ($0 < K_L > 1$). Apparently, when ($K_L > 1$), sorption is the favourable type of Langmuir isotherm [14]

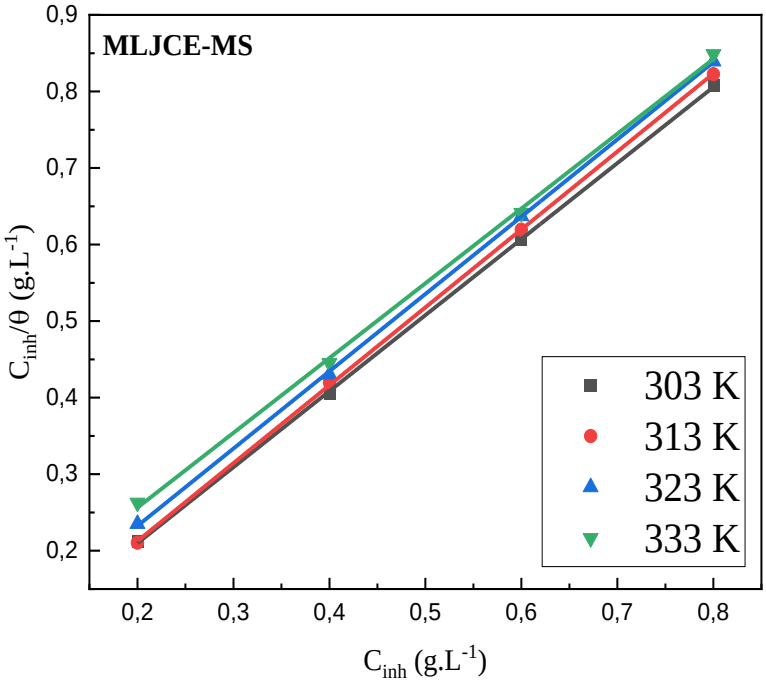

Figure 4. 38: Langmuir adsorption isotherm plots for MS, Zn, and Al corrosion in 1 M HCl in the presence of various concentrations of MLJCE

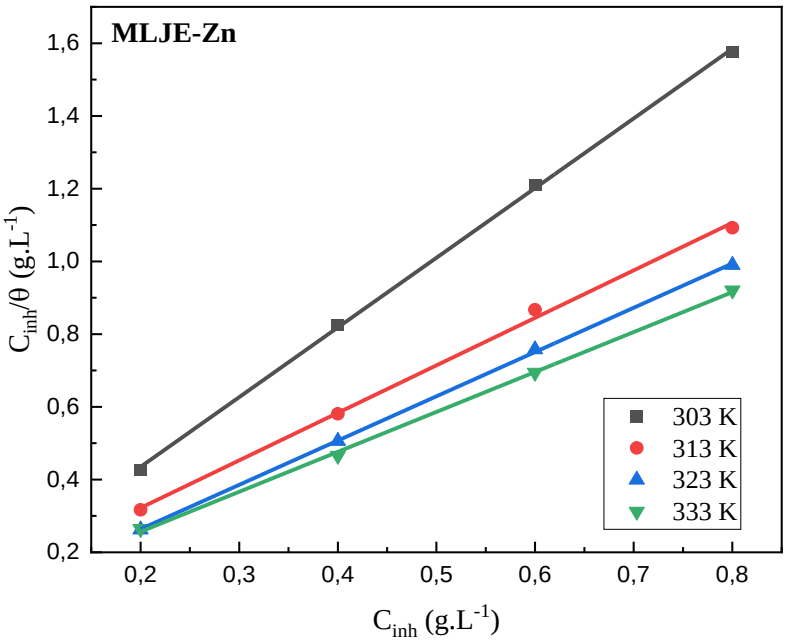

Figure 4.39: Langmuir adsorption isotherm plots for MS, Zn, and Al corrosion in 1 M HCl in the presence of various concentrations of MLJCE

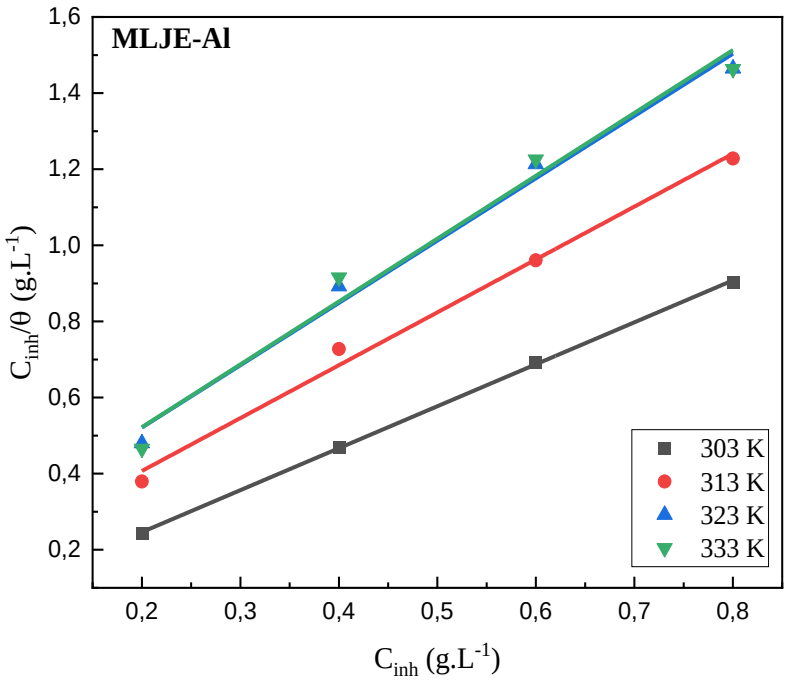

Figure 4.40: Langmuir adsorption isotherm plots for MS, Zn, and Al corrosion in 1 M HCl in the presence of various concentrations of MLJCE

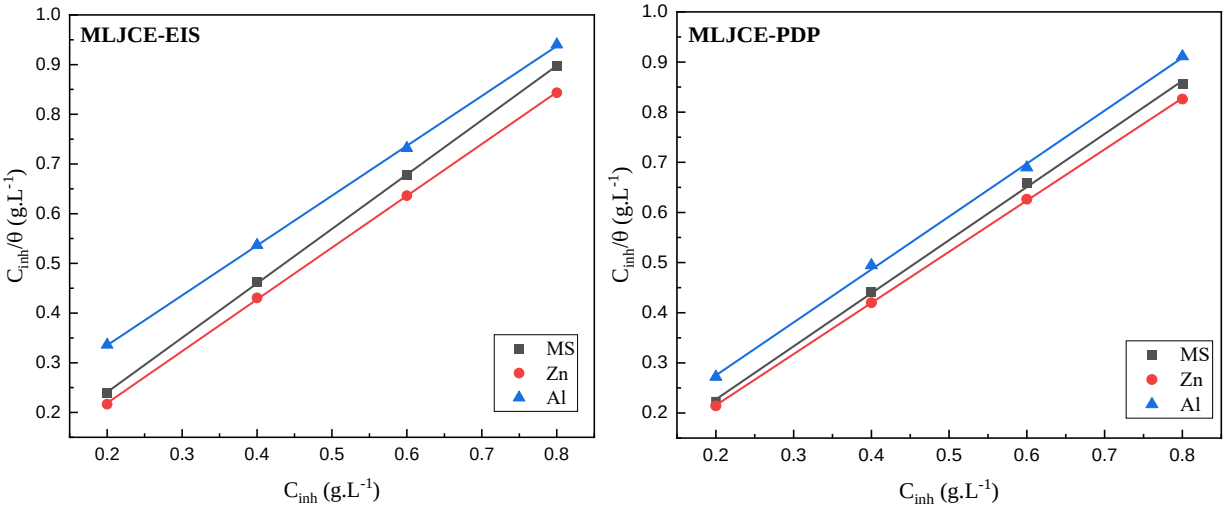

Figure 4.41: Langmuir adsorption isotherm plots for MS, Zn, and Al corrosion in 1 M HCl in the presence of various concentrations of MLJCE

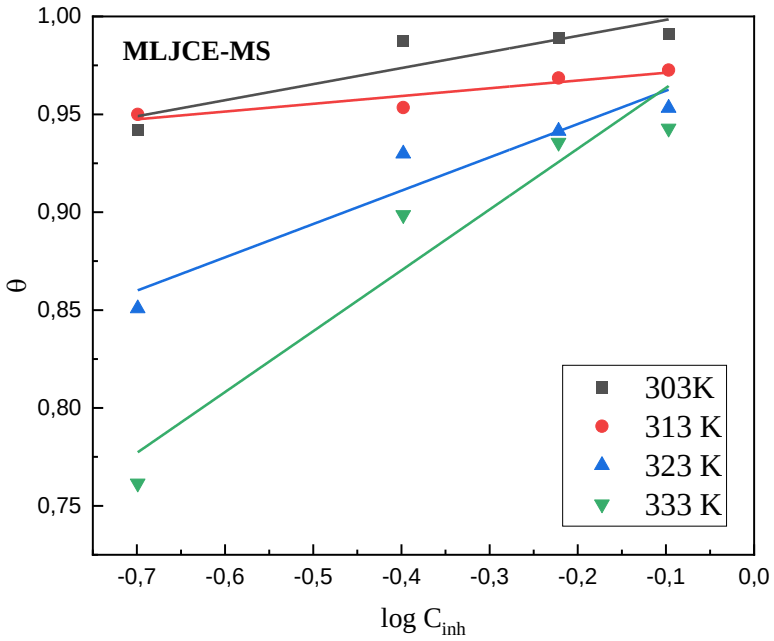

Figure 4.42: Temkin adsorption isotherm plots for MS, Zn, and Al corrosion in 1 M HCl in the presence of various concentrations of MLJCE

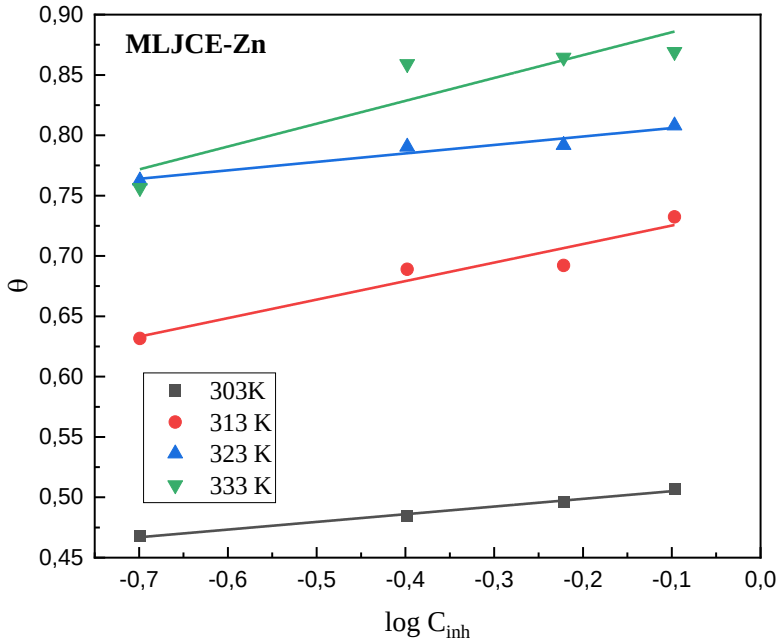

Figure 4.43: Temkin adsorption isotherm plots for MS, Zn, and Al corrosion in 1 M HCl in the presence of various concentrations of MLJCE

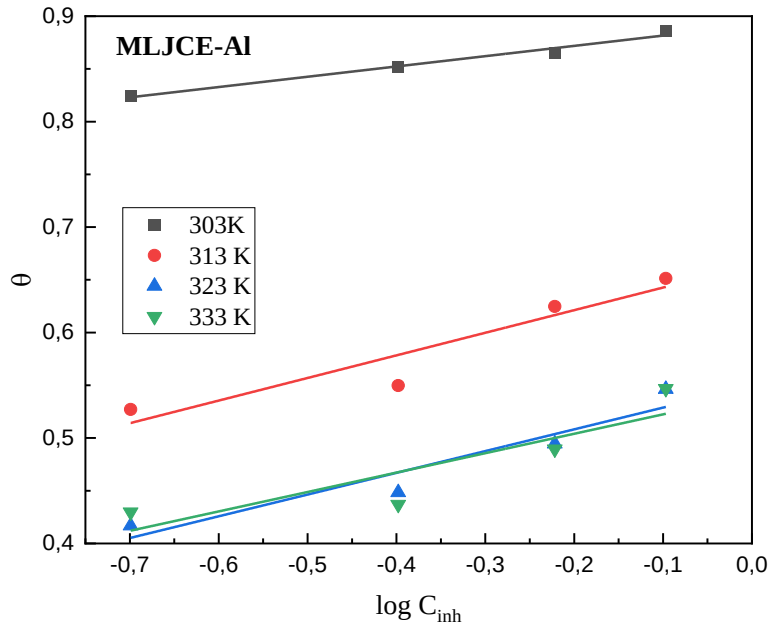

Figure 4.44: Temkin adsorption isotherm plots for MS, Zn, and Al corrosion in 1 M HCl in the presence of various concentrations of MLJCE

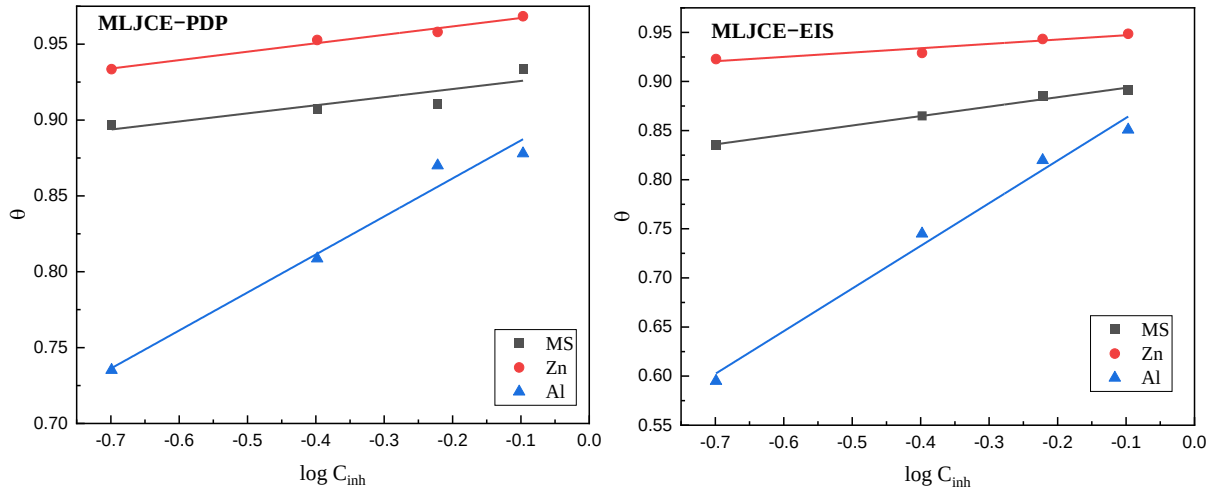

Figure 4.45: Temkin adsorption isotherm plots for MS, Zn, and Al corrosion in 1 M HCl in the presence of various concentrations of MLJCE

Other adsorption isotherms that consider the interaction of adsorbed species can be taken into account in addition to K_L [9]. One of these isotherms is the Temkin adsorption isotherm because it can account for lateral interactions that occur between inhibitors, and this was done by plotting θ against log C_{inh} (Figure 4.42−4.45), which has a slope of −2.303⁄2a and an intercept equal of $\left(-\frac{2.303}{2a}\right)\log K_{ads}$ using the following expression:

$$\theta = \frac{-2.303}{2a}\log K_{ads} - \frac{2.303}{2a}\log C_{inh}. \quad (58)$$

The applicability of the Temkin model to the adsorption of MLJCE on the surfaces of Al, Zn, and MS is confirmed by the relatively high R^2 values (Table 4.7). The presence of repulsion forces in the adsorption layer and surface heterogeneity is highlighted by the negative interaction parameters (a) [476]. Temkin's K_{ads} values are very high and associated with a strong interaction between the three metal surfaces and the extract [477]. The negative ΔG^{o}_{ads} values support the spontaneity of the MLJCE adsorption process on the Al, MS, and Zn surfaces and the stability of the formed adsorption layers. The Langmuir isotherm ΔG^{o}_{ads} values pointed to a mixed-type adsorption process whereases the values obtained from Temkin isotherm predict chemisorption adsorption isotherm since the values are way above or near −40 kJ.mol^{-1}. This points to a complex interaction between the metal surface and the MLJCE involving chemisorption and physisorption mechanisms [478].

Table 4.8: The K_L values for MLJCE at varying concentrations at 303 to 333 K for MS, Al, and Zn corrosion in 1 M HCl calculated from weight loss Langmuir isotherm parameters

Metal	Conc. of MLJCE (ppm)	K_L			
		303 K	313 K	323 K	333 K
MS	200	0.0526	0.0431	0.1323	0.2334
	400	0.0270	0.0220	0.0708	0.1321
	600	0.0182	0.0148	0.0484	0.0921
	800	0.0134	0.0111	0.0367	0.0707
Mean		0.0278	0.0228	0.0721	0.1321
Zn	200	0.2054	0.2331	0.0921	0.1561
	400	0.1145	0.1319	0.0483	0.0847
	600	0.0793	0.0920	0.0327	0.0581
	800	0.0607	0.0706	0.0247	0.0442
Mean		0.1150	0.1319	0.0495	0.0858
Al	200	0.1143	0.3923	0.4920	0.4893
	400	0.0606	0.2440	0.3263	0.3239
	600	0.0412	0.1771	0.2440	0.2420
	800	0.0312	0.1390	0.1949	0.1932
Mean		0.0618	0.2381	0.3143	0.3121

MLJCE showed high ΔG^{o}_{ads} values of up to –165.1740, –90.2690, –70.3833 kJ.mol^{-1} for MS, Zn, and Al metals, respectively. These high values could be due to the lateral interaction between the adsorbed MLJCE species on the metal surfaces. This is supported by Nnaji *et al*. [479], who noted the complex nature of the adsorption process and indicated that different adsorption isotherms could explain it; their results also showed high ΔG^{o}_{ads} values obtained via the Temkin adsorption isotherm.

4.8. FT-IR analysis of the MLJCE adsorption layer formed on the surface of Al, Zn, and MS in the 400-4000 cm^{-1} range

FT-IR analysis is a popular technique for analyzing the functional groups of corrosion inhibitor compounds responsible for interacting with the inhibitor and the metal surface. As a result, FT-IR was used to confirm the MLJCE's adsorption and assign the functional groups responsible for such a process on the surfaces of Al, Zn, and MS. This type of determination can aid in the selection of inhibitors to study or use in the industry. Most corrosion inhibition studies are carried out in a system that contains liquid water that is used to prepare various concentrations of inhibitor and corrosive solutions. When analyzing the adsorption layer formed by the inhibitors on the metal surface, liquid water could be recorded in the spectrum instead of the inhibitors. Although many liquids have a noticeable FT-IR absorption capacity, water is one of the more difficult liquids to assign because it produces intense and broad absorption bands across the entire mid-infrared region. Due to its extensive ability to form hydrogen bonds, water is a largely self-associating liquid. The resulting hydrogen bonds network fluid shows an almost continuous light absorption from the terahertz to the near IR range [480]. The FT-IR spectrum for water also shows the oscillation of O–H bonds around the 3000–4000 cm^{-1} region, which is one of the most critical absorption regions as it can overlap with absorption signals from important functional groups of inhibitors or hydrated systems. The absorption O–H band is usually characterized by two vibrations, the first vibration being associated with an asymmetrical stretch while the second is associated with an asymmetrical stretch [481, 482]. Another smaller combination band in the centre, around 2000 cm^{-1}, is the result of the coupling of the scissors bending and a near-infrared liberation band [480, 483]. The signal at around the 1600 cm^{-1} region is associated with the water scissors bend, while the signal around the 500–700 cm^{-1} region is associated with characteristic fingerprint-zone vibrations [374]. Besides these absorption bands, one of the main features of the water spectrum is its simplicity [374].

The water spectrum with only four significant signals means that the presence of any other substance should be easy to distinguish and assess. On the contrary, the vibration bands of liquid water can sometimes overlap with that of alcoholic compounds, with most overlap occurring when the concentration of the alcohol is very low. This is because both alcohol and water contain an O–H group, which produces intense broad stretching peaks in the 3000–4000 cm^{-1} region. This implies that water and alcoholic compounds share a spectral feature (O–H stretch), making it

challenging to identify the alcoholic compounds in the water solution [484]. Most studies have ascribed the contribution to corrosion inhibition to the liquid water molecules absorbed on the surface of various metals [485, 486], and as a consequence, attributing corrosion inhibition to the functional groups of the water molecules and not the inhibition compound molecules. The current work aims to highlight some of the erroneous FT-IR spectrum-vibrational band assignments concerning corrosion inhibition. According to Smith (2017) [487], Table 4.9 can be used to assign O–H stretch to pure alcohol, water, or a mixture of the two.

Table 4.9: The assignment of the O–H stretch when a sample contains alcohol, water, or both

The sample Contains	**–OH stretch (3400 cm^{-1})**	**–OH scissors (1630 cm^{-1})**	**–CO stretch (1300–1000 cm^{-1})**
Alcohol	+	+	+
Water	+	–	–
Both	+	+	+

4.8.1. FTIR analysis of liquid water solutions in the presence and absence of a corrosion inhibitor

To confirm the adsorption and to correctly assign the functional groups responsible for the adsorption on the surface of Al, Zn, and MS, the FT-IR spectrum of a liquid water solution (1 M HCl) in the presence and absence of MLJCE for Al, MS, and Zn systems (Figure 4.46) were analyzed and compared to the spectrum of pure liquid water. The results indicate that the properties of the spectra are identical to those of liquid water [483], even in the presence of the extract/inhibitor. This suggests that high-water concentration makes it difficult for FT-IR to detect the functional groups of inhibitor molecules in the solution. Several authors [485, 486, 488] analyzed solutions used to protect metals from corrosion, and their results showed that the spectrum obtained is almost identical to that of water. This implies that they most likely attributed the inhibition of corrosion to the functional groups of liquid water molecules rather than to those of the inhibitor. For example, Loto (2017) [489] studied the spectrum of a corrosion inhibitor dissolved in an acidic solution before and after a corrosion test. Although the FT-IR peaks obtained could be assigned to the functional groups of inhibitors responsible for corrosion inhibition, as reported in the publication, the presence of major peaks near the 3300 and 1630 cm^{-1} range point to the analysis of liquid water molecules, as this region is associated with two distinct peaks of water molecules.

During the adsorption process, inhibitors displace water molecules and other ions primarily adsorbed at the metal-solution interface to form a compact inhibition barrier [490, 491]. As a result, when analyzing the adsorption film formed on the metal surface, it is possible to analyze the part of the metal where liquid water molecules have not been displaced by the inhibitor molecules, resulting in water being included in the spectrum. This can also be attributed to the metal samples not being given enough time to dry completely. This was observed in Husaini's paper [492], which indicated an intense peak at around 3000–4000 cm^{-1} wavenumber on the metal surface (corrosion products); however, the absence of this peak on the spectrum of the crude compound suggests that it could be due to the presence of water on the surface of the corroded metal which results in the formation of hydrated Al oxide molecule ($Al_2O_3.\times H_2O$). In addition to the existence of the OH peak, there is also the existence of another peak at around 1600 cm^{-1}, which are both the prominent peaks observed in the FT-IR of liquid water, which indicates that Husaini's allocation of the 1600 cm^{-1} to the C=O stretch of carbonyl group may be incorrect as it could be the result of the scissors bending of liquid water.

The analysis of compounds in the corrosive, liquid water-containing solution has the disadvantage of not being able to precisely assign the corrosion inhibition to the functional group of the inhibitor compounds. This was observed by several authors [493-495] who studied the inhibitor solution before and after corrosion. Although their spectra are identical, they are similar to those of liquid water, implying that no functional inhibitor groups were observed. Their spectrum is also identical to that of Husaini, which was indicated as liquid water. Kusumastuti (2017) [496] analyzed the adsorption layer formed by the inhibitor on the surface of low-carbon steel and attributed the corrosion inhibition to it. However, the spectrum obtained shows that functional water groups were analyzed instead of the inhibitor. This is due to the simplicity of the spectrum, which shows absorption bands similar to those of water.

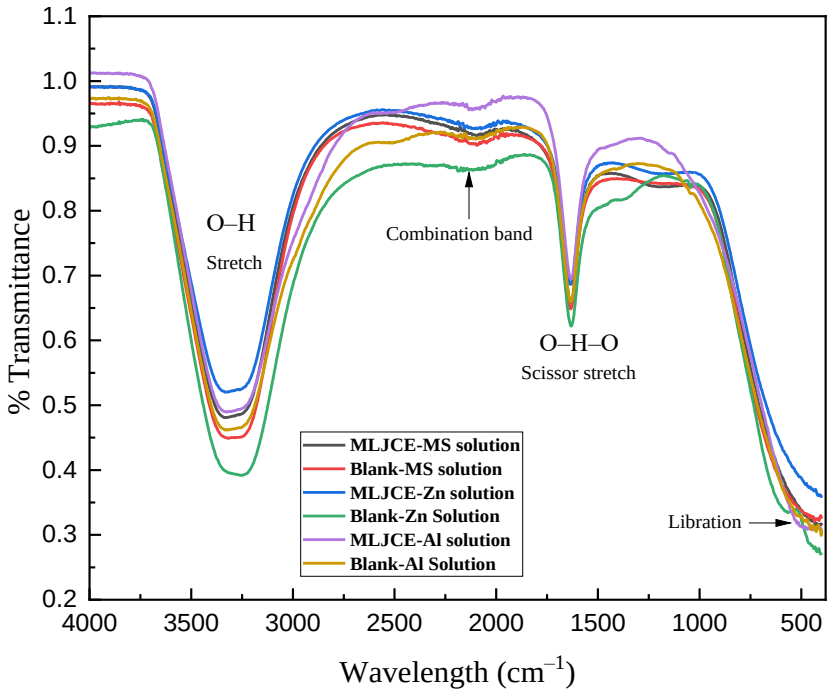

Figure 4.46: FTIR spectrum of the 1 M HCl solution of Zn, MS, and Al in the presence and absence of MLJCE corrosion inhibitor

In cases where corrosive liquid water solutions in the presence of the inhibitor are used to analyze the functional groups responsible for corrosion inhibition, an FT-IR analysis on the corrosive liquid water solution without an inhibitor is suggested to demonstrate whether inhibition has occurred successfully. This is because analysis of the two cases will highlight the difference in the intensity of the peaks in the two systems, indicating that an inhibition process had taken place. Renita (2015) [497], for example, analyzed the spectra of MS immersed in the corrosive solution in the presence and absence of the inhibitor and observed that the two spectra were identical. These spectra are similar to those obtained in the present study (Figure 4.46), in which Al, MS, and Zn samples were immersed in 1 M HCl without the corrosion inhibitor. The difference, however, was that the presence of the inhibitor in the solution resulted in a decrease in the intensity of the peaks associated with corrosion products such as Fe–O, suggesting that the presence of the inhibitor resulted in less iron oxide (rust) formation. The authors also suggest that the OH peak associated with liquid water had decreased in intensity, indicating that inhibitor adsorption on the MS surface reduced the surface area available for attack by HCl in liquid water.

4.8.2. FTIR analysis of corrosion products on the metal surfaces in the absence of MLJCE

After immersing MS, Zn, and Al in 1 M HCl without MLJCE for 7 hours, the samples were allowed to dry completely for a few days. The corrosion products on the metal samples were then scratched and analyzed to provide a basis for comparison with those in the presence of MLJCE. The blank-MS corrosion products spectrum (Figure 4.47) shows an intense broad stretch peak at around 3210 cm^{-1}, indicating the absorption of moisture from the liquid water, resulting in the formation of hydrated iron oxide ($Fe_2O_3.\times H_2O$), while the narrow stretch peak at 1620 cm^{-1} is due to the presence of water molecules (scissors) involved in the corrosion process. The absorption band at around 824 cm^{-1} is associated with goethite (α-FeOOH). The small peak located at about 1011 cm^{-1} is caused by lepidocrocite (γ–FeOOH), while the Fe–O bond stretching frequency peak appeared at 647 cm^{-1} based on research [498, 499]. The red colour of the rust of the corrosion products indicated the presence of ferric oxide (Fe_2O_3) in the rust formed.

The examination of the Al spectrum reveals a broad, intense peak around 3200 cm^{-1} and a narrow peak around 1620 cm^{-1}, indicating the presence of hydrated Al oxide ($Al_2O_3.\times H_2O$) and water. The stretching frequencies at around 1157 and 514 cm^{-1} correspond to γ–AlO_4 and γ–AlO_6, respectively, indicating that the γ–Al_2O_3 phase contains both octahedral and tetrahedral coordination's of Al oxide [500]. The characteristics of the absorption spectrum of the Zn corrosion products obtained in 1 M HCl are also shown in Figure 4.47. The spectrum shows a broad stretching peak around 3200 $cm^{-1,}$ which can be attributed to hydroxyl residue due to the hydrated zinc oxide molecule ($ZnO_3.\times H_2O$) stretching vibration. The characteristic peak at 1620 cm^{-1} is due to water molecules on the surface of Zn metal. A significant vibration band at 630 cm^{-1} is assigned to the characteristic stretching mode of the Zn–O bond, while the band at 460 cm^{-1} is due to the stretching and bending modes of the adsorbed water molecules.

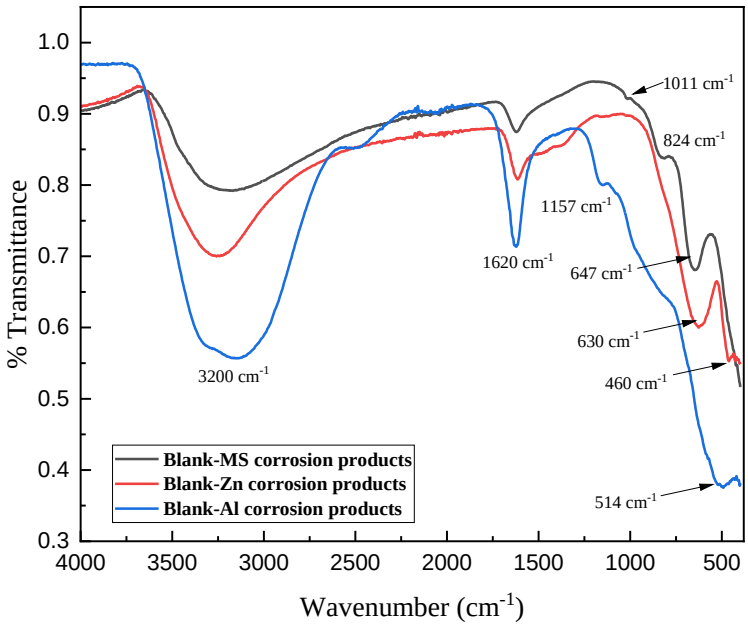

Figure 4.47: FT-IR spectrum of the corrosion products formed on Zn, MS, and Al surfaces after immersion in 1 M HCl solution without MLJCE

4.8.3. FT-IR analysis of adsorption film on the metal surfaces in the presence of MLJCE

The FT-IR spectrum of the adsorption film layer formed on the Zn, MS, and Al surface by MLJCE (MLJCE–MS, Zn, and Al adsorption films) in 1 M HCl solution were combined with those from Figure 4.46 and 4.47, and the results are shown in Figure 4.48–4.50. The figures show important peaks of MLJCE molecules present in the adsorption layer on three metal surfaces. The MLJCE–MS adsorption film spectrum indicates that the intense peak found around the 3200 cm^{-1} regions in the other spectra has shifted to form a broad, mild band at 3367 cm^{-1}. This suggests that the peak can be attributed to the hydroxyl group of the extracts, which binds to the MS surface (MS–OH) instead of water. The spectrum also indicates that the water scissors peak at around 1620 cm^{-1} has disappeared, and two new peaks appeared at about 1640 and 1610 cm^{-1}. This demonstrates that extracts adsorbed on the MS surface through the C–O, C=O, or the C=C groups. Also, the lepidocrocite peak at 1011 cm^{-1} shifted to a broad noticeable peak at around 837 cm^{-1}.

Meanwhile, the peaks at 824 and 647 cm^{-1} shifted to 642 and 433 cm^{-1} with reduced intensity. All these significant changes in peaks show that the extracts interacted with the MS surface, protecting it from the attack of the corrosive solution. In contrast, other peaks observed in the spectrum of the crude MLJCE disappeared after the inhibition of MS corrosion.

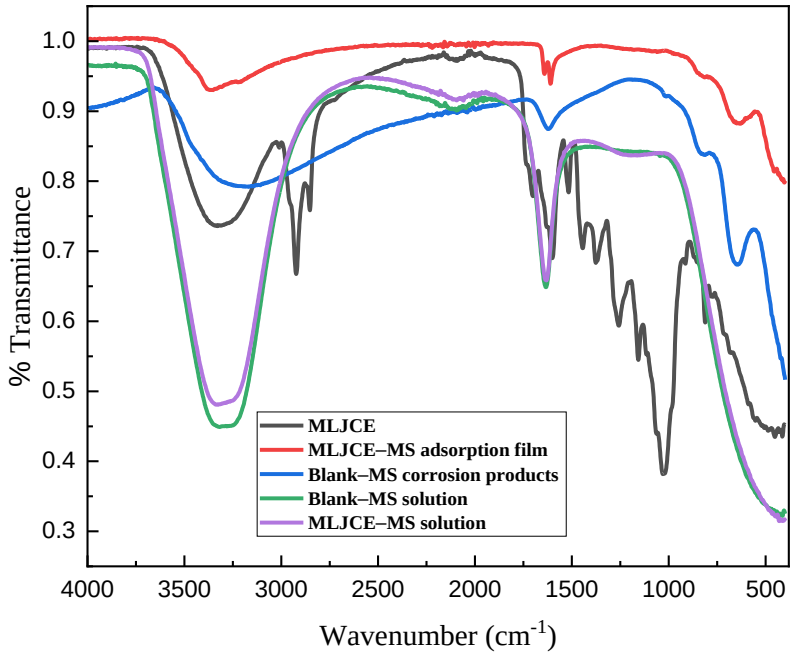

Figure 4.48: FTIR spectrum of the adsorption film formed on the MS surface (MLJCE-MS adsorption film) compared to the crude MLJCE, corrosion products formed on MS (Blank MS corrosion products), the 1 M HCl corrosion solution in the presence (MLJCE-MS solution) and the absence (Blank MS solution) of MLJCE

The corrosion of Zn was inhibited similarly to that of MS corrosion. There is a shift in the form of the hydrated zinc oxide ($ZnO_3.\times H_2O$) peak from an intense broad peak to a broader, narrower peak at 3350 cm^{-1}. This peak may have resulted due to the interaction of the O–H group of the extracts with the Zn surface. Meanwhile, at around 3209 $cm^{-1,}$ a new small peak was observed, and this might be due to the adsorption of either the methyl group ($C–H_3$) or methylene group ($C–H_2$) of the MLJCE. Two new peaks appeared at around 1634 and 1610 $cm^{-1,}$ which might have resulted from the binding of the C–O, C=O, or the C=C groups on the Zn surface. This indicates that the MLJCE prevented or limited the access of water molecules in HCl to the surface of Zn. Another new peak appeared at around 1022 $cm^{-1,}$ which could have resulted due to the adsorption of the C–O–C group on the Zn surface. The vibration band at 630 cm^{-1} has been reduced, suggesting that the Zn–O bond formed between Zn and the dissolved oxygen is weakened in the presence of the MLJCE and inhibits corrosion. The change and appearance of new peaks suggested that the MLJCE inhibited rust formation.

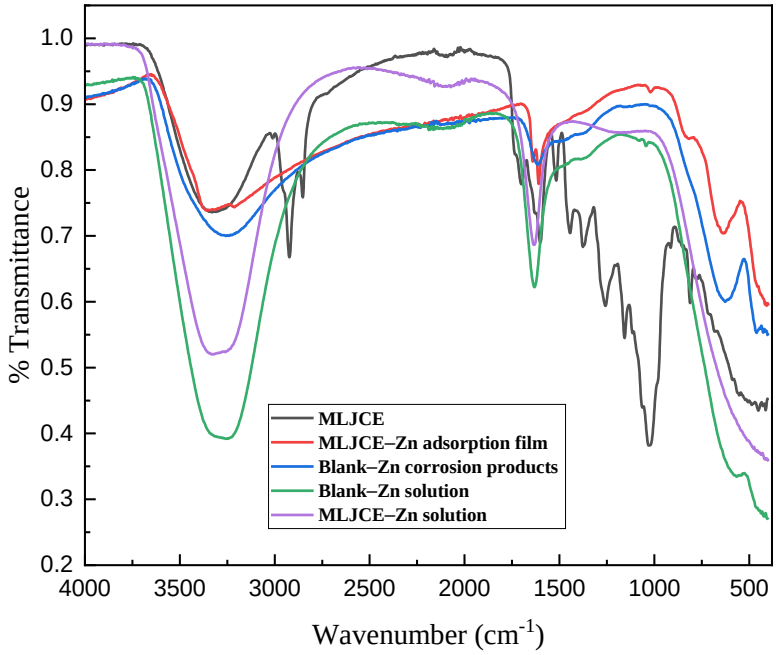

Figure 4.49: FTIR spectrum of the adsorption film formed on the Zn surface (MLJCE-Zn adsorption film) compared to the crude MLJCE, corrosion products formed on Zn (Blank-Zn corrosion products), the 1 M HCl corrosion solution in the presence (MLJCE-Zn solution) and absence (Blank-Zn solution) of MLJCE

The MLJCE adsorption film formed on the Al surface is shown in the spectrum in Figure 4.50, while Figure 4.51 is the expanded spectrum of the adsorption film formed on the Al surface. The spectrum indicates a peak at around 3000–3500 cm^{-1} can be assigned to both Al–OH of the MLJCE and the Al–H_2O bonds. The diffuse nature of this peak indicates a highly disordered structure formed by the extract, unlike the one observed for hydrated Al hydroxides [501]. This suggests that the extracts successfully reduced the access of water containing the 1 M HCl solution to the Al surface, thus protecting it from corrosion. The peak at 1620 $cm^{-1,}$ which is representative of the presence of water, has disappeared, and three peaks appeared at 1600, 1480, and 1420 cm^{-1}. These could be attributed to the adsorption of the amine groups and polyphenols on the Al surface. The absorption band observed around 1157 and 514 cm^{-1} have shifted to 860 and 507 $cm^{-1,}$ respectively. This shows that the MLJCE adsorption shifted the octahedral and tetrahedral Al oxide coordination. The shift and reduction in these peaks indicate that the extracts successfully reduced the Al rust formation.

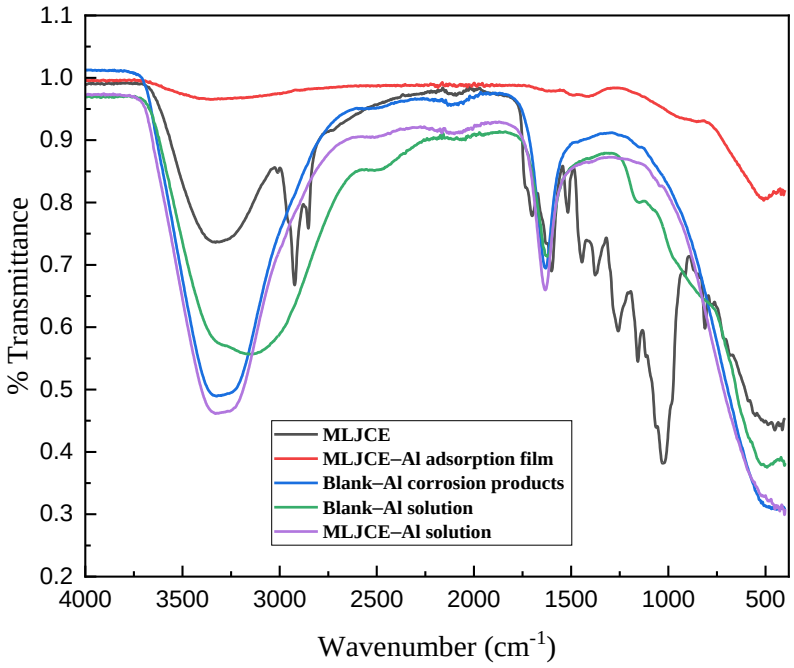

Figure 4.50: FTIR spectrum of the adsorption film formed on the Al surface (MLJCE-Al adsorption film) compared to the crude MLJCE, corrosion products formed on Al (Blank-Al corrosion products), the 1 M HCl corrosion solution in the presence (MLJCE-Al solution) and absence (Blank-Al solution) of MLJCE

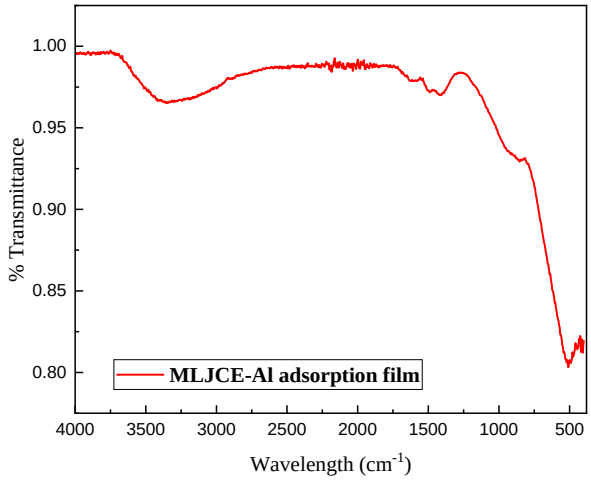

Figure 4.51: Expanded FTIR spectrum of the adsorption film formed on the Al surface (MLJCE-Al adsorption film)

4.9. UV-visible spectroscopy: Interaction of MLJCE with Al^{3+}, Fe^{2+}, and Zn^{2+} cations

Further confirmation of the interaction between the MLJCE components with the Al, MS, and Zn surface was examined using a UV–vis test. The spectra of the 1 M HCl solution before (1 M HCl) and after immersion of the three-metal specimen in the absence (Blank–Fe^{2+}, Blank–Zn^{2+}, and Blank–Al^{3+}) and presence of 800 ppm MLJCE (MLJCE–Fe^{2+}, MLJCE–Al^{3+} and MLJCE–Zn^{2+}) were compared to those of MLJCE (MLJCE in 1M HCl) as shown in Figure 4.52–4.54. The UV traces of the 1 M HCl and the uninhibited systems (Blank–Fe^{2+}, Blank–Zn^{2+}, and Blank–Al^{3+}) are almost identical and used as the control. The UV spectrum of MLJCE dissolved in 1 M HCl indicates an intense long-wavelength band (215–290 nm), and the immersion of the metal specimens in this solution (MLJCE–Fe^{2+}, MLJCE–Al^{3+} and MLJCE–Zn^{2+}) for 7 hours resulted in the shift of the band to around 342 nm. This shift is referred to as a bathochromic shift and could be attributed to the occurrence of π–π* and n–π* transitions which could be the result of the C=C, O–H, and C=O of the organic components of the MLJCE extract [502-504]. The bathochromic shift and the reduction in the absorbance intensity indicate that an intramolecular electron transfer from a ligand to inhibitor compounds, also known as ligand-to-metal charge transfer (LMCT), occurred [505-507].

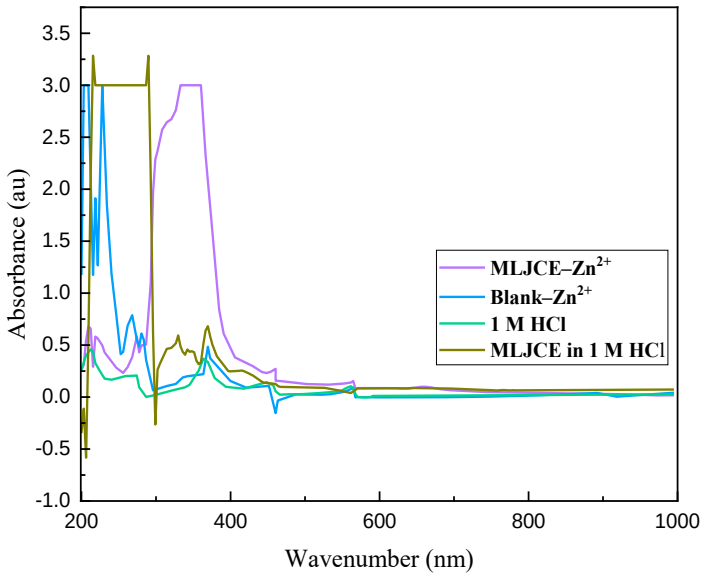

Figure 4.52: UV-vis spectra for 1 M HCl solution without and with MLJCE before immersion of the metal sample (MLJCE in 1M HCl), after immersion (MLJCE–Zn^{2+}), and the sample without MLJCE (Blank–Zn^{2+})

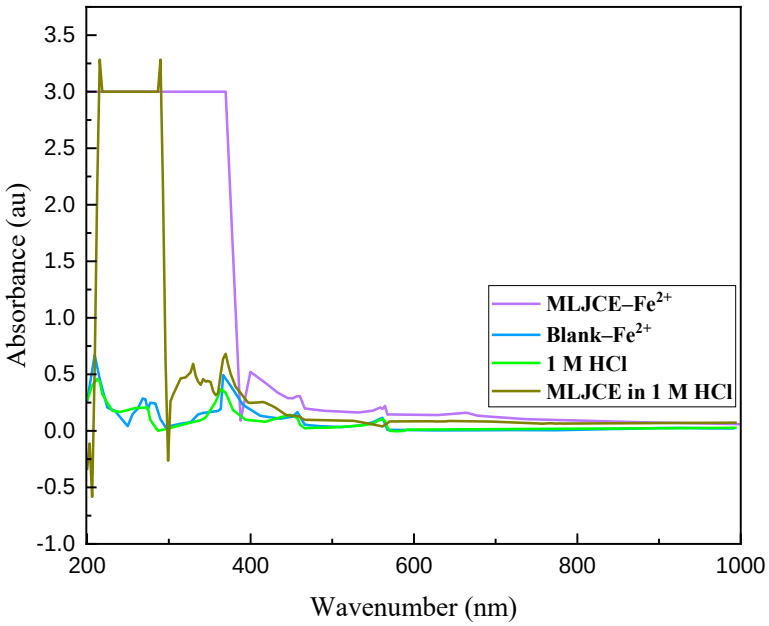

Figure 4.53: UV-vis spectra for 1 M HCl solution without and with MLJCE before immersion of the metal sample (MLJCE in 1M HCl), after immersion (MLJCE–Fe^{2+}), and the sample without MLJCE (Blank–Fe^{2+})

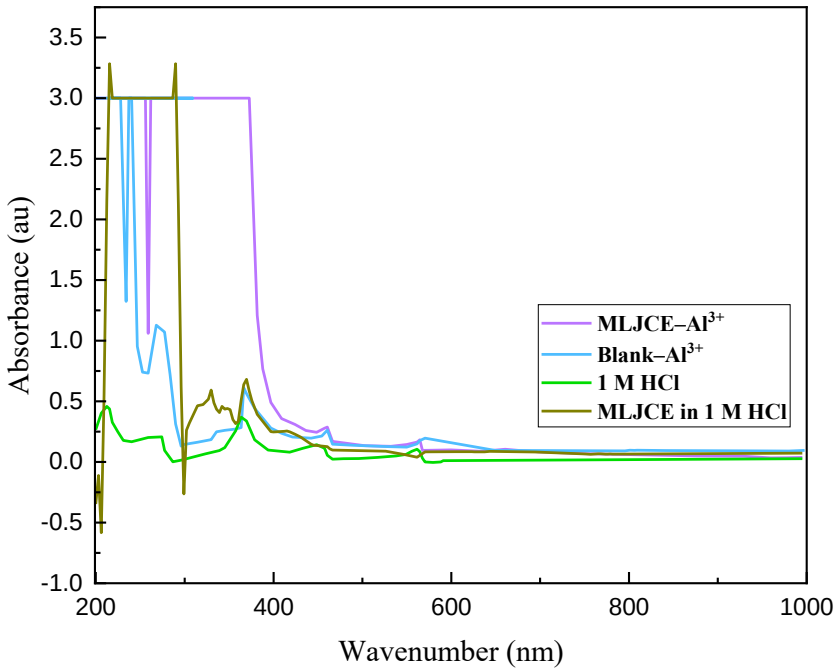

Figure 4.54: UV-vis spectra for 1 M HCl solution without and with MLJCE before immersion of the metal sample (MLJCE in 1M HCl), after immersion (MLJCE–Al^{3+}), and the sample without MLJCE (Blank–Al^{3+})

4.10. Water contact angle measurement

The characterization of the metal surface is crucial to determine the adsorbed layer formed by corrosion inhibitors. The adsorbed layer is said to be responsible for limiting the attachment of water molecules or O_2 diffusion to the metal surface, slowing down the kinetics of corrosion [508]. Contact angle measurements for polished untreated metal substrates, metal substrates immersed in 1 M HCl medium without inhibitor, and metal substrates immersed in the presence of 800 ppm MLJCE for 7 hours at 303 K are shown in Figure 4.55–4.57 for MS, Zn, and Al, respectively. Figure 4.55 reveals that the contact angle for MS decreased from 82.403° to 67.546° when the metal was immersed in 1 M HCl compared to the polished untreated metal sample. The reduction in contact angle in 1 M HCl results from the degradation of the MS surface, producing corrosion products that cause an increase in the surface roughness of the metal [509]. The reduction in contact angle to 67.546° indicates that the MS became more hydrophilic, suggesting that it became more wettable since the angle was well below 90° [347]. The contact angle for Zn and Al (Figures 4.56 and 4.57) decreased from 93.647° and 66.314° to 73.257° and 47.956°, respectively. This implies that the immersion of Zn and Al in the corrosive solution also increased the surface roughness of Zn and Al due to the attack of the exposed surfaces by Cl^- ions. Immersing the three metals in the corrosive solution in the presence of the optimum concentration of MLJCE (800 ppm) increased the contact angle, indicating an increase in the hydrophobicity of the metal surfaces. For instance, the contact angle increased to 98.977, 95.200, and 121.812° for MS, Zn, and Al, respectively. This increase in contact angle for Al, Zn, and MS in the presence of MLJCE reveals the formation of an adsorption film of MLJCE on the metal surfaces, which inhibits their corrosion [510, 511].

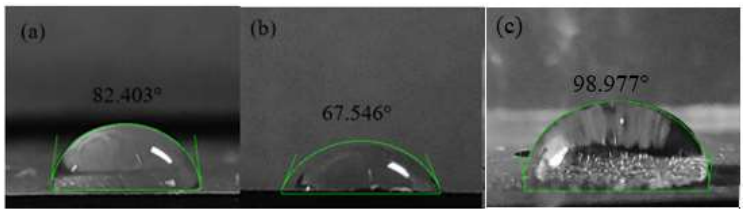

Figure 4.55: Surface wettability behaviour of (a) polished untreated MS substrate, (b) MS substrate after 7 hours of immersion in 1 M HCl medium with no inhibitor, and (c) in the presence of 800 ppm of MLJCE

Figure 4.56: Surface wettability behaviour of (a) polished untreated Zn substrate, (b) Zn substrate after 7 hours of immersion in 1 M HCl medium with no inhibitor, and (c) in the presence of 800 ppm of MLJCE

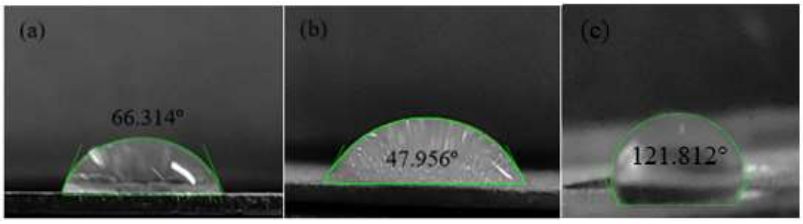

Figure 4.57: Surface wettability behaviour of (a) polished untreated Al substrate, (b) Al substrate after 7 hours of immersion in 1 M HCl medium with no inhibitor, and (c) in the presence of 800 ppm of MLJCE

4.11. SEM/EDS and Elemental Mapping

The morphology and the elemental composition of MS, Zn, and Al surfaces in 1 M HCl solution in the absence and presence of 800 ppm MLJCE were studied using SEM/EDS. In addition to the SEM/EDS analysis, elemental mapping of the MLJCE-inhibited surfaces was also performed. The SEM/EDS and elemental mapping results from the two environmental systems (uninhibited and MLJCE-inhibited systems) were compared to those obtained for the polished but untreated samples. SEM images with their respective EDS spectra for Zn, MS, and Al are shown in Figures 4.58, 4.60, and 4.61, respectively. The SEM images of the unexposed polished MS, Al, and Zn surfaces revealed a smooth and uniform surface with minor damage that may have occurred during the sample preparation process, which included abrasion with various grades of emery papers. At the same time, the EDS spectra revealed that these surfaces are primarily composed of 99.80 wt%, 97.07 wt%, and 99.51 wt%, respectively, with a low presence of other elements. SEM micrographs of the three metal electrodes exposed to 1 M HCl without protection show that the samples were severely damaged, with cavities and sizable pits indicating the corrosive Cl^- ions in the solution had penetrated much deeper into the electrode surfaces. The images suggest that the Al surface was more damaged than the two other metals, as large pits were revealed throughout its entire surface. While EDS spectra in this condition revealed the presence of similar elements on the metal surfaces as observed for the unexposed polished surface, but in slightly different proportions, Fe (99.74 wt%), Al (95.39 wt%), except for Zn (Fe, 99.58 wt%). The high Fe content of the Zn surface indicates that immersion in 1 M HCl dissolves the Zn-plated layer, exposing the high Fe content.

After adding 800 ppm MLJCE to the acidic solution, the surface morphology of the three metals showed a relatively smoother surface with some island areas and minor damages resembling the polished surface. The island parts could have formed due to MLJCE precipitation on the metal surfaces, which shielded them from the corrosive solution. The similarities between the MLJCE-treated surfaces and the unexposed polished surfaces suggest that the extracted molecules adsorb on the metal surfaces and form a protective film. Close inspection of the corresponding EDS spectra images in the presence of MLJCE reveals that the metals are primarily composed of Fe (99.86 wt%), Al (99.51 wt%), and Zn (0.17 wt%), with a high concentration of Fe (99.83 wt%). The precipitates observed in the presence of MLJCE were further analyzed using EDS mapping. The results were compared to a blank counterpart to determine their main composition, as shown in Figures 4.59, 4.61, and 4.63, respectively, for Zn, MS, and Al. The precipitates formed were

mainly O_2 for Zn and Al elements; for MS, it was carbon in the presence of MLJCE. The existence of O_2 elements attributes to the coverage of the metal surfaces by the corrosion products [512, 513]. The high O_2 content also indicates the existence of O_2-containing groups in the adsorbed MLJCE components [513]. The high content of carbon in the island areas for MS in the presence of the inhibitor was also observed by Ralkhal *et al*. [514], who attributed it to inhibitor adsorption on the metal surface.

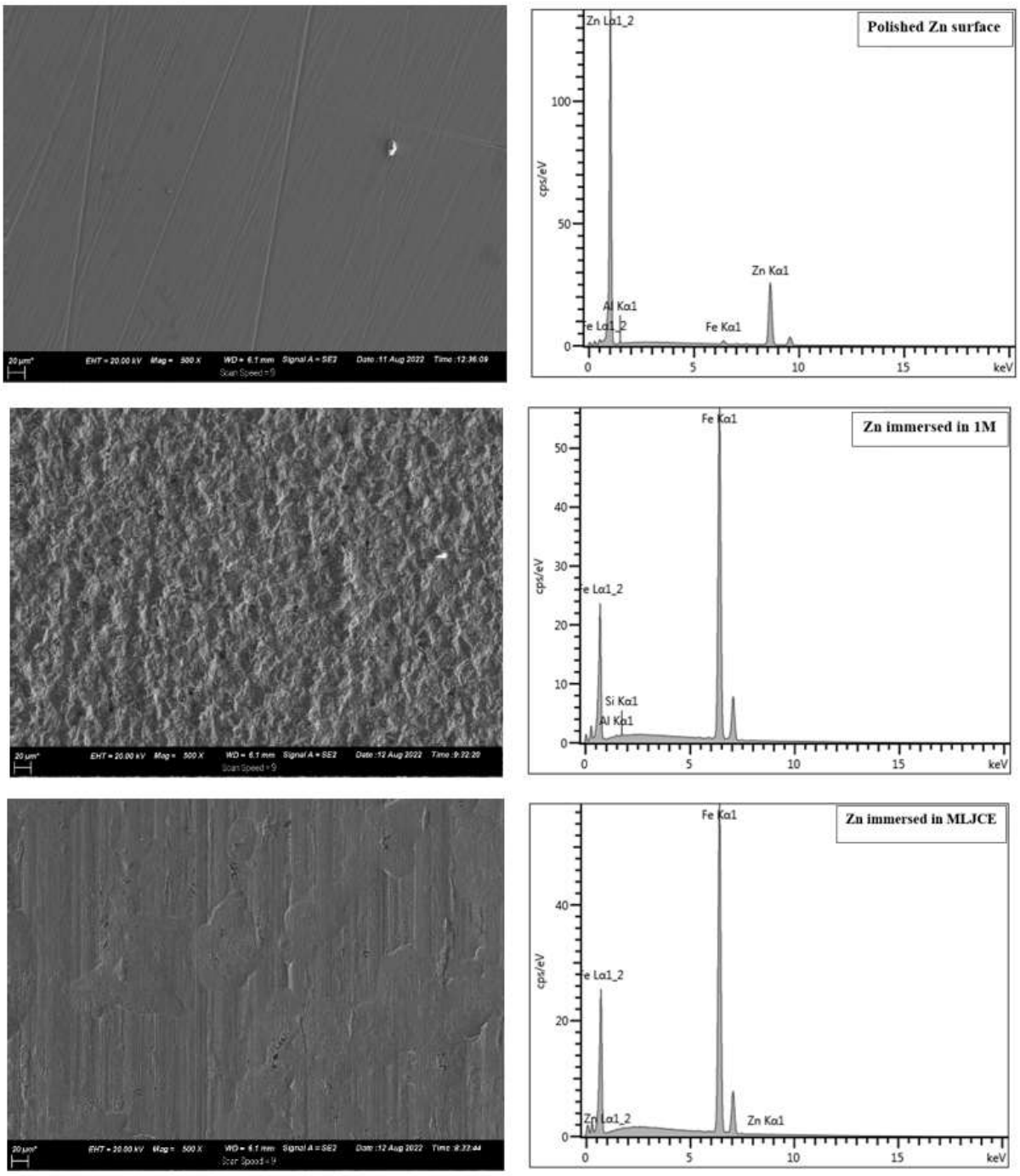

Figure 4.58: SEM images and EDS spectra of unexposed-polished Zn surface, Zn immersed in uninhibited 1 M HCl, and Zn immersed in MLJCE-inhibited 1 M HCl solution

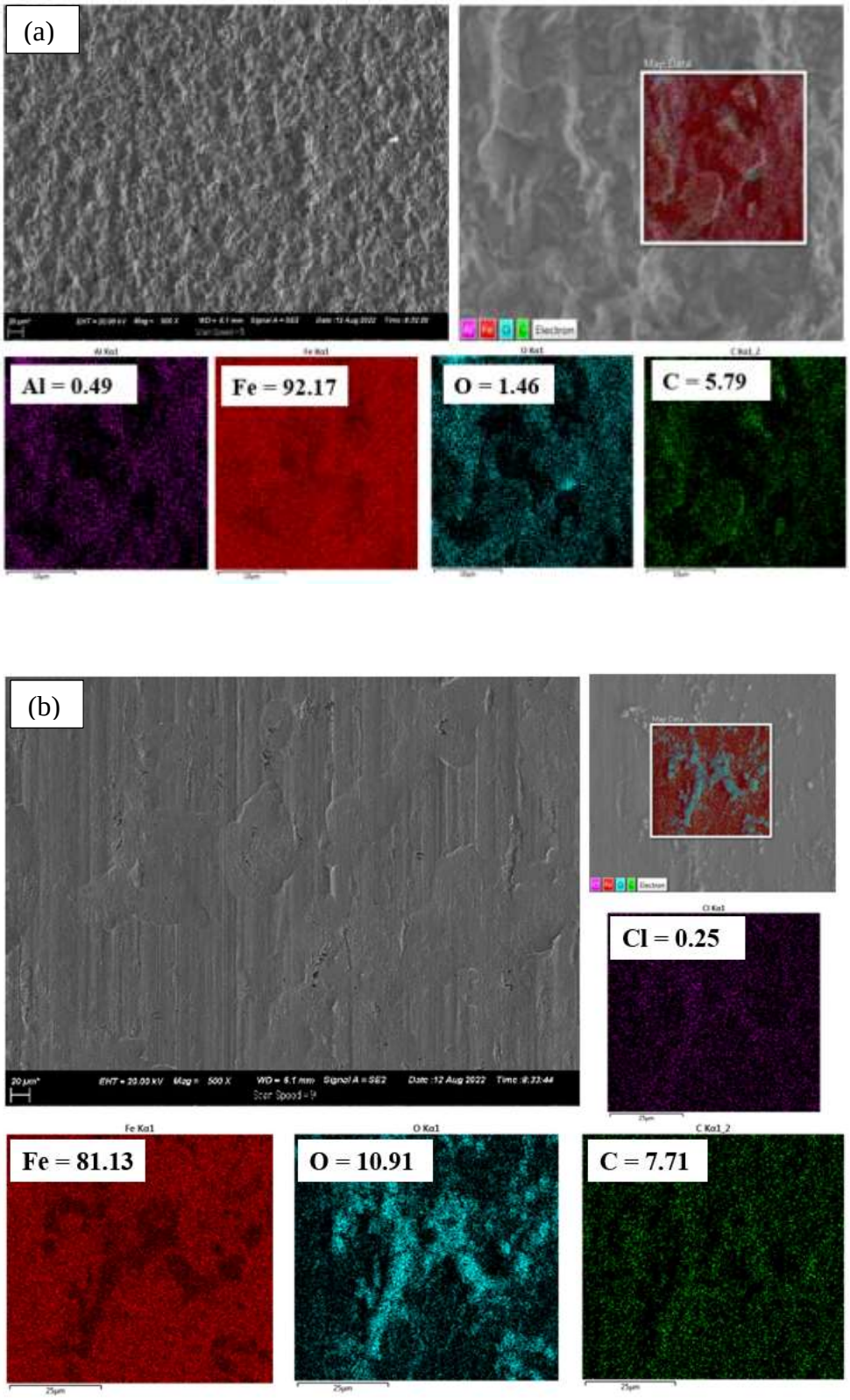

Figure 4. 59: EDS map analyses for Zn exposed to the corrosive solution in the (a) absence of the extract and the (b) presence of 800 ppm of the extract

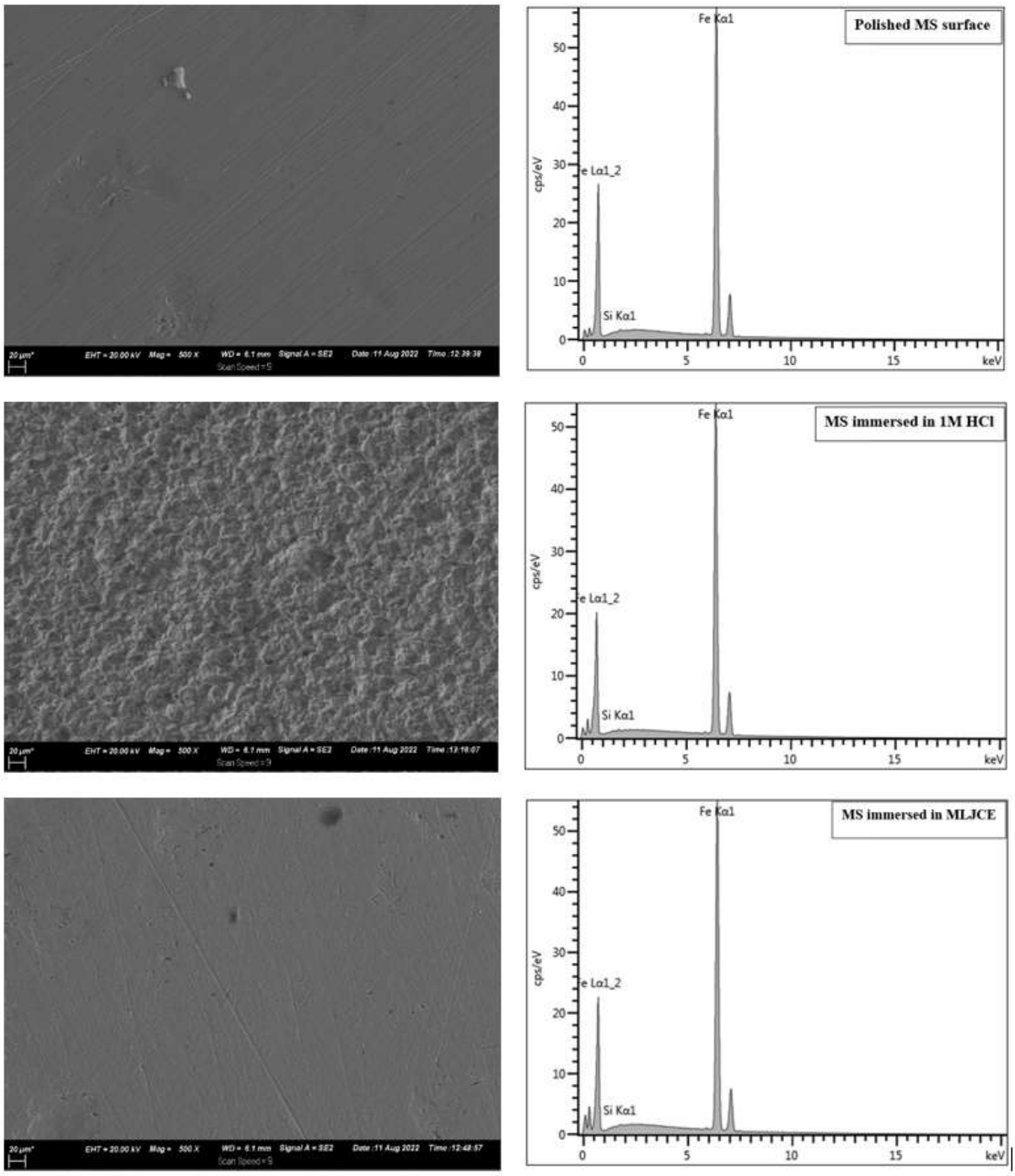

Figure 4.60: SEM images and EDS spectra of unexposed-polished MS surface, MS immersed in uninhibited 1 M HCl, and MS immersed in MLJCE-inhibited 1 M HCl solution

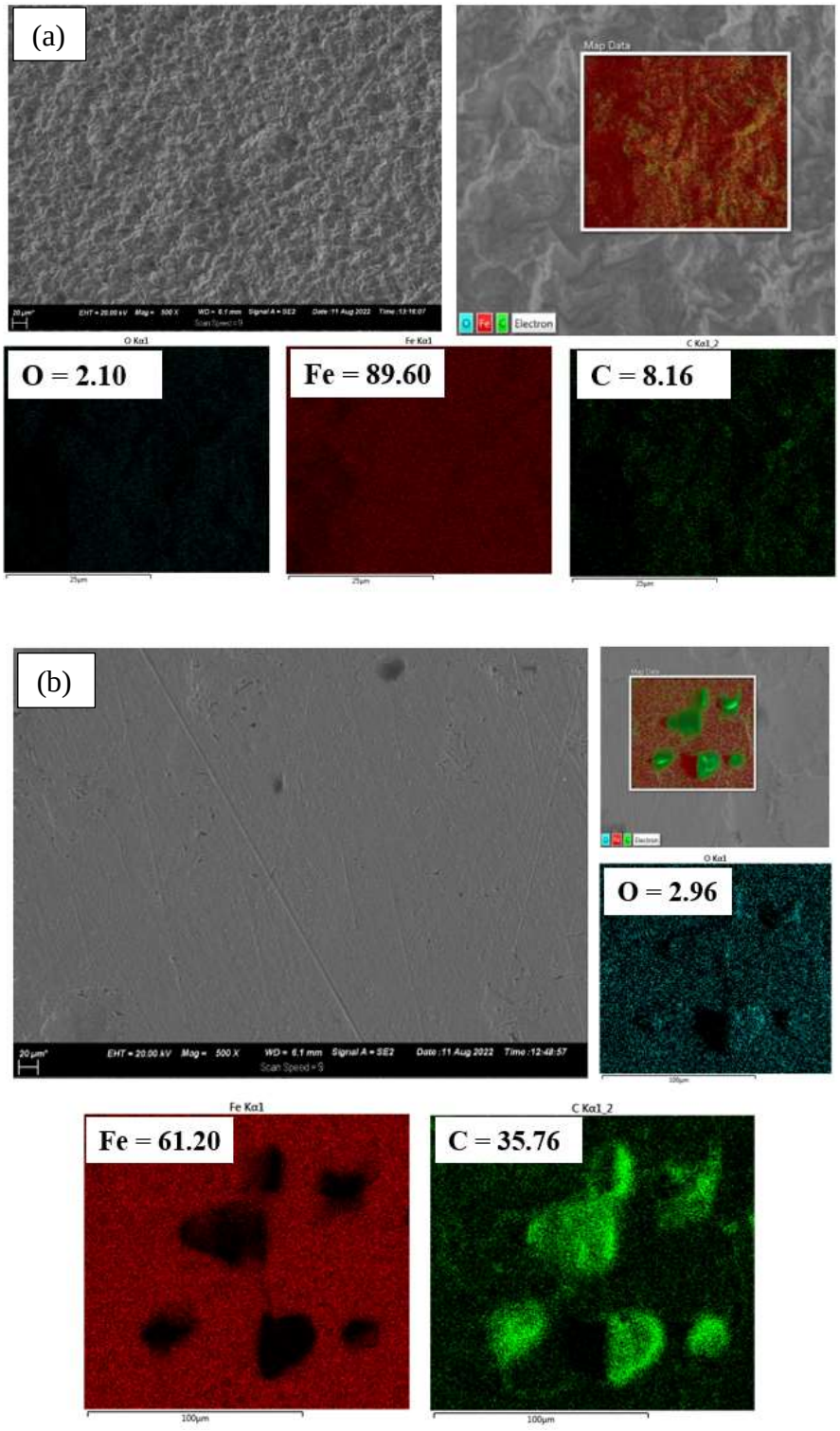

Figure 4.61: EDS map analyses for MS exposed to the corrosive solution in the (a) absence of the extract and the (b) presence of 800 ppm of the extract

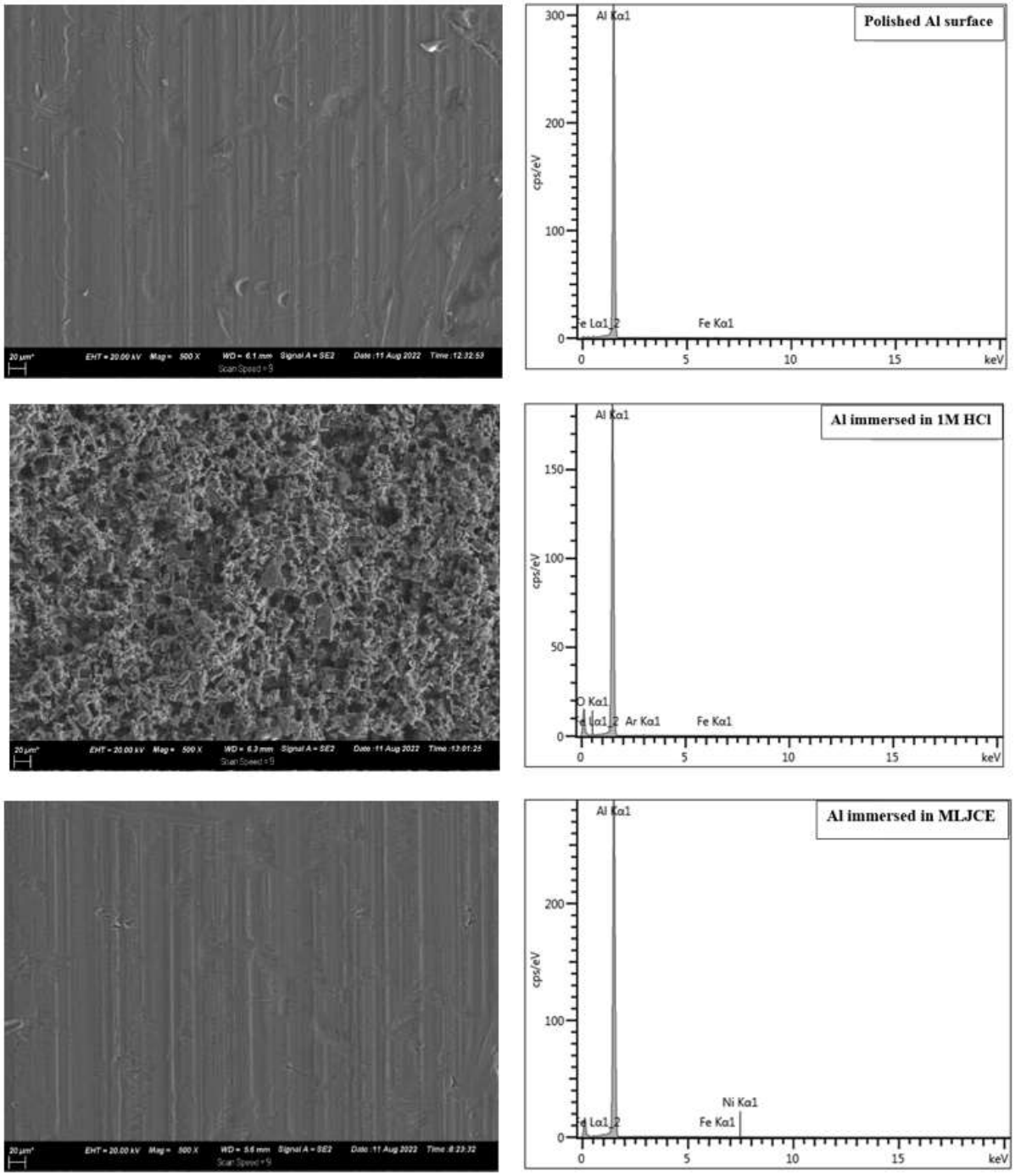

Figure 4.62: SEM images and EDS spectra of unexposed-polished Al surface, Al immersed in uninhibited 1 M HCl, and Al immersed in MLJCE-inhibited 1 M HCl solution

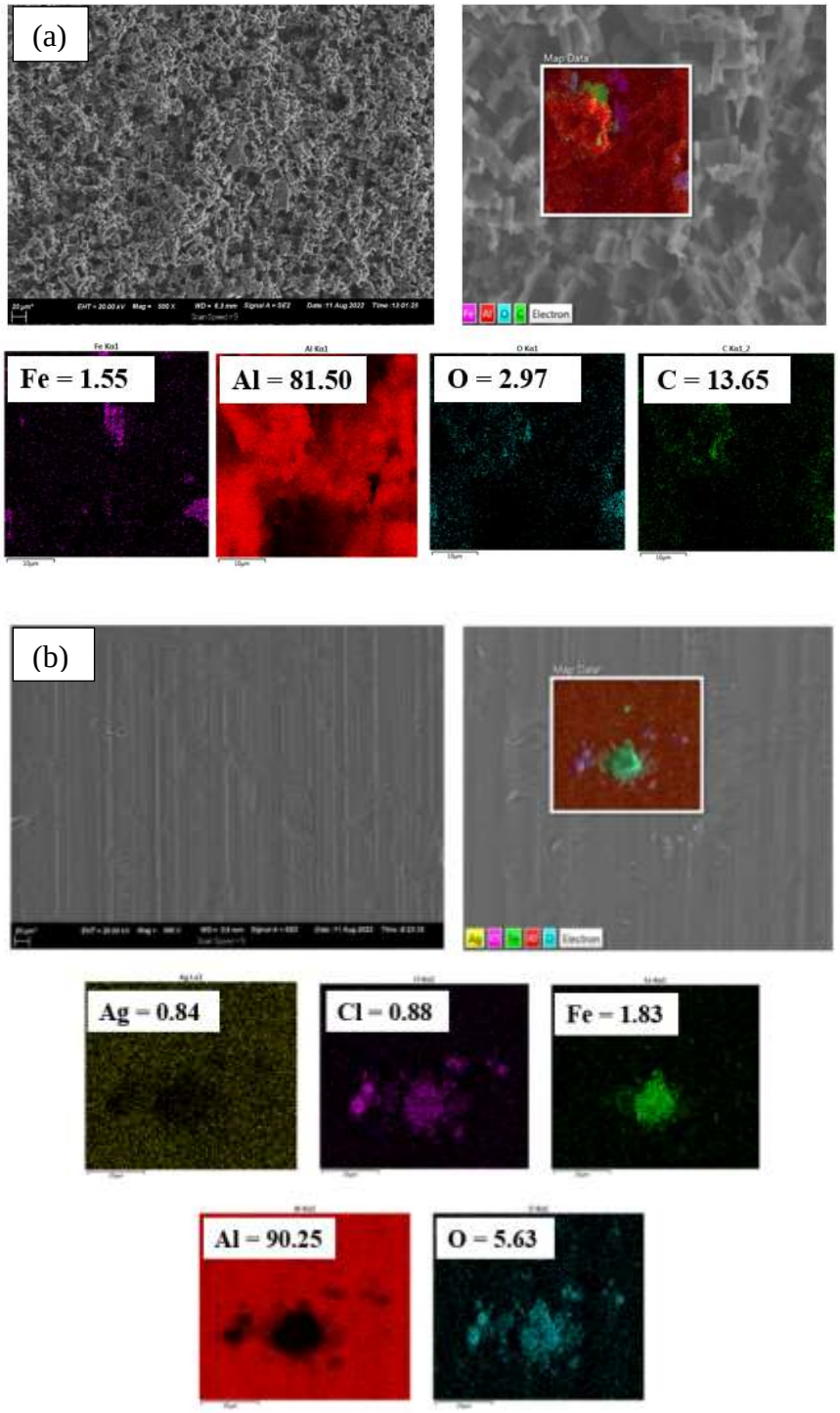

Figure 4.63: EDS map analyses for Al exposed to the corrosive solution in the (a) absence of the extract and the (b) presence of 800 ppm of the extract

CHAPTER 5

Ethanolic extract results and discussions

This chapter summarises and discusses the findings from the Ethanolic *L. javanica* crude leaf extract (ELJCE). The crude extracts were characterised using LC/MS and FT-IR spectroscopies. Weight loss analysis with a focus on the effect of temperature and inhibitor concentration, adsorption isotherms and thermodynamic parameters, and adsorption film analysis were all used to assess the corrosion potential of ELJCE. Electrochemical techniques were used to assess the corrosion resistance, degradation, and corrosion inhibition mechanisms of the inhibitors. Surface analysis of the extracts' protective film on metal surfaces was also performed.

5. Ethanolic *L. javanica* crude leaf extract (ELJCE) as a green inhibitor for Zn, Al, and MS corrosion

5.1. HPLC analysis of ELJCE

The ELJCE LC/MS chromatogram is shown in Figure 5.1. LC/MS analysis of the leaf extract identified several compounds, and 17 of the primary compounds identified are listed in Table 5.1, along with their molecular formula, retention time, and molecular weight. It can be seen from the listed compounds that the extract contains O_2 as the main heteroatom and also π-electrons in their molecules. Some of the compounds also consist of nitrogen atoms. Like the extracts from the methanol solution, the primary compound in the ELJCE was VBS [515]. The presence of phytochemicals with O_2 and π-electrons in their molecular structure and possible synergistic effects can be attributed to the ELJCE adsorption on the MS, Al, and Zn surfaces. The complex chemical compositions of plant extracts, similar to MLJCE, make it challenging to attribute inhibitory activity to any individual compound in the leaf extract.

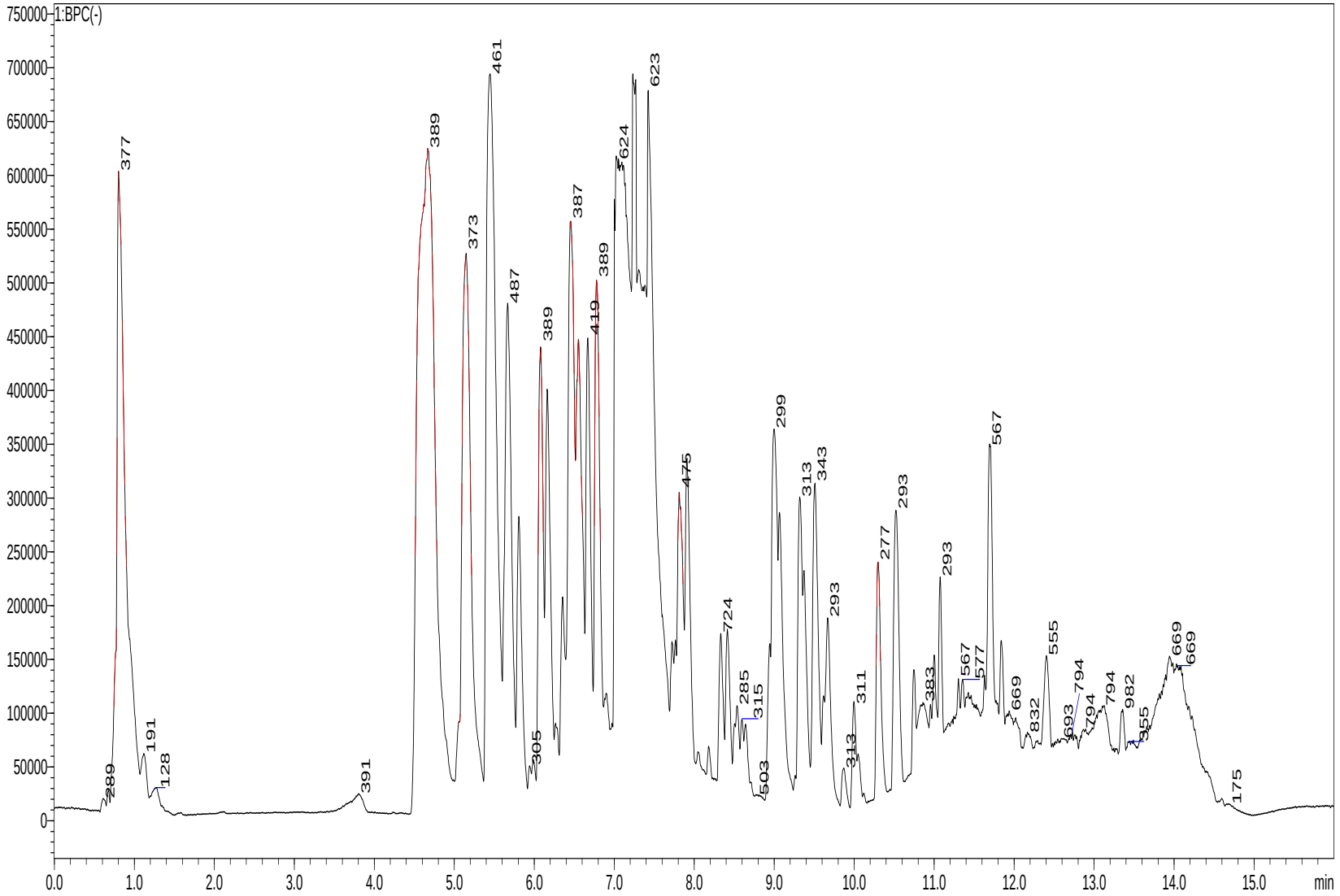

Figure 5.1: Total ion chromatograms of phytochemicals mixtures of ELJCE measured by LC/MS in negative ion mode

Table 5.1: Phytochemicals identified in the ELJCE

S.No.	RT (min)	Name of the compound	MF	MW
1	4.67	Bis(2-O,3-O,4-O,6-O-tetraacetyl-D-gluconic acid)tetramethylene ester		763.23
2	5.45	Decaffeoyl-acteoside	$C_{20}H_{30}O_{12}$	461.16
3	6.03	Heriguard	$C_{16}H_{18}O_9$	353.09
4	6.65	Dig3Ac(b1-4)Dig(b1-4)Dig	$C_{20}H_{34}O_{11}$	431.19
5	7.23	Acteoside/Verbascoside	$C_{29}H_{36}O_{15}$	623.19
6	7.42	Isoacteoside/Isoverbascoside	$C_{29}H_{36}O_{15}$	623.20
7	7.91	Cistanoside D	$C_{31}H_{40}O_{15}$	651.23
8	8.18	[(2R,3S,4R,5R,6S)-6-[2-(3,4-dihydroxyphenyl)ethoxy]-4,5-dihydroxy-2-[[(2R,3R,4S,5S,6S)-3,4,5-trihydroxy-6-methyloxan-2-yl]oxymethyl]oxan-3-yl] (E)-3-phenylprop-2-enoate	$C_{29}H_{36}O_{13}$	591.21
9	8.33	Cyclo[Leu-Leu-Leu-Leu-Leu-Leu]	$C_{36}H_{66}N_6O_6$	677.49
10	8.51	Tricoumaroyl spermidine	$C_{34}H_{37}N_3O_6$	582.26
11	9.41	3-methylidene-5-oxohexadecanedioic acid	$C_{17}H_{28}O_5$	311.18
12	10.25	13-OH-9Z, 11E, 15Z-octadecatrieoate	$C_{18}H_{29}O_3$	293.21
13	11.01	4-O-[3,4-bis[(1-ethoxycarbonyl-2,2,6,6-tetramethylpiperidine-4-carbonyl)oxy]cyclopentyl] 1-O-ethyl 2,2,6,6-tetramethylpiperidine-1,4-dicarboxylate	$C_{44}H_{73}N_3O_{12}$	834.52
14	11.38	[(3R,4R,4aR,5S,6R,6bR,9S,10S,12aR)-5,6,10-trihydroxy-4a,9-bis(hydroxymethyl)-2,2,6b,9,12a-pentamethyl-4-[(Z)-2-methylbut-2-enoyl]oxy-3,4,5,6,6a,6a,7,8,8a,10,11,12,13,14b-tetradecahydro-1H-picen-3-yl] (Z)-2-methylbut-2-enoate	$C_{39}H_{60}O_9$	653.40
15	11.86	[6-[6-[[10-(5,6-Dimethyloxan-2-yl)oxy-5-methoxy-9,16-dimethyl-2-oxo-7-(2-oxoethyl)-4-propanoyloxy-1-oxacyclohexadeca-11,13-dien-6-yl]oxy]-5-hydroxy-2-methyl-4-propan-2-yloxan-3-yl]oxy-4-hydroxy-2,4-dimethyloxan-3-yl] 3-methylbutanoate	$C_{51}H_{84}O_{16}$	951.57
16	13.36	2-[2-hydroxy-6-(1-{9-hydroxy-2-[5'-(6-hydroxy-3,5,6-trimethyloxan-2-yl)-3'-[(5-methoxy-6-methyloxan-2-yl)oxy]-2-methyl-[2,2'-bioxolan]-5-yl]-2,8-dimethyl-1,6-dioxaspiro[4.5]decan-7-yl}ethyl)-5-methoxy-4-[(5-methoxy-6-methyloxan-2-yl)oxy]-3-methyloxan-2-yl]acetic acid	$C_{52}H_{88}O_{18}$	981.58
17	13.36	[(2S)-1-[(9E,12E,15E)-octadeca-9,12,15-trienoyl]oxy-3-[(2R,5R,6R)-3,4,5-trihydroxy-6-[[(2R,5R,6R)-3,4,5-trihydroxy-6-(hydroxymethyl)oxan-2-yl]oxymethyl]oxan-2-yl]oxypropan-2-yl] (6E,9E,12E)-octadeca-6,9,12-trienoate	$C_{51}H_{84}O_{15}$	935.57

5.2. FT-IR screening of phytochemicals from ELJCE

The infrared spectrum of ELJCE, obtained in the frequency range of 4000-400 $cm^{-1,}$ was used to identify the characteristic absorption peaks corresponding to the stretching vibrations of different functional groups, as shown in Figure 5.2. The spectrum is characterized by a broad, intense peak associated with the hydroxyl (O–H) functional group in the 3330 cm^{-1} stretching frequencies. Strong methyl (C–H_3) and methylene (C–H_2) group absorption bands were found at 2924 cm^{-1} and 2855 cm^{-1}, respectively [375, 516, 517]. These two peaks suggest the presence of alkene and alkyl functional groups in the ethanolic crude extract [376]. The peak at 1700 cm^{-1} has been indicated to represent the stretching of the carbonyl (C=O) group [516], while other studies have attributed it to the aromatic carbons (–C=C–) found within the extract [381, 382]. The peak at 1603 cm^{-1} is linked to either a carbonyl, carboxylic acid and/or an ester group due to asymmetric and symmetric vibrational stretching for the carboxyl ion (COO–) [379, 380]. The presence of peaks around 1029, 1519, and 1156 cm^{-1} frequency ranges are said to be the result of skeletal aromatic rings, and the =C–O–C group suggests the presence of flavonoids.

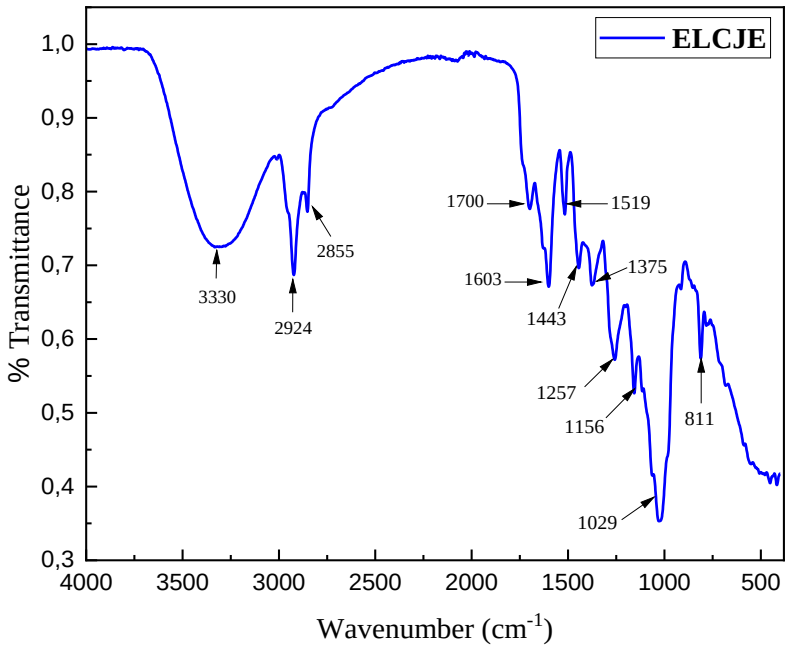

Figure 5.2: FTIR spectrum of the ELJCE used for the inhibition of Zn, MS, and Al corrosion

The bending vibration of the C–O–C group is associated with the peak at 1029 cm^{-1}, indicating the presence of carbohydrates in ELJCE [375]. The absorption bands around 1443 and 1375 cm^{-1} indicate the presence of amines and polyphenols in the ELJCE [518]. The absorption bands in the

800–1750 cm^{-1} region can be attributed to the meta-substitution of the aromatic protons, while those from 820 to 760 cm^{-1} resulted from ring vibrations [380, 519].

5.3. Variation of the open circuit potential (OCP) with immersion period

The OCP measurements are one of the critical parameters used to determine a system's resting potential, which forms the basis for the PDP and EIS measurements. Consequently, a potential was generated between the working electrodes (MS, Al, and Zn samples) and the corrosive solution with respect to the reference before performing the impedance and polarization scans. The electrodes were immersed in 1 M HCl with and without different concentrations of ELJCE for 1 hour, aiming for the potential where the rate of cathodic O_2 reduction processes equals the rate of anodic metal dissolution.

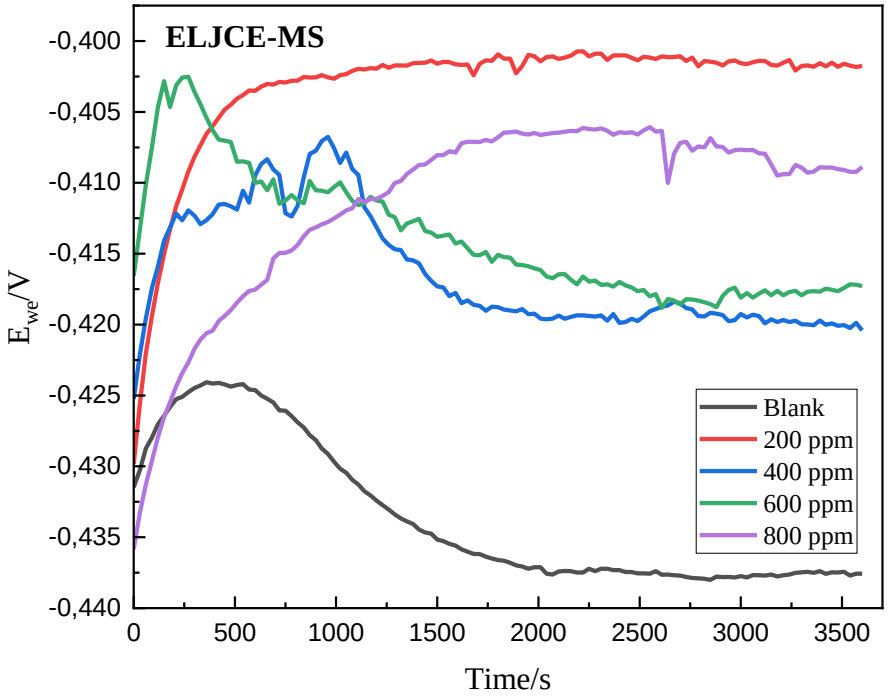

Figure 5.3: Evolution of open-circuit potential (E_{OCP}) versus exposure time for MS with and without ELJCE in 1 M HCl solution

In general, the OCP curves observed for MS (Figure 5.3) moved in a positive direction in the presence of ELJCE, while the curve observed in the absence of ELJCE moved positively for the first 500 seconds and then dropped to a more negative potential until a steady-state potential has been reached. The more negative the OCP value of the blank, the more corrosive electrolyte solution diffuses into the coating/metal interface [520]. The electropositive movement in the OCP in the presence of ELJCE for MS shows that the plant extracts effectively prevented the diffusion of corrosive electrolytes. In addition, it was found that the OCP values for 400 and 600 ppm ELJCE decreased as the immersion time increased. The presence of two opposing processes on the surface of MS is indicated by the movement of the OCP in both negative and positive directions. The two processes are ELJCE forming a protective film on the MS surface and corrosion of the MS surface due to a potential decrease in the negative direction [384-387].

The blank's Zn-OCP curve (Figure 5.4) shows that the OCP moves negatively for about 500 seconds before moving faster in a positive direction and reaching a constant value for the rest of the experiment. At 800 ppm, an abrupt change in potential in the positive direction was observed during the first 250 seconds of immersion. Stable OCP values achieved for the blank were almost at the same potential as ELJCE. The similarities in the OCP of the blank and ELJCE systems indicate that the extracts prevent both the anodic and cathodic Zn reactions and can be characterized as mixed-type corrosion inhibitors [388]. In the presence of 200, 400, and 600 ppm ELJCE, the steady-state potential was reached immediately and remained constant over time. The formation of corrosion products on the Zn surface, which provides some protection against corrosion, can explain the long-term stability of the potential for a blank solution. However, before such protection is offered to the Zn surface, it corrodes relatively quickly until protective corrosion product films cover it; as the surface is exposed for a more extended period to the corrosive environment, its corrosion rate decreases [521].

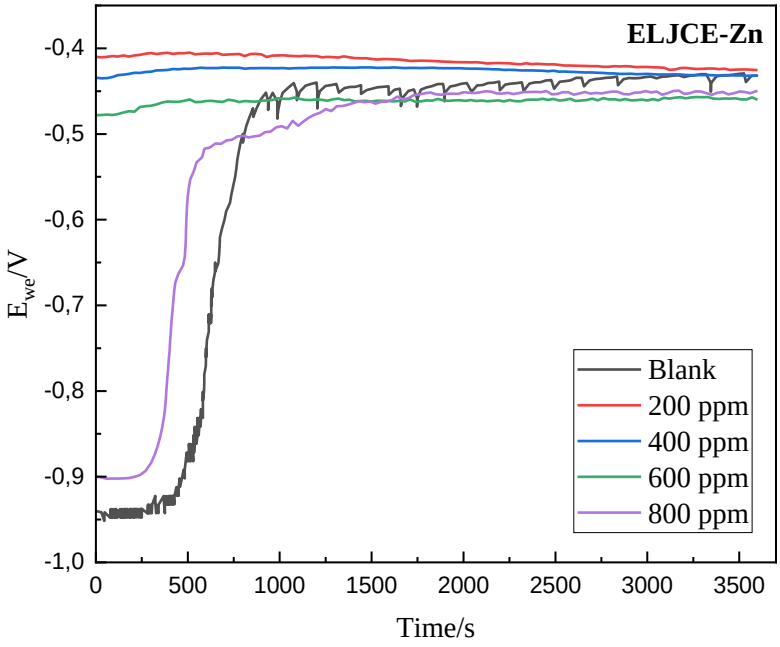

Figure 5.4: Evolution of open-circuit potential (E_{OCP}) versus exposure time for Zn with and without ELJCE in 1 M HCl solution

A careful examination of the OCP-time curves for Al (Figure 5.5) reveals that ELJCE shifts the steady-state potential in both directions. The curves' conflicting positive and negative shifts with respect to the uninhibited Al metal imply that ELJCE controlled both the anodic and cathodic response. This suggests that ELJCE acts as a mixed-type corrosion inhibitor for Al metal. The highest inhibitor concentration used shifted the potential values furthest in the positive direction, possibly due to the presence of more ELJCE compounds that can form anti-corrosion molecular films that limit attack of the Al surface by Cl^- ions in the corrosive solution. The OCP values become constant almost immediately and remain so for the entire 1-hour immersion time for the electrochemical measurements for the uninhibited and inhibited systems, as seen from the OCP time curves.

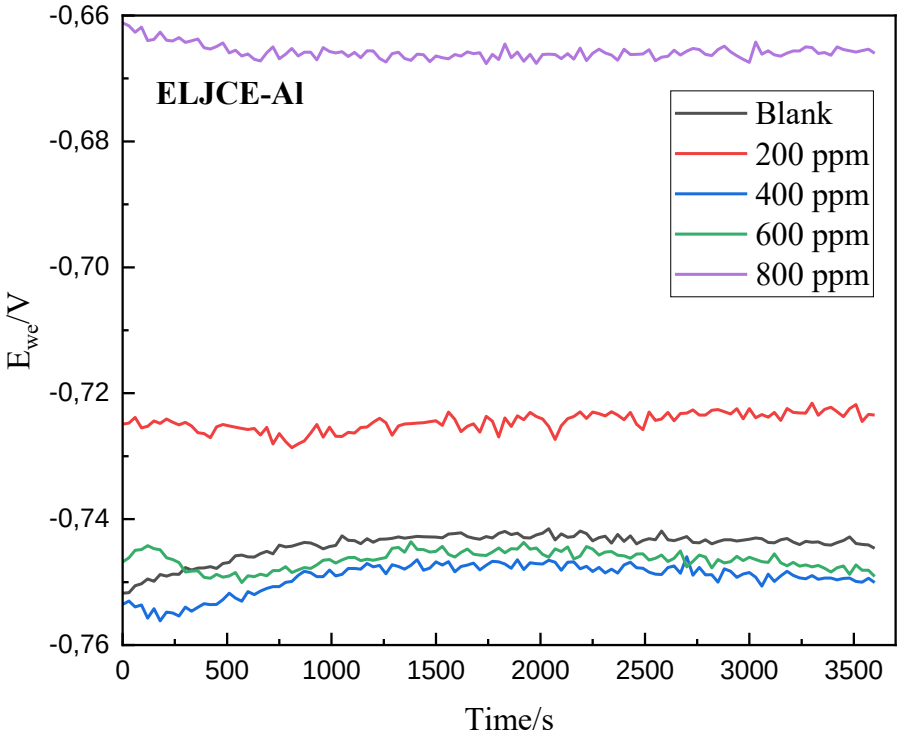

Figure 5.5: Evolution of open-circuit potential (E_{OCP}) versus exposure time for Al with and without ELJCE in 1 M HCl solution

5.4. Potentiodynamic polarization (PDP)

PDP scans were performed to obtain more information on the corrosion inhibition potential of ELJCEs, the stability and protection of the passive/adsorbent layer, and the pitting behaviour. Scans were performed in 1 M HCl in the presence and absence of ELJCE. The electrochemical parameters obtained, such as I_{corr}, E_{corr}, β_a and β_c and $\%IE_{PDP}$, are listed in Table 5.2. The Tafel slopes in Table 5.2 show that the plant extracts controlled the anodic and cathodic curves of Al, MS, and Zn. The MS and Zn slope values indicate that the anodic and cathodic reactions were controlled/inhibited to a similar extent. In contrast, the slope values for Al indicate that the cathodic reaction was more controlled than the anodic reaction process. Relatively higher E_{corr} values were obtained in the presence of ELJCE in the corrosive solution compared to the blank solution, more precisely for Al and Zn than for MS. This is because, in the presence of 600 and 800 ppm ELJCE, the E_{corr} values for MS decreased compared to the blank. Although E_{corr} values are higher in the presence of ELJCE for the three metals, their shift with respect to the blank value is less than 85 mV at all extract concentrations. A similar trend in E_{corr} values was reported by Mukhopadhyay *et al*. [522], who indicated that a change in E_{corr} values of more than 85 mV could be considered a result of preventing either the anodic or the cathodic reaction. This suggests that ELJCE can be regarded as a mixed-type inhibitor for the corrosion of Al, MS, and Zn samples, although the cathodic reaction is more affected in Al samples. The length of the Tafel plots for the inhibited and uninhibited systems is almost identical for all three metal samples. This is proposed [523] to support the mixed-type inhibition mechanism by corrosion inhibitors. Table 5.2 shows that as the concentration of the extracts increases, the E_{corr} for MS shifts to both less and more positive values, indicating that the ELJCE does indeed control the anodic and cathodic reactions of MS. For example, the E_{corr} value for the blank is −430.637 mV and has increased to a maximum of −444.586 mV at 400 ppm and fallen to a minimum of −401.550 mV at 800 ppm.

The small difference in E_{corr} values is due to the small amounts of alloying elements in MS, which are known to significantly affect the kinetics of iron dissolution [524, 525]. In addition, the reduction in the I_{corr} values without any significant shift in the E_{corr} values supports the classification of the extracts as mixed corrosion inhibitors of MS, Zn, and Al [526]. The I_{corr} values for the three metals indicate that in the absence of the plant extracts, the samples were corroded immediately after passing the corrosion potential, which is reflected in the high values obtained. The I_{corr} values appear to decrease from 570.249, 1144.688 and, 5831.281 $\mu A.cm^{-2}$ (blank) to

25.271, 28.912 and, 1252.243 μA.cm^{-2} (800 ppm) for MS, Zn, and Al, respectively, suggesting that ELJCE is an excellent inhibitor of MS, Al, and Zn corrosion in 1 M HCl solution. The increase in corrosion-inhibiting effectiveness of the extracts with increasing extract concentration is due to the adsorption of the extracts blocking the active parts of the electrode surfaces. It was found that the maximum %IE for MS and Zn is around 90%, while for Al, it is close to 80%, which implies that ELJCE acts as an excellent inhibitor for the three metals. The uninhibited anodic MS branch (Figure 5.6b) indicates that the potential above −270 mV vs Ag/AgCl can be described as the area in which stable corrosion products form. The addition of the extracts into the corrosive solution did not change the properties of the current-potential curves but shifted the point to around −180 mV. This indicates that the adsorption of the ELJCE on the MS surface delays the formation of the corrosion products and that the potential above −180 mV vs Ag/AgCl can be described as the desorption potential. The desorption process of the extracts from the MS surface makes the metal susceptible to attack by the corrosive solution. It suggests that the type of inhibition on the MS surface is due to the electrode potential. If the corrosion inhibition depends on the electrode's potential, as in this case, the inhibition phenomenon is accompanied by the formation of a two-dimensional layer formed by the extracts on the metal surface [527]. The MS and Zn cathodic branches for the uninhibited and inhibited systems form quasi-parallel lines (Figures 5.6 and 5.7), showing that the extracts do not alter aspects of the corrosion process but only decrease the corrosion current density. This can be seen from Table 5.2, which shows that hydrogen evolution and anodic metal dissolution reactions are slowed down by blocking the active site of the metal surface by the extract molecules. Tafel curve shows that neither a passive region nor a region of metastable pit growth was observed on the surface of MS in both the absence and presence of ELJCE. Because the current study's PDP test settings were set to observation pitting, the lack of a visible passive area on the Tefal scans has some drawbacks when evaluating corrosion inhibitors. The disadvantage is that it becomes difficult to conclude on passivation or pit growth separated by additional dissolution processes in the metal [528]. Areas of pitting and passivation were more evident on the surface of Al when PDP curves were scanned away from the OCP toward a more positive cathodic potential for both the inhibited and uninhibited systems. The occurrence of passivation and pitting on the Al surface indicate that the corrosive solution destroyed the natural passive layer that generally protects Al from corrosion [529]. Anions, such as Cl^- ions, are known to enhance pitting corrosion on the Al surface [530-534], which occurs in three steps: first,

adsorption of Cl^- ions on the oxide surface, second, penetration of Cl^- ions through the oxide film via O_2 vacancies, and finally, localized dissolution of Al below the oxide film to release hydrogen gas [535-539].

Table 5.2: Polarization electrochemical parameters of Al, Zn, and MS after 1-hour immersion at 303 K in 1 M HCl with and without different concentrations of ELJCE

Metal	Conc. of MLJCE (ppm)	C_R (mpy)	E_{corr} (mV vs Ag/AgCl)	β_a ($mV.dec^{-1}$)	β_c ($mV.dec^{-1}$)	I_{pass} ($\mu A.cm^{-2}$)	I_{corr} ($\mu A.cm^{-2}$)	$\%IE_{PDP}$
MS	**Blank**	261.26	−430.637	77.6	119.4	–	570.249	–
	200	21.791	−438.964	102.4	82.8	–	47.563	91.66
	400	18.4461	−444.586	73.0	85.2	–	40.262	92.94
	600	15.5208	−410.120	93.1	81.1	–	33.877	94.06
	800	11.5779	−401.550	68.5	85.6	–	25.271	95.57
Zn	**Blank**	675.025	−413.435	96.8	196.8	–	1144.688	–
	200	44.1899	−449.905	100.7	94.7	–	74.936	93.45
	400	26.545 4	−463.384	74.2	77.3	–	45.015	96.07
	600	21.9923	−445.407	88.3	86.4	–	37.294	96.74
	800	17.0495	−447.483	81.7	79.4	–	28.912	97.47
Al	**Blank**	2492.66	−740. 497	64.6	183.6	1.7399	5831.281	–
	200	999.255	−745.807	25.7	137.1	0.8913	2329.011	60.06
	400	600.1	−720.118	26.9	134.4	–	1398.681	76.01
	600	576.913	−747.225	28.4	141.9	1.2648	1344.639	76.94
	800	537.271	−745.360	24.2	137.3	0.8962	1252.243	78.53

The Al Tafel curves (Figure 5.8) revealed an E_{pp} region, which is a point where the potential increases due to activation control behaviour. This was preceded by a significant decrease in I_{corr}, implying the formation of a protective or passive layer on the surface of Al. The lowest point to which the I_{corr} falls is the I_{pass}. The fluctuations in the current of the curves around the passive region suggest that metastable pits were formed on the Al surface during the PDP test. Although the passive area was non-uniform, the I_{pass} values were obtained at the lowest point of the passive region. The I_{pass} for the blank was found to be 1.7399 $\mu A.cm^{-2}$ and decreased in the presence of the extract. The I_{pass} was not determined at 400 ppm, although passivation did occur, and this is because the I_{corr} did not drop to a point where the value could be identified. The lower I_{pass} values observed in the presence of ELJCE indicate that the protective/passive film formed on the surface of Al was relatively stable [540] and did not deteriorate entirely due to the attack by the corrosive solution.

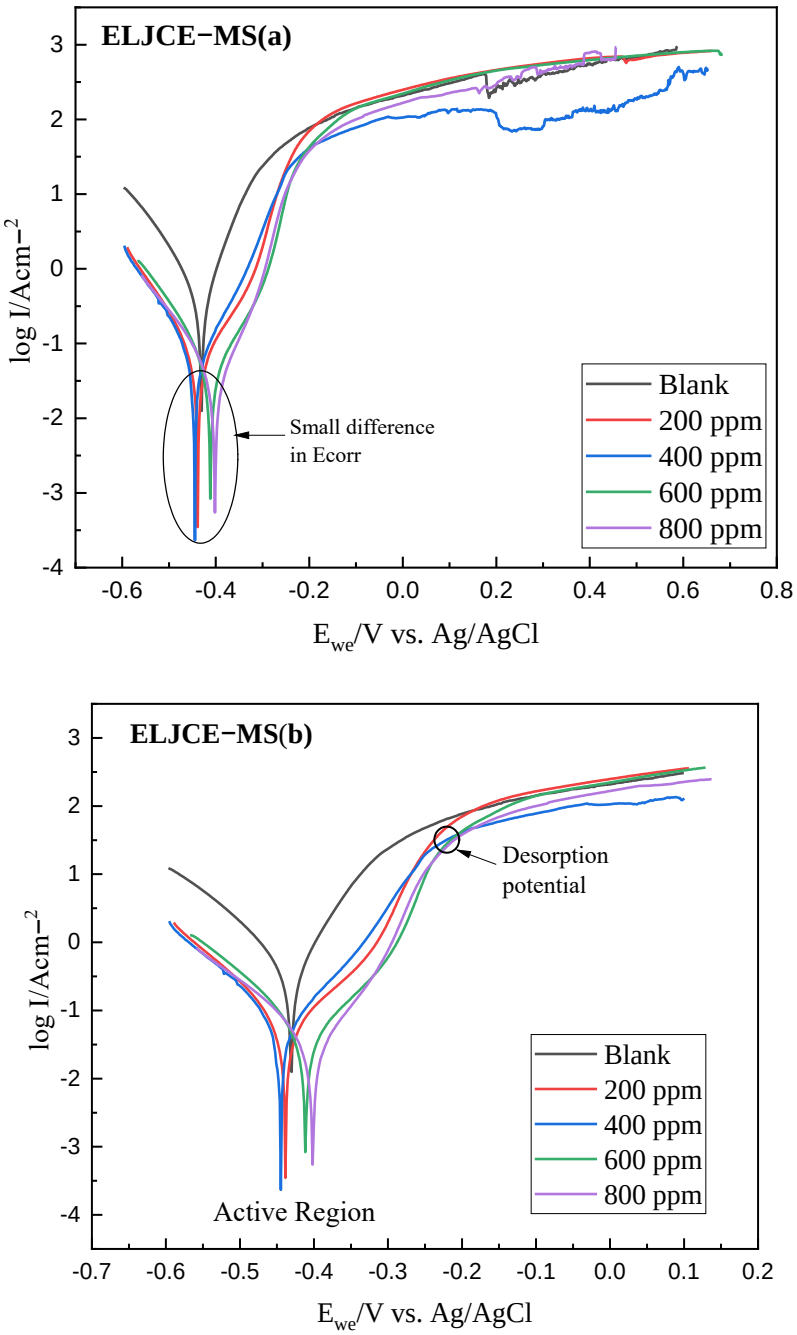

Figure 5.6: Tafel PDP curves for MS dissolution in 1 M HCl with and without different concentrations of ELJCE to observe pitting (a). The extrapolated (b) active area at 303 K, respectively

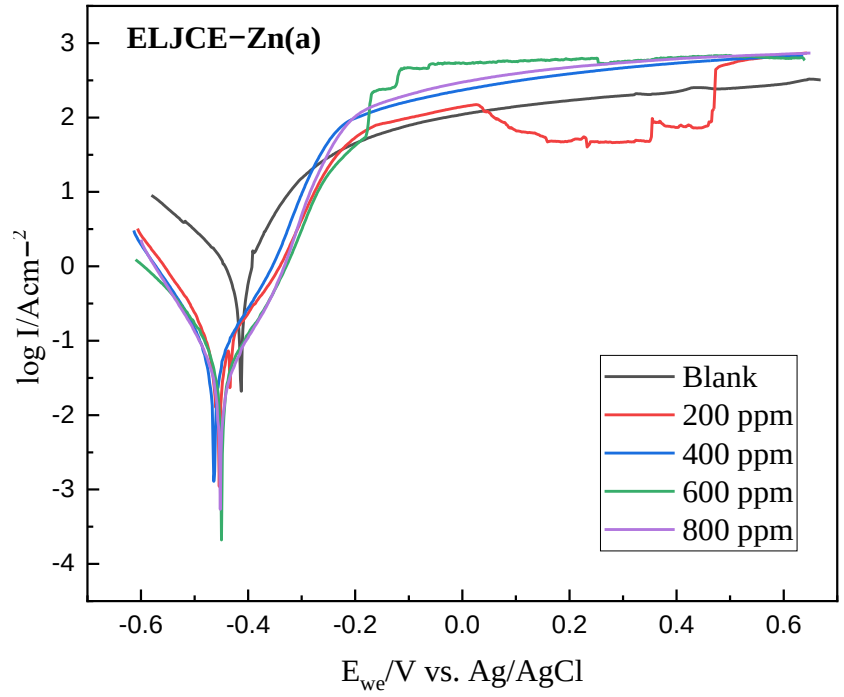

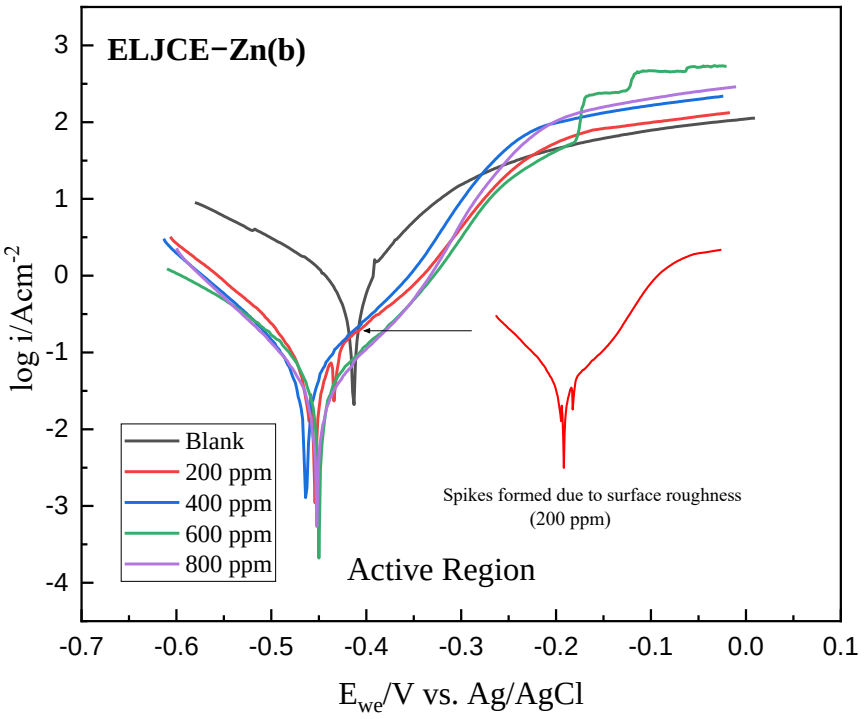

Figure 5.7: Tafel PDP curves for Zn dissolution in 1 M HCl with and without different concentrations of ELJCE to observe pitting (a). The extrapolated (b) active area at 303 K, respectively

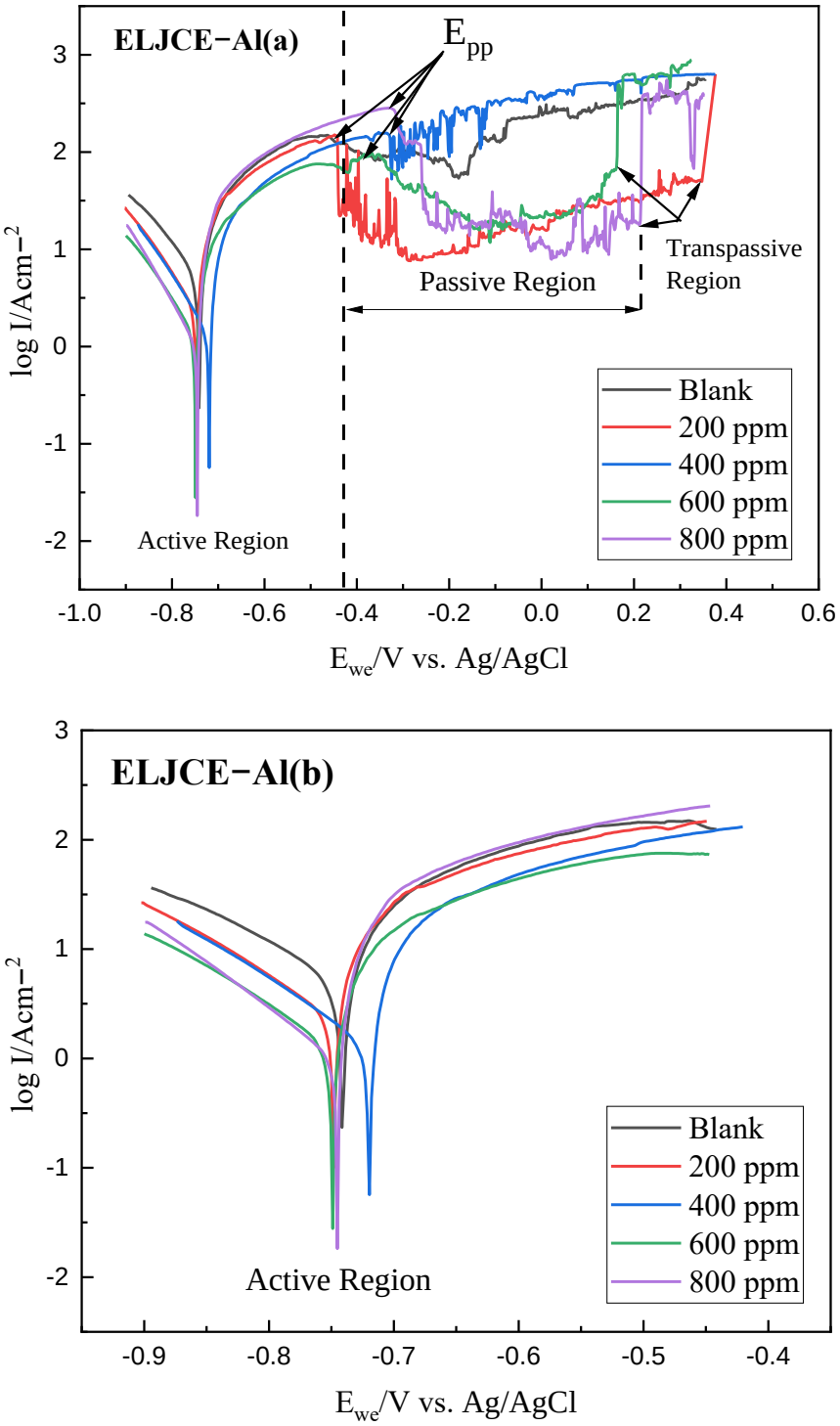

Figure 5.8: Tafel PDP curves for Al dissolution in 1 M HCl with and without different concentrations of ELJCE to observe pitting (a). The extrapolated (b) active area at 303 K, respectively

5.5. Electrochemical impedance spectroscopy (EIS)

Impedance analysis was performed to define the changes induced at the interface between the metal samples and 1 M HCl by the adding ELJCE to the corrosive solution. The test measurements were carried out at the OCP and then evaluated with regard to the equivalent circuit diagram shown in Figure 4.18 for MS and Zn and Figure 4.19 for Al in section 4. The Nyquist plots of Im(Z) versus Re(Z) with frequency implicitly included are shown in Figure 5.9−5.10 for the three metals. The diagrams show the higher frequency data on the right and the lower frequency data on the left side of the graph. In the presence and absence of ELJCE, the time constant obtained from the EEC appears as an imperfect semicircle in the Nyquist plots or as a peak in the phase angle in the Bode plots. The phase angles were represented by a single maximum for MS and Zn, representing a single constant phase element at the interface for the corrosion process present in the equivalent circuit diagram. The shift of the peaks compared to the blank value suggests a rather capacitive behaviour due to the adsorption of the ELJCE compounds on the MS and Zn surface. The phase angle of the Bode plots generally increases with the concentration of ELJCE. This is supported by the broadened phase diagrams showing the formation of a protective film on the metal surfaces [541].

On the other hand, the phase angles for Al were represented by two maxima, suggesting that two-time constants govern its corrosion process. The size of the phase angle |θ| and the slope obtained from Figure 5.12−5.13 for MS, Zn, and Al corrosion inhibition after the addition of ELJCE are shown in Table 5.3. It is reported in the literature that perfect capacitive performance would result in a phase angle of −90° and a slope value of −1 [542, 543]. The maximum |θ| values for MS and Zn are in the range of −70°, while the maximum value for Al is around −60°, which is less than −90°, indicating that a CPE should be included in the equivalent circuit to account for the non-ideal behaviour of the metal/solution interface [170]. The slope values taken from the linear relationship between log |Z| and log f in the medium-frequency region are closer to −1 in the presence of ELJCE than in its absence, which underlines the inhibitory capacity of the extracts for the Al, MS, and Zn surface. This behaviour is a characteristic of capacitive behaviour. The Re(Z) value for the blank (1 M HCl) was only 32.2, 20.76, and 6.617 Ω for MS, Zn, and Al, respectively, indicating the lowest R_{ct} of the corrosion reaction. When ELJCE was added to the corrosive solution, the Nyquist plots gradually increased in diameter, increasing concentration from 200 to 800 ppm. Despite the size change in diameter, the Nyquist plots obtained are nearly identical in

the absence and presence of ELJCE, indicating that the extracts do not alter the corrosion mechanism of the three metal samples, which is similar to the results obtained from PDP. The increase in Nyquist diameter with plant extracts concentration reflected an increase in R_{ct} values, indicating that ELJCE adsorbed on the surface of the three metals, resulting in lower CPE values compared to the blank, with Al being the exception.

For instance, the R_{ct} values increased from 32.2 Ω (blank) to a maximum of 604.8 Ω (800 ppm) for MS, suggesting that its charge transfer process is being slowed down due to a decrease in the exposed surface area susceptible to corrosive attack. This also applies to Zn and Al, where the values for the two metals have increased to 419.2 and 28.96 Ω (800 ppm), respectively. This reduces the electrodes' corrosion rate, which is in concord with the weight loss and PDP results obtained. These observations suggest that the change in CPE, R_s and R_{ct} values, as in Table 5.3, was caused by the gradual replacement of the water molecules and other corrosive ions that were initially adsorbed on the surface of the metals by the ELJCE compounds resulting in the reduction of the dissolution of the metals [544]. It can be argued that the ELJCE compounds replaced enough water molecules even at the lowest concentration evaluated (200 ppm) since an inhibition efficiency of 89.87, 88.16, and 68.19% was observed and increased to 94.71, 95.05, and 77.15% at 800 ppm for MS, Zn and Al respectively. The reduction in the double-layer pseudo-capacitance can be attributed to a decrease in the local dielectric constant and/or an increase in electric double-layer thickness [545-547]. The Nyquist plots for Zn and MS show that the capacitive loop curve deviates slightly from an imperfect semicircular shape, which is more noticeable at lower frequencies. The deviations in these diagrams are mainly caused by the heterogeneity and micro-roughness of the working electrode surface, which is a typical state of the corrosion system [426, 548, 549].

Most of the Al matrix consists of an oxide layer that protects it from corrosion, and such a layer contributes capacitively to the EEC. Such a capacitive loop is observed in the high-frequency range, while an inductive loop is observed in the low-frequency range. The capacitive loop at high frequencies is due to the charge transfer of the corrosion process and the formation of an oxidic passive layer [550]. The inductive loop's origin is largely unknown, and several studies attribute it to various factors. It has been attributed to the oxide film species' surface or bulk relaxation process and their dielectric properties [551, 552]. Bessone *et al*. [553] suggested that the inductive

time constant is due to the rearrangement of the Al surface charge at the metal-oxide interface. The loop was also attributed to the stabilization of the adsorption layer formed by the plant extract compounds on Al's surface and reactive products [554]. According to our previous investigations into the inhibition of Al corrosion [555], the inductive loop can be explained by the relaxation of the substances in the oxide layer covering the Al electrode surface, among other factors. The impedance plots of Al are also represented by imperfect circles, leading to the use of CPE in the EEC used to analyze the data. The use of CPE is due to the non-ideal behaviour of the electrochemical process at the metal/solution interface, which is usually attributed to several factors, including metallurgical problems such as surface roughness, grain boundaries, and the presence of impurities, among others. The non-ideal behaviour can also result from the movement of the extract compounds from the solution onto the metal surface during the adsorption process or even from the corrosion reaction process itself, which can lead to the formation of porous layers and corrosion products on the metal surfaces [556]. The values of the CPE exponent are close to unity in the presence of ELJCE, indicating that the electrode/electrolyte systems are pseudocapacitive for all three metal samples. The pseudocapacitive behaviour results from the inhomogeneities on the surface of the metals. These values did not vary significantly compared to the uninhibited system, suggesting that the charge transfer process controls the corrosion process of Zn, Al, and MS samples [430]. The surface of Zn became more homogeneous in the presence of ELJCE since the values of the CPE exponent increased significantly compared to the blank (0.5031).

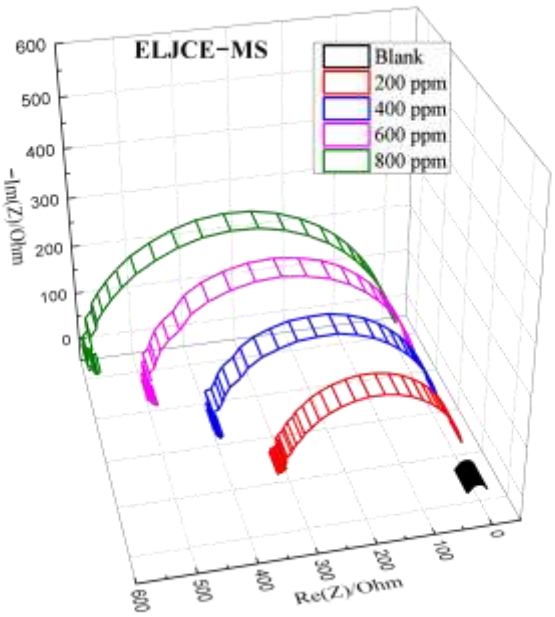

Figure 5.9: MS Nyquist plots in 1 M HCl solution with and without ELJCE at various concentrations at 303 K

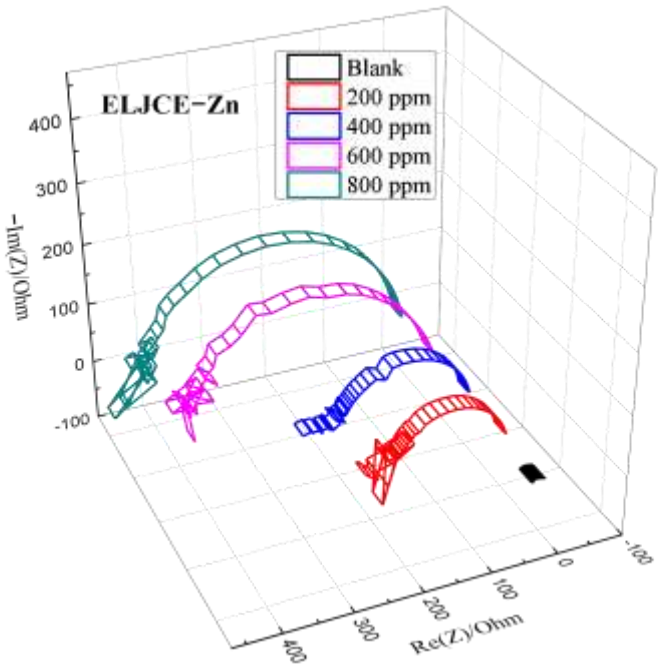

Figure 5.10: Zn Nyquist plots in 1 M HCl solution with and without ELJCE at various concentrations at 303 K

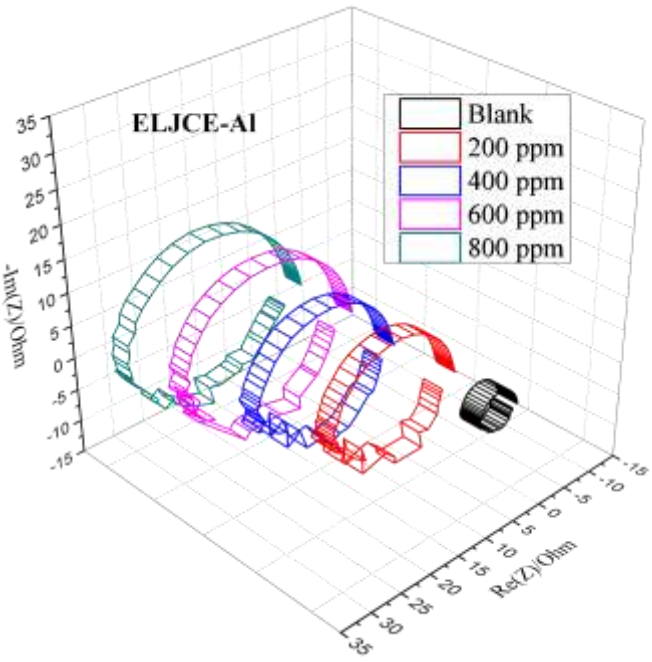

Figure 5.11: Al Nyquist plots in 1 M HCl solution with and without ELJCE at various concentrations at 303 K

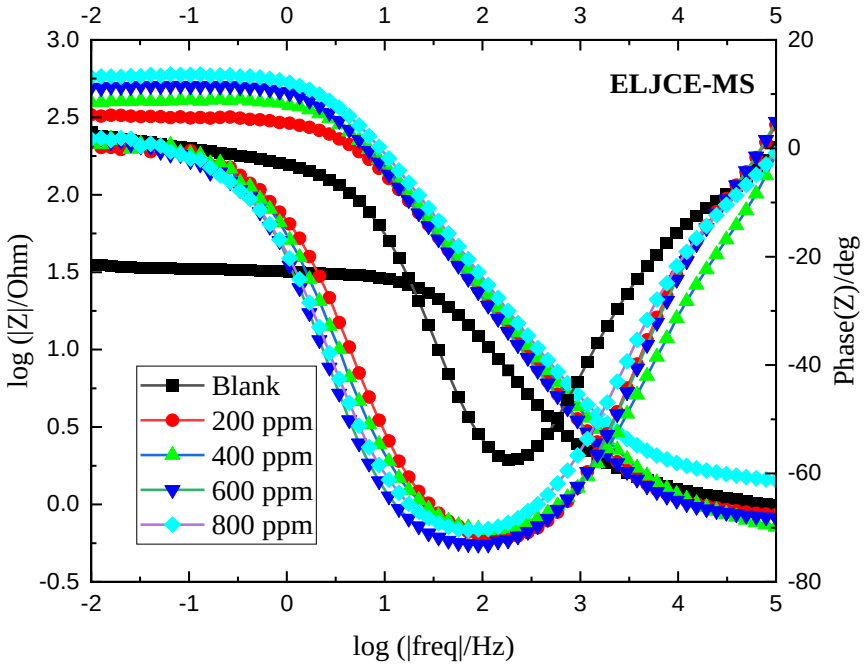

Figure 5. 12: MS Bode modulus and phase angle plot in 1 M HCl solution with and without ELJCE at various concentrations at 303 K

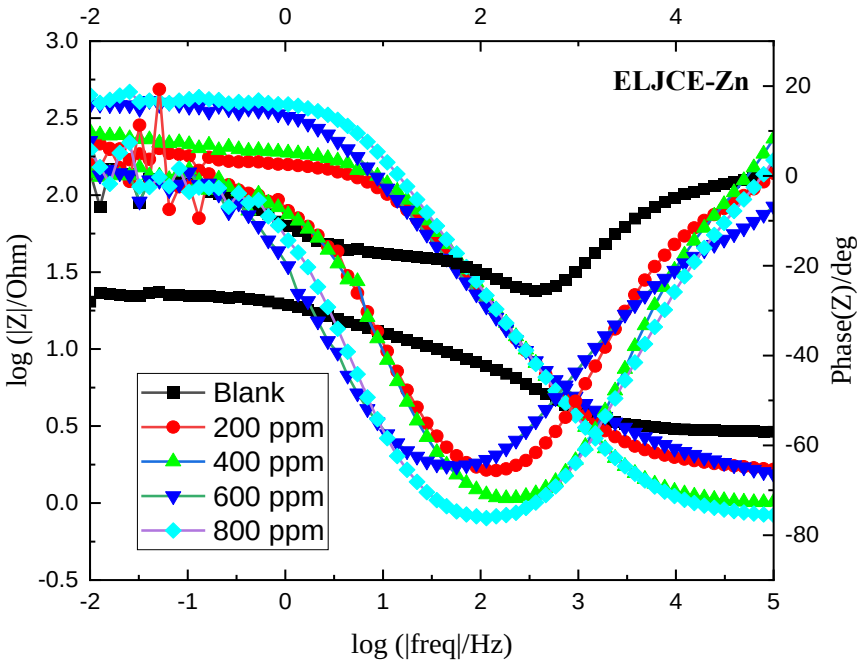

Figure 5.13: Zn Bode modulus and phase angle plot in 1 M HCl solution with and without ELJCE at various concentrations at 303 K

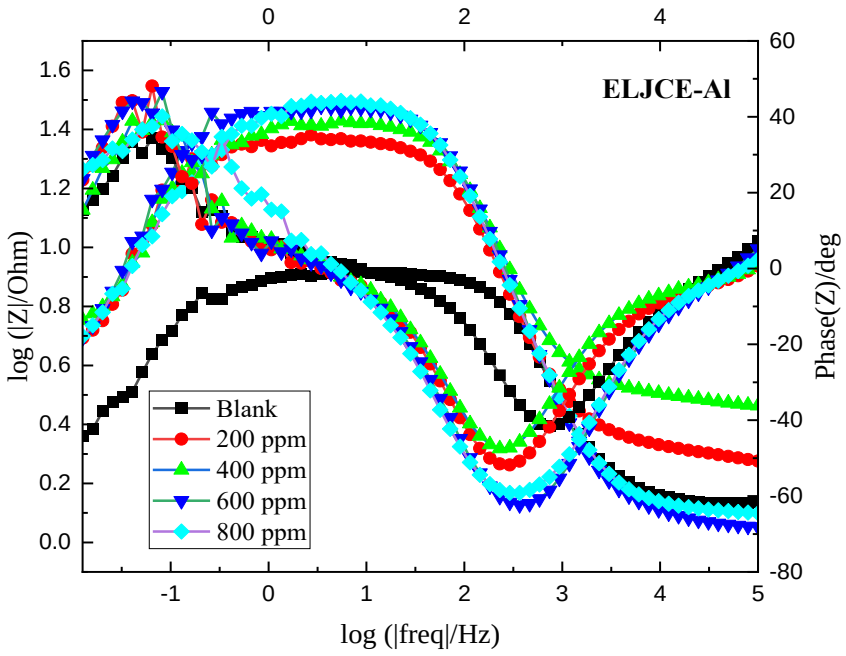

Figure 5.14: Al Bode modulus and phase angle plot in 1 M HCl solution with and without ELJCE at various concentrations at 303 K

Because impedance plots for composite metals such as Al, Zn, and MS are affected by frequency dispersion effects occurring during analysis, the actual value of capacitance (i.e., C_{dl}) for the three metal samples was estimated, as shown in Table 5.3. The adsorption and subsequent protection of Al, Zn, and MS corrosion by ELJCEs is based on increased corrosion resistance by decreasing electron flow and decreasing double-layer capacitance as ELJCE concentration increases. Table 2 shows that the C_{dl} values decreased when different concentrations of ELJCE were introduced. The C_{dl} values decreased for MS and Zn, with the decrease being more pronounced for Zn when compared to the blank values. This is owing to the fact that introducing an inhibitor into the electric double layer changes its composition and structure by altering the dielectric properties of the water molecules in the electric double layer. This typically results in a change in the alignment of the dipoles of the water molecules, which lowers the dielectric constant and, as a result, the C_{dl}. The decrease in capacitance of the double layer may also be due to the adsorption film covering a larger surface area of the metals, reducing the area where the corrosive electrolyte can attack [557]. There is no clear trend in Al C_{dl} values versus blank, as both increased and decreased C_{dl} values were observed. Although the difference in both directions is small, the high values can be attributed to the increased surface area of the electrode due to the unstable adsorption layer that forms on the Al surface, resulting in lower protection values compared to Zn and MS. An increasing trend in C_{dl} values was also observed by Kwolek [558], who noted that high C_{dl} values could be observed in certain alloys when selective corrosion occurs as a result of the increase in electrode surface area. This was caused by the movement of the electrolyte during testing, facilitating the release of hydrogen bubbles from the metal surface and aqueous solutions with a much higher dielectric constant than gases. In the current study, the lack of a clear trend could be attributed to the small effect that the variation in concentration of ELJCE had on the R_{ct} values since they are close together, which is related to an increase in surface area due to the release of hydrogen bubbles [558].

Table 5.3: Electrochemical impedance parameters of Al, Zn, and MS after 1-hour immersion at 303 K in 1 M HCl with and without different concentrations of ELJCE

Conc. of MLJCE (ppm)	R_s ($\Omega.cm^2$)	CPE parameters		L_1 (H)	R_{ct} ($\Omega.cm^2$)	C_{dl} ($\mu F.cm^{-2}$) $\times 10^{-4}$	(|θ|)	Slope	R_L ($\Omega.cm^2$)	%IE	χ^2 $\times 10^{-3}$
		Y_0 ($S.sec^n$) $\times 10^{-3}$	N								
MS											
0	1.107	0.385	0.8281	–	32.2	1.3884	−57.4165	−0.6904	–	–	2.949
200	0.8935	0.1697	0.8632	–	318	1.1532	−71.8296	−0.8246	–	89.87	0.8615
400	0.7872	0.1768	0.8336	–	421.8	1.0967	−70.3129	−0.7888	–	92.37	2.613
600	0.8576	0.1707	0.8667	–	516.4	1.1331	−73.4755	−0.8141	–	93.76	1.663
800	1.524	0.1475	0.8421	–	608.5	0.9616	−70.3188	−0.7833	–	94.71	1.722
Zn											
0	2.628	6.051	0.5031	–	20.76	28.1854	−25.5302	−0.2366	–	–	4.598
200	1.742	0.1962	0.8381	–	175.4	0.8175	−64.8177	−0.7511	–	88.16	7.213
400	1.021	0.1395	0.8798	–	209.4	0.8676	−71.8364	−0.8217	–	90.09	5.132
600	1.821	0.3025	0.7758	–	397.5	1.4720	−64.6796	−0.7398	–	94.78	7.987
800	0.8953	0.1238	0.8917	–	419.2	0.8748	−75.0797	−0.8682	–	95.05	2.891
Al											
0	1.392	0.1029	0.9548	10.24	6.617	0.8265	−41.5066	−0.5775	1.076	–	2.707
200	2.055	0.1495	0.9237	34.34	20.8	0.8455	−51.8097	−0.6787	2.568	68.19	3.824
400	3.117	0.1216	0.9338	27.84	22.69	0.7751	−47.4571	−0.6499	2.606	70.84	2.700
600	1.192	0.1127	0.9372	39.59	28.16	0.7894	−62.3475	−0.7891	4.033	76.50	3.349
800	1.295	0.1324	0.9205	25.65	28.96	0.9693	−59.1747	−0.7336	4.948	77.15	8.607

5.6. Weight loss measurement

5.6.1. The effect of ELJCE concentration on the anti-corrosive behaviour of Zn, Al, and MS

The effect of ELJCE concentration against MS, Al, and Zn corrosion in a 1 M HCl environment was evaluated by weight loss analysis, which involved immersing the three metal samples in 1 M HCl for 7 hours at different temperature ranges. The variation in corrosion rate as a function of ELJCE concentrations for the three metal samples at 303 to 333 K is shown in Figure 5.15. Figures 5.16–5.19 show the variation in inhibition efficiencies with respect to ELJCE concentrations for the three metal samples at 303 to 333 K. The calculated C_R and %IE from weight loss data are shown in Table 4. The table shows that the C_R values for the uninhibited Al, Zn, and MS systems are high compared to the inhibited systems and continue to increase with increasing temperature. Metal corrosion potential can be reduced by adding an inhibitor to a corrosive solution, and this reduction is usually directly proportional to increasing the concentration of the inhibitor [559]. The results of the current study showed a similar pattern, with the C_R of the MS, Al, and Zn samples decreasing with increasing ELJCE concentration. The decrease in C_R that occurs with increasing ELJCE concentration is highlighted in Figure 5.15, with the lowest C_R being reached at 800 ppm. The reduction in C_R is simultaneous with the increase in %IE as the inhibitor concentration is increased for all three metal samples. For example, at 333 K, the C_R for Zn the in the absence of the inhibitor was found to be 1.3485×10^{-2} g.cm^{-2}.h^{-1} and decreased with the addition of ELCE in the corrosive solution to 3.2580×10^{-3}, 3.1687×10^{-3}, 2.4587×10^{-3} and 1.9362×10^{-3} g.cm^{-2}.h^{-1} giving an inhibition efficiency of 75.84, 76.50, 81.77% and 85.64% at 200, 400, 600 and 800 ppm, respectively.

For MS, the corrosion rate at 333 K decreased from 8.6198×10^{-3} g.cm^{-2}.h^{-1} (blank) to 7.2359×10^{-4} g.cm^{-2}.h^{-1} (800 ppm), resulting in an inhibition efficiency of 85.64%. Similarly, in the presence of ELJCE, the corrosion rate for Al decreased from 6.7966×10^{-3} g.cm^{-2}.h^{-1} (blank) to 5.5815×10^{-3} g.cm^{-2}.h^{-1} (800 ppm), resulting in an inhibition efficiency of 50.64%. These results are consistent with data reported by other researchers [560, 561]. The decrease in C_R with increasing extract/inhibitor concentration indicates that a larger number of extract molecules are available to cover a larger area of the metal surface, resulting in less contact between the corrosive solution and the metal surface. This trend was observed for all three metals at all temperatures studied.

According to Table 5.4, the maximum ELJCE effectiveness against the corrosion of MS, Al and Zn samples was observed at the optimal inhibitor concentration of 800 ppm: 97.10% and 91.70% at 303 K for MS and Al, respectively, and 85.64% for Zn at 333 K.

Al has been shown to oxidize rapidly among the three metals studied, which is an essential property for its corrosion resistance. Although the oxide layer on the Al surface is said to be reliable and stable, it is not always impervious to deterioration. When the Al metal is exposed to a basic or acidic environment, the protective oxide layer tends to weaken, and its general reconstruction may not be fully appropriate or sufficient to prevent deterioration [562]. The inhibition efficiencies in Table 5.4 show that ELJCE has the potential to reduce the deterioration of the oxide film layer in the 1 M HCl medium but is not sufficient to provide adequate protection for the Al surface at all temperatures investigated. At 333 K, for example, increasing the concentration of ELJCE from 200 to 800 ppm resulted in an increase in %IE from 39.90 to 50.64%; however, despite the increased inhibition efficiency, the Al surface was corroded at an accelerated rate compared to MS and Zn samples at this temperature resulting in lower protection. Figure 5.15 shows that at all temperatures tested, increasing ELJCE concentrations resulted in a marked reduction in the C_R compared to the blank solution, even at the lowest concentration of 200 ppm. The decrease in overall inhibition efficiencies for MS and Al when the system temperature was raised from 303 to 333 K demonstrates that temperature and extract concentration affect the degree to which the corrosion rate is reduced. The high inhibition efficiencies as the extract concentration increased indicated that the weight loss of the three electrodes is more advanced in the blank solution than in the corresponding 1 M HCl solution containing a variety of ELJCE combinations. This shows that the adsorption of ELJCE on Al, Zn, and MS surfaces slows down their corrosion process.

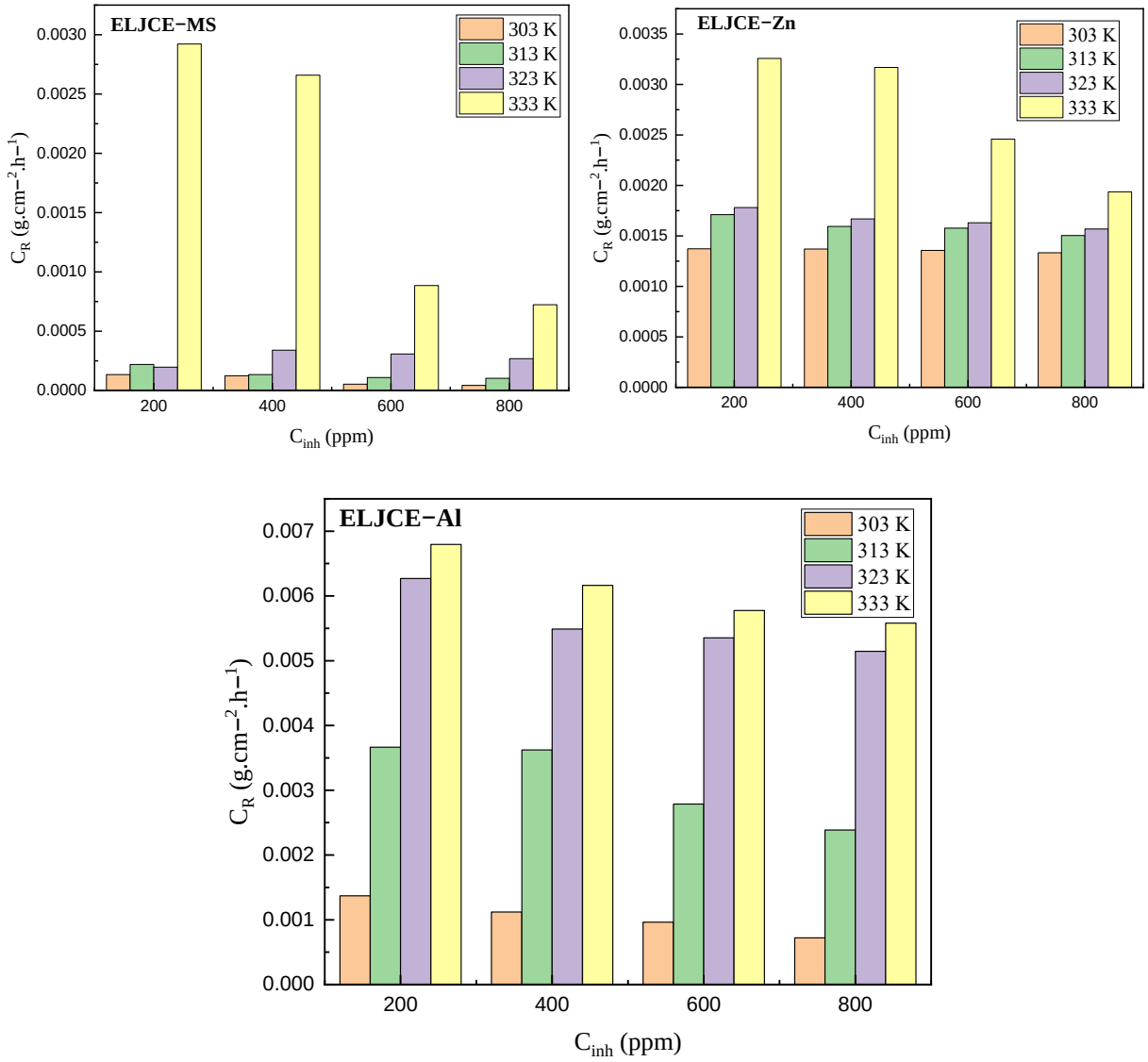

Figure 5.15: Variation of corrosion rate (C_R) obtained from weight loss for Zn, Al and MS in 1 M HCl as a function of concentration in the presence of ELJCE at 303-333 K

Table 5.4: Weight loss parameters for the uninhibited and ELJCE-inhibited Al, MS and Zn system in 1 M HCl corrosive solution at 303-333 K

Metal	Conc. of ELJCE (ppm)	303 K			313 K			323 K			333 K		
		C_R ($g.cm^{-2}.h^{-1}$)	C_R (mpy^1)	$\%IE_{CR}$	C_R ($g.cm^{-2}.h^{-1}$)	C_R (mpy^1)	$\%IE_{CR}$	C_R ($g.cm^{-2}.h^{-1}$)	C_R (mpy^1)	$\%IE_{CR}$	C_R ($g.cm^{-2}.h^{-1}$)	C_R (mpy^1)	$\%IE_{CR}$
MS	**Blank**	1.4988×10^{-3}	1.66944	–	2.8038×10^{-3}	3.12198	–	4.8840×10^{-3}	5.43455	–	8.6198×10^{-3}	9.58244	–
	200	1.3404×10^{-4}	0.14913	91.06	2.1968×10^{-4}	0.24450	92.16	1.9710×10^{-4}	0.21948	59.64	2.9217×10^{-3}	3.25069	66.10
	400	1.2412×10^{-4}	0.13808	91.72	1.3404×10^{-4}	0.14913	95.22	3.4008×10^{-4}	0.37829	93.04	2.6586×10^{-3}	2.95758	69.16
	600	5.3370×10^{-5}	0.05942	96.44	1.0922×10^{-4}	0.12163	96.10	3.0781×10^{-4}	0.34250	93.70	8.8494×10^{-4}	0.98510	89.73
	800	4.3440×10^{-5}	0.04829	97.10	1.0302×10^{-4}	0.11458	96.33	2.6809×10^{-4}	0.29858	94.51	7.2359×10^{-4}	0.80494	91.61
Zn	**Blank**	2.6325×10^{-3}	2.93086	–	4.3130×10^{-3}	4.80092	–	7.2024×10^{-3}	8.01864	–	1.3485×10^{-2}	15.00181	–
	200	1.3727×10^{-3}	1.52752	47.86	1.7103×10^{-3}	1.90284	60.35	1.7811×10^{-3}	1.98126	75.27	3.2580×10^{-3}	3.62318	75.84
	400	1.3702×10^{-3}	1.52494	47.95	1.5936×10^{-3}	1.77268	63.05	1.6681×10^{-3}	1.85731	76.84	3.1687×10^{-3}	3.52697	76.50
	600	1.3566×10^{-3}	1.50886	48.47	1.5775×10^{-3}	1.75652	63.42	1.6296×10^{-3}	1.81232	77.37	2.4587×10^{-3}	2.73460	81.77
	800	1.3330×10^{-3}	1.48241	49.36	1.5043×10^{-3}	1.67446	65.12	1.5688×10^{-3}	1.74368	78.22	1.9362×10^{-3}	2.15323	85.64
Al	**Blank**	8.6931×10^{-3}	9.67804	–	8.9549×10^{-3}	9.96442	–	1.0930×10^{-2}	12.16097	–	1.1308×10^{-2}	12.59214	–
	200	1.3702×10^{-3}	1.52494	84.24	3.6651×10^{-3}	4.07900	59.07	6.2691×10^{-3}	6.97378	42.64	6.7966×10^{-3}	7.57160	39.90
	400	1.1208×10^{-3}	1.24642	87.11	3.6217×10^{-3}	4.02917	59.56	5.4884×10^{-3}	6.11305	49.79	6.1648×10^{-3}	6.85702	45.48
	600	9.6190×10^{-4}	1.07006	88.93	2.7864×10^{-3}	3.10099	68.88	5.3544×10^{-3}	5.95773	51.01	5.7763×10^{-3}	6.41971	48.92
	800	7.2111×10^{-4}	0.80127	91.70	2.3867×10^{-3}	2.65767	73.35	5.1458×10^{-3}	5.72730	52.92	5.5815×10^{-3}	6.21520	50.64

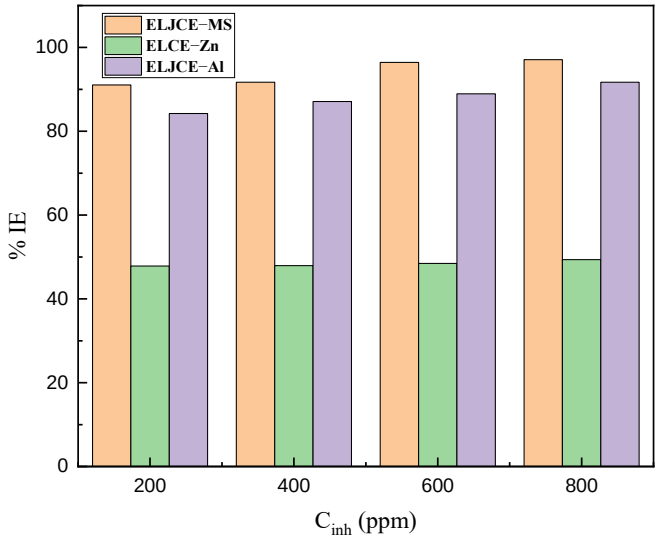

Figure 5.16: Variation of inhibition efficiencies ($\%IE_{WL}$) obtained from weight loss for Zn, Al, and MS samples in 1 M HCl as a function of ELJCE concentration at 303 K

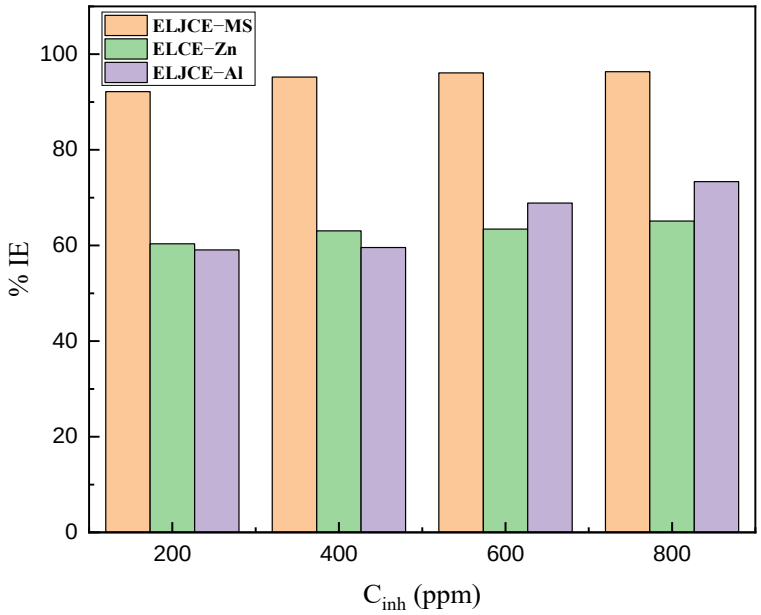

Figure 5.17: Variation of inhibition efficiencies ($\%IE_{WL}$) obtained from weight loss for Zn, Al, and MS samples in 1 M HCl as a function of ELJCE concentration at 313 K

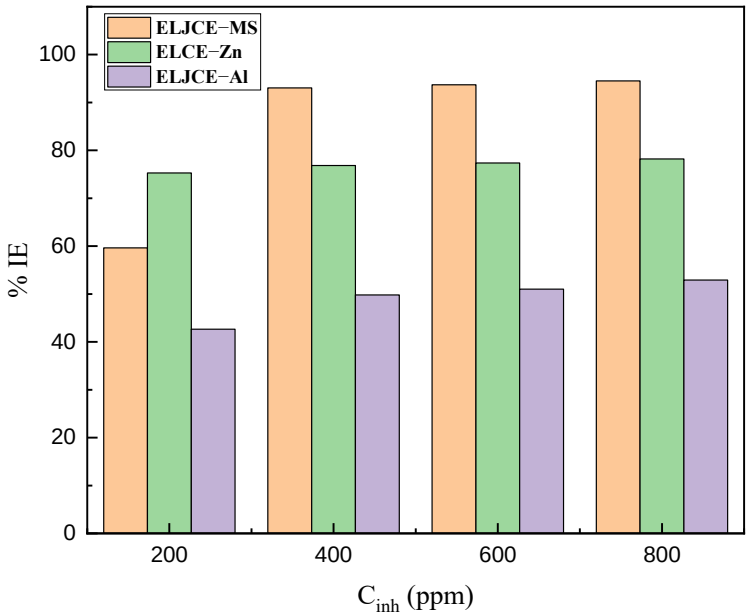

Figure 5.18: Variation of inhibition efficiencies ($\%IE_{WL}$) obtained from weight loss for Zn, Al, and MS samples in 1 M HCl as a function of ELJCE concentration at 323 K

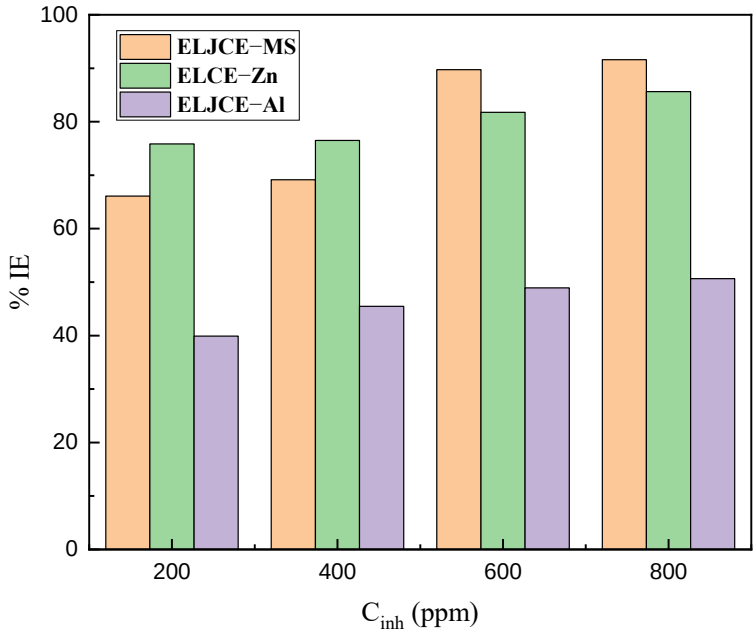

Figure 5.19: Variation of inhibition efficiencies ($\%IE_{WL}$) obtained from weight loss for Zn, Al, and MS samples in 1 M HCl as a function of ELJCE concentration at 333 K

5.6.2. Influence of immersion time on MS, Al, and Zn corrosion inhibition in 1 M HCl with an optimal concentration of ELJCE at 303 K

When examining an inhibitor's inhibiting effect against certain metals' corrosion, it is crucial to consider its performance over time. Immersion studies were carried out for 6, 7, 12, 18, and 24 hours to assess the stability of ELJCE and the rate of adsorption. Figure 5.20 shows the variation in inhibition efficiencies for Zn, Al, and MS at the optimal concentration (800 ppm) of ELJCE with immersion time. Table 5.5 shows inhibition efficiency at different exposure times (6-24 h). As shown in Figure 5.20, a maximum inhibition efficiency of 91.70% for Al was observed after 7 hours, which decreased to 72.89% with increasing exposure time. The figure also shows that the highest protection efficiency for MS was achieved around the 6- and 7-hour immersion times and was 98.10% and 97.10%, respectively. The inhibitory efficiency of ELJCE against corrosion of MS samples decreases with the contact time. Still, the decrease is minimal and even after a long contact time (i.e., 24 hours), the inhibitory efficiency remains close to 90%. This is also true for the Al sample, where the efficiency stabilizes at around 70%, suggesting that the protective effect of ELJCE is maintained for more than 24 hours, despite possible extract degradation. Exposing the Zn sample to the corrosive solution for the longest immersion time (24 hours) resulted in the

highest protection efficiency of ELJCE, which was 77.49%. This indicates that the protective effect increased with the immersion time and may be due to the development of the protective ELJCE film on the surface of the Zn sample. For example, a protective efficacy of 48.93% was found for the earliest immersion time, reaching a maximum at the final immersion time of 24 hours.

Table 5.5: Weight loss results showing the %IE for Al, Zn, and MS corrosion in 1M HCl in the absence and presence of 800 ppm ELJCE at various immersion times

Metal	Conc. of ELJCE (ppm)	Immersion period (hours)				
		6	7	12	18	24
		%IE				
MS	800	98.10	97.10	89.04	92.95	90.99
Zn	800	48.93	49.36	57.78	70.15	77.49
Al	800	82.56	91.70	80.89	73.96	72.89

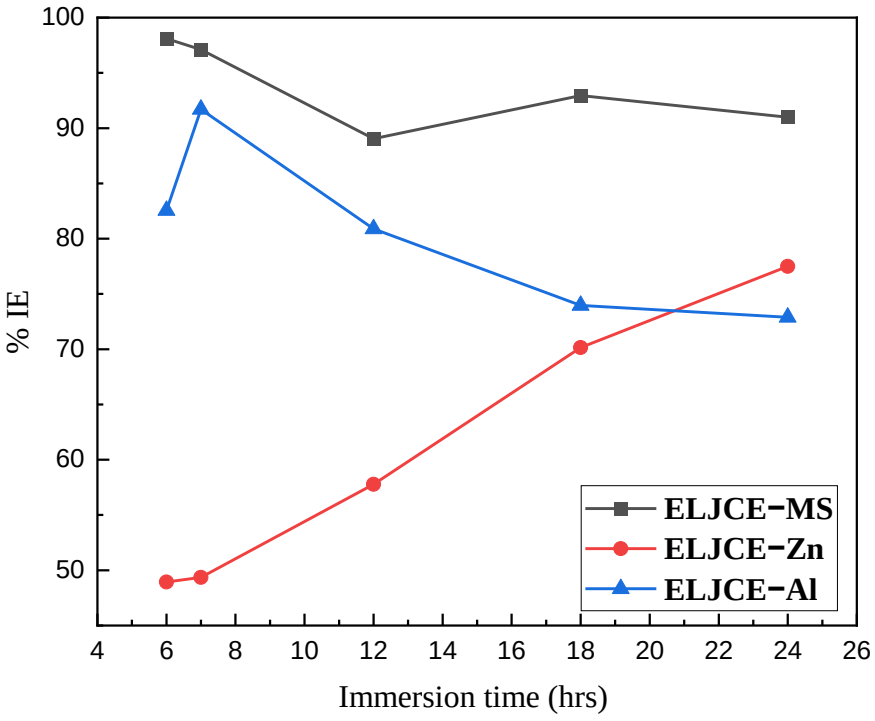

Figure 5.20: The variation of %IE for Al, Zn, and MS corrosion in 1 M HCl in the absence and presence of 800 ppm ELJCE at various immersion times

5.6.3. Effect of temperature on the corrosion of Zn, Al, and MS in 1 M HCl solution containing ELJCE

The effect of temperature on metal corrosion inhibitory reactions in an aqueous environment is a highly complex process considering that multiple modifications can occur on metal surfaces, such as rapid etching, inhibitor desorption, decomposition and inhibitor rearrangement [450]. At a constant bulk concentration of adsorptive inhibitor [563], a change in temperature affects the ability of inhibitor adsorption on the metal surface and the dissolution process of metals. The effect of temperature on the anti-corrosion efficacy of the inhibitory extracts of Al, MS, and Zn in 1 M HCl was investigated in the range of 303 K to 333 K in the absence and presence of different concentrations of ELJCE during 7 hours of immersion. The resulting details are summarized in Table 5.4. The table shows that the C_R increases significantly as the temperature of both the uninhibited and inhibited solutions increase. In the presence of ELJCE, this behaviour only applies to MS and Al surfaces but not to Zn metal surfaces. For example, the C_R for MS in the uninhibited system was 1.498810^{-3} $g.cm^{-2}.h^{-1}$ and that for Al was 8.6931×10^{-3} $g.cm^{-2}.h^{-1}$ at 303 K. The increase in temperature to 333 K led to an increase in C_R to 8.6198×10^{-3} and 1.1308×10^{-2} $g.cm^{-2}.h^{-1}$ for MS and Al, respectively. In the presence of ELJCE (200 ppm), the C_R was 1.3404×10^{-4} and 1.3702×10^{-3} at 303 K and increased to 2.9217×10^{-3} and 6.7966×10^{-3} $g.cm^{-2}.h^{-1}$ with the increase in temperature to 333 K for MS and Al samples, respectively. This implies that the protection efficiency decreased as temperature increased, as evidenced by the low %IE at high temperatures. This is thought to be due to physical adsorption on metal surfaces by ELJCE [564]. The decrease in inhibition efficiencies for MS and Al surfaces in 1 M HCl solution with temperature could be attributed to an increase in hot agitation of the plant extracts, which would affect the stability of the protective layer formed on the metal surfaces [565, 566]. The weakening of the adsorption film implies that the attack of H^+ and OH^- on metal surfaces increases with increasing system temperature, thereby increasing the corrosion rate.

The Zn surface inhibition efficiency increased with temperature, as evidenced by high inhibition efficiencies at higher temperatures. For instance, at 800 ppm, the %IE increased from 49.36, 65.12, and 78.22 to 85.64% at 303, 313, 323, and 333 K, respectively. This suggests that as the temperature rises, ELJCE adsorption film on the Zn surfaces strengthens, implying a chemical adsorption process [170]. Figures 5.21 and 5.22 shows that the inhibition efficiency for MS and Al decreases with temperature, whereas the inhibition efficiency for the Zn surface (Figure 5.23)

increases. The increase in the rate of corrosion with the temperature rise can be attributed to two factors: firstly, when the inhibitor molecules are at high temperatures and accumulate sufficient energy, they tend to desorb quickly from the metal surface, thus shortening the duration between the adsorption process and the desorption process, which results in the metal surface being exposed to aggressive species. Secondly, the decrease in hydrogen evolution over potential accelerates the cathodic reduction process.

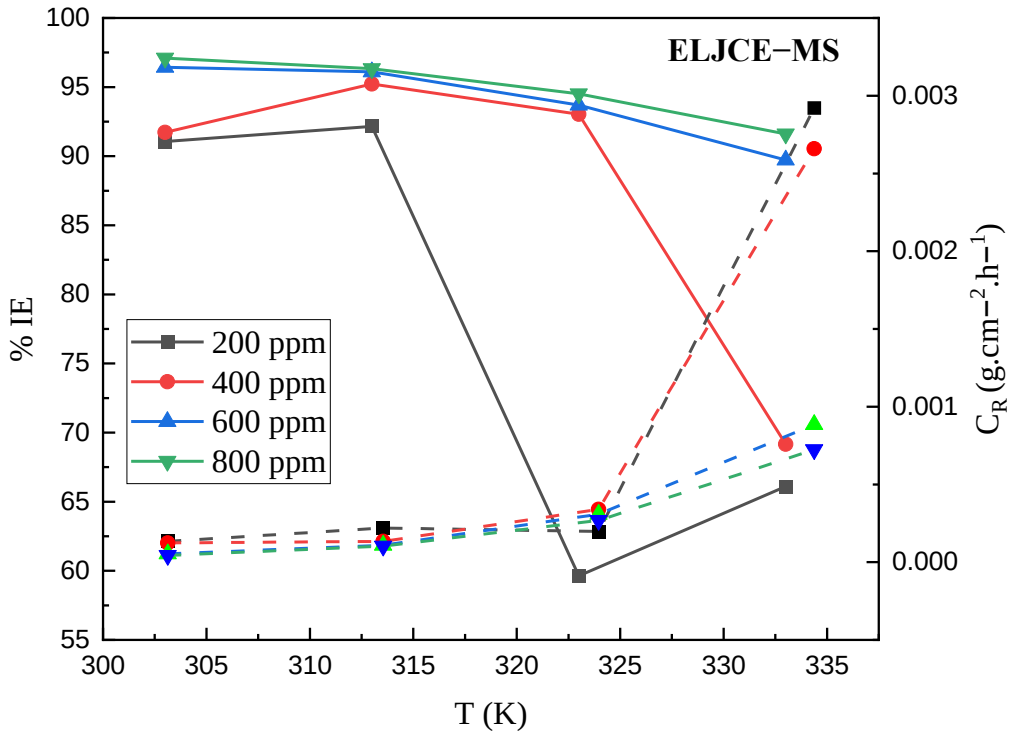

Figure 5.21: The dependence of (a) IE_{WL}(%) (solid lines) and (b) C_R (dashed lines) on temperature after 7 h of immersion of MS samples in 1 M HCl at different ELJCE concentrations

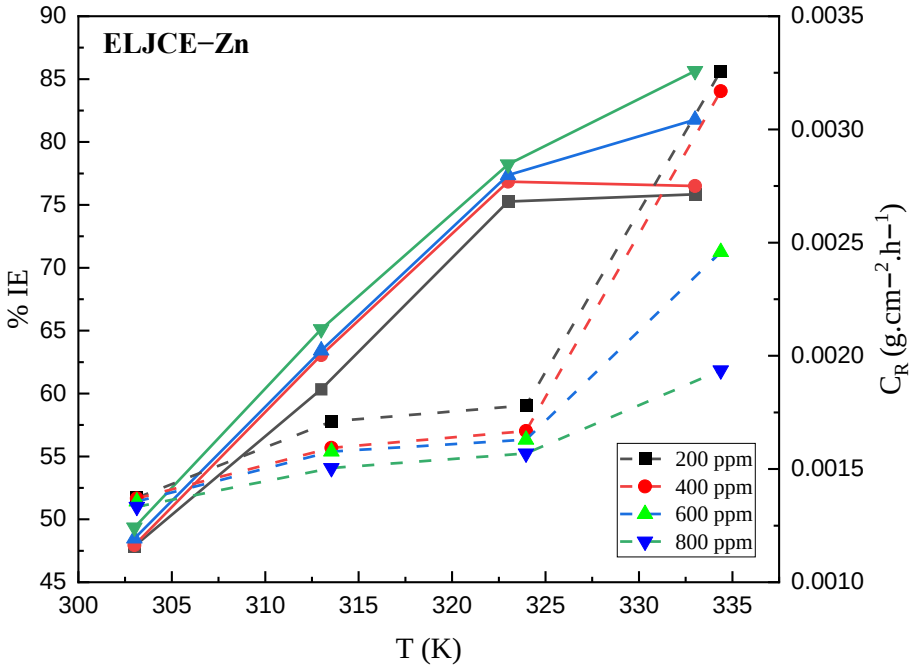

Figure 5.22: The dependence of (a) IE_{WL}(%) (solid lines) and (b) C_R (dashed lines) on temperature after 7 h of immersion of Zn samples in 1 M HCl at different ELJCE concentrations

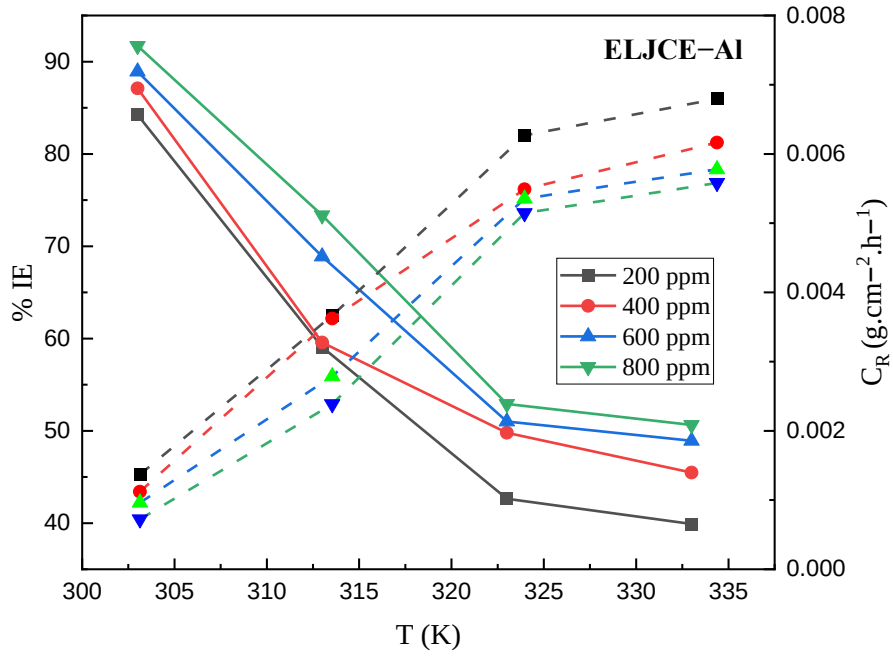

Figure 5.23: The dependence of (a) IE_{WL}(%) (solid lines) and (b) C_R (dashed lines) on temperature after 7 h of immersion of Zn samples in 1 M HCl at different ELJCE concentrations

5.6.4. Thermodynamic and kinetic Parameters

Linear regression of log C_R vs $10^3/T$ (Figure 5.23−5.25) yielded straight-line plots in the presence and absence of ELJCE with a slope of (E_a/2.303R), while the plotting of log C_R/T vs 10^3/T (Figure 5.26−5.28) also produced straight lines with a slope of (ΔH_a^*/2.303R) and an intercept of [(log RT/hN + (ΔS_a^*/2.303R)]. These diagrams enabled the determination of the E_a, ΔH_a^*, and ΔS_a^* values are shown in Table 5.6. The linear regression coefficients obtained from log C_R vs 10^3/T plots approached unity for all three metals, indicating that these plots can be used to explain the kinetics process of Zn, Al, and MS corrosion in 1 M HCl solution with a reasonable degree of confidence. It was found that the E_a values (Table 5.6) for the inhibited Zn surface were lower and continued to decrease with increasing concentration of ELJCE compared to the uninhibited Zn surface. For instance, the E_a value for the uninhibited system was found to be 45.0215 kJ.mol^{-1}. When ELJCE was introduced at a concentration of 200 ppm, the E_a value decreased to 21.9018 kJ.mol^{-1}. The E_a values continued to decline as the ELJCE concentration was further increased as more inhibitor molecules were added to the solution, reaching 21.2948, 15.1023, and 9.6680 kJ.mol^{-1} at 400, 600, and 800 ppm, respectively. Lower E_a values for the inhibited system imply that the ELJCE molecules modify the corrosion mechanism and that the modification occurs through chemical interaction with the active sites on the Zn surface [438, 567-569]. The decrease in E_a values for the inhibited Zn system suggests that the extracts were effective at higher temperatures. The increase in inhibition efficiencies of the Zn surface with increasing system temperature supports this. Higher E_a values were found in the presence of ELJCE in the acidic solution for MS and Al samples compared to those obtained for the dissolution of the two metals in the absence of ELJCE in the acidic solutions. The results in Table 5.6 show that for the Al and MS uninhibited system, the E_a value was 8.2165 and 48.2192 kJ.mol^{-1}. When the ELJCE was introduced at different concentrations of 200, 400, 600 and 800 ppm, the E_a value increased to 95.1306, 84.1970, 78.6765, 78.1250 kJ.mol^{-1} and 44.4164, 45.9885, 50.1532, 57.4468 kJ.mol^{-1} for MS and Al, respectively.

Since E_a represents a reaction's energy barrier, the increase in this value in the presence of ELJCE suggests that the presence of the extract/inhibitor induces an energy barrier that must be overcome to form corrosion products [570, 571]. This behaviour was observed for MS and Al samples, where for the Al sample, the increase in E_a values was found to be directly proportional to the concentration of ELJCE. The increase in E_a values for Al and MS following the addition of ELJCE indicates that the corrosion reaction of MS and Al was slowed down. Higher E_a values in the

presence of the ethanolic extracts also suggest that the extracts' adsorption on MS and Al surfaces was facilitated by a physical process that led to the formation of an electrostatic adsorption film [450, 572]. The high E_a values in the presence of ELJCE are due to the interaction of the inhibitor molecules with the MS and Al surfaces in the heterogeneous electrochemical corrosion process, which blocks the most active sites with the lowest E_a value, while areas with higher E_a participate in the subsequent corrosion process. This implies that at high E_a values, the dissolution of MS and Al surfaces is shifted to the uncovered portion of the metal surface where the extracts were not adsorbed [573]. Though the values of E_a for MS and Al are higher in the presence of ELJCE, they are also above the 40 kJ.mol^{-1} thresholds required for chemisorption [574]. This implies that the ELJCE's adsorption on the MS and Al surfaces also occurs via chemisorption. Also, due to the extracts' competitive adsorption with water molecules, the adsorption mechanism in this work cannot be considered a decisive criterion based on changes in E_a values. As a result, it is assumed that the adsorption mechanism in this work on Zn, MS, and Al is a combination of physisorption and chemisorption processes [575].

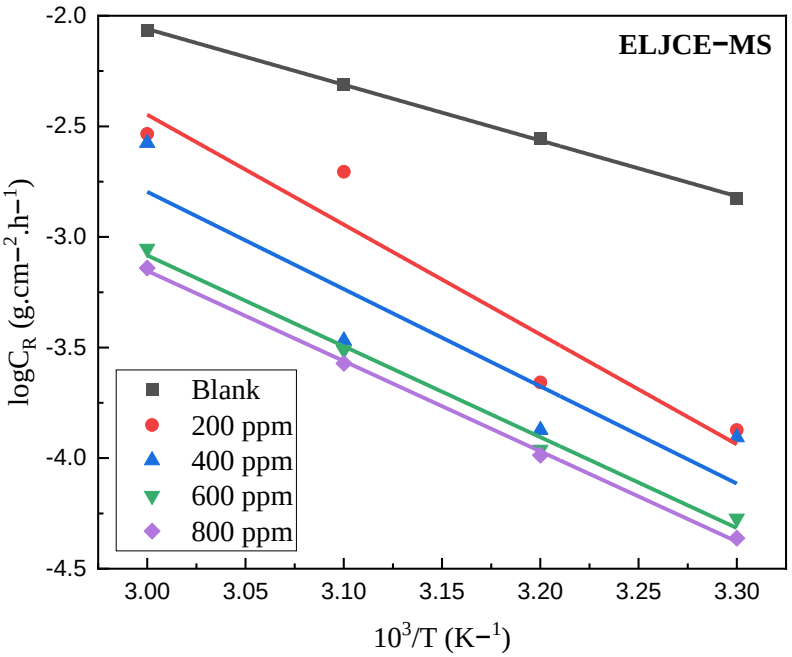

Figure 5.24: Arrhenius diagram (log C_R versus $10^3/T$) for the uninhibited (blank) and ELJCE-inhibited (200 to 800 ppm) MS system in corrosive 1 M HCl solution after 7 hours of immersion

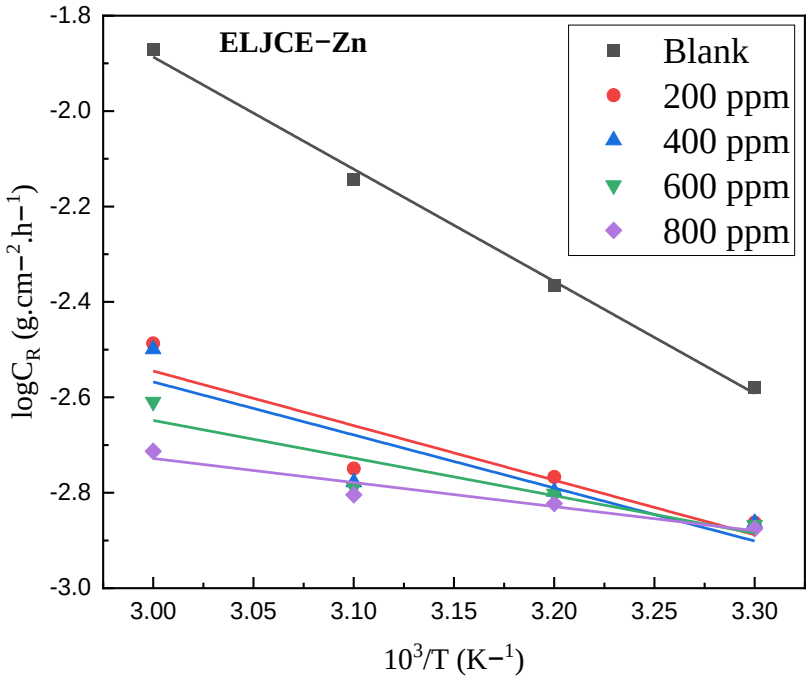

Figure 5.25: Arrhenius diagram (log C_R versus $10^3/T$) for the uninhibited (blank) and ELJCE-inhibited (200 to 800 ppm) Zn system in corrosive 1 M HCl solution after 7 hours of immersion

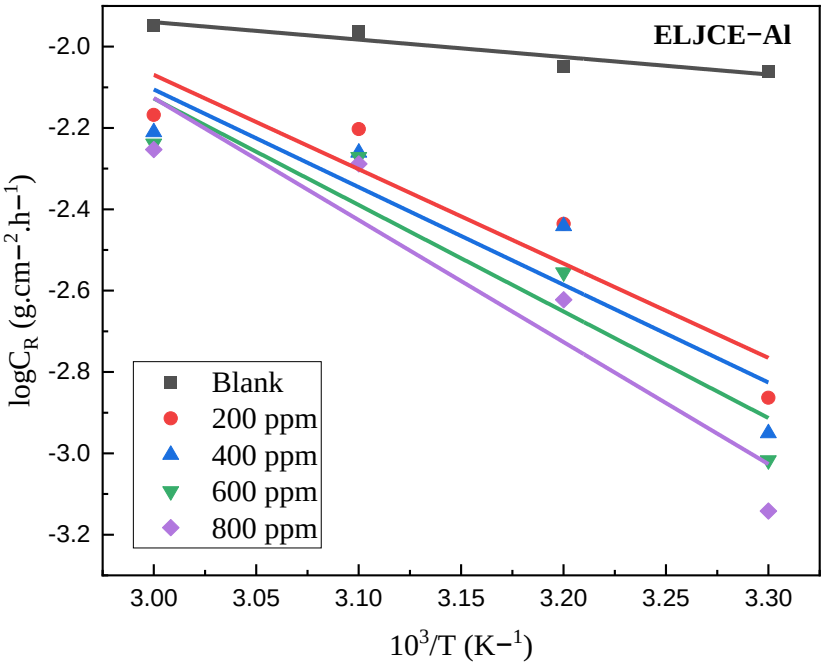

Figure 5.26: Arrhenius diagram (log C_R versus $10^3/T$) for the uninhibited (blank) and ELJCE-inhibited (200 to 800 ppm) Zn system in corrosive 1 M HCl solution after 7 hours of immersion

The positive ΔH_a^* values in the presence and absence of ELJCE indicate that the Zn, MS, and Al dissolution processes are endothermic. These values are also higher in the presence of the ELJCE than in their absence for Al and MS, indicating that their dissolution process is more difficult in the presence of the extracts [218, 575]. The difficulty of the dissolution process is due to a higher energy barrier caused by the presence of various concentrations of extracts, which raises the enthalpy of the corrosion process. Lower ΔH_a^* values were observed in the presence of extracts for the Zn system. This phenomenon could be explained by the extracts' chemisorption inhibition mechanism of Zn corrosion, which involves a charge transfer process from the extract's compounds to the Zn surface. Furthermore, the difference in E_a and ΔH_a^* values ($E_a - \Delta H_a^*$) indicates an average value of about 2.6 kJ.mol^{-1}, which is similar to the average value of RT and means that Al, Zn, and MS's corrosion process involves a unimolecular reaction [576]. The calculated entropy values for the corrosion of Al and MS in uninhibited HCl are −200.7138 and −194.5601 J.mol^{-1}.K^{-1}, respectively and decrease negatively in the presence of the extracts in the corrosive solution (Table 5.6). The negative decrease in entropy values when the extracts are present indicates that the ethanolic extracts formed an orderly, stable adsorption film on the Al and MS surfaces and that the activated complex is an association rather than a dissociation step during the rate-determination step [577]. Entropy values for Zn increased with increasing concentrations of ELJCE in 1 M HCl, reaching a high of −201.2758 J.mol^{-1}.K^{-1} at the maximum extract concentration of 800 ppm. The fact that the entropy values are negative indicates that the corrosion processes of the three metals are entropically favourable. Higher negative ΔS_a^* values were obtained for the ELJCE-inhibited 1 M HCl solution for MS and Al compared to that of the uninhibited solution, indicating a reduction in disorder or randomness as the inhibited corrosive reaction moves from the reagents to the activated complex [578]. While for Zn, lower negative ΔS_a^* values were obtained for the ELJCE-inhibited 1 M HCl solution compared to the uninhibited Zn solution. Such behaviour indicates the repulsive nature that occurs between the adsorbed ELJCE components. This results in the disordered arrangement of the extracts molecules on the Zn surface [459].

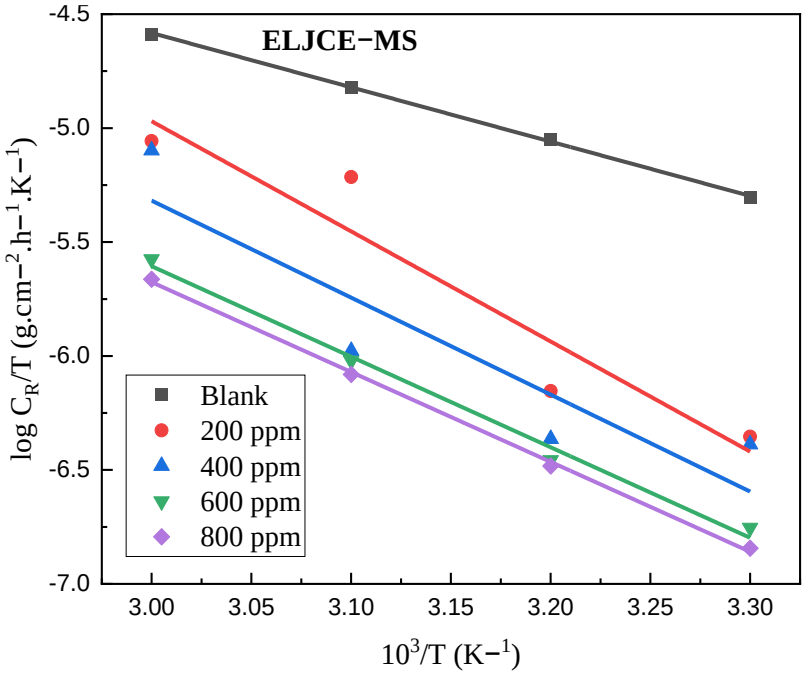

Figure 5.27: Transition state diagram (log C_R/T versus $10^3/T$) for the uninhibited (blank) and MLJCE-inhibited (200 to 800 ppm) MS system in corrosive 1 M HCl solution after 7 hours of immersion

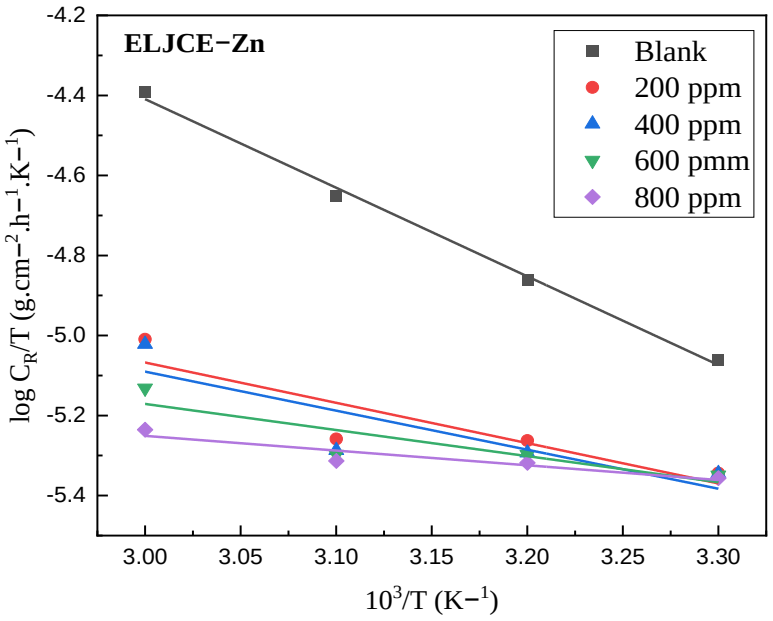

Figure 5.28: Transition state diagram (log C_R/T versus $10^3/T$) for the uninhibited (blank) and MLJCE-inhibited (200 to 800 ppm) Zn system in corrosive 1 M HCl solution after 7 hours of immersion

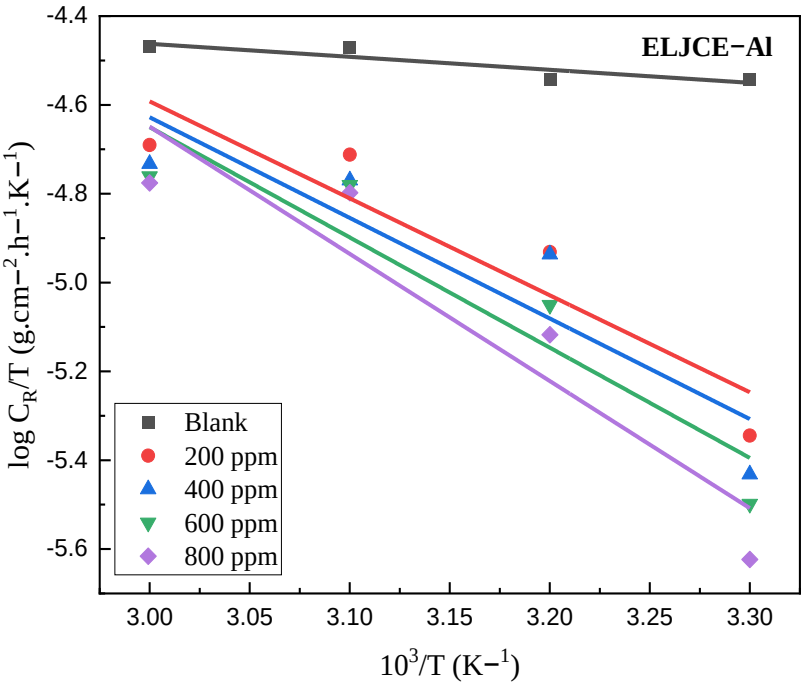

Figure 5.29: Transition state diagram (log C_R/T versus $10^3/T$) for the uninhibited (blank) and MLJCE-inhibited (200 to 800 ppm) Al system in corrosive 1 M HCl solution after 7 hours of immersion

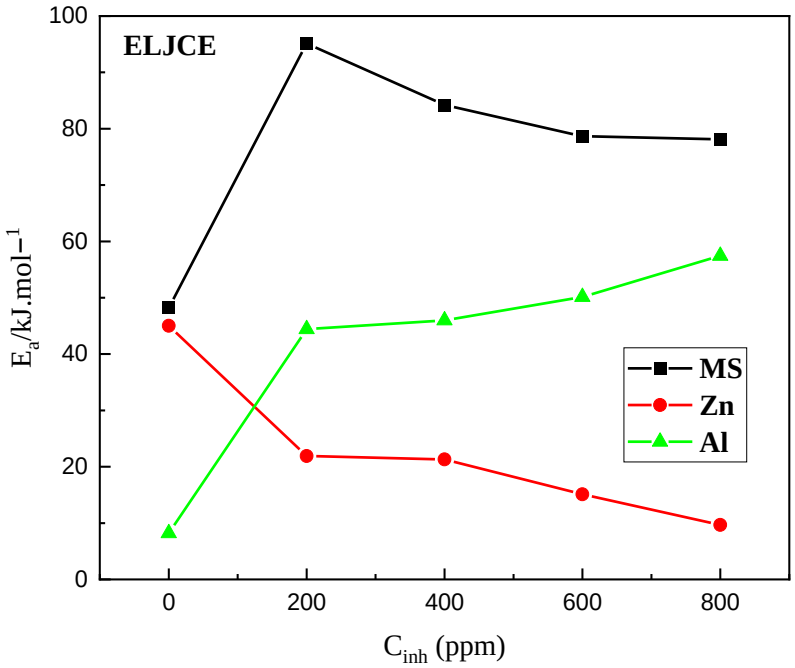

Figure 5.30: Relationship of E_a with the different concentrations of ELJCE for Zn, Al, and MS

The effect of temperature on the adsorption of ELJCE on the surface of Zn, Al, and MS was also evaluated by determining Q_{ads} values. At different temperatures, both negative and positive Q_{ads} values were obtained. The predominance of negative Q_{ads} values for Al suggests that the ELJCE binding on the Al surface is an exothermic process at all temperatures investigated. This behaviour is consistent with the physisorption adsorption mechanism on the Al surface [461]. Positive Q_{ads} values were observed at almost all temperatures except 303 to 313 K at 400 ppm, indicating that the extracts' inhibition efficiency against Zn corrosion increases with temperature. This suggests that the extracts form a chemical bond with the Zn surface [579]. Both negative and positive Q_{ads} values indicate that adsorption on the MS surface involves a hybrid adsorption mechanism involving both physical and chemical adsorption processes. Endothermic and exothermic adsorption processes occurred on the surfaces of Zn, Al, and MS. However, from Figure 5.30 it can be seen that the negative values for Zn are negligible and the adsorption process can be regarded as an endothermic process. This finding supports the comprehensive adsorption mechanism and is consistent with the obtained E_a values (Figure 5.29).

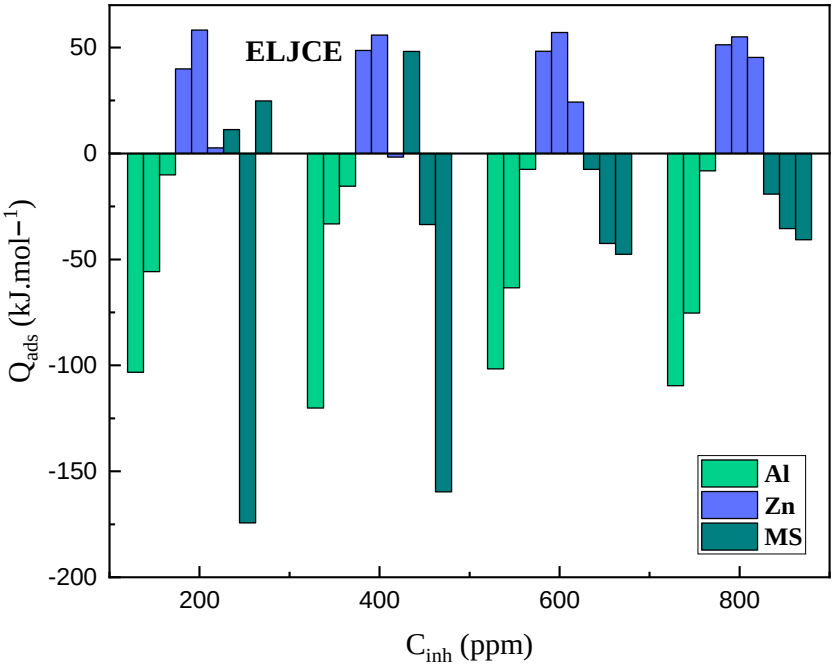

Figure 5.31: Heat of adsorption data for different concentrations of ELJCE for Zn, Al, and MS

Table 5.6: Kinetic and activation parameters for MS, Al, and Zn in uninhibited and MLJCE-inhibited 1 M HCl solution

Metal	Conc. of ELJCE (ppm)	E_a ($kJ.mol^{-1}$)	ΔH_a^* ($kJ.mol^{-1}$)	$E_a - \Delta H_a^* = RT$ ($kJ.mol^{-1}$)	ΔS_a^* ($J.mol^{-1}.K^{-1}$)	Q_{ads} ($kJ.mol^{-1}$)		
						303 to 313	313 to 323	323 to 333
MS	0	48.2192	45.6457	2.5735	−194.5601	–	–	–
	200	95.1306	92.5150	2.6156	−187.6044	11.3021	−174.3525	24.8004
	400	84.1970	81.4875	2.7095	−189.6804	48.1663	−33.5370	−159.6827
	600	78.6765	76.0589	2.6176	−190.8186	−7.4726	−42.4459	−47.5827
	800	78.1250	75.5113	2.6137	−190.9743	−19.1998	−35.4633	−40.7278
Zn	0	45.0215	42.4058	2.6157	−194.8944	–	–	–
	200	21.9018	19.2862	2.6156	−199.1747	39.8854	58.2628	2.6751
	400	21.2948	18.6792	2.6156	−199.2920	48.6150	55.9038	−1.7002
	600	15.1023	12.4923	2.6100	−200.3425	48.2276	57.0900	24.2863
	800	9.6680	7.0447	2.6233	−201.2758	51.2579	55.0024	45.3646
Al	0	8.2165	5.6009	2.6156	−200.7138	–	–	–
	200	44.4164	41.8007	2.6157	−195.1720	−103.2647	−55.7758	−10.1145
	400	45.9885	43.3709	2.6176	−194.9618	−120.1599	−33.2567	−15.4648
	600	50.1532	47.5356	2.6176	−194.3315	−101.6685	−63.4009	−7.4788
	800	57.4468	54.8235	2.6233	−193.1887	−109.6119	−75.2899	−8.1693

5.7. Thermodynamic parameters of adsorption

An adsorption isotherm is the most appropriate approach for expressing the nature of adsorption on the metal surface. The effectiveness of a corrosion inhibitor can be attributed to its adsorption capacity on the metal surface. Isotherms show how adsorbate molecules interact with the adsorbent electrode surface. The most applicable isotherm for the adsorption system and the various factors affecting adsorption must be determined to establish the most applicable correlation for the equilibrium system [580]. The adsorption process on a corroding metal surface never achieves true equilibrium but rather a state of dynamic equilibrium in which the adsorption and desorption rates are equal [581]. At this point, it is reasonable to assume quasi-equilibrium adsorption using the appropriate adsorption isotherm in a thermodynamic manner. This is also the point at which inhibitors are said to provide effective inhibition, significantly lowering the corrosion rate [582]. A correlation between the inhibitor concentration and the degrees of adsorbate covered on the surface for a given condition can be used to predict the chemical or physical nature of the adsorption process. The Langmuir adsorption isotherm was used in the current study to provide information on the ELJCE adsorption on the surfaces of Al, Zn, and MS because it best fits the data based on the correlation coefficients obtained.

The applicability of the data to isotherm was tested using equation 54 provided in section 4. Langmuir adsorption isotherms make several assumptions to explain the adsorption process of the adsorbate (inhibitor) [583-585]. The first assumption is that the reactive inhibitor molecules are distributed uniformly across the absorbent metal surface (monolayer adsorption process). Second, there is no lateral interaction between the inhibitor molecules at different adsorption sites, and each site can only accommodate one inhibitor molecule at a time. Finally, all adsorption sites on the adsorbent's surface are identical. Figure 5.31−5.34 shows the Langmuir plots for MS, Al, and Zn obtained after 7 hours of immersion in 1 M HCl in various concentrations of ELJCE at temperatures ranging from 303 to 323 K. The parameters obtained from the isotherm are represented in Table 5.7. The Langmuir plots show that straight lines were created by a plot of C_{inh}/θ versus C_{inh} with positive intercepts with an average R^2 of around 0.999. The fact that the R^2 is close to unity indicates strong adsorption on the metal surface at all temperatures. Langmuir plots are characterized by a slope near unity [585], and the slope values obtained for all three metals confirm the validity of the isotherm despite a minor deviation from unity. Although one of

the model's assumptions is that there is no interaction between the molecules of the adsorbed inhibitors, this assumption is invalid for large molecules. Thus, the variance observed from the slope unity may result from interactions between the adsorbed extract molecules on the metal surface, which is typical of natural product adsorption behaviour. In addition to the main active constituent (VBS), ELJCE contains several heterocyclic compounds capable of adsorbing onto metal surfaces, and an interaction between these compounds is highly anticipated. The hydroxyl functional groups in VBS are capable of interacting through the formation of hydrogen bonds between the partial negative charge (δ^-) of the O_2 atom and the partial positive charge (δ^+) of the hydrogen atom. The adsorption equilibrium constant (K_{ads}) denotes the adsorption process's strength.

Large K_{ads} values indicate that the extracts effectively inhibit corrosion, whereas smaller values indicate a weak interaction between the extracts and the metals' surfaces. Table 5.7 shows that the K_{ads} values are neither smaller nor larger, implying adequate interaction between the metal surface and the inhibitors. This holds for all three metals under consideration in this work. Both weak and strong interactions contribute to the inhibition of MS, Al and Zn corrosion by ELJCEs via physical electrostatic attraction and chemical adsorption. The interaction between the metal's surface and the extracts during corrosion inhibition can be characterized using the $\Delta G°_{ads}$ obtained from K_{ads} via the expression in equation 56. Negative $\Delta G°_{ads}$ values were obtained for both the inhibited and uninhibited systems, indicating that the adsorption of ELJCE onto the Al, Zn, and MS surfaces in 1 M HCl occurred by spontaneous processes. Generally, a magnitude of $\Delta G°_{ads}$ of -20 kJ.mol^{-1} or less negative indicates electrostatic interactions between the inhibitor and the charged metal surface. $\Delta G°_{ads}$ of -40 kJ.mol^{-1} or more negative represent the sharing or transfer of charges from the inhibitor molecules to the metal surface, resulting in the formation of a chemical bond [470-472]. Table 5.7 shows that the calculated $\Delta G°_{ads}$ values range between -20 and -40 kJ.mol^{-1}, indicating that ELJCEs adsorption is not solely physisorption nor chemisorption but follows a comprehensive mode of adsorption on the metals' surfaces.

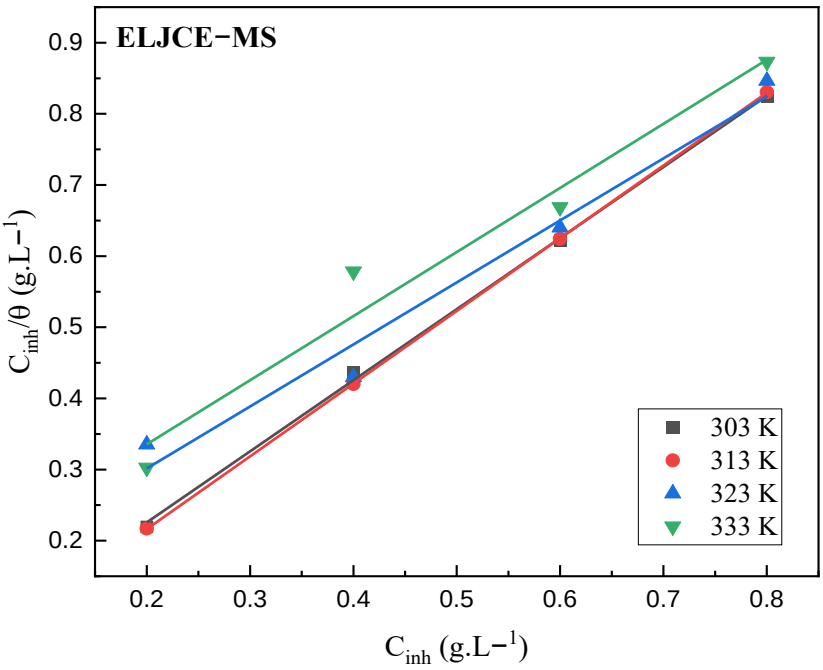

Figure 5.32: Langmuir adsorption isotherm plots for MS corrosion in 1 M HCl in the presence of various concentrations of ELJCE

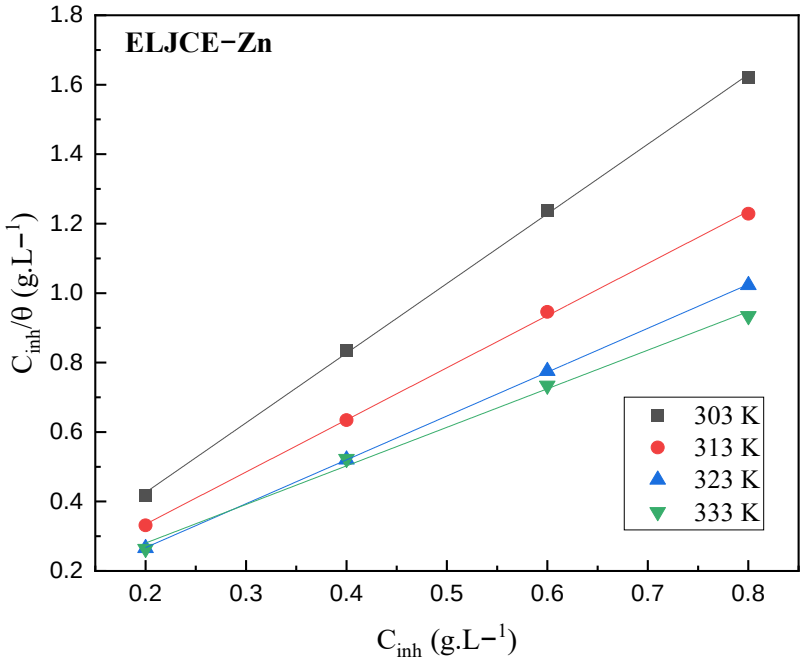

Figure 5.33: Langmuir adsorption isotherm plots for Zn corrosion in 1 M HCl in the presence of various concentrations of ELJCE

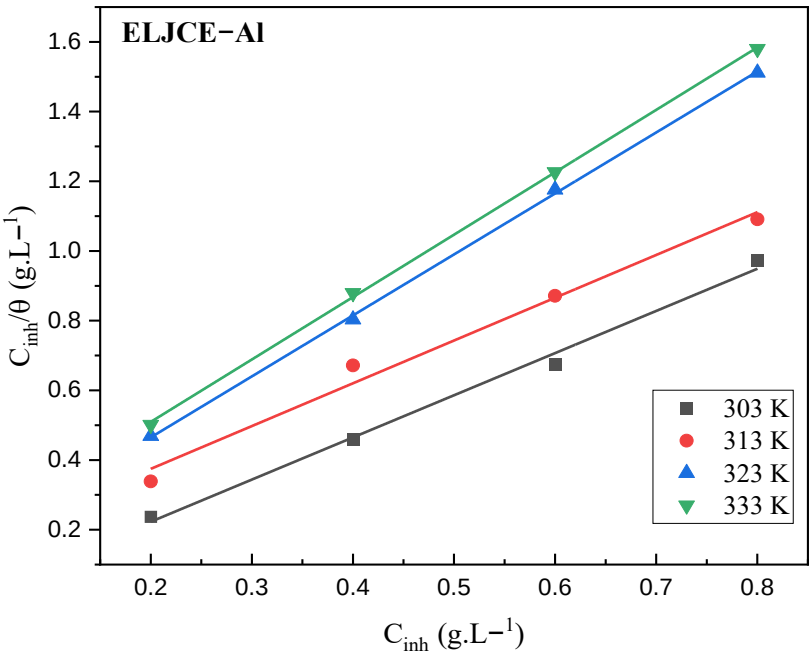

Figure 5.34: Langmuir adsorption isotherm plots for Al corrosion in 1 M HCl in the presence of various concentrations of ELJCE

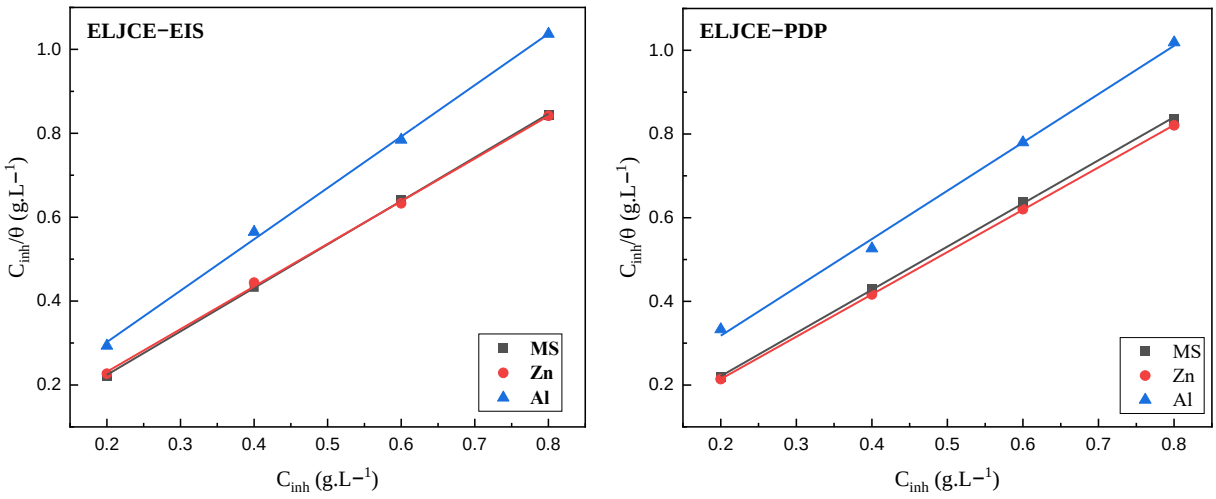

Figure 5.35: Langmuir adsorption isotherm plots for MS, Zn, and Al corrosion in 1 M HCl in the presence of various concentrations of ELJCE

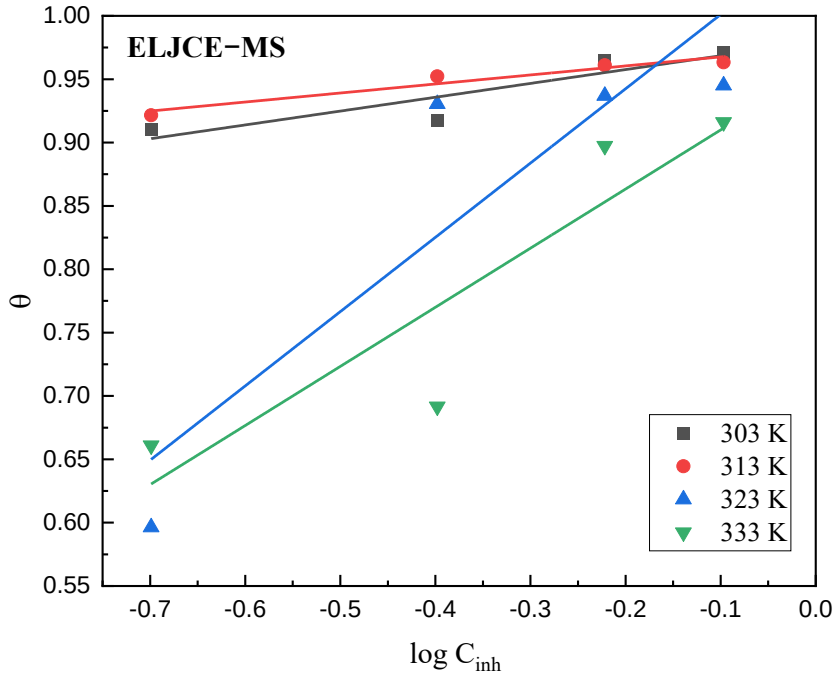

Figure 5.36: Temkin adsorption isotherm plots for MS corrosion in 1 M HCl in the presence of various concentrations of ELJCE

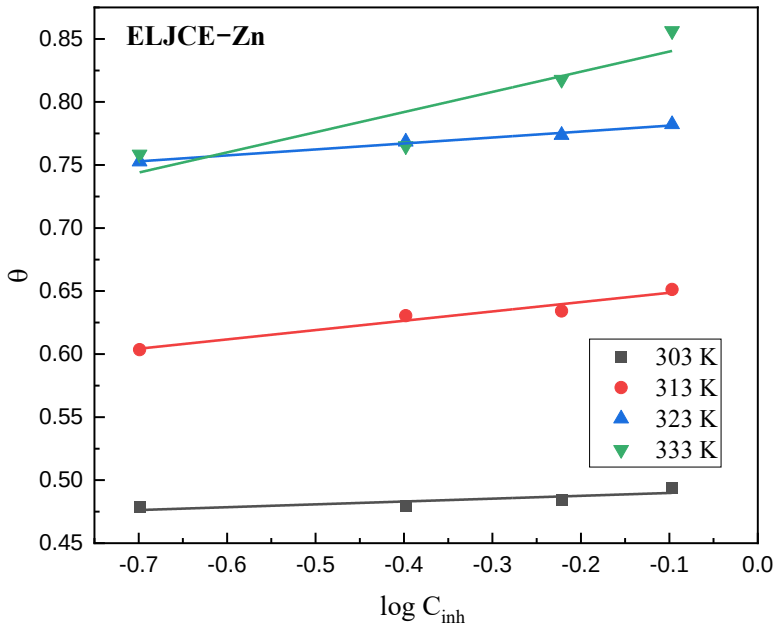

Figure 5.37: Temkin adsorption isotherm plots for Zn corrosion in 1 M HCl in the presence of various concentrations of ELJCE

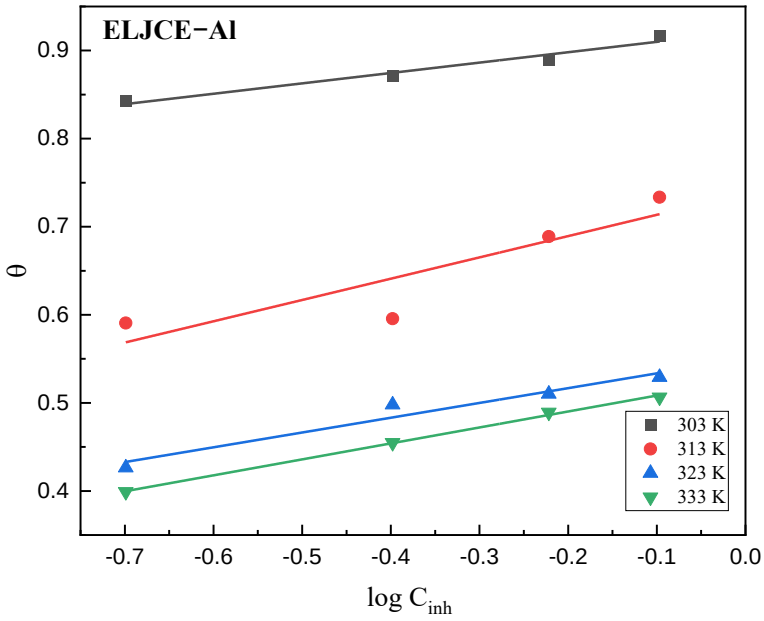

Figure 5.38: Temkin adsorption isotherm plots for MS corrosion in 1 M HCl in the presence of various concentrations of ELJCE

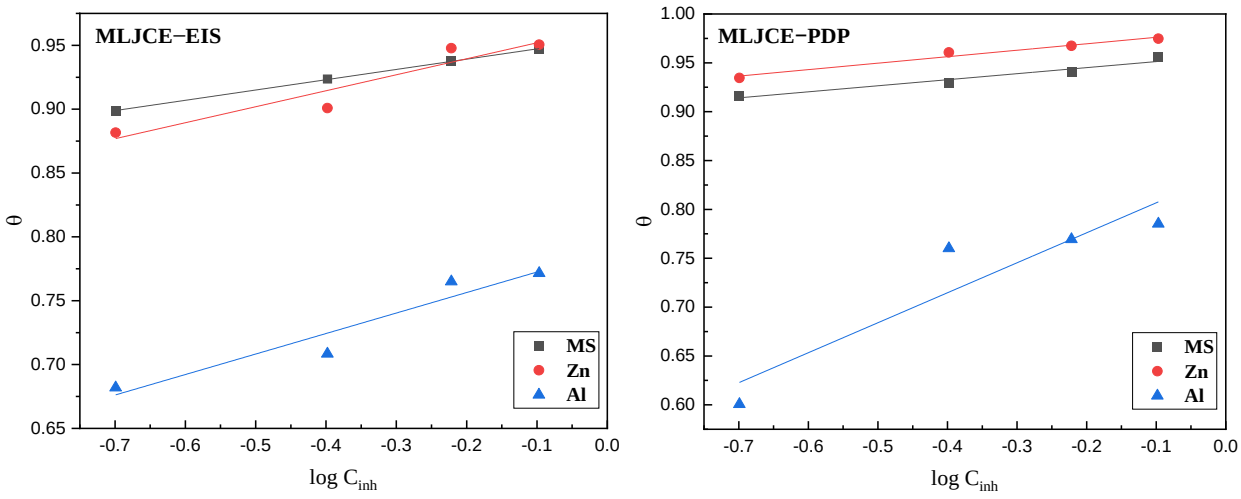

Figure 5.39: Temkin adsorption isotherm plots for MS, Zn, and Al corrosion in 1 M HCl in the presence of various concentrations of ELJCE

The K_L was calculated as a further physical description of the adsorption isotherm and to confirm the fit of the experimental data to the Langmuir adsorption isotherm using equation 57 [469, 474, 475]. It can be seen from Table 5.8 that all K_L values obtained at all extract concentrations are below one ($K_L < 1$), confirming that the adsorption of ELJCE onto MS, Zn, and Al surfaces is

favourably aligned with the Langmuir adsorption isotherm. The estimated mean values of K_L show that Langmuir's description of adsorption is more favourable at the lowest temperature (303 K) for MS and Zn. Whereases for Al it is favourable at both the lowest (303 K) and the highest temperatures (333 K) [586]. The deviation in slope values indicates the involvement of more than one molecule or atom during the adsorption on the surface of the three metals and the interaction between the ELJCEs compounds. This necessitates using an isotherm like the Temkin adsorption isotherm model, which considers such interaction. The isotherm model's adsorption parameters are shown in Table 5.8. The Temkin model fitted data for all three metals is depicted in Figure 5.35−5.38. The interaction parameters (a) values found are high and point to the presence of repulsion forces as the values were negative [476]. Straight lines with R^2 close to unity represent the plots, confirming that the experimental data is well-fitted to this isotherm.

Table 5.7: Gravimetric, EIS, and PDP Langmuir and Temkin adsorption isotherm parameters

Metal	Isotherm	Method	T (K)	R^2	Slope	Intercept	K_{ads} (L.g^{-1})	$\Delta G°_{ads}$ (kJ.mol^{-1})	–a
MS	Langmuir	Weight loss	303	0.999	0.9995	0.0257	38.9105	–26.6265	–
			313	1	1.0224	0.0118	84.7458	–29.5309	
			323	0.975	0.8720	0.1270	7.8740	–24.0932	
			333	0.966	0.9012	0.1552	6.4433	–24.2840	
		PDP	303	0.999	1.0321	0.01485	67.3401	−28.0083	
		EIS	303	0.999	1.0367	0.01672	59.8086	−27.7095	
	Temkin	Weight loss	303	0.831	0.1092	0.9795	$9.3282x10^{8}$	–69.4355	10.5449
			313	0.937	0.0713	0.9748	$4.6968x10^{13}$	–99.9030	16.1501
			323	0.805	0.5863	1.0597	$6.4180x10^{1}$	–29.7279	1.9640
			333	0.829	0.4666	0.9566	$1.1225x10^{2}$	–32.1961	2.4679
		PDP	303	0.945	0.0619	0.9575	$5.1801x10^{6}$	−56.3518	8.0775
		EIS	303	1	0.0806	0.9553	$7.1188x10^{11}$	−86.1571	6.2035
Zn	Langmuir	Weight loss	303	1	2.0061	0.0247	40.4858	–26.7264	–
			313	1	1.5015	0.0344	29.0698	–26.7464	
			323	1	1.2631	0.0146	68.4932	–29.9026	
			333	0.996	1.1111	0.0581	17.2117	–27.0044	
		PDP	303	0.999	1.0121	0.01182	84.6024	−28.5832	
		EIS	303	0.999	1.0167	0.02803	35.6761	−26.4078	
	Temkin	Weight loss	303	0.735	0.0226	0.4921	$5.9470x10^{21}$	–143.7129	50.9513
			313	0.957	0.0740	0.6560	$7.3266x10^{8}$	–71.0984	15.5608
			323	0.988	0.0473	0.7860	$4.1429x10^{16}$	–121.3092	24.3446
			333	0.812	0.1600	0.8560	$2.2387x10^{5}$	–53.2332	7.1969
		PDP	303	0.972	0.0661	0.9827	$7.3600x10^{14}$	−103.6438	7.5643
		EIS	303	0.905	0.1252	0.9645	$5.0542x10^{7}$	−62.0907	3.9936
Al	Langmuir	Weight loss	303	0.994	1.2103	0.0192	52.0833	–27.3610	–
			313	0.987	1.2279	0.1291	7.7459	–23.3046	
			323	1	1.7505	0.1149	8.7032	–24.3621	
			333	1	1.7913	0.1512	6.6138	–24.3563	
		PDP	303	0.997	1.1554	0.08676	11.5260	−23.5613	
		EIS	303	0.999	1.2253	0.05715	17.4978	−24.6131	
	Temkin	Weight loss	303	0.964	0.1179	0.9217	$6.5720x10^{7}$	–62.7522	9.7668
			313	0.800	0.2418	0.7377	$1.1243x10^{3}$	–36.2589	4.7622
			323	0.953	0.1679	0.5503	$1.8945x10^{3}$	–38.8187	6.8582
			333	0.998	0.1812	0.5265	$8.0467x10^{2}$	–37.6497	6.3549
		PDP	303	0.865	0.3068	0.8374	$5.3632x10^{2}$	−33.2357	1.6297
		EIS	303	0.922	0.1606	0.7885	$8.1192x10^{4}$	−45.8822	3.1132

Table 5.8: The K_L values for ELJCE at varying concentrations at 303 to 333 K for MS, Al, and Zn corrosion in 1 M HCl calculated from weight loss Langmuir isotherm parameters

Metal	Conc. of ELJCE (ppm)	K_L			
		303 K	313 K	323 K	333 K
MS	200	0.1139	0.0570	0.3884	0.4369
	400	0.0604	0.0286	0.2410	0.2795
	600	0.0411	0.0193	0.1747	0.2055
	800	0.0311	0.0145	0.1370	0.1625
Mean		0.0616	0.1085	0.2353	0.2711
Zn	200	0.1099	0.1468	0.0680	0.2251
	400	0.0582	0.0792	0.0352	0.1268
	600	0.0395	0.0542	0.0238	0.0882
	800	0.0300	0.0412	0.0179	0.0677
Mean		0.0594	0.0804	0.0898	0.1270
Al	200	0.0876	0.3923	0.3649	0.0703
	400	0.0458	0.2440	0.2232	0.0364
	600	0.0310	0.1771	0.1607	0.0246
	800	0.0234	0.1390	0.1256	0.0185
Mean		0.0470	0.2381	0.2186	0.0375

High ΔG^{o}_{ads} values, obtained by fitting the data to Temkin adsorption isotherm, confirm chemical interaction between the inhibitor molecules and the surface of the three metals. For example, the ΔG^{o}_{ads} values for MS were found to be –69.4355, –99.9030, –29.7279, –32.1961 kJ.mol^{-1} at 303, 313, 323 and 333 K, respectively. The spontaneity of ELJCE adsorption on the MS, Zn, and Al surfaces was also confirmed by negative Temkin ΔG^{o}_{ads} values. While ΔG^{o}_{ads} values from the Langmuir isotherm suggested a mixed-type adsorption process, the values obtained from the Temkin isotherm predict a chemisorption-adsorption process as the values are well above or near −40 kJ.mol$^{-1,}$ particularly for MS and Zn. When both results are considered, they support the complex interaction between the metal surfaces and ELJCE components, involving both chemisorption and physisorption mechanisms [478]. The high ΔG^{o}_{ads} values obtained from the Temkin data indicate intermolecular interactions between the adsorbed ELJCE components on the Al, Zn, and MS surfaces.

5.8. FT-IR analysis of the ELJCE adsorption layer formed on the surface of Al, Zn, and MS in the 400-4000 cm^{-1} range

FT-IR analysis of the functional groups responsible for MLJCE adsorption on the surface of metal samples (section 4.8) revealed that it is critical to analyze the entire system to obtain a complete picture of the functional groups responsible for slowing down the corrosion process. As a result, Figure 5.39–5.41 compares the spectrum of functional groups responsible for ELJCE adsorption on MS, Al, and Zn surfaces to those formed without the extracts and the corrosive 1 M HCl solution (i.e., liquid water) of the two systems. The spectra obtained from the corrosion solution in the presence and absence of ELJCE are identical to those obtained from liquid water, as shown in the three figures. Although these plots are similar, the addition of ELJCE to the corrosive MS and Zn solutions (ELJCE–Zn and MS solution) slightly alters the absorption bands around 1630 cm^{-1}, suggesting the involvement of the carboxyl ion group (COO^{-}) in preventing or controlling their corrosion process. When the liquid water contribution cannot be distinguished from that of the inhibitors solution, a comparison based on the intensity of the peaks and their movement or displacement should be used to determine whether corrosion inhibition occurred.

Figure 5.39 shows that the adsorption spectrum of ELJCE–MS is similar to that of water with an indication of corrosive products on the surface of MS. Figure 5.40 indicates that a similar type of spectrum was also observed for the adsorption of ELJCE on the surface of Zn (ELJCE–Zn adsorption film). Evidence of the adsorption of ELJCE on the surface of Zn and MS is highlighted by the minor differences in the spectra. For example, the ELJCE adsorption spectra on the surface of MS and Zn show a much broader peak at 3222 and 3250 cm^{-1}, respectively. This indicates the presence of the hydroxy group of the ELJCE in addition to that of water. The adsorption of ELJCE on the Al surface (ELJCE–Al adsorption film) shown in Figure 5.41 suggests that adding the extract to the corrosive solution protected the Al surface from being attacked by the corrosive solution. This is indicated by the less intense broad peak around the 3220 cm^{-1}, which can be assigned to both the Al–OH of the MLJCE and the Al–H_2O bonds. However, the reduction in the intensity of this peak indicates that it may just be the result of the disordered structure of ELJCE adsorbed on the Al surface instead of water [501]. The lack of the distinct scissor water peak at around 1620 cm^{-1} also supports the protection of the Al surface from the corrosive solution. The absorption bands around the 1380–1640 cm^{-1} could be due to the adsorption of amine and polyphenols groups on the Al surface. To observe the effect of ELJCE in retarding corrosion, the

expanded ELJCE adsorption film Al adsorption film spectrum is shown in Figure 5.42. The location absorption peaks at approximately 824 and 647 cm^{-1} remained almost unchanged in the presence of ELJCE in solution compared to the Blank-MS corrosion products spectrum. This is also evident in the Zn spectrum, as the absorption band at 630 cm^{-1} has remained constant, implying that the plant extract did not affect the Zn-O bond between the dissolved O_2 and the surface of Zn. The similarities in the FT-IR spectra of the blank and inhibited MS and Zn surfaces suggest that the corrosion mechanism of Zn and MS was not altered during the inhibition process, which is consistent with the results from PDP and EIS techniques.

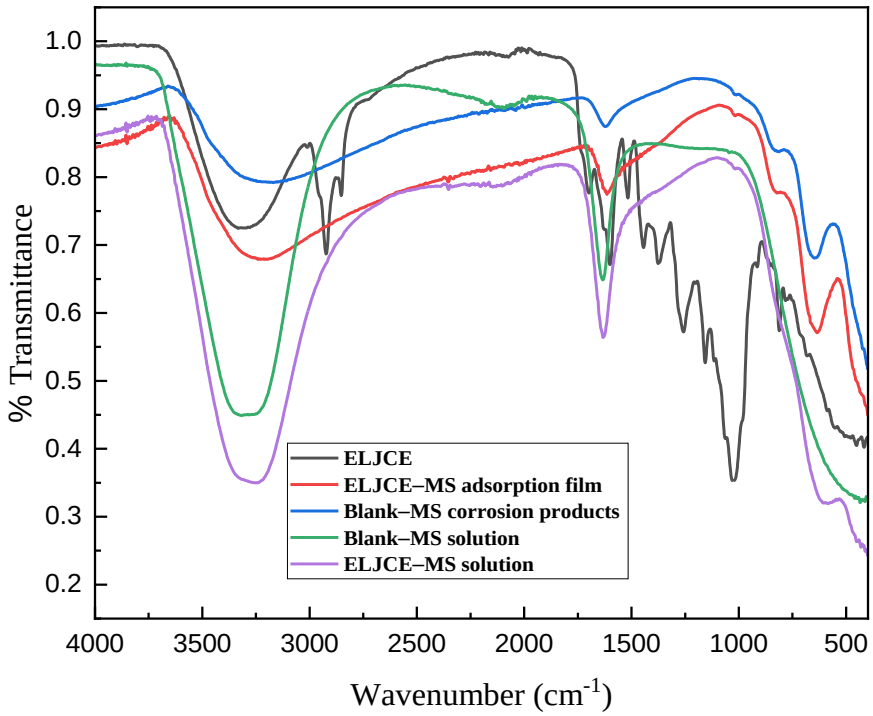

Figure 5.40: FT-IR spectrum of the adsorption film formed on the MS surface (ELJCE-MS adsorption film) compared to the crude ELJCE, corrosion products formed on MS (Blank-MS corrosion products), the 1 M HCl corrosion solution in the presence (ELJCE-MS solution) and the absence (Blank-MS solution) of ELJCE

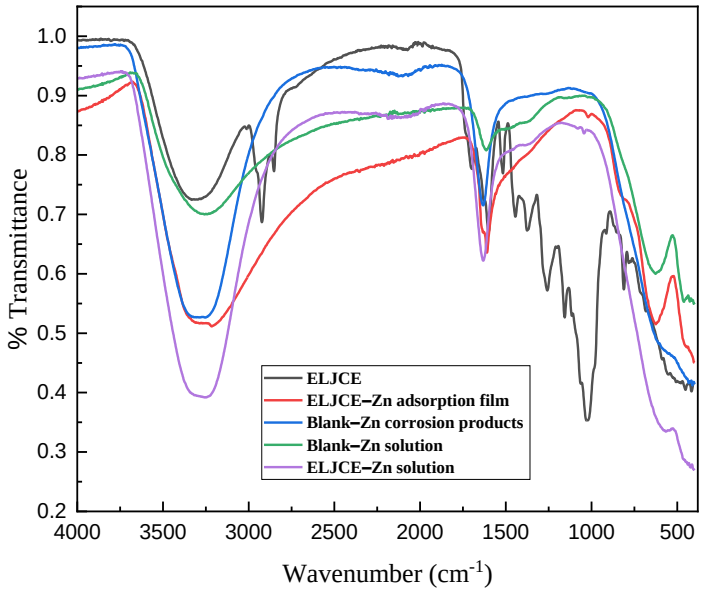

Figure 5.41: FT-IR spectrum of the adsorption film formed on the Zn surface (ELJCE-Zn adsorption film) compared to the crude ELJCE, corrosion products formed on Zn (Blank-Zn corrosion products), the 1 M HCl corrosion solution in the presence (ELJCE-Zn solution) and the absence (Blank-Zn solution) of ELJCE

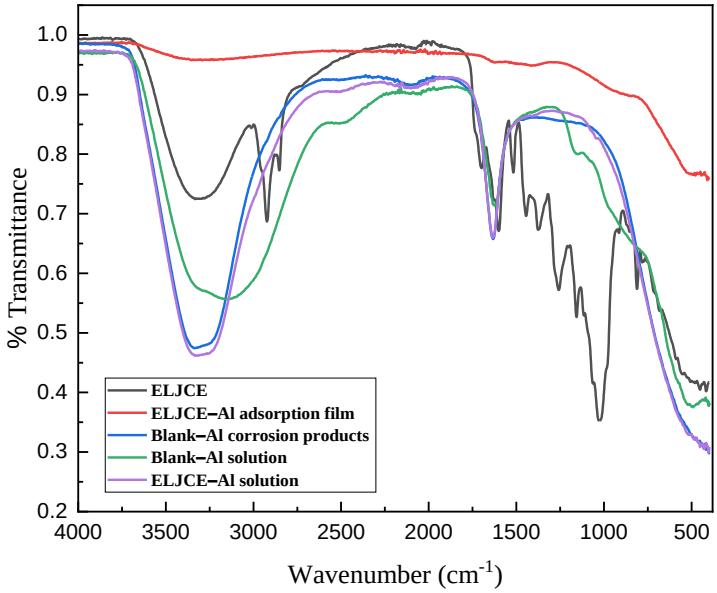

Figure 5.42: FT-IR spectrum of the adsorption film formed on the Al surface (ELJCE-Al adsorption film) compared to the crude ELJCE, corrosion products formed on Al (Blank-Al corrosion products), the 1 M HCl corrosion solution in the presence (ELJCE-Al solution) and the absence (Blank-Al solution) of ELJCE

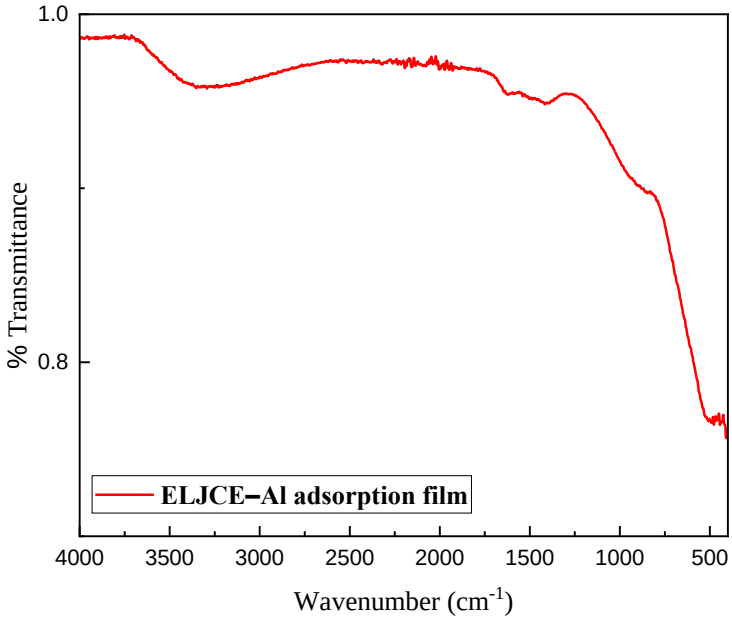

Figure 5.43: Expanded FT-IR spectrum of the adsorption film formed on the Al surface (ELJCE-Al adsorption film)

5.9. UV–visible spectroscopy: Interaction of ELJCE with Al^{3+}, Fe^{2+} and Zn^{2+} cations

The possible interactions at the interface between the ELJCE molecules and the Al, Zn, and MS surfaces were investigated using a UV–vis test. The tests were performed by analyzing the 1 M HCl acidic solution before and after immersion of the three-metal specimen in the absence (Blank–Fe^{2+}, Blank–Zn^{2+} and Blank–Al^{3+}) and presence of 800 ppm ELJCE (ELJCE–Fe^{2+}, ELJCE–Al^{3+} and ELJCE–Zn^{2+}) and the results compared to those of ELJCE (ELJCE in 1 M HCl) as shown in Figure 5.43–5.45. The UV traces for the ELJCE-inhibited solutions analyzed after the immersion of the three metals (ELJCE–Fe^{2+}, ELJCE–Al^{3+} and ELJCE–Zn^{2+}) showed reduced absorption bands in the 215–290 nm range compared to the solution analyzed before immersion of the metal samples (ELJCE in 1 M HCl) due to the interaction of the extract components with the metal surfaces. This effect is more pronounced for the MS coupons, indicating a stronger interaction between the metal and the plant extract than the other two metals, as evidenced by the %IE. These absorbance peaks could indicate the presence of π–π* and n–π* transitions that could result from the C=C and C=O groups present in the plant extract [502, 503]. The UV traces for the 1 M HCl solution after the immersion of Al and Zn samples without the extract (Blank–Al^{3+} and Blank–Zn^{2+}) showed absorption peaks around the 240 to 268 nm range, associated with the intra-orbital d-d transitions of the two metal cations. Such peaks correspond to those of Marhamati *et al*. [587] for the iron cation. The participation of the 215–290 nm peaks in the adsorption process has also been suggested as indicating intramolecular electron transfer from a ligand to inhibitor compounds [505-507]. The absorption bands observed for the 1 M HCl solution before and after immersion of the three metal samples (Blank–Al^{3+}, Blank–Fe^{2+}, and Blank–Zn^{2+}) without extract in the 669 nm region were compensated by the presence of extract (ELJCE–Fe^{2+}, ELJCE–Al^{3+} and ELJCE–Zn^{2+}). The change of these peaks in the presence of ELJCE indicates the appearance of the n–p* transitions of carbonyl and other functional groups found in the extract during the adsorption process [588, 589].

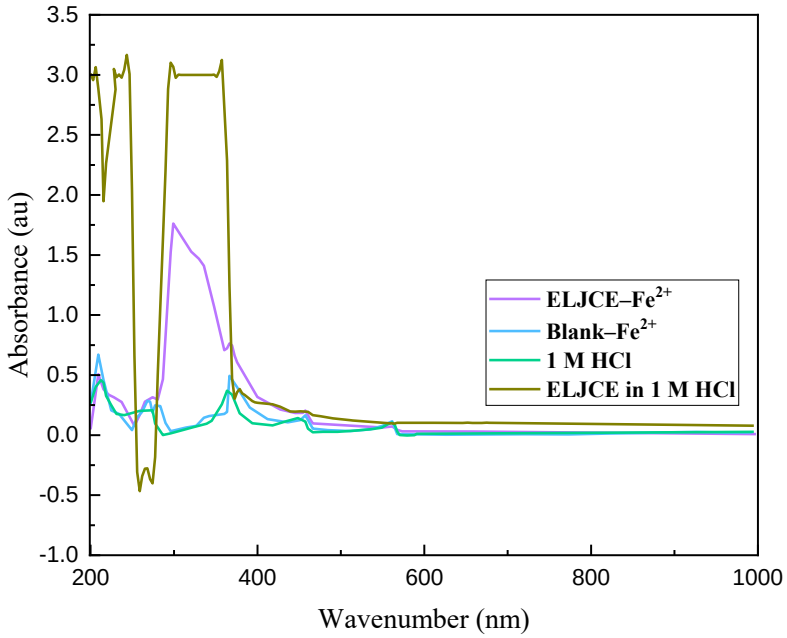

Figure 5.44: UV-vis spectra for 1 M HCl solution without and with ELJCE before immersion of the metal sample (ELJCE in 1M HCl), after immersion (ELJCE–Fe^{2+}), and the sample without ELJCE (Blank–Fe^{2+})

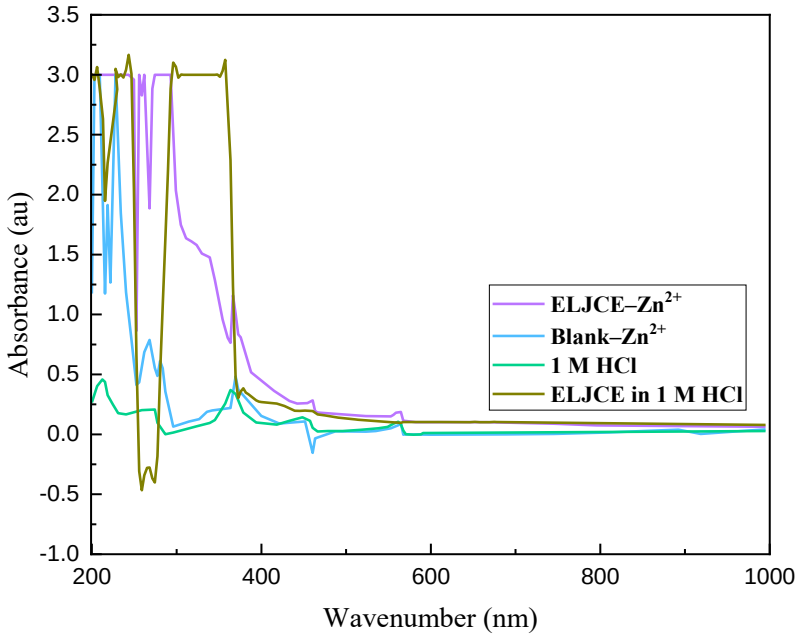

Figure 5.45: UV-vis spectra for 1 M HCl solution without and with ELJCE before immersion of the metal sample (ELJCE in 1M HCl), after immersion (ELJCE–Zn^{2+}), and the sample without ELJCE (Blank–Zn^{2+})

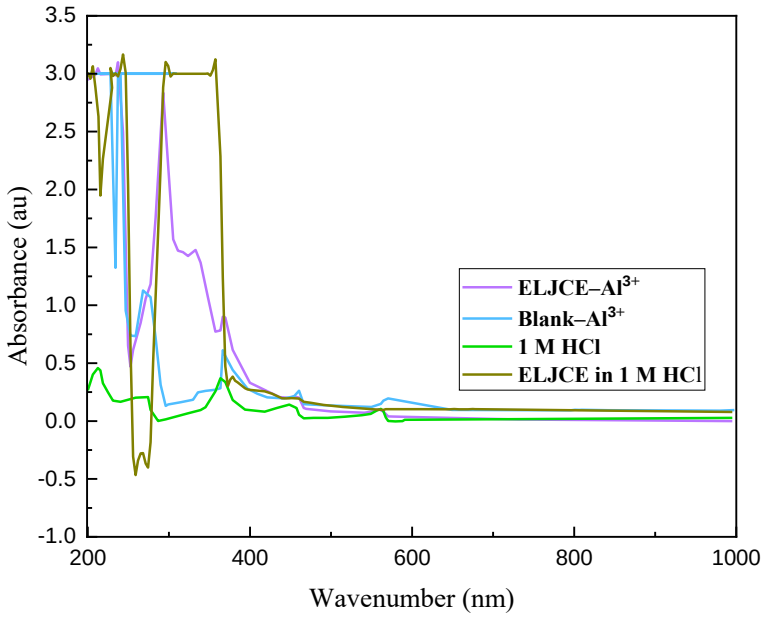

Figure 5.46: UV-vis spectra for 1 M HCl solution without and with ELJCE before immersion of the metal sample (ELJCE in 1M HCl), after immersion (ELJCE–Al^{3+}), and the sample without ELJCE (Blank–Al^{3+})

5.10. Water contact angle measurement

Contact angle tests were performed in a 1 M HCl corrosive environment in the absence and presence of 800 ppm ELJCE to determine the three metal surface properties related to hydrophobicity or hydrophilicity. The results shown in Figure 5.46–5.48 indicate that the contact angle starts at 82.403, 93.647 and 66.314° for the unexposed MS, Zn and Al surfaces and, upon exposure of the metals to 1 M HCl, the contact angles decrease to 67.546, 73.257 and 47.956°, respectively. The reduction in contact angle shows the hydrophilic nature of the metal surfaces as the water droplet was distributed over a large surface area. This behaviour is attributed to the formation of corrosion products (oxides/hydroxides) generated by the 1 M HCl solution, which tend to be suitable agents for forming H-bonds between the surrounding HCl electrolyte and the metal surface [590]. When the three metal samples were submerged in 1 M HCl solution containing 800 ppm ELJCE extract, the contact angle increased to 97.192, 97.232 and 95.356° for MS, Zn, and Al, respectively. Adsorption and numerous accumulations of the hydrophobic metabolites of the ELJCE extract resulted in the formation of a protective film on the metal surfaces. These engineered hydrophobic films protect the MS, Zn, and Al surfaces from corrosion by preventing the corrosive electrolyte from reaching the MS, Al and Zn/ELJCE interface [591].

Figure 5.47: Surface wettability behaviour of (a) polished untreated MS substrate, (b) MS substrate after 7 hours of immersion in 1 M HCl medium with no inhibitor, and (c) in the presence of 800 ppm of ELJCE

Figure 5.48: Surface wettability behaviour of (a) polished untreated Zn substrate, (b) Zn substrate after 7 hours of immersion in 1 M HCl medium with no inhibitor, and (c) in the presence of 800 ppm of ELJCE

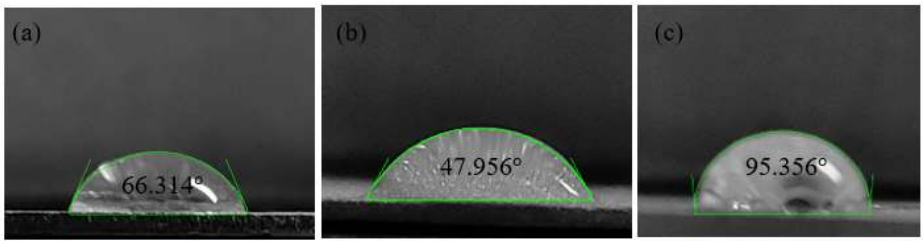

Figure 5.49: Surface wettability behaviour of (a) polished untreated Zn substrate, (b) Zn substrate after 7 hours of immersion in 1 M HCl medium with no inhibitor, and (c) in the presence of 800 ppm of ELJCE

5.11. SEM/EDX and Elemental Mapping

SEM analyzes were performed to examine the surface morphologies of MS, Zn, and Al after immersion in 1 M HCl solution for 7 hours at 303 K in the absence and presence of 800 ppm ELJCE inhibitor and the results are shown in Figure 5.49, 5.51 and 5.53, respectively. The results were compared to the morphologies of the untreated, polished Zn, MS, and Al surfaces. Zn and MS surfaces corroded uniformly when exposed to a 1 M HCl solution without ELJCE. In contrast, the Al surface exhibited pitting corrosion characteristics. The exposure of the metals in 1 M HCl with ELJCE resulted in smoother surfaces despite some minor visible imperfections in the form of scratches and pits, which could have formed during sample preparation or due to the formation of an inadequate adsorption film with some defects. ELJCE components were integrated into the passive film that inhibits the dissolution process by preventing the entry of H^+, Cl^-, and OH^- species to the active sites on the metal surfaces. The EDS spectrum for the polished, untreated MS surface is similar to the EDS spectrum for the MS surface exposed to 1 M HCl without the plant extract. However, additional lines were observed for the spectrum of MS surface exposed to the corrosive solution with ELJCE. The additional lines demonstrate the presence of oxygen and Cl^- species, among others. The Zn EDS spectrum indicated the presence of the Zn element before exposure to the corrosive solution (polished Zn surface); however, the element disappeared when the sample was exposed to the 1 M HCl solution with and without ELJCE. The absence of the Zn element indicates that upon exposure to the 1 M HCl, the galvanized Zn layer was destroyed by the corrosive solution revealing the Fe layer underneath. The precipitates detected on the Zn, Al, and MS surfaces were further analyzed by EDS elemental mapping, and the results (Figures 5.50, 5.52 and 5.54) were compared to a blank counterpart. From the figures, the element that seemed to have been impacted by the presence of ELJCE in the corrosive solution was carbon which can be attributed to the adsorption of the plant extract on the metal surfaces [514].

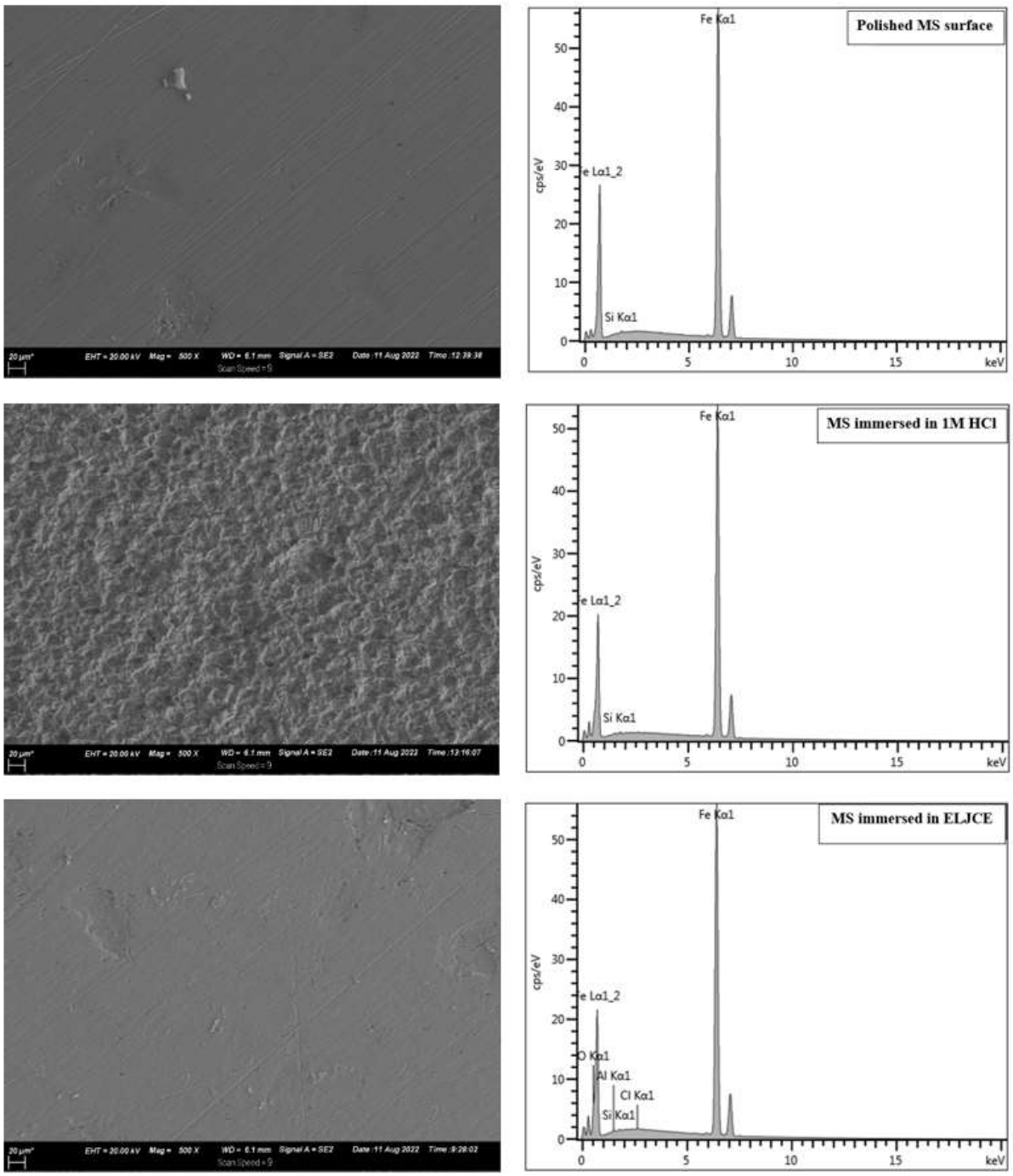

Figure 5.50: SEM images and EDS spectra of unexposed-polished MS surface, MS immersed in uninhibited 1 M HCl, and MS immersed in ELJCE-inhibited 1 M HCl solution

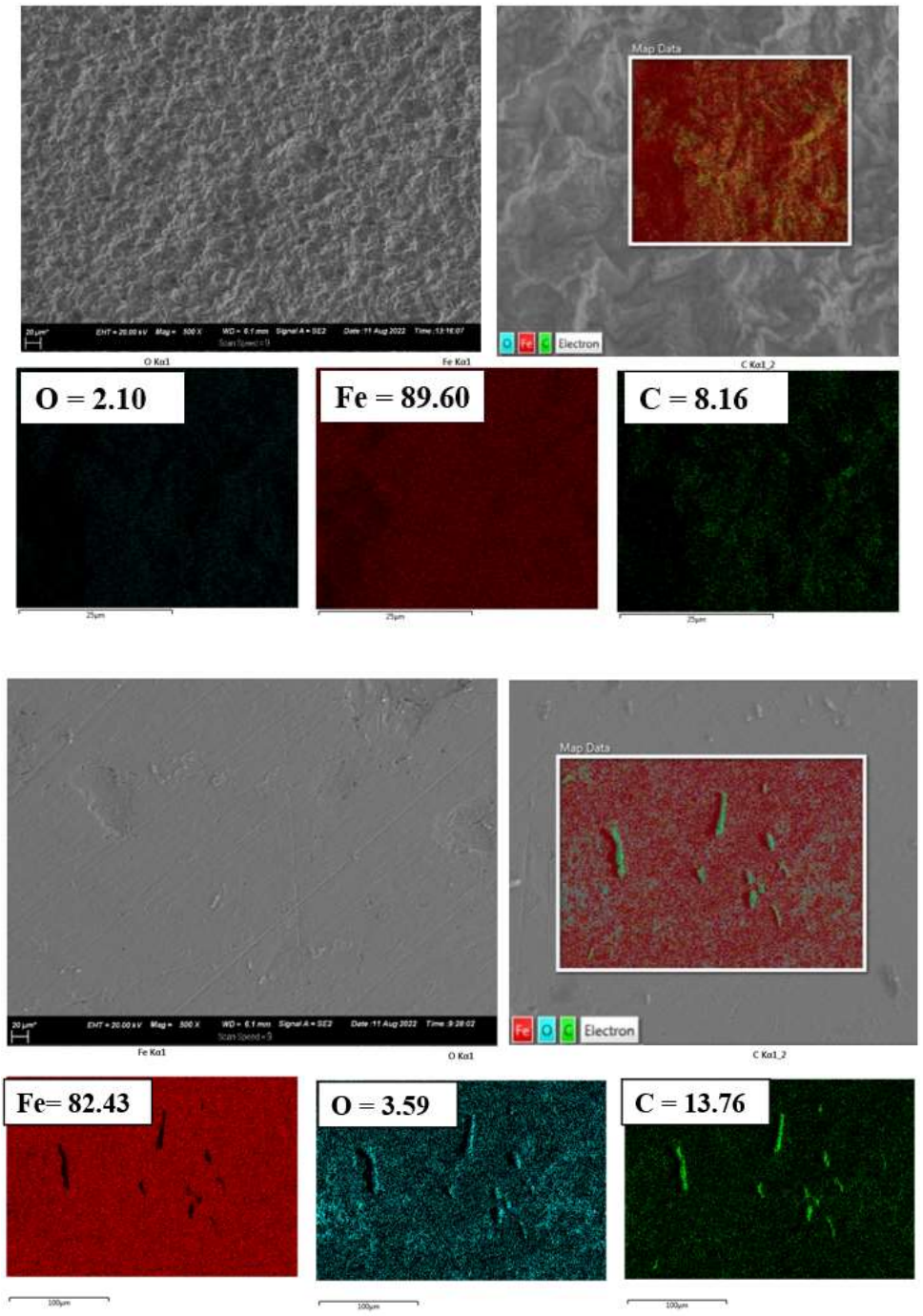

Figure 5.51: EDS map analyses for MS exposed to the corrosive solution in the (a) absence of the extract and the (b) presence of 800 ppm of the extract

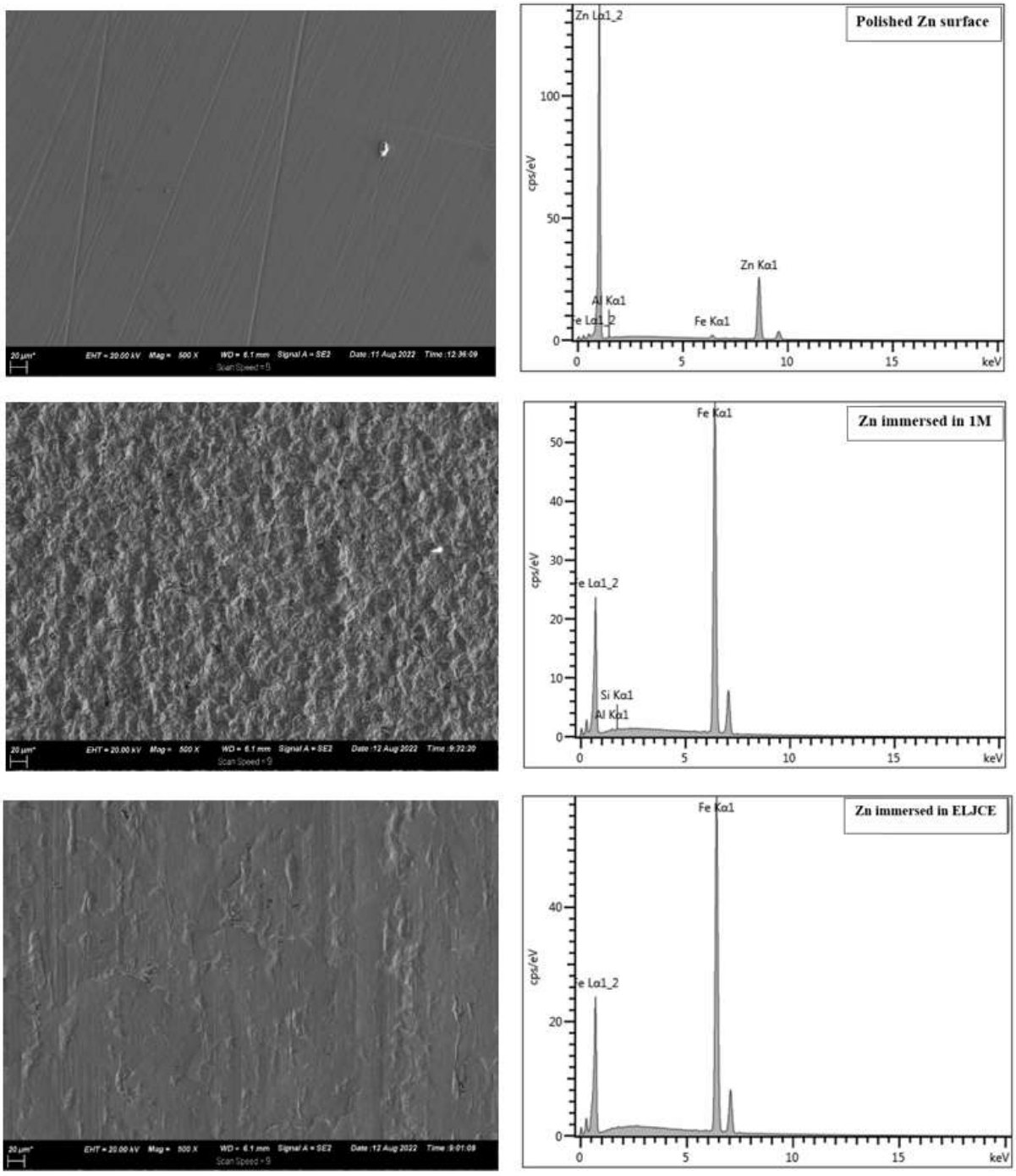

Figure 5.52: SEM images and EDS spectra of unexposed-polished Zn surface, Zn immersed in uninhibited 1 M HCl, and Zn immersed in ELJCE-inhibited 1 M HCl solution

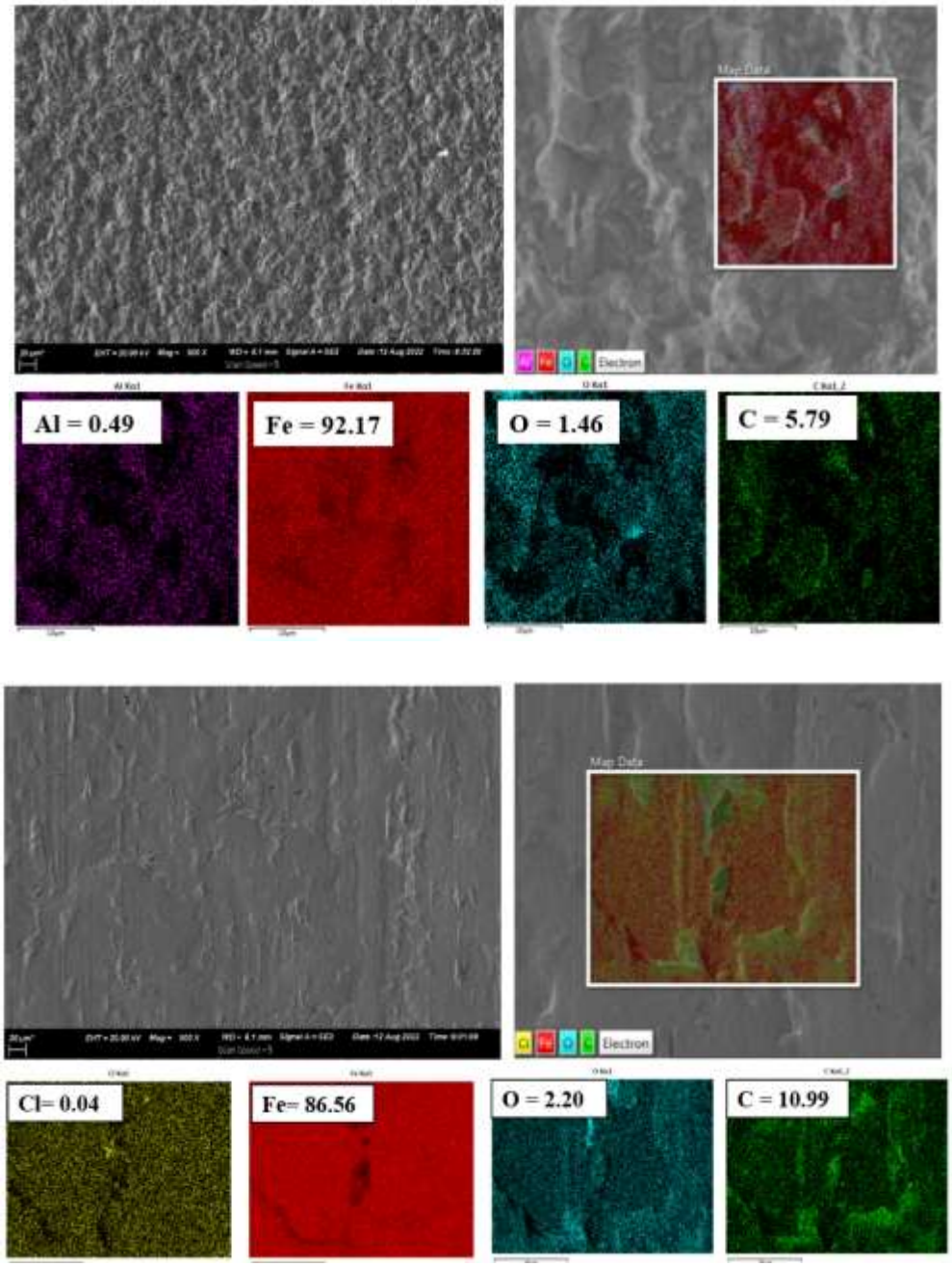

Figure 5.53: EDS map analyses for Zn exposed to the corrosive solution in the (a) absence of the extract and the (b) presence of 800 ppm of the extract

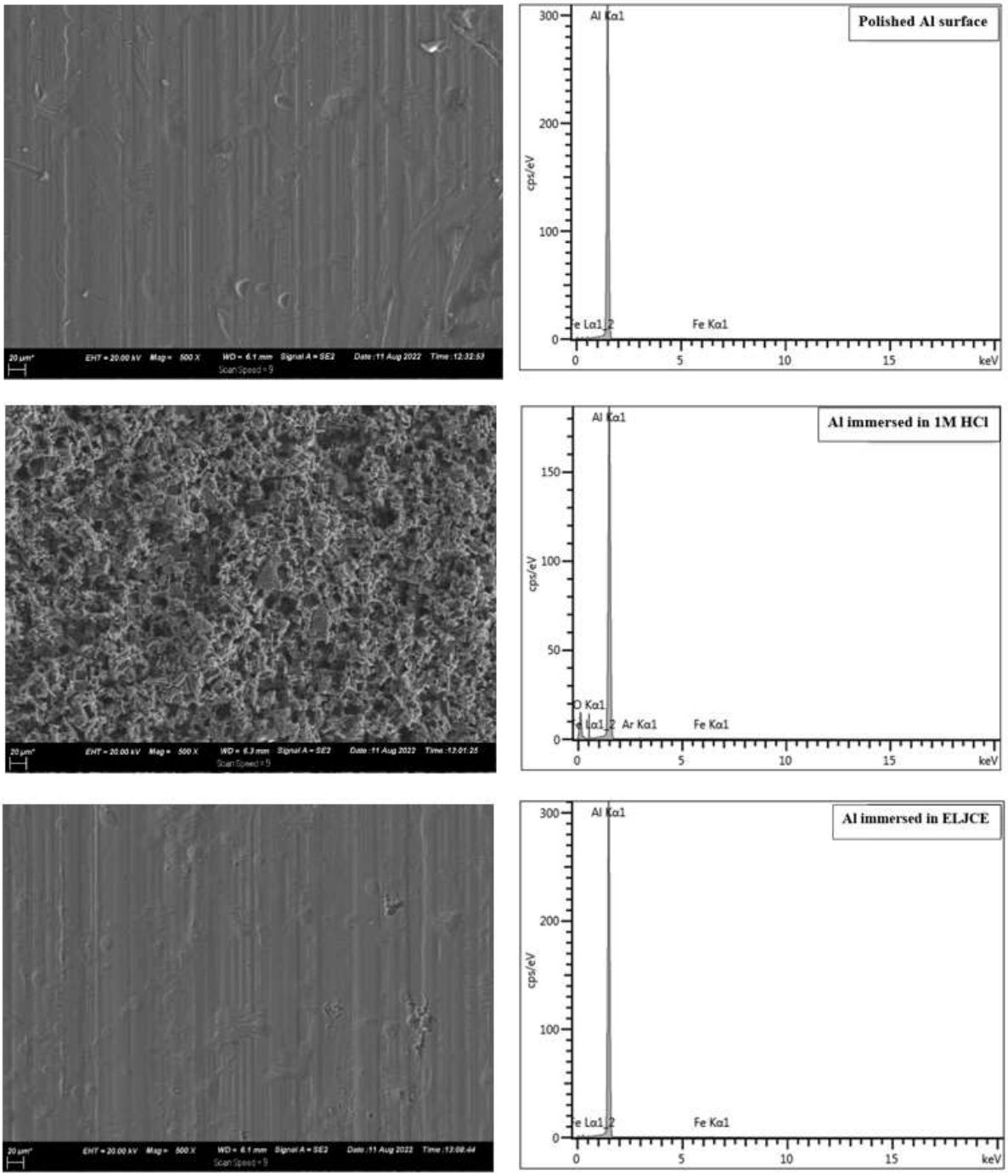

Figure 5.54: SEM images and EDS spectra of unexposed-polished Al surface, Al immersed in uninhibited 1 M HCl, and Al immersed in ELJCE-inhibited 1 M HCl solution

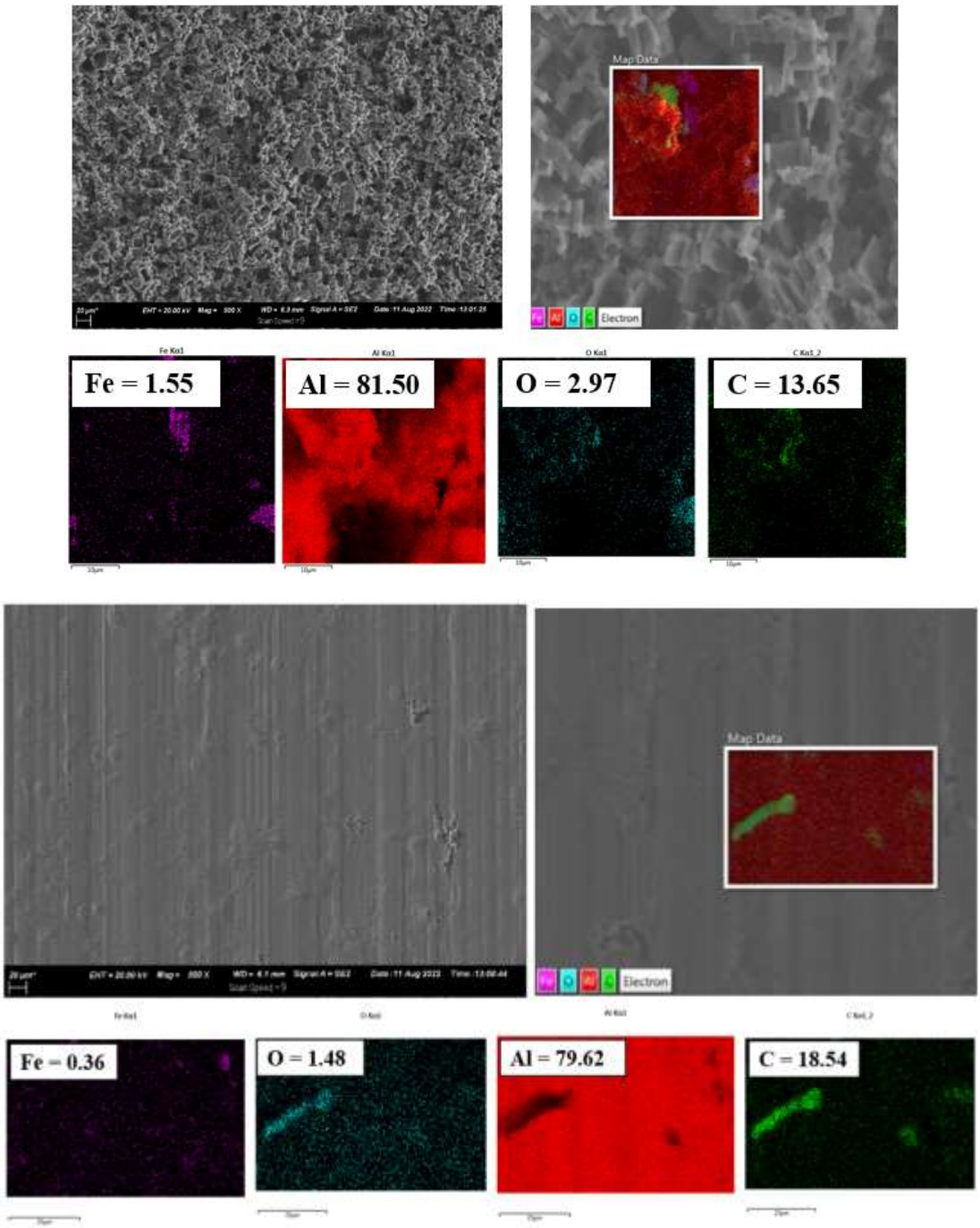

Figure 5.55: EDS map analyses for Al exposed to the corrosive solution in the (a) absence of the extract and the (b) presence of 800 ppm of the extract

CHAPTER 6

Acetonolic extract results and discussions

This chapter summarises and discusses the findings from the Acetonolic *L. javanica* crude leaf extract (ALJCE). The crude extracts were characterised using LC/MS and FT-IR spectroscopies. Weight loss analysis with a focus on the effect of temperature and inhibitor concentration, adsorption isotherms and thermodynamic parameters, and adsorption film analysis were all used to assess the corrosion potential of ALJCE. Electrochemical techniques were used to assess the corrosion resistance, degradation, and corrosion inhibition mechanisms of the inhibitors. Surface analysis of the extracts' protective film on metal surfaces was also performed.

6. Acetonolic *L. javanica* crude leaf extract (ALJCE) as a green inhibitor for MS, Al, and Zn corrosion

6.1. HPLC analysis of ALJCE

Figure 6.1 depicts the ALJCE components obtained from the LC/MS chromatographs. The chromatogram comprises several peaks, from which some of the main active compounds found in ALJCE were identified and listed in Table 6.1, along with their molecular formula, retention time, and molecular weight. From the chromatogram, VBS was found to have the highest peak, suggesting that it is the main active ingredient in the ALJCE. This compound was detected at two different retention times of 6.48 and 7.36 min and, in both cases, had the highest peak and a molecular weight of 623.19 g/mol and its molecular formula was $C_{29}H_{36}O_{15}$. Most of the compounds consist of carbonyl groups, hydroxyl functional groups and/or ether moieties in addition to other functional groups. The formation of ALJCE metal complexes can explain the anti-corrosion mechanism through electron donor and acceptor interactions due to the presence of an oxygen atom of the hydroxyl, carbonyl group or ether moieties of the extract components. The interactions of the plant extracts with the three metal surfaces studied via the ether moieties tend to lead to weaker interactions since it is an electron-withdrawing substituent and can also lead to lower inhibition efficiencies [592, 593]. The other mode of interaction can occur via other electron-donating substituents (NH_2, $–OCH_3$, $–CH_3$, $–CHCH_2$) [593] and the carbon double bonds present in the ALJCE.

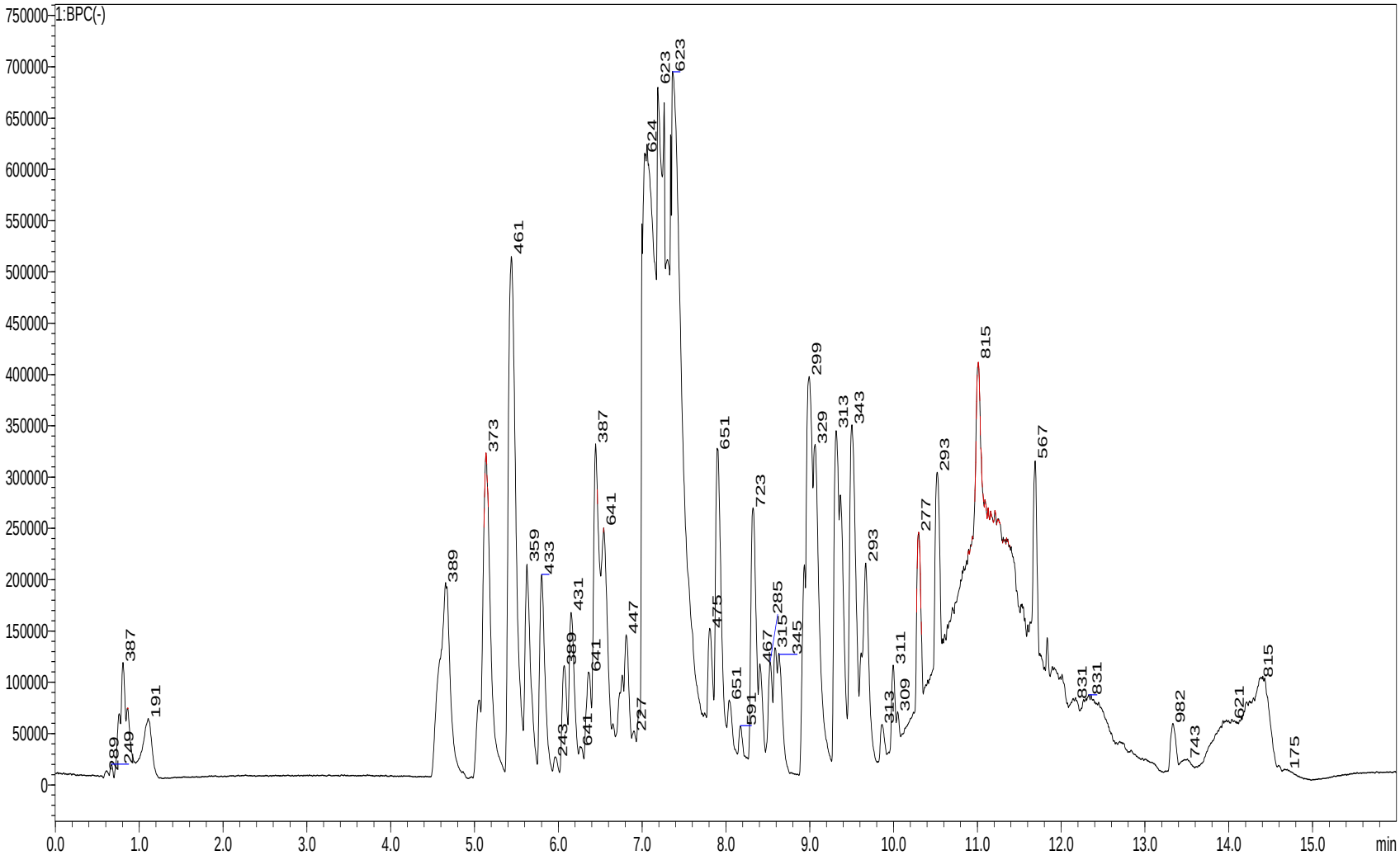

Figure 6.1: Total ion chromatograms of phytochemicals mixtures of ALJCE measured by LC/MS in negative ion mode

Table 6.1: Phytochemicals identified in the ALJCE

S.No.	RT (min)	Name of the compound	MF	MW
1	4.66	Scandoside	$C_{16}H_{22}O_{11}$	389.11
2	5.15	N-(3-methylphenyl)-3-[(3-nitrobenzoyl)amino]benzamide	$C_{21}H_{17}N_{30}O_4$	374.12
3	5.44	Decaffeoyl-acteoside	$C_{20}H_{30}O_{12}$	461.16
4	5.56	Mussaenosidic acid	$C_{16}H_{24}O_{10}$	375.13
5	5.63	8,8'-[(1S,2S)-1,2-Dihydroxyethylene]bis[2-amino-9H-purine-6(1H)-one]	$C_{12}H_{12}N_{10}O_4$	359.10
6	5.67	{3,5,6-trihydroxy-4-[(3,4,5-trihydroxy-6-methyloxan-2-yl)oxy]oxan-2-yl}methyl 3-(3,4-dihydroxyphenyl)prop-2-enoate	$C_{21}H_{28}O_{13}$	487.14
7	6.15	Benzyl gentiobioside	$C_{19}H_{28}O_{11}$	431.15
8	6.48/7.36	Verbascoside/Acteoside	$C_{29}H_{36}O_{15}$	623.19
9	6.51	6-(2-(3,4-dihydroxyphenyl)-2-hydroxyethoxy)-4,5-dihydroxy-2-(((3,4,5-trihydroxy-6-(hydroxymethyl)tetrahydro-2H-pyran-2-yl)oxy)methyl)tetrahydro-2H-pyran-3-yl 3-(3,4-dihydroxyphenyl)acrylate	$C_{29}H_{36}O_{17}$	655.19
10	7.09	2-[[4-[(2-Chlorophenyl)methoxy]-3,5-diiodophenyl]methylidene]indene-1,3-dione	$C_{23}H_{13}Cl_1I_2O_3$	624.85
11	7.30	[4'-(4-Aminophenoxymethyl)-2,2':6',2''-terpyridine-6,6''-diylbis(methylenenitrilo)]tetrakisacetic acid	$C_{32}H_{32}N_6O_9$	625.20
12	7.48	Isorhamnetin 3-glucuronide	$C_{22}H_{20}O_{13}$	491.08
13	7.66	1-[10-[(4,6-Diamino-2,2-dimethyl-1,3,5-triazin-1-yl)oxy]decoxy]-6,6-dimethyl-1,3,5-triazine-2,4-diamine	$C_{20}H_{40}N_{10}O_2$	451.33
14	7.90/8.24	Cistanoside D	$C_{31}H_{40}O_{15}$	651.23
15	8.17	[(2R,3R,4S,5R,6R)-2-(acetamidomethyl)-6-[(2R,3R,4S,5R,6R)-6-(acetamidomethyl)-3,4-diacetyloxy-5-hydroxyoxan-2-yl]oxy-5-acetyloxy-3-hydroxyoxan-4-yl] acetate	$C_{24}H_{36}N_{20}O_{15}$	591.21
16	9.08	[3-(4-Butoxybenzoyl)peroxycarbonyloxy-2-[(4-butoxybenzoyl)peroxycarbonyloxymethyl]-2-methylpropoxy]carbonyl4-butoxybenzenecarboperoxoate	$C_{41}H_{48}O_{18}$	827.27
17	10.37	Leukotoxin	$C_{18}H_{34}O_4$	313.24
18	13.34	[(2S)-1-[(9E,12E,15E)-octadeca-9,12,15-trienoyl]oxy-3-[(2R,5R,6R)-3,4,5-trihydroxy-6-[[(2R,5R,6R)-3,4,5-trihydroxy-6-(hydroxymethyl)oxan-2-yl]oxymethyl]oxan-2-yl]oxypropan-2-yl] (6E,9E,12E)-octadeca-6,9,12-trienoate	$C_{51}H_{84}O_{15}$	935.57
19	14.29	2-[[2-[3-[4-(3-aminopropylamino)butylamino]propylamino]acetyl]amino]-N-methyl-N-octadecyl-N'-[(2S,5R)-2,4,5-trihydroxy-6-(hydroxymethyl)oxan-3-yl]pentanediamide	$C_{42}H_{85}N_7O_8$	814.64
20	14.40	(2R)-2-[(2R,5S,6R)-6-[(2R,3S,4S,6R)-3-acetyloxy-6-[(3S,5S,7R,9S,10S,12R,15R)-15-acetyloxy-3-[(2R,5R,6S)-5-ethyl-5-hydroxy-6-methyloxan-2-yl]-3,10,12-trimethyl-4,6,8-trioxadispiro[4.1.57.35]pentadec-13-en-9-yl]-4-methyl-5-oxooctan-2-yl]-5-methyloxan-2-yl]butanoic acid	$C_{46}H_{74}O_{13}$	815.50

6.2. FT-IR screening of phytochemicals from ALJCE

The functional groups of the active compounds found in the ALJCE were identified using FT-IR analysis. The absorption peaks in the infrared radiation region of the spectrum were used to make this identification. Figure 6.2 shows the FT-IR spectrum of the ALJCE. The ALJCE absorption spectra exhibited a peak around the 3390 cm^{-1} region, indicating the presence of alcohols (O–H stretch) [377], amines (N–H) and amides (N–H) groups in the plant extract [378]. While the peaks appearing around wavenumbers 2924 and 2855 cm^{-1} may correspond to C–H stretching in the ALJCE molecules. Guo *et al*. [377] attributed these peaks to the stretching in methyl of aromatic and methylene groups of side chains and aromatic methoxy groups. The strong and sharp peak at 1702 cm^{-1} is attributed to the vibrational mode of C=O [594], which could be due to an aldehyde or carboxyl group in the plant extract. This peak also indicates the presence of an alkene group (C=C) [381, 382]. The peak at 1603 cm^{-1} is due to the asymmetric and symmetric vibrational stretching for the carboxyl ion (COO^{-}), indicating the presence of ester, carbonyl, and carboxylic acid groups in ALJCE [379, 380]. The peaks at 1030, 1519 and 1157 cm^{-1} showed the presence of flavonoids (=C–O–C stretch) in the extract. The peak at 1443 cm^{-1} indicates that the extract contains sulfates (S=O), alkane (C–H), and aromatic (C=C) functional groups in the extract. The presence of sulfonyl chloride (S=O), alkyl halide (C–F) and nitro (N=O) group is indicated by the peak at 1360 cm^{-1}. The peak around the 1223 cm^{-1} region represents the presence of carboxylic acid (C–O), phosphoramide (P=O), ester (C–O), alkyl halide (C–F), ether (C–O) and amine (C–N) groups [378]. The peaks around the region from 812 to 760 cm^{-1} could be assigned to the vibrations of the aromatic rings [380].

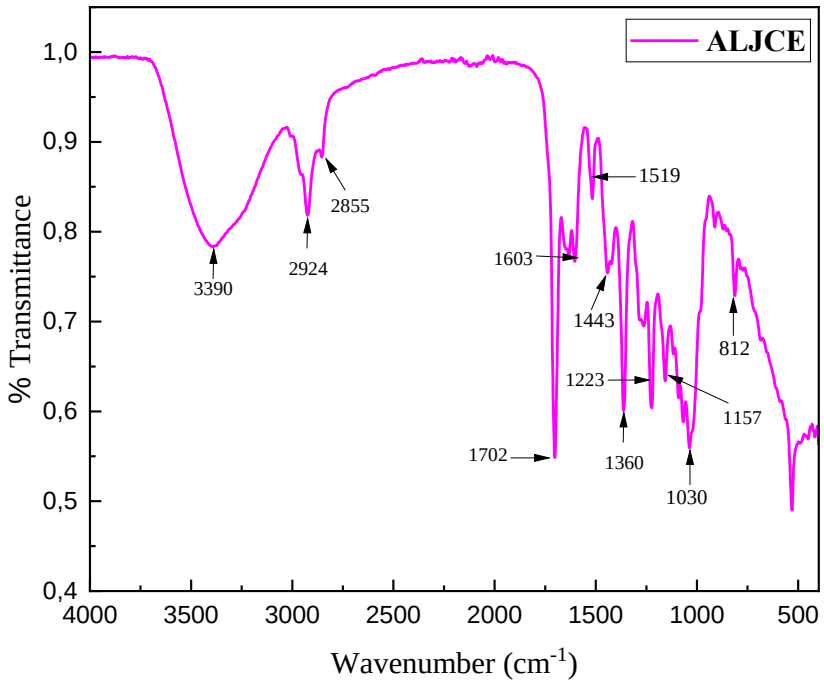

Figure 6.2: FTIR spectrum of the ALJCE used for the inhibition of Zn, MS, and Al corrosion

6.3. Variation of the open circuit potential (OCP) with immersion period

Prior to performing each PDP and EIS test, OCP tests were performed to determine if the OCP reached a steady-state after 1 hour. Figure 6.3–6.5 shows the variation over time of the OCP for MS, Al, and Zn in corrosive 1 M HCl solution in the absence and presence of several concentrations of ALJCE at 303 K. Figure 6.4 shows that the Zn OCP stabilizes in the presence of ALJCE towards the anodic potential. The positivity of the Zn OCP plots at all concentrations of ALJCE is attributed to the gradual adsorption of the extracts on the Zn surface [595, 596], which inhibits the anodic process. The blank OCP begins at a more negative potential than the inhibited solutions and moves toward a positive potential after 925 seconds of immersion, where stabilization is achieved. The relationship between MS electrode OCP and immersion time (Figure 6.3) indicates a positive shift for the uninhibited system in the first 7 minutes, which was also observed for the ALJCE-inhibited system within a few minutes of immersion at all concentrations. After the initial positive movement of the OCP, it was found that the overall shift in OCP with exposure time was towards negative potential until a stable potential after 1 hour of immersion was reached. The movement of the OCP away from the positive direction after a few minutes of

immersion is often attributed to the dissolution of a native oxide layer that was present on the MS surface before immersion in the corrosive environment as a result of its contact with the atmosphere [597]. As a result, the initial positive shift observed for the uninhibited system can be attributed to the presence of iron oxide on the MS surface. While such an oxide layer is known to provide significant protection for metals such as Zn and Al, for MS, it is flaky and unstable and promotes corrosion over time. Figure 6.5 indicates that the introduction of ALJPE into the corrosive 1 M HCl solution causes a shift of the OCP to more negative values as the concentration of ALJPE is increased, indicating the formation of a protective inhibitor film on the Al surface.

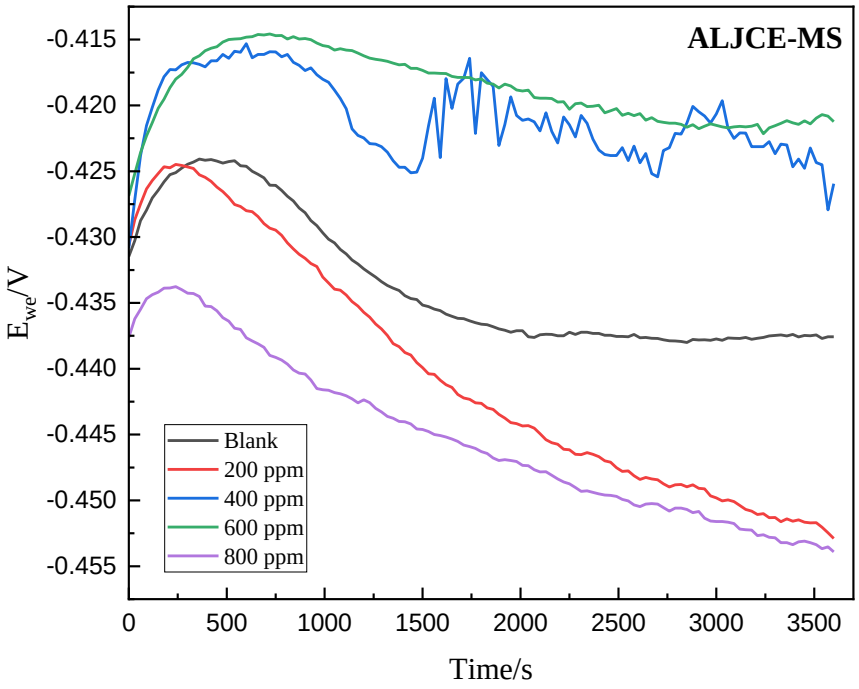

Figure 6.3: Evolution of open-circuit potential (E_{OCP}) versus exposure time for MS with and without MLJCE in 1 M HCl solution

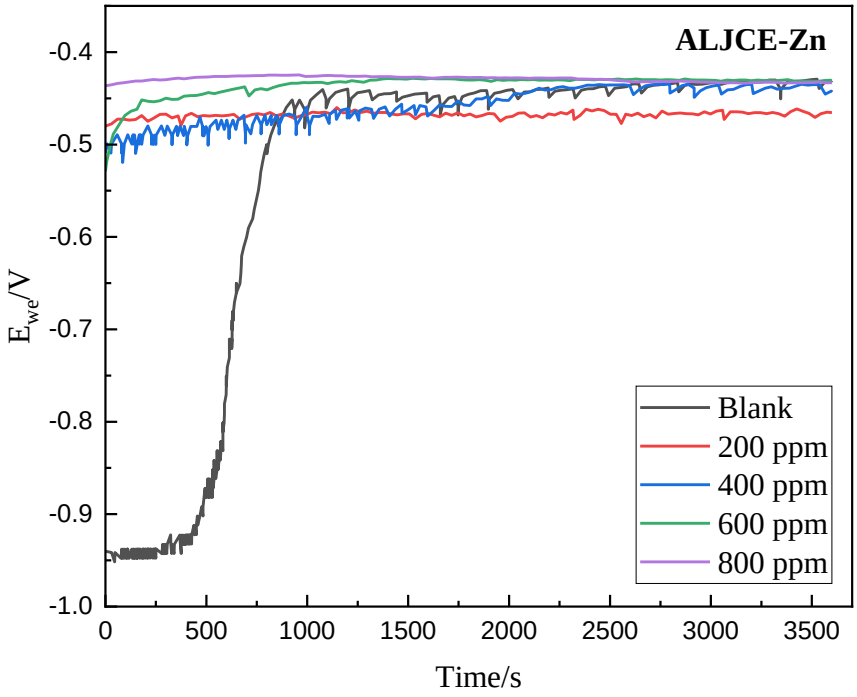

Figure 6.4: Evolution of open-circuit potential (E_{OCP}) versus exposure time for Zn with and without MLJCE in 1 M HCl solution

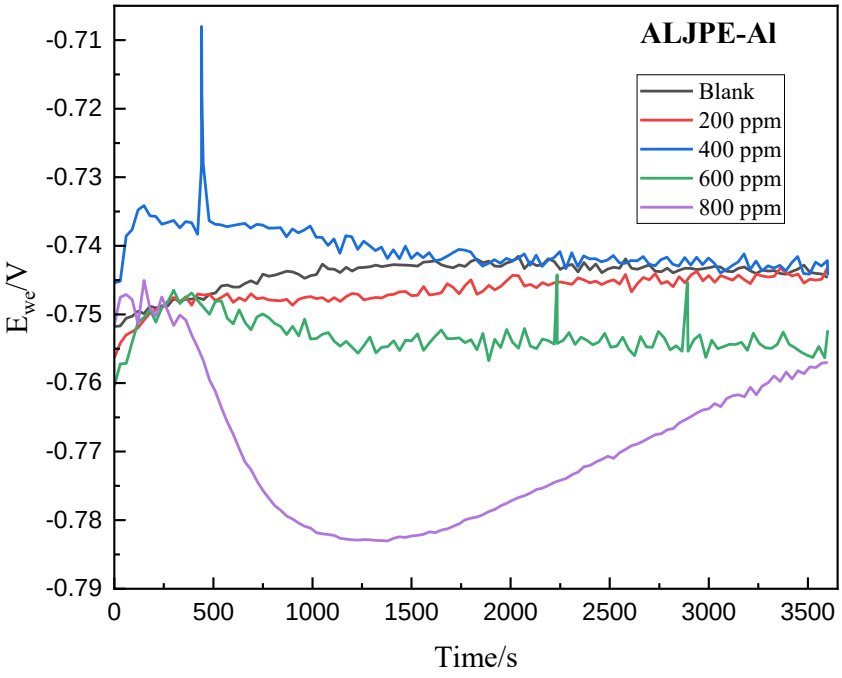

Figure 6.5: Evolution of open-circuit potential (E_{OCP}) versus exposure time for Al with and without MLJCE in 1 M HCl solution

6.4. Potentiodynamic polarization (PDP)

Polarization curves were recorded to study the kinetics of the anodic and cathodic corrosion reactions. The analysis was performed for MS, Al, and Zn samples in 1 M HCl at 303 K for various concentrations of the ALJCE and the curves are presented in Figure 6.6−6.8. The corrosion kinetic parameters derived from these plots are shown in Table 6.2. The rate of corrosion is one of the pieces of information that can be extracted from PDP scans. According to the PDP curves (Figure 6.6−6.8), adding ALJCE to the electrolyte solution influences both the anodic and cathodic Tafel slope values, resulting in a reduction in the corrosion rate of the anodic metal dissolution and a delay in the cathodic hydrogen evolution reaction for all three metals studied. Undulation-type curves with no pronounced passive zone are observed for Zn metal in both the absence and presence of ALJCE (Figure 6.7). The lack of an explicit passive zone in the anodic polarization curves suggests that ALJCE formed a stable adsorbent film layer on the surface of Zn.

A high entropic alloy such as Al is prone to passivation and pitting due to the dissolution of its passive natural oxide layer, which protects it from corrosion. The anodic Tafel curves for the Al substrate (Figure 6.8) emphasize the passivation behaviour of the Al substrate under anodic polarization. The occurrence of passivation without and with the addition of ALJCE in the anodic branch was observed from −500 mV up to 300 mV. The diagram shows that when the system's potential increases beyond E_{corr}, the I_{corr} initially rises due to activation-controlled behaviour and reaches a maximum at the passivation potential. After that, a rapid decrease in I_{corr} with increasing potential indicates the formation of a protective or passive film on the Al surface (i.e., passivation took place). According to the curves, a low constant I_{corr} is maintained regardless of the applied potential when the Al metal is in the passive state. The curves in the presence of 400 and 600 ppm ALJCE inhibitors show that the passive/protective film breaks down at higher potentials, which leads to the onset of the trans-passive region or pitting. The anodic current remains almost steady with the addition of a low concentration (200 ppm) of ALJCE even after the critical current has been attained, resulting in the absence of distinct features of the active-passive region.

The Al substrate undergoes an anodic and cathodic localized corrosion reaction process through equations 59 and 60 as follows [598]:

$$Al(s) \rightarrow Al^{3+}(aq) + 3e^{-} \quad (59)$$

$$2H^{+}(aq) + 2e^{-} \rightarrow H_2(s) \quad (60)$$

Outside the pits, other cathodic reactions are possible and include hydrogen evolution and oxygen reduction, which are shown by equations 61 and 62, respectively:

$$2H_2O(l) + 2e^- \rightarrow H_2(s) + 2OH^-(aq) \quad (61)$$

$$O_2(g) + 2H_2O(l) + 4e^- \rightarrow 4OH^-(aq) \quad (62)$$

Figure 6.6 shows the anodic polarization curve for MS in the presence of ALJCE at 200 ppm. The curves showed a current decrease between −510 and −350 mV vs Ag/AgCl. This is due to the desorption of the adsorption layer formed on the MS surface due to the solution's aggressive acidic ions. When the adsorption layer on the MS is removed, the MS corrodes further. The occurrence of this behaviour only at the lowest concentration (200 ppm) of ALJCE could be due to a low number of ALJCE molecules at this concentration, leaving parts of the MS surface vulnerable to corrosion. In the presence of 800 ppm ALJCE, a trans-passive region was observed at 350 mV, resulting in pitting corrosion. However, the extent of the trans-passive area was minimal, indicating that the ALJCE reduced the extent of the damage inflicted by pitting.

The PDP curve, at 200 ppm for Zn, showed minor spikes in the anodic region, possibly due to the surface roughness caused by polishing the sample before the experiment. In the presence of ALJCE, the resting potential decreased from −452.547 to −419.023 mV vs Ag/AgCl, despite the lack of a distinct passive zone. The decrease in resting potential could be attributed to the reduction in the concentration of Zn^{2+} in the solution (i.e., anodic reaction). At 200 ppm ALJCE, a decrease in the corrosion current density (61.615 μA.cm^{-2}) with a potential shift to the more noble side (−0.4525 V.Ag/AgCl) was observed. The trend remained constant, which reduced the corrosion current density to 22.882 μA.cm^{-2} and the potential to −0.419 mV vs Ag/AgCl at 800 ppm. A continuous decrease in I_{corr} values in the presence of ALJCE was observed with increasing concentration. The reduction in I_{corr} was observed for all three metal samples (i.e., MS, Al and Zn), indicating that ALJCE effectively prevented their dissolution, with maximum inhibitory effects of up to 94.21, 97.50 and 98%, respectively, being observed at 800 ppm. These results agree with Otaibi and Hammud [599], who used Harmal leaf extract as a corrosion inhibitor for carbon steel and found that the I_{corr} values decreased from 12.70 mA.cm^{-2} to 6.02 mA.cm^{-2} in the absence and presence of 513.83 ppm of the extract, respectively. As can be seen from Table 6.2, ALJCE offers an effective inhibitory effect for Zn than MS and Al at all concentrations tested. This suggests that the extracts created a stronger interaction with the three metal surfaces.

Generally, a corrosion inhibitor is classified as either anodic or cathodic based on whether the difference in E_{corr} between the inhibited and uninhibited systems is greater than 85 mV; if the difference is less than 85 mV, the inhibitor is classified as a mixed-type [403]. The current study shows that ALJCE has a maximum displacement of approximately 23, 39 and 17 mV vs Ag/AgCl for MS, Zn, and Al, respectively, indicating that ALJCE is a mixed-type inhibitor, controlling both the anodic and cathodic reactions [33]. The influence of both the anodic and cathodic reactions shows that adding ALJCE to the corrosive solution had little effect on the E_{corr} values. For instance, the free corrosion potential of the corrosive 1 M HCl solution without ALJCE was −740.497 mV. After adding different concentrations of ALJCE, it stayed around this value up to 400 ppm. Still, when the concentration was increased to 600 and 800 ppm, the E_{corr} reached more active values than those obtained without the extract, namely −756.712 and −757.873 mV for Al. Though the E_{corr} values were not significantly affected, the I_{corr} values improved (decreased) by adding various concentrations of ALJCE. The I_{corr} values fell from 5831.281 (blank) down to 594.661 $\mu A.cm^{-2}$ (200 ppm), and the lowest I_{corr} value obtained was with the addition of 800 ppm (145.823 $\mu A.cm^{-2}$). The reduction in the I_{corr} values with ALJCE concentrations can be linked to the adsorption of the extracts on the Al surface [600-602].

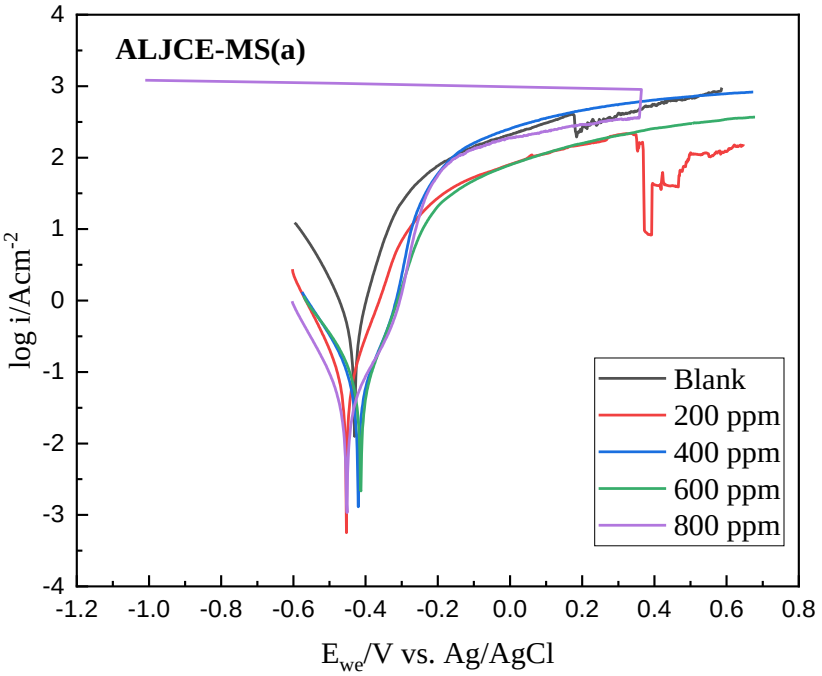

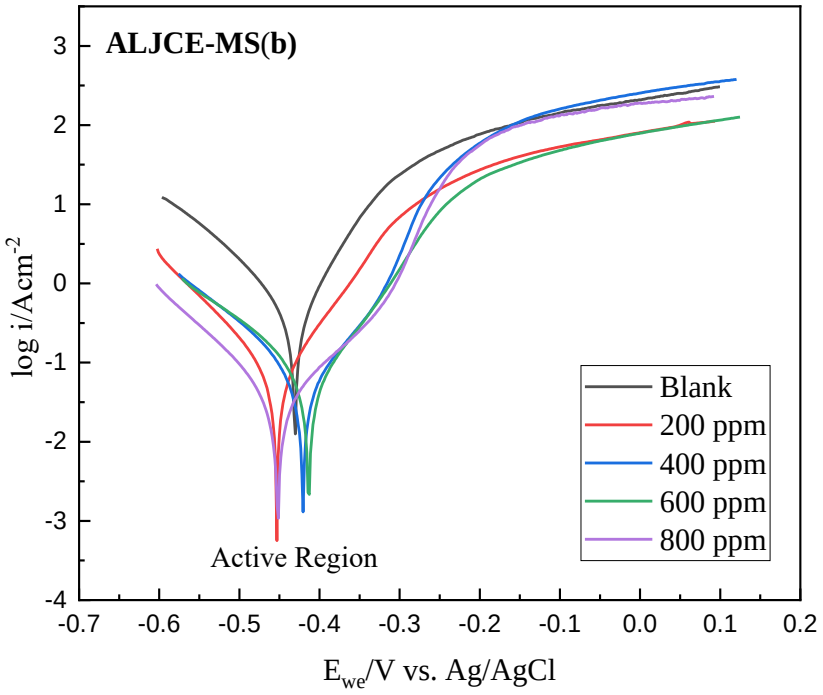

Figure 6.6: Tafel PDP curves for MS dissolution in 1 M HCl with and without different concentrations of ELJCE to observe pitting (a). The extrapolated (b) active area at 303 K, respectively

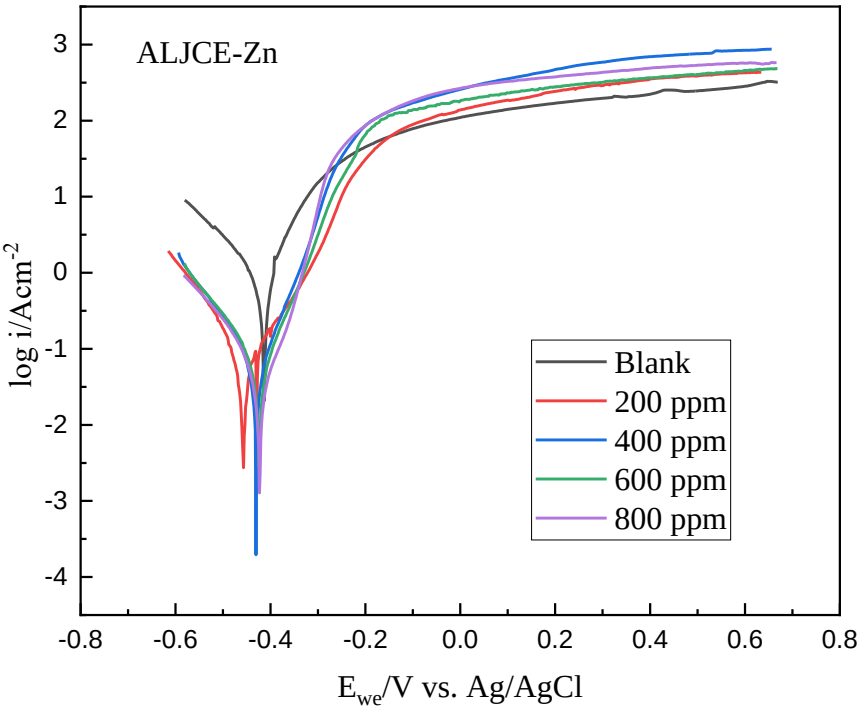

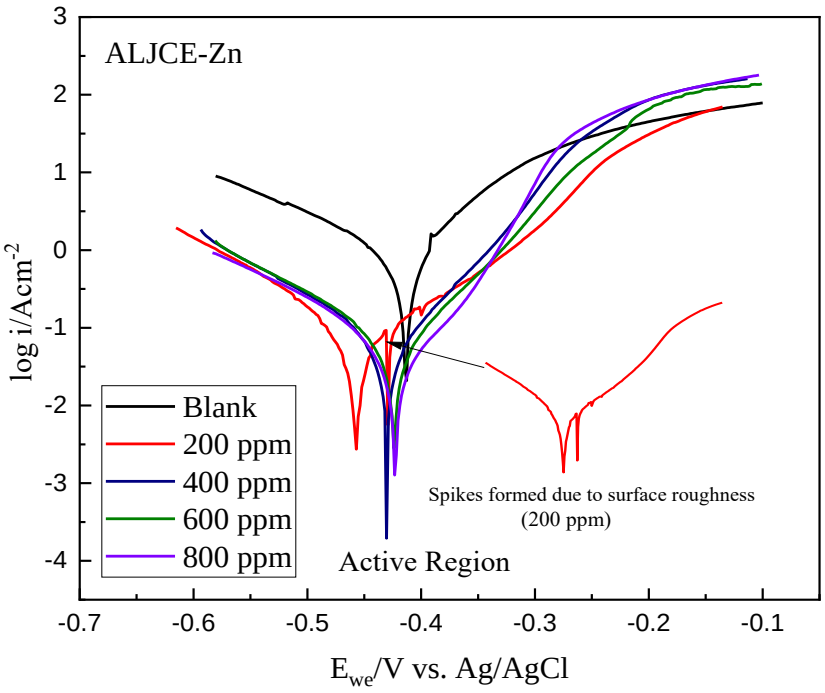

Figure 6.7: Tafel PDP curves for Zn dissolution in 1 M HCl with and without different concentrations of ALJCE to observe pitting (a). The extrapolated (b) active area at 303 K, respectively

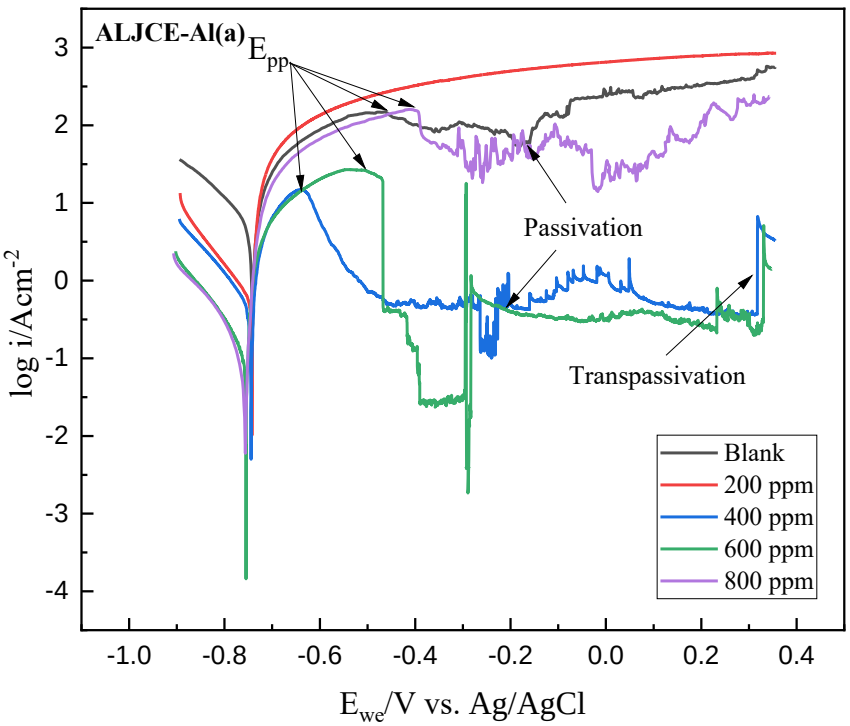

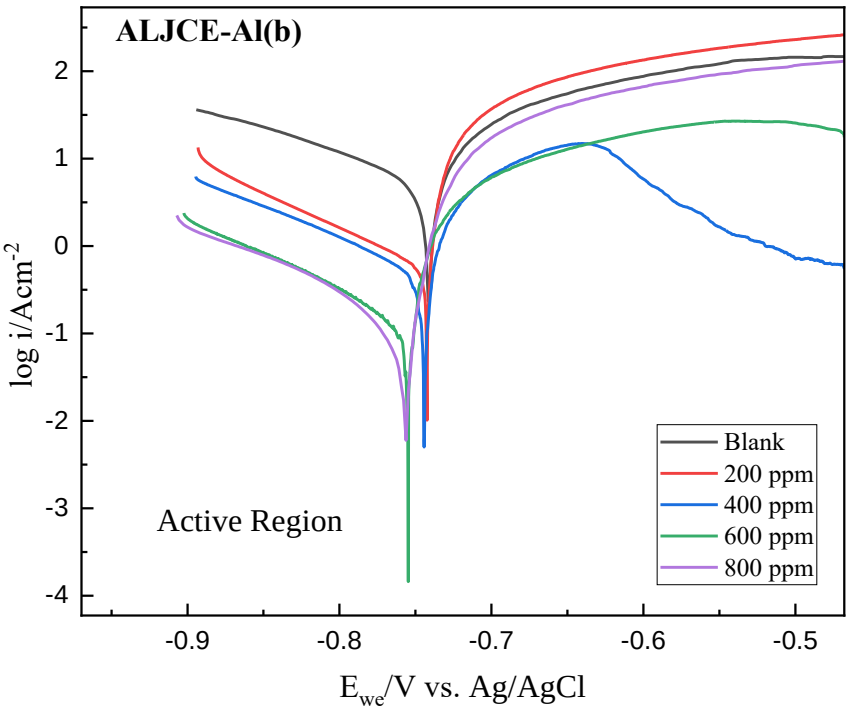

Figure 6.8: Tafel PDP curves for Al dissolution in 1 M HCl with and without different concentrations of ELJCE to observe pitting (a). The extrapolated (b) active area at 303 K, respectively

Table 6.2: Polarization electrochemical parameters of Al, MS, and Zn after 1-hour immersion at 303 K in 1 M HCl with and without different concentrations of ALJCE

Metal	Conc. of ALJCE (ppm)	C_R (mpy)	E_{corr} (mV)	β_a (mV.dec^{-1})	β_c (mV.dec^{-1})	I_{pass} (µA.cm^{-2})	I_{corr} (µA.cm^{-2})	%IE_{PDP}
MS	0	261.26	−430.637	77.6	119.4	–	570.249	–
	200	37.1959	−453.357	84.8	103.0	–	81.187	85.76
	400	31.5134	−420.815	105.9	114.9	–	68.784	87.94
	600	21.955	−413.445	73.5	96.1	–	47.921	91.60
	800	15.1313	−447.202	111.1	107.5	–	33.027	94.21
Zn	0	675.025	−413.435	96.8	196.8	–	1144.688	–
	200	36.3345	−452.547	112.9	96.4	–	61.615	94.62
	400	26.7347	−426.443	66. 3	98.8	–	50.150	95.62
	600	24.3057	−422.314	67.1	85.1	–	41.217	96.40
	800	13.4936	−419.023	58.1	66.3	–	22.882	98.00
Al	0	2492.66	−740.497	64.6	183.6	1.7399	5831.281	–
	200	255.138	−744.354	13.3	127.8	–	594.661	89.80
	400	236.015	−745.596	33.8	146.5	0.3631	553.166	90.51

	600	74.5641	−756.712	22.8	137.4	0.4574	173.790	97.02
	800	62.5649	−757.873	19.4	122.8	1.2041	145.823	97.50

6.5. Electrochemical impedance spectroscopy (EIS)

EIS measurements were used as a complementary electrochemical technique to understand the charge transfer mechanism of the ALJCE inhibitors and to quantitatively assess the effectiveness of extract performance as corrosion inhibitors for Zn, MS, and Al substrates. Using a small amplitude AC signal (10 mV) in the frequency range of 100 kHz to 10 mHz, EIS was used to demonstrate the frequency response of the electrochemical system in the absence and presence of ALJCE. The experimental data were recorded as real and imaginary ohmic impedance components and plotted as Nyquist diagrams (Figure 6.9−6.11). The Nyquist plots in Figures 6.9 and 6.10 showed imperfect semicircular loops for both the uninhibited and ALJCE-inhibited systems of Zn and MS substrates. The loop defects become more noticeable in the low-frequency range, indicating non-ideal capacitive behaviour of the electrochemical metal-liquid interface [603, 604] due to surface inhomogeneities resulting from surface defects, roughness on the metal surface, and electrode porosity, and this phenomenon is known as the dispersing effect [605]. The semi-circular curves in the Nyquist plots for Al show that the charge transfer process also controls Al's dissolution process. Al Nyquist plots are known to consist primarily of a small inductive loop in the intermediate frequency compared to a sizeable capacitive loop in the higher frequency ranges [606]. However, the shape of the curves in the present study showed an inductive loop in the intermediate frequency ranges almost as large as the capacitive loop in the higher frequency ranges. Other researchers studying Al corrosion in HCl observed similarly shaped EIS plots [607-610]. The depressed semi-circular nature of the Nyquist curves with a centre below the real axis, like in the MS and Zn systems, can be attributed to the scattering/dispersing effect, which is one of the properties of solid electrodes like Al [611, 612]. The similarity of the Nyquist curves for the uninhibited and inhibited systems shows that the plant product species prevents MS, Zn, and Al dissolution through an adsorption mode that does not alter the electrochemical properties. The non-linear least-squares method can be used to fit electrochemical data [613], and for a metal corroding in an aqueous solution (e.g., 1.0 M HCl), an ECC known as the Randles circuit, consisting of a parallel combination of capacitance and resistance, representing the corrosive interface are used in series with a second uncompensated resistor.

The modified Randles equivalent circuit (Figure 4.18, section 4.5) was found to be the best-fitting circuit for MS and Zn in this study as it was found to account for the dispersion effects exhibited by the two metals. The circuit was modified by replacing the pure capacitor with a CPE. Besides

the CPE, the circuit also consists of R_s (uncompensated resistor), which represents the electrolyte resistance created by the movement of electric charge, while R_{ct} is the charge transfer resistance, which determines the rate of corrosion. While for Al, two other elements were added, which included the inductance resistance (R_L) and inductance (L), to compensate for the induction loop in lower frequency ranges, as shown in Figure 4.19 (section 4.5). The fitting of the EIS data by the two circuits using the ZSim software (version 3.3) allowed the chi-square value (χ^2, i.e., the sum of the squared differences between theoretical and experimental points) to be used for evaluating the quality of the equivalent circuit adaptation [614]. The χ^2 values obtained for MS, Al, and Zn are shown in Table 6.3 and indicate a good fit for the proposed circuits. Higher R_{ct} values in corrosion inhibition studies indicate the formation of a barrier that must be overcome to promote the charge transfer process during corrosion, which implies a reduction in the rate of corrosion [613]. As such, R_{ct} values were used as the baseline values to calculate the inhibition efficiencies of ALJCE for Al, Zn, and MS corrosion inhibitory effects of ALJCE and are recorded in Table 6.3. The values increased with the increasing concentration of the extracts, which shows that the charge transfer phenomenon mainly controls the corrosion of MS, Zn, and Al. This indicates that the conductivity of the 1 M HCl solution was reduced as the protection of the metal surfaces by the extracts increased with the increase in the concentration of ALJCE, implying that the plant species significantly reduces the contact between the surface of the metals and the corrosive solution, thus protecting the metal from corrosion.

The C_{dl} values calculated as a replacement for the CPE values to represent an ideal behaviour using equation 49 are shown in Table 6.3. The results show that the C_{dl} values in the blank solution for MS and Zn were 1.3884 and 28.1854 $\mu F.cm^{-2}$, respectively. Compared to their respective blank values, these values are significantly lower in the presence of ALJCE, indicating that the extracts effectively formed a barrier layer that protected the metals from corrosion. The low C_{dl} values in the presence of ALJCE could be attributed to the decrease in the dielectric constant or an increase in the thickness of the protective film created by the extracts on the surface of the metals [615]. Bode phase angle diagrams were developed to analyze the impedance data further, as shown in Figures 6.12−6.14. The figures show that the phase angles for ALJCE-inhibited samples increased with ALJCE concentration and were larger than those of non-inhibited samples with a single time constant for both MS and Zn substrates.

The increase in the phase angles with the ALJCE concentration shows that the Zn and MS surfaces become noticeably smoother as the ALJCE compounds form a protective film over the metal surfaces [616]. In the presence of ALJCE, the average phase angle shift for both Zn and MS was about −70°, which is less than −90°, suggesting that these systems are not ideal capacitors in the presence of ALJCE concentrations. While for Al, the phase angle for the uninhibited system was found to be −41.5066° and the introduction of ALJPE into the system increased it to a maximum of −59.1747° at 800 ppm, indicating a deviation from the ideal capacitive behaviour. These results suggest that ALJCE acted as a resistor in the lower and higher frequency range by forming an adsorption layer on the Al, Zn, and MS surfaces. The Bode-Modulus diagrams showed that the slope of the mid-frequency range was almost a straight line and close to −1 for all three metal samples in the presence of an ALJCE concentration, which means that they approximate the real capacity behaviour. The phase angles approaching an ideal capacitor (phase angle = −90°; slope = −1) indicate the lowering in the metal specimens' corrosion rate, which suggests that ALJCE were effective in protecting the metals from attack by the corrosive solution [617]. These findings are consistent with those reported in the literature [613, 617, 618] on the general behaviour of a suitable/good inhibitor preventing the dissolution of metals.

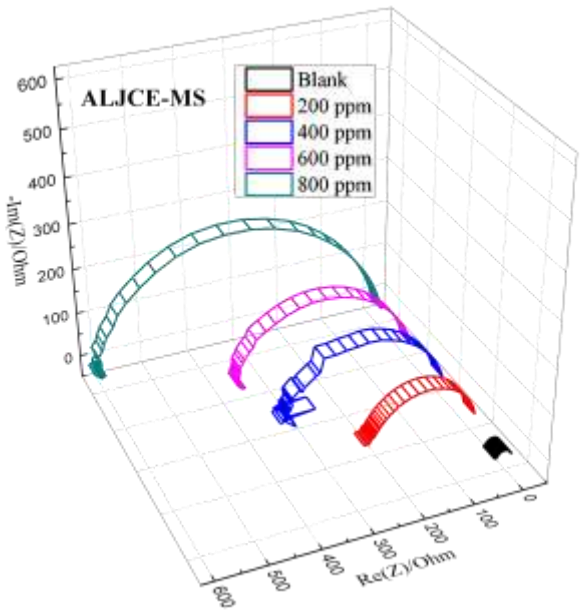

Figure 6.9: MS Nyquist plots in 1 M HCl solution with and without ALJCE at various concentrations at 303 K

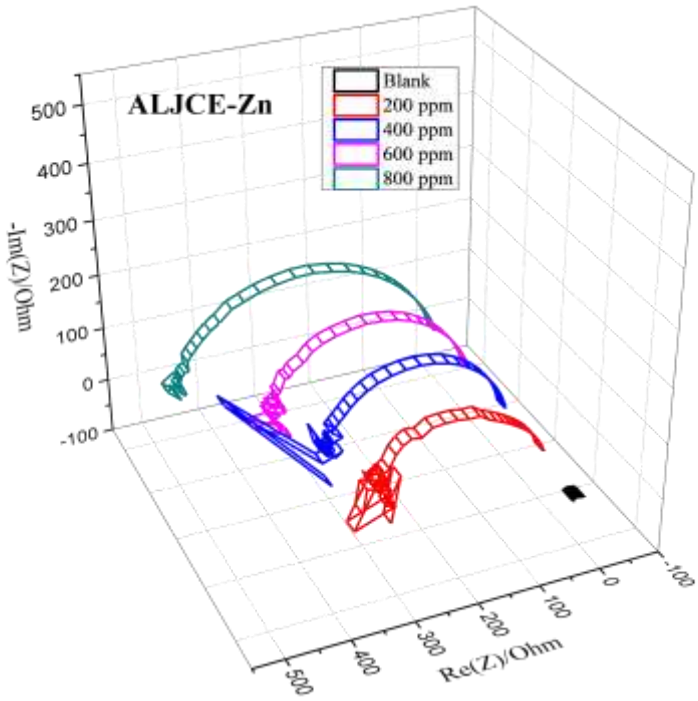

Figure 6.10: Zn Nyquist plots in 1 M HCl solution with and without ALJCE at various concentrations at 303 K

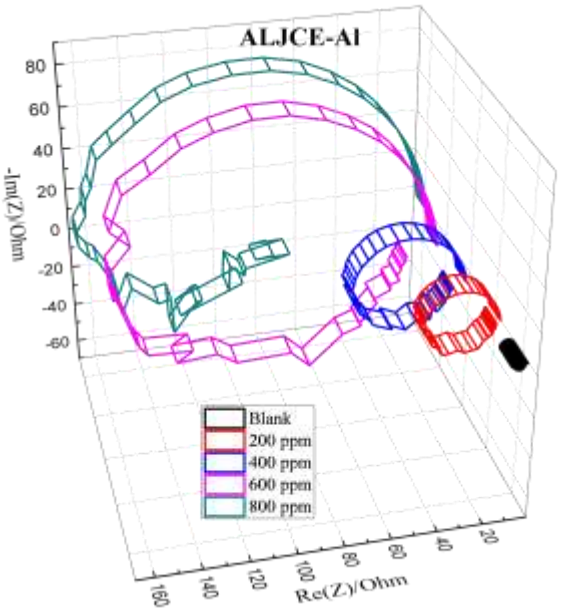

Figure 6.11: Al Nyquist plots in 1 M HCl solution with and without ALJCE at various concentrations at 303 K

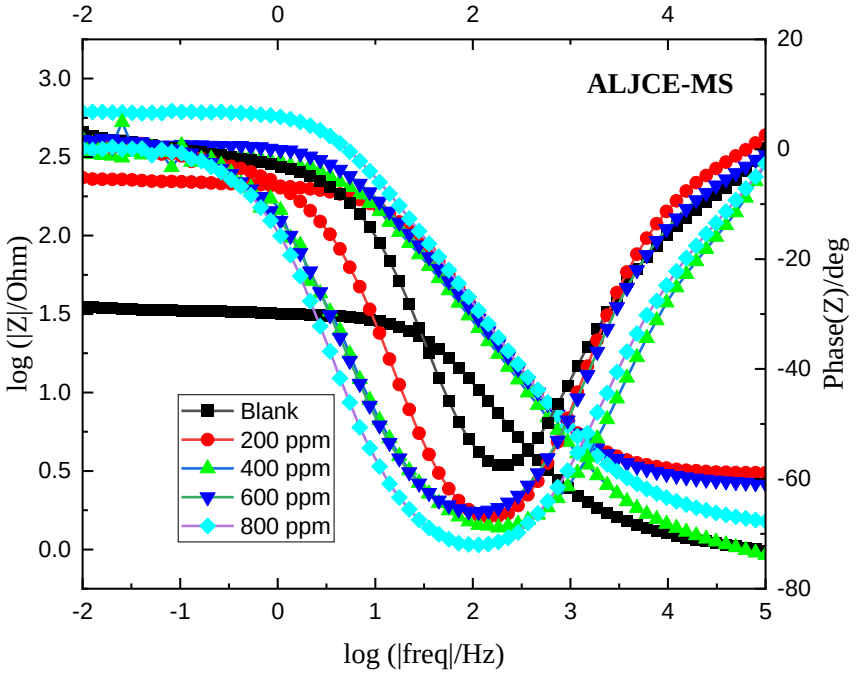

Figure 6.12: MS Bode modulus and phase angle plot in 1 M HCl solution with and without ALJCE at various concentrations at 303 K

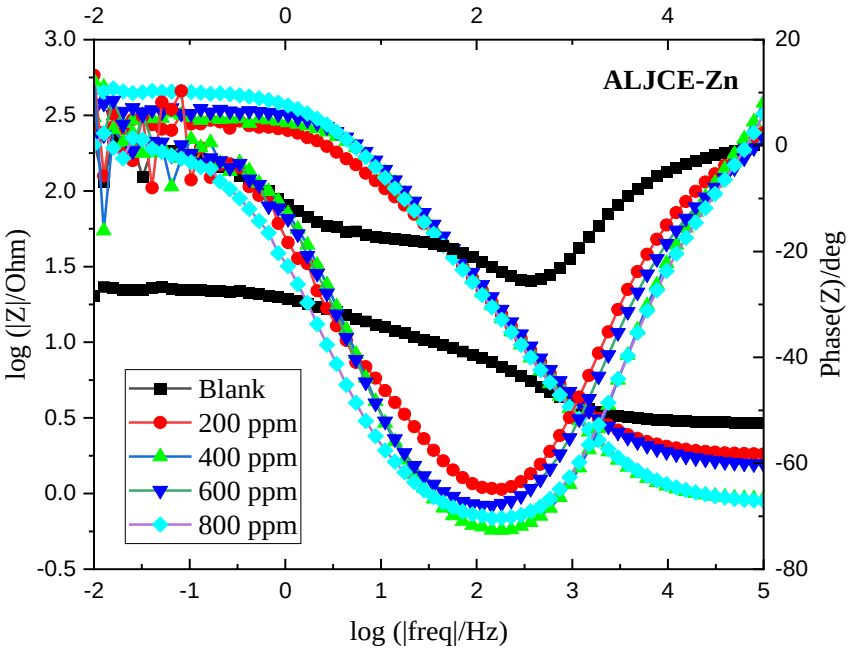

Figure 6.13: Zn Bode modulus and phase angle plot in 1 M HCl solution with and without ALJCE at various concentrations at 303 K

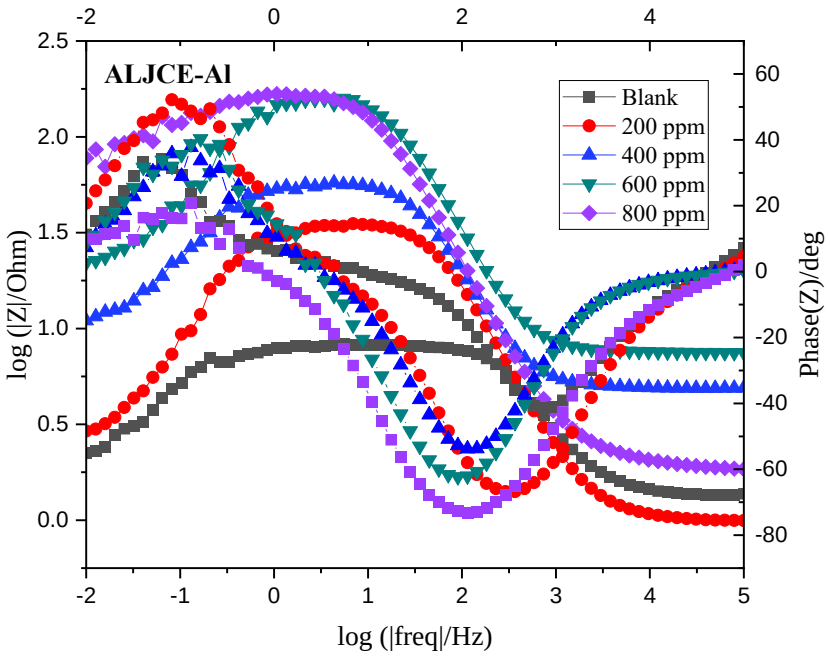

Figure 6.14: Al Bode modulus and phase angle plot in 1 M HCl solution with and without ALJCE at various concentrations at 303 K

Table 6.3: Electrochemical impedance parameters of Zn, Al, and MS in 1 M HCl in the presence and absence of different concentrations of ALJCE

Conc. of ALJCE (ppm)	R_s ($\Omega.cm^2$)	CPE parameters		L_1 (H)	R_{ct} ($\Omega.cm^2$)	C_{dl} ($\mu F.cm^{-2}$) $\times 10^{-4}$	(|θ|)	Slope	R_L ($\Omega.cm^2$)	%IE	χ^2 $\times 10^{-3}$
		Y_0 ($S.sec^n$) $\times 10^{-3}$	N								
MS											
0	1.107	0.385	0.8281	–	32.2	1.3884	−57.4165	−0.6904	–	–	2.949
200	3.099	0.0956	0.8811	–	214.4	0.5302	−67.0625	−0.7934	–	84.98	1.015
400	1.017	0.1742	0.8214	–	328.6	0.8822	−68.8694	−0.7744	–	90.20	2.401
600	2.709	0.1413	0.8354	–	376.6	0.9738	−65.9465	−0.7547	–	91.45	0.711
800	1.675	0.1087	0.8513	–	625.0	0.7403	−72.0325	−0.8174	–	94.85	2.83
Zn											
0	2.628	0.6051	0.5031	–	20.76	28.1854	−25.5302	−0.2366	–	–	4.598
200	1.785	0.2502	0.7998	–	280	2.0897	−64.9094	−0.7363	–	92.59	6.354
400	0.9354	0.1542	0.8715	–	316.8	0.9151	−72.6262	−0.8282	–	93.45	9.114
600	1.604	0.1718	0.8365	–	344.6	1.0642	−68.0094	−0.7774	–	93.98	1.666
800	0.9045	0.2107	0.8325	–	451.4	1.2963	−70.3684	−0.7943	–	95.40	1.921
Al											
0	1.392	0.1029	0.9548	10.24	6.617	0.8265	−41.5066	−0.5775	1.076	–	2.707
200	1.027	0.1089	0.9600	14.5	32.75	0.8571	−51.8097	−0.6787	2.109	79.80	4.270
400	4.926	0.1006	0.9702	35.36	50.25	0.8897	−47.4571	−0.6499	8.858	86.83	2.481
600	7.561	0.0585	0.977	67.25	143.3	0.6310	−62.3475	−0.7891	20.22	95.38	5.006
800	1.989	0.1054	0.9346	429	165.6	0.8658	−59.1747	−0.7336	165.3	96.00	4.269

6.6. Weight loss measurement

6.6.1. The effect of ALJCE concentration on the anti-corrosive behaviour of Zn, Al, and MS

The data obtained from weight loss analysis, such as C_R and %IE of Al, Zn, and MS coupons in the 1 M HCl corrosion test solution with and without various concentrations of ALJCE, are summarized in Table 6.4. Several concentrations (200 to 800 ppm) of the extracts were tested to determine the optimal ALJCE concentration that can effectively protect the metal surfaces from attack by corrosive species. According to Table 6.4, the C_R of the three metal samples is concentration-dependent and markedly decreases with increasing ALJCE concentration at each temperature examined. The C_R decreases as the concentrations of the extracts increase from 200 to 800 ppm, as shown in Figure 6.15. In contrast, the variation of the %IE with inhibitor concentrations at different temperatures (Figures 6.16−6.19) shows that the addition and subsequent increase in the concentration of ALJCE improve the inhibitory effect (%IE) of Al, Zn, and MS. This type of effect is accompanied by an increase in mass and charge towards the surface of the three metals, which favours the adsorption of ALJCE components and reduces the dissolution of the metals. According to the figures, the lowest corrosion protection for the three metals was observed at 200 ppm, owing to the poor coverage that the ALJCE offers due to the limited number of extract molecules available, leaving part of the metal surfaces vulnerable to attack by Cl^- ions. The %IE values show that at the optimal concentration of 800 ppm, the plant extracts had the greatest inhibitory effect. The higher %IE values at 800 ppm are due to the greater availability of ALJCE components compared to the other concentrations tested, resulting in increased binding propensity at the metal/solution interfaces. Higher binding implies that the three metal surfaces are effectively separated from the corrosive medium (1 M HCl), slowing their dissolution [619]. For example, in the presence of 800 ppm ALJCE, maximum inhibition efficiencies of 98.01 and 91.89%, respectively, were achieved for MS and Al at 303 K, while for Zn, an optimal protection efficiency of 87.77% at 333K. The C_R and %IE for surface Zn were nearly constant with increasing ALJCE. In contrast, those for MS and Al fluctuated, either decreasing or increasing as the extracts' concentration increased. This shows that the ALJCE strongly bonded to the surface of Zn and offered stronger protection than Al and MS.

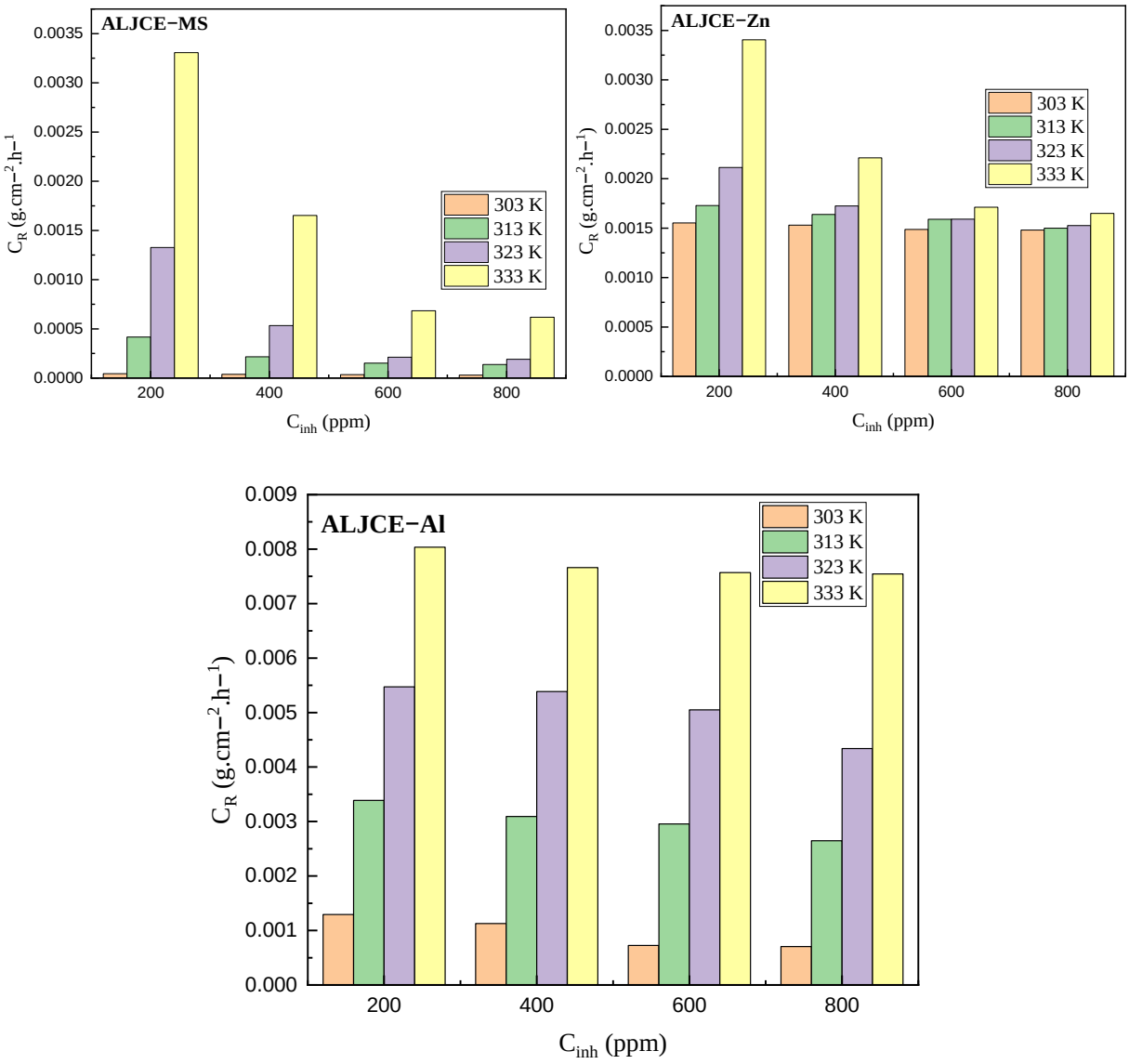

Figure 6.15: Variation of corrosion rate (C_R) obtained from weight loss for Zn, Al, and MS in 1 M HCl as a function of concentration in the presence of MLJCE at 303-333 K

Table 6.4: Weight loss parameters for the uninhibited and ALJCE-inhibited Al, MS, and Zn systems in 1 M HCl corrosive solution at 303-333 K.

Metal	Conc. of ALJCE (ppm)	303 K			313 K			323 K			333 K		
		C_R ($g.cm^{-2}.h^{-1}$)	C_R (mpy^1)	$\%IE_{CR}$	C_R ($g.cm^{-2}.h^{-1}$)	C_R (mpy^1)	$\%IE_{CR}$	C_R ($g.cm^{-2}.h^{-1}$)	C_R (mpy^1)	$\%IE_{CR}$	C_R ($g.cm^{-2}.h^{-1}$)	C_R (mpy^1)	$\%IE_{CR}$
MS	Blank	1.4988×10^{-3}	1.66944	–	2.8038×10^{-3}	3.11968	–	4.8840×10^{-3}	5.43776	–	8.6198×10^{-3}	9.59376	–
	200	4.4682×10^{-5}	0.04988	97.02	4.1703×10^{-4}	0.46540	85.13	1.3268×10^{-3}	1.47536	72.83	3.3064×10^{-3}	3.67408	61.64
	400	3.8476×10^{-5}	0.04288	97.43	2.1596×10^{-4}	0.24008	92.30	5.3370×10^{-4}	0.59392	89.07	1.6520×10^{-3}	1.83840	80.83
	600	3.4752×10^{-5}	0.03864	97.68	1.5142×10^{-4}	0.16848	94.60	2.1224×10^{-4}	0.23616	95.65	6.8388×10^{-4}	0.76080	92.07
	800	2.9788×10^{-5}	0.03320	98.01	1.3777×10^{-4}	0.15328	95.09	1.9114×10^{-4}	0.21280	96.09	6.1810×10^{-4}	0.68784	92.83
Zn	Blank	2.6325×10^{-3}	2.93086	–	4.3130×10^{-3}	4.79822	–	7.2024×10^{-3}	8.01758	–	1.3485×10^{-2}	14.99706	–
	200	1.5527×10^{-3}	1.72898	41.02	1.7289×10^{-3}	1.92586	59.91	2.1137×10^{-3}	2.35418	70.65	3.4057×10^{-3}	3.78978	74.74
	400	1.5304×10^{-3}	1.70330	41.87	1.6383×10^{-3}	1.82254	62.01	1.7240×10^{-3}	1.91816	76.06	2.2117×10^{-3}	2.46042	83.60
	600	1.4869×10^{-3}	1.65564	43.52	1.5899×10^{-3}	1.76946	63.14	1.5912×10^{-3}	1.76974	77.91	1.7116×10^{-3}	1.90656	87.31
	800	1.4807×10^{-3}	1.64814	43.75	1.4993×10^{-3}	1.67086	65.24	1.5266×10^{-3}	1.69824	78.80	1.6495×10^{-3}	1.83654	87.77
Al	0	8.6931×10^{-3}	9.67492	–	8.9549×10^{-3}	9.96434	–	1.0930×10^{-2}	12.14630	–	1.1308×10^{-2}	12.59214	–
	200	1.2924×10^{-3}	1.43760	85.13	3.3875×10^{-3}	3.77050	62.17	5.4723×10^{-3}	6.08270	49.93	8.0348×10^{-3}	8.93804	28.95
	400	1.1265×10^{-3}	1.25370	87.04	3.0917×10^{-3}	3.43758	65.47	5.3870×10^{-3}	5.99338	50.71	7.6616×10^{-3}	8.53320	32.25
	600	7.2606×10^{-4}	0.80784	91.65	2.9539×10^{-3}	3.28792	67.01	5.0490×10^{-3}	5.61880	53.81	7.5698×10^{-3}	8.41304	33.06
	800	7.0499×10^{-4}	0.78432	91.89	2.6474×10^{-3}	2.94786	70.44	4.3387×10^{-3}	4.82754	60.30	7.5433×10^{-3}	8.39078	33.29

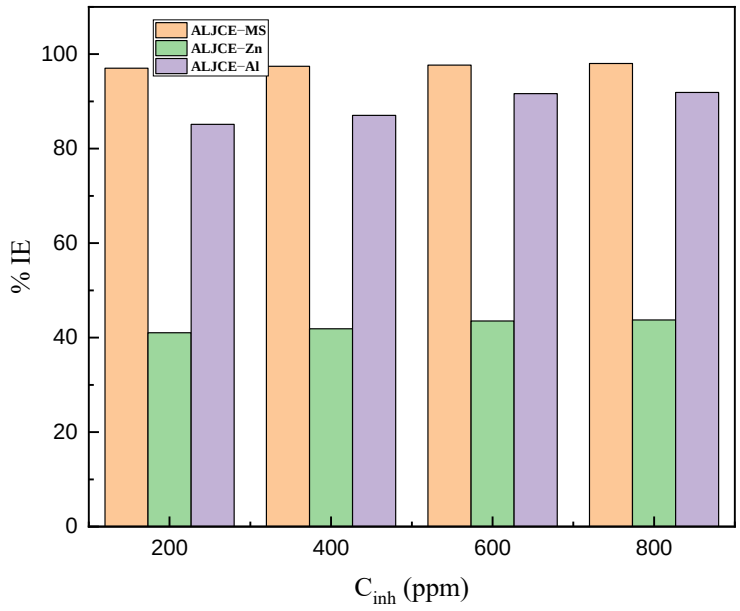

Figure 6.16: Variation of inhibition efficiencies ($\%IE_{WL}$) obtained from weight loss for Zn, Al, and MS samples in 1 M HCl as a function of ALJCE concentration at 303 K

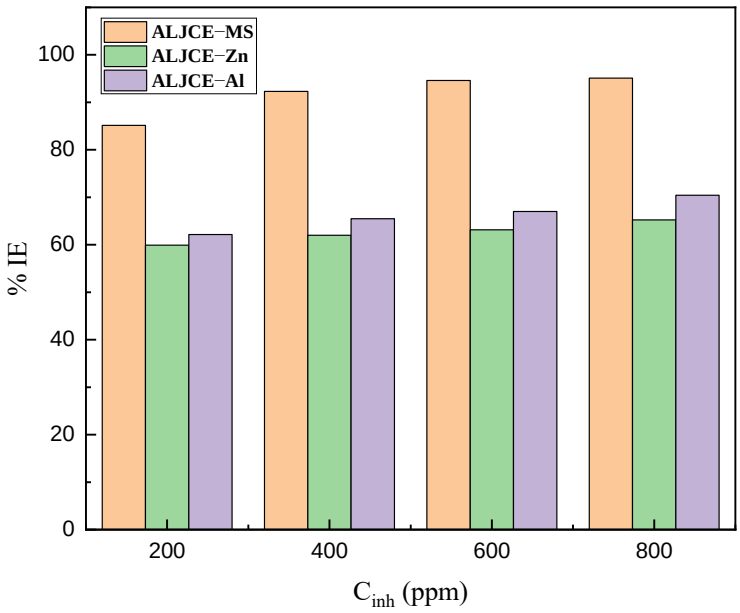

Figure 6.17: Variation of inhibition efficiencies ($\%IE_{WL}$) obtained from weight loss for Zn, Al, and MS samples in 1 M HCl as a function of ALJCE concentration at 313 K

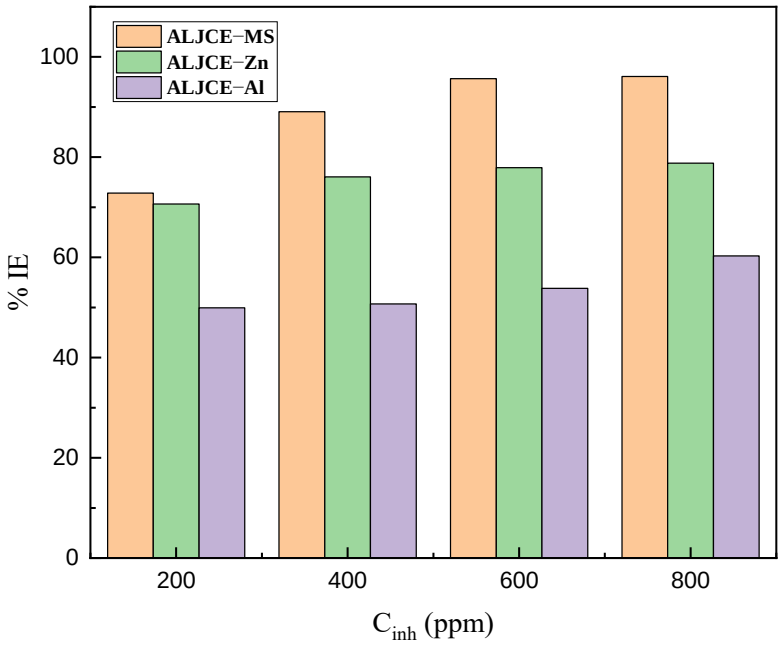

Figure 6.18: Variation of inhibition efficiencies (%IE$_{WL}$) obtained from weight loss for Zn, Al, and MS samples in 1 M HCl as a function of ALJCE concentration at 323 K

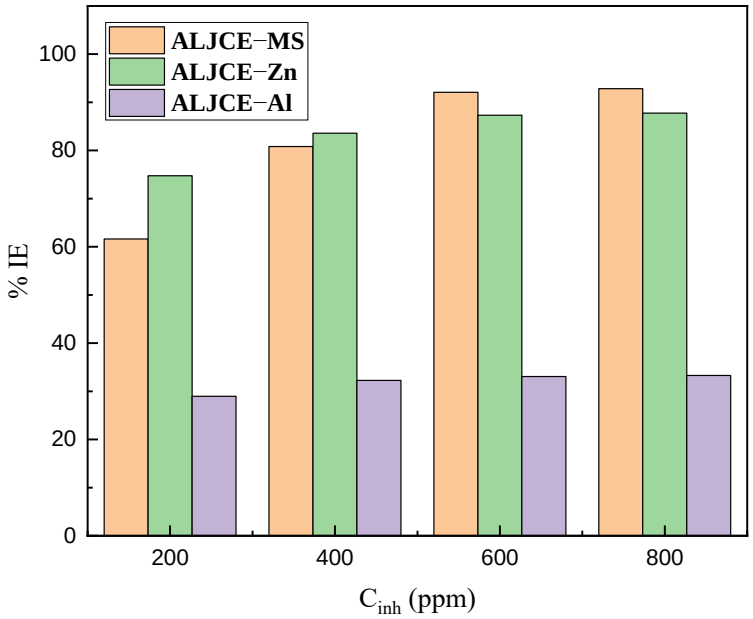

Figure 6.19: Variation of inhibition efficiencies (%IE$_{WL}$) obtained from weight loss for Zn, Al, and MS samples in 1 M HCl as a function of ALJCE concentration at 333 K

6.6.2. Influence of immersion time on MS, Al, and Zn corrosion inhibition in 1 M HCl with an optimal concentration of ALJCE at 303 K

Time is an important parameter in evaluating the effectiveness of an inhibitor against the corrosion of metals. A time study gives an indication of the stability of the adsorption film; therefore, the effect of long-term exposure (6 to 24 hours) of Al, Zn, and MS samples to 1 M HCl solution in the presence of 800 ppm ALJCE was examined using weight loss analysis. Figure 6.20 and Table 6.5 shows the weight loss results obtained at the optimum concentration of 800 ppm after immersing the test samples for 6, 7, 12, 18 and 24 hours and the corresponding %IE calculated from the results obtained. According to Table 6.5, the %IE for MS remained relatively constant at around 90% over the entire test period. The %IE of Al was found to decrease from 91.03% at 6 hours to 79.72% at 24 hours. This means that the decrease in %IE with exposure time was relatively small, and even after a long exposure time, the efficiency remains around 80%. Retaining the protection efficiency at approximately 80% indicates that the adsorption film formed on the Al surface had stabilized. The Zn %IE increased from 49.72 to 78.68% with immersion time (Figure 6.20) from 6 to 24 hours. The increase in %IE up to 24 h demonstrates that ALJCE is an effective Zn corrosion inhibitor due to the strong adsorption of ALJCE components on the Zn surface, resulting in the formation of a protective layer at the Zn/acid solution interface.

The high protective effect for all three metals achieved between 6 and 12 hours of immersion demonstrates rapid adsorption of ALJCE compounds at 800 ppm, indicating that ELJCE provides adequate corrosion protection for Al, MS, and Zn. Similarly, Baghdadi *et al*. [621] reported similar findings and observed a high inhibitory effect at the early exposure times of about 5–10 hours. After 10 hours of immersion, they observed a decrease in the protective effect, which they attributed to the desorption of inhibitor molecules from the metal surfaces. The fact that high inhibitory effects were maintained after 10 hours of immersion in the current study supports that ALJCE is an efficient inhibitor for all three metal samples in 1 M HCl solution.

Table 6.5: Weight loss results showing the %IE for Al, Zn, and MS corrosion in 1M HCl in the absence and presence of 800 ppm ALJCE at various immersion times

Metal	Conc. of ALJCE (ppm)	Immersion period (hours)				
		6	7	12	18	24
		%IE				
MS	800	91.77	98.01	99.45	98.60	97.00
Zn	800	49.72	43.75	60.61	72.37	78.68
Al	800	91.03	97.22	87.46	81.45	79.72

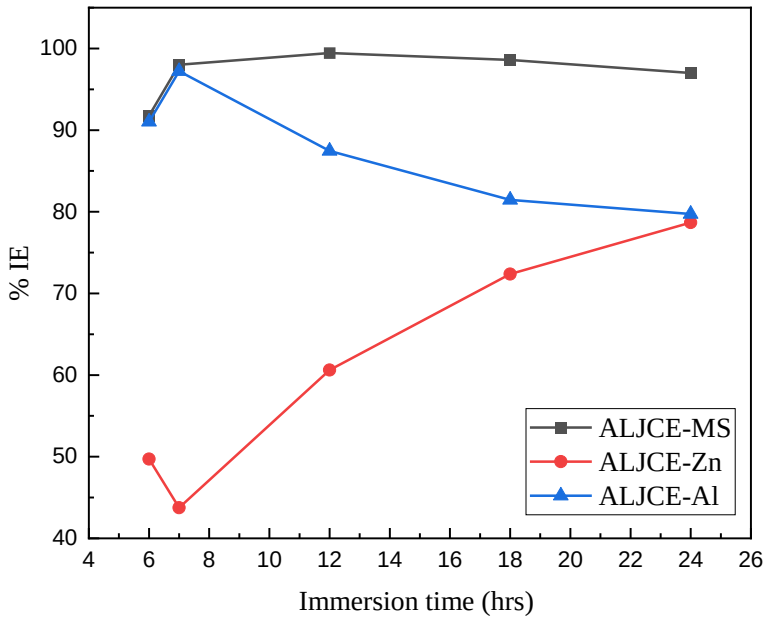

Figure 6.20: The variation of %IE for Al, Zn, and MS corrosion in 1M HCl in the absence and presence of 800 ppm ALJCE at various immersion times

6.6.3. Effect of temperature on the corrosion of Zn, Al, and MS in 1 M HCl solution containing ALJCE

Corrosion inhibitors regulate the corrosion process by altering the kinetics of metallic corrosion, thereby slowing the rate of either the anodic or cathodic reactions [620]. Temperature is one of the factors affecting the performance of a given inhibitor function because of its ability to alter the interaction between the metal and inhibitor surfaces. Therefore, to gain more insight into the nature of ALJCE adsorption, the effect of temperature on the %IE and C_R of MS, Al, and Zn samples in a 1 M HCl solution was investigated. In the absence of ALJCE, Al, MS, and Zn, dissolution

occurred acceleratedly. With an increasing temperature of the corrosive solutions from 303 to 333 K, the acceleration was ramped up even further (Table 6.4), indicating that the 1 M HCl molecules collided with the Al, MS, and Zn surface more frequently. The dissolution process slowly occurred when various concentrations of ALJCE were introduced in the corrosive medium (Figure 6.21–6.23). The reduction in the C_R indicates the participation of ALJCE at the metal/acidic solution interface, which forms a protective film. According to 6.21–6.23 and Table 6.4, as the temperature is raised from 303 K to 333 K, the value of inhibition efficiencies decreases while C_R increases. However, the increase in corrosion rates and subsequent decrease in inhibition efficiencies with temperature is only observed for MS and Al samples and can be attributed to the two metals' accelerated dissolution process at higher temperatures as a result of the desorption of the ALJCE molecules from the three metal surfaces. The desorption reduces the interaction between the metal surface and the extract/inhibitor molecules at elevated temperatures. These processes follow the general rule of chemical reaction at elevated temperature, which states that an increase in temperature causes faster etching and desorption of inhibitor molecules [621]. For instance, for MS at 200 ppm, the C_R increased from 4.4682×10^{-5}, 4.1703×10^{-4}, 1.3268×10^{-3} up to 3.3064×10^{-3} $g.cm^{-2}.h^{-1}$, at 303, 313, 323 and 333 K, respectively. Whereases for Al, the C_R increased from 1.2924×10^{-3}, 3.3875×10^{-3}, 5.4723×10^{-3}, up to 8.0348×10^{-3} $g.cm^{-2}.h^{-1}$ at 303, 313, 323 and 333 K, respectively.

On the other hand, the Zn sample demonstrated a decrease in corrosion rates as the temperature of the inhibited system was raised, resulting in an increase in %IE; this behaviour is associated with the chemisorption inhibition process [170]. For example, at 200 ppm, the C_R decreased from 1.5527×10^{-3}, 1.7289×10^{-3}, 2.1137×10^{-3}, up to 3.4057×10^{-3} $g.cm^{-2}.h^{-1}$ at 303, 313, 323 and 333 K, respectively. As such, the highest inhibition process for Zn corrosion was achieved at the highest temperature of 333 K.

During the corrosion inhibition process, an equilibrium exists between the adsorption and desorption of inhibitor molecules (e.g., ALJCE) on the metal surfaces, which occurs continuously at a specific temperature. As the temperature of the system rises, the equilibrium of Al and MS shifts towards the desorption direction until an equilibrium is achieved at a different value of the equilibrium constant. At higher temperatures, this results in lower %IE values. The decrease in %IE with temperature is due to electrostatic interactions (physical adsorption), which disappear at

elevated temperatures [622]. The increase in %IE with temperature for Zn indicates that the equilibrium is shifted towards adsorption, meaning that film is formed at higher temperatures, leading to a chemisorption inhibition mechanism. In the presence of ALJCE, the C_R decreased with temperature and at nearly a constant rate at all temperatures for Zn, indicating the presence of a robust adsorption film on the metal surface. However, for MS and Al, the C_R increased with temperature but at a much slower rate than the blank, especially at 303 K, where the highest %IE was achieved, as shown in Figures 6.21 and 6.22. The %IE was found to decrease with increasing temperature at all extract concentrations tested for MS and Al, though the decrease is more pronounced at the lowest concentration of the extracts tested, 200 ppm. When the temperature was raised from 303 to 333 K, the %IE was maintained at around 90% at higher concentrations of 600 and 800 ppm for MS. The retention of the %IE around 90% demonstrates the thermal stability of the adsorption film on the MS surface at various temperatures, even though there is a slight onset of the desorption process. Among the three metals studied, the %IE for Al decreased at a faster rate as the system temperature increased, with the lowest %IE of 35.75% obtained at the highest temperature and the lowest extract concentration of 333 K and 200 ppm, respectively. In the presence of ALJCE, the decrease in %IE with increasing temperature may indicate a weakening of the physical adsorption mechanism on the Al and MS surfaces at high temperatures.

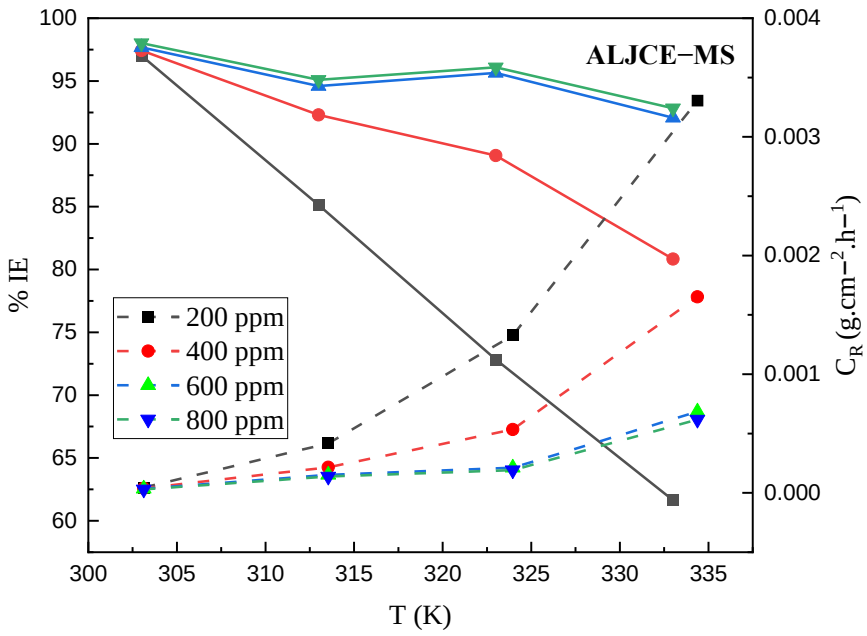

Figure 6.21: The dependence of (a) IE_{WL}(%) (solid lines) and (b) C_R (dashed lines) on temperature after 7 h of immersion of MS samples in 1 M HCl at different ALJCE concentrations

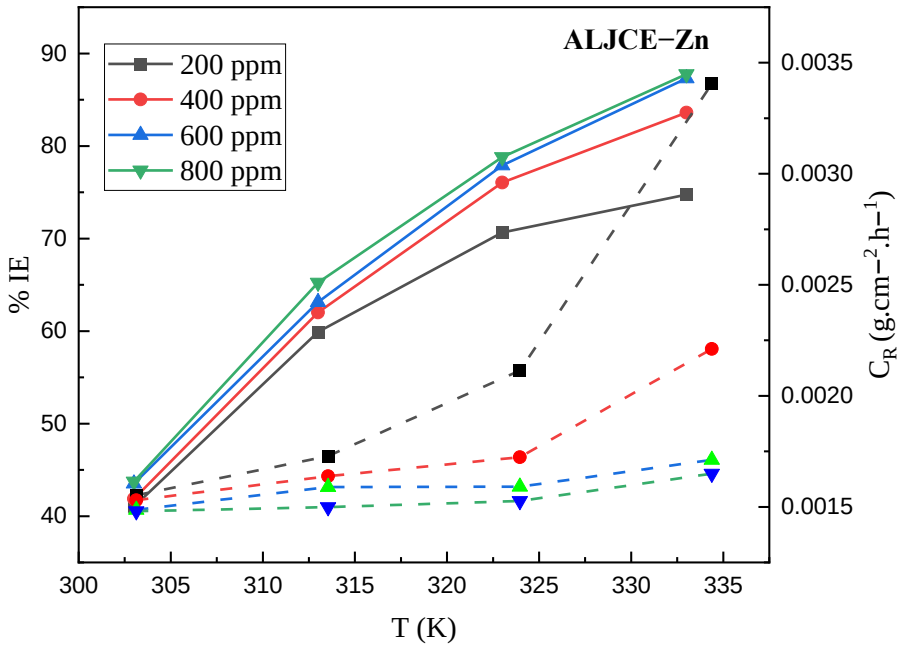

Figure 6.22: The dependence of (a) IE_{WL}(%) (solid lines) and (b) C_R (dashed lines) on temperature after 7 h of immersion of Zn samples in 1 M HCl at different ALJCE concentrations

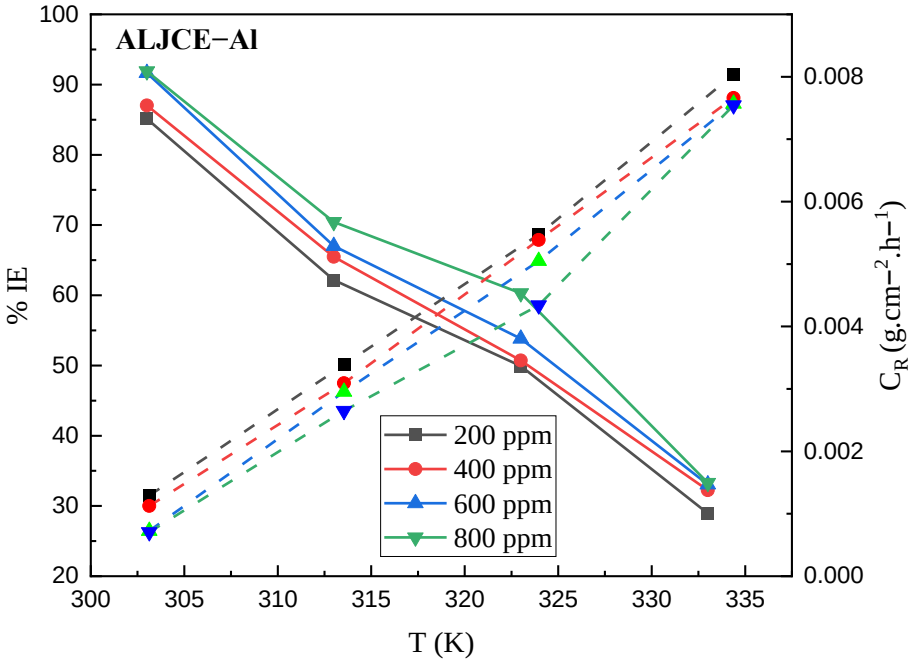

Figure 6.23: The dependence of (a) IE_{WL}(%) (solid lines) and (b) C_R (dashed lines) on temperature after 7 h of immersion of Al samples in 1 M HCl at different ALJCE concentrations

6.6.4. Thermodynamic and kinetic Parameters

The nature of MS, Al, and Zn corrosion inhibition can be further elucidated using kinetic and thermodynamic parameters in 1 M HCl with and without ALJCE. The apparent E_a for the corrosion of Zn, Al, and MS in 1 M HCl with and without various concentrations of ALJCE were calculated using Arrhenius equation 51. The slope ($-E_a/2.303R$) obtained from the linear Arrhenius plots of log C_R against $10^3/T$ (Figures 6.24−6.26) for the blank and each concentration of ALJCE was employed to calculate the E_a for the corrosion phenomena of Zn, Al, and MS and the results are indexed in Table 6.6. Inspection of Table 6.6 demonstrates that the activation energies were altered by the presence of ALJCE in the corrosive solution highlighting their adsorption of the surface of MS, Zn and Al. The temperature, inhibition efficiency, and E_a of the inhibited system are all related in the following ways:

i. If the E_a remains constant in the presence and absence of an inhibitor, the inhibition efficiency does not vary with system temperature.
ii. If the E_a of the inhibited solution is less than that of the uninhibited system, then the inhibition efficiency increases with temperature.
iii. If the E_a of the inhibited solution is greater than that of the uninhibited system, the inhibition efficiency decreases as the temperature rises.

It is experimentally evident from Table 6.6 that the E_a values for MS and Al are higher in the presence of ALJCE than in its absence. The increase in E_a values in the presence of the extract/inhibitor could be due to the participation of ALJCE molecules during the adsorption process on the Al and MS surfaces, leading to the formation of a physical barrier, which in turn blocks the corrosive charge and mass transfer [623], leading to a decrease in its rate of dissolution. An analogous increase in apparent E_a in the presence of ALJCE compared to its absence, along with a reduction in IE(%) with increasing temperature, can be interpreted as indicating the formation of electrostatic adsorption (physisorption) nature. The electrostatic adsorption of ALJCE on the Al and MS surfaces leads to a barrier that prevents charge and mass transfer processes. Table 6.6 shows that the E_a for the uninhibited MS surface was 48.2192 $kJ.mol^{-1}$, whereas the E_a for different concentrations of ALJCE (200–800 ppm) ranged from 117.0056 to 78.3835 $kJ.mol^{-1}$, indicating that while the E_a is higher in the presence of the extracts (implying a physical adsorption mechanism), it decreases with increasing extract concentration.

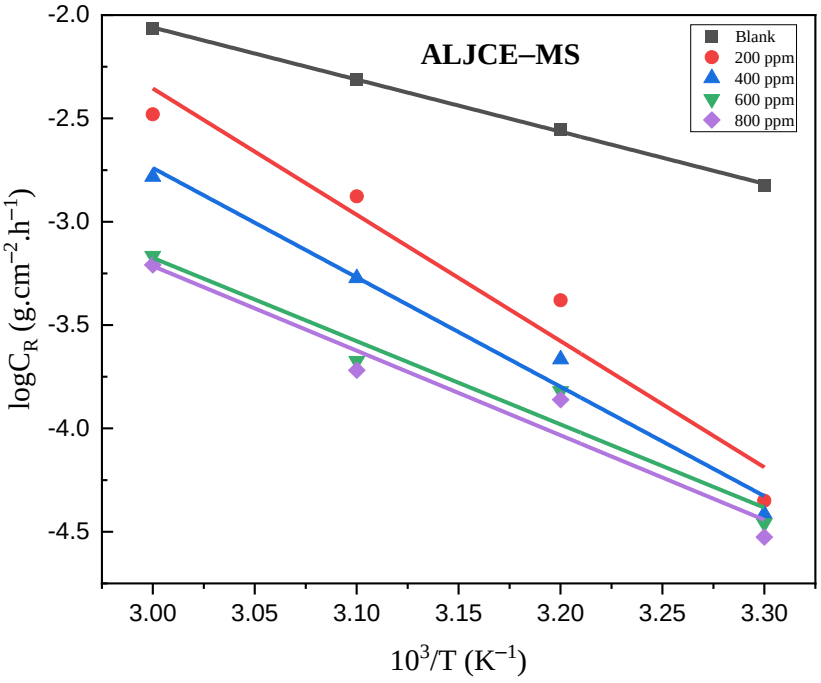

Figure 6.24: Arrhenius diagram (log C_R versus $10^3/T$) for the uninhibited (blank) and ALJCE-inhibited (200 to 800 ppm) MS system in corrosive 1 M HCl solution after 7 hours of immersion

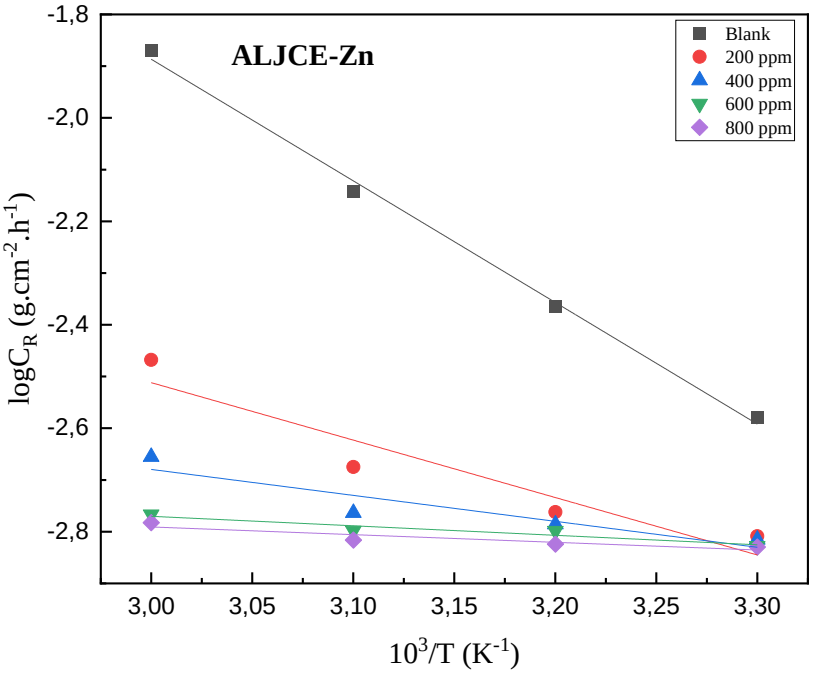

Figure 6.25: Arrhenius diagram (log C_R versus $10^3/T$) for the uninhibited (blank) and ALJCE-inhibited (200 to 800 ppm) Zn system in corrosive 1 M HCl solution after 7 hours of immersion

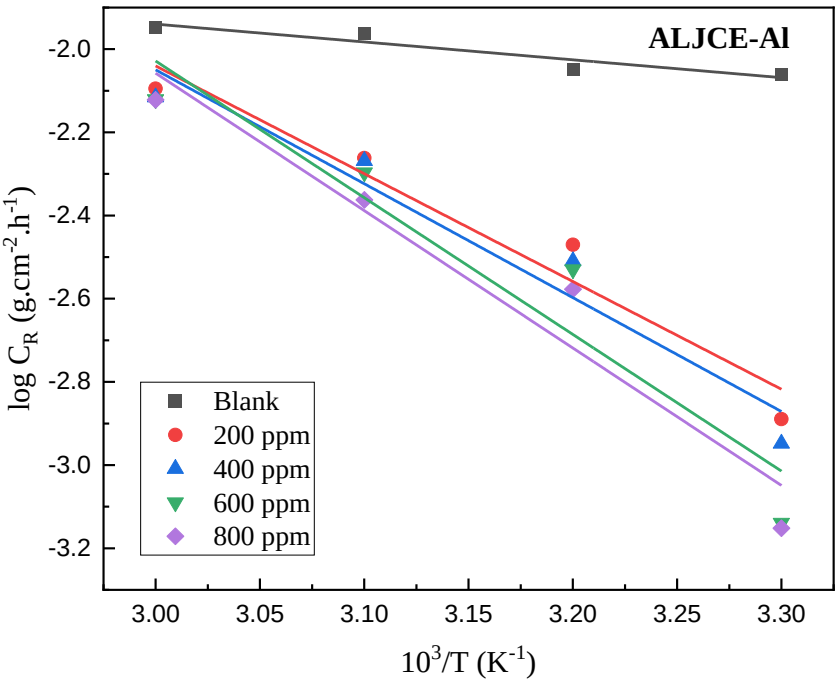

Figure 6.26: Arrhenius diagram (log C_R versus 10^3/T) for the uninhibited (blank) and ALJCE-inhibited (200 to 800 ppm) Al system in corrosive 1 M HCl solution after 7 hours of immersion

The decrease in E_a values could be attributed to chemical interactions between the metal surface and the extracts molecules, such as electron sharing or transfer from the extracts to the MS surface, resulting in the formation of a film that acts as a barrier between the metal surface and the HCl solution [624]. This suggests that both physical and chemical adsorption inhibition mechanisms control MS corrosion.

Further examination of the results (Table 6.6) reveals that adding ALJCE to the corrosive solution reduced the E_a values for Zn to a low of 2.8435 kJ.mol^{-1} compared to the blank (45.0215 kJ.mol^{-1}). The decrease in E_a values with temperature can be explained in several ways, as in the literature. According to Riggs and Hurd [625], the rate at which metals corrode can be summarized into two corrosion rates; the rate at which the metal surface corrodes in the absence of the corrosion inhibitor and the rate at which the metal surface covered by the adsorbed inhibitor molecules corrodes. At higher metal surface coverage, the first process has no significant contribution, and the corrosion process is inhibited by a direct reaction that occurs between the inhibitor molecules and the metal surfaces, and the E_a can be smaller or higher than in the absence of the inhibitor. Putilova *et al*. [456] demonstrated the phenomenon by showing that the surface area of the metal

protected by the inhibitor increases with increasing temperature. At the same time, the rate-determining step of metal dissolution becomes diffusion through the corrosion product and inhibitor film. Other researchers [626-628] state that the reduction in E_a values in the presence of the inhibitors is attributed to the chemisorption inhibition mechanism against metal corrosion due to the large size of the inhibitor compounds.

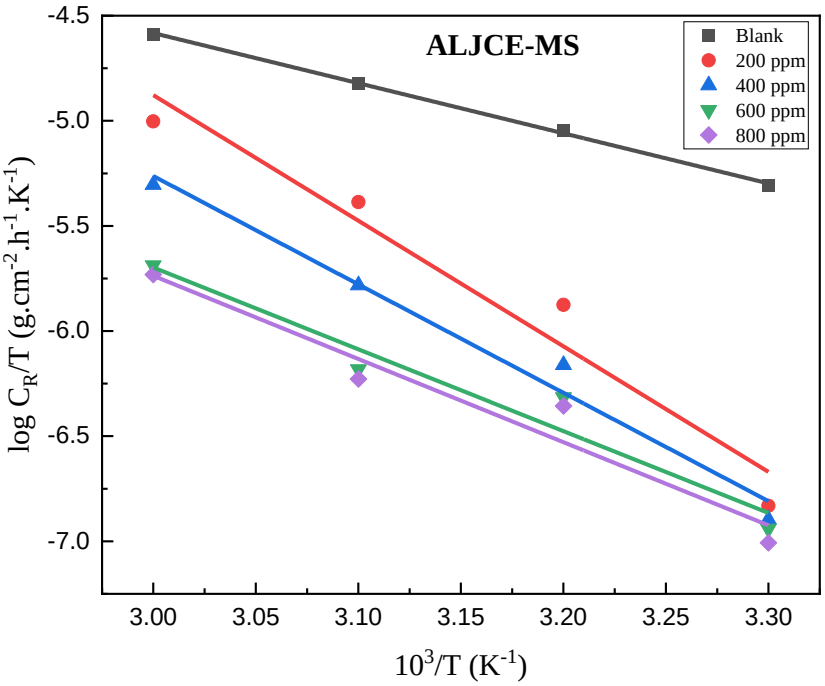

Figure 6.27: Transition state diagram (log C_R/T versus 10^3/T) for the uninhibited (blank) and ALJCE-inhibited (200 to 800 ppm) MS system in corrosive 1 M HCl solution after 7 hours of immersion

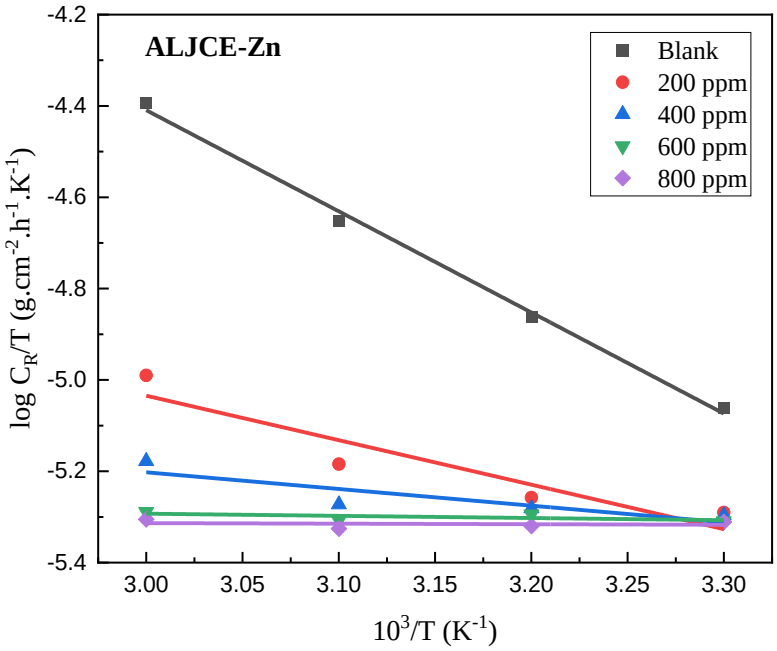

Figure 6.28: Transition state diagram (log C_R/T versus 10^3/T) for the uninhibited (blank) and ALJCE-inhibited (200 to 800 ppm) Zn system in corrosive 1 M HCl solution after 7 hours of immersion

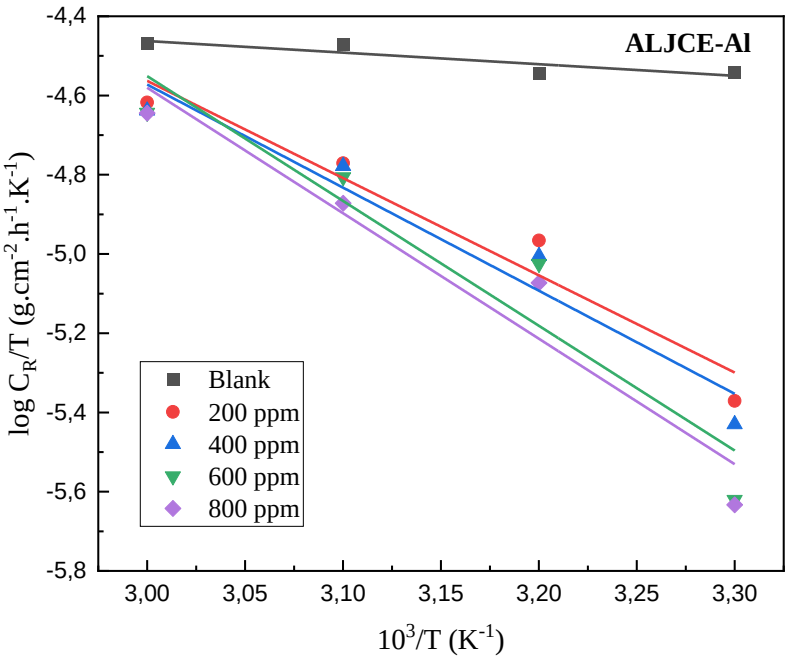

Figure 6.29: Transition state diagram (log C_R/T versus 10^3/T) for the uninhibited (blank) and ALJCE-inhibited (200 to 800 ppm) Al system in corrosive 1 M HCl solution after 7 hours of immersion

Plotting log (C_R/T) vs 10^3/T resulted in straight lines graphs (Figures 6.27−6.29) with a slope of ($-\Delta H_a^*/2.303R$) and an intercept of (log R/Nh) + $\Delta S_a^*/2.303R$), from which the values of ΔH_a^* and ΔS_a^* were calculated using equation 52 and tabulated in Table 6.6. The ΔH_a^* values are all positive in the absence and presence of the leaf extract, demonstrating the difficulty of the endothermic nature of MS, Al, and Zn dissolution, which is attributed to physisorption adsorption [44]. The ΔH_a^* values for MS and Al are higher in the presence of the extracts than in the uninhibited system, indicating a greater protective effect. These high efficiencies result from an energy barrier formed by the extract adsorption process on the metal surface, which increases the corrosion process's enthalpy. Though the ΔH_a^* values are higher in the presence of the extracts; they decrease with the concentration of the extracts from 200 to 800 ppm for MS specimens. For the Al surface, a strong parallelism exists between ΔH_a^* and E_a as they increase with the increase in %IE when the concentration of the extract is increased. The ΔH_a^* values for the inhibited Zn system are lower than for the uninhibited system and continue to decrease when the concentration of the extracts is increased from 200 to 800 ppm. The decrease in ΔH_a^* with the extract concentration is related to the chemical interaction between the Zn surface and the extract compounds. This is supported by the increase in %IE with solution temperature, suggesting a chemisorption binding mechanism. In addition, the mean value of the difference between the E_a and ΔH_a^* values ($E_a - \Delta H_a^*$) is about 2.6 kJ.mol^{-1}, which is almost the exact value of the product of the gas constant (R = 8.3145 J.mol^{-1}.K^{-1}) and the lowest temperature of the experiment (T = 303 K). This applies to all three metals examined. This finding is consistent with Benabbouha *et al*. [629], who reported that the metal corrosion process involves a unimolecular reaction. The negative ΔS_a^* signs in the absence and presence of ALJCE indicate that the formation of the activated complex in the rate-limiting step occurred through an association process rather than a dissociation process [630], implying that the reactants were less disordered during the formation of the activated complex. The entropy values in the presence of the ALJCE extracts have a less negative value than in the bare system for Al and MS, suggesting that the addition of the extracts into the corrosive solution has shifted the corrosion system close to equilibrium, suggesting that a greater degree of disorder occurs during the conversion of the leaf extract species from reactants to an active complex for the two systems.

Table 6.6: Kinetic and activation parameters for MS, Al, and Zn in uninhibited and ALJCE-inhibited 1 M HCl solution

Metal	Conc. of ALJPE (ppm)	E_a (kJ.mol^{-1})	ΔH_a^* (kJ.mol^{-1})	$E_a - \Delta H_a^* = RT$ (kJ.mol^{-1})	ΔS_a (J.mol^{-1}.K^{-1})	Q_{ads} (kJ.mol^{-1})		
						303 to 313	303 to 313	303 to 313
MS	Blank	48.2192	45.6457	2.5774	−194.5601	–	–	–
	200	117.0056	114.3846	2.6210	−184.0860	−137.0854	−63.7968	−45.7712
	400	101.3251	98.7095	2.6156	−186.9265	−90.8091	−32.4452	−58.9369
	600	77.1408	74.5252	2.6156	−191.1505	−69.1572	19.1067	−57.1224
	800	78.3835	75.7602	2.6233	−190.9966	−73.6143	20.0262	−57.3245
Zn	Blank	45.0215	42.4058	2.6157	−194.8944	–	–	–
	200	21.2642	18.6543	2.6099	−199.2408	60.3227	40.0805	18.4570
	400	9.6086	6.9930	2.6155	−201.2355	64.5208	55.9931	42.2892
	600	3.5156	0.9057	2.6099	−202.2798	63.0072	60.7183	59.7698
	800	2.8435	0.2279	2.6156	−202.4067	69.4765	57.4482	58.8480
Al	Blank	8.2165	5.6009	2.6156	−200.7138	–	–	–
	200	49.6190	46.9957	2.6233	−194.3290	−98.4324	−42.0008	−80.0554
	400	52.4376	49.8219	2.6157	−193.8955	−99.7474	−51.3996	−68.9368
	600	62.9424	60.3248	2.6176	−192.2288	−133.0566	−46.7402	−76.7598
	800	63.2660	60.6484	2.6176	−192.2074	−122.9676	−37.8634	−99.5605

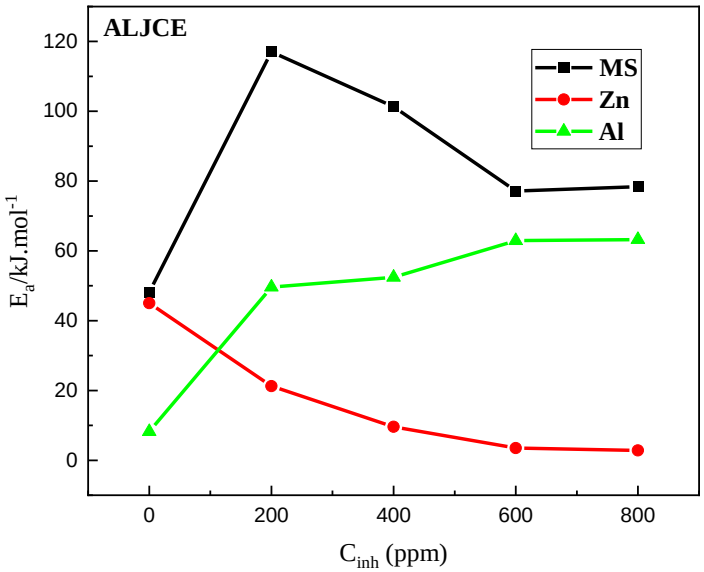

Figure 6.30: Relationship of E_a with the different concentrations of ALJCE for Zn, Al, and MS

Using equation 53, the Q_{ads} of the ALJCE on the surface of Zn, MS, and Al metals were estimated using surface coverage and temperature. The Q_{ads} values allow for the determination of the type of adsorption process that occurred during corrosion inhibition, and these values are shown in Table 4. Positive Q_{ads} values indicate chemical adsorption, whereas negative Q_{ads} values indicate physical adsorption, which is associated with decreased %IE as the system temperature rises. According to the table, the Q_{ads} values for Zn are positive at all temperatures, indicating a chemical adsorption inhibition mechanism. The ALJCE's physical adsorption mode is suggested by the negative Q_{ads} values on the surface of Al metal. The negative and positive values of Q_{ads} for MS surface represented both chemical and physical adsorption processes.

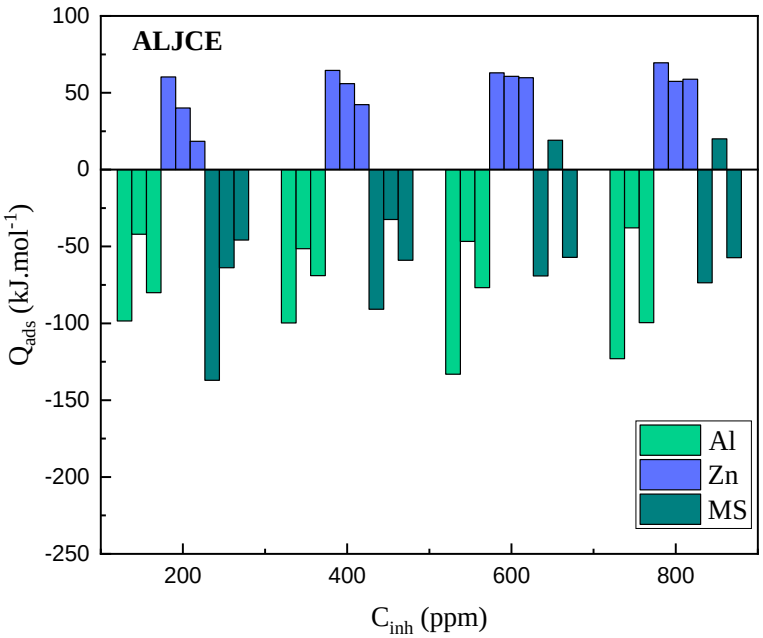

Figure 6.31: Heat of adsorption data for different concentrations of ALJCE for Zn, Al, and MS

6.7. Thermodynamic parameters of adsorption

Adsorption isotherms are the best method to quantitatively analyze the adsorbed layer formed by the inhibitor molecules responsible for the reduced access of corrosive species to the metal surface [170]. The adsorption of inhibitors on the surface of metals is generally recognized as the primary step in the action of inhibitors in corrosive solutions. It provides crucial information about the thermodynamic properties of corrosion. The adsorption process implies that no corrosion reactions occur on the metal or alloy surfaces covered by the adsorbed inhibitor species (or active sites). Still, these corrosion reactions typically occur on the inhibitor-free surface [631]. Adsorption by a substance relies primarily on the molecular structure, size and electrical potential of the substrate/corrosive solution interface. Adsorption isotherms are crucial in determining the corrosion-inhibiting mechanism of inhibitors on metal surfaces. Adsorption is a process in which water molecules with dissolved corrosive species are displaced from the substrate surface by the inhibitor molecules (e.g., ALJCE), and such a process can be explained according to equation 63 below [631, 632]:

$$ALJCE\ (sol) + nH_2O(ads) \rightarrow ALJCE(ads) + nH_2O(sol) \quad (63)$$

For adsorption to occur, the interaction energy between the substrate surface and the inhibitor species must be higher than the energy between the metal surfaces and the water molecules [170]. Therefore, depending on the inhibitor's concentration and the solution's temperature, the proportion of the metal surface covered by the inhibitor species can be monitored. Surface coverage data are helpful in describing the properties of adsorption. The dependence of ALJCE on the surface area was tested graphically by fitting to several adsorption isotherms, with the Langmuir isotherm described by equation 54 being found to be the most appropriate isotherm (Figures 6.32−6.35). The Langmuir model describes how the adsorption of inhibitors like ALJCE on metals' surfaces occurs in corrosive solutions. The isotherm assumes that the solid surface has a fixed number of locations where the adsorbed species are located and that each adsorption location contains an inhibitor species [633]. In other words, a single layer of adsorption forms on the surface of the metal with no contact between the individual components from the plant extract. The adsorption of ALJCE on Zn, Al, and MS surfaces leads to the formation of a stable, insoluble protective layer, which effectively suppresses the dissolution reaction of the three electrodes. The intercept lines on the C_{inh}/θ axis of the Langmuir isotherms was used to calculate the K_{ads} values

at different temperatures, which were then used to determine the $\Delta G°_{ads}$ and results are indexed in Table 6.7. The values of R^2 from the plots were around unity, which indicates strict isothermal compliance with the Langmuir adsorption isotherm. High K_{ads} values strongly imply a better ability of ALJCE to bond to Al, Zn, and MS surfaces when immersed in the 1 M HCl solution. It also indicates that corrosion only occurs on the part of the metal that is not protected by plant extracts. The K_{ads} values decreased with increasing ambient temperature for MS and Al surfaces, implying the decrease in the strength of the interaction between ALJCE and the two metal surfaces as a result of the desorption process when the system temperature is increased from 303 K to 333 K. While K_{ads} values for Zn increase with temperature, implying that the strength of adsorption increases with temperature, a behaviour associated with chemical adsorption. Negative $\Delta G°_{ads}$ values indicate a spontaneous adsorption mechanism on MS, Al, and Zn surfaces. The higher negative energy values of $\Delta G°_{ads}$ also indicate favourable adsorption of thermodynamically more stable extracts on the metal surface. It is generally accepted that $\Delta G°_{ads}$ values of -20 kJ mol^{-1} or less indicate a physisorption adsorption mechanism [470-472]. In such cases, the adsorption of the plant extracts on the metal surface is attributed to the electrostatic attraction between the charged extract molecules and the charged metal surface. About -40 kJ.mol^{-1} or more negative $\Delta G°_{ads}$ values indicate that charges (electrons) are shared or transferred from the inhibitor species to the metal surface to form a bond (i.e., chemisorption) [470-472]. The present work shows that the calculated $\Delta G°_{ads}$ values are neither at -20 kJ.mol^{-1} nor -40 kJ mol^{-1} but lie between the two ranges, which means that both physical and chemical adsorption processes occur on the surface of the three metals. For Al, however, the values are close to the -20 kJ mol^{-1} range, suggesting that the ALJCE acts primarily through a physical adsorption process to retard its dissolution.

The slope values for the three metal samples are at or near unity, with some variation, suggesting that the ALJCE adsorption process on these surfaces cannot be described by the Langmuir isotherm alone, as it does not represent the uptake of large interacting molecules or their adsorption ability at more than one active site on the metal surfaces. The Temkin adsorption isotherm has been plotted to describe such processes as outlined in equation 58. The R^2 values for the Temkin isotherm shown in Table 6.7 are close to unity, indicating that the extracts obey such an isotherm. The lateral interaction parameter "a" values show that up to 31 forms of interactions or extract components absorption onto the MS surface is possible.

Table 6.7: Gravimetric, EIS, and PDP Langmuir adsorption isotherm parameters for ALJCE-inhibited Al, MS, and Zn systems in 1 M HCl corrosive solution at different temperatures.

Metal	Isotherm	Method	T (K)	R^2	Slope	Intercept	K_{ads} (L.g^{-1})	$\Delta G°_{ads}$ (kJ.mol^{-1})	–a
MS	Langmuir	Weight loss	303	1	1.0170	0.00330	303.0303	−31.7975	–
			313	1	1.0100	0.03095	32.3102	−27.0215	
			323	0.998	0.9261	0.08285	12.0700	−25.2404	
			333	0.996	0.8845	0.14100	7.0922	−24.5496	
		PDP	303	0.999	1.0241	0.03605	27.7393	−25.7739	
		EIS	303	0.999	1.0185	0.03536	28.2805	−25.8226	
	Temkin	Weight loss	303	0.979	0.0158	0.98095	1.2176×10^{62}	−377.5537	31.6456
			313	0.942	0.1709	0.97828	5.3004×10^{5}	−52.2790	2.9257
			323	0.945	0.4047	1.02733	3.4557×10^{2}	−34.2491	1.2355
			333	0.965	0.5472	1.01207	7.0706×10^{1}	−30.9164	0.9137
		PDP	303	0.934	0.1392	0.94804	6.4672×10^{6}	−56.9109	3.5920
		EIS	303	0.971	0.1546	0.95841	1.5826×10^{6}	−53.3645	3.2342
Zn	Langmuir	Weight loss	303	1	2.2250	0.05035	19.8610	−24.9322	–
			313	0.999	1.4921	0.04295	23.2829	−26.1688	
			323	1	1.2203	0.03845	26.0078	−27.3020	
			333	1	1.0702	0.05110	19.5695	−27.3598	
		PDP	303	1	1.0094	0.01240	80.6452	−28.4625	
		EIS	303	1	1.0391	0.01070	93.4579	−28.8340	
	Temkin	Weight loss	303	0.933	0.0486	0.44261	1.2801×10^{9}	−70.2328	10.2881
			313	0.957	0.0833	0.65524	7.3456×10^{7}	−65.1129	6.0024
			323	0.968	0.1377	0.80727	7.2871×10^{5}	−54.8041	3.6311
			333	0.954	0.2259	0.91348	1.1061×10^{4}	−44.9058	2.2134
		PDP	303	0.899	0.0518	0.97994	8.2745×10^{18}	−127.1424	9.6525
		EIS	303	0.884	0.0424	0.95357	3.0899×10^{22}	−147.8646	11.7925
Al	Langmuir	Weight loss	303	0.999	1.0511	0.0294	34.0136	−26.2876	–
			313	0.998	1.3632	0.05935	16.8492	−25.3271	
			323	0.9838	1.5523	0.13165	7.5959	−23.9967	
			333	1	2.8558	0.1094	9.1408	−25.2522	
		PDP	303	0.9431	0.6674	0.26910	3.7161	−20.7097	
		EIS	303	0.998	0.9583	0.0643	15.5521	−24.3161	
	Temkin	Weight loss	303	0.905	0.1229	0.93278	3.8874×10^{7}	−61.4294	4.0683
			313	0.948	0.1281	0.70805	3.3676×10^{5}	−51.0986	3.9032
			323	0.724	0.1537	0.59126	7.0284×10^{3}	−42.3395	3.2531
			333	0.925	0.0740	0.34506	4.6026×10^{4}	−48.8534	6.7568
		PDP	303	0.809	0.1419	0.98728	9.0690×10^{6}	−57.7627	3.5236
		EIS	303	0.960	0.2891	0.99732	2.8166×10^{3}	−37.4141	1.7295

These values decrease for all three metals with increasing system temperature, suggesting that temperature drives the extracts components' desorption from the metals' surface. Temkin $\Delta G°_{ads}$

values go beyond the –40 kJ.mol^{-1} value associated with the chemical adsorption process; this indicates that the lateral interaction of the adsorbed species contributes significantly to the inhibition process leading to high protection efficiencies as suggested by the values of the lateral interaction parameter.

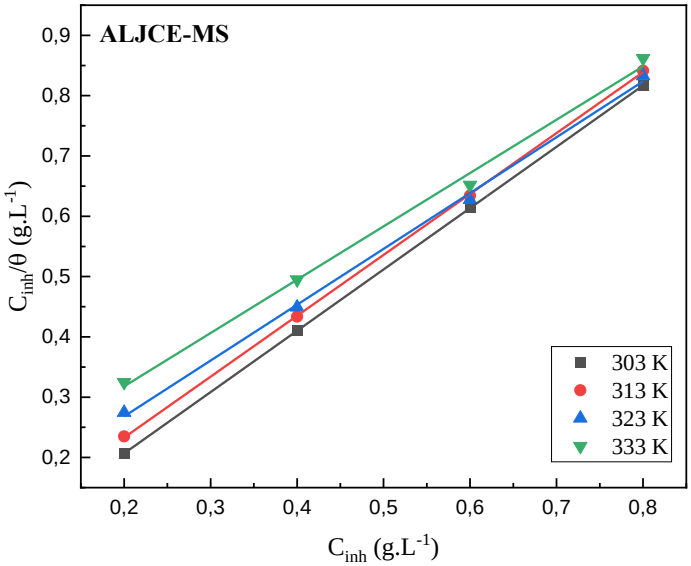

Figure 6.32: Langmuir adsorption isotherm plots for MS corrosion in 1 M HCl in the presence of various concentrations of ALJCE

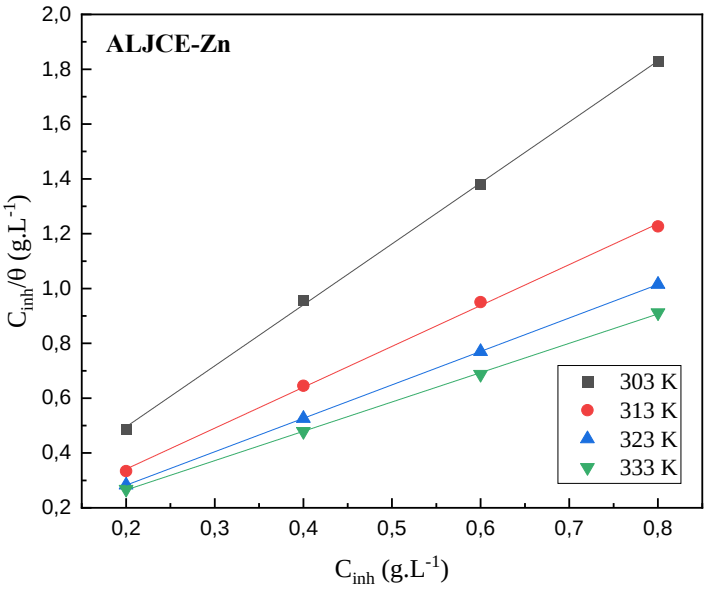

Figure 6.33: Langmuir adsorption isotherm plots for Zn corrosion in 1 M HCl in the presence of various concentrations of ALJCE

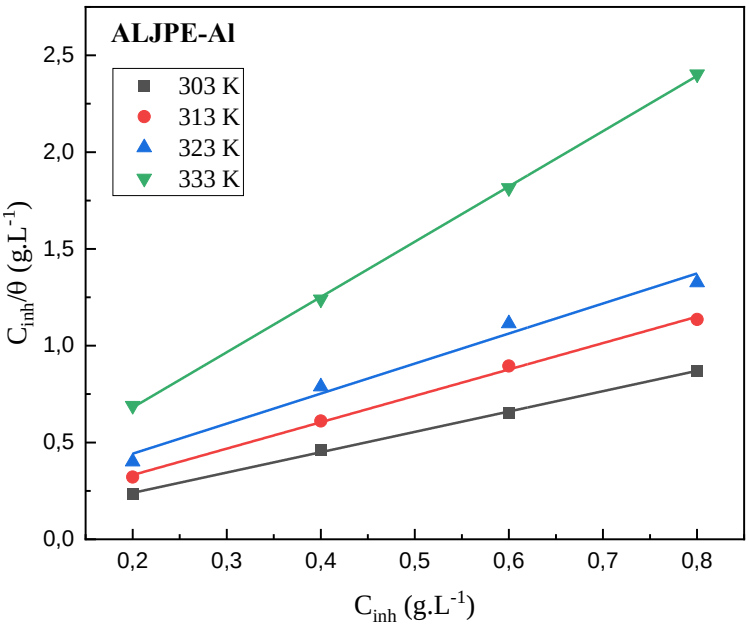

Figure 6.34: Langmuir adsorption isotherm plots for Al corrosion in 1 M HCl in the presence of various concentrations of ALJCE

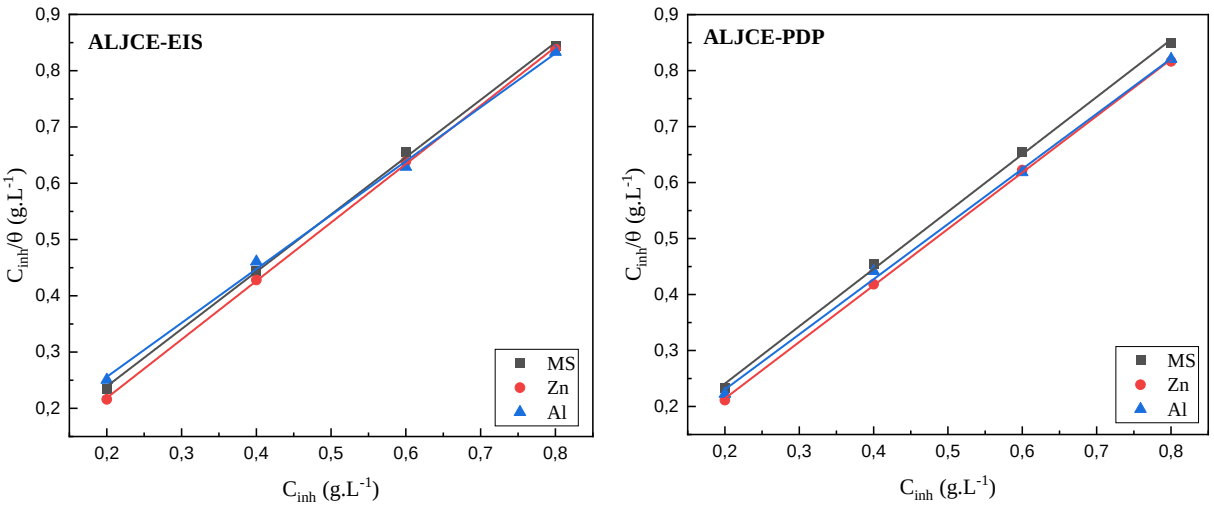

Figure 6.35: Langmuir adsorption isotherm plots for MS, Zn, and Al corrosion in 1 M HCl in the presence of various concentrations of ALJCE

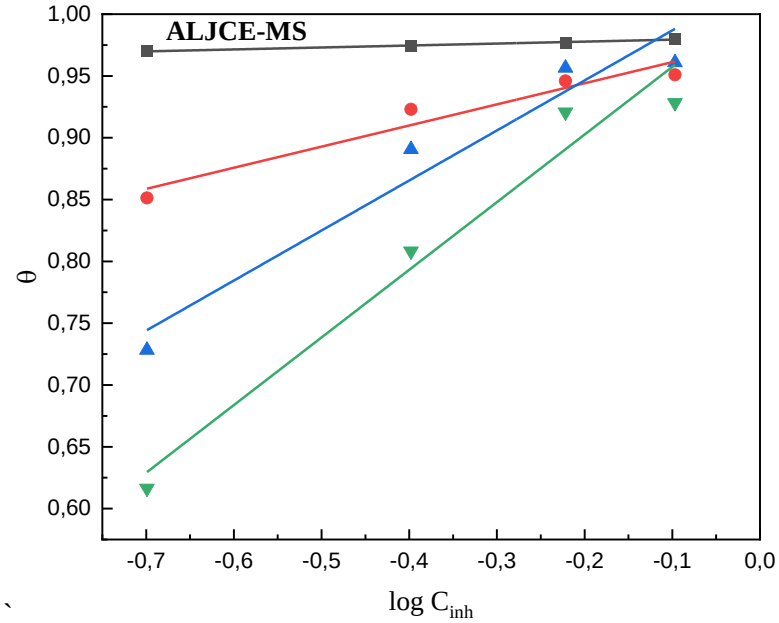

Figure 6.36: Temkin adsorption isotherm plots for MS corrosion in 1 M HCl in the presence of various concentrations of ALJCE

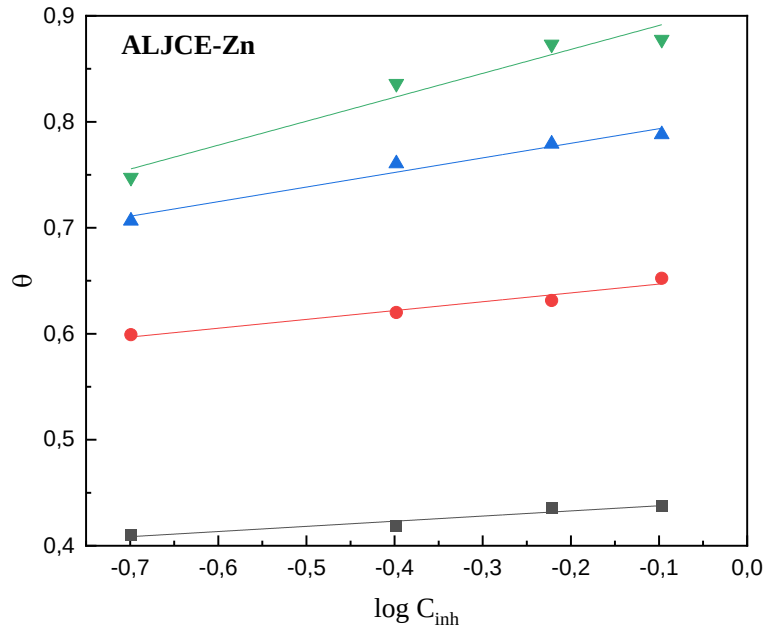

Figure 6.37: Temkin adsorption isotherm plots for Zn corrosion in 1 M HCl in the presence of various concentrations of ALJCE

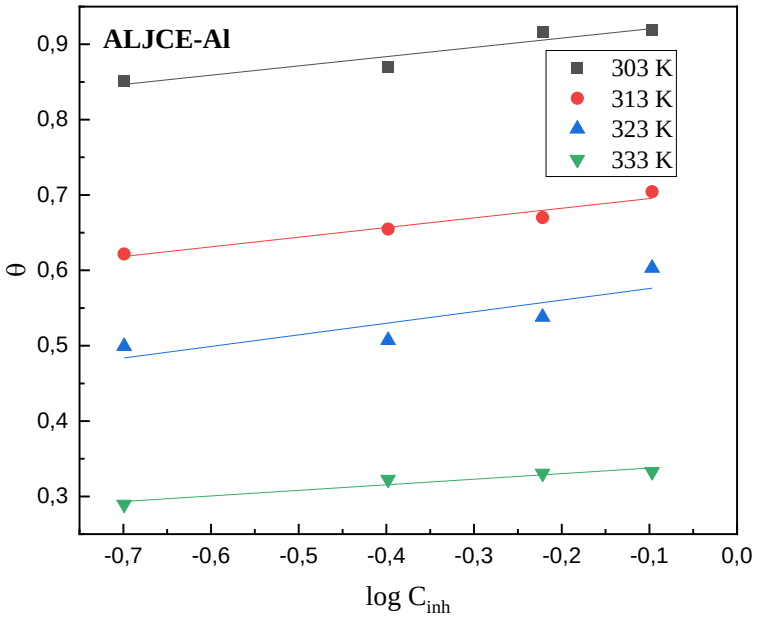

Figure 6.38: Temkin adsorption isotherm plots for Al corrosion in 1 M HCl in the presence of various concentrations of ALJCE

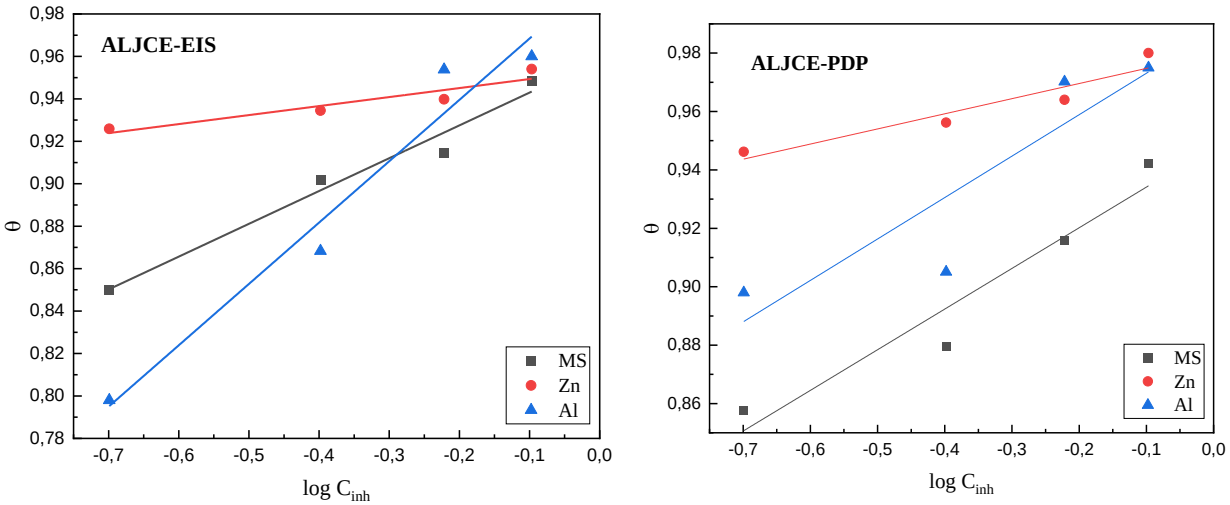

Figure 6.39: Temkin adsorption isotherm plots for MS, Zn, and Al corrosion in 1 M HCl in the presence of various concentrations of ALJCE

The physical property of the adsorption isotherm, K_L, was also considered to evaluate the fitness of the surface coverage data to the Langmuir adsorption isotherm in addition to the slope and R^2 values [469, 474, 475]. When $K_L > 1$ or $K_L = 1$, the adsorption process is unfavourable or

considered irreversible and does not agree with the Langmuir adsorption isotherm [475]. If K_L < 1, the experimental data are favourable and fit the Langmuir adsorption isotherm. The results in Table 6.8 show that the K_L values are less than one, implying that the Langmuir adsorption isotherm can interpret the adsorption process of ALJPE on the Al, Zn and MS surfaces.

Table 6.8: The K_L values for ALJCE at varying concentrations at 303 to 333 K for MS, Al and Zn corrosion in 1 M HCl calculated from weight loss Langmuir isotherm parameters

Metal	Conc. of MLJCE (ppm)	K_L			
		303 K	313 K	323 K	333 K
MS	200	0.0162	0.1340	0.2929	0.4135
	400	0.0082	0.0718	0.1716	0.2606
	600	0.0055	0.0491	0.1213	0.1903
	800	0.0041	0.0372	0.0938	0.1498
Mean		0.0085	0.0730	0.1699	0.2536
Zn	200	0.2011	0.1768	0.1612	0.2035
	400	0.1118	0.0970	0.0877	0.1133
	600	0.0774	0.0668	0.0602	0.0785
	800	0.0592	0.0510	0.0459	0.0600
Mean		0.1124	0.0979	0.0888	0.1138
Al	200	0.1282	0.2288	0.3970	0.3536
	400	0.0685	0.1292	0.2476	0.2148
	600	0.0467	0.0900	0.1799	0.1542
	800	0.0354	0.0691	0.1413	0.1203
Mean		0.0697	0.1293	0.2414	0.2107

6.8. FTIR analysis of the ALJCE adsorption layer formed on the surface of Al, MS, and Zn in the 400-4000 cm^{-1} range

The ALJCE functional groups responsible for the inhibition of Zn, Al and MS corrosion were analyzed using FTIR. The resulting spectra were compared to those of a blank and their respective corrosive solutions. The FTIR spectra of the blank and inhibitor solutions for all three metal samples showed the same peaks as those of liquid water, which was expected since water produces intense and broad absorption bands in the mid-infrared range. The O–H peak around 3000–4000 cm^{-1} and a small, less intense peak at 2000 cm^{-1} due to the coupling of the scissor bending and a near-infrared liberation band are examples of such peaks [480, 483]. Around the 1600 cm^{-1} region, there is a peak caused by the scissors bending of the water molecule (H–O–H) and small peaks caused by vibrations in the fingerprint region [374]. As a result, the FTIR spectrum of the adsorption film formed on the metal surfaces was compared with that of the bare metal surface (blank) to determine the ALJCE functional groups responsible for reducing the corrosion rate of MS, Zn and Al, and the results are shown in Figure 6.40–6.42. Figure 6.40 shows the presence of a broad peak around the 3265 cm^{-1} regions in the ALJCE–MS adsorption film spectrum. This peak is less intense than that of the O–H peak of the corrosive solutions of the inhibited and uninhibited systems, indicating that it is caused by the interaction of the ALJCE's hydroxyl group with the MS surface (MS–OH). This is supported by the disappearance of the intense scissor peak of around wavenumber 1620 cm^{-1} and the appearance of a new broad distinct peak around 1350–1665 cm^{-1}, indicating the involvement of carboxyl or aldehyde functional groups (i.e., flavonoids) in the adsorption process on the MS surface, resulting in the decrease in its corrosion rate. There is also the appearance of two new peaks around the 650 and 820 $cm^{-1,}$ which are said to be due to the Fe–O bond and the α–FeOOH corrosion products. The ALJCE–Zn adsorption film spectrum indicates the reduction in the intensity of the $ZnO_3.\times H_2O$ peak found at about 3350 cm^{-1} to a narrower peak in the presence of ALJCE which shows that the extract was successful in reducing the C_R of Zn. This could have been caused by the crude extract's O–H and N–H groups. The adsorption of ALJCE on the Zn surface can also be attributed to two new peaks that appeared at around 1647 and 1606 $cm^{-1,}$ which might be from the binding of the C=O, COO^-, C–O, or the C=C groups onto the Zn surface. Around 820 $cm^{-1,}$ there is a new small peak (ALJCE–Zn adsorption film); such a peak was not observed in the blank–Zn corrosion products spectrum. This peak can be attributed to the interaction of the ALJCE with the Zn surface through the C=C groups of the aromatic rings.

The absorption bands in the 450–820 cm^{-1} region correspond to the passivating Zn oxide layers, which are formed during the corrosion process of Zn in 1 M HCl. The passivation layers protect the Zn surface from further degradation by the aggressive ions in acidic solutions [170]. The blank-Al corrosion products spectrum is also identical to that of liquid water except for the two peaks identified at 1151 and 502 $cm^{-1,}$ which in our previous paper [555] on the inhibition of Al, these peaks were stated to represent the γ–AlO_4 and γ–AlO_6, respectively, indicating the presences of both octahedral and tetrahedral coordination of alumina in γ–Al_2O_3 [500]. The ALJCE-Al adsorption spectrum is distinctively different from the other spectra showing the participation of ALJPE in the dissolution process of Al. The spectrum showed a reduction in the intensity of the $Al_2O_3.\times H_2O$ peak found at about 3000–4000 cm^{-1} to a narrower peak. This indicates that the presence of ALJPE in the corrosive solution decreased Al's C_R, which the O–H group could have caused in the crude extract. A less intense peak at 1620 cm^{-1} is evidence that the ALJPE adsorption layer protected the Al surface since this peak can be linked to the scissor band of water molecules. Additionally, the uniqueness of this peak from that of water could be the result of the interaction of ALJPE with the Al surface via the C=O and C=C groups (Figure 6.43). The characteristic absorption bands around the 1496 and 1406 cm^{-1} can be linked to the adsorption of ALJPE via the S=O, C–H C=C, and =C–O–C functional groups in the extract. The absorption band observed around 1151 cm^{-1} in the blank-Al corrosion products spectrum has shifted to around 900 cm^{-1} in the presence of ALJPE, while the peak at 502 cm^{-1} has shifted to higher transmittance value. This indicates that the extract successfully altered the formation of both the octahedral and tetrahedral coordination of alumina.

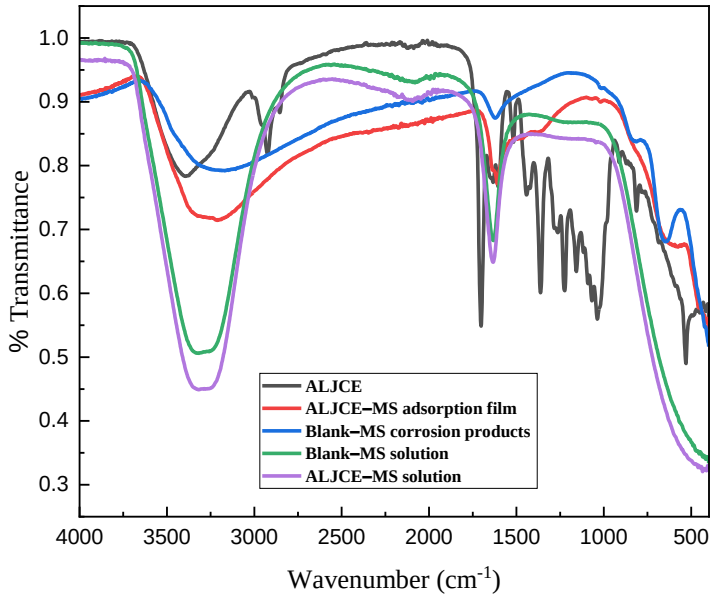

Figure 6.40: FT-IR spectrum of the adsorption film formed on the MS surface (ALJCE-MS adsorption film) compared to the crude ALJCE, corrosion products formed on MS (Blank-MS corrosion products), the 1 M HCl corrosion solution in the presence (ALJCE-MS solution) and absence (Blank-MS solution) of ALJCE

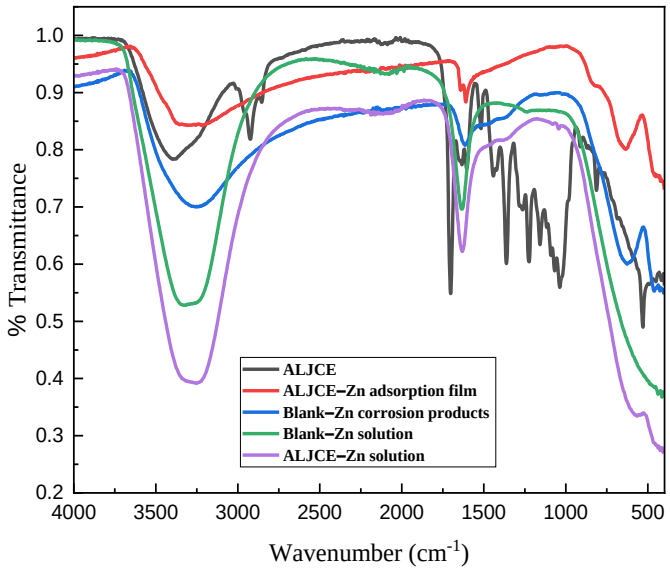

Figure 6.41: FTIR spectrum of the adsorption film formed on the Zn surface (ALJCE-Zn adsorption film) compared to the crude ALJCE, corrosion products formed on Zn (Blank-Zn corrosion products), the 1 M HCl corrosion solution in the presence (ALJCE-Zn solution) and absence (Blank-Zn solution) of ALJCE

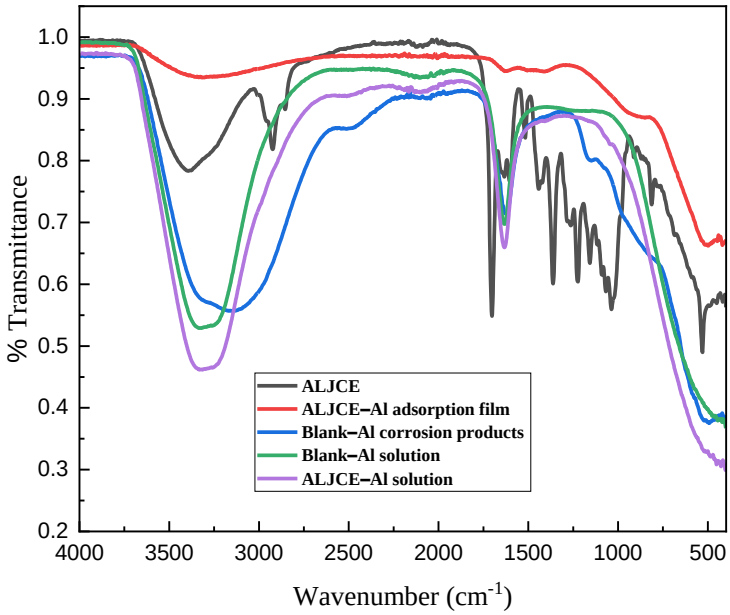

Figure 6.42: FTIR spectrum of the adsorption film formed on the Al surface (ALJCE-Al adsorption film) compared to the crude ALJCE, corrosion products formed on Al (Blank-Al corrosion products), the 1 M HCl corrosion solution in the presence (ALJCE-Al solution) and absence (Blank-Al solution) of ALJCE

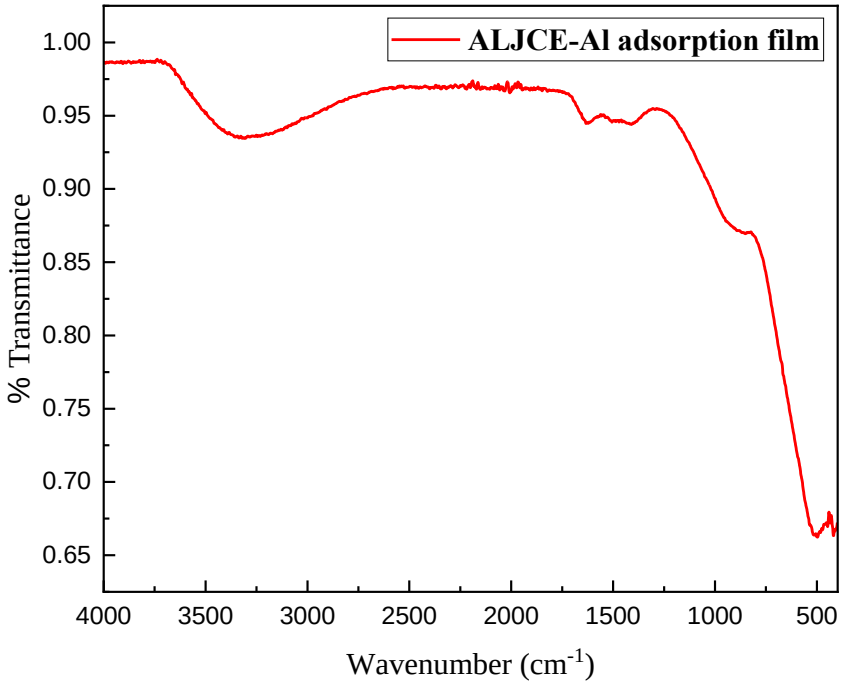

Figure 6.43: Expanded FTIR spectrum of the adsorption film formed on the Al surface (ALJCE-Al adsorption film)

6.9. UV-visible spectroscopy: Interaction of MLJCE with Al^{3+}, Fe^{2+} and Zn^{2+} cations

Plant extracts contain chromophores, molecules that absorb light at a specific frequency and thus give colour to a molecule [87]. Figures 6.44–6.42 show the UV-vis spectrum in terms of wavelength and absorbance obtained for ALJCE dissolved in the acidic solution (ALJCE in 1 M HCl) without the immersion of the metal samples. The spectra obtained after immersing the metal samples in the corrosive 1 M HCl solution with optimal concentration (800 ppm) of the extract for 7 hours are shown by ALJCE–Fe^{2+}, ALJCE–Al^{3+} and ALJCE–Zn^{2+}. As a control, in addition to the 1 M HCl solution, the Zn, Al, and MS samples immersed in the acidic solution (1 M HCl + Zn^{2+}) without the inhibiting extract (Blank–Fe^{2+}, Blank–Zn^{2+} and Blank–Al^{3+}) for 7 hours were analyzed. The ALJCE spectra fingerprint shows a significant change in the shape of the spectra after contact with the immersed Zn, Al, and MS samples, indicating that the extract adsorbs onto the metal surfaces and prevents their dissolution. The Blank–Zn^{2+} spectrum shows two bands at 209 and 227 nm, the intensity of which is significantly reduced in the presence of the extract. This indicates the adsorption of ALJCE on the Zn surface and is supported by absorption bands at 218 and 237 nm (ALJCE–Zn^{2+}) that have decreased in intensity compared to the spectrum of ALJCE in 1 M HCl. A more prominent band, indicative of ALJCE binding to the Zn surface, is shown at about 339 nm. Other notable absorption bands, indicating binding of the extract to the Zn surface and formation of the ALJCE–Zn^{2+} complex, are observed at 663, 418 nm regions. The bands responsible for the inhibition of Zn corrosion can be assigned to the $n \rightarrow \pi^*$ and $\pi \rightarrow \pi^*$ transitions [88, 89]. The UV traces for MS and Al (Figures 6.44 and 6.46) show that the long-wavelength band observed before immersion of the two metals in a corrosive solution containing ALJPE molecules was shifted from the 215–290 to 265–366 nm regions due to a bathochromic shift produced by the introduction of the metals. These absorbance peaks could be interpreted as indicating the presence of π–π^* and n–π^* transitions, which could result from the C=C, O–H and C=O groups present in the plant extract [502, 503]. The shift in the long-wavelength band (265–366 nm) also indicates intramolecular electron transfer from a ligand to ALJCE components [505-507]. Other absorption peaks around the 418 and 663 nm that point to the adsorption of ALJPE onto the Al and Zn surface may be due to the n–p* transitions of carbonyl and other functional groups found in the extract [588, 589].

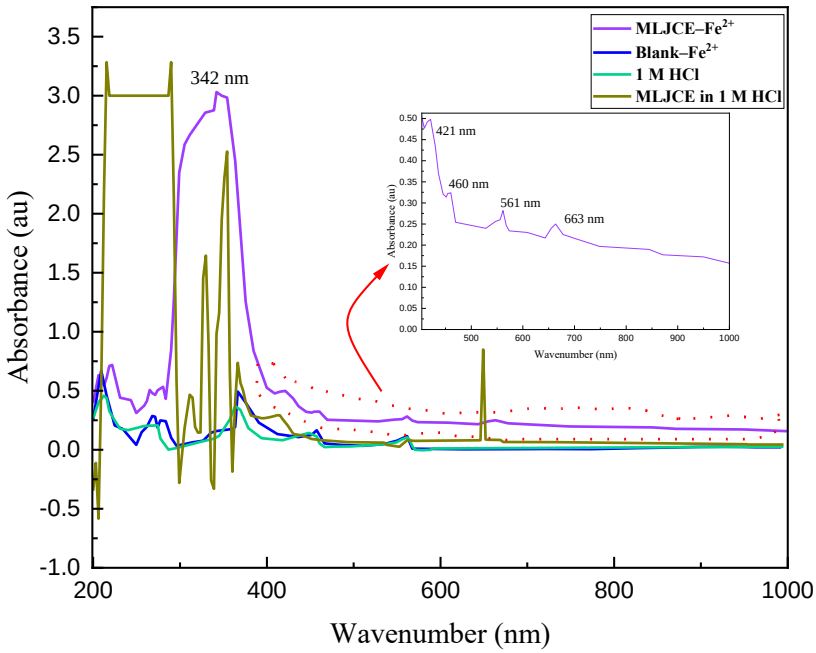

Figure 6.44: UV-vis spectra for 1 M HCl solution without and with ALJCE before immersion of the metal sample (ALJCE in 1 M HCl), after immersion (ALJCE–Fe^{2+}), and the sample without ALJCE (Blank–Fe^{2+})

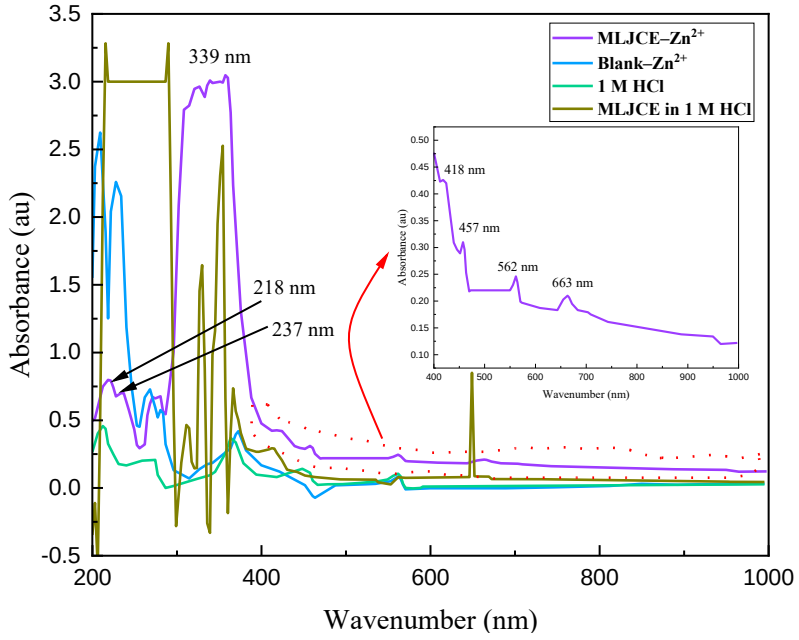

Figure 6.45: UV-vis spectra for 1 M HCl solution without and with ALJCE before immersion of the metal sample (ALJCE in 1M HCl), after immersion (ALJCE–Zn^{2+}), and the sample without ALJCE (Blank–Zn^{2+})

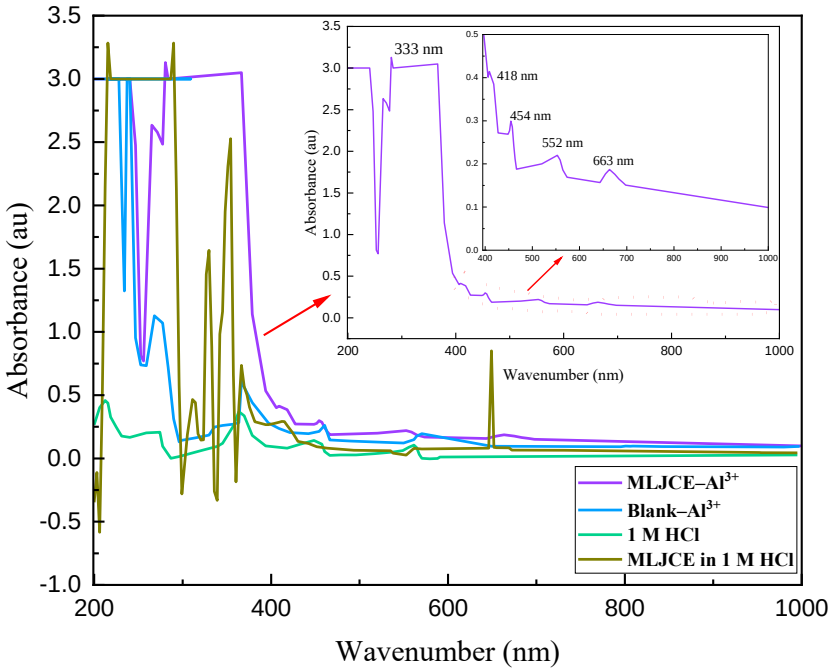

Figure 6.46: UV-vis spectra for 1 M HCl solution without and with ALJCE before immersion of the metal sample (ALJCE in 1M HCl), after immersion (ALJCE–Al^{3+}), and the sample without ALJCE (Blank–Al^{3+})

6.10. Water contact angle measurement

The polarity of the water molecules and the surface sites, impurities, and the roughness of the metal surface all affect the contact angle between a static water droplet and the metal surface, and these factors can be used to verify the binding of an inhibitor on the surface of a metal [634]. Figures 6.47–6.49 shows contact angle images of the surfaces of the Zn, MS, and Al coupons in the uninhibited acid test solution, the surface inhibited by ALJCE adsorption, and the polished untreated surface. The contact angle of water droplets was determined to be 82.403, 93.647, and 66.314° for the polished untreated MS, Zn, and Al surfaces, respectively, but when exposed to the corrosive solution in the absence of the plant extracts, the contact angles decreased to 67.546, 73.257, and 47.956°. Other authors found similar results [564, 634], where the contact angles were high for the bare (untreated) metal, decreased in the unconstrained acidic solution, and increased in the presence of the inhibitor. Generally, a metal surface is considered hydrophilic when the water droplet contact angle is less than 90°, and when it is greater than 90°, the contact angle is hydrophobic [635, 636]. The reduction in the water droplet contact angles when the Zn, MS and Al surfaces were exposed to the 1 M HCl solution indicates that the surfaces have become more

hydrophilic than their polished, unexposed counterparts. This shows that the acidic solution severely damaged the surfaces, allowing the water droplet to spread over the large area of the surfaces. The addition of ALJCE to the corrosive solution had the opposite effect as the metallic surfaces became hydrophobic, indicating the decrease in its wettability, implying that ALJCE formed a protective film on the Zn, MS, and Al surfaces.

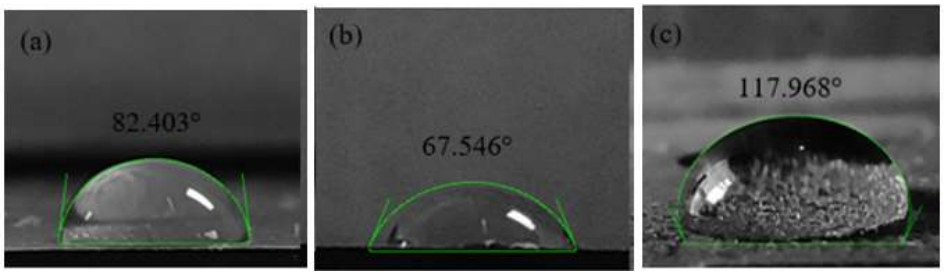

Figure 6.47: Surface wettability behaviour of (a) polished untreated MS substrate, (b) MS substrate after 7 hours of immersion in 1 M HCl medium with no inhibitor, and (c) in the presence of 800 ppm of ALJCE

Figure 6.48: Surface wettability behaviour of (a) polished untreated Zn substrate, (b) Zn substrate after 7 hours of immersion in 1 M HCl medium with no inhibitor, and (c) in the presence of 800 ppm of ALJCE

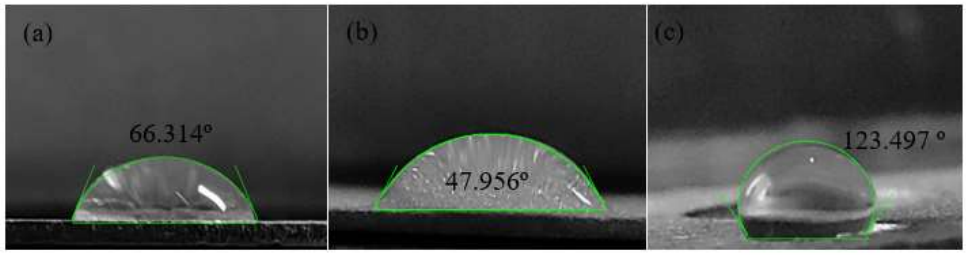

Figure 6.49: Surface wettability behaviour of (a) polished untreated Al substrate, (b) Al substrate after 7 hours of immersion in 1 M HCl medium with no inhibitor, and (c) in the presence of 800 ppm of ALJCE

6.11. SEM/EDS and Elemental Mapping

Figures 6.50, 6.52, and 6.54 show the untreated, polished MS, Zn, and Al metal samples in the form of SEM images, which are smooth and show minor scratches created during preparation. The roughness of the surfaces suggests that they were corroded after immersion in the 1 M HCl solution (MS, Zn, and Al immersed in 1 M HCl), as the surfaces appeared very rough and badly damaged. The Al corroded surface had more visible cracks and pits than the Zn and MS surfaces, implying that Al suffered from pitting while MS and Zn suffered from a uniform form of corrosion. However, immersing the three metal surfaces in 1 M HCl solution in the presence of 800 ppm ALJCE revealed smoother surfaces, indicating that the rate of deterioration and surface damage was significantly reduced. The smoothness of the surfaces in the presence of ALJCE is due to the formation of protective inhibitor films onto the Al, MS, and Zn surfaces. The elemental composition of polished but untreated metal surfaces and those immersed in 1 M HCl with and without ALJCE was determined using EDS, and the results are displayed alongside the SEM micrographs. The EDS spectrum of Zn was the most affected by immersion in the corrosive solution with and without extracts of the three metal samples. The spectrum indicated a high Zn concentration prior to immersion in the corrosive solution. However, when the sample was immersed in 1 M HCl solution, there was no such peak. In contrast, a minute Zn peak was observed when exposed to the corrosive solution containing the ALJCE. The lack of a Zn peak without the extracts could be due to the dissolution and destruction of the plated Zn layer. However, the low Zn peak in the presence of 800 ppm ALJCE suggests that the destruction of the Zn layer or element was prevented due to the protective film formed by the plant extract [637]. Some island regions were observed on the metal surfaces exposed to 1M HCl with ALJCE. These were analyzed by elemental mapping to gather information on the element responsible for corrosion inhibition and compared to that obtained for the blank solutions, as shown in Figures 6.51, 6.53, and 6.55. EDS analysis revealed that oxygen and carbon were the elements affected significantly by the presence of ALJCE in the corrosive solution for all three metals, indicating the adsorption of extracted components on the surfaces of the three metals [514, 638].

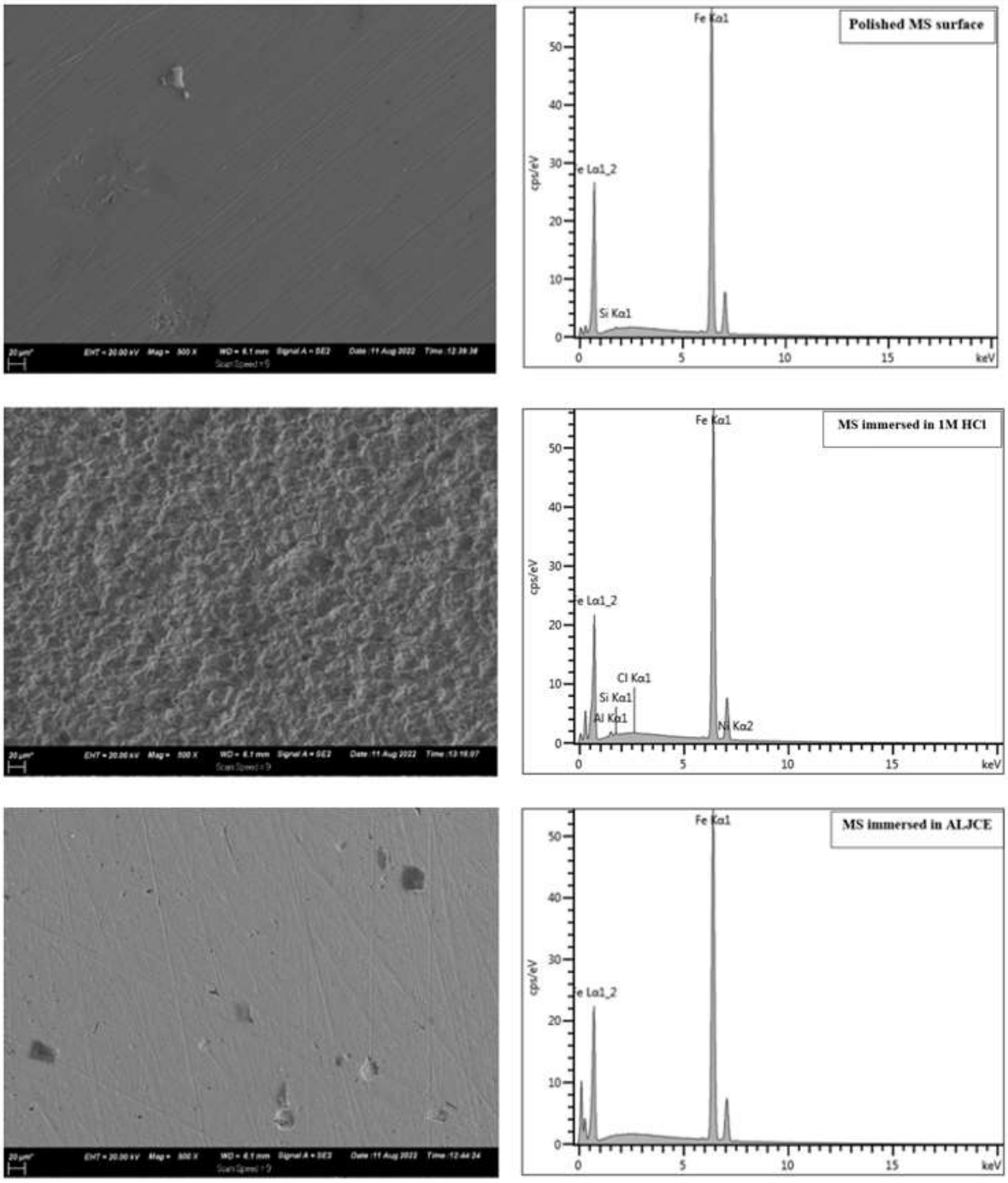

Figure 6.50: SEM images and EDS spectra of unexposed-polished MS surface, MS immersed in uninhibited 1 M HCl, and MS immersed in ALJCE-inhibited 1 M HCl solution

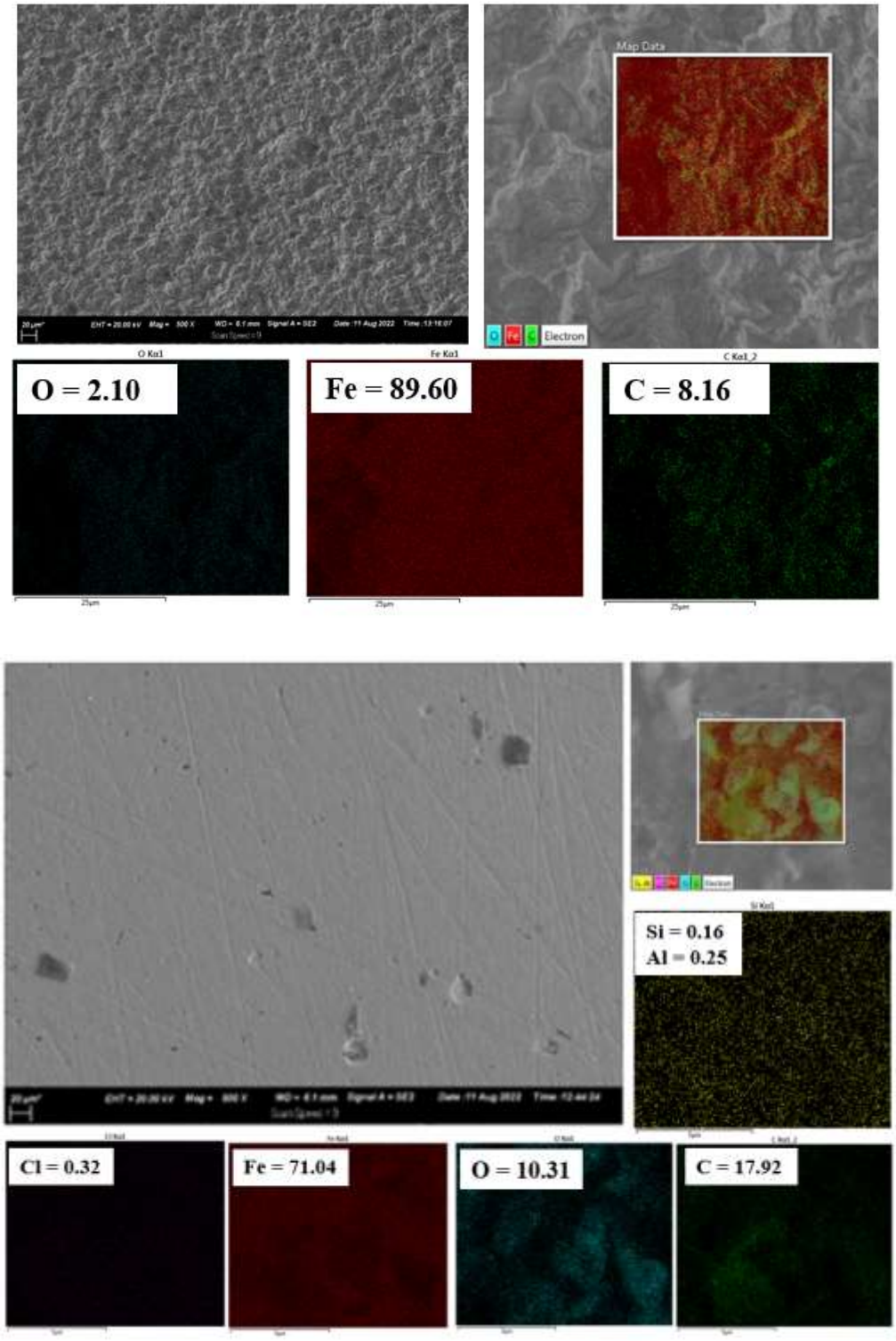

Figure 6.51: EDS map analyses for MS exposed to the corrosive solution in the (a) absence of the extract and the (b) presence of 800 ppm of the extract

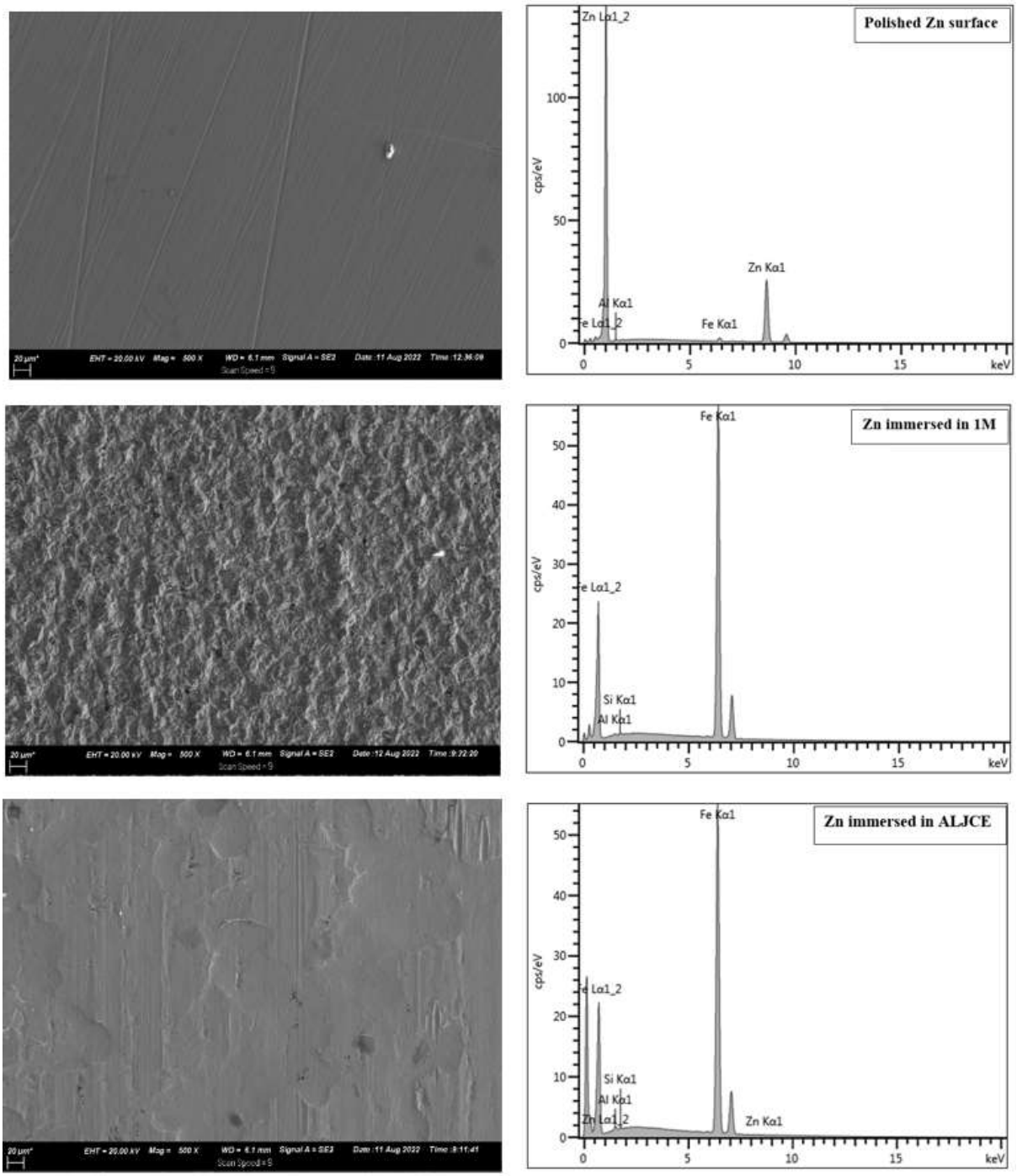

Figure 6.52: SEM images and EDS spectra of unexposed-polished Zn surface, Zn immersed in uninhibited 1 M HCl, and Zn immersed in ALJCE-inhibited 1 M HCl solution

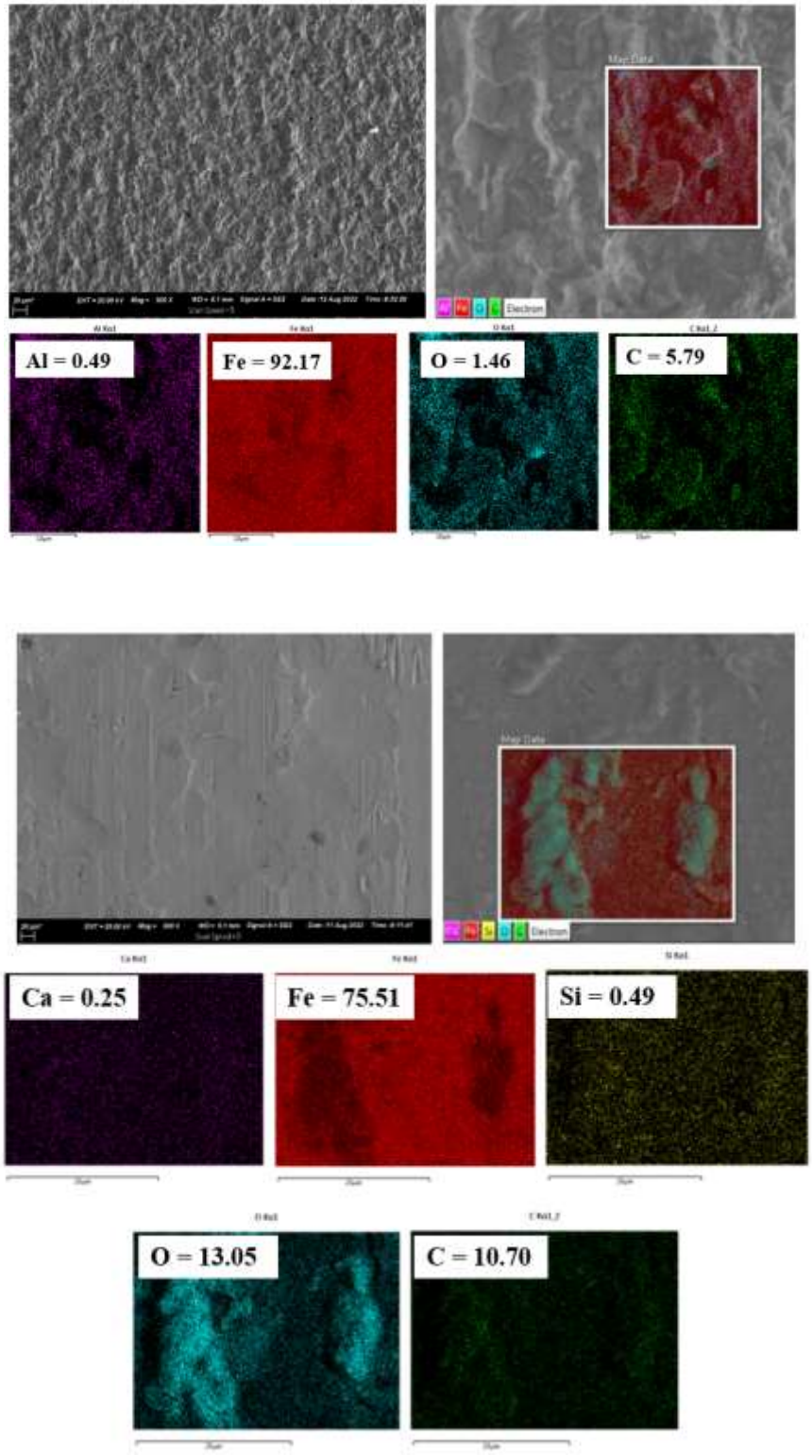

Figure 6.53: EDS map analyses for Zn exposed to the corrosive solution in the (a) absence of the extract and the (b) presence of 800 ppm of the extract

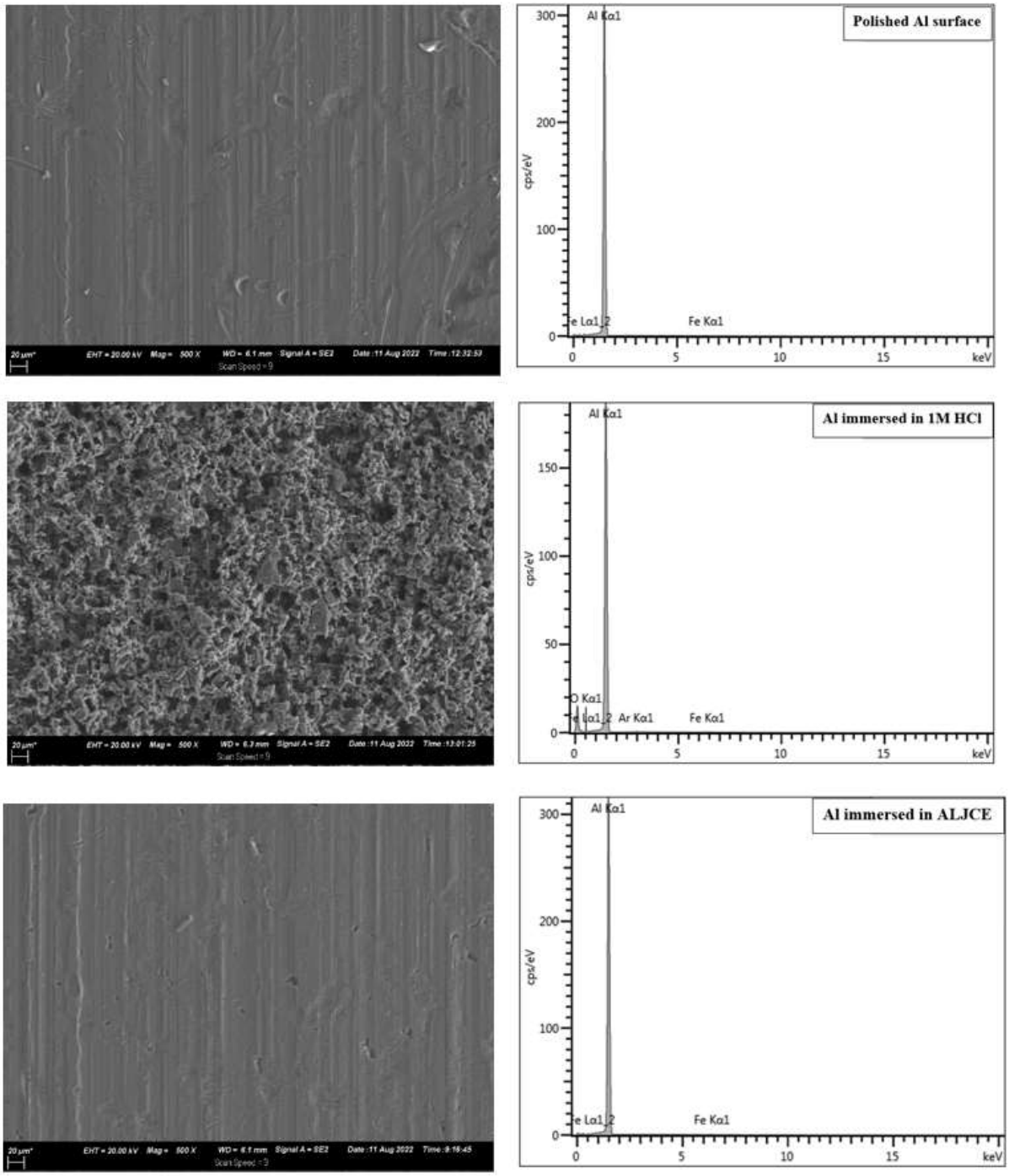

Figure 6.54: SEM images and EDS spectra of unexposed-polished Al surface, Al immersed in uninhibited 1 M HCl, and Al immersed in ALJCE-inhibited 1 M HCl solution

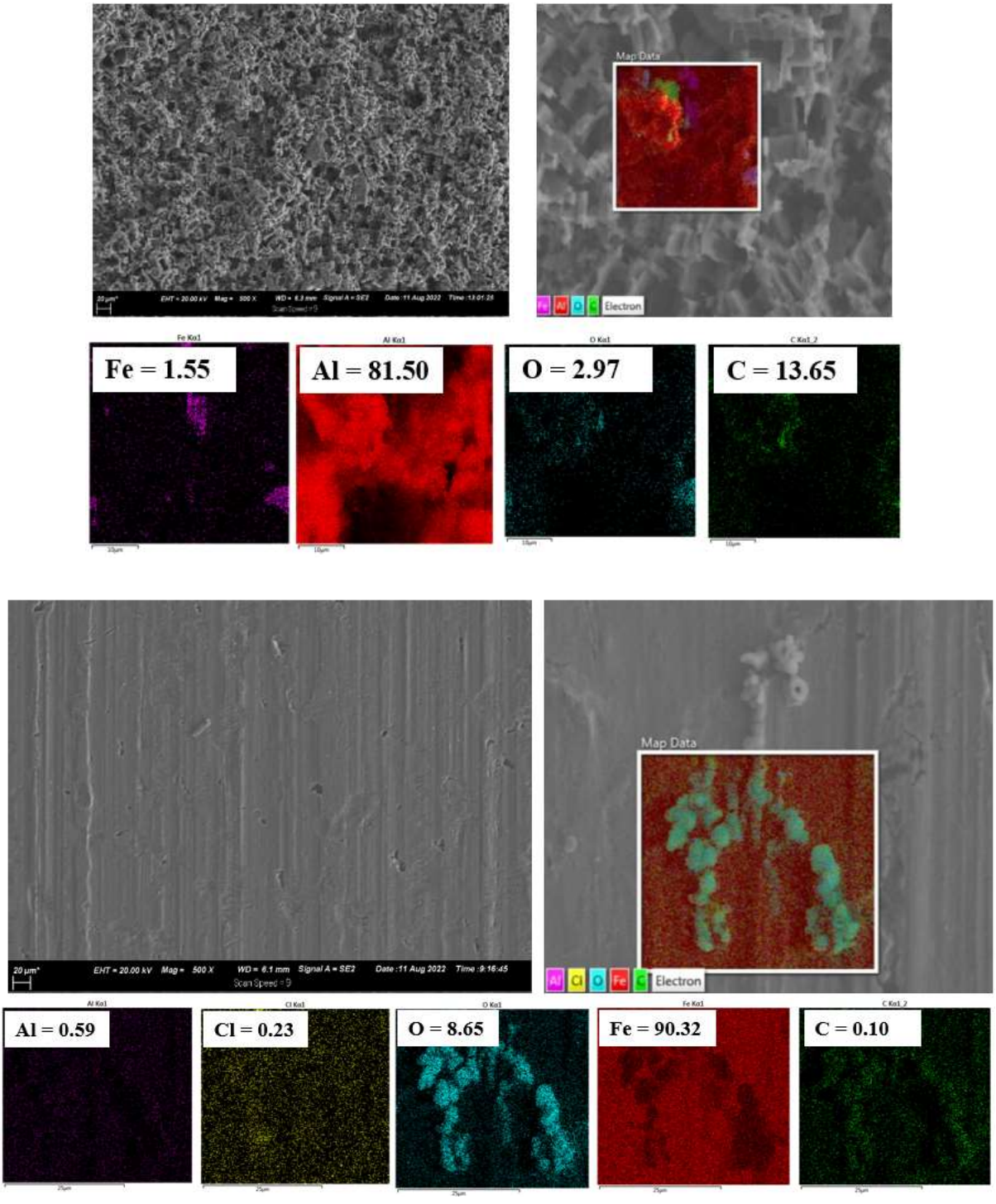

Figure 6.55: EDS map analyses for Al exposed to the corrosive solution in the (a) absence of the extract and the (b) presence of 800 ppm of the extract

CHAPTER 7

Verbascoside binding process results and discussions

The main metabolite isolated from the three extracts was theoretically evaluated using quantum chemical calculations to determine the stable binding geometry that produces the highest binding energies of the Fe, Zn, and MS surfaces. A corrosion inhibition mechanism by which the plant extracts could have prevented the three metals from corroding has also been proposed.

7. Quantum chemical studies on the interaction between *L. javanica* components and the metal surfaces of Al, MS, and Zn

Adsorption is a chemical bonding process between a solid surface and a molecule via an exothermic process, generating heat as the mixture components are adsorbed [639], favouring configurations that minimize Gibbs's free energy. When adsorbing molecules on metal surfaces, care must be taken to select suitable model surface plates for such metals. This is achieved by selecting the lowest energy, most stable surfaces, as they are most likely to be the predominantly exposed crystal faces in a realistic system. The face-centred cubic (FCC) surface plane chosen for the study on the Al surface was Al(111), as it is believed to be one of the most stable planes for this metal [640]. The body-centred cubic (BCC) flat surface of Fe(110) was chosen because it has the lowest energy [641], indicating that it is the dominant surface on real Fe crystals [642]. The Zn(110) surface was chosen for Zn because it is one of the most commonly reported surfaces in the literature [643, 644]. The complex nature of the chemical makeup of the *L. javanica* plant makes it difficult to ascribe its inhibitory activity to a single specific component. For example, the plant contains a wide range of compounds that can be extracted and isolated, with up to 173 combinations identified in one study [645]. Therefore, the contribution to corrosion inhibition through the mutual influence of the connections and their interaction cannot be ruled out. VBS is a compound abundant in *L. javanica* extracts obtained from methanol, ethanol and acetone solvents, and the high antioxidant activities of the plant can be attributed in part to it [515]. Therefore, this work investigates the binding structures and energies between VBS and the Al(111), Zn(110), and Fe(110) surfaces using quantum mechanical methods and DFT to find the highest energy adsorption sites. The adsorption properties of VBS on the MS, Al, Zn surfaces have been simulated in both vacuum and solution phases to simulate a realistic situation and the results are discussed below:

7.1. Binding structures and energies of the VBS/Al(111) system

Four interaction sites were evaluated for the solution phase (VBS1 to VBS4) and for the vacuum phase (VBS5 to VBS8) to discern the equilibrium adsorption configuration of VBS on the Al(111) surface, and the PBE-optimized geometry structures are shown in Figure 7.1. The calculated interaction and binding energies obtained through equation 30 are listed in Table 7.1. It can be seen from Figure 7.1 that the optimization configurations of VBS/Al(111) in the solution phase resulted in higher binding energies compared to the vacuum phase [646]. For instance, the VBS2

binding structure produced the highest binding energy (114.620 kcal/mol) for the solution phase. It occurred preferentially through the phenylethanoid group with the oxygen atom near the Al surface (Al−O43).

In comparison, the VBS8 binding structure resulted in the highest binding energy (86.939 kcal/mol) for the vacuum phase and occurred through the hydroxy group located at carbon 31. The parallel adsorption configurations (VBS1 and VBS8) in the two different environmental conditions suggest that this is the best binding configuration to ensure that the VBS molecules cover a larger surface area of the Al surface. The other adsorbed geometries at different adsorption sites for the two phases also showed high binding energies with the oxygen atom close to the Al surface. Binding energies can be interpreted to indicate whether the mode of adsorption is physisorption or chemisorption. Chemisorption has been linked to high binding energies, which are thought to occur in conjunction with physisorption when the molecule of interest is close to the metal surface [647]. The interaction of oxygen in its 2p state with the sp band of a metal, such as Al, results in chemisorption. [647]. It has been reported that binding energy of about 13 kcal/mol indicates chemisorption [647]. All eight binding geometries revealed binding energies greater than 13 kcal/mol for the VBS/Al(111) systems, indicating a chemical binding process.

Table 7.1: Calculated optimized energies for stable VBS adsorption sites on Al(111) surface

Environment	System	d_{Al-O} (Å)	h (Å)	E_{int} (kcal/mol)	E_{bind} (kcal/mol)
Solution Phase	VBS1/Al(111)	3.321	(Al−H) 2.879	−112.937	112.937
	VBS2/Al(111)	2.590	(Al−O) 2.590	−114.620	114.620
	VBS3/Al(111)	3.153	(Al−H) 3.079	−107.975	107.975
	VBS4/Al(111)	3.661	(Al−H) 2.936	−109.975	109.975
Vacuum	VBS5/Al(111)	2.585	(Al−O) 2.585	−76.224	76.224
	VBS6/Al(111)	3.101	(Al−O) 3.101	−75.319	75.319
	VBS7/Al(111)	3.553	(Al−H) 2.964	−75.364	75.364
	VBS8/Al(111)	2.157	(Al−O) 2.157	−86.939	86.939

d_{Al-O} represents the distance between the nearest O_2 atom to the Al surface, and h is the interlayer distance between the topmost atom of the Al surface and the nearest atom of the VBS molecule.

The experimental results (PDP, EIS, and gravimetric analysis) suggested that the inhibition of Al corrosion in 1M HCl occurred via a mixed-type inhibition process involving both physical and

chemical processes. This supports the assumption that the chemisorption binding process is generally coupled with physisorption. Compared to the others, the high binding energies for the VBS2 and VBS5/Al(111) systems can be attributed to the aromatic rings, and the oxygen atom since their structures contain π-electrons from the conjugated double bonds that could interact with the sp band of the metal.

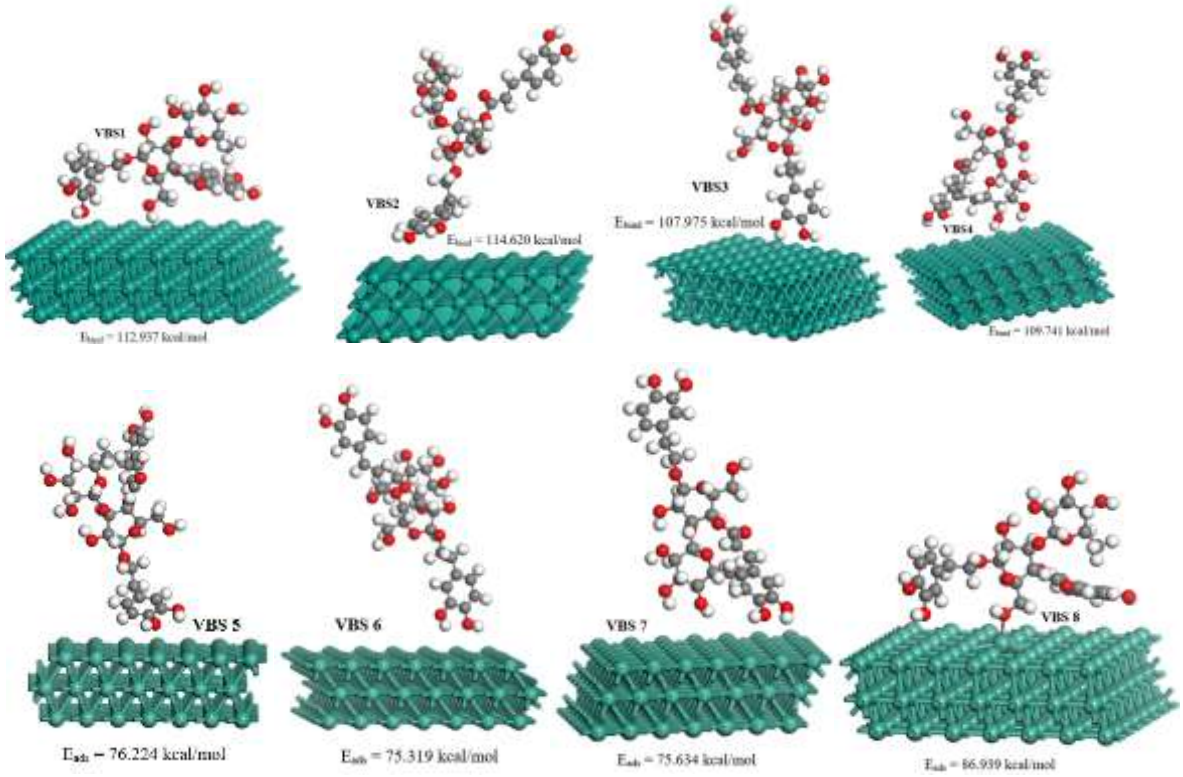

Figure 7.1: Different adsorption geometries of the VBS molecules for the solution (VBS1 to VBS4) and vacuum phase (VBS5 to VBS8) on the Al(111) surface

The bond distance for the optimized VBS2/Al(111) structure between the O43 atom and the Al atom is 2.590 Å. As a result of the interaction process, the initial bond distances of C41=C40 and C40–O43 of the non-interacting phenylethanoid group were lengthened from 1.391 and 1.388 Å to 1.395 and 1.399 Å, and that of C39–C40 was compressed from 1.406 to 1.405 Å, respectively. Although these bond lengths indicate a slight or minor distortion of the VBS molecule when it binds through the phenylethanoid group, the small change is indicative of the stability of the final binding structure.

7.2. Binding structures and energies of the VBS/Zn(110) system

Three possible interaction sites between VBS molecules on the Zn(110) surface were tested for the solution (VBS1 to VBS3) and vacuum phases (VBS4 to VBS6). The preferred binding sites for the VBS molecule on the Zn surface are shown in Figure 7.2, while the interaction and binding energies are indexed in Table 7.2. The results suggest that the strongest interaction strengths involve the interaction between VBS and the Zn(110) surface in the solution phase. In contrast, the weakest interaction strengths were observed for the vacuum phase. The strongest binding strengths for the vacuum were 31.398 and 23.806 kcal/mol observed when the VBS molecules interacted with the Zn(110) surface via the oxygen atom of the hydroxyl group (–C31–OH) (VBS7) and that of the sugar group (VBS6). The weakest binding strength of 15.527 kcal/mol was observed for the VBS4 when the molecule interacted with the Zn surface via the phenylpropanoid group. The difference between the weakest and the strongest binding energy for the vacuum phase shows a difference of 15.871 kcal/mol, indicating an energetic difference between the two binding sites. The binding strength observed for VBS in the solution phase was fairly similar for all three binding geometries, with the strongest binding strengths of 64.061 kcal/mol observed for VBS3, while the weakest binding strength of 58.411 kcal/mol was observed for VBS1. The highest binding energy for both the vacuum and solution phase indicates the preference for binding to the metal surface by the oxygen atom and could be attributed to the opposite electronegative charge of the Zn and oxygen atoms, resulting in a strong attraction between them and could be proposed as the most stable binding site on the Zn(110) surface.

The binding energies obtained for the VBS/Zn(110) systems indicate a mixed-type adsorption process involving chemisorption and physisorption binding process, as all the energies are greater than 13 kcal/mol. The binding process of the VBS2 and VBS5 can be attributed to the π-electrons of the aromatic rings that interact with the Zn surface's sp band. The bond distance for the optimized structure between the O29 atom and the nearest Zn atom is 2.251 Å for the VBS6 geometry, while for the VBS7, the distance between the O32 atom and the Zn atom is 2.198 Å. The interaction in VBS6 resulted in the lengthening of the bond distances of C24–O29 and O29–H from 1.430 and 0.977 Å to 1.456 and 0.987 Å, respectively. At the same time, the bond distances of C24–C25 and C24–C23 were compressed from 1.527 Å of the non-interacting sugar group to 1.523 Å during the interaction of the sugar group with the metal surface. This indicates that the VBS molecule experienced a slight distortion through the sugar group as it interacted with the

atoms on the Zn surface. The binding of the adsorbate (VBS7) through the oxygen atom of the hydroxyl group attached to C31 also indicates that the bond distance between these two atoms (C31–O32) before and after the interaction with the Zn surface was lengthened from 1.435 to 1.454 Å.

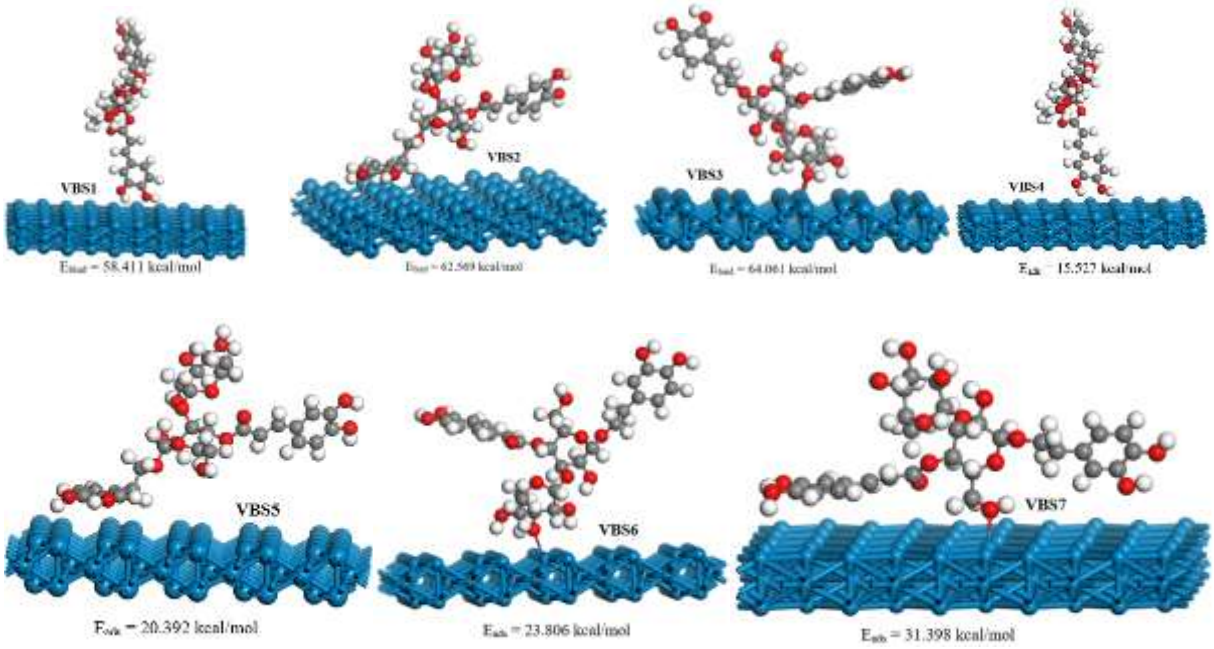

Figure 7.2: Different adsorption geometries of the VBS molecules for the solution (VBS1 to VBS3) and vacuum phase (VBS4 to VBS7) on the Zn(110) surface

Table 7.2: Calculated optimized energies for stable VBS adsorption sites on Fe(110) surface

Environment	System	d_{Fe-O} (Å)	h (Å)	E_{int} (kcal/mol)	E_{bind} (kcal/mol)
Solution Phase	VBS1/Zn(110)	2.840	(Zn−H) 2.824	−58.411	58.411
	VBS2/Zn(110)	2.742	(Zn−O) 3.310	−62.569	62.569
	VBS3/Zn(110)	2.286	(Zn−O) 2.286	−64.061	64.061
Vacuum	VBS4/Zn(110)	2.713	(Zn−O) 2.713	−15.527	15.527
	VBS5/Zn(110)	3.014	(Zn−H) 2.829	−20.392	20.392
	VBS6/Zn(110)	2.251	(Zn−O) 2.251	−23.806	23.806
	VBS7/Zn(110)	2.198	(Zn−O) 2.198	−31.398	31.398

d_{Zn-O} represents the distance between the nearest O atom to the Zn surface, and h is the interlayer distance between the topmost atom of the Zn surface and the nearest atom of the VBS molecule.

7.3. Binding structures and energies of the VBS/Fe(110) system

Full DFT-level geometry optimization produced optimized equilibrium geometries and energies in the vacuum (VBS1 to VBS3) and solution phases (VBS4 and VBS5), as shown in Figure 7.3. The figure demonstrates that the interaction of VBS with the uppermost of the Fe(110) slab occurs preferably via the oxygen atom; as such, it is worth noting the Fe–O bond distance. Strong adsorption of molecules on the metal surfaces is believed to result in a shorter surface molecule bond. VBS3 adsorption geometry indicates two covalent bonds (Fe–O) above 2.414 Å and 2.092 Å producing an adsorption energy of 63.401 kcal/mol. The interaction of VBS with the Fe(110) surface through the oxygen atom indicates hybridization between the 2p orbital of the oxygen atom and the 3d orbital of the surface Fe atom. Besides the interaction of VBS via the oxygen atom, the molecules were also aligned parallel to the top layer of the Fe(110) slab via the phenylpropanoid group, with the −O−H pointing to the surface via the hydrogen atom at a distance of 2.670 Å, as indicated by the VBS4 geometry. The interaction via the phenylpropanoid group suggests the participation of CH−π (physisorption) and π−π interactions (chemisorption). Adsorption energy values of molecular VBS on Fe(110) in two different environments indicate a chemisorption adsorption nature on the surface of metals typically coupled with physisorption [647]. This implies that VBS interacts with the Fe(110) surface through a complex adsorption process involving both physisorption and chemisorption, which supports the experimental data. Comparing the adsorption energies from the vacuum and the solution phase, it is clear that the adsorption of VBS in the gas phase produced the highest adsorption energies (35,993 and 63,401 kcal/mol) which is in contradiction to what was observed with the VBS/Al(111) and VBS/Zn(110) systems. This behaviour can be attributed to the fact that VBS molecules, considered ideal gases, do not have adsorptive-adsorptive interaction problems, whereas considering water in the system (i.e. solution phase) leads not only to an adsorptive-adsorptive interaction but also results in solute-solvent interaction, indicating competitive behaviour between solute and solvent in adsorption on the Fe(110) plate, making it difficult for VBS to adsorb on the Fe surface [642, 648]. The low binding energies for the solution phase can also be attributed to the salvation effects affecting the degree of inhibitor adsorption on metallic surfaces, as the inhibitor molecules are trapped in the solvent

cavity, resulting in less strong interactions with the metal surface compared to the vacuum phase [649-651].

Table 7.3: Calculated optimized energies for stable VBS adsorption sites on Fe(110) surface

Environment	System	d_{Fe-O} (Å)	h (Å)	E_{int} (kcal/mol)	E_{bind} (kcal/mol)
Vacuum	VBS1/Fe(110)	2.430	(Fe−O) 2.430	−13.476	13.476
	VBS2/Fe(110)	2.212	(Fe−O) 2.212	−35.993	35.993
	VBS3/Fe(110)	2.414	(Fe−O) 2.092	−63.401	63.401
Solution Phase	VBS4/Fe(110)	2.867	(Fe−H) 2.670	−22.762	22.762
	VBS5/Fe(110)	2.460	(Fe−O) 2.460	−14.168	14.168

d_{Fe-O} represents the distance between the nearest O atom to the Fe surface, and h is the interlayer distance between the topmost atom of the Fe surface and the nearest atom of the VBS molecule.

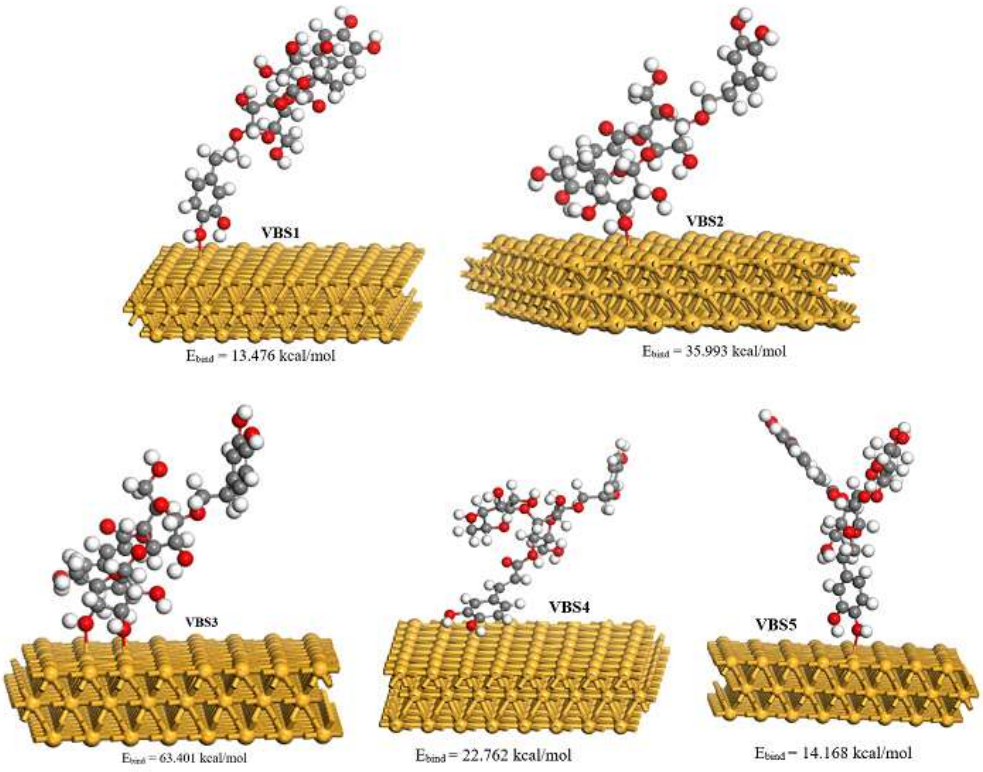

Figure 7.3: Different adsorption geometries of the VBS molecules for the vacuum (VBS1 to VBS3) and solution phase (VBS4 and VBS5) on the Fe(110) surface

The above configurations resulted in a different binding geometry, indicating multiple possible, stable binding sites for the VBS molecule on the Fe(111), Al(111), or Zn(110) surfaces, determined

by the initial arrangement of the VBS molecule in the supercell. A comparison of the binding energy in the solution and vacuum phases is shown in Figure 7.3. For both simulated environments, the interactions producing the strongest binding strengths were between VBS and the Al(111) surface compared to Fe(110) and Zn (110) surfaces. Since the Zn^{2+} has an electron configuration of $[Ar]3d^{10}$, it is unlikely to donate more than the 4s orbital electrons since the 3d orbital is fully filled and reasonably stable, which could be the reason for the low binding energies. The electron configuration of Fe^{2+}, $[Ar]3d^6$, suggests that the partially filled 3d orbitals bind with the VBS molecule's highest occupied molecular orbitals. Al is the most thermodynamically reactive metal compared to Zn and Fe, as indicated by its position in the electromotive force series, but is nevertheless less corrosive. This behaviour can be explained by the fact that Al loses three electrons ($3s^2p^1$) to become stable (Al^{3+}) with an electron configuration of $[Ne]1s^22s^2sp^6$. So when Al encounters a molecule like VBS with an abundance of oxygen atoms, one of the possible interactions is that two Al atoms donate six electrons to three oxygen atoms, resulting in a much stronger interaction.

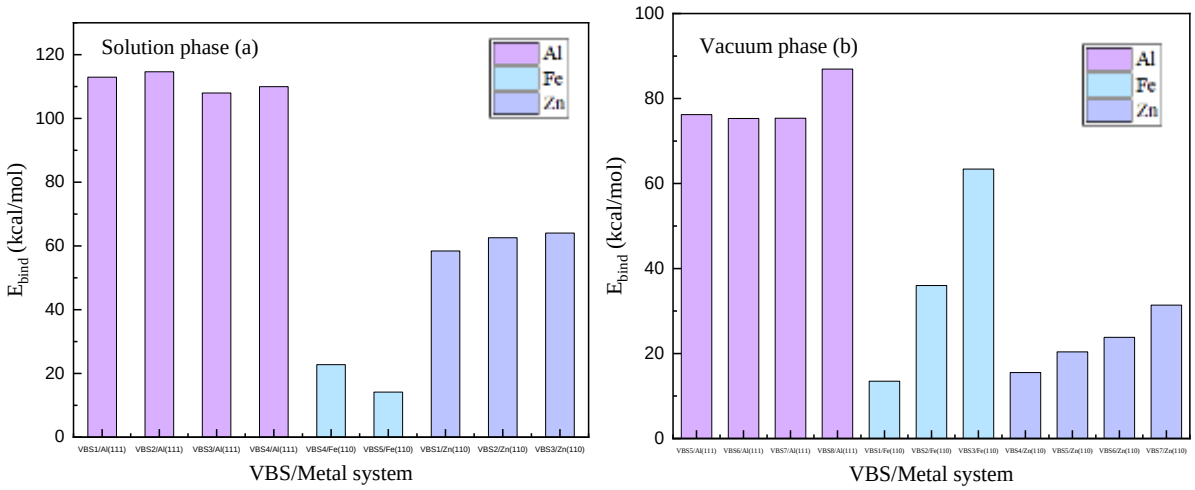

Figure 7.4: Comparison of surface plane binding energies of Fe(110), Zn(110) and Al(111) for binding VBS in solution (a) and vacuum phase (b)

7.4. Corrosion inhibition mechanism

Most corrosion inhibitors are believed to inhibit corrosion primarily through adsorption and coordination processes [652]. The π-electron clouds in the aromatic ring of organic compounds and the lone pair of electrons in the donor atoms can form a strong interaction bond between the inhibitor and the metal surfaces [653]. Although lone pairs of electrons in oxygen, sulphur, and

nitrogen heteroatoms play an essential role in forming a protective layer [654], the unique properties of metals such as Al, MS, and Zn imply the formation of such a layer is unique to each metal. For instance, the absence of d orbitals in the outer shell of Al suggests that few compounds containing such atoms can directly form covalent bonds with the Al surface via the chemisorption mechanism [655]. On the other hand, several studies have shown that Al^{3+} chelate complexes can be easily created through coordination with heterocyclic, hydroxy, and carboxyl groups [652, 656, 657]. In acidic corrosive solutions, the Al surface possesses a positive charge that creates an attractive force for the negatively charged Cl^- ions adsorbed on the Al surface [555, 658], which act as adsorption centres for the protonated extract components (e.g., VBS+). This adsorption type is linked to the proposed physical adsorption mode [659]. Chelation of freshly oxidized Al^{3+} ions (equation 59) *L. javanica* components can lead to the formation of Al^{3+}– *L. javanica* complexes as proposed in equation 64, similar to that reported by Nnaji *et al*. [658]:

$$Al^{3+}(aq) + inh(ads) \rightarrow [Al - inh]^{3+}(ads) \quad (64)$$

The formation of Al^{3+}- *L. javanica* complexes led to the passivation of the Al surface, as supported by the PDP results in this work. Nnaji *et al*. [658] also suggested possible reactions that might be involved during the corrosion process. These include acid ionization (equation 65), water hydrolysis (equation 66), metal oxidation or corrosion (equation 67), formation of corrosion products (equation 68 and 69), and protective film formation (equations 70 and 71).

$$3HCl(aq) \leftrightarrow 3H^+(aq) + 3Cl^-(aq) \quad (65)$$

$$3H_2O(l) \leftrightarrow 3H^+(aq) + 3OH^+(aq) \quad (66)$$

$$2Al(s) \rightarrow 2Al^{3+}(aq) + 6e^- \quad (67)$$

$$Al^+(aq) + 3Cl^-(aq) \leftrightarrow AlCl_3(s) \quad (68)$$

$$Al^{3+}(aq) + 3OH^-(aq) \leftrightarrow Al(OH)_3(s) \quad (69)$$

$$ACl_3(s) + xinh^{n+} \leftrightarrow [AlCl_3 xinh^{n+}](s) \quad (70)$$

$$Al(OH)_3(s) + xinh^{n+} \leftrightarrow [Al(OH)_3 xinh^{n+}](s) \quad (71)$$

where *x* is the number of inhibitor molecules and *n* can be 1, 2, 3, or 4 for the different components of ALJPE.

The mixed-type Al corrosion inhibition mechanism was also proposed for Zn and MS through the different techniques used in the study. These could occur either through the electrostatic interaction of plant components with positively charged Zn and MS surfaces or through the lone pairs of electrons on atoms such as oxygen. The same behaviour, where the Al surface becomes positively charged in the acidic solution, applies to MS and Zn surfaces, which then become covered with negatively charged Cl- ions, and the *L. javanica* components electrostatically interact with such surfaces. After getting adsorbed, the plant species compete with H^+ ions for electrons on the Zn and MS surfaces. This results in the release of H_2 gas, and the plant species return to their neutral form, where they can interact with the Zn and MS surfaces via the electron-dense atoms. The MS and Zn surfaces become negatively charged due to the accumulation of electrons. For instance, the 3d orbital of Fe might release an electron to a vacant π^* (antibonding) orbital of the *L. javanica* components through retro-donation to relieve the MS surface from extra negative charge resulting in stronger adsorption of the *L. javanica* components on the MS surface [660]. It is important to note that the mechanism of action of green inhibitors such as *L. javanica* extracts in inhibiting corrosion depends on the structure of the active ingredient present. Other theories have been put forward to support this [661, 662]. Another process that might aid in Al, Zn, and MS corrosion inhibition is the intermolecular interactions between the *L. javanica* components, such as hydrogen bonding between the VBS molecules. This process is supported by the Langmuir slope's departure from unity in this study.

CHAPTER 8

Summary, comparison, conclusions, list of publications, recommendations, and future

This chapter contains a summary of some of the current study's findings. It also summarizes some of the most important findings from current research on plant extracts as potential corrosion inhibitors. There is a list of publications that have been submitted and those that have yet to be submitted. Recommendations and potential future studies derived from the current work have been outlined.

8. Summary and comparative analysis of the corrosion inhibition performance of L. javanica leaf extracts on Al, MS, and Zn

In the present study, ethanol, methanol, and acetone extracts from *L. javanica* leaves were investigated for their anticorrosive properties towards Al, Zn, and MS in 1 M HCl solution at 303–333 K. The characterized extracts showed that the three solvents extracted similar compounds, and their anti-corrosion behaviour for Zn, Al, and MS corrosion was comparable. Some of the results are summarized in Table 8.1.

Table 8.1: Comparison of the performance of MLJCE, ELJCE, and ALJCE on the corrosion inhibition of Al, Zn, and MS in 1 HCl solution

Technique	Metal		
	Al	**MS**	**Zn**
PDP	• Less than 85 mV E_{corr} values • Mixed-type adsorption • PDP curves with a pronounced passive region • Maximum %IE were 87.79, 97.54 and 97.47% from the three extracts	• Less than 85 mV E_{corr} values • Mixed-type adsorption • Undulation PDP curves with no pronounced passive region • Maximum %IE were 93.40, 95.57 and 94.21% from the three extracts	• Less than 85 mV E_{corr} values • Mixed-type adsorption with dominating cathodic protection • Undulation PDP curves with no pronounced passive region • Maximum %IE were 96.84, 98.00 and 97.47% from the three extracts
EIS	• Circuit for data fitting: $R_s(Q\ R_{ct}\ (L_1/R_L))$ • Imperfect Nyquist plots with a pronounced passive region (inductive loop) • More capacitive behaviour than MS and Zn • Maximum %IE were 85.08, 77.15 and 97.50% from the three extracts	• Circuit for data fitting: $R_s(Q\ R_{ct})$ • Imperfect Nyquist plots • Pseudo-capacitive behaviour, n-values approach unity in the presence of the extracts • Maximum %IE were 89.13, 94.71 and 94.85% from the three extracts	• Circuit for data fitting: $R_s(Q\ R_{ct})$ • Imperfect Nyquist plots • Pseudo-capacitive behaviour, n-values approach unity in the presence of the extracts • Maximum %IE were 94.85, 95.05 and 95.40% from the three extracts
Adsorption and Adsorption Isotherms	• Obeys Langmuir model • Mixed type adsorption • Spontaneous adsorption • Lateral molecular interaction (Temkin)	• Obeys Langmuir model • Mixed type adsorption • Spontaneous adsorption • Lateral molecular interaction (Temkin)	• Obeys Langmuir model • Mixed type adsorption • Spontaneous adsorption • Lateral molecular interaction (Temkin)
SEM/EDS	• Pitting corrosion • Traces of oxygen and carbon precipitate	• Uniform corrosion • Traces of oxygen and carbon precipitate	• Uniform corrosion • Traces of oxygen and carbon precipitate
Weight loss	• Increasing positive ΔH_a^* and E_a values with extract concentration • Q_{ads} indicate exothermic adsorption linked with physisorption • Maximum %IE were 88.58, 91.70 and 91.89% from the three extracts • Decreasing %IE with temperature	• Increasing positive ΔH_a^* and E_a values with extract concentration • Q_{ads} indicate exothermic adsorption linked with physisorption • Maximum %IE were 99.09, 97.01 and 98.01% from the three extracts • Decreasing %IE with temperature	• Decreasing positive ΔH_a^* and E_a values with extract concentration • Q_{ads} indicate endothermic adsorption linked with chemisorption • Maximum %IE were 86.92, 85.64 and 87.77% from the three extracts • Increasing %IE with temperature
Contact angle	• Increase in hydrophobic nature of the metal surface in the presence of extract	• Increase in hydrophobic nature of the metal surface in the presence of extract	• Increase in hydrophobic nature of the metal surface in the presence of extract

8.1. Conclusions

The current study has successfully shown that *L. javanica* leaf extracts are excellent inhibitors of Al, Zn and MS corrosion in 1 M HCl as they promote the formation of a passive or protective layer on the three metal surfaces, and they are cheap to produce, biodegradable and non-toxic. Some of the key findings of this work are discussed below:

The extraction of different components contained in *L. javanica* leaves was successfully performed with methanol, ethanol, and acetone. LC/MS and FT-IR characterized the extracted components, and their inhibition performance was evaluated using weight loss, FT-IR, UV-vis, SEM/EDS, PDP, EIS and water contact angle studies.

All examined extracts (i.e., MLJCE, ELJCE, and ALJCE) showed appreciable protective activity against Al, Zn and MS corrosion in 1 M HCl solution. The protection provided by the extracts for Zn was found to be more effective and possibly irreversible compared to MS and Al. This conclusion is based on the fact that it has been found that the protective effect for Zn increases with the temperature of the corrosive environment, and this is associated with a chemical inhibition process. For MS and Al, the decrease in protection efficiency with temperature indicates a reversible weaker protection resulting from a dominant physical inhibition process. The optimum extract concentration that provided good protection for MS, Al, and Zn was 800 ppm for all three examined extracts.

The thermodynamic and kinetic parameters of corrosion and corrosion inhibition of Zn, MS, and Al were evaluated by performing temperature studies. The decrease in the thermodynamic ΔH_a^* and E_a values with increasing concentrations of MLJCE, ELJCE, and ALJCE up to 800 ppm for Zn were observed, while parameters increased for MS and Al. The increase in these parameters with extract concentration indicates the formation of a physical barrier that prevents corrosive charge and mass transfer, requiring more energy to move from the reactants to the activated complex. On the other hand, it has been proposed that the decrease in these parameters is due to the surface area covered by the extracts expanding with increasing temperature and is associated with the chemical adsorption of the extracts on the Zn surface. The heat of adsorption studies indicates that the adsorption mechanism for MS and Al occurred through both an endothermic and

an exothermic nature. In contrast, for Zn, for all three extracts, it mainly occurred through an endothermic nature.

All extracts investigated herein are mixed-type corrosion inhibitors. Adsorption of MLJCE, ELJCE, and ALJCE onto active sites of Zn, Al, and MS surfaces to inhibit their corrosion occurred without changing their corrosion mechanisms. According to the isotherm data, MLJCE, ELJCE, and ALJCE adsorption on three metal surfaces occurred spontaneously, and the adsorption mechanism followed the Langmuir adsorption isotherm. The Temkin adsorption isotherm accounted for the lateral interaction of the adsorbed species since the Langmuir adsorption slopes differed from unity for all three metals.

Spectroscopic measurements confirmed the presence of interactions between Zn, Al, and MS and extracted components, resulting in the formation of extract-metal complexes. Water contact angle studies confirmed the construction of a widespread protective layer on the MS, Zn, and Al surfaces. This corresponds to the formation of a hydrophobic film that reduces their wettability.

The extracts generated an adsorption film with pseudocapacitive behaviour on the MS, Zn, and Al surfaces, with Al also showing an inductive behaviour. The pseudocapacitive behaviour of the MS, Al, and Zn electrodes is also confirmed by the CPE exponent values being near unity in the presence of the extracts.

The verbascoside molecule identified to be the main component of the three plant extracts as evidenced by its presence in all fractions collected through column fractionation was used for the DFT calculations. The binding process of verbascoside on the MS, Zn, and Al surfaces showed that the molecule interacted with the surface preferentially via the oxygen atoms, which can donate lone pairs of electrons to the metal surfaces. The calculations also revealed the involvement of the aromatic π-bonds during the interaction of the molecule with the metal surfaces, resulting in high bond energies.

Potentiodynamic results showed that the extracts are capable of preventing the pitting of MS and Zn surfaces, while the lack of pitting in the absence of the extracts could be due to the protective nature of the Zn patina and the oxide layer on the MS surface. As indicated by SEM results, the Al surface suffered from pitting, while the corrosion mode on the MS and Zn surfaces was uniform.

8.2. Recommendations and future studies

The present study found that plant-derived green inhibitors can be used to control the corrosion of metals that come in contact with a corrosive environment. The use of plant extracts as metal protectors is limited, and this study recommends their use because of their high level of protection. Also, evaluating the plant extract used in this study in a high-temperature environment could be considered in the future. For investigations into corrosion protection, the use of quantum mechanical methods to simulate the interactions between adsorbent and adsorbate is recommended since these can better describe chemical processes with the bond formation or bond breakage. Future studies could also include isolating some main components and evaluating their inhibitory abilities in an isolated state. This is based on the effectiveness of the plant used in this study and could potentially lead to the discovery of more highly effective corrosion inhibitors.

8.3. Study contribution to the field of corrosion

In a breakthrough discovery, this study uncovers the potential of plant extracts as remarkable corrosion inhibitors. The extracts stood strong even after 24 hours, showcasing enduring inhibition. Their performance shined under high temperatures, especially for Zn, an unexpected and rare trait. This research affirmed that these extracts could protect MS, Zn, and Al and aluminium. A standout finding: quantum calculations beat common methods for understanding extract-metal interactions. By revealing bond behavior, these results promise practical impact. In short, this study open doors to effective, sustainable corrosion protection.

8.4. List of publications

- **Tshimangadzo Nesane**, Ntakadzeni E. Madala, Mwadham M. Kabanda and Lutendo C. Murulana, Experimental and theoretical studies on the inhibitory potential of *Lippia javanica* leaf extract for aluminium corrosion in 1M HCl medium. ***Journal of Adhesion Science and Technology, (2023), https://doi.org/10.1080/01694243.2023.2211788***
- **Tshimangadzo Nesane**, Ntakadzeni E. Madala, Mwadham M. Kabanda and Lutendo C. Murulana, Indra Bahadur, *Lippia javanica* leaf extract as an effective anti-corrosion agent against mild steel corrosion in 1 M HCl and its characterization by UHPLC/Q-TOF-MS and quantum chemical evaluation of its adsorption process on Fe(110). ***Colloids and Surfaces A: Physicochemical and Engineering Aspects, 667 (2023) 131405***

- **Tshimangadzo Nesane**, Ntakadzeni E. Madala, Mwadham M. Kabanda and Lutendo C. Murulana, *Lippia javanica* extract as a green inhibitor of zinc corrosion in hydrochloric acid solution ***(Submitted to Current Material Science)***

References

References

1. McCafferty, E., *Introduction to corrosion science*. 2010: Springer Science & Business Media.
2. Zarras, P. and J.D. Stenger-Smith, *Smart Inorganic and Organic Pretreatment Coatings for the Inhibition of Corrosion on Metals/Alloys*, in *Intelligent Coatings for Corrosion Control*. 2015, Elsevier. p. 59-91.
3. Eddy, N., S. Odoemelam, and A. Odiongenyi, *Joint effect of halides and ethanol extract of Lasianthera africana on inhibition of corrosion of mild steel in H 2 SO 4.* Journal of applied electrochemistry, 2009. **39**(6): p. 849-857.
4. Raghavendra, N. and J.I. Bhat, *Natural products for material protection: an interesting and efficacious anticorrosive property of dry arecanut seed extract at electrode (aluminum)–electrolyte (hydrochloric acid) interface.* Journal of Bio-and Tribo-Corrosion, 2016. **2**(4): p. 21.
5. Oguzie, E.E., *Corrosion inhibition of aluminium in acidic and alkaline media by Sansevieria trifasciata extract.* Corrosion science, 2007. **49**(3): p. 1527-1539.
6. El-Etre, A., *Inhibition of aluminum corrosion using Opuntia extract.* Corrosion science, 2003. **45**(11): p. 2485-2495.
7. Abiola, O.K. and J. Otaigbe, *The effects of Phyllanthus amarus extract on corrosion and kinetics of corrosion process of aluminum in alkaline solution.* Corrosion Science, 2009. **51**(11): p. 2790-2793.
8. Chira, A., B. Bucur, and G.-L. Radu, *Electrodeposited Organic Layers Formed from Aryl Diazonium Salts for Inhibition of Copper Corrosion.* Materials, 2017. **10**(3): p. 235.
9. Verma, C., E.E. Ebenso, and M. Quraishi, *Ionic liquids as green and sustainable corrosion inhibitors for metals and alloys: an overview*. Journal of Molecular Liquids, 2017. **233**: p. 403-414.
10. Roberge, P.R., *Handbook of corrosion engineering*. 2000: McGraw-Hill.
11. Tait, W.S., *Electrochemical Corrosion Basics*, in *Handbook of Environmental Degradation of Materials*. 2018, Elsevier. p. 97-115.
12. Popov, B.N., *Corrosion engineering: principles and solved problems*. 2015: Elsevier.
13. Garverick, L., *Corrosion in the petrochemical industry*. 1994: ASM international.

14. Ugi, B., et al., *Aluminium corrosion abatement using non toxic and eco-friendly organic inhibitors.* Journal of Global Ecology and Environment, 2016: p. 242-252.
15. Rao, B., *Handbook of condition monitoring*. 1996: Elsevier.
16. Koch, G.H., et al., *Corrosion cost and preventive strategies in the United States*. 2002, United States. Federal Highway Administration.
17. Koch, G.H., et al., *Cost of corrosion in the United States*, in *Handbook of environmental degradation of materials*. 2005, Elsevier. p. 3-24.
18. Gong, Z., et al., *Investigation the corrosion inhibition effect of itraconazole on copper in H2SO4 at different temperatures: Combining experimental and theoretical studies.* Materials, 2018. **11**(11): p. 2107.
19. Koch, G., *Cost of corrosion*, in *Trends in Oil and Gas Corrosion Research and Technologies*. 2017, Elsevier. p. 3-30.
20. Canale, L.d.C.F., G.E. Totten, and R.A. Mesquita, *Failure analysis of heat treated steel components*. 2008: ASM international.
21. Veronika, B.K., *Knowledge about metals in the first century.* Korrozios Figyelo, 2008. **48**(5): p. 133-+.
22. Fontana, M.G., *Corrosion engineering*. 2005: Tata McGraw-Hill Education.
23. Odio, B., et al., *Investigation of the effect of corrosion on mild steel in five different environments.* International Journal of Scientific & Technology Research, 2014. **3**(7).
24. Li, X., S. Deng, and H. Fu, *Inhibition effect of methyl violet on the corrosion of cold rolled steel in 1.0 M HCl solution.* Corrosion Science, 2010. **52**(10): p. 3413-3420.
25. Fayomi, O. and I. Akande, *Corrosion mitigation of aluminium in 3.65% NaCl medium using hexamine.* Journal of Bio-and Tribo-Corrosion, 2019. **5**(1): p. 23.
26. Xhanari, K., et al., *Green corrosion inhibitors for aluminium and its alloys: a review.* RSC advances, 2017. **7**(44): p. 27299-27330.
27. Papavinasam, S., *Corrosion control in the oil and gas industry*. 2013: Elsevier.
28. Regulator, A.E., *Report 2013-B: Pipeline Performance in Alberta, 1990-2012*. 2013: Alberta Energy Regulator.
29. Askari, M., M. Aliofkhazraei, and S. Afroukhteh, *A comprehensive review on internal corrosion and cracking of oil and gas pipelines.* Journal of Natural Gas Science and Engineering, 2019: p. 102971.

30. Winning, I.G., D. Mcnaughtan, and N. Bretherton. *Evaluation of weld corrosion behavior and the application of corrosion inhibitors and combined scale/corrosion inhibitors*. in *CORROSION 2004*. 2004. NACE International.
31. Zardasti, L., et al. *The consequence assessment of gas pipeline failure due to corrosion*. in *Solid State Phenomena*. 2015. Trans Tech Publ.
32. Dugstad, A., L. Lunde, and S. Nesic. *Control of internal corrosion in multi-phase oil and gas pipelines*. in *Proceedings of the conference Prevention of Pipeline Corrosion, Gulf Publishing Co*. 1994.
33. Goulart, C.M., et al., *Experimental and theoretical evaluation of semicarbazones and thiosemicarbazones as organic corrosion inhibitors.* Corrosion Science, 2013. **67**: p. 281-291.
34. Loto, R.T. and C.A. Loto, *Corrosion behaviour of S43035 ferritic stainless steel in hot sulphate/chloride solution.* Journal of Materials Research and Technology, 2018. **7**(3): p. 231-239.
35. Okafor, P., et al., *Inhibitory action of Phyllanthus amarus extracts on the corrosion of mild steel in acidic media.* Corrosion Science, 2008. **50**(8): p. 2310-2317.
36. Zhang, G., et al., *Evaluation of inhibition efficiency of an imidazoline derivative in CO2-containing aqueous solution.* Materials Chemistry and Physics, 2007. **105**(2-3): p. 331-340.
37. Lopez, D.A., S. Simison, and S. De Sanchez, *The influence of steel microstructure on CO2 corrosion. EIS studies on the inhibition efficiency of benzimidazole.* Electrochimica Acta, 2003. **48**(7): p. 845-854.
38. Hong, T., Y. Sun, and W. Jepson, *Study on corrosion inhibitor in large pipelines under multiphase flow using EIS.* Corrosion science, 2002. **44**(1): p. 101-112.
39. Okafor, P., et al., *Corrosion inhibition and adsorption behavior of imidazoline salt on N80 carbon steel in CO 2-saturated solutions and its synergism with thiourea.* Journal of Solid State Electrochemistry, 2010. **14**(8): p. 1367-1376.
40. Ahamad, I., R. Prasad, and M. Quraishi, *Thermodynamic, electrochemical and quantum chemical investigation of some Schiff bases as corrosion inhibitors for mild steel in hydrochloric acid solutions.* Corrosion Science, 2010. **52**(3): p. 933-942.

41. Ju, H., Z.-P. Kai, and Y. Li, *Aminic nitrogen-bearing polydentate Schiff base compounds as corrosion inhibitors for iron in acidic media: a quantum chemical calculation.* Corrosion Science, 2008. **50**(3): p. 865-871.
42. Yurt, A., et al., *Investigation on some Schiff bases as HCl corrosion inhibitors for carbon steel.* Materials Chemistry and Physics, 2004. **85**(2-3): p. 420-426.
43. Fajobi, M., R.T. Loto, and O. Oluwole, *Corrosion in Crude Distillation Overhead System: A Review.* Journal of Bio-and Tribo-Corrosion, 2019. **5**(3): p. 67.
44. Okewale, A. and A. Olaitan, *The use of rubber leaf extract as a corrosion inhibitor for mild steel in acidic solution.* International Journal of Materials and Chemistry, 2017. **7**(1): p. 5-13.
45. Sunday, J.O., et al., *Gravimetric and electrochemical studies of corrosion inhibition potential of acid and ethanol extract of siam weed on mild steel.* Leonardo Journal of Sciences, 2016(29): p. 25-42.
46. Pathak, R. and P. Mishra, *Drugs as corrosion inhibitors: a review.* International journal of Science and Research, 2016. **5**(4): p. 671-677.
47. Chetouani, A., B. Hammouti, and M. Benkaddour, *Corrosion inhibition of iron in hydrochloric acid solution by jojoba oil.* Pigment & resin technology, 2004.
48. Bouyanzer, A. and B. Hammouti, *A study of anti-corrosive effects of Artemisia oil on steel.* Pigment & resin technology, 2004.
49. Ebenso, E., et al., *Corrosion inhibition studies of some plant extracts on aluminium in acidic medium.* Transactions-Society for the Advancement of Electrochemical Science and Technology, 2004. **39**(4): p. 117.
50. BENDAHOU, M., M. BENABDELLAH, and B. HAMMOUTI, *A study of rosemary oil as a green corrosion inhibitor for steel in 2M H3PO4.* Pigment & resin technology, 2006. **35**(2): p. 95-100.
51. Umoren, S.A. and U.M. Eduok, *Application of carbohydrate polymers as corrosion inhibitors for metal substrates in different media: a review.* Carbohydrate polymers, 2016. **140**: p. 314-341.
52. Hu, K., et al., *Effect of novel cytosine-l-alanine derivative based corrosion inhibitor on steel surface in acidic solution.* Journal of Molecular Liquids, 2016. **222**: p. 109-117.

53. Ramezanzadeh, B., H. Vakili, and R. Amini, *The effects of addition of poly (vinyl) alcohol (PVA) as a green corrosion inhibitor to the phosphate conversion coating on the anticorrosion and adhesion properties of the epoxy coating on the steel substrate.* Applied Surface Science, 2015. **327**: p. 174-181.
54. Mohammadinejad, R., et al., *Plant-derived nanostructures: types and applications.* Green Chemistry, 2016. **18**(1): p. 20-52.
55. Varma, R.S., *Journey on greener pathways: from the use of alternate energy inputs and benign reaction media to sustainable applications of nano-catalysts in synthesis and environmental remediation.* Green Chemistry, 2014. **16**(4): p. 2027-2041.
56. MináLee, J., *Chemical assay-guided natural product isolation via solid-supported chemodosimetric fluorescent probe.* Chemical science, 2015. **6**(5): p. 2806-2811.
57. Sathiyanathan, R., et al., *Corrosion inhibition of mild steel by ethanolic extracts of Ricinus communis leaves.* Indian Journal of Chemical Technology, 2005. **12**(3): p. 356-360.
58. Sathiyanathan, R.A.L., et al., *Inhibitory effect of Ricinus communis (Castor-oil plant) leaf extract on corrosion of mild steel in low chloride medium.* Journal of the Indian Chemical Society, 2005. **82**(4): p. 357-359.
59. Poongothaia, N., et al., *Wood bark oils as vapour phase corrosion inhibitors for metals in NaCl and SO2 environments.* Indian Journal of Chemical Technology, 2005. **12**: p. 641-647.
60. Verma, C., et al., *An overview on plant extracts as environmental sustainable and green corrosion inhibitors for metals and alloys in aggressive corrosive media.* Journal of molecular liquids, 2018. **266**: p. 577-590.
61. Chigondo, M. and F. Chigondo, *Recent natural corrosion inhibitors for mild steel: an overview.* Journal of Chemistry, 2016. **2016**.
62. Umoren, S., *Polymers as corrosion inhibitors for metals in different media-A review.* The Open Corrosion Journal, 2009. **2**(1).
63. Hasan, S.K. and P. Sisodia, *Paniala (Flacourtia Jangomas) plant extract as eco friendly inhibitor on the corrosion of mild steel in acidic media.* Rasayan J. Chem, 2011. **4**(3): p. 548-553.

64. Laqhaili, A., et al., *Effect of lavandula stoechas oil on welded material corrosion in 5.5 M H3PO4 solution.* Journal of Chemical and Pharmaceutical Research, 2013. **5**(12): p. 1297-1306.
65. Johnsirani, V., et al., *The Effect of Eclipta Alba Leaves Extract on the Corrosion Inhibition Process of Carbon Steel in Sea Water.* Portugaliae electrochimica acta, 2013. **31**(2): p. 95-106.
66. Awizar, D.A., et al., *Nanosilicate extraction from rice husk ash as green corrosion inhibitor.* International Journal of Electrochemical Science, 2013. **8**(2): p. 1759-1769.
67. Fouda, A. and A.H. Badr, *Aqueous extract of propolis as corrosion inhibitor for carbon steel in aqueous solutions.* Afr J Pure Appl Chem, 2013. **7**(10): p. 350-359.
68. Kumar, C.P. and K. Mohana, *Adsorption and thermodynamic characteristics of Plumeria rubra plant extracts on mild steel corrosion in industrial water medium.* International research journal of Pure and Applied Chemistry, 2013: p. 330-346.
69. Jekayinfa, S., et al., *Effect of cassava fluid on corrosion performance of mild steel.* Anti-Corrosion Methods and Materials, 2005. **52**(5): p. 286-292.
70. Alvarez, P.E., et al., *Rollinia occidentalis extract as green corrosion inhibitor for carbon steel in HCl solution.* Journal of industrial and engineering chemistry, 2018. **58**: p. 92-99.
71. Kraka, E. and D. Cremer, *Computer design of anticancer drugs. A new enediyne warhead.* Journal of the American Chemical Society, 2000. **122**(34): p. 8245-8264.
72. Vosta, J. and J. Eliasek, *Study on corrosion inhibition from aspect of quantum chemistry.* corrosion science, 1971. **11**(4): p. 223-229.
73. Rg, P. and W. Yang, *Density-functional theory of atoms and molecules*. 1989, Oxford University Press, New York.
74. Rodríguez-Valdez, L.M.a., A. Martínez-Villafañe, and D. Glossman-Mitnik, *CHIH-DFT determination of the molecular structure, infrared and ultraviolet spectra of potentially organic corrosion inhibitors.* Journal of Molecular Structure: THEOCHEM, 2004. **681**(1-3): p. 83-88.
75. Blajiev, O. and A. Hubin, *Inhibition of copper corrosion in chloride solutions by amino-mercapto-thiadiazol and methyl-mercapto-thiadiazol: an impedance spectroscopy and a quantum-chemical investigation.* Electrochimica Acta, 2004. **49**(17-18): p. 2761-2770.

76. Henríquez-Román, J.H., et al., *The influence of aniline and its derivatives on the corrosion behaviour of copper in acid solution: a theoretical approach.* Journal of Molecular Structure: THEOCHEM, 2005. **757**(1-3): p. 1-7.
77. Jamalizadeh, E., A. Jafari, and S. Hosseini, *Semi-empirical and ab initio quantum chemical characterisation of pyridine derivatives as HCl inhibitors of aluminium surface.* Journal of Molecular Structure: THEOCHEM, 2008. **870**(1-3): p. 23-30.
78. Gece, G. and S. Bilgic, *A theoretical study on the inhibition efficiencies of some amino acids as corrosion inhibitors of nickel.* Corrosion Science, 2010. **52**(10): p. 3435-3443.
79. Abdulazeez, M.O., A.K. Oyebamiji, and B. Semire, *DFT and QSAR study of corrosion inhibition on 3, 5-di-substituted pyrazole derivatives with heteroatom on position one.* Lebanese Science Journal, 2016. **17**(2): p. 217.
80. Beech, I.B. and J. Sunner, *Biocorrosion: towards understanding interactions between biofilms and metals.* Current opinion in Biotechnology, 2004. **15**(3): p. 181-186.
81. Samina, M., A. Karim, and A. Venkatachalam, *Corrosion study of iron and copper metals and brass alloy in different medium.* Journal of Chemistry, 2011. **8**(S1): p. S344-S348.
82. Abdulmaruf, S. and D. Dajab, *Corrosion behavior of Copper immersed in different environment.* Materials Society of Nigeria (MSN) Zaria chapter book of proceedings, 2007: p. 67-70.
83. Kumar, A., R. Shukla, and A. Venkatachalam, *Studies of Corrosion and Electrochemical Behavior of Some Metals and Brass Alloy under Different Media.* Rasayan J. Chem, 2013. **6**: p. 12-14.
84. Ikpesu, J., *Investigation of Weight Loss and Corrosion Rate of Bi-metals and Tri-metal in Acidic Environment. J. of Res.* Env. Sci. and Toxicology, 2014. **3**: p. 15-20.
85. Fontana, M.G. and N.D. Greene, *Corrosion engineering*. 2018: McGraw-hill.
86. Brondel, D., et al., *Corrosion in the oil industry.* Oilfield review, 1994. **6**(2): p. 4-18.
87. Roberge, P.R., *Corrosion basics: an introduction*. 2006.
88. Jones, D.A., *Principles and prevention of corrosion*. 1992: Macmillan.
89. Bard, A.J. and L.R. Faulkner, *Fundamentals and applications.* Electrochemical Methods, 2001. **2**(482): p. 580-632.
90. Sarin, P., et al., *Physico-chemical characteristics of corrosion scales in old iron pipes.* Water Research, 2001. **35**(12): p. 2961-2969.

91. De Waard, C., U. Lotz, and D. Milliams, *Predictive model for CO2 corrosion engineering in wet natural gas pipelines.* Corrosion, 1991. **47**(12): p. 976-985.
92. Taylor, C., et al., *Multiphysics modelling, quantum chemistry and risk analysis for corrosion inhibitor design and lifetime prediction.* Faraday discussions, 2015. **180**: p. 459-477.
93. Pourbaix, M., *Atlas of electrochemical equilibria in aqueous solutions.* NACE, 1966.
94. Obot, I., D. Macdonald, and Z. Gasem, *Density functional theory (DFT) as a powerful tool for designing new organic corrosion inhibitors. Part 1: an overview.* Corrosion Science, 2015. **99**: p. 1-30.
95. Macdonald, D. and G. Cragnolino, *Corrosion and erosion–corrosion of steam cycle materials.* Water Technology for Thermal Power Systems, 1989.
96. Momeni, M. and J. Wren, *A mechanistic model for oxide growth and dissolution during corrosion of Cr-containing alloys.* Faraday discussions, 2015. **180**: p. 113-135.
97. Finšgar, M. and J. Jackson, *Application of corrosion inhibitors for steels in acidic media for the oil and gas industry: a review.* Corrosion science, 2014. **86**: p. 17-41.
98. Popoola, L.T., et al., *Corrosion problems during oil and gas production and its mitigation.* International Journal of Industrial Chemistry, 2013. **1**(4): p. 1-15.
99. Tiu, B.D.B. and R.C. Advincula, *Polymeric corrosion inhibitors for the oil and gas industry: Design principles and mechanism.* Reactive and Functional Polymers, 2015. **95**: p. 25-45.
100. Bonis, M.R. and J.L. Crolet. *Why So Low Free Acetic Acid Thresholds, in Sweet Corrosion at Low PCO2?* in *CORROSION 2005*. 2005. NACE International.
101. Weeter, R., *Desorption of oxygen from water using natural gas for countercurrent stripping.* Journal of Petroleum Technology, 1965. **17**(05): p. 515-520.
102. FOUDA, A.E.A.E.S., M.A. IBRAHEEM, and M.T. RASHAD, *Sweet Corrosion Inhibition on API 5L-B Pipeline Steel.* Journal of dispersion science and technology, 2014. **35**(4-6): p. 739-752.
103. Groysman, A., *Corrosion problems and solutions in oil, gas, refining and petrochemical industry.* Koroze a ochrana materialu, 2017. **61**(3): p. 100-117.
104. Jia, Z., et al., *Effect of acetic acid on CO2 corrosion of 3Cr low-alloy steel.* Materials Chemistry and Physics, 2012. **132**(2-3): p. 258-263.

105. Palmer-Jones, R. and D. Paisley, *Repairing Internal Corrosion Defects in Pipelines-A Case Study*.
106. Nyborg, R. and A. Dugstad. *Understanding and prediction of mesa corrosion attack*. in *CORROSION 2003*. 2003. NACE International.
107. Tems, R.D., *Downhole corrosion*, in *Trends in Oil and Gas Corrosion Research and Technologies*. 2017, Elsevier. p. 79-94.
108. Ali, T. and R.F.S.E. Center, *TECHNOECONOMIC ANALYSIS OF AREA II HYDROGEN PRODUCTION-PART*.
109. Koteeswaran, M., *CO2 and H2S Corrosion in Oil Pipelines.* 2010.
110. Sun, W. and S. Nesic. *A Mechanistic Model Of H2S Corrosion Of Mild Steel*. in *CORROSION 2007*. 2007. NACE International.
111. Nesic, S., et al., *A new updated model of CO2/H2S corrosion in multiphase flow.* CORROSION 2008, 2008.
112. Smith, J. and J. Miller, *Nature of sulphides and their corrosive effect on ferrous metals: a review*. British Corrosion Journal, 1975. **10**(3): p. 136-143.
113. Ning, J., et al., *Thermodynamic study of hydrogen sulfide corrosion of mild steel.* Corrosion, 2014. **70**(4): p. 375-389.
114. MR, N., *Petroleum, Petrochemical, and Natural Gas Industries—Materials for Use in H2S-Containing Environments in Oil and Gas Production*. 2015, NACE: Houston, TX, USA.
115. Agarwal, A., et al., *Corrosion aspect of dental implants—An overview and.* Open Journal of Stomatology, 2014. **4**: p. 56-60.
116. Shreir, L.L., *Corrosion: corrosion control*. 2013: Newnes.
117. Cottis, R., *Shreir's corrosion*. 2010: Elsevier Amsterdam, The Netherlands:.
118. Revie, R.W., *Corrosion and corrosion control: an introduction to corrosion science and engineering*. 2008: John Wiley & Sons.
119. Godinez-Alvarez, J., et al. *Inhibition of ferrous metal corrosion by carboxylates*. in *CORROSION 2004*. 2004. NACE International.
120. ISO, D., *Corrosion of metals and alloys–basic terms and definitions*. 1999, ISO.
121. Papavinasam, S., *Corrosion Control in the Oil and Gas Industry*. 2014, Elsevier.
122. Richardson, T.J., *Shreir's corrosion*. 2009: Elsevier.

123. Boffardi, B.P., *Control of environmental variables in water-recirculating systems.* ASM Handbook., 1987. **13**: p. 487-497.
124. Sørensen, P.A., et al., *Anticorrosive coatings: a review.* Journal of Coatings Technology and Research, 2009. **6**(2): p. 135-176.
125. Lourenço, M. and C.d. SOUZA, *Métodos de proteção e aumento da durabilidade do concreto armado.* Corrosão em Estruturas de Concreto Armado: Teoria, Controle e Métodos de Análise. 1st ed. Rio de Janeiro: Elsevier, 2014: p. 51-73.
126. Rivetti, M.L.S. and D.V. Ribeiro, *Corrosion inhibitors for reinforced concrete.* Corrosion inhibitors, principles and recent applications, 2018: p. 35-58.
127. Fontana, M. and N. Greene, *Modern Theory—Principles.* Corrosion Engineering, 1986: p. 445-481.
128. Dariva, C.G. and A.F. Galio, *Corrosion inhibitors–principles, mechanisms and applications.* Developments in corrosion protection, 2014. **16**: p. 365-378.
129. Myrdal, R., *Corrosion Inhibitors-State of the art: FA 3.2 Service life: SP 3.2. 5 Preventive measures.* 2010.
130. Trépanier, S., B. Hope, and C. Hansson, *Corrosion inhibitors in concrete: Part III. Effect on time to chloride-induced corrosion initiation and subsequent corrosion rates of steel in mortar.* Cement and concrete research, 2001. **31**(5): p. 713-718.
131. Brunella, M.F., L. Bertolini, and S. Candiani. *Effect of Chloride Environments on Fatigue Behavior of AA6061*-A1203* Particle Composite*. in *CORROSION 98*. 1998. NACE International.
132. Thorpe, T., et al., *Corrosion fatigue of BS 4360: 50D structural steel in seawater.* International journal of fatigue, 1983. **5**(3): p. 123-133.
133. Ebara, R., *Corrosion fatigue crack initiation in 12% chromium stainless steel.* Materials Science and Engineering: A, 2007. **468**: p. 109-113.
134. de Rincon, O.T., et al., *Long-term performance of ZnO as a rebar corrosion inhibitor.* Cement and concrete composites, 2002. **24**(1): p. 79-87.
135. Söylev, T.A. and M. Richardson, *Corrosion inhibitors for steel in concrete: State-of-the-art report.* Construction and Building Materials, 2008. **22**(4): p. 609-622.
136. Soeda, K. and T. Ichimura, *Present state of corrosion inhibitors in Japan.* Cement and Concrete Composites, 2003. **25**(1): p. 117-122.

137. Kondratova, I., P. Montes, and T. Bremner, *Natural marine exposure results for reinforced concrete slabs with corrosion inhibitors.* Cement and Concrete Composites, 2003. **25**(4-5): p. 483-490.

138. Elsener, B. and U. Angst, *Corrosion inhibitors for reinforced concrete,* in *Science and Technology of Concrete Admixtures*. 2016, Elsevier. p. 321-339.

139. Fouda, A., et al., *Quinazolin derivatives as eco-friendly corrosion inhibitors for low carbon steel in 2 M HCl solutions.* African Journal of Pure and Applied Chemistry, 2013. **7**(5): p. 198-207.

140. Ryu, H.-S., et al., *Effect of LiNO2 inhibitor on corrosion characteristics of steel rebar in saturated Ca (OH) 2 solution containing NaCl: an electrochemical study.* Construction and Building Materials, 2017. **133**: p. 387-396.

141. Lourenço, M. and C.d. SOUZA, *Métodos de Proteção e aumento da durabilidade do concreto armado.* Corrosão em estruturas de concreto armado. Rio de Janeiro: Campus, 2014.

142. Cao, Z.L., M. Hibino, and H. Goda, *Effect of Nitrite Concentration and pH on Steel Corrosion Induced by Chloride in Simulated Concrete Pore Environment.* Applied Mechanics and Materials, 2012. **193**: p. 314-318.

143. Fei, F.-l., et al., *Corrosion performance of steel reinforcement in simulated concrete pore solutions in the presence of imidazoline quaternary ammonium salt corrosion inhibitor.* Construction and Building Materials, 2014. **70**: p. 43-53.

144. Bryan, N.S., et al., *Ingested nitrate and nitrite and stomach cancer risk: an updated review.* Food and Chemical Toxicology, 2012. **50**(10): p. 3646-3665.

145. Ormellese, M., et al., *A study of organic substances as inhibitors for chloride-induced corrosion in concrete.* Corrosion Science, 2009. **51**(12): p. 2959-2968.

146. Liu, Z.Y., et al. *Electrochemical behavior of carbon steel in neutral chloride solution adding amine-carboxylate based corrosion inhibitor*. in *Applied Mechanics and Materials*. 2012. Trans Tech Publ.

147. Li, Z.Y., L.Q. Tu, and M.Q. Qin. *Effectiveness of Amino Alcohol-Based Corrosion Inhibitor and its influence on concrete properties*. in *Applied Mechanics and Materials*. 2014. Trans Tech Publ.

148. Larouj, M., et al., *Adsorption properties and inhibition of carbon steel corrosion in hydrochloric acid solution by Ethyl 3-hydroxy-8-methyl-4-oxo-6-phenyl-2-(p-toly)-4, 6-dihydropyrimido [2, 1-b][1, 3] thiazine-7-carboxylate.* J. Mater. Environ. Sci, 2015. **6**(11): p. 3251-3267.

149. Ryu, H.-S., et al., *Evaluation of corrosion resistance properties of N, N'-Dimethyl ethanolamine corrosion inhibitor in saturated Ca (OH) 2 solution with different concentrations of chloride ions by electrochemical experiments.* Construction and Building Materials, 2016. **114**: p. 223-231.

150. Abdulrahman, A., M. Ismail, and M.S. Hussain, *Corrosion inhibitors for steel reinforcement in concrete: A review.* Scientific Research and Essays, 2011. **6**(20): p. 4152-4162.

151. Hmamou, D.B., et al., *Inhibition of C38 steel corrosion in hydrochloric acid solution by 4, 5-Diphenyl-1H-Imidazole-2-Thiol: Gravimetric and temperature effects treatments.* Journal of Chemical and Pharmaceutical Research, 2012. **4**(7): p. 3498-3504.

152. Singh, A. and M. Quraishi, *Piroxicam; A novel corrosion inhibitor for mild steel corrosion in HCl acid solution.* J Mater Environ Sci, 2010. **1**(2): p. 101-110.

153. Abdulrahman, A. and M. Ismail, *Green Plant Extract as a passivation-promoting Inhibitor for Reinforced Concrete.* International Journal of Engineering Science and Technology, 2011. **3**(8): p. 6484-6490.

154. Redman, E. and A. Redman, *Transforming sustainable food and waste behaviors by realigning domains of knowledge in our education system.* Journal of Cleaner Production, 2014. **64**: p. 147-157.

155. Okeniyi, J.O., C.A. Loto, and A.P.I. Popoola, *Electrochemical performance of Anthocleista djalonensis on steel-reinforcement corrosion in concrete immersed in saline/marine simulating-environment.* Transactions of the Indian Institute of Metals, 2014. **67**(6): p. 959-969.

156. Raja, P.B., S. Ghoreishiamiri, and M. Ismail, *Natural Corrosion Inhibitors For Steel Reinforcement In Concrete—A Review.* Surface Review and Letters (SRL), 2015. **22**(03): p. 1-8.

157. Logan, H.L., *Film-rupture mechanism of stress corrosion.* Journal of Research of the National Bureau of Standards, 1952. **48**(2): p. 99-105.

158. Sastri, V.S., *Corrosion inhibitors: principles and applications*.
159. Palmer, J.W., W. Hedges, and J.L. Dawson, *A Working Party Report on the Use of Corrosion Inhibitors in Oil and Gas Production*. Vol. 840. 2004: Routledge.
160. Binks, B., et al. *Comparison of the Effects of Air, Carbon Dioxide and Hydrogen Sulphide on Corrosion of a Low Carbon Steel under Water and Its Inhibition by a Quaternary Ammonium Salt*. in *CORROSION 2005*. 2005. NACE International.
161. McMahon, A., *The mechanism of action of an oleic imidazoline based corrosion inhibitor for oilfield use.* Colloids and surfaces, 1991. **59**: p. 187-208.
162. Ramachandran, S., et al., *Self-assembled monolayer mechanism for corrosion inhibition of iron by imidazolines.* Langmuir, 1996. **12**(26): p. 6419-6428.
163. Jovancicevic, V., S. Ramachandran, and P. Prince, *Inhibition of carbon dioxide corrosion of mild steel by imidazolines and their precursors.* Corrosion, 1999. **55**(5): p. 449-455.
164. Schweitzer, P.A., *Corrosion Engineering Handbook, -3 Volume Set*. 1996: CRC Press.
165. Masel, R.I., *Principles of adsorption and reaction on solid surfaces*. Vol. 3. 1996: John Wiley & Sons.
166. Ibach, H., *Physics of Surfaces and Interfaces*. 2006: Springer Science & Business Media.
167. Bagotsky, V.S., *Fundamentals of electrochemistry*. Vol. 44. 2005: John Wiley & Sons.
168. Monk, P.M., *Physical chemistry: understanding our chemical world*. 2005: John Wiley & Sons.
169. Morales Gil, P., *Exploring corrosion inhibition in acidic and oilfield environments*. 2013, University of Manchester.
170. BenSalah, M., et al., *Passivity of Sanicro28 (UNS N-08028) stainless steel in polluted phosphoric acid at different temperatures studied by electrochemical impedance spectroscopy and Mott–Schottky analysis.* Corrosion Science, 2014. **86**: p. 61-70.
171. Bentiss, F., M. Traisnel, and M. Lagrenee, *The substituted 1, 3, 4-oxadiazoles: a new class of corrosion inhibitors of mild steel in acidic media.* Corrosion science, 2000. **42**(1): p. 127-146.
172. Mernari, B., et al., *Inhibiting effects of 3, 5-bis (n-pyridyl)-4-amino-1, 2, 4-triazoles on the corrosion for mild steel in 1 M HCl medium.* Corrosion Science, 1998. **40**(2-3): p. 391-399.
173. Ita, B. and O. Effiong, *Adsorption Study on the Corrosion Inhibition Properties of 2-Acetylpyrole and 2-Acetylpyrrole-(2-Acethylthiosemi-Carbazone) on Mild Steel in*

Hydrochloric Acid Medium. Global Journal of Pure and Applied Sciences, 1999. **5**: p. 497-502.

174. Touham, F., et al., *New pyrazolic compounds as corrosion inhibitors for Iron Armco in HCI media.* Bulletin of Electrochemistry, 2000. **16**(6): p. 245-249.
175. Ebenso, E., et al., *Inhibition of mild steel corrosion in sulphuric acid using alizarin yellow GG dye and synergistic iodide additive.* Int. J. Electrochem. Sci, 2008. **3**(12): p. 1325-1339.
176. Masel, R.I., *Principles of adsorption and reaction on solid surfaces.* 1996.
177. Hackerman, N. and A. Makrides, *Action of polar organic inhibitors in acid dissolution of metals.* Industrial & Engineering Chemistry, 1954. **46**(3): p. 523-527.
178. Ishihara, S., et al., *Prediction of corrosion fatigue lives of aluminium alloy on the basis of corrosion pit growth law*. Fatigue & Fracture of Engineering Materials & Structures, 2006. **29**(6): p. 472-480.
179. Akid, R., *The initiation and growth of short fatigue cracks in an aqueous saline environment*. 1987, University of Sheffield.
180. Abd El-Maksoud, S., *The effect of organic compounds on the electrochemical behaviour of steel in acidic media. A review.* International Journal of Electrochemical Science, 2008. **3**(5): p. 528-555.
181. Ebadi, M., et al., *Corrosion inhibition properties of pyrazolylindolenine compounds on copper surface in acidic media.* Chemistry Central Journal, 2012. **6**(1): p. 163.
182. Wang, H., et al., *Characterization of inhibitor and corrosion product film using electrochemical impedance spectroscopy (EIS).* CORROSION 2001, 2001.
183. Ivušić, F., et al., *Synergistic inhibition of carbon steel corrosion in seawater by cerium chloride and sodium gluconate.* 2015. **98**: p. 88-97.
184. Umoren, S.A. and M.M.J.J.o.e.c.e. Solomon, *Synergistic corrosion inhibition effect of metal cations and mixtures of organic compounds: a review.* 2017. **5**(1): p. 246-273.
185. Peyrat-Maillard, M., et al., *Effect of vitamin E and vitamin C on the antioxidant activity of malt rootlets extracts.* 2001. **34**(3): p. 176-182.
186. Yechiel, E., *Interactive Vehicles in Synergistic Cosmeceuticals: Advances in Nanoencapsulation, Transportation, Transfer, and Targeting*, in *Delivery System Handbook for Personal Care and Cosmetic Products*. 2005, Elsevier. p. 303-319.

187. Mobin, M., M. Parveen, and M.J.A.J.o.C. Rafiquee, *Synergistic effect of sodium dodecyl sulfate and cetyltrimethyl ammonium bromide on the corrosion inhibition behavior of l-methionine on mild steel in acidic medium.* 2017. **10**: p. S1364-S1372.

188. Javadian, S., A. Yousefi, and J.J.A.S.S. Neshati, *Synergistic effect of mixed cationic and anionic surfactants on the corrosion inhibitor behavior of mild steel in 3.5% NaCl.* 2013. **285**: p. 674-681.

189. Umoren, S., I. Obot, and E.J.J.o.C. Ebenso, *Corrosion Inhibition of Aluminium Using Exudate Gum from Pachylobus edulis in the Presence of Halide Ions in HCl.* **5**(2): p. 355-364.

190. Aramaki, K. and N. Hackerman, *Inhibition mechanism of medium-sized polymethyleneimine.* Journal of the electrochemical society, 1969. **116**(5): p. 568.

191. Agosta, W.C., *Bombardier beetles and fever trees: a close-up look at chemical warfare and signals in animals and plants*. 1996.

192. Abdallah, M., et al., *Performance of tramadol drug as a safe inhibitor for aluminum corrosion in 1.0 M HCl solution and understanding mechanism of inhibition using DFT.* Egyptian Journal of Petroleum, 2019. **28**(2): p. 173-181.

193. Gupta, A., M. Naraniwal, and V. Kothari, *Modern extraction methods for preparation of bioactive plant extracts.* International journal of applied and natural sciences, 2012. **1**(1): p. 8-26.

194. Karban, R. and I. Baldwin, *Induced Responses to Herbivory University of Chicago Press, 319p.* 1997.

195. Abdallah, M., et al., *Antihypertensive drugs as an inhibitors for corrosion of aluminum and aluminum silicon alloys in aqueous solutions.* Arabian Journal of Chemistry, 2012. **5**(2): p. 225-234.

196. Abdollahi, F., et al., *Electrochemical investigation of meloxicam drug as a corrosion inhibitor for mild steel in hydrochloric and sulfuric acid solutions.* Progress in Color, Colorants and Coatings, 2020. **13**(3): p. 155-165.

197. Alwash, A., et al., *Inhibitive effect of atenolol on the corrosion of zinc in hydrochloric acid.* Rasayan J Chem, 2017. **10**: p. 922-8.

198. Bashir, S., et al., *Inhibition Performances of Nicotinamide Against Aluminum Corrosion in an Acidic Medium.* Portugaliae Electrochimica Acta, 2020. **38**(2): p. 107-123.

199. Bensouda, Z., et al., *Corrosion inhibition of mild steel in 1 M HCl solution by Artemisia Abrotanum essential oil as an eco-friendly inhibitor*. J Mater Environ Sci, 2018. **9**: p. 1851-1865.

200. PELIKÁN, J.B., *Conservation of iron with tannin.* Studies in conservation, 1966. **11**(3): p. 109-116.

201. Hem, J.D., *Complexes of ferrous iron with tannic acid*. 1960: US Government Printing Office.

202. Xu, W., E.-H. Han, and Z. Wang, *Effect of tannic acid on corrosion behavior of carbon steel in NaCl solution.* Journal of Materials Science & Technology, 2019. **35**(1): p. 64-75.

203. Rocca, E. and F. Mirambet, *Corrosion inhibitors for metallic artefacts: temporary protection*, in *Corrosion of Metallic Heritage Artefacts*. 2007, Elsevier. p. 308-334.

204. Jalajaa, D., et al., *Moringa oleifera gum exudate as corrosion inhibitor on mild steel in acidic medium.* Rasayan Journal Chemistry, 2019. **12**: p. 545-548.

205. Murthy, Z. and K. Vijayaragavan, *Mild steel corrosion inhibition by acid extract of leaves of Hibiscus sabdariffa as a green corrosion inhibitor and sorption behavior*. Green Chemistry Letters and Reviews, 2014. **7**(3): p. 209-219.

206. Ji, G., et al., *Aqueous extract of Argemone mexicana roots for effective protection of mild steel in an HCl environment.* Research on Chemical Intermediates, 2016. **42**(2): p. 439-459.

207. Haida, S., et al., *Cistus monspeliensis extract as antioxidant and corrosion inhibitor of ordinary steel in 1 M hydrochloric acid medium.* Mediterranean Journal of Chemistry, 2020. **10**(2): p. 185-196.

208. Odidika, C.C., et al., *Corrosion Inhibition and Adsorption Properties of Commelina benghalensis Leaves Extract on Mild Steel in 1M H2SO4 Solution.* Science, 2020. **8**(2): p. 86-92.

209. Sivakumar, P. and A. Srikanth, *Green corrosion inhibitor: A comparative study.* Sādhanā, 2020. **45**(1): p. 1-11.

210. Boudalia, M., et al., *Green approach to corrosion inhibition of stainless steel in phosphoric acid of Artemesia herba albamedium using plant extract.* Journal of Materials Research and Technology, 2019. **8**(6): p. 5763-5773.

211. Ogunleye, O., et al., *Green corrosion inhibition and adsorption characteristics of Luffa cylindrica leaf extract on mild steel in hydrochloric acid environment.* Heliyon, 2020. **6**(1): p. e03205.

212. Eddy, N. and E. Ebenso, *Inhibitive and adsorption properties of Musa sapientum for the corrosion of mild steel in acid medium.* Pure and Applied Chemistry, 2008. **2**: p. 46-54.

213. Singh, M.R., *A green Approach: A corrosion inhibition of mild steel by adhatoda vasica plant extract in 0.5 MH2so4.* environments. **10**: p. 19.

214. Kumar, K., M. Pillai, and G.R. Thusnavis, *Pericarp of the fruit of garcinia mangostana as corrosion inhibitor for mild steel in hydrochloric acid medium.* Portugaliae Electrochimica Acta, 2010. **28**(6): p. 373-383.

215. Vijayalakshmi, P., R. Rajalakshmi, and S. Subhashini, *Cocos nucifera shell as a potential inhibitor for mild steel corrosion in acidic medium.* Asian Journal of Chemistry, 2010. **22**(6): p. 4537.

216. Okafor, P.C., E.E. Ebenso, and U.J. Ekpe, *Azadirachta indica extracts as corrosion inhibitor for mild steel in acid medium.* Int. J. Electrochem. Sci, 2010. **5**(7): p. 978-993.

217. Ekanem, U., et al., *Inhibition of mild steel corrosion in HCl using pineapple leaves (Ananas comosus L.) extract.* Journal of materials science, 2010. **45**(20): p. 5558-5566.

218. Satapathy, A., et al., *Corrosion inhibition by Justicia gendarussa plant extract in hydrochloric acid solution.* Corrosion science, 2009. **51**(12): p. 2848-2856.

219. Singh, A., I. Ahamad, and M.A. Quraishi, *Piper longum extract as green corrosion inhibitor for aluminium in NaOH solution.* Arabian Journal of Chemistry, 2016. **9**: p. S1584-S1589.

220. Vijayalakshmi, P., R. Rajalakshmi, and S. Subhashini, *Corrosion inhibition of aqueous extract of Cocos nucifera-coconut palm-petiole extract from destructive distillation for the corrosion of mild steel in acidic medium.* Portugaliae Electrochimica Acta, 2011. **29**(1): p. 9-21.

221. Lebrini, M., F. Robert, and C. Roos, *Inhibition effect of alkaloids extract from Annona squamosa plant on the corrosion of C38 steel in normal hydrochloric acid medium.* International Journal of Electrochemical Science, 2010. **5**(11): p. 1698-1712.

222. Van Wyk, B.-E. and N. Gericke, *People's plants: A guide to useful plants of Southern Africa*. 2000: Briza publications.

223. Leistner, O.A., *Seed plants of southern Africa: families and genera*. 2000: National Botanical Institute.
224. Viljoen, A., et al., *The composition, geographical variation and antimicrobial activity of Lippia javanica (Verbenaceae) leaf essential oils.* 2005. **96**(1-2): p. 271-277.
225. Fabian, A. and G. Germishuizen, *Wild flowers of northern South Africa*. 1997: Fernwood Press.
226. Van Wyk, B.-E., B.v. Oudtshoorn, and N. Gericke, *Medicinal Plants of South Africa*. 1997: Briza.
227. Pascual, M., et al., *Lippia: traditional uses, chemistry and pharmacology: a review.* 2001. **76**(3): p. 201-214.
228. Chagonda, L.S. and J.-C. Chalchat, *Essential oil composition of Lippia javanica (Burm. f.) spreng chemotype from Western Zimbabwe.* Journal of Essential Oil Bearing Plants, 2015. **18**(2): p. 482-485.
229. Smith, C.A., *Common names of South African plants.* 1966.
230. Watt, J., M.G.J.T.M. Breyer-brandwijk, and P.P.o.S. Africa., *The Medicinal and Poisonous Plants of Southern Africa.* 1932.
231. Hutchings, A., N.J.V. Press, and Flora, *Zulu medicinal plants. an inventory.* 1998: p. 27.
232. Hutchings, A. and J.J.J.o.E. van Staden, *Plants used for stress-related ailments in traditional Zulu, Xhosa and Sotho medicine. Part 1: Plants used for headaches.* 1994. **43**(2): p. 89-124.
233. Chagonda, L.S. and J.-C.J.J.o.E.O.B.P. Chalchat, *Essential oil composition of Lippia javanica (Burm. f.) spreng chemotype from Western Zimbabwe.* 2015. **18**(2): p. 482-485.
234. Lukwa, N., et al., *Lippia javanica (Burm F) Spreng: its general constituents and bioactivity on mosquitoes.* 2009. **26**(1): p. 85-91.
235. Manenzhe, N.J., N. Potgieter, and T.J.P. van Ree, *Composition and antimicrobial activities of volatile components of Lippia javanica.* 2004. **65**(16): p. 2333-2336.
236. Mwangi, J., et al., *Essential oils of Kenyan Lippia species. Part III.* 1991. **6**(3): p. 221-224.
237. Pooley, E., *A field guide to wildflowers: KwaZulu-Natal and the eastern region*. 1998: Natal Flora Publ. Trust.
238. Wang, H., et al., *Atomic bonding between metal and graphene.* 2013. **117**(9): p. 4632-4638.

239. Hage, D.S. *Reference module in chemistry, molecular sciences and chemical engineering*. in *Elsevier Inc.* 2013.
240. Young, D.C., *Computational Chemistry: A Practical Guide for Applying Techniques to Real World Problems. 2001*. 1999.
241. Lewars, E., *Computational chemistry*. Introduction to the theory and applications of molecular and quantum mechanics, 2003: p. 318.
242. Burkert, U. and N. Allinger, *Molecular Mechanics, 1982, ACS Monograph 177*. Am. Chem. Soc., Washington, DC.
243. Taylor, C.D. and P. Marcus, *Molecular modeling of corrosion processes: scientific development and engineering applications*. 2015: Wiley Online Library.
244. Vanommeslaeghe, K. and O.J.C.p.d. Guvench, *Molecular mechanics*. 2014. **20**(20): p. 3281-3292.
245. Allinger, N.L., *Conformational Analysis. III. Applications to Some Medium Ring Compounds1, 2*. Journal of the American Chemical Society, 1959. **81**(21): p. 5727-5733.
246. Leach, A.R. and A.R. Leach, *Molecular modelling: principles and applications*. 2001: Pearson education.
247. Jansen, S.A., et al., *Evolution of the electronic states of polyaniline: an ab initio analysis of the orbital states of PAni synthons.* Synthetic metals, 1999. **105**(2): p. 107-113.
248. GUND, T., *Molecular modeling of small molecules*, in *Guidebook on molecular modeling in drug design*. 1996, Elsevier. p. 55-92.
249. Young, D., *Computational chemistry: a practical guide for applying techniques to real world problems*. 2004: John Wiley & Sons.
250. Atkins, P.W. and R.S. Friedman, *Molecular quantum mechanics*. 2011: Oxford university press.
251. Schulten, K., *Notes on quantum mechanics*. University of Illinois at UrbanaChampaign, 2000.
252. Born, M. and R.J.A.d.p. Oppenheimer, *Zur quantentheorie der molekeln.* 1927. **389**(20): p. 457-484.
253. Balachandran, V., V. Karpagam, and A.J.J.o.M.S. Lakshmi, *Conformational stability, theoretical and experimental vibrational spectral analysis of 2, 4, 6-trihydroxybenzaldehyde.* 2012. **1021**: p. 13-21.

254. Denpo, K. and H.J.C. Ogawa, *Fluid flow effects on CO2 corrosion resistance of oil well materials.* 1993. **49**(6): p. 442-449.
255. Jensen, F., *Introduction to Computational Chemistry*. 2007.
256. Dewar, M.J., et al., *Development and use of quantum mechanical molecular models. 76. AM1: a new general purpose quantum mechanical molecular model.* Journal of the American Chemical Society, 1985. **107**(13): p. 3902-3909.
257. Stewart, J.J., *Optimization of parameters for semiempirical methods II. Applications.* Journal of computational chemistry, 1989. **10**(2): p. 221-264.
258. Abdulsattar, M.A. and K.H. Al-Bayati, *Corrections and parametrization of semiempirical large unit cell method for covalent semiconductors.* Physical Review B, 2007. **75**(24): p. 201-245.
259. Foresman, J., *Exploring chemistry.*
260. Foresman, J. and E. Frish, *Exploring chemistry*. Gaussian Inc., Pittsburg, USA, 1996.
261. Stewart, J.J., *Optimization of parameters for semiempirical methods V: modification of NDDO approximations and application to 70 elements.* Journal of Molecular modeling, 2007. **13**(12): p. 1173-1213.
262. Kohn, W., *Time-dependent Kohn–Sham density-functional theory*. Physical Review A, 1965. **1133**: p. 140-148.
263. PERDEW, J.J.P.R.L., *Generalized gradient approximation made simple.* 1996. **77**: p. 3865-3868.
264. Hammer, B., L.B. Hansen, and J.K.J.P.R.B. Nørskov, *Improved adsorption energetics within density-functional theory using revised Perdew-Burke-Ernzerhof functionals.* 1999. **59**(11): p. 7413-7421.
265. Burke, K.J.T.J.o.c.p., *Perspective on density functional theory.* 2012. **136**(15): p. 150901-150901.
266. Sousa, S.F., P.A. Fernandes, and M.J.J.T.J.o.P.C.A. Ramos, *General performance of density functionals.* 2007. **111**(42): p. 10439-10452.
267. Grossman, J.C., L. Mitas, and K.J.P. Raghavachari, *Structure and stability of molecular carbon: Importance of electron correlation.* 1995. **75**(21): p. 3870-3873.

268. Zupan, A., et al., *Pressure-induced phase transitions in solid Si, SiO 2, and Fe: Performance of local-spin-density and generalized-gradient-approximation density functionals.* 1998. **58**(17): p. 11266-11272.
269. Skelton, J.M., et al., *Influence of the exchange-correlation functional on the quasi-harmonic lattice dynamics of II-VI semiconductors.* 2015: p. 064710-064710.
270. Giese, T. and D.J.T.J.o.C.P. York, *Density-functional expansion methods: evaluation of LDA, GGA, and meta-GGA functionals and different integral approximations.* 2010. **133**(24): p. 244107-244107.
271. PERDEW, J. and Y.J.P.r.B. WANG, Condensed matter, *Accurate and simple analytic representation of the electron-gas correlation energy.* 1992. **45**(23): p. 13244-13249.
272. Payne, M., et al., *Iterative minimization techniques for ab initio total-energy calculations: molecular dynamics and conjugate gradients.* 1992. **64**(4): p. 1045-1098.
273. Orio, M., D.A. Pantazis, and F.J.P.r. Neese, *Density functional theory.* 2009. **102**(2-3): p. 443-453.
274. Wellendorff, J., et al., *A benchmark database for adsorption bond energies to transition metal surfaces and comparison to selected DFT functionals.* 2015. **640**: p. 36-44.
275. Klimeš, J., D. Bowler, and A.J.J.o.p.C.m.a.I.o.P.j. Michaelides, *Chemical accuracy for the van der Waals density functional.* 2010. **22**(2): p. 022201-022201.
276. Hensley, A.J., et al., *DFT-based method for more accurate adsorption energies: an adaptive sum of energies from RPBE and vdW density functionals.* 2017. **121**(9): p. 4937-4945.
277. Perdew, J., K. Burke, and M.J.P.R.L. Ernzerhof, *Perdew, burke, and ernzerhof reply*. 1998. **80**(4): p. 891.
278. Ernzerhof, M. and G.E.J.T.J.o.c.p. Scuseria, *Assessment of the Perdew–Burke–Ernzerhof exchange-correlation functional.* 1999. **110**(11): p. 5029-5036.
279. Cohen-Tannoudji, C., B. Diu, and F.J.Q.F.T. Laloë, McGraw-Hill, New York, USA, *Méchanique Quantique, vol 1, chapter 5. G, Hermann, 1977. C Itzykson, JB Zuber, ".*
280. Groß, A., *Theoretical Surface Science: A Microscopic Perspective*. 2013: Springer Science & Business Media.
281. Blöchl, P.J.P., *Projector augmented-wave method.* 1994. **50**(24): p. 17953-17979.

282. Vanderbilt, D.J.P., *Soft self-consistent pseudopotentials in a generalized eigenvalue formalism.* 1990. **41**(11): p. 7892-7895.
283. KRESSE, G.J.P.R.B., *From ultrasoft pseudopotentials to the projector augmented-wave method.* 1999. **59**: p. 1758-1775.
284. TROULLIER, N. and J.J.P.r.B. MARTINS, Condensed matter, *Efficient pseudopotentials for plane-wave calculations.* 1991. **43**(3): p. 1993-2006.
285. Rappe, A.M., et al., *Optimized pseudopotentials.* 1990. **41**(2): p. 1227-1230.
286. Schlapka, A., et al., *Surface strain versus substrate interaction in heteroepitaxial metal layers: Pt on Ru (0001).* 2003. **91**(1): p. 016101-016101.
287. Zakharov, M.J.I.J.o.Q.C., *Performance of numerical atom-centered basis sets in the ground-state correlated calculations of noncovalent interactions: Water and methane dimer cases.* 2013. **113**(15): p. 1899-1918.
288. Hohenberg, P. and W.J.P. Kohn, *Inhomogeneous Electron Gas.* 1964. **136**(3B): p. 864-871.
289. Davidson, E.R. and D.J.C.R. Feller, *Basis set selection for molecular calculations.* 1986. **86**(4): p. 681-696.
290. Migahed, M., E. Zaki, and M.J.R.a. Shaban, *Corrosion control in the tubing steel of oil wells during matrix acidizing operations.* 2016. **6**(75): p. 71384-71396.
291. Zhou, Y., et al., *Corrosion control of mild steel in 0.1 MH 2 SO 4 solution by benzimidazole and its derivatives: an experimental and theoretical study.* 2017. **7**(39): p. 23961-23969.
292. Bello, M., et al., *Modified cassava starches as corrosion inhibitors of carbon steel: An electrochemical and morphological approach.* 2010. **82**(3): p. 561-568.
293. Fouda, A., et al., *Experimental and theoretical studies on corrosion inhibition of 4-amidinophenyl-2, 2'-bifuran and its analogues in acidic media.* 2017. **7**(73): p. 46414-46430.
294. Jensen, F., *Introduction to computational chemistry*. 2017: John wiley & sons.
295. Civalleri, B., et al., *Hartree–Fock geometry optimisation of periodic systems with the CRYSTAL code.* 2001. **348**(1-2): p. 131-138.
296. Cramer, C.J., *Essentials of computational chemistry: theories and models*. 2013: John Wiley & Sons.

297. Delley, B.J.T.J.o.c.p., *An all-electron numerical method for solving the local density functional for polyatomic molecules.* 1990. **92**(1): p. 508-517.
298. Delley, B.J.T.J.o.c.p., *From molecules to solids with the DMol 3 approach.* 2000. **113**(18): p. 7756-7764.
299. Janousch, M., et al., *Role of oxygen vacancies in Cr-doped SrTiO3 for resistance-change memory.* 2007. **19**(17): p. 2232-2235.
300. Kaneti, Y.V., et al., *Experimental and theoretical studies of gold nanoparticle decorated zinc oxide nanoflakes with exposed {1 0 1 0} facets for butylamine sensing.* 2016. **230**: p. 581-591.
301. Delley, B.J.M.S., *The conductor-like screening model for polymers and surfaces.* 2006. **32**(2): p. 117-123.
302. Low, J.J., et al., *Virtual high throughput screening confirmed experimentally: porous coordination polymer hydration.* 2009. **131**(43): p. 15834-15842.
303. Basiuk, V.A., M.J.J.o.C. Bassiouk, and T. Nanoscience, *Interaction of amino acids with single-walled carbon nanotubes: Insights from density functional theory calculations.* 2008. **5**(7): p. 1205-1209.
304. Hayashi, Y., et al., *Prediction of the interaction between spermidine and the GG mismatch containing acceptor stem in tRNAIle: Molecular modeling, density functional theory, and molecular dynamics study.* 2013. **441**(4): p. 999-1004.
305. Bockstedte, M., et al., *Density-functional theory calculations for poly-atomic systems: electronic structure, static and elastic properties and ab initio molecular dynamics.* 1997. **107**(1-3): p. 187-222.
306. Brivio, G. and M.J.R. Trioni, *The adiabatic molecule-metal surface interaction: Theoretical approaches.* 1999. **71**(1): p. 231-265.
307. Sun, W. and G.J.S.S. Ceder, *Efficient creation and convergence of surface slabs.* 2013. **617**: p. 53-59.
308. Boettger, J.J.P., *Nonconvergence of surface energies obtained from thin-film calculations.* 1994. **49**(23): p. 16798-16800.
309. Fiorentini, V. and M.J.J.o.P.C.M. Methfessel, *Extracting convergent surface formation energies from slab calculations.* 1998. **10**(4): p. 895-895.

310. FU, C.-L. and K.-M.J.P.r.B. HO, Condensed matter, *First-principles calculation of the equilibrium ground-state properties of transition metals: applications to Nb and Mo.* 1983. **28**(10): p. 5480-5486.
311. Kokalj, A., *On the HSAB based estimate of charge transfer between adsorbates and metal surfaces.* Chemical Physics, 2012. **393**(1): p. 1-12.
312. Besora, M., et al., *Calculation of reaction free energies in solution: A comparison of current approaches.* 2018. **122**(5): p. 1392-1399.
313. Mennucci, B.J.T.J.o.P.C.L., *Continuum solvation models: What else can we learn from them?* 2010. **1**(10): p. 1666-1674.
314. Borowski, P., et al., *The vibrational spectrum of 1, 4-dioxane in aqueous solution–theory and experiment.* 2016. **40**(9): p. 7663-7670.
315. Könczöl, Á. and G.J.D.D.T.T. Dargó, *Brief overview of solubility methods: recent trends in equilibrium solubility measurement and predictive models.* 2018. **27**: p. 3-10.
316. Wang, J., T.J.C.c. Hou, and h.t. screening, *Recent advances on aqueous solubility prediction.* 2011. **14**(5): p. 328-338.
317. Skyner, R., et al., *A review of methods for the calculation of solution free energies and the modelling of systems in solution.* 2015. **17**(9): p. 6174-6191.
318. Hughes, L.D., et al., *Why are some properties more difficult to predict than others? A study of QSPR models of solubility, melting point, and Log P.* 2008. **48**(1): p. 220-232.
319. Yalkowsky, S.H. and S.C.J.J.o.p.s. Valvani, *Solubility and partitioning I: solubility of nonelectrolytes in water.* 1980. **69**(8): p. 912-922.
320. Jain, N. and S.H.J.J.o.p.s. Yalkowsky, *Estimation of the aqueous solubility I: application to organic nonelectrolytes.* 2001. **90**(2): p. 234-252.
321. Beveridge, D.L., F.J.A.r.o.b. DiCapua, and b. chemistry, *Free energy via molecular simulation: applications to chemical and biomolecular systems.* 1989. **18**(1): p. 431-492.
322. Mark, P. and L.J.T.J.o.P.C.A. Nilsson, *Structure and dynamics of the TIP3P, SPC, and SPC/E water models at 298 K.* 2001. **105**(43): p. 9954-9960.
323. van der Spoel, D., P.J. Van Maaren, and H.J.J.T.J.o.c.p. Berendsen, *A systematic study of water models for molecular simulation: derivation of water models optimized for use with a reaction field.* 1998. **108**(24): p. 10220-10230.

324. Takano, Y., K.J.J.o.C.T. Houk, and Computation, *Benchmarking the conductor-like polarizable continuum model (CPCM) for aqueous solvation free energies of neutral and ionic organic molecules.* 2005. **1**(1): p. 70-77.

325. Mullins, E., et al., *Sigma-profile database for using COSMO-based thermodynamic methods.* 2006. **45**(12): p. 4389-4415.

326. Andzelm, J., C. Kölmel, and A.J.T.J.o.c.p. Klamt, *Incorporation of solvent effects into density functional calculations of molecular energies and geometries.* 1995. **103**(21): p. 9312-9320.

327. Klamt, A.J.W.I.R.C.M.S., *The COSMO and COSMO-RS solvation models.* 2018. **8**(1): p. e1338.

328. Klamt, A., et al., *Refinement and parametrization of COSMO-RS.* 1998. **102**(26): p. 5074-5085.

329. von Ragué Schleyer, P., et al., *Encyclopedia of computational chemistry.* 1998.

330. Klamt, A. and F.J.F.P.E. Eckert, *COSMO-RS: a novel and efficient method for the a priori prediction of thermophysical data of liquids.* 2000. **172**(1): p. 43-72.

331. Klamt, A.C.-R., *From Quantum Chemistry to Fluid Phase Thermodynamics and Drug Design (2005)*. Amsterdam: Elsevier.

332. Levandi, T., et al., *Capillary electrophoresis time-of-flight mass spectrometry for comparative metabolomics of transgenic versus conventional maize.* Analytical chemistry, 2008. **80**(16): p. 6329-6335.

333. García-Villalba, R., et al., *Comparative metabolomic study of transgenic versus conventional soybean using capillary electrophoresis–time-of-flight mass spectrometry.* Journal of Chromatography A, 2008. **1195**(1-2): p. 164-173.

334. Dinelli, G., et al., *Determination of phenolic compounds in modern and old varieties of durum wheat using liquid chromatography coupled with time-of-flight mass spectrometry.* Journal of Chromatography A, 2009. **1216**(43): p. 7229-7240.

335. Grata, E., et al., *UPLC–TOF-MS for plant metabolomics: a sequential approach for wound marker analysis in Arabidopsis thaliana.* Journal of Chromatography B, 2008. **871**(2): p. 261-270.

336. Levandi, T., et al., *Principal component analysis of HPLC-MS/MS patterns of wheat (Triticum aestivum) varieties.* Proceedings of the Estonian Academy of Sciences, 2014. **63**(1): p. 86.
337. Snyder, L.R., J.J. Kirkland, and J.W. Dolan, *Introduction to modern liquid chromatography*. 2011: John Wiley & Sons.
338. Poole, C.F. and S.K. Poole, *Chromatography today*. 2012: Elsevier.
339. Unger, K.K., R. Skudas, and M.M. Schulte, *Particle packed columns and monolithic columns in high-performance liquid chromatography-comparison and critical appraisal.* Journal of Chromatography A, 2008. **1184**(1-2): p. 393-415.
340. Svec, F., *Porous polymer monoliths: amazingly wide variety of techniques enabling their preparation.* Journal of Chromatography A, 2010. **1217**(6): p. 902-924.
341. Lomsadze, K., et al., *Comparative high-performance liquid chromatography enantioseparations on polysaccharide based chiral stationary phases prepared by coating totally porous and core–shell silica particles.* Journal of Chromatography A, 2012. **1234**: p. 50-55.
342. Paek, C., et al., *Development of a carbon clad core-shell silica for high speed two-dimensional liquid chromatography*. Journal of Chromatography A, 2012. **1229**: p. 129-139.
343. Szyszka, D., *Study of contact angle of liquid on solid surface and solid on liquid surface.* Mining Science, 2012(135): p. 131-146.
344. Kubiak, K., et al., *Wettability versus roughness of engineering surfaces.* Wear, 2011. **271**(3-4): p. 523-528.
345. Holdich, R., et al., *Spreading of liquid drops from a liquid source.* Colloids and Surfaces A: Physicochemical and Engineering Aspects, 2006. **282**: p. 247-255.
346. Li, X.-M., D. Reinhoudt, and M. Crego-Calama, *What do we need for a superhydrophobic surface? A review on the recent progress in the preparation of superhydrophobic surfaces.* Chemical Society Reviews, 2007. **36**(8): p. 1350-1368.
347. Samanta, A., et al., *Roles of chemistry modification for laser textured metal alloys to achieve extreme surface wetting behaviors.* Materials & Design, 2020. **192**: p. 108744.
348. Erbil, H.Y., *The debate on the dependence of apparent contact angles on drop contact area or three-phase contact line: A review*. Surface Science Reports, 2014. **69**(4): p. 325-365.

349. Bard, A., et al., *Electrochemical methods: fundamentals and applications, vol 2 John Wiley & Sons.* New York, NY.[Google Scholar], 1980.
350. Mueller, W., *Theory of the polarization curve technique for studying corrosion and electrochemical protection.* Canadian Journal of Chemistry, 1960. **38**(4): p. 576-587.
351. Bard, A., et al., *Electrochemical Methods: Fundamentals and Applications Vol. 2 wiley.* New York, 1980: p. 231.
352. Stern, M. and A.L. Geary, *Electrochemical polarization: I. A theoretical analysis of the shape of polarization curves.* Journal of the electrochemical society, 1957. **104**(1): p. 56.
353. Barsoukov, E. and J.R. Macdonald, *Impedance Spectroscopy Theory, Experiment, and.* Applications, 2nd ed.(Hoboken, NJ: John Wiley &Sons, Inc., 2005), 2005.
354. Choi, W., et al., *Modeling and applications of electrochemical impedance spectroscopy (EIS) for lithium-ion batteries.* Journal of Electrochemical Science and Technology, 2020. **11**(1): p. 1-13.
355. Djoumbou Feunang, Y., et al., *ClassyFire: automated chemical classification with a comprehensive, computable taxonomy.* Journal of cheminformatics, 2016. **8**(1): p. 1-20.
356. Kim, H.W., et al., *NPClassifier: a deep neural network-based structural classification tool for natural products.* Journal of natural products, 2021. **84**(11): p. 2795-2807.
357. Dührkop, K., et al., *SIRIUS 4: Turning tandem mass spectra into metabolite structure information.*
358. Dührkop, K., et al., *Systematic classification of unknown metabolites using high-resolution fragmentation mass spectra.* Nature Biotechnology, 2021. **39**(4): p. 462-471.
359. Ludwig, M., et al., *Database-independent molecular formula annotation using Gibbs sampling through ZODIAC.* Nature Machine Intelligence, 2020. **2**(10): p. 629-641.
360. Böcker, S. and K. Dührkop, *Fragmentation trees reloaded.* Journal of cheminformatics, 2016. **8**(1): p. 1-26.
361. Böcker, S., et al., *SIRIUS: decomposing isotope patterns for metabolite identification.* Bioinformatics, 2009. **25**(2): p. 218-224.
362. Dührkop, K., et al., *Searching molecular structure databases with tandem mass spectra using CSI: FingerID.* Proceedings of the National Academy of Sciences, 2015. **112**(41): p. 12580-12585.

363. Hoffmann, M.A., et al., *Assigning confidence to structural annotations from mass spectra with COSMIC.* bioRxiv, 2021.

364. Chen, H., J.L. Muros-Cobos, and A. Amirfazli, *Contact angle measurement with a smartphone.* Review of Scientific Instruments, 2018. **89**(3): p. 035117.

365. Williams, D., et al., *Contact angle measurements using cellphone cameras to implement the Bikerman method.* Galvanotechnik, 2011. **102**(8): p. 1718.

366. Tran, T., et al., *A study of bacteria adhesion and microbial corrosion on different stainless steels in environment containing Desulfovibrio vulgaris.* Royal Society open science, 2021. **8**(1): p. 201577.

367. Stalder, A.F., et al., *Low-bond axisymmetric drop shape analysis for surface tension and contact angle measurements of sessile drops.* Colloids and Surfaces A: Physicochemical and Engineering Aspects, 2010. **364**(1-3): p. 72-81.

368. Delley, B., *From molecules to solids with the DMol 3 approach.* The Journal of chemical physics, 2000. **113**(18): p. 7756-7764.

369. Hehre, W.J., R. Ditchfield, and J.A. Pople, *Self—consistent molecular orbital methods. XII. Further extensions of Gaussian—type basis sets for use in molecular orbital studies of organic molecules.* The Journal of Chemical Physics, 1972. **56**(5): p. 2257-2261.

370. Francl, M.M., et al., *Self-consistent molecular orbital methods. XXIII. A polarization-type basis set for second-row elements.* The Journal of Chemical Physics, 1982. **77**(7): p. 3654-3665.

371. Mashhadzadeh, A.H., et al., *Theoretical studies on the mechanical and electronic properties of 2D and 3D structures of beryllium-oxide graphene and graphene nanobud.* Applied Surface Science, 2019. **476**: p. 36-48.

372. Wang, J., et al., *Gas sensing performances and mechanism at atomic level of Au-MoS2 microspheres.* Applied Surface Science, 2019. **490**: p. 124-136.

373. Attia, Y.M., et al., *Verbascoside: identification, quantification, and potential sensitization of colorectal Cancer cells to 5-FU by targeting PI3K/AKT pathway.* Scientific reports, 2018. **8**(1): p. 1-12.

374. Palencia, M., *Functional transformation of Fourier-transform mid-infrared spectrum for improving spectral specificity by simple algorithm based on wavelet-like functions.* Journal of advanced research, 2018. **14**: p. 53-62.

375. Vasincu, A., et al., *Vernonia kotschyana roots: Therapeutic potential via antioxidant activity*. Molecules, 2014. **19**(11): p. 19114-19136.

376. Kgatshe, M., et al., *Characterization and antibacterial activity of biosynthesized silver nanoparticles using the ethanolic extract of Pelargonium sidoides DC.* Journal of Nanomaterials, 2019. **2019**.

377. Guo, X., S. Zhang, and X.-q. Shan, *Adsorption of metal ions on lignin.* Journal of hazardous materials, 2008. **151**(1): p. 134-142.

378. Hari, N., et al., *IR Spectroscopic Analysis of Critically Endangered Jasminum Species.* Int. Jn. of innovative science and research technology, 2018.

379. Chang, H., et al., *Characterization of natural dye extracted from wormwood and purple cabbage for dye-sensitized solar cells.* International Journal of Photoenergy, 2013. **2013**.

380. Muchuweti, M. and Z. Chikwambi, *Isolation and identification of anthocyanins in the fruit peels of starkrimson and marx red bartlett common pear cultivars and their bud mutants.* Am. J. Food Technol, 2008. **3**: p. 1-12.

381. Kumari, M.M., S.A. Aromal, and D. Philip, *Synthesis of monodispersed palladium nanoparticles using tannic acid and its optical non-linearity*. Spectrochimica Acta Part A: Molecular and Biomolecular Spectroscopy, 2013. **103**: p. 130-133.

382. Mallikarjuna, K., et al., *Palladium nanoparticles: single-step plant-mediated green chemical procedure using Piper betle leaves broth and their anti-fungal studies.* International Journal of Chemical and Analytical Science, 2013. **4**(1): p. 14-18.

383. Norsworthy, R., *Understanding corrosion in underground pipelines: basic principles*, in *Underground Pipeline Corrosion*. 2014, Elsevier. p. 3-34.

384. M'hiri, N., et al., *Corrosion inhibition of carbon steel in acidic medium by orange peel extract and its main antioxidant compounds.* Corrosion Science, 2016. **102**: p. 55-62.

385. Yıldız, R., *An electrochemical and theoretical evaluation of 4, 6-diamino-2-pyrimidinethiol as a corrosion inhibitor for mild steel in HCl solutions.* Corrosion Science, 2015. **90**: p. 544-553.

386. Ansari, K., M. Quraishi, and A. Singh, *Schiff's base of pyridyl substituted triazoles as new and effective corrosion inhibitors for mild steel in hydrochloric acid solution.* Corrosion science, 2014. **79**: p. 5-15.

387. Rehim, S.S.A., et al., *On the corrosion inhibition of low carbon steel in concentrated sulphuric acid solutions. Part I: Chemical and electrochemical (AC and DC) studies.* Corrosion Science, 2008. **50**(8): p. 2258-2271.

388. Dhouibi, I., et al., *A study of the anti-corrosive effects of essential oils of rosemary and myrtle for copper corrosion in chloride media.* Arabian Journal of Chemistry, 2021. **14**(2): p. 102961.

389. Fayomi, O. and I. Akande, *Corrosion mitigation of aluminium in 3.65% NaCl medium using hexamine.* Journal of Bio-and Tribo-Corrosion, 2019. **5**(1): p. 1-7.

390. Gupta, R.K., et al., *Aminoazobenzene and diaminoazobenzene functionalized graphene oxides as novel class of corrosion inhibitors for mild steel: experimental and DFT studies.* Materials Chemistry and Physics, 2017. **198**: p. 360-373.

391. Carroll, W. and C. Breslin, *Stability of passive films formed on aluminium in aqueous halide solutions.* British Corrosion Journal, 1991. **26**(4): p. 255-259.

392. El-Shafei, A., S. Abd El-Maksoud, and A. Fouda, *The role of indole and its derivatives in the pitting corrosion of Al in neutral chloride solution.* Corrosion science, 2004. **46**(3): p. 579-590.

393. AlKharafi, F. and W. Badawy, *Stability of anodically passivated Al, Al-Cu, Al-6061 and Al-7075 in nitric acid and nitric acid solutions containing chloride.* Indian journal of chemical technology, 1996. **3**(4): p. 212-218.

394. Badawy, W., F. Al-Kharafi, and A. El-Azab, *Electrochemical behaviour and corrosion inhibition of Al, Al-6061 and Al–Cu in neutral aqueous solutions.* Corrosion Science, 1999. **41**(4): p. 709-727.

395. Tang, Y., et al., *The metastable pitting potential and its relation to the pitting potential for four materials in chloride solutions.* Corrosion Science, 2014. **80**: p. 111-119.

396. HEINE, B. and R. KIRCHHEIM, *Dissolution rates of iron and chromium and Fe-Cr-alloys in the passive state.* Corrosion science, 1990. **31**: p. 533-538.

397. Mahdavian, M. and S. Ashhari, *Corrosion inhibition performance of 2-mercaptobenzimidazole and 2-mercaptobenzoxazole compounds for protection of mild steel in hydrochloric acid solution.* Electrochimica Acta, 2010. **55**(5): p. 1720-1724.

398. Aljourani, J., K. Raeissi, and M. Golozar, *Benzimidazole and its derivatives as corrosion inhibitors for mild steel in 1M HCl solution.* Corrosion science, 2009. **51**(8): p. 1836-1843.

399. Rozenfel′d, I., *Corrosion inhibitors. 1981*. New York: McGraw-Hill.
400. Sastri, V., *Corrosion inhibitors: principles and applications. 1998*. Wiley New York.
401. Geethamani, P. and P. Kasthuri, *The inhibitory action of expired asthalin drug on the corrosion of mild steel in acidic media: a comparative study*. Journal of the Taiwan Institute of Chemical Engineers, 2016. **63**: p. 490-499.
402. Benabbouha, T., et al., *Red Algae Halopitys Incurvus extract as a green corrosion inhibitor of carbon steel in hydrochloric acid.* Journal of Bio-and Tribo-Corrosion, 2018. **4**(3): p. 1-9.
403. Liu, M., et al., *Analysis of the Anti-Corrosion Performance of Dextrin and Its Graft Copolymer on J55 Steel in Acid Solution.* Processes, 2021. **9**(9): p. 1642.
404. Xu, B., et al., *Experimental and theoretical evaluation of two pyridinecarboxaldehyde thiosemicarbazone compounds as corrosion inhibitors for mild steel in hydrochloric acid solution.* Corrosion Science, 2014. **78**: p. 260-268.
405. Abd El-Lateef, H.M., *Experimental and computational investigation on the corrosion inhibition characteristics of mild steel by some novel synthesized imines in hydrochloric acid solutions.* Corrosion Science, 2015. **92**: p. 104-117.
406. Abd El Rehim, S., M.A. Ibrahim, and K. Khalid, *The inhibition of 4-(2′-amino-5′-methylphenylazo) antipyrine on corrosion of mild steel in HCl solution.* Materials Chemistry and Physics, 2001. **70**(3): p. 268-273.
407. Li, X., S. Deng, and H. Fu, *Triazolyl blue tetrazolium bromide as a novel corrosion inhibitor for steel in HCl and H2SO4 solutions.* Corrosion Science, 2011. **53**(1): p. 302-309.
408. Yadav, M., et al., *Corrosion inhibition effect of spiropyrimidinethiones on mild steel in 15% HCl solution: insight from electrochemical and quantum studies.* RSC advances, 2015. **5**(87): p. 70832-70848.
409. Ammal, P.R., M. Prajila, and A. Joseph, *Effective inhibition of mild steel corrosion in hydrochloric acid using EBIMOT, a 1, 3, 4-oxadiazole derivative bearing a 2-ethylbenzimidazole moiety: Electro analytical, computational and kinetic studies.* Egyptian Journal of Petroleum, 2018. **27**(4): p. 823-833.

410. Oguzie, E., et al., *Biomass extracts for materials protection: corrosion inhibition of mild steel in acidic media by Terminalia chebula extracts.* Chemical engineering communications, 2014. **201**(6): p. 790-803.

411. Mobin, M., R. Aslam, and J. Aslam, *Non toxic biodegradable cationic gemini surfactants as novel corrosion inhibitor for mild steel in hydrochloric acid medium and synergistic effect of sodium salicylate: Experimental and theoretical approach.* Materials Chemistry and Physics, 2017. **191**: p. 151-167.

412. Karthik, G. and M. Sundaravadivelu, *Studies on the inhibition of mild steel corrosion in hydrochloric acid solution by atenolol drug.* Egyptian Journal of Petroleum, 2016. **25**(2): p. 183-191.

413. Tao, Z., et al., *Electrochemical study of cyproconazole as a novel corrosion inhibitor for copper in acidic solution.* Industrial & Engineering Chemistry Research, 2013. **52**(50): p. 17891-17899.

414. Macdonald, D.D., *Review of mechanistic analysis by electrochemical impedance spectroscopy*, in *Electrochemical and Optical Techniques for the Study and Monitoring of Metallic Corrosion*. 1991, Springer. p. 31-68.

415. Brett, C., *The application of electrochemical impedance techniques to aluminium corrosion in acidic chloride solution.* Journal of applied electrochemistry, 1990. **20**(6): p. 1000-1003.

416. Amin, M.A., Q. Mohsen, and O.A. Hazzazi, *Synergistic effect of I− ions on the corrosion inhibition of Al in 1.0 M phosphoric acid solutions by purine.* Materials Chemistry and Physics, 2009. **114**(2-3): p. 908-914.

417. Li, W.-h., et al., *Some new triazole derivatives as inhibitors for mild steel corrosion in acidic medium.* Journal of Applied Electrochemistry, 2008. **38**(3): p. 289-295.

418. Kliškić, M., et al., *Aqueous extract of Rosmarinus officinalis L. as inhibitor of Al–Mg alloy corrosion in chloride solution.* Journal of applied electrochemistry, 2000. **30**(7): p. 823-830.

419. Chugh, B., et al., *Comparative investigation of corrosion-mitigating behavior of thiadiazole-derived bis-schiff bases for mild steel in acid medium: experimental, theoretical, and surface study.* ACS omega, 2020. **5**(23): p. 13503-13520.

420. Abeng, F.E., et al., *Metolazone compound as corrosion inhibitor for API 5L X-52 steel in hydrochloric acid solution.* Bulletin of the Chemical Society of Ethiopia, 2020. **34**(2): p. 407-418.

421. Yadav, D.K., M. Quraishi, and B. Maiti, *Inhibition effect of some benzylidenes on mild steel in 1 M HCl: an experimental and theoretical correlation.* Corrosion science, 2012. **55**: p. 254-266.

422. Singh, J.K., et al., *Effect of Chloride Ions Concentrations to Breakdown the Passive Film on Rebar Surface Exposed to L-Arginine Containing Pore Solution.* Materials, 2021. **14**(19): p. 5693.

423. Zheludkevich, M., et al., *Triazole and thiazole derivatives as corrosion inhibitors for AA2024 aluminium alloy.* Corrosion Science, 2005. **47**(12): p. 3368-3383.

424. Rosero-Navarro, N.C., et al., *Effects of Ce-containing sol–gel coatings reinforced with SiO2 nanoparticles on the protection of AA2024.* Corrosion Science, 2008. **50**(5): p. 1283-1291.

425. Chaitra, T.K., K.N. Mohana, and H.C. Tandon, *Comparative study of Levofloxacin and its amide derivative as efficient water soluble inhibitors for mild steel corrosion in hydrochloric acid solution.* International journal of industrial chemistry, 2017. **8**(1): p. 1-15.

426. Lgaz, H., et al., *Evaluation of 2-mercaptobenzimidazole derivatives as corrosion inhibitors for mild steel in hydrochloric acid.* Metals, 2020. **10**(3): p. 357.

427. Quraishi, M.A., *2-Amino-3, 5-dicarbonitrile-6-thio-pyridines: new and effective corrosion inhibitors for mild steel in 1 M HCl.* Industrial & Engineering Chemistry Research, 2014. **53**(8): p. 2851-2859.

428. Saady, A., et al., *Experimental and theoretical tools for corrosion inhibition study of mild steel in aqueous hydrochloric acid solution by new indanones derivatives.* Materials discovery, 2018. **12**: p. 30-42.

429. Rahmani, H., et al., *Experimental, quantum chemical studies of oxazole derivatives as corrosion inhibitors on mild steel in molar hydrochloric acid medium.* International Journal of Corrosion and Scale Inhibition, 2018. **7**(4): p. 509-527.

430. Özcan, M., F. Karadağ, and I. Dehri, *Investigation of adsorption characteristics of methionine at mild steel/sulfuric acid interface: an experimental and theoretical study.*

Colloids and Surfaces A: Physicochemical and Engineering Aspects, 2008. **316**(1-3): p. 55-61.

431. Xu, B., et al., *Experimental and theoretical evaluation of N, N-Bis (2-pyridylmethyl) aniline as a novel corrosion inhibitor for mild steel in hydrochloric acid.* Journal of the Taiwan Institute of Chemical Engineers, 2016. **59**: p. 526-535.
432. Machnikova, E., et al., *Corrosion study of PVD coatings and conductive polymer deposited on mild steel: Part I: Polypyrrole.* Surface and Coatings Technology, 2008. **202**(8): p. 1543-1550.
433. Hassan, H.H., *Perchlorate and oxygen reduction during Zn corrosion in a neutral medium.* Electrochimica acta, 2006. **51**(26): p. 5966-5972.
434. Macdonald, J.R., *Impedance spectroscopy and its use in analyzing the steady-state AC response of solid and liquid electrolytes.* Journal of electroanalytical chemistry and interfacial electrochemistry, 1987. **223**(1-2): p. 25-50.
435. Palanisamy, G., *Corrosion Inhibitors*, in *Corrosion Inhibitors*. 2019, IntechOpen.
436. Jayakumar, S., et al., *Corrosion inhibition of mild steel in 1 M HCl using Tamarindus indica extract: electrochemical, surface and spectroscopic studies.* Journal of Adhesion Science and Technology, 2020. **34**(7): p. 713-743.
437. Mobin, M., S. Zehra, and R. Aslam, *L-Phenylalanine methyl ester hydrochloride as a green corrosion inhibitor for mild steel in hydrochloric acid solution and the effect of surfactant additive.* RSC advances, 2016. **6**(7): p. 5890-5902.
438. Alhaffar, M.T., et al., *Isoxazolidine derivatives as corrosion inhibitors for low carbon steel in HCl solution: experimental, theoretical and effect of KI studies.* Rsc Advances, 2018. **8**(4): p. 1764-1777.
439. Fares, M.M., A. Maayta, and J.A. Al-Mustafa, *Corrosion inhibition of iota-carrageenan natural polymer on aluminum in presence of zwitterion mediator in HCl media.* Corrosion Science, 2012. **65**: p. 223-230.
440. Quy Huong, D., T. Duong, and P.C. Nam, *Effect of the structure and temperature on corrosion inhibition of thiourea derivatives in 1.0 M HCl solution.* ACS omega, 2019. **4**(11): p. 14478-14489.

441. Prabhu, R., T. Venkatesha, and B. Praveen, *Electrochemical study of the corrosion behavior of zinc surface treated with a new organic chelating inhibitor.* International Scholarly Research Notices, 2012. **2012**.

442. Bentiss, F., M. Lebrini, and H. Vezin, *F., Chai, M., Traisnel, M. Lagrene, Enhanced corrosion resistance of carbon steel in normal sulfuric acid medium by some macrocyclic polyether compounds containing a 1, 3, 4-thiadiazole moiety AC impedance and computational studies.* Corr. sci, 2005. **51**: p. 2165-2173.

443. Alkhathlan, H.Z., et al., *Launaea nudicaulis as a source of new and efficient green corrosion inhibitor for mild steel in acidic medium: a comparative study of two solvent extracts.* Int J Electrochem Sci, 2014. **9**: p. 870-889.

444. Ahmed, A.H., et al., *Mn2+-complexes of N, O-dihydrazone: Structural studies, indirect band gap energy and corrosion inhibition on aluminum in acidic medium.* Journal of the Chilean Chemical Society, 2018. **63**(4): p. 4180-4189.

445. Hamdy, A. and N.S. El-Gendy, *Thermodynamic, adsorption and electrochemical studies for corrosion inhibition of carbon steel by henna extract in acid medium.* Egyptian Journal of Petroleum, 2013. **22**(1): p. 17-25.

446. Shukla, S.K. and M. Quraishi, *The effects of pharmaceutically active compound doxycycline on the corrosion of mild steel in hydrochloric acid solution.* Corrosion Science, 2010. **52**(2): p. 314-321.

447. Onyeachu, I.B., et al., *Corrosion inhibition effect of a benzimidazole derivative on heat exchanger tubing materials during acid cleaning of multistage flash desalination plants.* Desalination, 2020. **479**: p. 114283.

448. Smith, W. and F. Goodwin, *Hot Dip Coatings.* 2017.

449. Kairi, N.I. and J. Kassim, *The effect of temperature on the corrosion inhibition of mild steel in 1 M HCl solution by Curcuma longa extract.* International Journal of Electrochemical Science, 2013. **8**(5): p. 7138-7155.

450. Bentiss, F., M. Lebrini, and M. Lagrenée, *Thermodynamic characterization of metal dissolution and inhibitor adsorption processes in mild steel/2, 5-bis (n-thienyl)-1, 3, 4-thiadiazoles/hydrochloric acid system.* Corrosion science, 2005. **47**(12): p. 2915-2931.

451. Hegazy, M. and M. Zaky, *Inhibition effect of novel nonionic surfactants on the corrosion of carbon steel in acidic medium.* Corrosion science, 2010. **52**(4): p. 1333-1341.

452. Obot, I. and N. Obi-Egbedi, *An interesting and efficient green corrosion inhibitor for aluminium from extracts of Chlomolaena odorata L. in acidic solution.* Journal of Applied Electrochemistry, 2010. **40**(11): p. 1977-1984.

453. Popova, A., et al., *AC and DC study of the temperature effect on mild steel corrosion in acid media in the presence of benzimidazole derivatives.* Corrosion science, 2003. **45**(1): p. 33-58.

454. Masroor, S., et al., *The novel iminium surfactant p-benzylidene benzyldodecyl iminium chloride as a corrosion inhibitor for plain carbon steel in 1 M HCl: electrochemical and DFT evaluation.* RSC advances, 2017. **7**(37): p. 23182-23196.

455. Kumar, A.D., et al., *Design and Amberlyst-15 mediated synthesis of novel thienyl-pyrazole carboxamides that potently inhibit Phospholipase A2 by binding to an allosteric site on the enzyme.* Bioorganic Chemistry, 2018. **80**: p. 444-452.

456. Putilova, I.N., S.A.e. Balezin, and V.P. Barannik, *Metallic corrosion inhibitors*. 1960: Pergamon Press.

457. El-Anadouli, B., B. Ateya, and F. El-Nizamy, *The effect of temperature on the polarization resistance—I. Activation control.* Corrosion science, 1986. **26**(6): p. 419-424.

458. Ating, E., et al., *Leaves extract of Ananas sativum as green corrosion inhibitor for aluminium in hydrochloric acid solutions.* Green Chemistry Letters and Reviews, 2010. **3**(2): p. 61-68.

459. Lei, J., L. Li, and F. Pan, *Environmental friendly corrosion inhibitors for magnesium alloys.* Magnesium Alloys-Corrosion and Surface Treatments, 2011: p. 47-64.

460. Avci, G., *Corrosion inhibition of indole-3-acetic acid on mild steel in 0.5 M HCl.* Colloids and Surfaces A: Physicochemical and Engineering Aspects, 2008. **317**(1-3): p. 730-736.

461. Umoren, S., I. Obot, and E. Ebenso, *Corrosion inhibition of aluminium using exudate gum from Pachylobus edulis in the presence of halide ions in HCl.* E-journal of Chemistry, 2008. **5**(2): p. 355-364.

462. Oguzie, E., et al., *Effect of hexamethylpararosaniline chloride (crystal violet) on mild steel corrosion in acidic media.* Corrosion Science, 2008. **50**(12): p. 3480-3486.

463. Valcarce, M.B. and M. Vázquez, *Carbon steel passivity examined in solutions with a low degree of carbonation: The effect of chloride and nitrite ions.* Materials Chemistry and Physics, 2009. **115**(1): p. 313-321.

464. Zhao, T. and G. Mu, *The adsorption and corrosion inhibition of anion surfactants on aluminium surface in hydrochloric acid.* Corrosion Science, 1999. **41**(10): p. 1937-1944.

465. John, S. and A. Joseph, *Effective inhibition of mild steel corrosion in 1 M hydrochloric acid using substituted triazines: an experimental and theoretical study.* RSC advances, 2012. **2**(26): p. 9944-9951.

466. Noor, E.A., *Temperature effects on the corrosion inhibition of mild steel in acidic solutions by aqueous extract of fenugreek leaves.* International Journal of Electrochemical Science, 2007. **2**(12).

467. Osial, M. and D. Wiliński, *Organic substances as corrosion inhibitors for steel in concrete–an overview.* Journal of Building Chemistry, 2016. **1**(1): p. 43-53.

468. Milonjić, S.K., *A consideration of the correct calculation of thermodynamic parameters of adsorption.* Journal of the Serbian chemical society, 2007. **72**(12): p. 1363-1367.

469. Deng, S. and X. Li, *Inhibition by Jasminum nudiflorum Lindl. leaves extract of the corrosion of aluminium in HCl solution.* Corrosion Science, 2012. **64**: p. 253-262.

470. Raghavendra, N. and J.I. Bhat, *Inhibition of Al corrosion in 0.5 M HCl solution by Areca flower extract.* Journal of King Saud University-Engineering Sciences, 2019. **31**(3): p. 202-208.

471. Saeed, M.T., et al., *Corrosion inhibition of mild steel in 1 M HCl by sweet melon peel extract.* Journal of King Saud University-Science, 2019. **31**(4): p. 1344-1351.

472. Benarioua, M., et al., *Mild steel corrosion inhibition by Parsley (Petroselium Sativum) extract in acidic media.* Egyptian Journal of Petroleum, 2019. **28**(2): p. 155-159.

473. Oguzie, E., et al., *Evaluation of the inhibitory effect of methylene blue dye on the corrosion of aluminium in hydrochloric acid.* Materials Chemistry and Physics, 2004. **87**(2-3): p. 394-401.

474. Singh, A., et al., *Effect of electron donating functional groups on corrosion inhibition of J55 steel in a sweet corrosive environment: experimental, density functional theory, and molecular dynamic simulation.* Materials, 2018. **12**(1): p. 17.

475. Eduok, U.M. and M. Khaled, *Corrosion inhibition for low-carbon steel in 1 M H2SO4 solution by phenytoin: evaluation of the inhibition potency of another "anticorrosive drug".* Research on Chemical Intermediates, 2015. **41**(9): p. 6309-6324.

476. Iroha, N.B. and R.A. Ukpe, *Investigation of the Inhibition of the Corrosion of carbon steel in Solution of HCl by Glimepiride.* Communication in Physical Sciences, 2010. **5**(1, 2, 3).

477. Iroha, N.B. and N.A. Madueke, *Effect of Triumfetta rhomboidea leaves extract on the corrosion resistance of carbon steel in acidic environment.* Chemical Science International Journal, 2018. **25**(2): p. 1-9.

478. Dehghani, A., G. Bahlakeh, and B. Ramezanzadeh, *A detailed electrochemical/theoretical exploration of the aqueous Chinese gooseberry fruit shell extract as a green and cheap corrosion inhibitor for mild steel in acidic solution.* Journal of Molecular Liquids, 2019. **282**: p. 366-384.

479. Nnaji, N., et al., *Corrosion Resistance of Aluminum against Acid Activation: Impact of Benzothiazole-Substituted Gallium Phthalocyanine.* Molecules, 2019. **24**: p. 207.

480. Verma, P.K., et al., *The bend+ libration combination band is an intrinsic, collective, and strongly solute-dependent reporter on the hydrogen bonding network of liquid water.* The Journal of Physical Chemistry B, 2017. **122**(9): p. 2587-2599.

481. Maréchal, Y., *The molecular structure of liquid water delivered by absorption spectroscopy in the whole IR region completed with thermodynamics data.* Journal of Molecular Structure, 2011. **1004**(1-3): p. 146-155.

482. Sun, Q., *Local statistical interpretation for water structure.* Chemical Physics Letters, 2013. **568**: p. 90-94.

483. Eisenberg, D. and W. Kauzmann, *The structure and properties of water*. 2005: OUP Oxford.

484. Smith, B.C., *Alcohols—The Rest of the Story.* 2017.

485. Idir, B. and F. Kellou-Kerkouche, *Experimental and theoretical studies on corrosion inhibition performance of phenanthroline for cast iron in acid solution.* Journal of Electrochemical Science and Technology, 2018. **9**(4): p. 260-275.

486. Loto, R.T., et al. *Anti-corrosion properties of rosemary oil and vanillin on low carbon steel in dilute acid solutions*. in *TMS Annual Meeting & Exhibition*. 2018. Springer.

487. Smith, B.C., *IR Spectral Interpretation Workshop Alcohols The Rest of the Story.* Spectroscopy, 2017. **32**(4): p. 19-23.

488. Fouda, A.E.-A.E.-S., E.-S.G. Zaki, and M.A. Khalifa, *Evaluation of Some New Synthesized Surfactants Based on Maleic Acid as Inhibitors for Low Carbon Steel (LCS) Corrosion in 1.0 M HCl Solution.* Zeitschrift für Physikalische Chemie, 2020. **234**(2): p. 171-199.

489. Loto, R.T., *Study of the synergistic effect of 2-methoxy-4-formylphenol and sodium molybdenum oxide on the corrosion inhibition of 3CR12 ferritic steel in dilute sulphuric acid.* Results in physics, 2017. **7**: p. 769-776.

490. Wang, X., J. Xing, and Z. Huang, *Study on the Corrosion Inhibition Performance of a Schiff Base for Carbon Steel in 1 M HCl Solution.* INTERNATIONAL JOURNAL OF ELECTROCHEMICAL SCIENCE, 2021. **16**(9).

491. Kadhim, A., et al., *A mini review on corrosion, inhibitors and mechanism types of mild steel inhibition in an acidic environment.* International Journal of Corrosion and Scale Inhibition, 2021. **10**(3): p. 861-884.

492. Husaini, M., *Corrosion inhibition effect of benzaldehyde (Methoxybenzene) for Aluminium in sulphuric acid solution.* Algerian Journal of Engineering and Technology, 2021. **4**: p. 74-80.

493. Hassan, K.H., A.A. Khadom, and N.H. Kurshed, *Citrus aurantium leaves extracts as a sustainable corrosion inhibitor of mild steel in sulfuric acid.* south african journal of chemical engineering, 2016. **22**: p. 1-5.

494. Loto, R.T., *Electrochemical analysis of the corrosion inhibition properties of L-leucine and trypsin complex admixture on high carbon steel in 1 MH 2 SO 4 solution.* Revista Colombiana de Química, 2018. **47**(2): p. 12-20.

495. Loto, R.T., *Electrochemical analysis of the corrosion inhibition effect of trypsin complex on the pitting corrosion of 420 martensitic stainless steel in 2M H2SO4 solution.* Plos one, 2018. **13**(4): p. e0195870.

496. Kusumastuti, R., R.I. Pramana, and J.W. Soedarsono. *The use of morinda citrifolia as a green corrosion inhibitor for low carbon steel in 3.5% NaCl solution*. in *AIP Conference proceedings*. 2017. AIP Publishing LLC.

497. Renita, D., et al., *Green approach to corrosion inhibition by Emblica officinalis (NA-7) leaves extract.* International Journal of Nano Corrosion Science and Engineering, 2015. **2**(3): p. 29-45.

498. Raman, A., B. Kuban, and A. Razvan, *The application of infrared spectroscopy to the study of atmospheric rust systems—I. Standard spectra and illustrative applications to identify rust phases in natural atmospheric corrosion products.* Corrosion Science, 1991. **32**(12): p. 1295-1306.

499. Nasrazadani, S., *The application of infrared spectroscopy to a study of phosphoric and tannic acids interactions with magnetite (Fe3O4), goethite (α-FeOOH) and lepidocrocite (γ-FeOOH).* Corrosion Science, 1997. **39**(10-11): p. 1845-1859.

500. Potdar, H.S., et al., *Synthesis of nano-sized porous γ-alumina powder via a precipitation/digestion route.* Applied Catalysis A: General, 2007. **321**(2): p. 109-116.

501. Nail, S.L., J.L. White, and S.L. Hem, *IR studies of development of order in aluminum hydroxide gels.* Journal of Pharmaceutical Sciences, 1976. **65**(2): p. 231-234.

502. Majd, M.T., et al., *Production of an environmentally stable anti-corrosion film based on Esfand seed extract molecules-metal cations: Integrated experimental and computer modeling approaches.* Journal of hazardous materials, 2020. **382**: p. 121029.

503. Nematian, B., et al., *Adsorption of eco-friendly carthamus tinctorius on steel surface in saline solution: A combination of electrochemical and theoretical studies.* Colloids and Surfaces A: Physicochemical and Engineering Aspects, 2020. **601**: p. 125042.

504. Kesavan, D., M. Gopiraman, and N. Sulochana, *Green inhibitors for corrosion of metals: a review.* Chem. Sci. Rev. Lett, 2012. **1**(1): p. 1-8.

505. Alorabi, A.Q., M. Abdelbaset, and S.A. Zabin, *Colorimetric detection of multiple metal ions using schiff base 1-(2-thiophenylimino)-4-(N-dimethyl) benzene.* Chemosensors, 2019. **8**(1): p. 1.

506. Bahlakeh, G., et al., *Highly effective mild steel corrosion inhibition in 1 M HCl solution by novel green aqueous Mustard seed extract: Experimental, electronic-scale DFT and atomic-scale MC/MD explorations.* Journal of Molecular Liquids, 2019. **293**: p. 111559.

507. Bonardi, A.-H., et al., *Organometallic vs organic photoredox catalysts for photocuring reactions in the visible region.* Beilstein Journal of Organic Chemistry, 2018. **14**(1): p. 3025-3046.

508. Monticelli, C., *Corrosion inhibitors.* 2018.

509. Atta, A.M., et al., *A new green ionic liquid-based corrosion inhibitor for steel in acidic environments.* Molecules, 2015. **20**(6): p. 11131-11153.

510. Li, W., et al., *Electrochemical and computational studies of proline and captopril as corrosion inhibitors on carbon steel in a phase change material solution.* Int. J. Electrochem. Sci, 2020. **15**(1): p. 722-739.

511. Reddy, C.M., B.D. Sanketi, and S.N. Kumar, *Corrosion inhibition of mild steel by Capsicum annuum fruit paste.* Perspectives in Science, 2016. **8**: p. 603-605.

512. Li, Y., et al., *Exploration the inhibition mechanism of sodium dodecyl sulfate on Mg alloy.* Corrosion Science, 2020. **168**: p. 108559.

513. Dehghani, A., et al., *Estimating the synergistic corrosion inhibition potency of (2-(3, 4-)-3, 5, 7-trihydroxy-4H-chromen-4-one) and trivalent-cerium ions on mild steel in NaCl solution.* Construction and Building Materials, 2020. **261**: p. 119923.

514. Ralkhal, S., et al., *A combined electrochemical, molecular dynamics, quantum mechanics and XPS analysis of the mild steel surface protected by a complex film composed of neodymium (III) and benzimidazole.* Applied Surface Science, 2019. **464**: p. 178-194.

515. Olivier, D., et al., *Phenylethanoid glycosides from Lippia javanica.* South African Journal of Botany, 2010. **76**(1): p. 58-63.

516. Patle, T.K., et al., *Phytochemical screening and determination of phenolics and flavonoids in Dillenia pentagyna using UV–vis and FTIR spectroscopy.* Spectrochimica Acta Part A: Molecular and Biomolecular Spectroscopy, 2020. **242**: p. 118717.

517. Karpagasundari, C. and S. Kulothungan, *Analysis of bioactive compounds in Physalis minima leaves using GC MS, HPLC, UV-VIS and FTIR techniques.* Journal of Pharmacognosy and Phytochemistry, 2014. **3**(4): p. 196-201.

518. Jayaseelan, C., et al., *Toxicity studies of nanofabricated palladium against filariasis and malaria vectors.* Environmental Science and Pollution Research, 2018. **25**(1): p. 324-332.

519. Pantoja-Castro, M.A. and H. González-Rodríguez, *Study by infrared spectroscopy and thermogravimetric analysis of tannins and tannic acid.* Revista latinoamericana de química, 2011. **39**(3): p. 107-112.

520. Li, J., et al., *Silanized graphene oxide reinforced organofunctional silane composite coatings for corrosion protection.* Progress in Organic Coatings, 2016. **99**: p. 443-451.

521. Quintana, P., et al., *Study of the composition and morphology of initial stages of corrosion products formed on Zn plates exposed to the atmosphere of southeast Mexico.* Applied surface science, 1996. **99**(4): p. 325-334.

522. Mukhopadhyay, S., et al., *Corrosion Inhibition of Mild Steel by Aqueous Leaf Extract of Purple Hedge Plant: Experimental and Theoretical Investigation.* Journal of Bio-and Tribo-Corrosion, 2021. **7**(4): p. 1-20.

523. Olanrewaju, A., et al. *Corrosion Inhibition Study of Cratevaadansonii Plant Extract on Mild Steel in Acidic Media*. in *Journal of Physics: Conference Series*. 2019. IOP Publishing.

524. Barnartt, S., *Corrosion Kinetics of Iron in Acid Sulfate Solutions: Effects of Impurities in the Metal.* Journal of the Electrochemical Society, 1972. **119**(7): p. 812.

525. BARNARTT, S., *Tafel slopes for iron corrosion in acidic solutions.* Corrosion, 1971. **27**(11): p. 467-470.

526. Saratha, R., S. Priya, and P. Thilagavathy, *Investigation of Citrus aurantiifolia leaves extract as corrosion inhibitor for mild steel in 1 M HCl.* E-Journal of chemistry, 2009. **6**(3): p. 785-795.

527. Bentiss, F. and M. Traisnel, *N Chaibi, B Mernari, H Vezin, M Lagrenée.* Corros. Sci, 2002. **44**: p. 2271.

528. Bösing, I., J. Thöming, and M. Baune, *Electrolyte composition for distinguishing corrosion mechanisms in steel alloy screening.* International Journal of Corrosion, 2017. **2017**.

529. Yan, X. and J. Sun, *Effect of water hardness and pH value on the corrosion behavior of copper in an emulsion.* Int. J. Electrochem. Sci, 2017. **12**: p. 11580-11593.

530. Rehim, S.S.A., H.H. Hassan, and M.A. Amin, *Corrosion and corrosion inhibition of Al and some alloys in sulphate solutions containing halide ions investigated by an impedance technique.* Applied Surface Science, 2002. **187**(3-4): p. 279-290.

531. Amin, M.A., et al., *Pitting corrosion studies on Al and Al–Zn alloys in SCN− solutions.* Electrochimica Acta, 2009. **54**(18): p. 4288-4296.

532. Amin, M.A., *Metastable and stable pitting events on Al induced by chlorate and perchlorate anions—Polarization, XPS and SEM studies.* Electrochimica acta, 2009. **54**(6): p. 1857-1863.

533. Amin, M.A., S.S. Abd El Rehim, and A.S. El-Lithy, *Pitting and pitting control of Al in gluconic acid solutions–Polarization, chronoamperometry and morphological studies.* Corrosion Science, 2010. **52**(9): p. 3099-3108.

534. Amin, M.A., S.S. Abd El Rehim, and A.S. El-Lithy, *Corrosion, passivation and breakdown of passivity of Al and Al–Cu alloys in gluconic acid solutions.* Electrochimica acta, 2010. **55**(20): p. 5996-6003.

535. McCafferty, E., *Sequence of steps in the pitting of aluminum by chloride ions.* Corrosion science, 2003. **45**(7): p. 1421-1438.

536. Munoz, A. and J. Bessone, *Pitting of aluminium in non-aqueous chloride media.* Corrosion science, 1999. **41**(7): p. 1447-1463.

537. McCafferty, E., *The electrode kinetics of pit initiation on aluminum.* Corrosion Science, 1995. **37**(3): p. 481-492.

538. Tomcsanyi, L., et al., *Electrochemical study of the pitting corrosion of aluminium and its alloys—II. Study of the interaction of chloride ions with a passive film on aluminium and initiation of pitting corrosion.* Electrochimica acta, 1989. **34**(6): p. 855-859.

539. Atanasoska, L.D., et al., *Chloride ion penetration into oxide films on aluminum: Auger and XPS studies.* Journal of electroanalytical chemistry and interfacial electrochemistry, 1985. **182**(1): p. 179-186.

540. Heine, B. and R. Kirchheim, *Dissolution rates of iron and chromium and Fe・Cr・alloys in the passive state.* Corrosion science, 1990. **31**: p. 533-538.

541. Ashassi-Sorkhabi, H., B. Shaabani, and D. Seifzadeh, *Corrosion inhibition of mild steel by some Schiff base compounds in hydrochloric acid.* Applied Surface Science, 2005. **239**(2): p. 154-164.

542. Aslam, J., et al., *Inhibitory effect of 2-Nitroacridone on corrosion of low carbon steel in 1 M HCl solution: An experimental and theoretical approach.* Journal of Materials Research and Technology, 2020. **9**(3): p. 4061-4075.

543. Al-Sabagh, A., et al., *Scale and corrosion inhibition performance of the newly synthesized anionic surfactant in desalination plants: Experimental, and theoretical investigations.* Desalination, 2018. **437**: p. 45-58.

544. Payer, J., et al., *Economic effects of metallic corrosion in the United States. Appendix B. Part II. A report to NBS by Battelle Columbus Laboratories. Final report*. 1978, National Bureau of Standards, Washington, DC (USA).

545. Kaczerewska, O., et al., *Effectiveness of O-bridged cationic gemini surfactants as corrosion inhibitors for stainless steel in 3 M HCl: Experimental and theoretical studies.* Journal of Molecular Liquids, 2018. **249**: p. 1113-1124.

546. Prathibha, B., P. Kotteeswaran, and V.B. Raju, *Study on the inhibition of mild steel corrosion by cationic surfactant in HCl medium.* IOSR J Appl Chem, 2012. **2**: p. 45-53.

547. Wang, X., H. Yang, and F. Wang, *An investigation of benzimidazole derivative as corrosion inhibitor for mild steel in different concentration HCl solutions.* Corrosion science, 2011. **53**(1): p. 113-121.

548. Radwan, A.B., et al., *Corrosion inhibition of API X120 steel in a highly aggressive medium using stearamidopropyl dimethylamine.* Journal of Molecular Liquids, 2017. **236**: p. 220-231.

549. Usman, B.J., S.A. Umoren, and Z.M. Gasem, *Inhibition of API 5L X60 steel corrosion in CO2-saturated 3.5% NaCl solution by tannic acid and synergistic effect of KI additive.* Journal of Molecular Liquids, 2017. **237**: p. 146-156.

550. Abd El Rehim, S.S., H.H. Hassan, and M.A. Amin, *Corrosion inhibition of aluminum by 1, 1 (lauryl amido) propyl ammonium chloride in HCl solution.* Materials chemistry and physics, 2001. **70**(1): p. 64-72.

551. Frers, S., et al., *AC-Impedance measurements on aluminium in chloride containing solutions and below the pitting potential.* Journal of Applied Electrochemistry, 1990. **20**(6): p. 996-999.

552. Mansfeld, F., et al., *Electrochemical impedance spectroscopy as a monitoring tool for passivation and localized corrosion of aluminum alloys.* Materials and Corrosion, 1988. **39**(11): p. 487-492.

553. Bessone, J., et al., *AC-impedance measurements on aluminium barrier type oxide films.* Electrochimica Acta, 1983. **28**(2): p. 171-175.

554. Langmuir, I., *The constitution and fundamental properties of solids and liquids. II. Liquids.* Journal of the American chemical society, 1917. **39**(9): p. 1848-1906.

555. Nesane, T., S.S. Mnyakeni-Moleele, and L.C. Murulana, *Exploration of synthesized quaternary ammonium ionic liquids as unharmful anti-corrosives for aluminium utilizing hydrochloric acid medium.* Heliyon, 2020. **6**(6): p. e04113.

556. Mazkour, A., et al., *Investigation of Corrosion Protection of Austenitic Stainless Steel in 5.5 M Polluted Phosphoric Acid Using 5-Azidomethyl-7-morpholinomethyl-8-hydroxyquinoline as an Ecofriendly Inhibitor*. International Journal of Corrosion, 2021. **2021**.

557. Wang, H., et al. *Characterization of inhibitor and corrosion product film using electrochemical impedance spectroscopy (EIS)*. in *CORROSION 2001*. 2001. OnePetro.

558. Kwolek, P., *Corrosion behaviour of 7075 aluminium alloy in acidic solution.* RSC advances, 2020. **10**(44): p. 26078-26089.

559. Mikhail, S., et al., *Comprehensive Study of the Action of Corrosion Inhibitors Based on Quaternary Ammonium Compounds in Solutions of Hydrochloric and Sulfamic Acids.* Energies, 2021. **15**(1): p. 1-18.

560. Obot, I., et al., *Progress in the development of sour corrosion inhibitors: Past, present, and future perspectives.* Journal of Industrial and Engineering Chemistry, 2019. **79**: p. 1-18.

561. Alamiery, A., *Corrosion inhibition effect of 2-N-phenylamino-5-(3-phenyl-3-oxo-1-propyl)-1, 3, 4-oxadiazole on mild steel in 1 M hydrochloric acid medium: Insight from gravimetric and DFT investigations.* Materials Science for Energy Technologies, 2021. **4**: p. 398-406.

562. Sharma, A., et al., *Effect of temperature on inhibitory efficacy of Azadirachta indica fruit on acid corrosion of aluminum.* International Journal of Innovative Research in Science Engineering and Technology, 2013. **2**(12): p. 7982-7992.

563. Popova, A., *Temperature effect on mild steel corrosion in acid media in presence of azoles.* Corrosion Science, 2007. **49**(5): p. 2144-2158.

564. Ibrahim, S., et al., *Effect of 3-Nitroacetophenone on Corrosion Inhibition of Mild Steel in Acidic Medium.* International Journal of Photoenergy. **2022**.

565. Li, W., et al., *Investigation on inhibition behavior of S-triazole–triazole derivatives in acidic solution.* Corrosion science, 2008. **50**(11): p. 3261-3266.

566. Prabhu, R., A. Shanbhag, and T. Venkatesha, *Influence of tramadol [2-[(dimethylamino) methyl]-1-(3-methoxyphenyl) cyclohexanol hydrate] on corrosion inhibition of mild steel in acidic media.* Journal of Applied Electrochemistry, 2007. **37**(4): p. 491-497.

567. Martinez, S. and I. Štern, *Inhibitory mechanism of low-carbon steel corrosion by mimosa tannin in sulphuric acid solutions.* Journal of Applied Electrochemistry, 2001. **31**(9): p. 973-978.

568. Ikeuba, A., et al., *Alkaloid and non-alkaloid ethanolic extracts from seeds of Garcinia kola as green corrosion inhibitors of mild steel in H2SO4 solution.* International Journal of Electrochemical Science, 2013. **8**(5): p. 7455-7467.

569. Thirumoolan, D., et al., *Hyperbranched poly (cyanurateamine): a new corrosion inhibitor for mild steel in hydrochloric acid medium.* Progress in Organic Coatings, 2014. **77**(8): p. 1253-1263.

570. Donahue, F.M. and K. Nobe, *Theory of organic corrosion inhibitors: adsorption and linear free energy relationships.* Journal of the Electrochemical Society, 1965. **112**(9): p. 886.

571. Zhang, Q. and Y. Hua, *Corrosion inhibition of mild steel by alkylimidazolium ionic liquids in hydrochloric acid.* Electrochimica Acta, 2009. **54**(6): p. 1881-1887.

572. Abd El Rehim, S.S., H.H. Hassan, and M.A. Amin, *The corrosion inhibition study of sodium dodecyl benzene sulphonate to aluminium and its alloys in 1.0 M HCl solution.* Materials Chemistry and Physics, 2003. **78**(2): p. 337-348.

573. Quraishi, M., et al., *Green approach to corrosion inhibition of mild steel in hydrochloric acid and sulphuric acid solutions by the extract of Murraya koenigii leaves.* Materials chemistry and Physics, 2010. **122**(1): p. 114-122.

574. Boparai, H.K., M. Joseph, and D.M. O'Carroll, *Kinetics and thermodynamics of cadmium ion removal by adsorption onto nano zerovalent iron particles.* Journal of hazardous materials, 2011. **186**(1): p. 458-465.

575. Vračar, L.M. and D.M. Dražić, *Adsorption and corrosion inhibitive properties of some organic molecules on iron electrode in sulfuric acid.* Corrosion Science, 2002. **44**(8): p. 1669-1680.

576. Abboud, Y., et al., *Corrosion inhibition of carbon steel in hydrochloric acid solution using pomegranate leave extracts.* Corrosion Engineering, Science and Technology, 2016. **51**(8): p. 557-565.

577. Husaini, M., B. Usman, and M.B. Ibrahim, *Study of corrosion inhibition of Aluminum in nitric acid solution using Anisaldehyde (4-methoxy benzaldehyde) as corrosion inhibitor.* Algerian Journal of Engineering and Technology, 2019. **1**: p. 11-18.

578. Singh, A.K., E.E. Ebenso, and M. Quraishi, *Adsorption behaviour of cefapirin on mild steel in hydrochloric acid solution.* Int. J. Electrochem. Sci, 2012. **7**: p. 2320-2333.

579. Umoren, S., et al., *Gum arabic as a potential corrosion inhibitor for aluminium in alkaline medium and its adsorption characteristics.* Anti-corrosion methods and materials, 2006.

580. Mall, I.D., et al., *Removal of congo red from aqueous solution by bagasse fly ash and activated carbon: kinetic study and equilibrium isotherm analyses.* Chemosphere, 2005. **61**(4): p. 492-501.

581. Langmuir, I., *The constitution and fundamental properties of solids and liquids. Part I. Solids.* Journal of the American chemical society, 1916. **38**(11): p. 2221-2295.

582. Raja, P.B., et al., *Evaluation of green corrosion inhibition by alkaloid extracts of Ochrosia oppositifolia and isoreserpiline against mild steel in 1 M HCl medium.* Industrial & Engineering Chemistry Research, 2013. **52**(31): p. 10582-10593.

583. Langmuir, I., *The adsorption of gases on plane surfaces of glass, mica and platinum.* Journal of the American Chemical society, 1918. **40**(9): p. 1361-1403.

584. Villamil, R.F., et al., *Effect of sodium dodecylsulfate on copper corrosion in sulfuric acid media in the absence and presence of benzotriazole.* Journal of Electroanalytical chemistry, 1999. **472**(2): p. 112-119.

585. Lagrenee, M., et al., *Study of the mechanism and inhibiting efficiency of 3, 5-bis (4-methylthiophenyl)-4H-1, 2, 4-triazole on mild steel corrosion in acidic media.* Corrosion Science, 2002. **44**(3): p. 573-588.

586. Umoren, S., et al., *Coconut coir dust extract: a novel eco-friendly corrosion inhibitor for Al in HCl solutions.* Green chemistry letters and Reviews, 2012. **5**(3): p. 303-313.

587. Marhamati, F., M. Mahdavian, and S. Bazgir, *Corrosion mitigation of mild steel in hydrochloric acid solution using grape seed extract.* Scientific reports, 2021. **11**(1): p. 1-16.

588. Elavarasan, S. and M. Gopalakrishnan, *Synthesis, structural analysis, theoretical studies of some lawsone derivatives.* Spectrochimica Acta Part A: Molecular and Biomolecular Spectroscopy, 2014. **133**: p. 1-6.

589. Singh, D.K., S. Luqman, and A.K. Mathur, *Lawsonia inermis L.–A commercially important primaeval dying and medicinal plant with diverse pharmacological activity: A review.* Industrial Crops and Products, 2015. **65**: p. 269-286.

590. Guruprasad, A., et al., *Corrosion inhibition of zinc in 0.1 M hydrochloric acid medium with clotrimazole: Experimental, theoretical and quantum studies.* Surfaces and Interfaces, 2020. **19**: p. 100478.

591. Haddadi, S.A., et al., *Detailed experimental investigation of the highly active corrosion inhibitive green molecules based on zinc cations/Nepeta Pogonosperma extract and toward the corrosion mitigation of mild steel in the saline solution.* Colloids and Surfaces A: Physicochemical and Engineering Aspects, 2022. **642**: p. 128613.

592. Kim, J.-Y., I. Shin, and J.-W. Byeon, *Corrosion Inhibition of Mild Steel and 304 Stainless Steel in 1 M Hydrochloric Acid Solution by Tea Tree Extract and Its Main Constituents.* Materials, 2021. **14**(17): p. 5016.

593. Hadisaputra, S., et al. *Theoretical study on the corrosion inhibition performance of dibenzo-18-crown-6 and its derivatives*. in *IOP Conference Series: Materials Science and Engineering*. 2019. IOP Publishing.

594. Bhawani, S.A., T.S. Sen, and M.N.M. Ibrahim, *Synthesis of molecular imprinting polymers for extraction of gallic acid from urine.* Chemistry Central Journal, 2018. **12**(1): p. 1-7.

595. Abbout, S., et al., *Gravimetric, electrochemical and theoretical study, and surface analysis of novel epoxy resin as corrosion inhibitor of carbon steel in 0.5 M H2SO4 solution.* Journal of Molecular Structure, 2021. **1245**: p. 131014.

596. Abbout, S., et al., *Ceratonia Siliqua L seeds extract as eco-friendly corrosion inhibitor for carbon steel in 1 M HCl: Characterization, electrochemical, surface analysis, and theoretical studies.* Journal of Molecular Structure, 2021. **1240**: p. 130611.

597. Deyab, M., et al., *Mitigation of acid corrosion on carbon steel by novel pyrazolone derivatives.* RSC advances, 2017. **7**(71): p. 45232-45240.

598. Gudić, S., I. Smoljko, and M. Kliškić, *The effect of small addition of tin and indium on the corrosion behavior of aluminium in chloride solution.* Journal of alloys and compounds, 2010. **505**(1): p. 54-63.

599. Al Otaibi, N. and H.H. Hammud, *Corrosion Inhibition Using Harmal Leaf Extract as an Eco-Friendly Corrosion Inhibitor.* Molecules, 2021. **26**(22): p. 7024.

600. Ji, G., et al., *Musa paradisica peel extract as green corrosion inhibitor for mild steel in HCl solution.* Corrosion Science, 2015. **90**: p. 107-117.

601. Ngobiri, N., et al., *Eco-friendly corrosion inhibition of pipeline steel using Brassica oleracea.* International Journal of Corrosion, 2015. **2015**.

602. El Hamdani, N., et al., *Alkaloids extract of Retama monosperma (L.) Boiss. seeds used as novel eco-friendly inhibitor for carbon steel corrosion in 1 M HCl solution: Electrochemical and surface studies.* Applied Surface Science, 2015. **357**: p. 1294-1305.

603. RameshKumar, S., et al., *Quantum chemical and experimental investigations on equipotent effects of (+) R and (−) S enantiomers of racemic amisulpride as eco-friendly corrosion inhibitors for mild steel in acidic solution.* Journal of Molecular Liquids, 2015. **212**: p. 168-186.

604. Ghasemi, O., et al., *Inhibition effect of a synthesized N, N′-bis (2-hydroxybenzaldehyde)-1, 3-propandiimine on corrosion of mild steel in HCl.* Journal of Central South University, 2013. **20**(2): p. 301-311.

605. Fouda, A., G. El-Ewady, and A. Ali, *Modazar as promising corrosion inhibitor of carbon steel in hydrochloric acid solution.* Green chemistry letters and reviews, 2017. **10**(2): p. 88-100.

606. Lorenz, W. and F. Mansfeld, *Determination of corrosion rates by electrochemical DC and AC methods.* Corrosion Science, 1981. **21**(9-10): p. 647-672.

607. Murthy, H.A., *Electroanalytical study on the corrosion behaviour of TiO2 particulate reinforced Al 6061 composites.* Material Science Research India, 2015. **12**(2): p. 112-126.

608. Charitha, B. and P. Rao, *Carbohydrate biopolymer for corrosion control of 6061 Al-alloy and 6061Aluminum-15%(v) SiC (P) composite—Green approach.* Carbohydrate polymers, 2017. **168**: p. 337-345.

609. Charitha, B. and P. Rao, *Pullulan as a potent green inhibitor for corrosion mitigation of aluminum composite: electrochemical and surface studies.* International journal of biological macromolecules, 2018. **112**: p. 461-472.

610. Shetty, D., et al., *Anticorrosion behaviour of a hydrazide derivative on 6061 Al-15%(v) SiC (P) composite in acid medium: experimental and theoretical calculations.* Journal of Bio-and Tribo-Corrosion, 2020. **6**(2): p. 1-15.

611. Pourbaix, M., *Atlas of electrochemical equilibria in aqueous solution.* NACE, 1974. **307**.

612. Butler, J.A.V., *Studies in heterogeneous equilibria. Part II.—The kinetic interpretation of the nernst theory of electromotive force.* Transactions of the Faraday Society, 1924. **19**(March): p. 729-733.

613. Chauhan, D.S., et al., *Thiosemicarbazide and thiocarbohydrazide functionalized chitosan as ecofriendly corrosion inhibitors for carbon steel in hydrochloric acid solution.* International journal of biological macromolecules, 2018. **107**: p. 1747-1757.

614. Elgyar, O.A., et al., *The inhibition action of viscum album extract on the corrosion of carbon steel in hydrochloric acid solution.* Biointerface Res. Appl. Chem, 2021. **11**(6): p. 14344.

615. Mohd, N.K., et al., *Corrosion inhibition, adsorption behaviour and thermodynamic properties of n-cinnamalidene palmitohydrazide on mild steel in hydrochloric acid solution.* J. Oil Palm Res, 2020. **32**: p. 124-138.

616. Verma, C., et al., *Corrosion inhibition of mild steel in 1M HCl by D-glucose derivatives of dihydropyrido [2, 3-d: 6, 5-d'] dipyrimidine-2, 4, 6, 8 (1H, 3H, 5H, 7H)-tetraone.* Scientific Reports, 2017. **7**(1): p. 1-17.

617. Chauhan, D.S., et al., *Triazole-modified chitosan: a biomacromolecule as a new environmentally benign corrosion inhibitor for carbon steel in a hydrochloric acid solution.* RSC advances, 2019. **9**(26): p. 14990-15003.

618. Quraishi, M., et al., *Vanillin modified chitosan as a new bio-inspired corrosion inhibitor for carbon steel in oil-well acidizing relevant to petroleum industry.* Cellulose, 2020. **27**(11): p. 6425-6443.

619. Chetouani, A., et al., *New synthesised pyridazine derivatives as effective inhibitors for the corrosion of pure iron in HCl medium.* Progress in Organic Coatings, 2002. **45**(4): p. 373-378.

620. Oguzie, E., *Portugaliae Electrochim.* Acta, 2008. **26**: p. 303.

621. Singh, P., et al., *Electrochemical, theoretical, and surface morphological studies of corrosion inhibition effect of green naphthyridine derivatives on mild steel in hydrochloric acid.* The Journal of Physical Chemistry C, 2016. **120**(6): p. 3408-3419.

622. Ghazi, I., et al., *Corrosion Inhibition of Carob Pod Pulp (Ceratonia siliqua L.) on Carbon Steel Surface C38 in Hydrochloric Acid.* Journal of Bio-and Tribo-corrosion, 2022. **8**(1): p. 1-23.

623. Chen, Y., Z. Chen, and Y. Zhuo, *Newly Synthesized Morpholinyl Mannich Bases as Corrosion Inhibitors for N80 Steel in Acid Environment.* Materials, 2022. **15**(12): p. 4218.
624. Badr, G., A. Ali, and A. Fouda, *The Efficiency of Ecballium Elaterium Extract as Green Inhibitor for Carbon Steel Corrosion in Sulfuric Acid.* INTERNATIONAL JOURNAL OF ELECTROCHEMICAL SCIENCE, 2021. **16**(8).
625. RIGGS JR, O.L. and R.M. Hurd, *Temperature coefficient of corrosion inhibition.* Corrosion, 1967. **23**(8): p. 252-260.
626. Go, L.C., et al., *Kinetic and thermodynamic analyses of the corrosion inhibition of synthetic extracellular polymeric substances.* PeerJ Materials Science, 2020. **2**: p. e4.
627. Amin, M.A., et al., *Monitoring corrosion and corrosion control of iron in HCl by non-ionic surfactants of the TRITON-X series–Part II. Temperature effect, activation energies and thermodynamics of adsorption.* Corrosion science, 2011. **53**(2): p. 540-548.
628. Aiad, I., et al., *Cationic surfactant based on alignate as green corrosion inhibitors for the mild steel in 1.0 M HCl.* Egyptian journal of petroleum, 2018. **27**(4): p. 877-885.
629. Singh, A., S. Mohapatra, and B. Pani, *Corrosion inhibition effect of Aloe Vera gel: gravimetric and electrochemical study.* Journal of Industrial and Engineering Chemistry, 2016. **33**: p. 288-297.
630. Ramesh Saliyan, V. and A.V. Adhikari, *Inhibition of corrosion of mild steel in acid media by N'-benzylidene-3-(quinolin-4-ylthio) propanohydrazide.* Bulletin of Materials Science, 2008. **31**(4): p. 699-711.
631. Hosseini, M., S.F. Mertens, and M.R. Arshadi, *Synergism and antagonism in mild steel corrosion inhibition by sodium dodecylbenzenesulphonate and hexamethylenetetramine.* Corrosion Science, 2003. **45**(7): p. 1473-1489.
632. Rudresh, H. and S. Mayanna, *Adsorption of n-Decylamine on Zinc from Acidic Chloride Solution.* Journal of The Electrochemical Society, 1977. **124**(3): p. 340.
633. Yüce, A.O., R. Solmaz, and G. Kardaş, *Investigation of inhibition effect of rhodanine-N-acetic acid on mild steel corrosion in HCl solution.* Materials Chemistry and Physics, 2012. **131**(3): p. 615-620.
634. Mathew, Z.P., et al., *Corrosion inhibition of mild steel using poly (2-ethyl-2-oxazoline) in 0.1 M HCl solution.* Heliyon, 2020. **6**(11): p. e05560.

635. Singh, P., A.K. Singh, and V.P. Singh, *Synthesis, structural and corrosion inhibition properties of some transition metal (II) complexes with o-hydroxyacetophenone-2-thiophenoyl hydrazone.* Polyhedron, 2013. **65**: p. 73-81.

636. Jafari, H., et al., *Electrochemical and theoretical studies of adsorption and corrosion inhibition of N, N'-bis (2-hydroxyethoxyacetophenone)-2, 2-dimethyl-1, 2-propanediimine on low carbon steel (API 5L Grade B) in acidic solution.* Industrial & Engineering Chemistry Research, 2013. **52**(20): p. 6617-6632.

637. Yadav, M., et al., *Experimental and theoretical studies on corrosion inhibition effect of synthesized benzothiazole derivatives on mild steel in 15% HCl solution.* Int. J. Electrochem. Sci, 2015. **10**: p. 602-624.

638. Mahdi, S.M., *Study the pomegranate's peel powder as a Natural Inhibitor for Mild steel corrosion.* International Journal of Materials Chemistry and Physics, 2015. **1**(1): p. 74-81.

639. Torres-Knoop, A., et al., *Behavior of the enthalpy of adsorption in nanoporous materials close to saturation conditions.* Journal of chemical theory and computation, 2017. **13**(7): p. 3326-3339.

640. Liu, Y., et al., *Study of adsorption of hydrogen on Al, Cu, Mg, Ti surfaces in Al alloy melt via first principles calculation.* Metals, 2017. **7**(1): p. 21.

641. Xu, L., et al., *Atomic and molecular adsorption on Fe (110).* Surface Science, 2018. **667**: p. 54-65.

642. Jenkins, S.J. and S.J. Pratt, *Beyond the surface atlas: A roadmap and gazetteer for surface symmetry and structure.* Surface science reports, 2007. **62**(10): p. 373-429.

643. Rahmanzadeh, A., M. Rezvani, and M.D. Ganji, *Understanding the interaction properties of an eco-friendly corrosion inhibitor on Zn (1 1 0) surface: Comprehensive DFT-based MD simulation.* 2021.

644. Chen, Z. and S. Li, *Molecular Dynamics Simulation of Adsorption Behavior of Schiff base Gemini Surfactants on Zn (1 1 0) Surface.* Int. J. Electrochem. Sci, 2017. **12**: p. 6622-6637.

645. Maroyi, A., *Lippia javanica (Burm. F.) Spreng.: traditional and commercial uses and phytochemical and pharmacological significance in the african and indian subcontinent.* Evidence-based complementary and alternative medicine, 2017. **2017**.

646. Guo, L., et al., *Theoretical evaluation of the corrosion inhibition performance of 1, 3-thiazole and its amino derivatives.* Arabian Journal of Chemistry, 2017. **10**(1): p. 121-130.

647. Rocca, M., T. Rahman, and L. Vattuone, *Springer Handbook of Surface Science*. 2020: Springer.

648. Goto, T., et al., *Effect of polarity of activated carbon surface, solvent and adsorbate on adsorption of aromatic compounds from liquid phase.* Chemical and Pharmaceutical Bulletin, 2015. **63**(9): p. 726-730.

649. Bartley, J., et al., *Computer simulation of the corrosion inhibition of copper in acidic solution by alkyl esters of 5-carboxybenzotriazole.* Corrosion Science, 2003. **45**(1): p. 81-96.

650. Guo, L., et al., *Comparative theoretical study on the corrosion inhibition properties of benzoxazole and benzothiazole.* Research on Chemical Intermediates, 2015. **41**(6): p. 3729-3742.

651. Verma, C., et al., *Molecular dynamics and Monte Carlo simulations as powerful tools for study of interfacial adsorption behavior of corrosion inhibitors in aqueous phase: a review.* Journal of Molecular Liquids, 2018. **260**: p. 99-120.

652. Cen, H., et al., *Carbon dots as effective corrosion inhibitor for 5052 aluminium alloy in 0.1 M HCl solution.* Corrosion Science, 2019. **161**: p. 108197.

653. Li, S., et al., *Investigation on some Schiff bases as HCl corrosioninhibitors for copper.* Corrosion Science, 1999. **41**(7): p. 1273-1287.

654. Punitha, R., et al., *Synthesis and corrosion inhibition studies of modified polyacrylic acid bearing triazole moieties on aluminium in alkaline medium.* Journal of Polymer Research, 2019. **26**(12): p. 1-12.

655. Li, X., S. Deng, and X. Xie, *Experimental and theoretical study on corrosion inhibition of oxime compounds for aluminium in HCl solution.* Corrosion Science, 2014. **81**: p. 162-175.

656. Abdallah, M., M. Sobhi, and H. Altass, *Corrosion inhibition of aluminum in hydrochloric acid by pyrazinamide derivatives.* Journal of Molecular Liquids, 2016. **223**: p. 1143-1150.

657. Liu, J., et al., *Synergism between cerium nitrate and sodium dodecylbenzenesulfonate on corrosion of AA5052 aluminium alloy in 3 wt.% NaCl solution.* Applied Surface Science, 2016. **389**: p. 369-377.

658. Nnaji, N.J., et al., *Morpholine and piperazine based carboxamide derivatives as corrosion inhibitors of mild steel in HCl medium.* Journal of Molecular Liquids, 2017. **230**: p. 652-661.

659. Shahini, M., et al., *Superior inhibition action of the Mish Gush (MG) leaves extract toward mild steel corrosion in HCl solution: Theoretical and electrochemical studies.* Journal of Molecular Liquids, 2021. **332**: p. 115876.

660. Olivares-Xometl, O., et al., *Synthesis and corrosion inhibition of α-amino acids alkylamides for mild steel in acidic environment.* Materials Chemistry and Physics, 2008. **110**(2-3): p. 344-351.

661. Pais, M. and P. Rao, *Biomolecules for corrosion mitigation of zinc: a short review.* Journal of Bio-and Tribo-Corrosion, 2019. **5**(4): p. 1-11.

662. Yadav, M., et al., *Corrosion inhibition performance of pyranopyrazole derivatives for mild steel in HCl solution: Gravimetric, electrochemical and DFT studies.* Journal of Molecular Liquids, 2016. **216**: p. 78-86.